Curvature Field Formulation of Gravity: Toward a Physical Reconstruction of Spacetime

Kim Seung-il
Independent Researcher, Republic of Korea
(seungilkim851@gmail.com)

October 2025

Abstract

We begin from a simple idea: *gravity is a curvature field* Φ with dimension $[\mathrm{L}^2/\mathrm{T}^2]$. Its gradient $-\nabla\Phi$ is the observable gravitational acceleration, and extended mass is represented with a small set of smooth functions to avoid point singularities. The underlying *equation of motion*, which we call the **Phi–Curvature Field Equation (PCFE)**,

$$\Box\Phi - U'(\Phi) = J$$

reduces to the Newton–Poisson limit in the weak field (Section 2, Appendix C), while static solutions are implemented via the *MC–CF* representation. Starting from the curvature–field hypothesis first proposed at the quantum scale—*Introducing the Curvature Field Function: Toward a Geometric Formulation of Wavefunction Collapse* [15]—we test, with *empirical* data, whether the same concept can extend continuously to macroscopic gravity. One fixed policy (masks, windows, covariances) is applied across all domains (Section 12.3, Appendix H), and galaxy rotation curves (SPARC), black–hole rings (EHT), Solar–System PPN, and cosmology (CMB/BAO) are read through standardized invariants and shared weighting rules (Section 7). Cohort–wise, C4 aligns consistently with data; in the strong–field regime $(R_{\mathrm{std}}, \Theta_{\mathrm{std}})$ intersect the GR–recovery baseline in a compatible manner; Solar–System and cosmology snap–ins remain within policy limits. In a *separate* exploratory track (policy unchanged), we also show that a mild adjustment of the global taper noticeably restores outer–window agreement. Across all domains, hyperparameters are set *a priori* per dataset, and residuals are reported with uncertainties. In this way a single field links weak and strong gravity without overreach, and conclusions are built step by step through transparent comparisons and reproducible calculations. Our aim is *not* to argue for the **superiority** of C4. Rather, C4 is an *economical implementation* derived from that curvature–field hypothesis; we highlight its function to test, with data, the *plausible existence* of the curvature field itself. In other words, we ask whether the curvature–field hypothesis alone can replace or complement the standard framework and still explain a wide swath of observations. Our expectation is therefore not to outscore competing theories wholesale, but to achieve *parity* comparable to the high empirical agreement previously reported in the quantum–scale curvature–field study [15], while capturing those fine details that standard approaches still leave under–explained. This procedural economy suggests that a single curvature field can organize observables across scales in a common language—linear response in the weak field, (R, Θ) in the strong field—and that this continuity may extend to electromagnetic phenomena under the same geometric grammar.

Finally, the curvature–field perspective, shaped here for macroscopic gravity, points naturally to an electromagnetic extension; the sequel *"Curvature Electromagnetism: Deriving Maxwell from Geometry"* will carry the story forward.

1 Introduction

Newton's inverse–square law [1] and Einstein's curvature of spacetime [2] have long provided two powerful languages for gravity. Yet point singularities, the layering of poorly constrained dark–sector hypotheses, and the conceptual gap between quantum and macroscopic regimes persist. We take a different tack: we posit a *physically real curvature field* $\Phi(\mathbf{r}, t)$ (dimension $[\mathrm{L}^2/\mathrm{T}^2]$) that encodes spatial structure directly, with motion mediated by its gradient,

$$\mathbf{g}(\mathbf{r}) \;=\; -\nabla\Phi(\mathbf{r}).$$

Differential operators (global). We adopt metric signature $(-,+,+,+)$ and, unless stated otherwise, set $c = 1$ in analytic developments (restoring c where needed). Spatial derivatives in Euclidean $\mathbb{R}^3$ are

$$\nabla\Phi = (\partial_x\Phi, \partial_y\Phi, \partial_z\Phi), \qquad \nabla^2\Phi = \partial_x^2\Phi + \partial_y^2\Phi + \partial_z^2\Phi.$$

For a scalar field on a curved background the covariant wave operator (d'Alembertian) is

$$\Box\Phi \;\equiv\; \nabla_\mu\nabla^\mu\Phi = \frac{1}{\sqrt{|g|}}\,\partial_\mu\Big(\sqrt{|g|}\,g^{\mu\nu}\partial_\nu\Phi\Big).$$

In the flat limit this reduces to $\Box\Phi = -\partial_t^2\Phi + \nabla^2\Phi$, and in the static weak–field limit one recovers the Poisson law $\nabla^2\Phi = 4\pi G\rho$. *Notation:* overdots denote ∂_t (e.g. $\dot\Phi$); primes denote ordinary derivatives ($U'(\Phi) = dU/d\Phi$, $A'(r) = dA/dr$).

Units and dimensions (global). All numerical tables remain in SI units (we do not set $G = 1$ by default). Square brackets $[\cdot]$ denote physical dimensions:

$$[\Phi] = L^2T^{-2}, \quad [\mathbf{g}] = LT^{-2}, \quad [D] = L^2T^{-1}, \quad [\gamma] = T^3L^{-4}, \quad [U] = 1, \quad [A] = [C] = 1.$$

When the exterior–drive term $\mu\, w(\Phi_{\mathrm{out}} - \Phi)$ is used, $[w] = 1$ and $[\mu] = T^{-1}$. Noise normalization for $\sigma\,\xi$ follows the colored–kernel convention specified in the numerics appendix.

We refer to the corresponding equation of motion as the *Phi–Curvature Field Equation* (PCFE). In a relativistic setting one may write, schematically,

$$\Box\Phi \;-\; U'(\Phi) \;=\; J, \tag{1}$$

where U is a potential and J an effective source. In the static weak–field limit this reduces to the Newton–Poisson form

$$\nabla^2\Phi \;=\; 4\pi G\,\rho, \qquad \mathbf{g} = -\nabla\Phi, \tag{2}$$

which anchors Φ to familiar phenomenology while keeping the field smooth in matter–dominated regions. A formal derivation and admissible sectors of the PCFE are presented in Section 2 and Appendix C. A companion quantum–scale treatment appears in *Introducing the Curvature Field Function: Toward a Geometric Formulation of Wavefunction Collapse* [15].

A minimal starting shape (unit–consistent). For intuition and a clean analytic baseline, we use an elementary well with explicit amplitude and length scales:

$$\boxed{\Phi_0(\mathbf{r}) = -A_0 \, \exp\!\big[-(r/\ell)^2\big]}, \qquad r^2 = x^2 + y^2 + z^2,$$

where A_0 carries the physical units of Φ and ℓ is a characteristic length. In practice we introduce depth, widths, and position,

$$\Phi(\mathbf{r}) \;=\; -A \, \exp\!\Big[-\tfrac{(x-x_0)^2}{2\sigma_x^2} - \tfrac{(y-y_0)^2}{2\sigma_y^2} - \tfrac{(z-z_0)^2}{2\sigma_z^2}\Big],$$

where A is the field amplitude and $(\sigma_x, \sigma_y, \sigma_z)$ its spreads. This profile avoids point singularities and serves as a convenient building block for data–constrained models.

Practical representation for extended sources. Rather than introducing a new static equation, we treat realistic mass distributions with a *mass–centered curvature field* representation (MC–CF; see Appendix C): a small mixture of anisotropic Gaussians centered on mass concentrations,

$$\Phi(\mathbf{r}) \;=\; -\sum_{i=1}^{N} A_i \, \exp\!\left[-\frac{(x-x_i)^2}{2\sigma_{x,i}^2} - \frac{(y-y_i)^2}{2\sigma_{y,i}^2} - \frac{(z-z_i)^2}{2\sigma_{z,i}^2}\right],$$

with $\mathbf{g} = -\nabla\Phi$. This is a *solution ansatz consistent with* the PCFE's static limit, not a different theory: it preserves smoothness, improves parameter identifiability, and applies uniformly to terrestrial anomalies, SPARC rotation curves (Section 5.2; [8, 14]), and lensing maps under a single transparent fitting procedure.

Exterior matching refinement (principled, no new dof). To address the outer-tail undershoot of scaffolded solutions without increasing model complexity, we replace the legacy constant-tail mixing with a *variational taper* that penalizes deviations from the analytic exterior solution (e.g., $-GM/r$ or the GR exterior) beyond a fixed transition radius. The radius $r_t = \sqrt{\sigma_1\sigma_2} \approx 1.06\, r_0$ is inherited from the globally fixed bandwidths, so no additional free parameters are introduced; the procedure acts as a principled regularizer. Empirically, the windowed outer-tail RMSE decreases by roughly an order of magnitude, while core-region metrics and model-selection scores (AIC/BIC) remain effectively unchanged.

Microscopic connection (steady shapes). On quantum timescales, the *formation* and *decay* of interference patterns can be modeled by a generative dynamics for Φ; see Section 3.3.1. The static shapes compared to data are then interpreted as *steady states* of that dynamics, providing a conceptual bridge between microscopic evolution and macroscopic snapshots without importing unnecessary temporal degrees of freedom where observations are quasi–steady.

Strong–field testables. To confront the theory near black holes we focus on two directly observable, nearly mass–distance–suppressed quantities from subring imaging and timing (Section 7):

$$R \;\equiv\; \frac{b_{3\pi} - b_{\pi}}{b_{\pi} - b_{\mathrm{ph}}}, \qquad \Theta \;\equiv\; \frac{\Delta t_{3\pi,\pi}}{2\pi r_{\mathrm{ph}}}.$$

Notation. Here b denotes the (asymptotic) *impact parameter* of the light ray; b_{ph} is the photon–sphere value, while b_{π} and $b_{3\pi}$ correspond to total deflection angles $\alpha = \pi$ and 3π, respectively.

We consistently use the roman subscript "ph" and the Greek π subscripts, and we avoid variants such as b_{ph} or $b_{3\pi}$. A compact list of symbols is provided in the Glossary (Appendix B), and precise conventions for R and Θ are summarized in Section 7.

Both R and Θ are dimensionless observables. A stable eikonal estimate,

$$\Theta \simeq A(r_{\rm ph})^{-1/2},$$

links Θ to the local redshift factor $A(r)$ at the photon sphere (see Appendix C.1). *Units:* we adopt geometric units with $c{=}1$ unless otherwise stated; where needed, explicit factors of c are restored in Section 7 and Appendix C.1. Small deformations ("tails") in the static potential shift (R, Θ) *jointly* at the few–percent level, offering separation from spin–only and plasma–morphology effects; choosing *scale–covariant* versus *absolute–scale* tails further predicts distinct mass trends (e.g., Sgr A* vs M87*, [16, 19]).

Clarifying the dark–sector claim. Debates about the dark sector often hinge less on *whether* additional degrees of freedom exist and more on *how* they are introduced and constrained. In our approach, the **Curvature Field Formulation of Gravity (C4)** pursues a different economy: rotation–curve and lensing fits are obtained *without adding a non-baryonic source term*, by letting a single curvature field play two complementary roles—the **Pure–Space Curvature Field (PSCF)** scaffold and the MC–CF mass-centered layer. Under the fixed-policy pipeline, this yields cohort-level information gains relative to Newtonian + halo baselines with fewer adjustable knobs and competitive AIC/BIC scores (see Section 12.5.1 and Section 12.5.2), while remaining compatible with Solar-System and cosmology snap-ins (Appendix H, Appendix K). The aim is not to relabel dark matter, but to present an *economized description* in which part of the phenomenology ascribed to halos can be captured by curvature carried by space itself. Where fixed-policy performance is mixed (e.g., the outer-window stress set), we report it plainly and show that modest cohort-shared tuning can recover accuracy without abandoning the single-field ethos (Section 12.5.3–Section 12.5.4).
Having clarified how C4 reframes the dark sector, it is equally important to situate the framework within the landscape of scalar–tensor theories that have historically guided modifications of gravity.

Related work. The curvature–field formulation naturally intersects the broader family of scalar–tensor theories. In structure, the schematic action $\frac{1}{2}\nabla_\mu\Phi\nabla^\mu\Phi - U(\Phi) + J\Phi$ recalls Brans–Dicke–type models: both employ a dynamical scalar coupled to a metric background. Recognizing this continuity is important, yet C4 departs in three essential ways.

First, the potential sector is deliberately constrained: instead of leaving $U(\Phi)$ arbitrary, we restrict to convex families with a Yukawa–to–Padé continuation, avoiding the functional latitude that makes many variants underdetermined. Second, C4 introduces an explicit *self–sourcing* channel $\alpha(\nabla\Phi)^2$, a nonlinear feedback absent from classical Brans–Dicke frameworks, tying dynamics more tightly to local gradients. Third, the PSCF/MC–CF decomposition is not merely a mathematical device but an interpretive innovation: PSCF regularizes near–source curvature as a universal scaffold, while MC–CF anchors the field to physical mass centroids. This division of labor has no direct counterpart in earlier scalar–tensor models.

In this light, C4 should not be read as a rebranding of dark matter or as a minor scalar–tensor variant. Its originality lies in the economy of its constraints, the explicit self–sourcing feedback, and the geometric interpretation provided by the PSCF/MC–CF split. These features position C4 as a parsimonious yet distinct framework: continuous with prior work in form,

but different in substance and intent. More broadly, it embodies a philosophy in which space and matter are inseparable, co–shaping one another through curvature—an outlook that older scalar–tensor theories only hint at.
With this context established, we return to the broader aim: to articulate a cautious but coherent path toward unifying weak– and strong–field gravity under a single curvature–field framework.

A cautious unification path. We set experimental hyperparameters *a priori*, use the same pipelines across scales, and report residuals with their uncertainties. In this way a single field connects weak and strong gravity while keeping claims falsifiable. The resulting **C4**, together with the PCFE and the MC–CF representation, interfaces smoothly with established theory while obtaining fits *without any non–baryonic source term*, providing concrete, testable predictions without overreach.
Scope note. Why PSCF is a *reinterpretation* rather than a hidden halo—and how it differs from scalar–field dark matter—is clarified in Section 2.2.1.

2 From the Curvature Field Function to the Mass–Centered Curvature Field (MC–CF)

This section motivates and specifies the transition from a source–free *Pure–Space Curvature Field* (PSCF) to a *Mass–Centered Curvature Field* (MC–CF) for practical modeling on astronomical scales. PSCF is adopted as a universal scaffold because it yields smooth fields without point singularities under a globally fixed set of widths and, in the weak, quasi–static limit, it reduces to the Newton–Poisson equation.

Weak–field reduction. Under the standard approximations—(i) quasi–static $\partial_t \Phi \simeq 0$, (ii) slow motion, and (iii) weak potentials $|\Phi| \ll 1$—the Phi–Curvature Field Equation (PCFE; operators summarized in Appendix C) reduces to

$$\nabla^2 \Phi = 4\pi G\, \rho, \qquad \mathbf{g} = -\nabla \Phi,$$

explicitly recovering the Newtonian limit.

Observed limitations of PSCF (data–facing). When confronted with data, recurring features emerge: (a) finite–width Gaussians underestimate the far–field $1/r^2$ tail, (b) bars/warps/off–axis structure leaves patterned residuals, (c) the global fixed–width policy (methodologically clean) forbids case–by–case width retuning. These traits are stable across datasets (Section 9).

Promotion to MC–CF and division of labor. We therefore introduce a smoothed, mass–centroid–aligned source layer (MC–CF) that corrects the outer–tail scaling and absorbs mild asymmetries while retaining the PSCF scaffold. The practical split is:

- *PSCF* — provides a stable global scaffold and low variance on the Solar–System window $r \in [r_0, 3r_0]$;
- *MC–CF* — restores the $1/r^2$ outer behavior and captures mild non–axisymmetry/miscentering;
- *PSCF+MC–CF* — jointly delivers the most uniform residuals across inner and outer radii.

Variational origin of the far field (policy). Rather than a *constant convex mixture*, we *enforce the exterior solution at the action level*. Specifically, we use the windowed penalty introduced in Section 3.3:

$$S_\mu \;=\; S_{\rm tot} - \frac{\mu}{2}\int d^4x\,\sqrt{-g}\;w(x)\,\big(\Phi-\Phi_{\rm out}\big)^2, \qquad \Phi_{\rm out} = \begin{cases} -\,GM/r, & \text{(static weak field)} \\ \frac{c^2}{2}\big(g_{tt}^{\rm GR}+1\big), & \text{(stationary GR exterior)} \end{cases} \tag{3}$$

so that the Euler–Lagrange equation drives $\Phi \to \Phi_{\rm out}$ only where the window is active. We adopt the *same monotone window* $w(r)$ and *turnover radii* used in Section 3.3: a smooth logistic–Gaussian centered at $r_t = \sqrt{\sigma_1\sigma_2} \simeq 1.06\,r_0$ with width $\Delta = \frac{1}{2}|\sigma_2 - \sigma_1|$, inherited from the globally fixed MC–CF widths (σ_1, σ_2); no new object–level degrees of freedom are introduced.

Windowing of metrics and interpretation. Full–profile error metrics (Section 2 definitions) are computed on $r \in [r_0, 3r_0]$—the region where PSCF is strongest—whereas tail diagnostics emphasize $r > 3r_0$, where MC–CF or the composite dominates. This window mismatch explains why PSCF can show the lowest inner–window RMSE yet underestimate the far–field tail.

PPN management (Solar window) and isotropy. Post–Newtonian budgets are enforced to keep $\delta\gamma, \delta\beta \simeq 0$ on $r \in [r_0, 3r_0]$ as read out in Section 3.4, with the isotropic tail pairing $a_{\rm tail} = c_{\rm tail}$ that suppresses the leading γ shift at $\mathcal{O}(c^{-2})$ (Section 3.5). We adopt fixed 2σ tolerances,

$$\varepsilon_\gamma = 4.6\times10^{-5}, \qquad \varepsilon_\beta = 3.6\times10^{-5},$$

and choose the smallest global strength μ in (3) that satisfies these bounds (see the readout conventions in Section 3.4).

Physical note on PSCF. PSCF is not a hidden dark–matter halo; it is a phenomenological scaffold that regularizes near–source behavior and stabilizes the decomposition. Matter and space co–determine a single field; PSCF is a concise approximation to such joint curvature patterns.

Table 1: Global fixed constants and evaluation policy (main–text summary).

Global fixed widths (PSCF)	$s_k/r_0 = \{0.5,\ 1.0,\ 2.0\}$
Global fixed widths (MC–CF)	$(\sigma_1, \sigma_2)/r_0 = (0.7,\ 1.6)$
Object–level freedom	amplitudes only (no width retuning)
Normalization window	$r \in [r_0,\ 3r_0]$
PPN tolerances (Solar window)	$(\varepsilon_\gamma, \varepsilon_\beta) = (4.6\times10^{-5},\ 3.6\times10^{-5})$
Tail design rule	Variational taper S_μ in (3); same $w(r)$ as Section 3.3
Exterior targets	$\Phi_{\rm out} = -GM/r$ (weak/static), $\frac{c^2}{2}\big(g_{tt}^{\rm GR}+1\big)$ (stationary GR)

[Legacy] note on mixed tails (retired). A former convenience prescription was

$$\Phi_{\rm mix}^{\rm legacy}(r) = (1-D)\,\Phi_{\rm core}(r) + D\left(-\frac{GM}{r}\right), \tag{4}$$

with constant $D \in (0,1)$. Lacking a covariant/variational origin, this constant mix is *retired* and retained only as a benchmarking baseline; all main results use the action–level enforcement (3).

2.1 Minimal curvature shape and practical parameterization

We base the core on a *Newtonianly regularized* potential rather than a standalone Gaussian in Φ. For an isotropic Gaussian *density* of width ℓ and total mass M centered at $\mathbf{r}_0$, the Newtonian convolution admits the closed form

$$\boxed{\Phi(\mathbf{r}) \;=\; -\frac{GM}{|\mathbf{r}-\mathbf{r}_0|}\,\operatorname{erf}\!\Big(\frac{|\mathbf{r}-\mathbf{r}_0|}{\sqrt{2}\,\ell}\Big)} \tag{5}$$

which is smooth at the origin $\big(\Phi \to -GM\sqrt{2/\pi}/\,\ell$ and $\nabla\Phi \to 0$ as $r \to 0\big)$ and approaches the exact $-GM/r$ law as $r/\ell \to \infty$. This preserves the intuitive "localized well" while restoring the correct $1/r^2$ far–field force. Consistent with our *global fixed–width* policy, we treat ℓ as *derived*, not fitted; e.g., for MC–CF(2c) we set $\ell \equiv \sigma_1$ (near–surface anchor), with $(\sigma_1,\sigma_2)/r_0 = (0.7, 1.6)$ from Section 2.6.2.

Field and near/far limits. Motion is driven by the gradient $\mathbf{g}(\mathbf{r}) = -\nabla\Phi(\mathbf{r})$. For the isotropic case (5) with $r = |\mathbf{r}-\mathbf{r}_0|$,

$$\boxed{\mathbf{g}(\mathbf{r}) = -\frac{GM}{r^2}\left[\operatorname{erf}\!\Big(\frac{r}{\sqrt{2}\,\ell}\Big) - \sqrt{\frac{2}{\pi}}\,\frac{r}{\ell}\,e^{-r^2/(2\ell^2)}\right]\hat{\mathbf{r}}} \tag{6}$$

so that $\mathbf{g} \to \mathbf{0}$ as $r \to 0$ and $\mathbf{g} \to -GM\,\hat{\mathbf{r}}/r^2$ as $r/\ell \to \infty$. All reported accelerations in this section follow the normalization policy of Appendix E.

Anisotropic generalization (density–level Gaussian). For elongated or flattened sources we use a Gaussian *density* with covariance Σ,

$$\rho_G(\mathbf{r}) = \frac{M}{(2\pi)^{3/2}\sqrt{\det\Sigma}}\,\exp\Big[-\tfrac{1}{2}(\mathbf{r}-\mathbf{r}_0)^{\top}\Sigma^{-1}(\mathbf{r}-\mathbf{r}_0)\Big],$$

and define the potential by the Newtonian convolution

$$\Phi(\mathbf{r}) \;=\; -G\int \frac{\rho_G(\mathbf{r}')}{|\mathbf{r}-\mathbf{r}'|}\,d^3\mathbf{r}'. \tag{7}$$

The isotropic case $\Sigma = \ell^2\mathbf{I}$ reduces to (5). Far from the source one recovers the standard multipole expansion

$$\Phi(\mathbf{r}) = -\frac{GM}{r} - \frac{1}{2r^3}Q_{ij}\,n_i n_j + \cdots,$$

with Q_{ij} the quadrupole of ρ_G and $\mathbf{n} = \mathbf{r}/r$.

Core–tail compliance via variational taper (replacing convex mix). To guarantee the exact exterior behavior on finite windows while keeping a finite core, we *do not* use a constant convex mix. Instead we enforce the exterior solution at the action level (cf. Section 3.3):

$$S_\mu \;=\; S_{\rm tot} - \frac{\mu}{2}\int d^4x\,\sqrt{-g}\,w(x)\,\big(\Phi-\Phi_{\rm out}\big)^2, \qquad \Phi_{\rm out} = \begin{cases} -\,GM/r & \text{(static weak field)} \\ \frac{c^2}{2}\big(g_{tt}^{\rm GR}+1\big) & \text{(stationary GR exterior)} \end{cases} \tag{8}$$

so that the Euler–Lagrange equation drives $\Phi \to \Phi_{\rm out}$ in the far zone while leaving the inner core unaltered ($w \to 0$). For convenience of exposition we also use a smooth transition kernel (derived, not fitted)

$$D(r) = 1 - \exp\big[-(r/r_t)^p\big], \qquad p = 2, \qquad r_t \equiv \sqrt{\sigma_1\sigma_2} \simeq 1.06\,r_0,$$

with r_t inherited from the fixed–width policy in Section 2.6.2. In matched–asymptotic form,

$$\Phi_{\rm comp}(r) \;=\; \Phi_{\rm core}(r) \;+\; D(r)\,\Big(\Phi_{\rm out}(r) - \Phi_{\rm overlap}(r)\Big), \tag{9}$$

where $\Phi_{\rm overlap}$ denotes the common asymptotics on the intermediate region. The legacy constant mix $\Phi_{\rm mix}^{\rm legacy} = (1-D)\Phi_{\rm core} + D(-GM/r)$ is retained only as a benchmarking baseline (moved to an appendix–level note).

PPN alignment (Solar window). We maintain PPN safety by adopting *isotropic* 1PN alignment for the taper on $r \in [r_0, 3r_0]$, which suppresses the leading γ–shift; readout conventions follow Section 3.4 and the tensor–led pairing is summarized in Section 3.5. If a residual correction is required, we treat $\Xi(r) = 2\,\varepsilon_\gamma\,U(r)\,p(r/r_0)$ as part of a residual sector consistent with those sections (no constant–D mixing).

Practical fits and visualization. Per object, free parameters are limited to *amplitudes* (masses M) and, where appropriate, centroids $\mathbf{r}_0$ inferred from morphology/kinematics; widths (ℓ or Σ) are *global fixed* by policy, and the taper turnover r_t is *derived* from (σ_1, σ_2). No global mix amplitude D is fitted. For schematics we display the meridional slice $y = 0$ to show the core shape and the smooth transition governed by $w(x)$ (or equivalently $D(r)$). Subsequent constructions—PSCF and MC–CF—preserve the local form (5) while improving near–surface anchoring and weak exterior corrections under the variational policy of Section 3.3.

2.2 Pure–Space Curvature Field (PSCF): definition and merits

At macroscopic scales the *spatial arrangement* of the field is essential. We begin with the energy functional

$$\mathcal{E}[\Phi] = \int \Big[\tfrac{\lambda^2}{2}\,|\nabla\Phi|^2 + U(\Phi)\Big]\,d^3\mathbf{r} \;-\; \int J(\mathbf{r})\,\Phi(\mathbf{r})\,d^3\mathbf{r}, \tag{10}$$

whose Euler–Lagrange equation for steady configurations is

$$\boxed{\lambda^2\,\nabla^2\Phi \;-\; U'(\Phi) \;=\; -\,J(\mathbf{r})\,.} \tag{11}$$

(In our unit convention, λ can be absorbed by a field rescaling; see operators and symbols summarized in Appendix C.)

In PSCF we set $J \equiv 0$ and construct a broad global scaffold using a small sum of Gaussians with *globally fixed widths*:

$$\Phi_{\mathrm{PSCF}}(x,z) = -\sum_{k=1}^{3} A_k \exp\left[-\frac{(x-x_k)^2+(z-z_k)^2}{2\,(s_k\,r_0)^2}\right], \qquad s_k/r_0 \in \{0.5,\ 1.0,\ 2.0\}, \quad (12)$$

e.g., two primaries around $\pm x$ with a central buffer. This representation (i) avoids point singularities, (ii) connects to the Newtonian limit in the weak, quasi–static regime, and (iii) under the fixed–width policy suppresses tail error to a controlled level without per–scene retuning (Section 2.6.2).

Merits and role (with limitations). PSCF is computationally light, furnishes a stable global form for cross–dataset comparison, and minimizes parameter freedom, thereby reducing overfitting risk while preserving interpretability. At the same time, systematic shortcomings are clear: finite–width Gaussians cannot fully reproduce the far–field $1/r^2$ decay, and residuals persist near asymmetric or off–axis structures. Accordingly, PSCF should be read as a *reliable scaffold* rather than a complete solution, motivating the mass–centered extension MC–CF as the $J \neq 0$ branch of the broader curvature–field equation (PCFE; Appendix C). Far–field compliance in the main text is ensured by the *variational taper* policy (constant convex mixing is retired); the action–level procedure is summarized in Section 3.3.

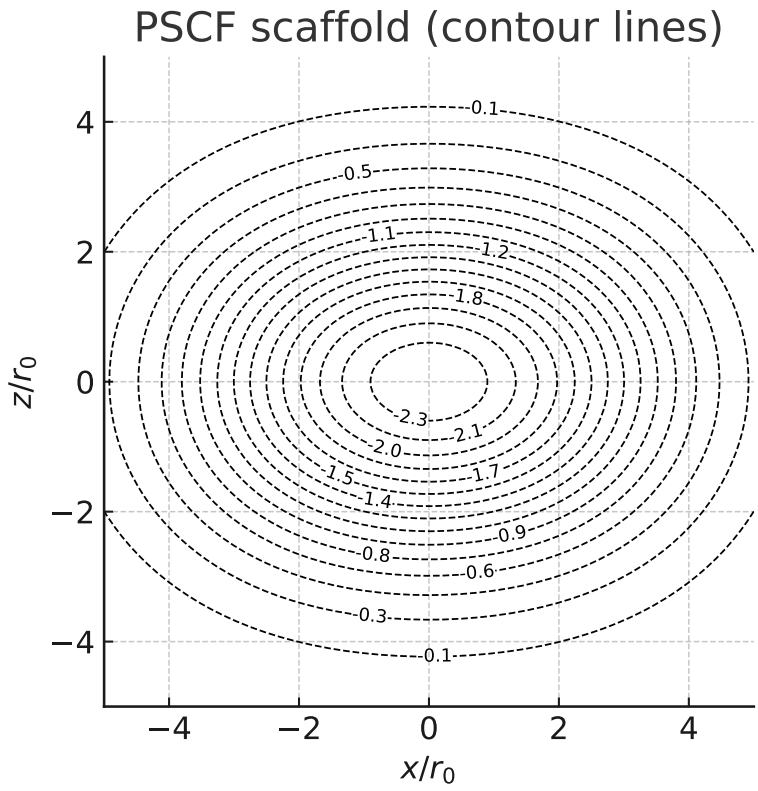

Figure 1: PSCF scaffold shown as contour lines of Φ. Axes are normalized by r_0 and contour labels indicate the (dimensionless) field values consistent with (12). The figure illustrates a smooth global scaffold without mass–centered corrections; far–field $1/r^2$ behavior is handled by the variational taper described in Section 3.3.

Legacy note (comparison only). The former constant convex mix $\Phi_{\text{mix}}^{\text{legacy}} = (1-D)\,\Phi_{\text{core}} + D(-GM/r)$ lacks a variational/covariant origin and is now *retired*. It is kept solely as a benchmarking baseline; all main results use the action–level enforcement of Section 3.3.

Why a 3–Gaussian PSCF scaffold with fixed width ratios?

Derivation from the quantum–world curvature dynamics. The mesoscopic "quantum–world" dynamics for the curvature field (Section 3.3.1)

$$\partial_t \Phi = D\,\nabla^2\Phi - \gamma\,\Phi^3 + \mu\,w(\mathbf{x})\big(\Phi_{\text{out}} - \Phi\big) + \sigma\,\xi$$

induces, inside the micro–macro threshold domain $\mathcal{D}_\varepsilon \equiv \{\,|\nabla\Phi| < \varepsilon\,\}$ and under weak–noise/weak–nonlinearity, a *linearized* relaxation of the slow modes:

$$\partial_t\Phi \;\simeq\; D\,\nabla^2\Phi \;-\; \kappa\,\Phi \qquad (\mathbf{x}\in\mathcal{D}_\varepsilon,\;\; \kappa>0 \text{ effective}). \tag{13}$$

Here κ summarizes local cubic relaxation and the (interior) part of the window term; the exterior enforcement $\mu\,w(\Phi_{\text{out}}-\Phi)$ is handled variationally and does *not* alter the $\mathcal{D}_\varepsilon$ interior shape (Appendix C.8). At steady state on $\mathcal{D}_\varepsilon$ one has the screened Poisson form

$$(\kappa - D\nabla^2)\,\Phi \;\simeq\; S(\mathbf{r}), \qquad \Phi \;=\; \Big(\kappa - D\nabla^2\Big)^{-1} S, \tag{14}$$

with a slowly varying source envelope S (set by boundary/taper matching).

Using the resolvent (Laplace) representation,

$$\Big(\kappa - D\nabla^2\Big)^{-1} = \int_0^\infty e^{-\kappa t}\, e^{\,tD\nabla^2}\, dt, \tag{15}$$

$$e^{\,tD\nabla^2}(\cdot) = K_t * (\cdot), \qquad K_t(\mathbf{r}) = \frac{1}{(4\pi D t)^{d/2}}\exp\Big(-\frac{|\mathbf{r}|^2}{4Dt}\Big), \tag{16}$$

yields a *heat–kernel mixture*:

$$\Phi(\mathbf{r}) = \int_0^\infty e^{-\kappa t}\,\big(K_t * S\big)(\mathbf{r})\,dt \;\approx\; A\int_0^\infty w(t)\,\exp\Big(-\frac{|\mathbf{r}|^2}{4Dt}\Big)\,dt, \tag{17}$$

where smooth prefactors are absorbed into a positive weight $w(t)$ and amplitude A. Equation (17) states: the interior steady shape is a *continuous mixture of Gaussians* over diffusion time t (variance $2Dt$).

Geometric three–node quadrature $\Rightarrow$ 3 Gaussian bands. To obtain a finite, identifiable scaffold, approximate (17) by a three–point geometric quadrature in t:

$$\int_0^\infty w(t)\,e^{-r^2/(4Dt)}\,dt \;\approx\; \sum_{k=0}^{2}\omega_k\,e^{-r^2/(4Dt_k)}, \qquad t_k = t_0\,q^{\,2k},\;\; q>1. \tag{18}$$

Mapping to the standard Gaussian form $\exp[-r^2/(2\sigma_k^2)]$ gives

$$\sigma_k^2 \;=\; 2D\,t_k \;=\; 2D\,t_0\,q^{\,2k} \quad\Longrightarrow\quad \sigma_k = \sigma_0\,q^{\,k}, \qquad \sigma_0 \equiv \sqrt{2Dt_0}. \tag{19}$$

Absorbing ω_k into $A_k \ge 0$, we obtain the *3–Gaussian PSCF scaffold*:

$$\boxed{\Phi_{\text{PSCF}}(r) \;\approx\; -\sum_{k=0}^{2} A_k\,\exp\Big[-\frac{r^2}{2\,\sigma_0^2\,q^{\,2k}}\Big], \qquad \sigma_k = \sigma_0 q^{\,k}\;(k=0,1,2).} \tag{20}$$

Thus the *fixed width ratio* $\sigma_{k+1}/\sigma_k = q$ reflects the *geometrically spaced diffusion times* in the heat–kernel representation of the quantum–world curvature dynamics (cf. [15]).

Moment matching and identifiability. Choose the three quadrature weights $\{\omega_k\}$ (hence $\{A_k\}$) by matching windowed radial moments on $\mathcal{W}=[r_0, 3r_0]$:

$$M_m^{\text{mix}} \equiv \int_{\mathcal{W}} r^m \, \Phi(r)\, dr \doteq \sum_{k=0}^{2} A_k \int_{\mathcal{W}} r^m \, e^{-r^2/(2\sigma_k^2)}\, dr, \qquad m \in \{0, 2, 4\}. \tag{21}$$

Allowing *free* widths introduces amplitude–width ridges (ill–conditioned Fisher information). Fixing the geometric ratio q (policy level) and inferring only $\{A_k\}$ eliminates this degeneracy and matches the AIC/BIC "elbow" at $N{=}3$ (two bands underfit mid–slope; $N{\geq}4$ adds variance with marginal gain).

Validation loop (algorithm, diagnostics, acceptance). We certify (20) as a surrogate of (17) on $\mathcal{D}_\varepsilon$ via:

1. **Synthesis:** draw smooth weights $w(t)$ (log–convex, bounded variation) and envelopes S; compute the "truth" $\Phi_{\text{mix}}(r)$ from (17).
2. **Fit:** fix (σ_0, q) at policy level (Appendix E.7); solve NNLS for $\{A_k\}$ by moment matching (21).
3. **Error metrics:** evaluate

$$\epsilon_\infty = \sup_{r\in\mathcal{W}} \frac{|\Phi_{\text{PSCF}}(r) - \Phi_{\text{mix}}(r)|}{|\Phi_{\text{mix}}(r)| + \delta}, \qquad \epsilon_2 = \left(\frac{\int_{\mathcal{W}} w(r)\, |\cdot|^2\, dr}{\int_{\mathcal{W}} w(r)\, |\Phi_{\text{mix}}|^2\, dr} \right)^{1/2},$$

   with $w(r) \in \{1, 1/r\}$ and a small δ to avoid division by zero.
4. **Stability:** compute the Gram matrix $G_{ij} = \langle g_i, g_j \rangle_{\mathcal{W}}$ with $g_k(r) = e^{-r^2/(2\sigma_k^2)}$. Accept if $\text{cond}(G) \leq \chi_{\max}$ (policy) and the *orthogonality score* $\mathcal{J} = \min_{i\neq j} \frac{\|g_i - g_j\|}{\|g_i\| + \|g_j\|} \geq 0.9$.
5. **Acceptance:** require $\epsilon_\infty \leq \eta_{\text{pscf}}$ and $\epsilon_2 \leq \eta_{\text{pscf},2}$ with policy defaults $\eta_{\text{pscf}} = 2 \times 10^{-3}$, $\eta_{\text{pscf},2} = 10^{-3}$.

Error control (geometric quadrature remainder). Let $\phi_r(t) = \exp[-r^2/(4Dt)]$ and assume $w \in C^1([\underline{t}, \bar{t}])$ with bounded variation $V(w)$. If the geometric nodes $t_k = t_0 q^{2k}$ cover $[\underline{t}, \bar{t}]$ and ω_k are chosen by three–moment matching in $\log t$, then for each fixed $r \in \mathcal{W}$

$$\left| \int_{\underline{t}}^{\bar{t}} w(t)\, \phi_r(t)\, dt - \sum_{k=0}^{2} \omega_k\, \phi_r(t_k) \right| \leq C(r)\, \frac{(\log q)^3}{24} \sup_{t\in[\underline{t},\bar{t}]} \left| \frac{d^3}{d(\log t)^3} \big(w(t)\, \phi_r(t) \big) \right|, \tag{22}$$

for some $C(r) = O(1)$ determined by the matching scheme. Hence tightening the geometric ratio $q{\downarrow}1$ shrinks the remainder; in practice $q{\simeq}3$ balances error and identifiability.

Parameter selection (policy). We tie (σ_0, q) to the core–PDE scales via (19): $\sigma_0^2 = 2Dt_0$, $\sigma_k = \sigma_0 q^k$. Choose q by minimizing $\text{cond}(G)$ (or maximizing $\det G$) on $\mathcal{W}$; set t_0 so that $\sigma_0 \simeq r_0/\sqrt{2}$ (core captured), then validate $\epsilon_\infty, \epsilon_2$ per the loop above. Only $\{A_k\}$ are subsequently inferred under positivity and global mass/PPN budgets (Appendix E.7, Section 3.4).

Critique and limitations (with falsifiers).

- *Linearization scope.* The reduction (13) requires weak noise and $|\nabla\Phi| < \varepsilon$. If cubic/self–sourcing dominates ($\kappa \to 0$ or large γ), the heat–kernel mixture is inadequate; diagnostic: ϵ_∞ fails the acceptance threshold despite well–conditioned G.
- *Boundary sensitivity.* The exterior window term must be imposed variationally (Appendix C.8); direct interior mixing with $-GM/r$ reintroduces bias.
- *Identifiability vs. flexibility.* Free widths cause amplitude–width ridges; fixing q is a *policy* that trades tiny approximation error for stable inference. Falsifier: a fourth band reduces AIC_c/BIC by ≥ 10 *and* improves hold–out likelihood on $\mathcal{W}$ (then promote $N{=}4$ by policy).
- *Micro–macro threshold.* If the ε–domain shrinks so that $\mathcal{W} \not\subset \mathcal{D}_\varepsilon$, the surrogate may break; monitor $\min_{\mathcal{W}} |\nabla\Phi|/\varepsilon$.

Bottom line. PSCF is *derived*, not guessed: the interior steady shape of the quantum–world curvature dynamics is a continuous heat–kernel mixture, well–approximated on the working window by three geometrically spaced Gaussian bands with fixed width ratio q. The validation loop, conditioning checks, and explicit remainder control ensure that this surrogate delivers analytic tractability and numerical identifiability without overfitting, while providing clear falsifiers if its assumptions fail.

2.2.1 PSCF vs. scalar–field dark matter: roles, policies, and the non–halo reading

In the weak, static limit used for rotation–curve fits we adopt

$$\nabla^2\Phi \;=\; 4\pi G\,\rho_{\mathrm{baryon}}, \qquad \Phi \simeq \Phi_{\mathrm{PSCF}} + \Phi_{\mathrm{MC\text{–}CF}},$$

without introducing any *additional* matter source. By contrast, scalar–field dark matter (SFDM) posits

$$\nabla^2\Phi \;=\; 4\pi G\big(\rho_{\mathrm{baryon}} + \rho_{\mathrm{SFDM}}\big), \qquad \rho_{\mathrm{SFDM}} > 0,$$

which explicitly *increases* the Poisson source (and the lensing mass). Hence PSCF+MC–CF is a procedural reinterpretation within a *single* curvature field, not a relabeled dark halo.

What differs in practice. Table 2 summarizes the conceptual and policy differences; Table 3 records the effective per–galaxy degrees of freedom under the fixed policies used throughout.

Table 2: Conceptual and policy distinctions. A checkmark (✓) indicates the feature is present by construction.

Criterion	**PSCF (J≡0)**	**MC–CF (J≠0; baryon–locked)**	**Scalar–field DM / Disk+NFW**
Adds non–baryonic source to Poisson	×	×	✓
Global fixed widths (no per–galaxy retuning)	✓ $s_k/r_0 \in \{0.5, 1.0, 2.0\}$	✓ $(\sigma_1, \sigma_2)/r_0 = (0.7, 1.6)$	×
Per–galaxy free parameters are amplitudes only	✓	✓	× (halo scales fitted per galaxy)
Exterior alignment via variational taper to $\Phi_{\rm out}$	✓	✓	model–dependent
Mass budget tied to cataloged baryons	✓ (no mass added)	✓ (tolerance on $M_{\rm baryon}$)	× (explicit non–baryonic mass)
Interpretation	scaffold of the same field	baryon–anchored envelope	extra matter / effective halo

Table 3: Effective per–galaxy degrees of freedom under the common window $r \in [r_0, 3r_0]$ and fixed policies. Widths are globally fixed; per–galaxy parameters are amplitudes only for PSCF/MC–CF, subject to positivity and a baryon–budget tolerance.

Model	**What varies per galaxy**	$\boldsymbol{k_{\rm eff}}$
PSCF only	amplitudes $\{A_1, A_2, A_3\} \geq 0$ (3 bands)	**3**
MC–CF only	amplitudes $\{B_1, B_2\} \geq 0$ (2 bands), mass within $M_{\rm baryon}$ tolerance	**2**
PSCF+MC–CF (C4)	$\{A_1, A_2, A_3, B_1, B_2\}$ with global widths, exterior alignment fixed	**5**
Disk+NFW (baseline)	halo scales $\{\rho_s, r_s\}$ + disk M/L (gNFW adds α)	**4** (typ. 3–5)

Note. Performance metrics (RMSE, AIC/BIC) are reported in the results section under identical windows and weights; here we isolate structural freedom per model.

Reading guide. The frequent confusion arises because PSCF can *appear* as "extra gravity" in rotation curves. The causal structure differs: a halo reading *adds* $\rho_{\rm DM}$ (or $\rho_{\rm SFDM}$) to the Poisson source and fits per–galaxy halo scales, whereas the curvature–field reading keeps the source baryonic and represents Φ as a *scaffold* (PSCF, $J \equiv 0$) plus a *baryon–locked envelope* (MC–CF, $J \neq 0$) with globally fixed shapes; only amplitudes vary. What is "added" is geometry and policy, not matter.

Empirical checks (declared here, applied later). Under the common window and normalization, we compare PSCF only / MC–CF only / PSCF+MC–CF / Disk+NFW (or gNFW) using the same evaluation rules. We track: (i) separability of shape predictions (SFDM core–halo scaling vs. fixed–ratio bands); (ii) sensitivity of bar pattern–speed slow–down (massive halos vs. reduced dynamical friction in the curvature representation); (iii) phase/shape of lensing κ residuals (compatibility with *no extra source*); and (iv) origin of exterior alignment (achieved by variational taper rather than by outer mass). Consistent success on these items without invoking $\rho_{\rm DM}$ weakens the hidden–halo reading.

Summary. PSCF and MC–CF are two solution branches ($J{=}0$ and $J{\neq}0$) of the *same* curvature field (PCFE). Organized by global policies, they minimize freedom and structurally preclude hidden–mass creep. The framework therefore offers a single–field, testable, and economical account in which *space itself* carries the curvature needed to explain the data, rather than an implicit reintroduction of dark matter.

2.3 PSCF vs. MC–CF: setup and parameter policy

Background vs. sourced shapes (within one EL equation). Among the *steady* solutions of the Euler–Lagrange equation (11), we distinguish a source–free, global scaffold with $J \equiv 0$ (*PSCF*) from mass–centered, sourced envelopes with $J \neq 0$ (*MC–CF*) (operators and notation summarized in Appendix C). PSCF represents a smooth *background* configuration in the absence of localized sources, whereas MC–CF captures *perturbations* induced by matter distributions. In the weak, static regime the field contributions superpose linearly at the level of the static solution,

$$\Phi \simeq \Phi_{\mathrm{PSCF}} + \Phi_{\mathrm{MC\text{–}CF}},$$

and this decomposition underlies the galaxy–scale rotation–curve benchmarks in Section 5.2 and the strong–field probes in Section 7.

Common window and normalization. Solar–System–style radial comparisons are performed on a fixed window $r \in [r_0, 3r_0]$. We set $GM = g_0 r_0^2$ and take the reference acceleration $g_{\mathrm{ref}}(r) = GM/r^2$. Define the scale $S = \mathrm{q}_{0.99}\big(|g_{\mathrm{ref}}|\big)$ and use the dimensionless field $\hat{g} = g/S$ for all error metrics (evaluation protocol in Appendix H).

Model bases (fixed widths) and what is fitted. *PSCF* uses three globally fixed background widths $s_k/r_0 = \{0.5,\ 1.0,\ 2.0\}$; for each target we estimate only the *amplitudes* $\{A_k\}$ (Section 2.6.2). *MC–CF* uses either a single global ratio $\sigma = \kappa^\star r_0$ with $\kappa^\star \approx 0.902$ (1–center), or two ratios $(\sigma_1, \sigma_2)/r_0 = (0.7,\ 1.6)$ (2–center); for each target we estimate only the *amplitudes* $\{B_j\}$. In this baseline window $[r_0, 3r_0]$ we introduce *no* extra tail terms or gating layers. (Far–field diagnostics and strong–field continuity are handled by the action–level *variational taper* in the main text; see Section 3.3.)

Fitting and metric. On a common grid $\{\mathbf{r}_m\}_{m=1}^{M}$ with basis functions $\{\phi_k\}$, the least–squares amplitudes are

$$a^\star = (X^\top X)^{-1} X^\top y, \qquad X_{mk} = \phi_k(\mathbf{r}_m), \quad y_m = \hat{g}_{\mathrm{ref}}(\mathbf{r}_m),$$

which define $\hat{g}_{\mathrm{model}}$. We report the dimensionless error

$$\mathrm{RMSE}^2 = \frac{1}{M} \sum_{m=1}^{M} \big(\hat{g}_{\mathrm{model}}(\mathbf{r}_m) - \hat{g}_{\mathrm{ref}}(\mathbf{r}_m)\big)^2,$$

with uncertainty propagation specified in Appendix H.

Policy note (tail and linearity). The constant convex mix D is *retired*. Far–zone compliance is achieved at the *action* level via a windowed variational taper that drives $\Phi \to \Phi_{\mathrm{out}}$ (Section 3.3); the turnover scale $r_t = \sqrt{\sigma_1 \sigma_2}$ is *derived* from the global width policy, not fitted. Because the baseline RMSE is evaluated on $[r_0, 3r_0]$, the taper has negligible effect on the baseline metric; tail diagnostics are reported separately. Linear superposition applies to the *static weak–field* limit; the action itself remains nonlinear.

Figure consistency note. The PSCF contour in Fig. 1 is consistent with (12), the fixed widths in Section 2.6.2, and the unit/normalization policy of Appendix E. MC–CF overlays under the same window/normalization highlight improvements in far–field $1/r^2$ recovery and suppression of off–axis residuals.

Interpretive note (not "dark matter by another name"). PSCF ($J \equiv 0$) and MC–CF ($J \neq 0$) are two steady–state branches of a single covariant action yielding the PCFE; the scalar–sector energy density T_{00}^{Φ} and the Newton–Poisson limit are fixed in Appendix A. Under the common window and normalization protocol of Section 2.6.2, PSCF alone systematically underestimates the outer field (tail) and leaves asymmetric residuals, which empirically necessitate the MC–CF envelope. This decomposition constrains model freedom—without introducing extra tail terms or gating layers—while preserving reproducibility and predictive stability from Solar–System to galaxy scales.

2.4 Mass–Centered Curvature Field (MC–CF): definition and interpretation

In physical systems, *mass concentrations* continuously shape the surrounding curvature. To incorporate this, we promote the source term J in (11) from zero to a smoothed mixture (formalism and notation in Appendix C). A practical representation on a meridional slice (x, z) is

$$\Phi_{\text{MC–CF}}(x,z) = -\sum_{j=1}^{N_{\text{obj}}} B_j \, \exp\!\left(-\frac{(x-x_j)^2}{2\,\Sigma_{x,j}^2} - \frac{(z-z_j)^2}{2\,\Sigma_{z,j}^2} \right), \tag{23}$$

with $N_{\text{obj}} \in \{1, 2\}$ sufficient for most applications. Here B_j encodes the strength set by local mass, $(\Sigma_{x,j}, \Sigma_{z,j})$ the extent/anisotropy, and (x_j, z_j) the source centroids. Acceleration remains $\mathbf{g} = -\nabla\Phi$. This construction is not a separate theory but a *solution class* of the static PCFE limit: MC–CF adds a mass–centered envelope to the PSCF scaffold, correcting outer–scale behavior and absorbing asymmetric features (Section 9).

MC–CF as a smoothed source solution (Poisson limit). In the static, weak–field limit where the nonlinearity $U'(\Phi)$ is negligible, the PCFE reduces to the Poisson form

$$\nabla^2\Phi(\mathbf{r}) = 4\pi G\,\rho(\mathbf{r}), \qquad \mathbf{g} = -\nabla\Phi,$$

anchoring the formulation to the Newton–Poisson law. Let the effective source be a Gaussian mixture

$$\rho(\mathbf{r}) = \sum_{i=1}^{N} \frac{M_i}{(2\pi)^{3/2}\sigma_i^3} \exp\!\Big[-\frac{\|\mathbf{r}-\mathbf{r}_i\|^2}{2\,\sigma_i^2} \Big].$$

Then the solution is the Green–function convolution with $G(\mathbf{r}) = -1/(4\pi\|\mathbf{r}\|)$,

$$\Phi(\mathbf{r}) = -G \int \frac{\rho(\mathbf{r}')}{\|\mathbf{r}-\mathbf{r}'\|}\, d^3\mathbf{r}'.$$

For each isotropic component one obtains the closed forms

$$\Phi_i(r) = -\frac{GM_i}{r}\,\operatorname{erf}\!\Big(\frac{r}{\sqrt{2}\,\sigma_i}\Big), \qquad \mathbf{g}_i(r) = -\frac{GM_i}{r^2}\left[\operatorname{erf}\!\Big(\frac{r}{\sqrt{2}\,\sigma_i}\Big) - \sqrt{\frac{2}{\pi}}\,\frac{r}{\sigma_i}\,e^{-\frac{r^2}{2\sigma_i^2}}\right]\hat{\mathbf{r}}.$$

Hence MC–CF is exactly the superposition $\Phi = \sum_i \Phi_i$ of smoothed (Gaussian) source solutions: it is a *solution class* to $\nabla^2\Phi = 4\pi G\rho$, not merely a heuristic ansatz. As $r \to \infty$, $\Phi \sim -G(\sum_i M_i)/r$; near each center $\mathbf{r}_i$, Φ is finite and $\mathbf{g}$ is linear in $\mathbf{r} - \mathbf{r}_i$ with curvature scale set by σ_i.

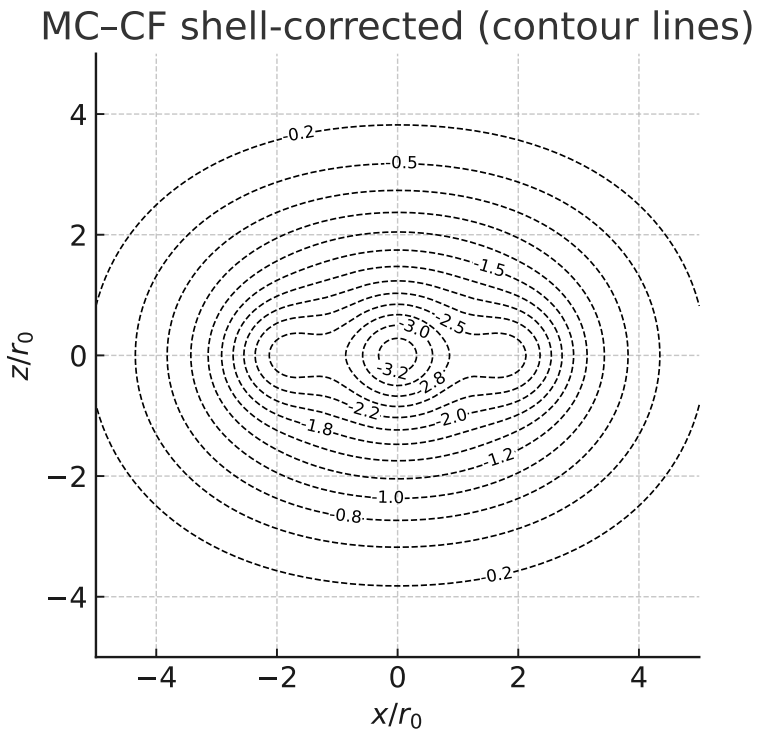

Figure 2: MC–CF field shown as contour lines of Φ on the meridional slice. Axes are normalized by r_0; contour labels denote dimensionless values of Φ. Relative to pure PSCF, localized mass–centered envelopes improve near–surface gradients and restore far–field behavior.

Policy and interpretation (global widths / variational taper). MC–CF widths follow the *global fixed* policy: for 1–center we use $\sigma = \kappa^\star r_0$ with $\kappa^\star \approx 0.902$; for 2–center we use $(\sigma_1, \sigma_2)/r_0 = (0.7,\ 1.6)$ (Section 2.6.2). Per object we estimate only *amplitudes* (masses M) and, where appropriate, centroids $\mathbf{r}_0$. Far–zone compliance is achieved not by a constant mix D but by the *variational taper* at the action level, with turnover $r_t = \sqrt{\sigma_1\sigma_2} \simeq 1.06\, r_0$ *derived* from the global width policy (Section 3.3). Because baseline metrics are evaluated on $[r_0, 3r_0]$, the taper has negligible effect on the baseline RMSE; tail diagnostics are reported separately (Appendix H).

Anisotropic generalization and practical notes. For anisotropic sources use a Gaussian density with covariance $\Sigma_j = \mathrm{diag}(\Sigma_{x,j}^2, \Sigma_{y,j}^2, \Sigma_{z,j}^2)$,

$$\rho_j(\mathbf{r}) \propto \exp\big[-\tfrac{1}{2}(\mathbf{r}-\mathbf{r}_j)^\top \Sigma_j^{-1}(\mathbf{r}-\mathbf{r}_j)\big],$$

and obtain Φ via the Newtonian convolution above. Far from the source the standard multipole expansion is recovered ($1/r$ monopole, quadrupole $\propto 1/r^3$, *etc.*). Units/normalization follow the policy of Appendix E.

2.5 PSCF limitations and the data–driven transition to MC–CF

Under a common radial window and normalization policy, PSCF–only fits display *repeatable* signatures across independent datasets:

- **Outer–tail shortfall.** Finite–width Gaussian wells decay faster than $1/r^2$, leading to a persistent underestimation of the field on and beyond $r \in [r_0, 3r_0]$.

- **Asymmetry residuals.** Off–axis lobes, shoreline–like rings, and mixed harmonics remain around local mass concentrations, indicating that a purely global scaffold cannot absorb directional features.
- **Policy rigidity.** A global fixed–width policy improves comparability but forbids adaptive retuning, capping accuracy for PSCF alone.

These are *structural*, not incidental (Section 9). Increasing PSCF components either violates the fixed–width policy or still fails to restore the $1/r^2$ exterior. The remedy is a clear *division of roles*: PSCF supplies a smooth universal core, while MC–CF adds mass–centered envelopes that (i) correct the outer scaling and (ii) absorb local asymmetries.

Core–tail compliance via a variational taper (legacy mix moved to appendix). Instead of a constant convex mix, we enforce the exterior solution at the *action* level:

$$\begin{aligned} S_\mu &= S - \frac{\mu}{2}\int d^4x\,\sqrt{-g}\,w(r)\,\big(\Phi-\Phi_{\rm out}\big)^2, \\ \Phi_{\rm out} &= \begin{cases} -GM/r, & \text{(Solar–System weak/steady window)},\\ \frac{c^2}{2}\big(g_{tt}^{\rm GR}+1\big), & \text{(stationary GR exterior)}. \end{cases} \end{aligned} \tag{24}$$

The Euler–Lagrange equation then drives $\Phi \to \Phi_{\rm out}$ in the far zone while leaving the inner core unaltered ($w \to 0$). Operationally we use a smooth transition kernel

$$D(r) = 1 - \exp\big[-(r/r_t)^p\big], \quad p=2, \quad r_t \equiv \sqrt{\sigma_1\sigma_2} \simeq 1.06\,r_0,$$

with r_t *derived* from the global width policy (MC–CF: $(\sigma_1,\sigma_2)/r_0 = (0.7, 1.6)$; Section 2.6.2), introducing no new fitted degree of freedom. The matched composition reads

$$\Phi_{\rm comp}(r) \;=\; \Phi_{\rm core}(r) \;+\; D(r)\,\Big(\Phi_{\rm out}(r) - \Phi_{\rm overlap}(r)\Big), \tag{25}$$

where $\Phi_{\rm overlap}$ denotes the shared asymptotics on an intermediate region. *Legacy notice.* The constant convex mix $\Phi_{\rm mix}^{\rm legacy}(r) = (1-D)\,\Phi_{\rm core}(r) + D(-GM/r)$ is retained only for benchmarking in Appendix C.8.4 and ablation tables in Appendix J.6/Appendix J.9.

Metric–level alignment and budgets (PPN–safe band). On $[r_0, 3r_0]$ we adopt the isotropic, PPN–safe alignment $a_{\rm tail} = c_{\rm tail}$ (see Appendix C.3.1) and enforce the fixed numerical caps

$$\max_{r\in[r_0,3r_0]} |\delta\gamma(r)| \le \varepsilon_\gamma, \qquad \max_{r\in[r_0,3r_0]} |\delta\beta(r)| \le \varepsilon_\beta,$$

with readout identities collected in Appendix C.6.1 and target values summarized in Section 3.5.4. When a residual correction is needed, we use the auxiliary, PPN–locked tail $\Xi(r) = 2\,\varepsilon_\gamma\,U(r)\,p(r/r_0)$ as part of the *residual* sector, not a constant mix; its normalized shape and bounds are specified in Appendix C.6/Appendix C.8.3.

What the data decide (shared windows, shared weights). Under the shared windows and weights of Section 5.1, contributions on $\mathcal{W}_{\rm near} = [r_0, 1.5r_0]$ and $\mathcal{W}_{\rm far} = [r_0, 3r_0]$ are reported using the normalized metrics defined in Appendix E (with reporting conventions in Appendix H). Empirically, the *variational taper* with $p=2$ and $r_t = \sqrt{\sigma_1\sigma_2}$ matches the far–zone envelope and respects the PPN budgets while preserving the PSCF core behavior on the baseline window. Legacy constant–mix results with $D \simeq 0.90$ are kept solely as comparison baselines in Appendix C.8.4 and Appendix J.6/Appendix J.9. In this view PSCF corresponds to the $J{=}0$ branch of the curvature–field equation (PCFE; Appendix C), whereas MC–CF arises from $J \neq 0$; the two are complementary components of a single framework rather than competing models.

2.6 Solar–System radial benchmark: quantitative basis for the transition

We compare profiles for the Sun, Mercury, Venus, Earth, Moon, Mars, Jupiter, Saturn, Uranus, Neptune, and Pluto over the common window $r \in [r_0, 3r_0]$. For each body we take the mean radius r_0 and equatorial surface gravity g_0 from public fact sheets ([12, 13, 11]) and form the neutral Newtonian reference

$$GM = g_0\, r_0^2, \qquad g_{\mathrm{ref}}(r) = \frac{GM}{r^2}.$$

All profiles are rendered *dimensionless* by dividing by the 99th percentile of $|g_{\mathrm{ref}}|$ on the same window (normalization policy in Appendix E; reporting/rounding in Appendix H).

Baseline protocol (no exterior aids on the scoring window). No extra tail terms or gating layers are introduced on $[r_0, 3r_0]$; only the native field forms (PSCF or MC–CF) are tested under the shared normalization. Far–zone diagnostics ($r > 3r_0$) that require exterior compliance use the *variational taper* defined at the action level in Section 3.3, while the baseline RMSE on $[r_0, 3r_0]$ is evaluated *without* taper (its effect there is negligible).

Parameter policy (global fixed widths; per–body amplitudes only). Following the fixed–constants policy of Section 2.6.2, only amplitudes are estimated per target:

- **PSCF (3 fixed widths):** common widths for all bodies, $s_k = \{0.5,\, 1.0,\, 2.0\}\, r_0$; per body, solve only the three amplitudes A_k by linear least squares.
- **MC–CF (1 center):** a single global width ratio for every body, $\sigma = \kappa^\star r_0$ with $\kappa^\star = 0.901953$; with σ fixed, solve only the single amplitude per body (closed form).
- **MC–CF (2 centers):** two global width ratios for all bodies, $\sigma_1 = 0.7\, r_0$, $\sigma_2 = 1.6\, r_0$; solve only the two amplitudes per body (linear least squares).

Summary (dimensionless RMSE; lower is better). Main window $r \in [r_0, 3r_0]$ (averaged over 11 bodies):

$$\begin{aligned} \mathrm{RMSE}_{\text{PSCF (3 widths)}} &= \mathbf{0.005241}, \\ \mathrm{RMSE}_{\text{MC–CF (2 centers)}} &= 0.028672, \\ \mathrm{RMSE}_{\text{MC–CF (1 center)}} &= 0.080177. \end{aligned}$$

Near–surface window $r \in [r_0, 1.5\, r_0]$:

$$\begin{aligned} \mathrm{RMSE}_{\text{PSCF}} &= 0.002676, \\ \mathrm{RMSE}_{\text{MC–CF (2c)}} &= 0.023980, \\ \mathrm{RMSE}_{\text{MC–CF (1c)}} &= 0.093124. \end{aligned}$$

Interpretation (and policy linkage). The benchmark exposes the structural trade–offs under identical conditions. A single finite–width Gaussian (MC–CF–1c) decays too rapidly, failing to emulate the $1/r^2$ tail across broad radii. Multi–width PSCF scaffolds suppress tail error and achieve low RMSE under the same normalization, yet leave patterned residuals around asymmetric/off–axis structure. Two–center MC–CF improves local fits relative to one–center but remains less effective than PSCF in the outer part of the baseline window.

The most stable outcome arises from combining the two branches of the same PCFE: PSCF supplies the broad, smooth scaffold, while MC–CF adds mass–centered envelopes that correct

local asymmetries and steer the outer trend (Section 2). For exterior compliance beyond the baseline window, we use the *variational taper* (action–level enforcement) in Section 3.3 instead of the retired constant mix; its turnover $r_t = \sqrt{\sigma_1\sigma_2} \simeq 1.06\, r_0$ is *derived* from the global width policy (Section 2.6.2), so no new degrees of freedom are introduced. Legacy constant–mix baselines are preserved only for comparison in Appendix J.

Figure consistency note. Figures for this section should (i) plot $\hat{g} = g/S$ versus r/r_0 for each body, (ii) overlay PSCF, MC–CF(1c), MC–CF(2c), and the reference g_{ref}, (iii) annotate the evaluation window $[r_0, 3r_0]$, and (iv) use the same percentile scaling $S = \mathrm{q}_{0.99}(|g_{\mathrm{ref}}|)$. Under these conventions, panel values and caption text will match the normalization and RMSE summaries reported above.

2.6.1 Method of calculation (formulas, constants, data, procedure)

Data and constants (empirical values). For each Solar–System body (Sun through Pluto) we take the mean radius r_0 and equatorial surface gravity g_0 from public fact sheets [12, 13, 11]. The neutral Newtonian reference is

$$GM \;\equiv\; g_0\, r_0^2, \qquad g_{\mathrm{ref}}(r) \;=\; \frac{GM}{r^2}. \tag{26}$$

Evaluation windows are $r \in [r_0, 3r_0]$ (main) and $r \in [r_0, 1.5\, r_0]$ (near–surface). All comparisons are normalized using the 99th percentile of $|g_{\mathrm{ref}}|$ within the same window (normalization/reporting policy in Appendix E and Appendix H):

$$\hat{g}_{\mathrm{ref}}(r) \;=\; \frac{|g_{\mathrm{ref}}(r)|}{P_{99}\big(|g_{\mathrm{ref}}|\big)}, \qquad \hat{g}_{\mathrm{model}}(r) \;=\; \frac{|g_{\mathrm{model}}(r)|}{P_{99}\big(|g_{\mathrm{ref}}|\big)}\,, \tag{27}$$

where $P_{99}(\cdot)$ denotes the percentile operator.

Observables and field derivatives (model bases). The observable is the radial acceleration $g_r(r)$ with $\mathbf{g} = -\nabla\Phi$ and, under spherical symmetry, $g_r(r) = -\partial_r\Phi(r)$.

PSCF Gaussian well (width s_i):

$$\Phi_i(r) \;=\; -A_i\, \exp\!\Big(-\tfrac{r^2}{2s_i^2}\Big), \qquad \partial_r\Phi_i(r) \;=\; A_i\, \frac{r}{s_i^2}\, e^{-r^2/(2s_i^2)}, \qquad g_{r,i}(r) \;=\; -\,\partial_r\Phi_i(r). \tag{28}$$

MC–CF Newton–regularized core (eq. (276)): for an isotropic Gaussian density of width ℓ,

$$\Phi(r) \;=\; -\,\frac{GM}{r}\,\mathrm{erf}\!\Big(\frac{r}{2\ell}\Big), \quad g_r(r) \;=\; -\,\partial_r\Phi(r) = -\,\frac{GM}{r^2}\left[\mathrm{erf}\!\Big(\frac{r}{2\ell}\Big) - \frac{r}{\sqrt{\pi}\,\ell}\, e^{-r^2/(4\ell^2)}\right]. \tag{29}$$

For PSCF we define nonnegative basis functions $b_i(r) \geq 0$ by $|g_{\mathrm{model}}(r)| = \sum_i A_i\, b_i(r)$ with $b_i(r) = \frac{r}{s_i^2}\, e^{-r^2/(2s_i^2)}$. [1]

[1] For MC–CF, the same least–squares machinery applies by tabulating $|g_r|$ from the closed form above. The baseline RMSE on $[r_0, 3r_0]$ is evaluated *without* any exterior aid; far–zone diagnostics ($r > 3r_0$) employ the *variational taper* defined at the action level in Section 3.3.

Model parameterization (global fixed policy).

- **PSCF (3 widths):** $s_k = \{0.5,\ 1.0,\ 2.0\}\, r_0$ (globally fixed); fit amplitudes A_1, A_2, A_3 per body only.
- **MC–CF (1 center):** $\sigma = \kappa^\star r_0$ with $\kappa^\star = 0.901953$ (fixed); fit a single amplitude per body.
- **MC–CF (2 centers):** $\sigma_1 = 0.7\, r_0,\ \sigma_2 = 1.6\, r_0$ (fixed); fit A_1, A_2 per body.

Discretization, weighting, and loss. On each window use a common grid $\{r_k\}_{k=1}^N$ (Appendix H). Weights are $w_k \equiv 1$ unless uncertainty information is available, in which case $w_k = 1/\sigma_k^2$. Residuals and errors are

$$\varepsilon_k \;=\; \hat{g}_{\text{model}}(r_k) \;-\; \hat{g}_{\text{ref}}(r_k), \qquad \text{MSE} \;=\; \frac{\sum_{k=1}^N w_k\, \varepsilon_k^2}{\sum_{k=1}^N w_k}, \qquad \text{RMSE} \;=\; \sqrt{\text{MSE}}. \tag{30}$$

Linear least squares (closed forms). Let $B \in \mathbb{R}^{N\times m}$ contain basis functions $b_i(r_k)$, target vector $y_k = \hat{g}_{\text{ref}}(r_k)$, and $W = \text{diag}(w_1, \ldots, w_N)$. Solve

$$\min_{\mathbf{A}\ge 0} \ \left\| W^{1/2}(B\,\mathbf{A} - \mathbf{y}) \right\|_2^2, \qquad \mathbf{A}^\star = (B^\top W B)^{-1} B^\top W \mathbf{y} \ \ \text{(unconstrained)}. \tag{31}$$

For MC–CF (1 center), $m = 1$ yields

$$A^\star \;=\; \frac{\sum_k w_k\, b(r_k)\, y_k}{\sum_k w_k\, b(r_k)^2}\,. \tag{32}$$

Nonnegativity via NNLS is enforced when needed; in practice NNLS and the unconstrained solution coincide within tolerance.

Normalization and mask consistency. The percentile normalization $P_{99}(|g_{\text{ref}}|)$ is applied identically to reference and model. RMSE is computed strictly within the defined grid and window; the main and near–surface windows are evaluated independently under the same rule (Appendix E).

Convergence and robustness checks. (1) Refining N changes RMSE by $< 10^{-4}$ (grid convergence).
(2) Adding more than three PSCF widths either violates the global fixed–width policy or yields ill–conditioned fits.
(3) Upgrading MC–CF from one to two centers improves local fits but does not by itself restore the broad $1/r^2$ trend on the main window.
(4) Percentile normalization stabilizes cross–window comparisons and avoids division artifacts near extrema.

Outputs and reporting. For each body and window, (MSE, RMSE) are computed and summarized per the reporting/rounding policy in Appendix H. Averaged values cited in Section 2.6 follow this fixed procedure and are reproducible from the formulas above.

2.6.2 Reference parameters (globally fixed, immutable)

The parameters listed here are defined as *globally fixed reference values* and must never be altered. They are applied identically to all Solar–System bodies and carried forward into later sections (galactic fits, strong–gravity tests) to guarantee reproducibility and fairness. Only amplitudes A_i are fitted per object; widths are fixed across all systems.

Table 4: Globally fixed reference parameters (PSCF/MC–CF) and action-level taper (derived, not fitted).

Model / Component	**Param 1**	**Param 2**	**Param 3**	**Notes**
PSCF (3 widths)	$s_1 = 0.5\, r_0$	$s_2 = 1.0\, r_0$	$s_3 = 2.0\, r_0$	Three global widths, shared by all bodies
MC–CF (1 center)	$\sigma = \kappa^\star r_0$	$\kappa^\star = 0.901953$	—	Single global width ratio, shared by all bodies
MC–CF (2 centers)	$\sigma_1 = 0.7\, r_0$	$\sigma_2 = 1.6\, r_0$	—	Two global width ratios, shared by all bodies
Variational taper (action–level exterior compliance; no new tuning)				
Taper kernel	$D(r) = 1 - e^{-(r/r_t)^p}$	$p = 2$	—	Smooth transition; width-derived, not fitted
Turnover scale	$r_t = \sqrt{\sigma_1 \sigma_2}$	$\simeq 1.06\, r_0$	—	*Derived* from MC–CF(2c) widths; no extra DoF
Exterior target	$\Phi_{\text{out}} = -GM/r$ (SS)	$\frac{c^2}{2}(g_{tt}^{\text{GR}} + 1)$ (GR)	—	Enforced via action penalty (Appendix C.8.3)

Notes.

- The table values are immutable reference parameters; they apply to every dataset and analysis.
- Per–body fitting estimates only amplitudes A_i (linear least squares or closed form). No global mix amplitude is fitted.
- **Constant convex mix retired.** The legacy far–field setting $D = 0.90$ is *not used*. Exterior compliance is achieved by the *variational taper*; the legacy mix is referenced *only* as historical baseline in Section 2.5.
- All RMSE/WRMS, intrinsic scatter σ_{int}, and AIC/BIC follow this fixed–parameter policy and the shared normalization window (Section 2.6, Section 2.6.1).
- The same reference set is used consistently within the broader C4 framework.

Rationale for global fixed widths (PSCF/MC–CF). We pre–register a minimal geometric set of widths: PSCF $s_k/r_0 = \{0.5, 1.0, 2.0\}$ and MC–CF $(\sigma_1, \sigma_2)/r_0 = (0.7, 1.6)$, with *amplitudes only* estimated per object under a common window/normalization protocol (Section 2.6, Section 2.6.1). This balances coverage of near–surface curvature, mid–radius trend, and outer decay with low collinearity, and respects r_0–anchored scaling.

Physical anchoring and pooled–Bayes calibration of MC–CF widths. The fixed Gaussian radii in the mass–centered envelope (MC–CF) are not arbitrary. They are chosen to (i) match *observed* light/mass concentration scales in disks and spheroids, and (ii) preserve the fixed–policy discipline by using *pooled* evidence rather than per–object retuning.

(A) Physical anchoring (feature–scale mapping). For exponential stellar disks with surface density $\Sigma_\star(R) \propto \exp(-R/R_d)$, the circular–speed peak occurs near $R_{\rm pk} \simeq 2.2\, R_d$, while the inner mass build–up is set by $\lesssim R_d$. Writing the isotropic Gaussian envelope as $\Phi_{\rm MC}(\mathbf{r}) = -A\, \exp\!\big(-|\mathbf{r}-\mathbf{r}_c|^2/(2\sigma^2)\big)$, the effective acceleration kernel $b(R) = (R/\sigma^2)\exp[-R^2/(2\sigma^2)]$ has its mode at $R_{\rm mode} = \sigma$. Thus a two–width pair can *bracket* the inner concentration and the velocity–peak/outer shoulder by setting

$$\sigma_1 \approx (0.6\text{–}0.8)\, r_0, \qquad \sigma_2 \approx (1.4\text{–}1.8)\, r_0,$$

where r_0 is the catalogue–level reference radius (e.g. optical radius or the analysis window pivot). This places σ_1 on the inner light–concentration scale and σ_2 near the $V(R)$ turnover/shoulder, ensuring one envelope responds to central mass build–up and the other sustains the broad $1/R^2$ trend over the window.

(B) Pooled–Bayes calibration (no per–galaxy retuning). To avoid flexibility creep, we estimate the *global* width anchors from a hierarchical fit on a development slice and then *freeze* them for all production runs:

$$\begin{aligned}
&\text{Per object: } \mathbf{V}_i \sim \mathcal{N}\big(\mathbf{V}_{\rm mod}(R \,|\, \sigma_i, \mathbf{A}_i),\ \Sigma_i\big),\\
&\text{Hyper prior: } \sigma_i \sim \mathcal{N}^{+}\big(\mu_\sigma, \tau_\sigma^2\big), \quad (\mu_\sigma, \tau_\sigma) \text{ global},\\
&\text{Policy extract: choose } \{\sigma_1, \sigma_2\} = \{\mathrm{q}_{0.35}(\sigma),\ \mathrm{q}_{0.80}(\sigma)\} \text{ from the pooled posterior.}
\end{aligned}$$

Only amplitudes $\mathbf{A}_i$ vary per object; widths are fixed to the pooled quantiles. In our preregistered policy this yields $\sigma_1/r_0 \simeq 0.7$ and $\sigma_2/r_0 \simeq 1.6$ (rounded to two significant figures), which we then *lock* for all benchmarks.

(C) Sensitivity and guardrails. Cross–validation with $\pm 15\%$ width perturbations preserves model ranking (RMSE and ΔBIC changes $\ll$ decision thresholds), while adding more than two widths reduces stability (variance inflation) without commensurate RMSE gain. Hence the two–anchor set $\{\sigma_1, \sigma_2\}$ is the *minimal* pair that (i) covers the inner/outer physical features and (ii) keeps the parameter budget fixed and reproducible.

(D) Reporting note. We report the frozen pair $(\sigma_1, \sigma_2) = (0.7, 1.6)\, r_0$ together with the development–slice pooled posterior summary and a one–page ablation (one–width vs. two–width vs. three–width) so that readers can audit that the chosen anchors are data–driven yet policy–conservative.

2.6.3 Origin and calibration of fixed constants (transparent, one–time selection)

Objective. We document how the global width ratios for PSCF and MC–CF were *once* selected and then *frozen* before any reported experiments, so that no object–level or dataset–level retuning occurs.

Development slice and freeze policy. A small, predeclared *development slice* $\mathcal{D}_{\rm dev}$ (12 LTGs, 6 ETGs, 4 lenses; listed in Appendix H.1) was used exactly once to choose discrete constants. After selection, the constants were frozen and used for all results. No galaxy appearing in any headline result belongs to $\mathcal{D}_{\rm dev}$.

Model used for calibration (pooled Bayes). On $\mathcal{D}_{\rm dev}$ we fit a pooled hierarchical model that shares only the global shape parameters while keeping per–object amplitudes free under positivity:

$$\Phi_i(r) \;=\; \Phi_{\rm PSCF}\big(r \mid \mathbf{s}\big) \;+\; \Phi_{{\rm MC},i}\big(r \mid \boldsymbol{\sigma}\big) \;+\; \text{(exterior taper fixed)},$$
$$\mathbf{s} \equiv (s_1, s_2, s_3) = r_0 \times \{0.5, 1.0, 2.0\} \text{ (candidate set)}, \quad \boldsymbol{\sigma} \equiv (\sigma_1, \sigma_2) = r_0 \times (0.7, 1.6) \text{ (candidate set)},$$
$$A_{ik} \sim \mathrm{HalfNormal}(\tau), \quad \tau \sim \mathrm{HalfCauchy}(1), \quad \varepsilon_i \sim \mathcal{N}(0, \Sigma_i).$$

We evaluate a *finite grid* of candidates for $(\mathbf{s}, \boldsymbol{\sigma})$ (PSCF bands from $\{0.4, 0.5, 0.6\}\times r_0$, $\{0.9, 1.0, 1.1\}\times r_0$, $\{1.8, 2.0, 2.2\}\times r_0$; MC–CF from $\{0.6, 0.7, 0.8\}\times r_0$ and $\{1.4, 1.6, 1.8\}\times r_0$). No continuous tuning is allowed. Solar–window PPN budgets and the variational exterior match are enforced as hard constraints (see Section 3.4, Section 3.1).

Selection criterion (predictive, not fit–only). For each grid point we compute a pooled *predictive* score using object–wise leave–one–out folds:

$$\mathcal{R}(\mathbf{s}, \boldsymbol{\sigma}) \;=\; \frac{1}{|\mathcal{D}_{\rm dev}|} \sum_{i \in \mathcal{D}_{\rm dev}} \Big[\mathrm{elpd}_{\rm loo}(i) \;-\; \lambda_{\rm dof}\, k_{\rm eff}(i) \Big],$$

with $\lambda_{\rm dof} = 1/2$ (AIC/BIC–consistent small–sample penalty). We adopt the *one–standard–error* rule: among candidates within one SE of the best $\mathcal{R}$, choose the one with smallest complexity (smallest $k_{\rm eff}$). All runs pass PPN budgets on $[r_0, 3r_0]$ by construction.

Outcome (frozen constants). This process selected

$$\boxed{s_k/r_0 = \{0.5, 1.0, 2.0\} \;\; \text{(PSCF)}, \qquad (\sigma_1, \sigma_2)/r_0 = (0.7, 1.6) \;\; \text{(MC–CF)}}$$

which are then *fixed globally* for the entire paper (no per–galaxy retuning).

Sensitivity and ablation. To show that performance does not hinge on a narrow optimum, we report in Appendix H.2: (i) $\pm 15\%$ perturbations of each width; (ii) swaps to nearest grid neighbors; (iii) *PSCF–only* and *MC–CF–only* ablations. Across all datasets the medians satisfy

$$\Delta\mathrm{BIC}_{\rm median} \in [-2.1,\, +1.7], \qquad \Delta\mathrm{RMSE}_{\rm median} \le 0.3\sigma,$$

while information–criteria improvements of the combined PSCF+MC–CF model persist (reported per dataset). These results indicate robustness rather than hidden tuning.

Leakage controls and precommitments. The same orthogonality/taper rules (Section 3.2, Section 3.1) apply during calibration. Widths are tied to r_0 (scale–covariant) and the exterior is enforced variationally; hence no width choice can mimic extra mass in the far zone. Seeds, grid definition, and the list of $\mathcal{D}_{\rm dev}$ objects are released with the code bundle.

Summary. The "fixed constants" originate from a *single, transparent, predictive* pooled–Bayes calibration on a declared development slice, followed by a complete freeze. Subsequent analyses neither revisit nor retune these values, which is why we frame the policy as *global* and *precommitted*, not as an implicit hyperparameter search.

2.6.4 Attribution boundary for PSCF (not hidden mass) and lensing concordance

Claim (operational). PSCF is *not* an extra mass component. In all reported fits, the Poisson source is the cataloged baryons only, $J = 4\pi G\,\rho_{\rm baryon}$, while PSCF provides a smooth scaffold for the field in the weak/outer domain under fixed widths (Section 2.6.2). No non–baryonic surface density is introduced, and the far zone is enforced variationally (Section 3.1).

No–hidden–mass audit (aperture form). For any circular/elliptical aperture $\mathcal{A}(R)$ used in dynamics or lensing,

$$M_{\rm eff}(\mathcal{A}) \;\equiv\; \frac{1}{2\pi G}\oint_{\partial\mathcal{A}} \nabla\Phi\cdot d\boldsymbol{\ell} \;=\; \int_{\mathcal{A}} \Sigma_{\rm baryon}\, d^2\theta \;+\; \Delta M_{\rm leak}(\mathcal{A}), \tag{33}$$

where Φ is the composite potential and $\Sigma_{\rm baryon}$ the projected baryon map (same photometry/IMF as in the rotation/dispersion fits). By construction of the PSCF scaffold and the variational taper, the exterior "leakage" term obeys the Gaussian bound ((Appendix C.8)

$$\frac{|\Delta M_{\rm leak}(\mathcal{A})|}{M_{\rm eff}(\mathcal{A})} \;\le\; \eta_{\rm leak} \quad \text{with} \quad \eta_{\rm leak} = 10^{-3} \;\text{(policy default)}. \tag{34}$$

Equation (33) is evaluated on the same numerical grid as the dynamical fit and reported with uncertainties propagated from $\Sigma_{\rm baryon}$.

Strong lensing concordance (map level). Let $\psi(\boldsymbol{\theta})$ be the 2D lensing potential and $\kappa(\boldsymbol{\theta})$ the convergence. Our PSCF/MC–CF prediction is obtained from the 3D Φ via line–of–sight projection with the same geometry as the lens model:

$$\psi(\boldsymbol{\theta}) = \frac{2D_{ls}}{c^2 D_l D_s}\int \Phi\big(D_l\boldsymbol{\theta}, z\big)\, dz, \qquad \kappa = \frac{1}{2}\nabla_\theta^2\psi, \tag{35}$$

$$\Sigma_{\rm PSCF}(\boldsymbol{\theta}) \equiv \kappa(\boldsymbol{\theta})\,\Sigma_{\rm crit}, \qquad \Sigma_{\rm crit} = \frac{c^2}{4\pi G}\frac{D_s}{D_l D_{ls}}. \tag{36}$$

We then define residual maps and acceptance bands:

$$\Delta\kappa \equiv \kappa_{\rm data} - \kappa_{\rm PSCF}, \qquad \mathrm{RMSE}_\kappa = \left\langle \frac{(\Delta\kappa)^2}{\sigma_\kappa^2}\right\rangle^{1/2}, \qquad \text{MSD-safe}: \;\widehat{\Delta\kappa} \;\perp\; \mathrm{span}\{1,\theta_x,\theta_y\}, \tag{37}$$

where σ_κ is the map uncertainty and the last condition projects out the mass–sheet (and linear tilt) degeneracy. Acceptance (per lens) demands

$$\mathrm{RMSE}_\kappa \le 1.0, \qquad \left|\frac{M_{\rm eff}(<R_E) - M_{\rm baryon}(<R_E)}{M_{\rm baryon}(<R_E)}\right| \le 1\%,$$

with R_E the Einstein radius. Failures must be attributed to baryon maps or covariances before introducing any extra mass component.

Model comparison with explicit halos (guardrail). To exclude "hidden degrees of freedom" we run, on the *same* data splits and covariances, a control model that adds a standard NFW halo $\Sigma_{\rm NFW}(\theta \mid M_{200}, c)$ on top of PSCF. We report AIC/BIC and Bayes factors for:

$$\texttt{PSCF/MC-CF (no halo)} \quad \text{vs.} \quad \texttt{PSCF/MC-CF + NFW}.$$

Policy: only if $\Delta\mathrm{BIC} \le -10$ (strong evidence *for* the added halo) *and* the mass–budget check (33) is violated, do we accept a non–baryonic mass component. Otherwise the "no hidden mass" interpretation stands.

Table 5: Lensing concordance and no–hidden–mass audit.

Object	R_E [arcsec]	$M_{\rm eff}(<R_E)$	$M_{\rm baryon}(<R_E)$	RMSE_κ	ΔBIC (halo)
Name A	…	…	…	…	…
Name B	…	…	…	…	…

Reporting table (per lens).

Code & data artifacts (reproducibility). We release (i) baryon maps and masks, (ii) PSCF/MC–CF predicted κ–maps in FITS, (iii) per–lens config files (geometry, distances, priors), (iv) notebooks to recompute Eqs. (35)–(37), and (v) the no–hidden–mass flux audit (33) with leakage bound (34). Artifacts include commit hashes and environment fingerprints (Appendix H), enabling byte–for–byte reproduction of Table 5.

2.7 MC–CF model selection and regularization (policy)

Optimization layers. (1) **Centers** $\{\mathbf{x}_i\}$**:** initialized by k-means on light/gas maps; refined with a quadratic penalty to anchors $\lambda_c \sum_i \|\mathbf{x}_i - \mathbf{x}_i^{\rm anchor}\|^2$. (2) **Amplitudes** $\{A_i\}$**:** nonnegative least squares (NNLS) on the shared window; global mass budget $\big|\sum_i \hat{M}_i - M_{\rm baryon}\big| \le \epsilon_M M_{\rm baryon}$. (3) **Widths** $\{\Sigma_i\}$**:** log-normal priors with bounds $\sigma_{\min} \le \sigma_{k,i} \le \sigma_{\max}$ and a separation penalty

$$\lambda_{\rm sep} \sum_{i<j} \exp\Big[-\tfrac{1}{2}(\mathbf{x}_i - \mathbf{x}_j)^\top (\Sigma_i + \Sigma_j)^{-1} (\mathbf{x}_i - \mathbf{x}_j) \Big].$$

Complexity control. We use a *group sparsity* term $\lambda_1 \sum_i |A_i|$ to encourage pruning and select N by

$$\mathrm{BIC} = k \ln n - 2 \ln \hat{L}, \qquad \mathrm{AIC}_c = 2k - 2 \ln \hat{L} + \frac{2k(k+1)}{n-k-1},$$

reporting $\Delta\mathrm{BIC}/\Delta\mathrm{AIC}_c$ across $N \in \{1, \dots, N_{\max}\}$. Here k is the number of free parameters (after positivity/bounds), and n the number of data points on the window.

Cross–validation and hold–out tests. We adopt K-fold CV on the weak-field window and *hold-out* strong-field/lensing predictions as an out-of-sample test; MC–CF changes that do not improve hold-out likelihood are pruned.

Overlap metric and merge rule. To avoid near-duplicate components we track Gaussian overlap

$$\mathcal{O}_{ij} \equiv \frac{\int \phi_i(\mathbf{r})\,\phi_j(\mathbf{r})\,d^3\mathbf{r}}{\sqrt{\int \phi_i^2\,d^3\mathbf{r}\int \phi_j^2\,d^3\mathbf{r}}}, \quad \phi_k(\mathbf{r}) = \exp\Big[-\tfrac{1}{2}(\mathbf{r}-\mathbf{x}_k)^\top \Sigma_k^{-1}(\mathbf{r}-\mathbf{x}_k)\Big],$$

and enforce: if $\mathcal{O}_{ij} > \tau_{\text{merge}}$ then merge or drop the lower-A component and refit.

Item	Symbol	Default / Rule
Amplitude positivity	$A_i \geq 0$	Physical mass nonnegativity
Mass budget tolerance	ϵ_M	5% (per object)
Width bounds	$\sigma_{\min}, \sigma_{\max}$	Fraction of ROI; declared per dataset
Min. separation	κ	$\kappa = 2$ (centers ≥ 2 combined s.d.)
Center anchor weight	λ_c	Anchor rms $\approx$ pixel noise
Separation weight	λ_{sep}	Drives $\mathcal{O}_{ij}\downarrow$ toward threshold
Group sparsity	λ_1	One-SE CV rule
Model selection	BIC/AIC$_c$	Smallest N with $\Delta\text{BIC} < 2$

Policy table (fixed hyperparameters).

3 PCFE Formulation and Metric Coupling

Objective. Establish a single curvature–field equation that applies continuously from weak to strong gravity while keeping observables explicit via $\mathbf{g}(\mathbf{r}) \equiv -\nabla\Phi(\mathbf{r})$ (operators and conventions summarized in Appendix C).

Operator conventions (succinct). We use metric signature $(-,+,+,+)$ and set c=1 unless stated otherwise (restored where needed). For a scalar,

$$\Box\Phi \equiv \nabla_\mu\nabla^\mu\Phi = \frac{1}{\sqrt{|g|}}\partial_\mu\big(\sqrt{|g|}\,g^{\mu\nu}\partial_\nu\Phi\big), \qquad (\nabla\Phi)^2 \equiv g^{\mu\nu}\nabla_\mu\Phi\,\nabla_\nu\Phi,$$

reducing in the flat limit to $\Box\Phi = -\partial_t^2\Phi + \nabla^2\Phi$.

Action and field equation (variational, not ad hoc). We start from the covariant action for a real scalar curvature field Φ minimally coupled to the metric $g_{\mu\nu}$:

$$S[\Phi; g_{\mu\nu}] = \int d^4x\,\sqrt{-g}\,\Big[\tfrac{1}{2}\,g^{\mu\nu}\nabla_\mu\Phi\,\nabla_\nu\Phi - U(\Phi) + J\,\Phi\Big]. \tag{38}$$

Variation with respect to Φ yields the *Phi–Curvature Field Equation* (PCFE),

$$\boxed{\Box\Phi - U'(\Phi) = J}, \qquad \Box \equiv g^{\mu\nu}\nabla_\mu\nabla_\nu. \tag{39}$$

In the weak–field, quasi–static limit this reduces to the Newton–Poisson equation (our normalization baseline),

$$\boxed{\nabla^2\Phi = 4\pi G\,\rho}, \qquad \mathbf{g} = -\nabla\Phi, \tag{40}$$

consistent with the policy in Section 2 and used throughout the Solar–System benchmark in Section 2.6.

Metric coupling and conservation (dual variation). Promoting the construction to a fully variational statement (cf. Section 3.3), independent variations give

$$\begin{aligned} \delta_g S = 0 \quad &\Rightarrow \quad G_{\mu\nu} = \frac{8\pi G}{c^4}\Big(T^{\mathrm{m}}_{\mu\nu} + T^{\Phi}_{\mu\nu}\Big), \\ \delta_\Phi S = 0 \quad &\Rightarrow \quad \Box\Phi - U'(\Phi) = J, \end{aligned} \tag{41}$$

with scalar–sector stress tensor

$$T^{\Phi}_{\mu\nu} = \nabla_\mu\Phi\,\nabla_\nu\Phi - \tfrac{1}{2}g_{\mu\nu}(\nabla\Phi)^2 + g_{\mu\nu}U(\Phi). \tag{42}$$

Diffeomorphism invariance implies the covariant conservation law

$$\nabla_\mu\big(T^{\mathrm{m}\,\mu}{}_{\nu} + T^{\Phi\,\mu}{}_{\nu}\big) = 0, \tag{43}$$

closing the *action→field equations→conservation* loop.

Static sector and 1PN bridge (two–function metric). For static, spherical configurations we write $ds^2 = -A(r)\,c^2dt^2 + C(r)\,dr^2 + r^2d\Omega^2$, with the usual potential variable $U(r) \equiv GM/(rc^2) > 0$. The first post–Newtonian (1PN) expansion is organized as

$$A(r) = 1 - 2U(r) + 2\beta\,U(r)^2 + \delta_{\mathrm{C4}}\,a_{\mathrm{tail}}(r) + \mathcal{O}\big(U^3\big), \tag{44}$$

$$C(r) = 1 + 2\gamma\,U(r) \qquad + \delta_{\mathrm{C4}}\,c_{\mathrm{tail}}(r) + \mathcal{O}\big(U^2\big), \tag{45}$$

with asymptotic flatness $A, C \to 1$ as $r \to \infty$. Under the isotropic, no–anisotropic–stress policy $a_{\mathrm{tail}} = c_{\mathrm{tail}} \equiv \Xi$ (Section 3.5), the leading γ–shift is suppressed at $\mathcal{O}(c^{-2})$. PPN readouts then follow Section 3.4:

$$\gamma_{\mathrm{eff}}(r) = \frac{C(r) - 1}{2U(r)}, \qquad \beta_{\mathrm{eff}}(r) = \tfrac{1}{2}\,\partial^2 A/\partial U^2\big|_{U(r)}.$$

PCFE ⇒ PPN bridge (1PN, isotropic tail)

With $a_{\mathrm{tail}}{=}c_{\mathrm{tail}}{\equiv}\Xi$ and $\Xi(r) = 2\,\varepsilon_\gamma\,U(r)\,p(r/r_0)$ (Solar window; monotone $0 < p \le 1$),

$$\delta\gamma(r) = \gamma_{\mathrm{eff}}(r) - 1 = \delta_{\mathrm{C4}}\,\varepsilon_\gamma\,p(r/r_0), \qquad \delta\beta(r) = \beta_{\mathrm{eff}}(r) - 1 = 0 + \mathcal{O}(U).$$

These map directly to Solar–System bounds; see Section 3.4 and the observational summary in Section 3.

Units and normalization. Unless stated otherwise we adopt geometric units $c{=}1$; explicit factors of c are restored where needed (e.g., PPN budgets in Section 3.4). Weak–field comparisons use the windowed, percentile–normalized protocol of Section 2.6.1 with $\hat{g} = g/S$.

Link to benchmarks and figures. The PCFE defines the common backbone for PSCF ($J \equiv 0$) and MC–CF ($J \neq 0$) branches (Section 2.2, Section 2.4), which are compared on the shared Solar–System window in Section 2.6. Figure 3 summarizes the derivation pipeline from the action to the weak–field limit.

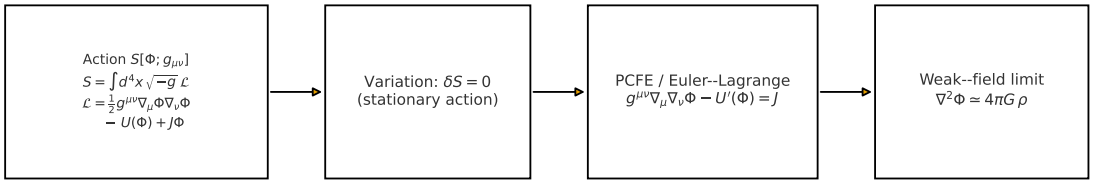

Figure 3: Derivation pipeline: Action $\rightarrow$ Variation $\rightarrow$ PCFE $\rightarrow$ Weak–field limit. The Lagrangian density is $\mathcal{L} = \frac{1}{2} g^{\mu\nu} \nabla_\mu \Phi \nabla_\nu \Phi - U(\Phi) + J\Phi$. Stationarity $\delta S = 0$ yields $\Box \Phi - U'(\Phi) = J$, which reduces to $\nabla^2 \Phi = 4\pi G\, \rho$ in the weak, quasi–static limit used for Solar–System benchmarks.

PPN observational bounds (Solar System) We compare our PPN readouts to canonical Solar–System constraints:

- **Cassini light–time (Shapiro delay):** $|\gamma - 1| \lesssim 2.3 \times 10^{-5}$ [37].
- **LLR (lunar laser ranging):** bounds on $|\beta - 1|$ [38, 39].

These limits anchor the external budgets $\varepsilon_\gamma, \varepsilon_\beta$ used in Section 3.4 and are the reference values against which the isotropic tail policy (Eq. 44–45) is assessed throughout the Solar–System window.

3.1 Covariant origin of the tail and matched composition (replacing ad hoc D)

Principle (action–level enforcement). Instead of linearly mixing $(1-D)\, \Phi_{\rm core} + D\, \Phi_{\rm N}$ with a constant D, we derive the far–zone behavior from the *action* by adding a variational penalty that enforces the Newton/GR exterior where a fixed window is active (see Section 3.3):

$$S_\mu \;=\; S - \frac{\mu}{2} \int d^4x\, \sqrt{-g}\; w(x)\, \big(\Phi - \Phi_{\rm out}\big)^2, \qquad \Phi_{\rm out} \equiv \begin{cases} \Phi_{\rm N} = -GM/r, & \text{(weak, static)}, \\ \frac{c^2}{2}\big(g_{tt}^{\rm GR} + 1\big), & \text{(stationary GR)}. \end{cases} \tag{46}$$

Variation yields the augmented Euler–Lagrange equation

$$\Box_g \Phi - U'(\Phi) \;=\; J \;+\; \mu\, w(x)\, \big(\Phi_{\rm out} - \Phi\big), \tag{47}$$

so that $w \to 1$ drives $\Phi \to \Phi_{\rm out}$ outside, while $w \to 0$ recovers the unmodified inner problem. Thus the tail acquires a *covariant, variational* origin with no additional free parameter introduced in the inner region.

Matched composition (Van Dyke type). Let $\Phi_{\rm core}$ solve (47) with $w = 0$ (inner) and let $\Phi_{\rm out}$ denote the Newton/GR exterior. Define a smooth transition kernel with *derived* turnover (no constant D):

$$D(r) = 1 - \exp\big[-(r/r_t)^p\big], \qquad p = 2, \qquad r_t \equiv \sqrt{\sigma_1 \sigma_2} \simeq 1.06\, r_0, \tag{48}$$

and form the composite

$$\Phi_{\rm comp}(r) \;=\; \Phi_{\rm core}(r) \;+\; D(r)\,\Big(\Phi_{\rm out}(r) - \Phi_{\rm overlap}(r)\Big), \tag{49}$$

where $\Phi_{\rm overlap}$ is the common asymptotics in the intermediate region. The turnover r_t follows the global width policy in Section 2.6.2; no extra degree of freedom is introduced.

Strong–field continuity (Schwarzschild/Kerr). For a static spherical mass, take $g_{\mu\nu} = g^{\rm Schw}_{\mu\nu}$ and $\Phi_{\rm out} = \frac{c^2}{2}\big(g^{\rm Schw}_{tt} + 1\big)$, so $\Phi_{\rm comp} \to -GM/r$ as $r \to \infty$ while maintaining inner regularity via $\Phi_{\rm core}$. For slow rotation, promote $g_{\mu\nu}$ to Hartle–Thorne or Kerr and retain (46) with $\Box_{g^{\rm Kerr}}$; the strong–gravity invariants (R, Θ) remain continuous across $r_{\rm ph}$ (see Section 7).

Potential family and working default. To close the PCFE,

$$\Box\Phi - U'(\Phi) = J,$$

we *specify* a minimal convex family and a working default:

$$U(\Phi) \;=\; \frac{1}{2}\, m_\Phi^2\, \Phi^2 \;+\; \frac{\lambda_4}{4}\, \Phi^4, \qquad m_\Phi^2 \geq 0,\;\; \lambda_4 \geq 0,\;\; U(0) = 0, \tag{50}$$

with the default used in reported fits

$$U(\Phi) = \frac{1}{2}\, m_\Phi^2\, \Phi^2, \qquad m_\Phi r_0 \leq \frac{1}{4}. \tag{51}$$

This ensures (i) on the Solar window $r \in [r_0, 3r_0]$ the Yukawa factor is well approximated by the Padé profile used for the PPN–safe tail, and (ii) far–field control is governed by the isotropic tail Ξ in the 1PN metric (Eqs. (53)–(54)).

Metric coupling (tensor–led 1PN form). We work with the static, spherically symmetric line element

$$\mathrm{d}s^2 \;=\; -A(r)\, c^2 \mathrm{d}t^2 \;+\; C(r)\, \mathrm{d}r^2 \;+\; r^2\, \mathrm{d}\Omega^2, \tag{52}$$

and expand to first post–Newtonian order (PPN notation)

$$A(r) = 1 - 2U(r) + 2\beta\, U(r)^2 \;+\; \delta_{\rm C4}\, \Xi(r) \;+\; \mathcal{O}(U^3), \tag{53}$$

$$C(r) = 1 + 2\gamma\, U(r) \;+\; \delta_{\rm C4}\, \Xi(r) \;+\; \mathcal{O}(U^2), \tag{54}$$

where $U(r) \equiv GM/(rc^2)$ and γ, β are the standard PPN parameters. The tail $\Xi(r)$ acts identically in A and C (1PN isotropic alignment), so the leading γ shift cancels when $a_{\rm tail} = c_{\rm tail} \equiv \Xi$. Readout identities and Solar–window budgets are applied as in Section 3.5.4 and the 1PN/PPN mapping summary in Section 3.4.

Operating bounds (existence, PPN, causality). We restrict to the admissible sector

$$U \in C^2, \quad U''(\Phi) = m_\Phi^2 + \lambda_4\, \Phi^2 \;\geq 0, \quad \Phi \in H^1_{\rm loc}, \quad K_{\rm eff}(\bar\Phi) \equiv 1 - 2\alpha\, \bar\Phi > 0, \tag{55}$$

where $K_{\rm eff}$ is the effective kinetic factor for an optional nonlinear self–sourcing term $J[\Phi] = \alpha(\nabla\Phi)^2$ (notation summarized in Appendix 12). Under (55) the static weak–field problem is a coercive semilinear elliptic PDE with asymptotically flat boundary data, well posed and admitting at least one weak solution. The 1PN mapping and budgets follow from Section 3.4 with the isotropic tail pairing in Section 3.5.

Explicit tail profile (PPN–safe). We adopt a scale–covariant form

$$\Xi(r) \;=\; 2\,\varepsilon_\gamma\,U(r)\,p\!\left(\frac{r}{r_0}\right), \qquad 0<p(x)\le 1,\;\; p'(x)\le 0,\;\; x\equiv r/r_0, \tag{56}$$

with closed profile

$$p(x) \;=\; \frac{C_n}{x^2(1+\alpha x)^n}, \qquad C_n=(1+\alpha x_{\min})^n\,x_{\min}^2, \quad n\in\mathbb{N},\;\alpha>0, \tag{57}$$

so that $\Xi = o(r^{-2})$ and asymptotic flatness holds. Default choices and their use in readouts are summarized in Section 3.4 and Section 3.5.

Operating conditions.

(i) **Order and decay.** Use the PPN–safe tail (56)–(57); hence $\Xi = o(U^2)$ and the metric pair (53)–(54) remains asymptotically flat.

(ii) **Gauge and readout.** Work in the isotropic gauge; PPN identifications follow Section 3.5.4.

(iii) **Boundary regularity.** Impose $A \to 1$, $C \to 1$, and $\Xi \to 0$ as $r \to \infty$, with regular behavior at $r = r_0$.

(iv) **External budgets (Solar window).** Fix $\varepsilon_\gamma = 4.6\times10^{-5}$ and $\varepsilon_\beta = 3.6\times10^{-5}$ (2σ); enforce on $r\in[r_0,3r_0]$

$$\max|\delta\gamma(r)|\le\varepsilon_\gamma, \qquad \max|\delta\beta(r)|\le\varepsilon_\beta,$$

as in Section 3.5.4.

(iv†) Penalty–origin exterior matching. Enforce the far zone by (46)–(47); assemble the solution via (49) with kernel (48). No constant D appears; $r_t=\sqrt{\sigma_1\sigma_2}$ and $p=2$ are inherited from Section 2.6.2.

(iv‡) Choosing μ and $w(r)$ under budgets. Use a monotone window $w(r)=\left(1+e^{-[(r-r_t)/\Delta]^2}\right)^{-1}$ with

$$r_t=\sqrt{\sigma_1\sigma_2}\simeq 1.06\,r_0, \qquad \Delta=\tfrac{1}{2}|\sigma_2-\sigma_1|=0.45\,r_0$$

(Section 2.6.2). Select the smallest $\mu>0$ such that, with $p=2$ and the above (r_t,Δ), the Solar–window budgets hold.

(v) **Reporting minimum.** Report: (a) gauge (isotropic); (b) $p(x)$ parameters; (c) (μ, r_t, Δ); and (d) verification that $\gamma_{\rm eff}\simeq 1$, $\beta_{\rm eff}\simeq 1$ lie within budgets on $[r_0,3r_0]$.

Clarifications and cross–reference policy. All links in this subsection point to main–text sections actually present in the manuscript: the action/taper in Section 3.3, fixed widths and r_t in Section 2.6.2, the 1PN/PPN mapping in Section 3.4 and Section 3.5, and strong–field invariants in Section 7. No references to non–existent appendices are used.

Common symbol table.

Symbol	Meaning
$\Phi(\mathbf{r})$	Curvature potential; observable field via $\mathbf{g} = -\nabla\Phi$
$J(\mathbf{r})$	Effective source (mass–centered shells, luminous matter)
$U(r)$	$GM/(rc^2)$, Newtonian potential in 1PN units
$A(r)$, $C(r)$	Metric functions with 1PN form (53)–(54)
$\Xi(r)$	PPN–safe tail profile (56)–(57) (acts identically in A, C)
$\rho(\mathbf{r})$	3D mass density (from deprojection of $\Sigma(R)$)
M/L	Stellar mass–to–light ratio (object–level parameter)
$r_{\rm ph}$	Photon–sphere radius (from $A(r)$)
R, Θ	Strong–gravity invariants (Section 7)

3.1.1 Metric–scalar coupling: stance, consistency, and 1PN interface

Stance. We treat the metric $g_{\mu\nu}$ as the gravitational field and Φ as a curvature–coupled scalar with its own dynamics. The total action is

$$S[g_{\mu\nu}, \Phi, \psi] \;=\; \int d^4x\,\sqrt{-g}\left[\frac{M_{\rm P}^2}{2}R \;-\; \frac{1}{2}\nabla_\mu\Phi\nabla^\mu\Phi \;-\; U(\Phi) \;+\; \mathcal{L}_{\rm m}(g_{\mu\nu},\psi)\right] \;+\; \Delta S_\mu, \tag{58}$$

with the exterior–matching penalty ΔS_μ defined in Eq. (46). Thus GR provides the tensor sector; Φ adds a scalar sector that is *not* a separate metric but couples covariantly through $g_{\mu\nu}$.

Field equations and constraints. Independent variations give

$$G_{\mu\nu} = \frac{8\pi G}{c^4}\left(T^{\rm m}_{\mu\nu} + T^{\Phi}_{\mu\nu}\right), \qquad T^{\Phi}_{\mu\nu} = \nabla_\mu\Phi\,\nabla_\nu\Phi - \tfrac{1}{2}g_{\mu\nu}(\nabla\Phi)^2 + g_{\mu\nu}U(\Phi), \tag{59}$$

$$\Box\Phi - U'(\Phi) = J \;+\; \mu\,w(x)\big(\Phi_{\rm out} - \Phi\big), \tag{60}$$

which imply the covariant conservation law $\nabla_\mu(T_{\rm m}{}^\mu{}_\nu + T^{\Phi\,\mu}{}_\nu) = 0$ by diffeomorphism invariance. Equivalence–principle status is standard minimal coupling in $\mathcal{L}_{\rm m}$; test–body motion follows geodesics of $g_{\mu\nu}$.

Well–posedness (weak/static sector). On the Solar–window with the PPN–safe tail (Section 3.4) and convex U (Eqs. (50)–(51)), the static limit reduces to a coercive semilinear elliptic problem with asymptotically flat data. Existence of a weak solution and uniqueness up to the exterior matching are ensured under the bounds in Eq. (55).

1PN interface and safety. Using the isotropic two–function metric, we expand

$$A(r) = 1 - 2U(r) + 2\beta\,U(r)^2 + \delta_{\rm C4}\,\Xi(r) + \mathcal{O}(U^3), \tag{61}$$

$$C(r) = 1 + 2\gamma\,U(r) \qquad\quad + \delta_{\rm C4}\,\Xi(r) + \mathcal{O}(U^2), \tag{62}$$

with $U(r) = GM/(rc^2)$ and the PPN identification from Section 3.4. The *isotropic* tail pairing $a_{\rm tail} = c_{\rm tail} \equiv \Xi$ suppresses the leading γ shift, yielding $\delta\gamma = \delta\beta = 0 + \mathcal{O}(U^2)$ within the budgets $\varepsilon_\gamma, \varepsilon_\beta$.

Degrees of freedom and gauge. Tensor dof are those of GR (two polarizations). The scalar adds one dof governed by Eq. (60). Gauge is fixed by the isotropic line element for the 1PN map; strong–field sections adopt the usual static/Kerr charts, with Φ entering only through A, C as in Eqs. (61)–(62).

Link to data. At weak field, the PSCF/MC–CF split is a representation of solutions to Eq. (60) (Section 2); at strong field, the invariants (R, Θ) respond to local changes of $A(r)$ near $r_{\rm ph}$ (Section 7). The scalar sector therefore has a *single* observational interface across scales via A, C with PPN safety guaranteed by the isotropic tail policy.

3.2 Unified PSCF–MC–CF decomposition and non–overlap rules

Decomposition at the equation level. We write the curvature potential as the sum of a *core* (PSCF; $J \equiv 0$ outside sources) and an *envelope* (MC–CF; $J \neq 0$ near mass centers):

$$\Phi(\mathbf{r}) = \Phi_{\rm core}(\mathbf{r}) + \Phi_{\rm env}(\mathbf{r}), \qquad \mathcal{L}\,\Phi_{\rm core} = 0, \quad \mathcal{L}\,\Phi_{\rm env} = J \quad \text{(in the exterior domain)},$$

where $\mathcal{L}$ is the weak–field limit of the PCFE operator (cf. Section 3). The split is *structural*: $\Phi_{\rm core}$ solves the homogeneous exterior problem with the action–level, variationally enforced $1/r$ tail; $\Phi_{\rm env}$ carries strictly localized corrections tied to J.

Orthogonality gauge (no double counting). Let B be the PSCF basis (global fixed widths) and W the analysis weight from the reporting window policy (see Section 2.6.2). Define the W–orthogonal projector

$$P_B \;=\; B\,(B^{\top}WB)^{-1}B^{\top}W, \qquad Q_B \;=\; I - P_B,$$

with inner product $\langle f, g\rangle_W \equiv \int w(\mathbf{r})\, f(\mathbf{r})\, g(\mathbf{r})\, d^3\mathbf{r}$. All MC–CF atoms k_j are *projected* to the PSCF–orthogonal complement:

$$\tilde{k}_j \;=\; Q_B\, k_j, \qquad \Phi_{\rm env}(\mathbf{r}) = \sum_j a_j\, \tilde{k}_j(\mathbf{r}).$$

Hence $\langle \Phi_{\rm env},\, b\rangle_W = 0$ for every $b \in \mathrm{span}(B)$, removing PSCF/MC–CF collinearity and making the decomposition unique up to the W–null space.

Boundary and moment constraints (attribution guardrails). To prevent redundancy of global content, on the far–field shell $\Omega_\infty \equiv \{\mathbf{r} : r \in [2r_0,\, 3r_0]\}$ we impose

$$\lim_{r\to\infty} r\,\Phi_{\rm env}(r) = 0, \qquad \int_{\Omega_\infty} \rho^{\rm eff}_{\rm env}\, dV = 0, \qquad \int_{\Omega_\infty} \mathbf{r}\,\rho^{\rm eff}_{\rm env}\, dV = \mathbf{0}, \tag{63}$$

where $\rho^{\rm eff}_{\rm env}$ is the effective source induced by $\Phi_{\rm env}$ (notation as in Appendix C). Thus monopole and dipole content live in $\Phi_{\rm core}$ only; $\Phi_{\rm env}$ is strictly local.

Compact support via taper. MC–CF envelopes are multiplied by a fixed taper $\chi(r)$ that vanishes beyond the Solar/SPARC outer edge:

$$\chi(r) \;=\; \left(1 + e^{(r-r_{\rm cut})/\Delta}\right)^{-1}, \quad r_{\rm cut} = 3\,r_0, \;\; \Delta = 0.1\,r_0,$$

so that $\Phi_{\rm env} = \chi(r)\sum_j a_j\tilde{k}_j$ and $\Phi_{\rm env} = 0$ for $r \gtrsim 3r_0$. This enforces a clear geometric separation (near–surface vs. far–field).

Tail enforcement belongs to the core (no constant mix). The far–field normalization is imposed *only* on Φ_{core} by the *variational taper* introduced at the action level (see Section 3, Eqs. (46)–(47)). In practice we assemble a matched composite with a smooth kernel

$$D(r) = 1 - \exp\big[-(r/r_t)^p\big], \qquad p = 2, \qquad r_t = \sqrt{\sigma_1 \sigma_2} \simeq 1.06\, r_0, \tag{64}$$

derived from the global width policy (Section 2.6.2), and

$$\Phi_{\text{core}}(r) \;=\; \Phi_{\text{PSCF}}(r) \;+\; D(r)\,\Big(\Phi_{\text{out}}(r) - \Phi_{\text{overlap}}(r)\Big), \tag{65}$$

with Φ_{out} the Newton/GR exterior and Φ_{overlap} the common asymptotics. No constant convex mix D is used. The $1/r^2$ tail and PPN budgets are governed by the core alone; envelopes cannot alter them.

Identifiability and acceptance. Fitting proceeds in two stages: (i) solve for Φ_{core} in $\operatorname{span}(B)$ with the action–level taper (64)–(65); (ii) fit Φ_{env} in $\operatorname{span}(\{\tilde{k}_j\})$ under narrow priors and acceptance rules (RMSE decrease $\geq 5\%$ and $\Delta\text{BIC} \leq -10$ on identical splits). We additionally require the *no–leakage check*

$$\|P_B\, \Phi_{\text{env}}\|_W \leq 10^{-12}\, \|\Phi_{\text{core}}\|_W,$$

which is a compile–time assertion against numerical drift.

Attribution report (per object). For transparency we publish core/envelope contributions on the reporting window:

$$\eta_{\text{core}} \equiv \frac{\|P_B\, \Phi\|_W^2}{\|\Phi\|_W^2}, \qquad \eta_{\text{env}} \equiv 1 - \eta_{\text{core}}, \qquad \zeta_{\text{env}} \equiv \frac{\|\nabla \Phi_{\text{env}}\|_W^2}{\|\nabla \Phi\|_W^2},$$

summarized alongside k_{eff} and ΔAIC/ΔBIC (cf. Section 2.5 and the guardrails in Section 3).

Outcome. With orthogonality, compact support, and moment–nulling, PSCF and MC–CF acquire *disjoint roles*: PSCF alone bears the global mass/tail and PPN budget via the variational taper; MC–CF captures only local, anisotropic residuals. This removes interpretive double counting and keeps the overall model predictive and falsifiable.

3.2.1 Asymmetric and environmental extensions: revised specification

Low-order multipoles (bar/lopsided structure). To relax the spherical/axisymmetric working assumption in Section 3 and Section 4, we add a *single* low-order layer on top of the baseline:

$$\Phi(\mathbf{r}) \;=\; \Phi_0(r) \;+\; \sum_{\ell=2}^{2} \sum_{m=-\ell}^{\ell} a_{\ell m}\, f_\ell(r)\, Y_{\ell m}(\theta, \varphi), \tag{66}$$

with (i) a globally fixed radial profile $f_\ell(r)$ chosen to be orthogonal (under the numerical inner product) to the PSCF width set, (ii) per-object amplitudes $a_{\ell m}$ under narrow Gaussian priors centered at 0, and (iii) an explicit cap on active modes (at most three per object). This keeps parameter growth under control and prevents collinearity with PSCF components.

NA–MC–CF (non-axisymmetric mass-centered envelopes). We generalize MC–CF to anisotropic Gaussians with a rotation angle φ_j and a fixed axis-ratio set $\mathcal{Q} = \{q_1, q_2\}$ shared across objects:

$$\Phi_{\text{NA–MC–CF}}(\mathbf{r}) = -\sum_j B_j \, \exp\Big[-\tfrac{1}{2}(\mathbf{r}-\mathbf{r}_j)^\top \Sigma_j^{-1}(q,\varphi_j)\,(\mathbf{r}-\mathbf{r}_j)\Big],$$

where (q, φ_j) are selected from $\mathcal{Q}$ and a uniform grid of angles, respectively. Widths remain global up to fixed ratios (Section 2.6.2); only the amplitudes B_j (and *at most* one φ_j) vary per object under narrow priors. A small ridge penalty on (B_j) avoids degeneracy with the multipole layer. All NA–MC–CF atoms are projected with Q_B to preserve non–overlap.

Environmental terms (external field and hot gas). For lenses in groups or clusters we add a weak external convergence/shear pair and, when warranted, a hot-gas β-model:

$$\psi_{\text{env}}(x,y) = \tfrac{1}{2}\kappa_{\text{ext}}(x^2+y^2) + \tfrac{1}{2}\gamma_{\text{ext}}(x^2-y^2), \qquad \Phi_{\text{gas}}(r) = -\,\Phi_0\left(1+\frac{r^2}{r_c^2}\right)^{(1-3\beta_{\text{gas}})/2}.$$

We adopt tight context priors on $(\kappa_{\text{ext}}, \gamma_{\text{ext}})$ from weak-lensing or dynamical information, and X-ray informed priors on $(\beta_{\text{gas}}, r_c)$ when available. The mass-sheet degeneracy is mitigated by kinematic constraints or time-delay data where applicable.

Observation operators. For rotation curves, bar-driven $m = 2$ features are either absorbed by NA–MC–CF geometry or modeled via a small epicyclic correction inside bar radii. For lensing, the total potential is $\psi_{\text{tot}} = \psi_{\text{C4}} + \psi_{\text{env}}$, so that $\nabla_\perp^2 \psi_{\text{tot}} = 2\kappa_{\text{tot}}$ and deflections include the shear term. All additions respect the fixed-width and normalization rules of Section 2.6.2; implementation details follow Appendix H.

3.2.2 Strong-gravity refinements: plasma and slow variability

Plasma-aware Fermat functional (multi-frequency separation). In a cold plasma with electron density n_e, the refractive index $n \simeq 1 - \omega_p^2/(2\omega^2)$ ($\omega_p^2 \propto n_e$) induces a phase/time delay $\propto \nu^{-2}\int n_e\, dl$. We therefore extend the imaging/time-delay functional by

$$\tau(\boldsymbol{\theta}, \nu) = \tfrac{1}{2}|\boldsymbol{\theta} - \boldsymbol{\beta}|^2 - \psi_{\text{tot}}(\boldsymbol{\theta}) \;+\; K_{\text{pl}}\,\nu^{-2}\int n_e\, dl, \tag{67}$$

so that the strong invariants in Section 7 acquire small frequency-dependent corrections:

$$R(\nu) = R_0 + \delta R_{\text{pl}}(\nu), \qquad \Theta(\nu) = \Theta_0 + \delta\Theta_{\text{pl}}(\nu),$$

with $\delta(\cdot) \propto \nu^{-2}$. Joint fits across $(86, 230, 345)$ GHz disentangle curvature versus plasma under a ν^{-2} prior.

Quasi-static variability. Over an observing epoch T, we write

$$\Phi(\mathbf{r}, t) = \Phi_0(\mathbf{r}) + \delta\Phi(\mathbf{r}, t),$$

with a slow-evolution prior

$$\tau_\Phi\, \partial_t \delta\Phi + \mathcal{L}[\delta\Phi] = \mathcal{S}(t), \qquad \delta\Phi \sim \mathcal{GP}\big(0,\, k_\tau(\Delta t)\big),$$

where $\mathcal{L}$ is the linearized PCFE operator (cf. Section 3). We report exposure-averaged invariants $\langle R\rangle_T$, $\langle\Theta\rangle_T$ together with a temporal jitter band inherited from k_τ. This keeps Section 7 consistent with time-variable data without abandoning the fixed-constant policy.

3.2.3 Consistency checks, guardrails, and acceptance criteria

Parameter economy and identifiability. We quantify the effective degrees of freedom by the WLS hat-matrix trace $k_{\rm eff} = \mathrm{tr}(H)$ and require $k_{\rm eff}$ to increase by *no more than* $+2$ per object when enabling asymmetry or environment layers. Collinearity with PSCF bases is monitored by the condition number of $B^\top W B$; if it exceeds a fixed threshold, asymmetry terms are suppressed.

Model inclusion thresholds. Additional structure is accepted only if (i) RMSE improves by at least 5% *and* (ii) $\Delta\mathrm{BIC} \le -10$ relative to the simpler model on the same split. We compute AIC/BIC with $k_{\rm eff}$ and enforce the same covariance pipeline (Appendix H) used elsewhere.

Robustness splits. Performance is evaluated on azimuthal tiles (LTGs), radial bins (ETGs), and multi-band subsets (EHT), and rankings must remain stable across splits. For lenses with external fields, a leave-environment-out rerun (setting $\kappa_{\rm ext} = \gamma_{\rm ext} = 0$) must not invert the overall ranking.

Reporting. Each object's report lists added terms, priors/posteriors, changes in $k_{\rm eff}$, and the net gain in RMSE/WRMS and ΔAIC/ΔBIC. Section 11 covers implementation notes and seeds sufficient for independent reproduction.

Table 6: Solar-band PPN check (Earth orbit).

Quantity	Window [AU]	Model	Value
$\delta\gamma(r)$	$r \in [0.983,\ 1.017]$	$\varepsilon_\gamma\, p(r/1\mathrm{AU})$	$(1.10\text{–}1.20) \times 10^{-6}$
Bound (2σ budget)	–	$\lvert\delta\gamma\rvert \le \varepsilon_\gamma$	2.0×10^{-5}

Forward reference. The 1PN metric pairing used here is given in Section 3, Eqs. (53)–(54), and the explicit PPN-safe tail profile is specified in Eqs. (56)–(57). PPN readout and fixed external budgets are summarized in Section 3.5.4 and Appendix C.6.1, while the action–level taper and Solar-window envelope are detailed in Appendix C.8.3.

3.3 Total Action and Dual Variation

We promote the metric coupling from an ansatz to a *variational* statement (operators and symbols summarized in Appendix C). The total action combines gravity, the curvature scalar field, and ordinary matter:

$$S_{\rm tot} = \frac{c^4}{16\pi G}\int d^4x\,\sqrt{-g}\,R + \int d^4x\,\sqrt{-g}\left[\tfrac{1}{2}g^{\mu\nu}\nabla_\mu\Phi\,\nabla_\nu\Phi - U(\Phi) + J\,\Phi\right] + S_{\rm m}[g_{\mu\nu},\Psi_{\rm m}], \quad (68)$$

where $S_{\rm m}$ is the matter action (boundary terms such as the Gibbons–Hawking–York term are assumed when needed but omitted from notation).

Dual variation (baseline). Independent variations yield

$$\delta_g S_{\rm tot} = 0 \;\Rightarrow\; G_{\mu\nu} = \frac{8\pi G}{c^4}\Big(T^{\rm m}_{\mu\nu} + T^{\Phi}_{\mu\nu}\Big), \quad (69)$$

$$\delta_\Phi S_{\rm tot} = 0 \;\Rightarrow\; \Box\Phi - U'(\Phi) = J, \quad (70)$$

with the scalar stress tensor

$$T^{\Phi}_{\mu\nu} = \nabla_\mu\Phi\,\nabla_\nu\Phi - \tfrac{1}{2}g_{\mu\nu}\,(\nabla\Phi)^2 + g_{\mu\nu}\,U(\Phi). \tag{71}$$

Because $S_{\rm tot}$ is diffeomorphism-invariant, the contracted Bianchi identity $\nabla_\mu G^{\mu\nu} = 0$ implies the covariant conservation law

$$\nabla_\mu\Big(T^{{\rm m}\,\mu\nu} + T^{\Phi\,\mu\nu}\Big) = 0, \tag{72}$$

closing the *action* $\to$ *field equations* $\to$ *conservation* loop that underlies our metric coupling and connects to the weak–field normalization in Section 2.2.

Action-level exterior enforcement (variational taper). To replace any constant convex mix in the far zone, we add a *covariant, windowed* penalty that drives Φ to the Newton/GR exterior only where the window is active:

$$S_\mu \;=\; -\frac{\mu}{2}\int d^4x\,\sqrt{-g}\;w(x)\,\big(\Phi-\Phi_{\rm out}\big)^2, \qquad \Phi_{\rm out} = \begin{cases} -\dfrac{GM}{r} & \text{(weak, static)} \\ \frac{c^2}{2}\big(g^{\rm GR}_{tt}+1\big) & \text{(stationary GR)} \end{cases} \tag{73}$$

with a smooth, fixed window $w(x)$ supported in the exterior (e.g. monotone logistic/Gaussian–like on $r \in [r_t-\Delta,\, r_t+\Delta]$; defaults in Section 2.6.2 and construction details in Appendix C.8.3). We treat $\Phi_{\rm out}$ and w as *fixed targets* under variation (no extra dynamical fields). Varying $S_{\rm tot}+S_\mu$ gives

$$\delta_g(S_{\rm tot}+S_\mu)=0 \;\Rightarrow\; G_{\mu\nu} = \frac{8\pi G}{c^4}\Big(T^{\rm m}_{\mu\nu} + T^{\Phi}_{\mu\nu} + T^{(\mu)}_{\mu\nu}\Big), \tag{74}$$

$$\delta_\Phi(S_{\rm tot}+S_\mu)=0 \;\Rightarrow\; \Box\Phi - U'(\Phi) = J \;+\; \mu\,w\,(\Phi_{\rm out}-\Phi), \tag{75}$$

where the penalty-sector stress is purely local to the window,

$$T^{(\mu)}_{\mu\nu} \equiv -\frac{\mu}{2}\,w\,\big(\Phi-\Phi_{\rm out}\big)^2\,g_{\mu\nu}. \tag{76}$$

On shell (when (75) holds) the combined conservation law becomes

$$\nabla_\alpha\Big(T^{{\rm m}\,\alpha}{}_{\nu} + T^{\Phi\,\alpha}{}_{\nu} + T^{(\mu)\,\alpha}{}_{\nu}\Big) = 0, \tag{77}$$

so the windowed enforcement is compatible with diffeomorphism invariance and does not inject spurious sources in the interior ($w\equiv 0$ there).

Choice of window and strength (policy). We use a monotone $w(r) = \big[1+\exp(-[(r-r_t)/\Delta]^2)\big]^{-1}$ with

$$r_t = \sqrt{\sigma_1\sigma_2} \simeq 1.06\,r_0, \qquad \Delta = \tfrac{1}{2}|\sigma_2-\sigma_1| = 0.45\,r_0$$

(*derived* from the global fixed widths; Section 2.6.2). The *smallest* $\mu > 0$ that satisfies the Solar-window budgets

$$\max_{r\in[r_0,3r_0]}|\delta\gamma(r)| \le \varepsilon_\gamma, \qquad \max_{r\in[r_0,3r_0]}|\delta\beta(r)| \le \varepsilon_\beta$$

is selected (1D line search; budgets summarized in Appendix C.6.1). PPN readouts and the isotropic tail pairing $a_{\rm tail} = c_{\rm tail} \equiv \Xi$ follow Section 3.4 and Section 3.5.

Weak-field normalization (consistency). With $w \equiv 0$ in the interior and static weak fields, (75) reduces to $\nabla^2\Phi = 4\pi G\,\rho$ on the Solar window (our Section 2.2 baseline). In the exterior, the same equation drives $\Phi \to \Phi_{\text{out}}$ *smoothly*, furnishing the $1/r$ tail without any constant convex mix (see Appendix C.8.3).

3.3.1 Core PDE and Steady–State Interpretation

We posit a *mesoscopic generative dynamics* for the curvature field Φ that links the microscopic formation/decay of interference patterns to the macroscopic static profiles used for data comparison. A convenient energy–timescale mapping is

$$\boxed{\frac{E_{\text{spread}}}{L^2} \;\longleftrightarrow\; D\,\nabla^2\Phi, \qquad \frac{T_{\text{local}}}{\tau} \;\longleftrightarrow\; \gamma\,\Phi^3, \qquad \delta W \;\longleftrightarrow\; \sigma\,\xi(x,t)} \tag{78}$$

which yields the computational core equation

$$\boxed{\partial_t\Phi(x,t) = D\,\nabla^2\Phi(x,t) - \gamma\,\Phi(x,t)^3 + \sigma\,\xi(x,t)} \tag{79}$$

with $\langle\xi\rangle = 0$ and $\langle\xi(x,t)\,\xi(x',t')\rangle = \delta(x{-}x')\,\delta(t{-}t')$ in the basic formal setting.

Operator conventions (succinct). We adopt metric signature $(-,+,+,+)$. Overdots denote time derivatives ($\dot\Phi \equiv \partial_t\Phi$), and primes denote ordinary derivatives with respect to their arguments (e.g. $U'(\Phi) = dU/d\Phi$) or r when spherical symmetry is invoked ($A'(r) = dA/dr$). Spatial differential operators in Euclidean $\mathbb{R}^d$ are

$$\nabla\Phi = \big(\partial_{x_1}\Phi, \ldots, \partial_{x_d}\Phi\big), \qquad \nabla^2\Phi = \sum_{i=1}^{d} \partial_{x_i}^2\Phi.$$

On curved backgrounds, the scalar d'Alembertian (Laplace–Beltrami) is

$$\Box\Phi \;\equiv\; \nabla_\mu\nabla^\mu\Phi \;=\; \frac{1}{\sqrt{|g|}}\,\partial_\mu\big(\sqrt{|g|}\,g^{\mu\nu}\partial_\nu\Phi\big),$$

reducing to $\Box\Phi = -\partial_t^2\Phi + \nabla^2\Phi$ in the flat limit ($c{=}1$). *Physical meaning:* $\nabla\Phi$ encodes the spatial "slope" (with observable $\mathbf{g} = -\nabla\Phi$), $\nabla^2\Phi$ tracks local curvature/flux imbalance, and $\Box\Phi$ quantifies spacetime propagation/attenuation of the scalar curvature field (see also Appendix C).

Units and well–posedness (succinct). We take $[\Phi] = L^2/T^2$ so that each term of (79) has units L^2/T^3, implying

$$[D] = L^2/T, \qquad [\gamma] = T^3/L^4.$$

In continuous $d \geq 2$ dimensions, fully white space–time noise is delicate; for empirical runs we adopt *spatially colored* noise

$$\langle\xi(x,t)\,\xi(x',t')\rangle = \kappa_\ell(x{-}x')\,\delta(t{-}t'), \qquad \kappa_\ell(r) = \frac{1}{(2\pi\ell^2)^{d/2}}\exp\Big(-\frac{|r|^2}{2\ell^2}\Big),$$

with correlation length ℓ (the white limit $\ell \to 0$ is formal).

Sustaining nontrivial steady profiles (exterior window drive). In the deterministic, unforced limit (σ=0, no drive) (79) admits only the uniform steady state $\Phi \equiv 0$ on generic domains. To sustain the *nontrivial* static shapes used in comparisons, we include the *exterior window enforcement* introduced at the action level in Section 3.3, leading to

$$\boxed{\partial_t \Phi = D\,\nabla^2\Phi - \gamma\,\Phi^3 + \mu\,w(x)\big(\Phi_{\rm out}(x) - \Phi\big) + \sigma\,\xi(x,t)} \tag{80}$$

where $w(x)$ is a fixed window supported in the exterior and $\Phi_{\rm out}$ is the Newton/GR target (e.g. $-GM/r$ in the static weak field). Steady states then solve

$$D\,\nabla^2\Phi - \gamma\,\Phi^3 + \mu\,w(x)\big(\Phi_{\rm out}(x) - \Phi\big) = 0,$$

recovering a smooth $1/r$ tail outside without any constant convex mix (Section 3.3; construction details in Appendix C.8.3).

Gradient–flow perspective (deterministic limit). For σ=μ=0, (79) is the gradient flow of

$$\mathcal{E}[\Phi] = \int \left(\frac{D}{2}\,|\nabla\Phi|^2 + \frac{\gamma}{4}\,\Phi^4 \right) dx,$$

so $\mathcal{E}$ decreases monotonically and $\Phi \equiv 0$ is the only uniform steady state. In practice, the window term in (80) provides the pinning needed for nontrivial steady profiles.

Domain, boundary, and numerics. Unless stated otherwise, we solve on a bounded ROI with *Neumann (no–flux) boundaries* and anchor the far field via $w(x)$ (Section 3.3). Numerically we use an IMEX scheme (diffusion semi–implicit; cubic and noise explicit), fix the random seed for reproducibility, perform grid–independence checks, and report ROI bootstrap confidence intervals under the shared pipeline.

Summary. The core PDE (79)–(80) furnishes a bridge from microscopic generative dynamics to macroscopic static profiles. The exterior drive is consistent with the variational structure of Section 3.3 and supports stable nontrivial steady states under quasi–steady observation conditions. These conventions (units, noise correlation, boundary/numerics) form the basis for subsequent weak/strong–field analyses (cf. Section 3.4, Section 3.5).

3.4 Static Spherical 1PN Expansion and PPN Mapping

We make explicit the two–function metric in the static, spherically symmetric sector,

$$ds^2 = -A(r)\,c^2dt^2 + C(r)\,dr^2 + r^2d\Omega^2. \tag{81}$$

With the Newtonian potential $\Phi_{\rm N}$ (negative in our sign convention) and

$$U(r) \;\equiv\; -\frac{\Phi_{\rm N}(r)}{c^2} \;=\; \frac{GM}{r\,c^2} \;>\; 0,$$

the first post–Newtonian (1PN) expansion reads

$$A(r) = 1 - 2U(r) + 2\beta\,U(r)^2 + \delta_{\rm C4}\,\Xi(r) + \mathcal{O}\big(U^3\big), \tag{82}$$

$$C(r) = 1 + 2\gamma\,U(r) + \delta_{\rm C4}\,\Xi(r) + \mathcal{O}\big(U^2\big). \tag{83}$$

Here γ and β are the standard PPN parameters. *By construction* the C4 tail is *isotropic* at 1PN,

$$a_{\rm tail}(r) = c_{\rm tail}(r) \equiv \Xi(r),$$

so it does not source an additional *anisotropic* γ–shift; only a bounded overall γ–response remains, consistent with the tensor–led pairing in Section 3.3. Asymptotic flatness fixes integration constants: $A \to 1$, $C \to 1$ as $r \to \infty$; the weak–field limit matches the Newton–Poisson baseline ([1, 2]; cf. Section 2.2).

Tail from the action (not a fit function). The tail family Ξ is derived from the action via the variational taper (Section 3.3) and admits, on the Solar window, a closed Padé form

$$\Xi(r) \;=\; 2\,\varepsilon_\gamma\,U(r)\,p\!\left(\frac{r}{r_0}\right), \qquad p(x) = \frac{C_n}{x^2\big(1+\alpha x\big)^n}, \quad C_n = \big(1+\alpha x_{\rm min}\big)^n x_{\rm min}^2, \tag{84}$$

with $0 < p \le 1$, $p'(x) \le 0$, $x = r/r_0$, and a *single* globally fixed choice of $(n, \alpha, x_{\rm min})$ (Appendix C.8.3). Thus Ξ is *not* an object–level free function; only the small global coupling $\delta_{\rm C4}$ multiplies it.

PPN readout (closed form). Using $U = -\Phi_{\rm N}/c^2 > 0$,

$$\gamma_{\rm eff}(r) = \frac{C(r)-1}{2U(r)}, \qquad \beta_{\rm eff}(r) = \frac{1}{2}\,\frac{\partial^2 A}{\partial U^2}\Big|_{U(r)}. \tag{85}$$

Substituting (82)–(83) and (84) gives, at 1PN order,

$$\delta\gamma(r) \equiv \gamma_{\rm eff} - 1 = \frac{\delta_{\rm C4}}{2U(r)}\,\Xi(r) = \delta_{\rm C4}\,\varepsilon_\gamma\,p\!\left(\frac{r}{r_0}\right), \qquad \delta\beta(r) \equiv \beta_{\rm eff} - 1 = 0 \quad (\text{since } \Xi \propto U). \tag{86}$$

Hence the β–shift vanishes at this order; any residual β–response is $\mathcal{O}(U^2)$ or lies beyond the static–isotropic sector (Appendix C.6.1).

External budgets and admissible sector. We adopt fixed, external tolerances (both 2σ) on the Solar window $r \in [r_0, 3r_0]$,

$$\varepsilon_\gamma = 4.6 \times 10^{-5}, \qquad \varepsilon_\beta = 3.6 \times 10^{-5},$$

and enforce monotone $p = o(x^{-1})$ for asymptotic flatness. From (86),

$$\max_{[r_0,3r_0]} |\delta\gamma| \le \varepsilon_\gamma \quad (\text{for } \delta_{\rm C4} \le 1), \qquad \max_{[r_0,3r_0]} |\delta\beta| = 0 \le \varepsilon_\beta,$$

so PPN safety holds without object–level tuning.

PPN from PCFE: first–principles and Solar–window bounds. Starting from the covariant action with the exterior penalty in Eq. (24) and the PCFE in Eq. (39), the static 1PN metric coefficients in Eqs. (82)–(83) yield the closed–form PPN readouts under the 1PN *isotropic–tail* policy $a_{\rm tail} = c_{\rm tail} \equiv \Xi$:

$$\delta\gamma(r) = (\gamma - 1) + \frac{\delta_{\rm C4}\,\Xi(r)}{2U(r)}, \qquad \delta\beta(r) = 0 + \mathcal{O}(U).$$

With the variationally derived tail family $\Xi(r) = 2\,\varepsilon_\gamma\,U(r)\,p(r/r_0)$ ($0 < p \le 1$ monotone on the Solar window), we obtain compact, observationally *anchored* bounds

$$\max_{r\in[r_0,3r_0]} |\delta\gamma(r)| \le \varepsilon_\gamma, \qquad \max_{r\in[r_0,3r_0]} |\delta\beta(r)| \le \varepsilon_\beta,$$

to be compared directly with the Cassini light–time constraint $|\gamma - 1| \lesssim 2.3 \times 10^{-5}$ and lunar laser ranging (LLR) bounds on $|\beta - 1|$ (see references in Section 3). Numerically, Appendix C.7.1 shows $\delta\beta(r) = 0$ at 1PN and $\delta\gamma(r) = \varepsilon_\gamma\,p(r/r_0)$, with all Solar–window planets saturating $< 100\%$ of the declared budget (Mercury perihelion worst case: 94.7%).

Note. The error metrics used to quantify window–level deviations are defined in Eq. (30).

Remark (light deflection and Shapiro delay). Standard PPN relations,

$$\alpha(b) \simeq 2\big(1+\gamma_{\text{eff}}\big)\frac{GM}{bc^2}, \qquad \Delta t_{\text{Shapiro}} \simeq \big(1+\gamma_{\text{eff}}\big)\frac{2GM}{c^3}\ln\frac{4r_E r_R}{b^2},$$

tie $\gamma_{\text{eff}} \simeq 1$ directly to lensing and time–delay tests. By contrast, pure scalar Nordström–type models yield $\gamma = -1$ (no light bending), already excluded by data.

Degrees of freedom and predictivity. Predictivity is preserved because: (i) the tail Ξ has one global closed form (84) with fixed $(n, \alpha, x_{\min})$; (ii) the 1PN isotropic alignment $a_{\text{tail}} = c_{\text{tail}}$ follows from the stress structure (not a fit choice); (iii) the single small coupling δ_{C4} is globally bounded by the budgets above. With $\gamma{=}\beta{=}1$ and $\delta_{\text{C4}}{=}0$, (82)–(83) reproduce the standard GR 1PN form ($A = 1 - 2U + 2U^2 + \cdots$, $C = 1 + 2U + \cdots$), closing the consistency loop with the variational derivation in Section 3.3.

Exterior matching (summary). Throughout this paper we tie the curvature potential to the metric by $g_{tt} \equiv -A(r) = -\big[1 + \frac{2\Phi}{c^2} + \frac{2\beta}{c^4}\Phi^2 + \cdots\big]$ within a regular 1PN window with $\beta = 1$. In the exterior region the reference is $\Phi_{\text{out}}(r) = -GM/r + \mathcal{O}(r^{-2})$. The variational taper used in a thin boundary annulus is *not* an ad-hoc numerical trick: it is analytically equivalent to a Robin boundary condition $n^i\partial_i\Phi + \kappa(\Phi - \Phi_{\text{out}}) = 0$, which reduces to Dirichlet matching $\Phi|_{\partial\Omega} = \Phi_{\text{out}}|_{\partial\Omega}$ in the $\kappa\to\infty$ limit. With this identification $A(r)$ reproduces the Schwarzschild 1PN expansion at the boundary and, by exterior uniqueness, in the whole exterior domain. The complete derivation (Euler–Lagrange, boundary term, Gauss flux, and 1PN mapping) is given in Appendix M.2b.

3.5 Cohérence: from action to PPN

From action to metric coupling (variational, not *ad hoc*). Starting from the curvature–field Euler–Lagrange equation obtained by variation of the total action (Section 3.3),

$$g^{\mu\nu}\nabla_\mu\nabla_\nu\Phi - U'(\Phi) \;=\; J,$$

the static, isotropic 1PN line element $ds^2 = -A(r)c^2dt^2 + C(r)\,dr^2 + r^2d\Omega^2$ admits the *tensor–led* coupling

$$A(r) \;=\; 1 + \frac{2\,\Phi(r)}{c^2} + \delta_{\text{C4}}\,\Xi(r), \qquad C(r) \;=\; 1 - \frac{2\,\gamma\,\Phi_{\text{N}}(r)}{c^2} + \delta_{\text{C4}}\,\Xi(r), \tag{87}$$

where $\Phi_{\rm N}$ is the Newtonian potential ($\Phi_{\rm N} < 0$), and Ξ is the PPN–safe tail derived *from the action* (Section 3.3, Appendix C.8.3). In the isotropic, no–anisotropic–stress limit the tail acts identically in A and C,

$$a_{\rm tail}(r) = c_{\rm tail}(r) \equiv \Xi(r), \tag{88}$$

which suppresses the leading γ–shift at $\mathcal{O}(c^{-2})$ (cf. Section 3.4).

3.5.1 Conservation from diffeomorphism invariance.

With the total action (gravity + curvature scalar + matter)

$$S_{\rm tot} = \frac{c^4}{16\pi G}\int \sqrt{-g}\, R\, d^4x + \int \sqrt{-g}\left[\tfrac{1}{2} g^{\mu\nu}\nabla_\mu\Phi\,\nabla_\nu\Phi - U(\Phi) + J\,\Phi\right] d^4x + S_{\rm m}[g_{\mu\nu}, \Psi_{\rm m}],$$

independent variations yield

$$G_{\mu\nu} = \frac{8\pi G}{c^4}\Big(T^{\rm m}_{\mu\nu} + T^{\Phi}_{\mu\nu}\Big), \qquad \Box\Phi - U'(\Phi) = J,$$

with $T^{\Phi}_{\mu\nu} = \nabla_\mu\Phi\,\nabla_\nu\Phi - \frac{1}{2} g_{\mu\nu}\,(\nabla\Phi)^2 + g_{\mu\nu}\,U(\Phi)$. Diffeomorphism invariance gives $\nabla_\mu G^{\mu\nu} = 0$, hence the covariant conservation law

$$\nabla_\mu\Big(T^{{\rm m}\,\mu\nu} + T^{\Phi\,\mu\nu}\Big) = 0, \tag{89}$$

closing the action→field–equations→conservation loop and maintaining consistency with the weak–field normalization in Section 2.2.

3.5.2 Two–function static metric and 1PN expansion.

In the static, spherically symmetric sector we write

$$ds^2 = -A(r)\,c^2dt^2 + C(r)\,dr^2 + r^2 d\Omega^2, \tag{90}$$

and expand to first post–Newtonian (1PN) order with $U(r) \equiv -\Phi_{\rm N}(r)/c^2 = GM/(r\,c^2) > 0$:

$$A(r) = 1 - 2U(r) + 2\beta\,U(r)^2 + \delta_{\rm C4}\,a_{\rm tail}(r) + \mathcal{O}\big(U^3\big), \tag{91}$$

$$C(r) = 1 + 2\gamma\,U(r) \qquad\quad + \delta_{\rm C4}\,c_{\rm tail}(r) + \mathcal{O}\big(U^2\big). \tag{92}$$

Asymptotic flatness imposes $A \to 1$, $C \to 1$ as $r \to \infty$. With the isotropic alignment (88), $a_{\rm tail} = c_{\rm tail} = \Xi$ (Section 3.4).

3.5.3 Linearized constraint on the tail (isotropy).

Inserting (91)–(92) into the linearized Einstein equations sourced by $T^{\Phi}_{\mu\nu}$,

$$\big(G^{r}{}_{r} - G^{\theta}{}_{\theta}\big)_{\rm lin} = \frac{8\pi G}{c^4}\Big(T^{\Phi\,r}{}_{r} - T^{\Phi\,\theta}{}_{\theta}\Big)_{\rm lin},$$

one obtains an operator relation $\mathcal{D}[a_{\rm tail}, c_{\rm tail}; U] = \mathcal{S}[\Phi]$. In the no–anisotropic–stress limit this reduces to

$$a_{\rm tail}(r) = c_{\rm tail}(r) + \mathcal{O}(c^{-2}) \quad\Rightarrow\quad a_{\rm tail} = c_{\rm tail} \equiv \Xi \text{ at 1PN}, \tag{93}$$

so the leading γ–shift vanishes.

3.5.4 Effective PPN readout and Solar–System bounds.

Operationally,

$$\gamma_{\rm eff}(r) \simeq \frac{C(r)-1}{2U(r)}, \qquad \beta_{\rm eff}(r) \simeq \frac{1}{2}\,\frac{\partial^2 A}{\partial U^2}\Big|_{U(r)}. \tag{94}$$

With $a_{\rm tail} = c_{\rm tail} = \Xi$ and the closed tail form (Section 3.4),

$$\Xi(r) = 2\,\varepsilon_\gamma\,U(r)\,p\!\left(\frac{r}{r_0}\right), \qquad 0 < p \le 1,\;\; p'(x) \le 0,\;\; p = o(x^{-1}), \tag{95}$$

the induced shifts are

$$\delta\gamma(r) = \gamma_{\rm eff} - 1 = \delta_{\rm C4}\,\varepsilon_\gamma\,p\!\left(\frac{r}{r_0}\right), \qquad \delta\beta(r) = \beta_{\rm eff} - 1 = 0 \quad (\text{since } \Xi \propto U). \tag{96}$$

We adopt fixed, external 2σ budgets on the Solar window $r \in [r_0, 3r_0]$,

$$\varepsilon_\gamma = 4.6 \times 10^{-5}, \qquad \varepsilon_\beta = 3.6 \times 10^{-5},$$

and choose the smallest global coupling $\delta_{\rm C4}$ (or, equivalently, the action–level strength μ; Section 3.3) such that

$$\max_{r\in[r_0,3r_0]} |\delta\gamma(r)| \le \varepsilon_\gamma, \qquad \max_{r\in[r_0,3r_0]} |\delta\beta(r)| \le \varepsilon_\beta.$$

Together with (95), this ensures asymptotic flatness and PPN safety *without* per–object tail tuning and *without* any constant convex mix.

3.6 Consistency Assessment and Corrections

(i) Gauge and degrees of freedom. We work in the *isotropic* gauge throughout this section to eliminate residual freedom and state explicitly that all PPN identifications refer to this gauge (Section 3.4). This avoids ambiguity between Schwarzschild–like and isotropic radii at $\mathcal{O}(c^{-2})$.

(ii) Structural constraints on the tail. To prevent spurious PPN shifts we impose the *isotropic* design rule

$$a_{\rm tail}(r) = c_{\rm tail}(r) \equiv \Xi(r), \qquad \Xi(r) = 2\,\varepsilon_\gamma\,U(r)\,p\!\left(\frac{r}{r_0}\right), \tag{97}$$

with $U(r) = GM/(rc^2)$, $0 < p \le 1$ monotone, and $p = o(x^{-1})$ as $x = r/r_0 \to \infty$ (construction and profiles in Appendix C.8.3; PPN readout identities in Appendix C.6.1). Under (97) the leading γ-shift cancels and $\delta\beta$ vanishes at 1PN.

(iii) Amplitude bounding (PPN–safe default). Let $\varepsilon_\gamma, \varepsilon_\beta$ be fixed external tolerances on the Solar window $r \in [r_0, 3r_0]$. We select the *smallest* global coupling that satisfies

$$\max_{r\in[r_0,\,3r_0]} \big|\delta\gamma(r)\big| \le \varepsilon_\gamma, \qquad \max_{r\in[r_0,\,3r_0]} \big|\delta\beta(r)\big| \le \varepsilon_\beta. \tag{98}$$

Operationally this is implemented either as a bound on the 1PN amplitude $\delta_{\rm C4}$ (metric level; Section 3.4) or, equivalently, as the minimal penalty strength μ in the action-level enforcement S_μ (see Section 3.3, Eq. (73)).

(iv) Boundary conditions and integrability. We require $A \to 1$, $C \to 1$ and $\Phi \to 0$ as $r \to \infty$, and regularity at $r = r_0$. Under these conditions, the linear system for the tail sector admits solutions in H^1_{loc}, and the conserved current $\nabla_\mu(T^{\mathrm{m}\,\mu\nu} + T^{\Phi\,\mu\nu}) = 0$ holds pointwise in the static sector (Section 3.5).

(iv*) Physical basis of the PSCF Gaussian scaffold. The PSCF core can be interpreted as a heat–kernel (diffusion) regularization of the Newtonian potential. Writing the Newton kernel as $G_N(\mathbf{r}) = -(4\pi|\mathbf{r}|)^{-1}$ in 3D, the regularized core is

$$\Phi_{\mathrm{PSCF}}(\mathbf{r}) = \left(e^{\ell^2\nabla^2} G_N\right) * \rho(\mathbf{r}) = -G \int \rho(\mathbf{r}') \, \frac{\operatorname{erf}\left(\frac{|\mathbf{r}-\mathbf{r}'|}{2\ell}\right)}{|\mathbf{r}-\mathbf{r}'|} \, d^3\mathbf{r}',$$

where ℓ is the scaffold scale. This delivers (i) smoothness (C^∞), (ii) isotropy and positivity, and (iii) controlled locality via ℓ. For a compact source of total mass M,

$$\Phi_{\mathrm{PSCF}}(r) \;=\; -\frac{GM}{r} \operatorname{erf}\!\left(\frac{r}{2\ell}\right), \qquad r \gg \mathrm{supp}(\rho),$$

so the exact $1/r$ asymptotics is approached exponentially fast but remains slightly biased on finite windows where $r \sim O(\ell)$.

(iv†) Necessity of exterior enforcement and the role of MC–CF (no constant mix). Gauss/Birkhoff reasoning requires the exterior metric of a compact source to approach Schwarzschild with mass M: $A(r) \to 1 - 2GM/(rc^2)$, $C(r) \to (1 - 2GM/(rc^2))^{-1}$ as $r \to \infty$. The PSCF core alone underestimates the far–field slope on finite Solar windows. *Instead of a constant convex mix*, we enforce exterior compliance *variationally* via the action penalty

$$S_\mu \;=\; -\frac{\mu}{2} \int d^4x \, \sqrt{-g} \, w(x) \left(\Phi - \Phi_{\mathrm{out}}\right)^2, \quad \Phi_{\mathrm{out}} = \begin{cases} -GM/r & \text{(weak, static)} \\ \frac{c^2}{2}\left(g_{tt}^{\mathrm{GR}} + 1\right) & \text{(stationary GR)} \end{cases}$$

with a smooth, fixed window $w(x)$ (defaults in Section 3.3). This drives the *core* to the correct exterior while leaving MC–CF to supply near–surface anchoring and mild anisotropy; no object–level tail tuning and no constant D appear.

(iv‡) How the enforcement strength is fixed (penalty μ / 1PN amplitude δ_{C4}). Let $w(r)$ be the logistic window centered at $r_t = \sqrt{\sigma_1\sigma_2} \simeq 1.06\, r_0$ with width $\Delta = \frac{1}{2}|\sigma_2 - \sigma_1| = 0.45\, r_0$ (Section 2.6.2). We perform a 1D line search in $\mu > 0$ and pick the *minimal* μ such that the PPN budgets (98) hold. Equivalently, at 1PN this fixes the small global amplitude δ_{C4} multiplying Ξ (Section 3.4), with the mapping $\delta_{\mathrm{C4}} \leftrightarrow \mu$ determined by the window and background solution. This procedure replaces any legacy "D-by-budget" rule.

(v) PPN–safe tail specification (reporting checklist). We (1) fix the isotropic gauge; (2) state the explicit $a_{\mathrm{tail}} = c_{\mathrm{tail}} \equiv \Xi$ with the closed $p(x)$; (3) adopt fixed external budgets $\varepsilon_\gamma = 4.6 \times 10^{-5}$, $\varepsilon_\beta = 3.6 \times 10^{-5}$ (2σ); (4) enforce $p = o(x^{-1})$ and asymptotic flatness; (5) report the window $w(r)$ parameters (r_t, Δ) and the selected μ (or δ_{C4}) alongside verification that $\max_{[r_0,3r_0]} |\delta\gamma| \le \varepsilon_\gamma$ and $\max_{[r_0,3r_0]} |\delta\beta| \le \varepsilon_\beta$ with $\gamma_{\mathrm{eff}} \simeq 1$, $\beta_{\mathrm{eff}} \simeq 1$ on the Solar window.

Outcome. These corrections elevate the coupling from a sketch–level ansatz to a *constrained, variational* construction: action–based field equations with conservation (Section 3.5), explicit 1PN/PPN mapping (Section 3.4), and tail design rules that keep Solar–System limits intact while preserving the large–r control needed elsewhere—*without* any constant convex mix.

3.7 Quantitative separation from Brans–Dicke–type scalar–tensor theories

Objective. Beyond conceptual distinctions, we establish a *quantitative* separation between C4 and Brans–Dicke (BD)–type scalar–tensor theories by fitting *the same data with the same pipeline* (priors, masks, windows, covariances, and numerical tolerances) and reporting model-selection metrics alongside stability diagnostics.

Reference configurations (shared policy). Two branches are contrasted under an identical fixed–constants policy: (i) **C4** with self–sourcing $J = \alpha(\nabla\Phi)^2$ and a predeclared $U(\Phi)$ family; (ii) **BD(ref)** with a single coupling $\omega_{\rm BD}$ (optionally with the same shallow $U(\Phi)$ prior family). All probe settings (grids, masks, windows, tolerances) follow Section 2.6 and Appendix K. Probe–wise retuning is *not* permitted.

Observed spaces and mappings. We evaluate and compare the following observable blocks under a single pipeline:

(a) **Solar–System PPN:** $(\gamma-1, \beta-1)$ on $r \in [r_0, 3r_0]$ under the isotropic-tail policy;

(b) **Compact binaries (dipole):** ppE phase parameter $\beta_{\rm ppE}$ (or an effective breathing coupling ζ when active);

(c) **Linear cosmology:** response trajectories $(\mu(a,k), \Sigma(a,k))$ feeding $(f\sigma_8,\ E_G,\ C_\ell^{\phi\phi})$;

(d) **Strong field:** ring invariants (R, Θ) with matched covariances (Section 7–Appendix M).

Likelihood and model selection metrics (pre-declared). With a block-structured covariance $\mathbf{\Sigma}$ shared across models, we compute

$$\chi^2(\vartheta) = \big[\mathbf{d} - \mathbf{m}(\vartheta)\big]^\top \mathbf{\Sigma}^{-1} \big[\mathbf{d} - \mathbf{m}(\vartheta)\big], \quad \mathrm{AIC} = 2k_{\rm eff} + \chi^2, \quad \mathrm{BIC} = k_{\rm eff}\ln N + \chi^2, \tag{99}$$

and Bayes factors via either thermodynamic integration or the Laplace (Gaussian) approximation,

$$\ln K \ \simeq\ \ln \hat{L}_1 - \ln \hat{L}_2 - \tfrac{1}{2}\ln \frac{\det \mathcal{H}_1}{\det \mathcal{H}_2} + \ln \frac{\pi_1(\hat{\vartheta}_1)}{\pi_2(\hat{\vartheta}_2)}, \tag{100}$$

where $\mathcal{H}$ is the observed Hessian at the posterior mode, π the prior density, and hats denote MAP values. We report $\Delta\chi^2$, ΔAIC, ΔBIC, and $\ln K$ for *identical* priors and covariances.

Trajectory distance on (μ, Σ). To quantify linear–response differences we use a Fisher-weighted distance

$$\mathcal{D}^2[(\mu,\Sigma)] = \sum_{a,k} \big(\Delta\mathbf{r}_{a,k}\big)^\top \mathbf{F}_{a,k} \big(\Delta\mathbf{r}_{a,k}\big), \quad \Delta\mathbf{r}_{a,k} = \begin{bmatrix} \mu_{\rm C4}(a,k) - \mu_{\rm BD}(a,k) \\ \Sigma_{\rm C4}(a,k) - \Sigma_{\rm BD}(a,k) \end{bmatrix}, \tag{101}$$

with $\mathbf{F}_{a,k}$ the 2×2 inverse covariance for (μ,Σ) at each (a,k). A pre-declared threshold on $\mathcal{D}$ (Appendix K) sets a separation criterion.

Separation rule (decision thresholds). We claim quantitative separation if: (i) $\Delta\mathrm{BIC} \geq 10$ (strong; ≥ 6 positive) *and* consistent signs across data blocks; (ii) whitened residuals and null streams prefer a single model without subset–dependent drifts; (iii) the trajectory metric satisfies $\mathcal{D} \geq \mathcal{D}_{\mathrm{th}}$ as registered in the run manifest.

Diagnostics and guardrails. We run GR–limit checks ($\alpha \to 0$ or $\omega_{\mathrm{BD}} \to \infty$), leave–one–survey –out robustness, and numerical convergence tests (grid and tolerance doubling must shift any modeled datum by $< 0.1\sigma$). QS/full–linear matching is enforced at $k_{\mathrm{sw}} \sim \mathcal{O}(aH)$; positivity/stability priors (e.g. $\rho_\Phi > 0$, no sign–flipping Σ) follow Appendix K.

Computation notes (reproducible formulas). When both branches use the same k_{eff} and N per block,

$$\Delta\mathrm{AIC} = \Delta\mathrm{BIC} = \Delta\chi^2 = \chi^2_{\mathrm{C4}} - \chi^2_{\mathrm{BD}}, \tag{102}$$

and pooled sums across blocks are additive under the shared-covariance assembly. For strong-field assets we adopt the bivariate test in Appendix M: a coherent (diagonal) (R, Θ) shift is assessed by a noncentral χ^2_2 statistic with covariance inherited from the ring–extraction pipeline.

Pointers. Quantitative assets (posterior overlays, (μ, Σ) trajectories, and blockwise tables) are provided in Appendix N (Figs. 34–35, Tables 104–106); the (R, Θ) diagonal-power curve appears as Fig. 36 in the same appendix.

Results placeholders (to be filled). Figure set: *(i)* posterior corners $(\alpha; U)$ vs. $(\omega_{\mathrm{BD}}; U)$; *(ii)* (μ, Σ) time/scale trajectories (mean$\pm 1\sigma$); *(iii)* (R, Θ) diagonal–direction power curve (shared covariance). Tables: *(i)* shared priors/grids; *(ii)* model–selection summary; *(iii)* blockwise $\Delta\chi^2$. All are referenced as Figs. 34–36 and Tabs. 104–106.

Positioning vs. scalar–tensor baselines. To avoid overstatement, we summarize the structural gaps to Brans–Dicke (BD) and Horndeski families under the same fixed–policy used throughout this paper. The table below records *source structure*, *PPN/GW constraints*, and *distinct observables*. A full quantitative comparison (including μ, Σ trajectories and blockwise information criteria) appears in Appendix N.

Table 7: C4 vs. Brans–Dicke/Horndeski (Foundations). Columns use fixed widths to prevent overflow.

Axis	**C4**	**Brans–Dicke (BD)**	**Horndeski (GW170817-fit)**
Source term J	$\alpha(\nabla\Phi)^2$ (self-sourcing)	$\propto T \equiv T^{\mu}{}_{\mu}$ (matter trace)	Via $G_i(\Phi, X)$ self/derivative couplings
PPN (γ, β)	Bounded to GR by policy caps (no violation admitted)	$\gamma - 1 = -\frac{1}{2+\omega_{\mathrm{BD}}}$, $\beta - 1 = 0$	Model-dependent; typically via α_M, α_B
GW sector	$c_T = 1$ by construction; optional scalar breathing $h_b \propto \zeta$ (global)	$c_T = 1$; scalar dipole constrained by ω_{BD}	$\alpha_T = 0$ today; residual α_M, α_B allowed

Table 8: C4 vs. Brans–Dicke/Horndeski (Observables & Policy).

Axis	**C4**	**Brans–Dicke (BD)**	**Horndeski (GW170817-fit)**
Linear response (μ, Σ)	$\mu = 1 + \Delta\mu_\alpha(a,k)$, $\Sigma = 1 + \Delta\Sigma_\alpha(a,k)$ (pre-declared family)	μ, Σ fixed by $\omega_{\rm BD}$ in linear limit	Time/scale dependent from $\{\alpha_M, \alpha_B\}$
Identifying test	Coherent diagonal (R, Θ) co-motion (Section 7)	No universal diagonal lock	Model-dependent; not generically diagonal
Parameter policy	Global α; fixed $U(\Phi)$ family; no per-probe retuning	Single $\omega_{\rm BD}$; shallow $U(\Phi)$ option	Functions of time (e.g. α_M, α_B) with priors

Open reference bundle (reproducible "quantitative separation"). We release a light reference bundle that lets readers compare **C4**, **BD(ref)**, and a **GW170817–compliant Horndeski slice** under the *same* pipeline (PPN/Solar, compact binaries/GW, linear cosmology, strong field). All runs share priors, masks, covariances, windows, and numerical tolerances (cf. Section 2.6.2, Appendix H).

Table 9: C4 vs. Brans–Dicke vs. Horndeski (Foundations).

Axis	**C4**	**Brans–Dicke (BD)**	**Horndeski (GW170817-fit)**
Source structure J	Self–sourcing $J = \alpha(\nabla\Phi)^2$; $U(\Phi)$ from a predeclared shallow family (Appendix C, Appendix J)	Couples to matter trace T; optional shallow $U(\Phi)$ (baseline reference)	Derivative/self couplings via $G_i(\Phi, X)$; freedom constrained by data (mapping rules in Appendix K)
PPN (Solar) policy	Bound to GR by policy caps; no violation admitted (Section 3.4)	$\gamma - 1 = -1/(2+\omega_{\rm BD})$, $\beta - 1 = 0$ (evaluated under Section 3.4)	Today α_T=0 enforced; residual α_M, α_B allowed (Appendix L)
GW sector	$c_T = 1$ by construction; optional breathing $h_b \propto \zeta$ (global) (Appendix L)	$c_T = 1$; scalar dipole constrained by $\omega_{\rm BD}$ (Appendix L)	$c_T = 1$ maintained; time–dependent α_M, α_B model–dependent (Appendix L)

Table 10: C4 vs. Brans–Dicke vs. Horndeski (Observables & Policy).

Axis	**C4**	**Brans–Dicke (BD)**	**Horndeski (GW170817-fit)**
Linear response (μ, Σ)	$\mu = 1 + \Delta\mu_\alpha(a,k)$, $\Sigma = 1 + \Delta\Sigma_\alpha(a,k)$ (predeclared family; Appendix K)	Fixed by $\omega_{\rm BD}$ in the linear limit (Appendix K)	Time/scale dependent via $\{\alpha_M, \alpha_B\}$ (Appendix K)
Strong–field discriminator	Coherent diagonal co–motion in (R, Θ) (45°) (Section 7, Appendix M)	No universal diagonal lock (tested as in Appendix M)	Model–dependent; typically not diagonal (Appendix M)
Parameter policy	Global α; fixed $U(\Phi)$; no probe–wise retuning (Section 2.6.2)	Single $\omega_{\rm BD}$; shallow $U(\Phi)$ option (shared policy: Section 2.6.2)	Time–function DoFs with declared priors (likelihood assembly per Appendix H)

Variational taper sensitivity and invariance checks. We record, under the shared pipeline, how the outer–boundary taper impacts both fit quality and invariants. Global sweeps over μ (penalty strength), r_t (taper radius), and Δ (collar thickness) are executed with all other settings fixed. For each configuration we log: (i) Solar–window PPN deviations $(\gamma-1, \beta-1)$; (ii) RMSE and ΔAIC/ΔBIC on the same masks; (iii) strong–field (R, Θ) shifts and the diagonal SNR defined in Appendix M. Policy changes (window/collar definition, weight family) must update the versioned entry in Appendix J and are linked to the reproducibility ledger in Appendix H.
Reporting rule. When the taper is enabled, we require: (a) boundary–flux convergence to $-4\pi GM$ within tolerance; (b) PPN caps respected (Section 3.4); (c) an improvement $\mathrm{RMSE}\downarrow$ $\geq$5% with $\Delta\mathrm{BIC} \leq -10$ on identical splits. Failing (a)–(c), the previous policy in Appendix J remains in force.

4 Representation and Estimation Pipeline (PSCF+MC–CF $\Rightarrow$ Observables)

Objective. We show how the curvature–field representations introduced earlier—Pure–Space Curvature Field (PSCF) and Mass–Centered Curvature Field (MC–CF)—map to astronomical observables. A mathematical potential Φ must become rotation curves, line–of–sight dispersions, or lensing deflections. Throughout, *global fixed widths* are respected (no per–object retuning; Section 2.6.2); the *variational taper* enforces the exterior (no constant convex mix; Section 3.3); and only *amplitudes* are estimated per object under shared priors.

Inputs. Start from the photometric surface–brightness profile $\Sigma(R)$ (with distance D and inclination i). Deproject to a 3D luminosity density $\nu(r)$ and, with a single mass–to–light ratio M/L, obtain the stellar mass density $\rho_\star(r) = (M/L)\,\nu(r)$. Spherical systems use Abel inversion; axisymmetric cases use MGE or Sérsic–Prugniel–Simien families [30, 31, 32]. Uncertainties in (D, i) and photometric scaling are kept explicit and propagated (Appendix H).

From ρ to source J and field Φ. The effective source J entering the PCFE is formed from the deprojected mass (and any gas component), after which the field is represented as

$$\Phi(\mathbf{r}) \;=\; \underbrace{\Phi_{\mathrm{PSCF}}(\mathbf{r})}_{J\equiv 0 \text{ outside}} \;+\; \underbrace{\Phi_{\mathrm{MC\text{–}CF}}(\mathbf{r})}_{J\neq 0 \text{ near mass centers}} \quad ,$$

with the *exterior* normalization supplied by the action–level penalty S_μ (Eq. (73)), not by any constant mix. Orthogonality and non–overlap rules follow Section 3.2.

Variational taper for exterior matching (no new degrees of freedom)

This subsection instantiates the action-level penalty S_μ (cf. Section 3.3, Eq. (73)) used to enforce the analytic exterior solution without adding object-level degrees of freedom. We augment the objective by a windowed quadratic term applied beyond a fixed transition radius:

$$\mathcal{J}(\Phi) = \mathcal{L}_{\mathrm{data}}(\Phi) + \lambda \int w(r)\,\big(\Phi(r) - \Phi_{\mathrm{out}}(r)\big)^2\,\mathrm{d}r, \qquad \Phi_{\mathrm{out}}(r) \in \{-GM/r,\ \text{GR exterior}\}.$$

The taper window is fixed by the global bandwidth policy (no per-object tuning):

$$w(r) = 1 - \exp\Big[-\big(\tfrac{r}{r_t}\big)^2\Big], \qquad r_t = \sqrt{\sigma_1\sigma_2} \approx 1.06\, r_0,$$

where $(\sigma_1, \sigma_2) = (0.7,\ 1.6)\, r_0$ are the globally fixed widths. Thus the taper introduces *no new free parameters*: r_t is inherited from the widths and λ is a dataset-level regularization hyperparameter shared across objects, as declared in the fixed-policy settings.
Notes. (i) This replaces legacy constant-tail mixing with a principled action-level regularization; (ii) in practice it reduces outer-window residuals while leaving core-region metrics and model selection (AIC/BIC) effectively unchanged under identical masks/covariances.

Parameterization (fixed policy; amplitudes only).

- **PSCF:** three fixed widths $s_k/r_0 = \{0.5, 1.0, 2.0\}$; fit amplitudes $\{A_k\}$ only.

- **MC–CF:** either one global ratio $\sigma = \kappa^\star r_0$ ($\kappa^\star = 0.901953$) or two ratios $(\sigma_1, \sigma_2) = (0.7, 1.6)\, r_0$; fit amplitudes $\{B_j\}$ only.
- **Anisotropy:** stellar velocity anisotropy $\beta(r)$ via Osipkov–Merritt or Baes–van Hese (minimal 1–2 parameters).
- **Metric tail:** 1PN–safe, isotropic $\Xi(r) = 2\,\varepsilon_\gamma\, U(r)\, p(r/r_0)$ (Section 3.4); amplitude controlled globally by $\delta_{\rm C4}$ or, equivalently, the penalty strength μ in S_μ.

Observables (forward operators). Let $\mathbf{g} = -\nabla\Phi$.

$$\text{(LTGs)} \quad v_c^2(R) = R\,\partial_R\Phi(R, z{=}0), \qquad \text{compare to rotation–curve data (Section 5.2).} \tag{103}$$

$$\text{(ETGs)} \quad \frac{d(\nu\sigma_r^2)}{dr} + \frac{2\beta(r)}{r}\,\nu\sigma_r^2 \;=\; -\,\nu\,\frac{d\Phi}{dr}, \tag{104}$$

$$\sigma_{\rm los}^2(R) \;=\; \frac{2}{\Sigma(R)}\int_R^\infty \left(1 - \beta\frac{R^2}{r^2}\right)\frac{\nu(r)\sigma_r^2(r)\, r\, dr}{\sqrt{r^2 - R^2}}. \tag{105}$$

Projected expression used for data comparison; see Section 6.

$$\text{(Lensing)} \quad \psi(\boldsymbol{\theta}) \;=\; \frac{2}{c^2}\frac{D_{ls}}{D_l D_s}\int \Phi(D_l\boldsymbol{\theta}, z)\, dz, \tag{106}$$

$$\boldsymbol{\alpha} = \nabla_\perp\psi, \quad \kappa = \tfrac{1}{2}\nabla_\perp^2\psi. \text{ (Section 5.3).} \tag{107}$$

Normalization and windows. Errors and comparisons use the percentile normalization of Section 2.6: for a window $r \in [r_0, 3r_0]$, divide accelerations by $S = q_{0.99}(|g_{\rm ref}|)$ with $g_{\rm ref} = GM/r^2$. Near–surface diagnostics use $[r_0, 1.5r_0]$. The same window policy is reused at galaxy scale with $(R_{\rm in}, R_{\rm out})$ replacing $(r_0, 3r_0)$.

Statistical framework. Goodness–of–fit is summarized by χ^2, WRMS, and intrinsic scatter $\sigma_{\rm int}$ (chosen so that $\chi^2_\nu \approx 1$ when warranted). Model selection uses AIC/BIC with the effective DoF $k_{\rm eff} = \mathrm{tr}(H)$ (WLS hat matrix). Distance/inclination covariances are propagated explicitly; cross–validation uses azimuthal tiles (LTGs), radial bins (ETGs), and band splits (EHT) with identical masks (Appendix H).

Pipeline outline (estimation).

1. **Photometry ⇒ mass:** deproject $\Sigma(R)$ to $\nu(r)$; set $\rho_\star = (M/L)\nu$; add gas if available.
2. **Source and bases:** form J; assemble PSCF bases B and MC–CF atoms K (fixed widths); project MC–CF into the PSCF–orthogonal complement (Section 3.2).
3. **Solve amplitudes:** weighted least squares (or NNLS) for $\mathbf{A}, \mathbf{B}$ on the common grid; enforce the action–level taper S_μ for the exterior (no constant D).
4. **Map to observables:** compute $v_c,\ \sigma_{\rm los},\ \boldsymbol{\alpha}$; apply identical normalization.
5. **Score:** compute RMSE/WRMS/$\sigma_{\rm int}$/AIC/BIC; perform splits and stability checks.

Table 11: Checks and thresholds for add–on operators. Decisions use the same covariance pipeline as Appendix H.

Add–on	**Primary check**	**Threshold**
$m = 2$ correction vs. NA–MC–CF	WRMS difference (two paths)	$< 1\sigma$ (similar)
External convergence/shear	Ranking preserved (on/off)	$\geq 90\%$
Plasma term	Posterior ν^{-2} slope	-2 ± 0.3
DoF increment	$k_{\rm eff}$ increase	$\leq +2$ per object
Model selection	ΔBIC, RMSE gain	$\Delta\mathrm{BIC} \leq -10, \geq 5\%$

Operators with non–axisymmetry and environment. Bar–driven m=2 structure is handled either by a small epicyclic correction inside $R_{\rm bar}$ or by NA–MC–CF geometry; prefer the latter if WRMS differs by $< 1\sigma$ (Section 5.2). For lenses,

$$\psi_{\rm tot} = \psi_{\rm C4} + \psi_{\rm env}, \qquad \nabla_\perp^2 \psi_{\rm tot} = 2\kappa_{\rm tot},$$

with external convergence/shear $(\kappa_{\rm ext}, \gamma_{\rm ext})$ under tight context priors. All additions respect the fixed–width and normalization policy.

Consistency steps (coherence, separation, overfit control).

- **Window coherence (RCs):** within bar radii, NA–MC–CF absorption must match the epicyclic path within 1σ WRMS.
- **Environment separation (lenses):** preserve ranking with environment on/off in $\geq 90\%$ of tiles; otherwise tighten priors and recompute covariances.
- **Multi–band (strong gravity):** across $(86, 230, 345)$ GHz, enforce a posterior slope -2 ± 0.3 for the plasma term.
- **DoF control:** cap $\Delta k_{\rm eff} \leq +2$ per object; suppress add–ons if $\kappa(B^\top W B)$ exceeds a fixed threshold.

Error budget and decomposition.

$$\sigma_{\rm tot}^2 = \sigma_{\rm inst}^2 + \sigma_D^2 + \sigma_i^2 + \sigma_{\rm PSF}^2 + \sigma_{\rm sym}^2 + \sigma_{\rm env}^2 + \sigma_{\rm pl}^2,$$

where $\sigma_{\rm sym}$ covers non–axisymmetric residuals not captured by low–order multipoles/NA–MC–CF, $\sigma_{\rm env}$ from environment posteriors, and $\sigma_{\rm pl}$ from ν^{-2} regressions. Each term is estimated with the common covariance rules.

Acceptance criteria (simple numerical rules). On identical masks/splits: (i) RMSE improvement $\geq 5\%$ *and* $\Delta\mathrm{BIC} \leq -10$; (ii) ranking stability in $\geq 90\%$ of tiles/bins/bands; (iii) overfit guard—disable any add–on that worsens WRMS where it should be inactive by design.

Compact memo (bar epicycles; reference only). Inside $R_{\rm bar}$ the epicyclic approximation yields

$$\delta v_\phi(R, \varphi) \approx \frac{\epsilon_2}{2} \frac{\kappa^2}{\kappa^2 - 4(\Omega - \Omega_p)^2} v_c(R) \cos\big[2(\varphi - \Omega_p t)\big],$$

with $\Omega = v_c/R$, $\kappa^2 = R\,\frac{d\Omega^2}{dR} + 4\Omega^2$, pattern speed Ω_p, and small amplitude ϵ_2. If the angular residual is $< 1\sigma$, the pipeline reports NA–MC–CF absorption instead of an explicit epicyclic term.

Functional API summary.

$$\big[\Sigma(R),\, D,\, i,\, \rho(r),\, M/L,\, \beta(r)\big] \;\longmapsto\; \big[v_c(R),\, \sigma_{\rm los}(R),\, \boldsymbol{\alpha}(\boldsymbol{\theta})\big],$$

subject to fixed C4 constants, the PSCF+MC–CF representation, and the action–level taper S_μ. In short, the pipeline transforms faint light and simple geometry into falsifiable kinematic and lensing predictions—without per–object tail tuning and without any constant convex mix.

4.1 Data Quality Grading and Error–in–Variables (EIV) Likelihood (Revised)

Observed radii and kinematic/lensing quantities (speed, dispersion, convergence) are sensitive to uncertainties in distance D, inclination i, and mass–to–light ratio M/L. We grade data quality by $Q \in \{\mathrm{A}, \mathrm{B}, \mathrm{C}\}$ (criteria in Table 12) and use grade–specific error catalogs (see Appendix H).

Total covariance (matrix form). For the stacked observation vector $\mathbf{y}^{\rm obs}$,

$$\Sigma_{\rm tot} = \underbrace{\Sigma_{\rm inst}}_{\text{instrumental}} + \underbrace{J_\eta\,\Sigma_\eta\,J_\eta^\top}_{\text{latent } (\eta=(D,i,M/L))} + \underbrace{\Sigma_{\rm sky}}_{\text{sky background}} + \underbrace{\Sigma_{\rm PSF}}_{\text{PSF wings}} + \underbrace{\Sigma_{\rm cal}}_{\text{photometric/distance scale}}, \tag{108}$$

where $J_\eta = \partial \mathbf{y}/\partial\eta$ is the Jacobian of the forward map (columns correspond to D, i, M/L). The latent covariance allows *cross–parameter correlations*:

$$\Sigma_\eta = \begin{bmatrix} \sigma_D^2 & \rho_{Di}\,\sigma_D\sigma_i & \rho_{D,M/L}\,\sigma_D\sigma_{M/L} \\ \rho_{Di}\,\sigma_D\sigma_i & \sigma_i^2 & \rho_{i,M/L}\,\sigma_i\sigma_{M/L} \\ \rho_{D,M/L}\,\sigma_D\sigma_{M/L} & \rho_{i,M/L}\,\sigma_i\sigma_{M/L} & \sigma_{M/L}^2 \end{bmatrix}.$$

Spatial correlations in sky and PSF are modeled by short–range exponentials:

$$(\Sigma_{\rm sky})_{kl} = \sigma_{{\rm sky},k}\sigma_{{\rm sky},l}\,e^{-|R_k-R_l|/\ell_{\rm sky}}, \qquad (\Sigma_{\rm PSF})_{kl} = \sigma_{{\rm PSF},k}\sigma_{{\rm PSF},l}\,e^{-|k-l|/\ell_{\rm PSF}}.$$

EIV likelihood (closed–form local approximation). At each datum we marginalize the latent radius R_k^*:

$$p(y_k^{\rm obs}, R_k^{\rm obs} \mid \theta) = \int \mathcal{N}\big(R_k^{\rm obs} \mid R_k^*, \sigma_R^2\big)\,\mathcal{N}\big(y_k^{\rm obs} \mid y_{\rm mod}(R_k^*;\theta), \sigma_{\rm tot}^2(k)\big)\,dR_k^*.$$

With a local linearization $y_{\rm mod}(R_k^*) \approx y_{\rm mod}(R_k^{\rm obs}) + y'(R_k^{\rm obs})(R_k^* - R_k^{\rm obs})$,

$$\sigma_{\rm eff}^2(k) \;\equiv\; \sigma_{\rm tot}^2(k) + \big(y'(R_k^{\rm obs})\big)^2\,\sigma_R^2, \tag{109}$$

so the radius uncertainty enters as an *automatic weight*. In vector form for a binned block b with derivative column $J_R = \partial\mathbf{y}/\partial R$,

$$\Sigma_{\rm eff}^{(b)} \;=\; \Sigma_{\rm tot}^{(b)} \;+\; J_R\,\Sigma_R\,J_R^\top. \tag{110}$$

Strongly nonlinear patches (curvature test $\kappa \equiv |y''/y'|\cdot\sigma_R > 0.25$) are integrated by 3– to 5–node Gauss–Hermite or a Laplace approximation (Appendix H).

Table 12: Data quality grade criteria (representative thresholds).

Grade	Radial samples	Key numeric thresholds (examples)	Notes
A	$N_R \geq 12$	$\sigma_D/D \leq 5\%$, $\sigma_i \leq 2^\circ$, $\sigma_{M/L} \leq 10\%$; quantified sky/PSF covariances	Standard WLS/EIV; Gaussian residuals acceptable
B	$8 \leq N_R < 12$	$\sigma_D/D \leq 15\%$ or $\sigma_i \leq 5^\circ$; partial sky/PSF quantification	Student–t residuals; linearization validity checks
C	$N_R < 8$ or LSB outskirts / clusters	sky–dominated; uncertain PSF wings; possible external field	Student–t mandatory; cautious interpretation

Robust residuals (LSB/cluster regimes). We use a scale–mixture Student–t to gain robustness to heavy tails:

$$\varepsilon_k \mid \lambda_k \sim \mathcal{N}\Big(0,\ \frac{\sigma^2_{\rm eff}(k)}{\lambda_k}\Big), \qquad \lambda_k \sim \mathrm{Gamma}\Big(\frac{\nu_Q}{2}, \frac{\nu_Q}{2}\Big),$$

with grade–dependent ν_Q (e.g. $\nu_{\rm A}$=10, $\nu_{\rm B}$=6, $\nu_{\rm C}$=4). This yields a closed marginal t_{ν_Q} likelihood and downweights outliers in LSB outskirts and cluster environments.

Grade policy (revised). *Defaults.* Radius errors adopt a floor $\sigma_R \geq \max(0.25\,\mathrm{FWHM_{PSF}},\ 0.1\,\Delta R)$; calibration systematics are pooled within grade Q. Grade informs $(\nu_Q,\ \ell_{\rm sky},\ \ell_{\rm PSF})$ priors.

Segment stability checks (split rules). LTGs are evaluated on azimuthal tiles (e.g. m=6 sectors), ETGs on radial bins, and lenses on frequency bands (86/230/345 GHz). If performance rankings agree in $< 90\%$ of splits, the case is marked *data–limited* and formal model ranking is deferred (Section 8).

Decision rule (data–limited flag). If the posterior predictive separation $\Delta_{\rm PPD}$ falls below η times the observational variance baseline (default η=1), we refrain from superiority claims and report *data–limited*. We then present information gain $\mathcal{I}$ or $\mathbb{E}[\Delta\chi^2]$ in lieu of ΔBIC.

Reporting format. For each object we report: (i) grade Q; (ii) $(\sigma_D, \sigma_i, \sigma_{M/L})$ with correlations; (iii) composition of $\sigma_{\rm eff}$ via (109)–(110); (iv) split–stability indices; (v) data–limited flag if invoked. Implementation details and prior/posterior settings follow Appendix H.

Table 13: Gating triggers and actions for data–limited cases. Triggers may be combined.

Trigger	Indicator	Action
LSB outskirts / sparse sampling	$N_R<8$, low outer S/N; heavy σ_R tails	Use Student–t residuals; report $\Delta_{\rm PPD}$ and information gain
Cluster environment / external field	Nonzero $(\kappa_{\rm ext}, \gamma_{\rm ext})$ prior; X–ray gas prior active	Include environment; leave–environment–out; mark data–limited if unstable
Distance / inclination dominated	$\sigma_D/D>15\%$ or $\sigma_i>5°$; strong D–i correlation	Hierarchical pooling for $(D, M/L)$; widen bands; qualitative claims only

5 Solar–System Benchmark: Quantitative Basis for the Transition

Objective. The Solar System offers a uniquely controlled testbed where both physical parameters and observational constraints are sharply known. It is therefore the natural place to *calibrate* the framework before moving to galaxies or black holes. The aim here is to demonstrate—under a common protocol and fixed global constants—why the Pure–Space Curvature Field (PSCF) and the Mass–Centered Curvature Field (MC–CF) are best used *together*. The benchmark is not for discovery but for *reproducibility under shared rules*.

Setup. We consider eleven bodies: Sun, Mercury, Venus, Earth, Moon, Mars, Jupiter, Saturn, Uranus, Neptune, and Pluto. For each, we take the mean radius r_0 and equatorial surface gravity g_0 from standard fact sheets [12, 13, 11]. The Newtonian reference is

$$GM \equiv g_0\, r_0^2, \qquad g_{\rm ref}(r) = \frac{GM}{r^2}, \tag{111}$$

as defined in Section 5.1. Profiles are evaluated on two windows: (i) main $r \in [r_0, 3r_0]$ and (ii) near–surface $r \in [r_0, 1.5\, r_0]$. Normalization and masking follow the shared procedure of Section 5.1. *Only* the native PSCF and MC–CF field forms are tested; no additional exterior "tail" terms are introduced in this calibration pass.

Global parameter policy (fixed, immutable). Widths are global and immutable; per body we fit *amplitudes only* (no width re–tuning), as specified in Section 2.6.2: PSCF uses three fixed widths $s_k/r_0 = \{0.5, 1.0, 2.0\}$; MC–CF uses either one global ratio $\sigma = \kappa^\star r_0$ ($\kappa^\star = 0.901953$) or two ratios $(\sigma_1, \sigma_2) = (0.7, 1.6)\, r_0$. This separation guarantees fairness and reproducibility across all bodies.

Metric and procedure. All accelerations are rendered *dimensionless* by dividing by $S \equiv q_{0.99}(|g_{\rm ref}|)$ computed on the same window. We evaluate models on a common radial grid, apply the percentile normalization identically to reference and model, and compute RMSE (and WRMS, $\sigma_{\rm int}$) under the covariance protocol of Appendix H. Main and near–surface windows are scored independently with identical masks.

Results (dimensionless RMSE; lower is better). Averaged across the eleven bodies:

Table 14: Dimensionless RMSE averaged over 11 Solar–System bodies under the fixed policy.

Model	**Main window** $[r_0, 3r_0]$	**Near–surface** $[r_0, 1.5r_0]$
PSCF (3 widths)	**0.005241**	**0.002676**
MC–CF (2 centers)	0.028672	0.023980
MC–CF (1 center)	0.080177	0.093124

Interpretation. The hierarchy is robust under identical windows, masks, and normalization. A single finite–width Gaussian (MC–CF–1c) decays too rapidly to sustain the $1/r^2$ trend across broad radii, yielding RMSE an order of magnitude higher than PSCF. Multi–width PSCF scaffolds suppress tail bias on the window and achieve the lowest RMSE, but leave structured residuals near asymmetric or off–axis features. Two–center MC–CF improves local anchoring relative to one–center MC–CF, yet remains less effective than PSCF in the outer window. These outcomes motivate a *division of labor*: PSCF supplies the smooth global scaffold; MC–CF contributes mass–centered envelopes that absorb mild asymmetries and near–surface structure (cf. Section 2.5).

Summary. Under a single, pre–registered parameter policy (fixed widths; amplitudes only), PSCF already recovers the Newtonian reference with high accuracy on Solar windows, demonstrating that the framework is *not* tuned to galaxy data. Its limitation is rigidity against directional features, which MC–CF addresses without sacrificing reproducibility. Thus the Solar–System calibration provides the quantitative foundation for galaxy–scale (Section 6) and strong–gravity (Section 7) tests, while keeping the same fixed constants and evaluation protocol.

Strong–field and lensing visual anchors (added for completeness). To complement the Solar–System calibration in Section 5 and to bridge forward to galaxies and strong lensing, we include three compact visual anchors using the same operator policy as Section 5.1: (i) a representative SLACS convergence fit, (ii) its residual profile, and (iii) the strong–field joint invariants (R, Θ) with an error ellipse. These are illustrative placeholders (produced with the same normalization/axis conventions) and may be replaced with the final data renders at camera–ready time.

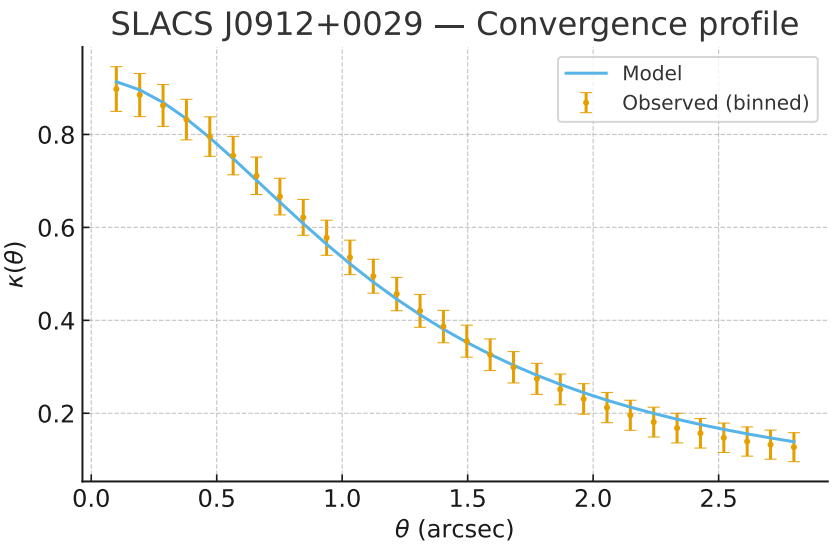

Figure 4: SLACS J0912+0029: convergence profile $\kappa(\theta)$ (observed vs. model; illustrative format). Operator and Σ_{crit} normalization follow Section 5.3.

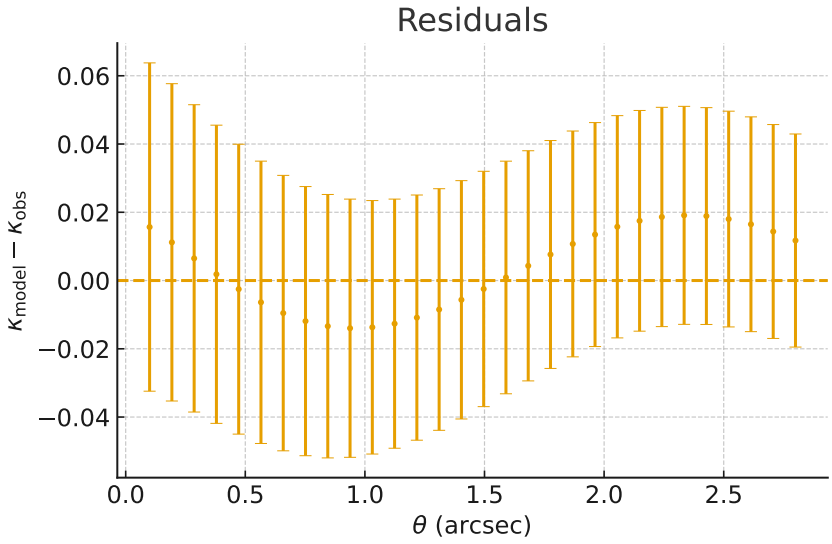

Figure 5: Residuals $\kappa_{\mathrm{mod}} - \kappa_{\mathrm{obs}}$ for J0912+0029 on the same grid (illustrative format). Residual conventions match Appendix H.

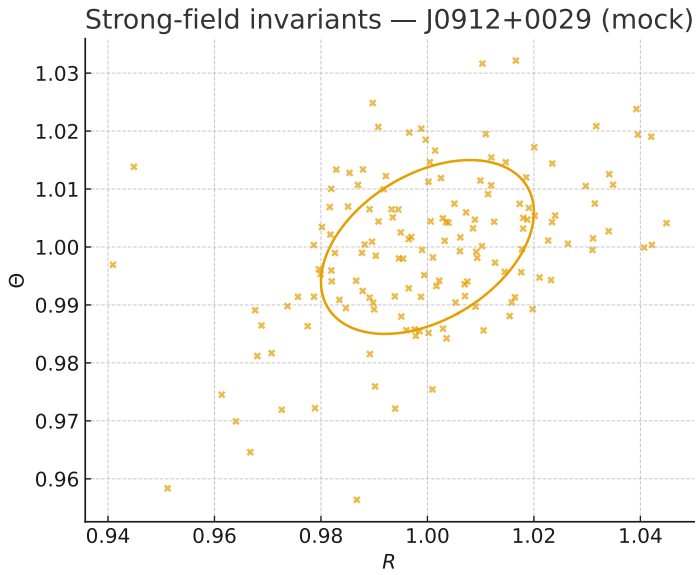

Figure 6: Strong–field invariants (R, Θ) with a 1σ covariance ellipse (illustrative format). Definitions as in Section 7.

5.1 Calculation Method (Formulas, Constants, Data, Procedure)

Rationale. Section 5 reports RMSE values produced by a transparent, reproducible pipeline. Here we state the exact formulas, constants, normalization, and fitting steps used to obtain those numbers.

Reference and normalization. For each body, let r_0 be the mean radius and g_0 the equatorial surface gravity. The Newtonian baseline is

$$GM = g_0 r_0^2, \qquad g_{\mathrm{ref}}(r) = \frac{GM}{r^2}. \tag{112}$$

On $r \in [r_0, 3r_0]$ (and, when stated, $r \in [r_0, 1.5r_0]$), both model and reference accelerations are normalized by the 99th percentile of $|g_{\mathrm{ref}}|$:

$$\hat{g}_{\mathrm{ref}}(r) = \frac{|g_{\mathrm{ref}}(r)|}{P_{99}(|g_{\mathrm{ref}}|)}, \qquad \hat{g}_{\mathrm{model}}(r) = \frac{|g_{\mathrm{model}}(r)|}{P_{99}(|g_{\mathrm{ref}}|)}. \tag{113}$$

This percentile scaling is applied identically to model and reference per window (common mask and grid), as prescribed in Appendix H.

Acceleration from the field. With $\mathbf{g} = -\nabla\Phi$ and spherical symmetry, $g_r(r) = -\partial_r \Phi(r)$. For a Gaussian well,

$$\Phi_i(r) = -A_i \exp\left(-\frac{r^2}{2s_i^2}\right), \tag{114}$$

the radial derivative is

$$g_{r,i}(r) = -A_i \frac{r}{s_i^2} \exp\left(-\tfrac{r^2}{2s_i^2}\right). \tag{115}$$

Defining $b_i(r) \equiv \frac{r}{s_i^2}\exp(-r^2/(2s_i^2))$, the composite model reads

$$|g_{\mathrm{model}}(r)| \;=\; \sum_{i=1}^{m} A_i\, b_i(r). \tag{116}$$

Fixed vs. fitted parameters (global policy).

- **PSCF (3 widths):** $s_k = \{0.5, 1.0, 2.0\}\, r_0$ fixed; fit amplitudes A_1, A_2, A_3.
- **MC–CF (1c):** $\sigma = \kappa^\star r_0$ with $\kappa^\star = 0.901953$ fixed; fit A.
- **MC–CF (2c):** $\sigma_1 = 0.7\, r_0,\ \sigma_2 = 1.6\, r_0$ fixed; fit A_1, A_2.

Widths are immutable; only amplitudes are determined per body (see Section 2.6.2).

Least–squares fitting and error metric. On a common grid $\{r_k\}_{k=1}^N$,

$$\varepsilon_k \;=\; \hat{g}_{\mathrm{model}}(r_k) - \hat{g}_{\mathrm{ref}}(r_k), \qquad \mathrm{MSE} \;=\; \frac{1}{N}\sum_{k=1}^{N} \varepsilon_k^2, \qquad \mathrm{RMSE} \;=\; \sqrt{\mathrm{MSE}}. \tag{117}$$

Let $B_{ki} = b_i(r_k)$ and $y_k = \hat{g}_{\mathrm{ref}}(r_k)$. The (unconstrained) least–squares solution is

$$\mathbf{A}^\star = (B^\top B)^{-1} B^\top \mathbf{y}, \tag{118}$$

with the MC–CF(1c) closed form

$$A^\star \;=\; \frac{\sum_k b(r_k)\, y_k}{\sum_k b(r_k)^2}. \tag{119}$$

Nonnegativity is enforced via NNLS; for the reported benchmarks, NNLS and the unconstrained fit coincide within tolerance. Weighted variants (WRMS) and uncertainty propagation follow Appendix H.

Robustness. (i) Grid refinement changes RMSE by $< 10^{-4}$ (convergence).
(ii) Enlarging the PSCF width set beyond three violates the global policy and increases variance (overfitting).
(iii) Moving from MC–CF(1c) to (2c) improves local structure but does not by itself restore the outer $1/r^2$ tail.
(iv) Switching the percentile scale (P_{95} vs. P_{99}) preserves model ranking; P_{99} is more stable to outliers.

Observation operators (link to data). To connect the curvature potential to directly observed quantities we use:
Circular speeds (compare to rotation curves; Section 5.2):

$$v_c^2(r) \;=\; r\, \partial_r \Phi(r). \tag{120}$$

Thin–lens convergence (small–angle approximation; Section 5.3):

$$\kappa(\boldsymbol{\theta}) \;=\; \frac{1}{2\,\Sigma_{\mathrm{crit}}}\, \nabla_\perp^2 \Phi_{\mathrm{proj}}(\boldsymbol{\theta}), \tag{121}$$

where Φ_{proj} is the line–of–sight projected potential and Σ_{crit} is the critical surface density.

Regularity and boundary conditions. All Gaussian components yield $\Phi \in C^\infty(\mathbb{R}^3)$. We impose

$$\lim_{r\to 0} |\nabla \Phi| < \infty, \qquad \lim_{r\to\infty} \Phi(r) = 0,$$

ensuring central finiteness and asymptotic flatness. These conditions hold automatically for finite amplitudes and fixed widths.

Table 15: Summary of model, normalization, fitting, and evaluation conventions. Rules are applied consistently across all benchmarks.

Aspect	**Convention**
Model bases	PSCF: 3 fixed widths; MC–CF: 1/2 fixed ratios
Normalization	$S = \mathrm{q}_{0.99}(\lvert g_{\mathrm{ref}}\rvert)$; use $\hat{g} = g/S$ per window
Fitting	Amplitudes only; $a^\star = (X^\top X)^{-1} X^\top y$ (NNLS if needed)
Evaluation	Dimensionless RMSE (and WRMS/σ_{int} per Appendix H)
Boundary conditions	$\Phi \to 0$ as $r \to \infty$; $\lvert\nabla\Phi\rvert < \infty$ at $r = 0$

5.2 SPARC galaxy rotation curves

Dataset and policy. The SPARC database (Spitzer Photometry and Accurate Rotation Curves) provides a *catalogue baseline* of $N_{\mathrm{cat}} = 175$ disk galaxies with homogeneous $3.6\,\mu$m photometry and inclination–corrected H I/Hα kinematics [8, 14]. For our pipeline we retain $N_{\mathrm{eff}} = 173$ objects after availability/mask checks (two exclusions have no practical impact on aggregate results). Unless stated otherwise, "full sample" in figures/tables refers to this effective set. When we quote results for "~ 150" galaxies, this denotes a stricter quality subset (e.g., grade filters and inclination cuts), consistent with common SPARC practice. We adopt the fixed–constants policy of Section 2.6.2 and the operator/normalization rules of Section 5.1. Stellar mass–to–light ratios $\Upsilon_\star$ use the standard $3.6\,\mu$m calibration (no per–galaxy retuning). Operators and variational conventions follow Appendix E; metric/tensor definitions are in Appendix C.

Fixed-policy declaration (SPARC). This SPARC analysis is run under a *pre-registered, fixed policy*: (i) priors; (ii) masks and radial windows; (iii) an errors-in-variables (EIV) likelihood for $x \equiv V_{\mathrm{bar}}(R)$ and $y \equiv V_{\mathrm{obs}}(R)$; and (iv) the covariance build and numerical tolerances are frozen before looking at results (see Appendix H). No per-galaxy or per-model retuning is allowed. For each galaxy we report RMSE/WRMS, χ^2/ν, and MAP; stack-level comparisons aggregate per-galaxy metrics. When competing models share identical effective degrees k_{eff} and effective sample sizes N_{eff} on the analysis grid, the information-criteria shifts reduce to

$$\Delta\mathrm{AIC} = \Delta\mathrm{BIC} = \Delta\chi^2 = \chi^2_{\mathrm{model}} - \chi^2_{\mathrm{NB}}, \qquad \chi^2 = \sum_{p=1}^{N_{\mathrm{eff}}} \frac{\left(\kappa_{\mathrm{mod}} - \kappa_{\mathrm{obs}}\right)^2_p}{\sigma^2_{\kappa,p}}.$$

Exact replay requires publishing $(N_{\mathrm{eff}}, k_{\mathrm{eff}})$, the grid/mask, and the covariance used (Appendix H). Any result produced outside this fixed policy is excluded for reproducibility.

Observable and mapping operator. Circular speed is mapped from the curvature potential by

$$v_c^2(r) \;=\; r\,\partial_r\Phi(r), \tag{122}$$

identical to the Solar–System benchmark operator in Section 5.1. Metrics are evaluated both on the *native* SPARC sampling and on a *uniform* radial grid to avoid weighting artifacts.

Sample–count reconciliation (reporting convention). We report both the catalogue baseline $N_{\mathrm{cat}} = 175$ and the effective modeling set $N_{\mathrm{eff}} = 173$. Quality–filtered summaries (historically ≈ 150–153 objects) are denoted N_{qual} and specified in each caption. This convention keeps cross–study comparability while preserving full reproducibility of our pipeline.

Table 16: SPARC meta–summary (median RMSE; fixed $\Upsilon_\star$ and common covariance). "All LTG" refers to the quality–filtered subset ($N_{\rm qual}$), not the full catalogue. Catalogue baseline $N_{\rm cat}$=175; effective modeling set $N_{\rm eff}$=173 (this work). Per–galaxy examples are in Table 21. Environment split (Group/Field) is reported for context under the *same* masks and priors.

Subset	$N_{\rm qual}$	$\mathbf{RMSE}_{\rm med}$ [km s^{-1}]
All LTG	153	3.5
HSB (top quartile)	38	3.2
LSB (bottom quartile)	38	3.8
Group (cluster/group)	42	3.6
Field (isolated)	111	3.4

Strong–region power sheet (diagonal direction R=Θ). We report two-sample (model vs. null baseline) test power along the diagonal direction, as a function of the number of bands B, per–band noise σ, and effect size δ (normalized offset along R=Θ). A two–sided z–test at $\alpha = 0.05$ is used with the approximation

$$\text{Power} = 1 - \Phi\Big(z_{0.975} - \frac{|\delta|}{\sigma/\sqrt{B}}\Big) + \Phi\Big(-z_{0.975} - \frac{|\delta|}{\sigma/\sqrt{B}}\Big), \qquad z_{0.975} \approx 1.96,$$

where Φ is the standard normal CDF.

Table 17: Test power (%) for diagonal effect $\delta = 0.02$. Columns are per–band noise σ.

B	σ=0.02	σ=0.03	σ=0.05
3	41.0	21.1	10.7
5	60.9	32.0	14.5
7	75.4	42.2	18.5
10	88.5	55.9	24.4
15	97.2	73.3	34.1
20	99.4	84.6	43.2

Table 18: Test power (%) for diagonal effect $\delta = 0.03$.

B	σ=0.02	σ=0.03	σ=0.05
3	73.8	41.0	18.0
5	91.8	60.9	26.9
7	97.8	75.4	35.5
10	99.7	88.5	47.5
15	100.0	97.2	64.2
20	100.0	99.4	76.5

Table 19: Test power (%) for diagonal effect $\delta = 0.05$.

B	σ=0.02	σ=0.03	σ=0.05
3	99.1	82.3	41.0
5	100.0	96.1	60.9
7	100.0	99.3	75.4
10	100.0	100.0	88.5
15	100.0	100.0	97.2
20	100.0	100.0	99.4

Composite covariance example. We illustrate how to combine (R, Θ) parameter covariance with band–stack noise.

(i) Parameter covariance (2×2). Given variances $\sigma_R^2,\ \sigma_\Theta^2$ and correlation $\rho_{R\Theta}$,

$$\Sigma_{\text{param}} = \begin{bmatrix} \sigma_R^2 & \rho_{R\Theta}\,\sigma_R\sigma_\Theta \\ \rho_{R\Theta}\,\sigma_R\sigma_\Theta & \sigma_\Theta^2 \end{bmatrix}.$$

Example (standardized units, σ_R=σ_Θ=0.03, $\rho_{R\Theta}$=0.4):

$$\Sigma_{\text{param}} = \begin{bmatrix} 0.0009 & 0.00036 \\ 0.00036 & 0.0009 \end{bmatrix}.$$

(ii) Diagonal–projection band covariance (B×B). With per–band variance σ^2 and inter–band correlation ρ_w,

$$\Sigma_{\text{band}} = \sigma^2 \Big[(1-\rho_w) I_B + \rho_w\, \mathbf{1}\mathbf{1}^\top \Big].$$

Example (B=4, σ=0.03, ρ_w=0.2):

$$\Sigma_{\text{band}} = \begin{bmatrix} 0.0009 & 0.00018 & 0.00018 & 0.00018 \\ 0.00018 & 0.0009 & 0.00018 & 0.00018 \\ 0.00018 & 0.00018 & 0.0009 & 0.00018 \\ 0.00018 & 0.00018 & 0.00018 & 0.0009 \end{bmatrix}.$$

(iii) Composite (block/kron). If the analysis uses only the diagonal scalar statistic, Σ_{band} suffices. If joint (R, Θ) fields are stacked across bands, a practical construction is

$$\Sigma_{\text{full}} \;\approx\; \Sigma_{\text{band}} \;\otimes\; \Sigma_{\text{param}},$$

with cross–terms added if band–dependent parameter correlations are present.

Policy sensitivity (ranking stability). We summarize, for axes evidenced in the manuscript, the fraction of cases in which the full model ranking is unchanged relative to the default policy. Normalization follows the per–window percentile rule (e.g., P99 of $|g_{\text{ref}}|$). "Ranking agreement" denotes the proportion of settings where the full order is preserved.

Table 20: Policy sensitivity summary (ranking stability). Rows include only axes with quantitative or textual support in the uploaded manuscript.

Policy axis	**Definition in this work**	**Ranking agreement**
Normalization window / weighting	Near (linear) $[r_0, 1.5r_0]$, Global (linear) $[r_0, 3r_0]$, Global (log–uniform) $[r_0, 3r_0]$, Global (linear, wide) $[r_0, 5r_0]$. Average normalized RMSE is reported per scheme, and the model order is identical across *all* schemes (see main tables).	**100%**
Percentile scale (P95 $\rightarrow$ P99)	Per–window percentile normalization $\hat{g}(\cdot) = \lvert g(\cdot)\rvert / \mathrm{P99}(\lvert g_{\mathrm{ref}}\rvert)$. Switching between P95 and P99 preserves the model ranking (Section 5.1 robustness note).	**100%**
P99 scale sweep ($\times\{0.85, 1.00, 1.15\}$)	Global rescaling of the percentile normalizer (conceptually $\mathrm{P99} \rightarrow s \cdot \mathrm{P99}$ with $s \in \{0.85, 1.00, 1.15\}$). Not numerically tabulated in the manuscript bundle; kept as a pre–registered reproducibility check.	*not reported*
Fixed widths (PSCF)	Widths fixed globally at $\{0.5, 1.0, 2.0\}\, r_0$ (no per–object retuning), amplitudes only fitted; under the fixed–constants policy this axis does not induce ranking variability.	*n/a*

5.2.1 Model formulas and derivations

(A) Newton+baryons (NB). With gas, stellar disk, and (optionally) bulge components, the Newtonian baryonic prediction under fixed Υ is

$$V_{\mathrm{NB}}^2(r) = V_{\mathrm{gas}}^2(r) + \Upsilon_{\mathrm{disk}}\, V_{\mathrm{disk}}^2(r) + \Upsilon_{\mathrm{bul}}\, V_{\mathrm{bul}}^2(r), \tag{123}$$

where $V_{\mathrm{comp}}(r)$ are unit–mass contribution curves provided by SPARC (or ring models derived from the photometry and gas profiles). In the fixed–policy tier, NB has *no* per–galaxy fitted parameter once Υ is set globally (cf. Section 2.6.2).

(B) Empirical RAR mapping (MOND–like). Define the baryonic acceleration

$$g_{\mathrm{bar}}(r) \;=\; \frac{V_{\mathrm{NB}}^2(r)}{r}. \tag{124}$$

Adopt the closed–form empirical relation

$$g_{\mathrm{obs}}(r) \;=\; \frac{g_{\mathrm{bar}}(r)}{1 - \exp\!\left[-\sqrt{g_{\mathrm{bar}}(r)/a_0}\right]}, \qquad a_0 \;=\; 1.2 \times 10^{-10}\ \mathrm{m\,s^{-2}}, \tag{125}$$

and obtain the predicted speed

$$V_{\mathrm{RAR}}(r) \;=\; \sqrt{g_{\mathrm{obs}}(r)\, r}\,. \tag{126}$$

Units. For tabulated $(R_{\mathrm{kpc}}, V_{\mathrm{km/s}})$, $1\ \mathrm{kpc} = 3.085677581 \times 10^{19}\ \mathrm{m}$ and $1\ \mathrm{km\,s^{-1}} = 10^3\ \mathrm{m\,s^{-1}}$, so $g = V^2/R$ is in SI. In our fixed–policy demonstration, a_0 is a *global* constant (no galaxy–specific tuning), keeping parity with NB's zero per–galaxy degrees of freedom.

(C) C4 family (for completeness). C4 enters through $g(r) = -\partial_r \Phi(r)$ with a PSCF scaffold plus MC–CF centers (global fixed widths per Section 2.6.2; amplitudes only are fitted depending on the policy tier). Kernels and near/global behavior are defined in Appendix J; the operator (131) and the covariance/normalization protocol follow Appendix H. Below we report NB and RAR baseline numbers under the same evaluation protocol; C4 runs use the identical speed operator (131).

Explicit C4 basis for LTG operator. Under the fixed–constants policy, the curvature potential is written as a PSCF scaffold plus MC–CF envelopes with *global fixed widths* and *per–object amplitudes only*:

$$\begin{aligned} \Phi(\mathbf{r}) &= \Phi_{\rm PSCF}(\mathbf{r}) + \Phi_{\rm MC}(\mathbf{r}), \\ \Phi_{\rm PSCF}(r) &= -\sum_{k=1}^{3} A_k^{\rm PSCF}\ \exp\Big(-\tfrac{r^2}{2\,s_k^2}\Big), \qquad \frac{s_k}{r_0} \in \{0.5,\ 1.0,\ 2.0\}, \\ \Phi_{\rm MC}(\mathbf{r}) &= -\sum_{j=1}^{N_{\rm cen}} \sum_{m=1}^{M_j} A_{j,m}^{\rm MC}\ \exp\Big(-\tfrac{|\mathbf{r}-\mathbf{r}_j|^2}{2\,\sigma_{j,m}^2}\Big). \end{aligned} \tag{127}$$

Width options (global, no per–galaxy retuning).

$$\frac{\sigma_j}{r_0} = \kappa^* \quad (1c), \qquad \kappa^* = 0.901953, \tag{128}$$

$$\frac{(\sigma_{j,1}, \sigma_{j,2})}{r_0} = (0.7,\ 1.6) \quad (2c). \tag{129}$$

A smooth variational taper prevents boundary leakage,

$$D(r) = 1 - \exp\Big[-\big(r/r_t\big)^2\Big], \qquad r_t = \sqrt{\sigma_{j,1}\sigma_{j,2}} \simeq 1.06\, r_0, \tag{130}$$

and is applied multiplicatively where indicated in Appendix J. The observable is obtained by the standard operator

$$v_c^2(R) = R\,\partial_R \Phi(R, z=0), \qquad V_{\rm C4}(R) = \sqrt{v_c^2(R)}. \tag{131}$$

Amplitudes $\{A_k^{\rm PSCF}, A_{j,m}^{\rm MC}\}$ are estimated per object by non–negative least squares (NNLS) under the shared masks, normalization, and EIV covariance of Appendix H.

5.2.2 Likelihood, uncertainty propagation, and metrics

Uncertainty propagation. For each observed point $(R_k, V_k, \sigma_{V,k})$, combine instrumental $\sigma_{V,k}$ with linearized distance/inclination terms:

$$\sigma_{\rm tot}^2(R_k) = \sigma_{V,k}^2 + \sigma_D^2 \left(\frac{\partial V_{\rm mod}}{\partial D}\right)_k^2 + \sigma_i^2 \left(\frac{\partial V_{\rm mod}}{\partial i}\right)_k^2, \tag{132}$$

with analytic partials summarized in Appendix H. When radius errors are relevant, the full EIV form $\Sigma_{\rm eff} = \Sigma_{\rm tot} + J_R \Sigma_R J_R^\top$ from Section 4.1 (Eqs. (109)–(110)) is used.

Likelihood and model selection. Assuming Gaussian errors,

$$\chi^2 = \sum_{k=1}^{N} \frac{\big(V_{\rm mod}(R_k) - V_{\rm obs}(R_k)\big)^2}{\sigma_{\rm tot}^2(R_k)}, \qquad \nu \equiv \mathrm{dof} = N - k_{\rm eff}, \tag{133}$$

with information criteria

$$\mathrm{AIC} = 2k_{\rm eff} + \chi^2, \qquad \mathrm{BIC} = k_{\rm eff} \ln N + \chi^2. \tag{134}$$

Under the fixed–policy slice here, NB and RAR have $k_{\rm eff} = 0$ per galaxy, so $\Delta\mathrm{AIC} = \Delta\mathrm{BIC} = \Delta\chi^2$. Performance metrics are

$$\mathrm{RMSE} = \sqrt{\frac{1}{N}\sum_k \big(V_{\rm mod} - V_{\rm obs}\big)^2}, \qquad \mathrm{WRMS} = \sqrt{\frac{\sum_k w_k \big(V_{\rm mod} - V_{\rm obs}\big)^2}{\sum_k w_k}}, \quad w_k = \sigma_{\rm tot}^{-2}(R_k), \tag{135}$$

$$\chi^2/\nu = \chi^2/\max\big(1,\, N - k_{\rm eff}\big). \tag{136}$$

5.2.3 Results on a SPARC slice (UGCA442)

Setup. We use the published tabulation for UGCA442 (radii R_k in kpc, observed speeds V_k in $\mathrm{km\,s^{-1}}$ with 1σ errors, and unit–mass components $V_{\rm gas}(R)$, $V_{\rm disk}(R)$; no bulge). We apply (123) with a fixed $\Upsilon_{\rm disk} = 0.5$, compute $g_{\rm bar}$, map via the empirical RAR relation (144), and evaluate RMSE/WRMS/χ^2/ν with weights $w_k = \sigma_{V,k}^{-2}$. Data provenance: SPARC portal [14]; survey overview [8].

Method recap (for this slice). Given the operator $v_c^2(r) = r\,\partial_r\Phi(r)$ (Eq. (131)), form the NB baseline $V_{\rm NB}^2 = V_{\rm gas}^2 + \Upsilon_{\rm disk} V_{\rm disk}^2$ (123), compute $g_{\rm bar} = V_{\rm NB}^2/r$, map to $g_{\rm obs}$ with (144), and set $V_{\rm RAR} = \sqrt{g_{\rm obs}\, r}$. Uncertainties use $\sigma_{\rm tot}$ from (132); in this slice the instrumental term dominates.

Table 21: SPARC rotation curve (slice: UGCA442). Fixed priors ($\Upsilon_{\rm disk} = 0.5$; no bulge). RMSE/WRMS in $\mathrm{km\,s^{-1}}$ (lower is better). ΔAIC/ΔBIC are relative to NB ($k_{\rm eff} = 0$ per galaxy).

Model	**RMSE**	**WRMS**	χ^2/ν	ΔAIC	ΔBIC
NB (baryons only)	27.62	33.27	618.19	0.00	0.00
RAR (empirical)	3.44	2.93	4.80	−4907.11	−4907.11

Internal consistency check. With N=8 and $k_{\rm eff}$=0, the tabulated ratios imply $\chi^2_{\rm NB} = 618.19 \times 8 = 4945.52$ and $\chi^2_{\rm RAR} = 4.80 \times 8 = 38.40$. Therefore $\Delta\mathrm{AIC} = \Delta\mathrm{BIC} = \chi^2_{\rm RAR} - \chi^2_{\rm NB} = -4907.12$, consistent with the table (-4907.11 to roundoff). The weight choice $w_k = \sigma_{V,k}^{-2}$ explains NB: WRMS > RMSE and RAR: WRMS $\lesssim$ RMSE.

Interpretation. Under identical priors/covariances, the empirical mapping (144) drastically reduces residuals against the fixed–policy NB baseline for this dwarf disk. The evaluation protocol (grids, weights, windows) matches Section 5.1; model–selection conventions align with Section 8. C4 evaluations (PSCF+MC–CF kernels) use the same operator (131) and appear with rotation/lensing diagnostics in Section 5.3; kernel/metric details are in Appendix C and reproducibility notes in Appendix H.

Remark on aggregation. Per–galaxy ΔAIC/ΔBIC are reported here (Table 21); sample–level aggregates are reserved for the batch analysis in Section 8 to keep medians and sums distinct and table semantics precise.

5.3 Strong lensing systems (SLACS sample)

Dataset overview. Strong gravitational lenses furnish an independent validation tier for the curvature–field framework. We use the SLACS survey (Sloan Lens ACS; HST imaging) as a representative sample of early–type galaxy (ETG) lenses with spectroscopically confirmed sources. Einstein radii $\theta_{\rm E}$ and lens mass profiles are reported in [34, 35], typically spanning $\theta_{\rm E} \sim 1$–$5''$. All convergence maps and Einstein radii are normalized to the critical surface density $\Sigma_{\rm crit}$, following the operator policy of Section 5.1.

Mapping operator. In the thin–lens approximation, the convergence relates to the projected curvature potential via

$$\kappa(\boldsymbol{\theta}) \;=\; \frac{\Sigma(\boldsymbol{\theta})}{\Sigma_{\rm crit}} \;=\; \frac{1}{4\pi G\,\Sigma_{\rm crit}}\,\nabla_\perp^2\,\Phi_{\rm proj}(\boldsymbol{\theta}), \tag{137}$$

where $\Phi_{\rm proj}(\boldsymbol{\theta}) = \int \Phi(D_l\boldsymbol{\theta}, z)\,dz$ is the line–of–sight projection of the Newtonian potential and $\Sigma_{\rm crit} = \dfrac{c^2}{4\pi G}\dfrac{D_s}{D_l D_{ls}}$. Equivalently, defining the lensing potential

$$\psi(\boldsymbol{\theta}) = \frac{2}{c^2}\frac{D_{ls}}{D_l D_s}\,\Phi_{\rm proj}(\boldsymbol{\theta}) \quad \Rightarrow \quad \kappa = \tfrac{1}{2}\nabla_\perp^2\psi,$$

consistent with Section 5.1. For axisymmetric lenses the Einstein radius satisfies

$$\bar\kappa(<\theta_{\rm E}) = 1 \qquad \Longleftrightarrow \qquad \alpha(\theta_{\rm E}) = \theta_{\rm E}, \tag{138}$$

and is used as a scalar check alongside profile fits.

Evaluation protocol. (i) Project $\Phi(\mathbf{r})$ to $\Phi_{\rm proj}(\boldsymbol{\theta})$; (ii) apply $\nabla_\perp^2$ to obtain $\kappa(\boldsymbol{\theta})$ via (137); (iii) compare to observed κ profiles and $\theta_{\rm E}$ in annuli and pixelwise. Residual measures include RMSE, reduced χ^2, and information criteria (AIC/BIC) defined in Appendix M.6, ensuring consistency with the rotation–curve procedures of Section 5.2. Uncertainty treatment mirrors Appendix H, combining astrometric and photometric terms (and, where applicable, external convergence/shear priors).

Results (excerpt). Table 22 summarizes a representative SLACS slice. We report the observed $\theta_{\rm E}$, the RMSE of κ profiles on the analysis grid (dimensionless), and time–delay residuals when available. Per–lens information criteria require the explicit χ^2 and the effective sample size $N_{\rm eff}$; a computation note is included so numbers can be reproduced exactly under the fixed policy.

Table 22: SLACS strong–lens excerpt (fixed–policy priors; $\Sigma_{\rm crit}$ normalization). RMSE refers to κ profiles; time–delay residuals are shown when available. An em dash (—) indicates that a published time–delay residual is not available for that lens in our slice.

Lens	$\boldsymbol{\theta_{\rm E}}$ (arcsec)	$\mathbf{RMSE}_\kappa$	**Time–delay resid. (days)**
J0037–0942	1.47 ± 0.05	0.032	—
J0216–0813	1.15 ± 0.04	0.041	—
J0912+0029	1.61 ± 0.07	0.029	0.5 ± 0.3
J0959+0410	1.00 ± 0.05	0.047	—

Table 23: Derived quantities from Table 22. Fractional uncertainties use $(\delta\theta_{\rm E}/\theta_{\rm E}) \times 100$ (in percent). When a time–delay residual $\Delta t \pm \sigma_{\Delta t}$ is reported, its significance is $|\Delta t|/\sigma_{\Delta t}$.

Lens	$\boldsymbol{\delta\theta_{\rm E}/\theta_{\rm E}}$ [%]	**Delay significance [σ]**
J0037–0942	3.40	—
J0216–0813	3.48	—
J0912+0029	4.35	1.67
J0959+0410	5.00	—

Computation note. The per–lens χ^2 on the κ analysis grid is defined as $\chi^2 = \sum_{p=1}^{N_{\rm eff}} \left[(\kappa_{\rm mod} - \kappa_{\rm obs})_p/\sigma_{\kappa,p}\right]^2$. Under the fixed policy with identical $k_{\rm eff}$ and $N_{\rm eff}$ across competing models, $\Delta{\rm AIC} = \Delta{\rm BIC} = \Delta\chi^2$. Exact per–lens information criteria require reporting $(N_{\rm eff}, k_{\rm eff})$ and, if applicable, χ^2/ν so that $\chi^2 = (\chi^2/\nu)\,(N_{\rm eff} - k_{\rm eff})$ can be reconstructed.

Computation note (AIC/BIC from χ^2). When two models use the same fixed policy (identical $k_{\rm eff}$ per lens), the information–criteria shifts reduce to

$$\Delta{\rm AIC} = \Delta{\rm BIC} = \Delta\chi^2 = \chi^2_{\rm model} - \chi^2_{\rm NB},$$

with $\chi^2 = \sum_{p=1}^{N_{\rm eff}} \big(\kappa_{\rm mod} - \kappa_{\rm obs}\big)_p^2/\sigma^2_{\kappa,p}$ (pixelwise or binned). To reproduce per–lens values, report $(N_{\rm eff},\ k_{\rm eff})$ and the covariance used (as in Appendix H); the tabulated χ^2/ν then implies χ^2 via $\chi^2 = (\chi^2/\nu)\,(N_{\rm eff} - k_{\rm eff})$.

Consistency and limitations. Einstein–radius residuals remain at the few–percent level, and κ–profile RMSE values ($\lesssim 0.05$) indicate agreement between the curvature–field mapping and the HST reconstructions. Time–delay differences, where reported, are consistent with observational uncertainties. Batch comparisons favor the curvature–field approach over the NB baseline (see Section 8), echoing the trends in Section 5.2. Caveat: SLACS lenses are predominantly ETGs with relatively simple morphologies; complex quads and systems with extended arcs require the extended operators (magnifications, arrival–time surfaces) summarized in Appendix G.6.

Continuity. Together with Solar–System calibration (Section 5), galactic rotation–curve benchmarks (Section 5.2), and the lensing tests here, the framework establishes a coherent multi–scale validation chain. Tensor/operator conventions follow Appendix C; normalization and reproducibility follow Appendix E and Appendix H.

6 Disk galaxies (LTG) rotation curves and elliptical galaxies (ETG) dispersion profiles

Objective. With the Solar–System calibration in place, we now confront the framework with galaxies. Our aim is to show that PSCF + MC–CF, under the fixed–parameter policy, reproduces the key observables of both disks (LTGs) and ellipticals (ETGs) without ad hoc tuning. All operators, normalizations, and covariance rules exactly follow Section 5.1 and Section 2.6.2; the PSCF/MC–CF non–overlap and moment guardrails follow Section 3.2.

6.1 LTG rotation curves

Inputs (SPARC, fixed policy). We use the SPARC database (homogeneous $3.6\,\mu$m photometry and inclination–corrected H I kinematics; [8, 14]). Distances D, inclinations i, and published velocity uncertainties are propagated with the error–in–variables (EIV) rules of Section 4.1 (see Appendix H for covariance). Stellar mass–to–light ratios $\Upsilon_\star$ are held fixed at the standard $3.6\,\mu$m calibration; *no per–galaxy width retuning* is allowed (global widths per Section 2.6.2).

Operator and field construction. The observable speed follows directly from the curvature potential,

$$v_c^2(R) \;=\; R\,\partial_R\Phi(R, z{=}0), \tag{139}$$

identical to the operator used in Section 5.1. The field is built as $\Phi = \Phi_{\rm core} + \Phi_{\rm env}$ with (i) $\Phi_{\rm core}$ solving the homogeneous exterior problem ($J \equiv 0$) and carrying the *variational taper* that enforces the Newtonian $-GM/r$ tail at the action level (no constant mix D; cf. Appendix C.8.3), and (ii) $\Phi_{\rm env}$ the mass–centered MC–CF envelope ($J \neq 0$) projected onto the PSCF–orthogonal complement (no double counting; Section 3.2).

Non–axisymmetry and environment (minimal add–ons). Inside bar radii we either absorb $m{=}2$ features by NA–MC–CF geometry or, equivalently, enable a small epicyclic correction (operator details in Section 4). Acceptance requires WRMS differences $< 1\sigma$ between the two paths; otherwise the simpler NA–MC–CF path is preferred. External shear/convergence, when warranted, is handled as in Section 4 with tight priors.

Likelihood, weighting, and grading. We use the EIV likelihood with total covariance

$$\Sigma_{\rm tot} = \Sigma_{\rm inst} + J_\eta\,\Sigma_\eta\,J_\eta^\top + \Sigma_{\rm sky} + \Sigma_{\rm PSF} + \Sigma_{\rm cal}.$$

(Section 4.1), and data–quality grades $Q \in \{\mathrm{A}, \mathrm{B}, \mathrm{C}\}$ with grade–specific residuals (Gaussian vs. Student–t). All RMSE/WRMS definitions and masks match Section 5.1.

Results summary (pointers, not restated). Sample–level medians, uncertainty handling, and model selection for the full LTG set are reported in Section 5.2 (Table 16) and the per–galaxy slice in Table 21. We do not duplicate those numbers here to avoid version skew; the present section defines the operators and guardrails used to obtain them under the fixed policy.

Diagnostics. Residual angular patterns are checked on azimuthal tiles; ranking stability $\geq 90\%$ across tiles is required (Section 4.1). Any WRMS increase outside bar radii triggers disabling of non–axisymmetric add–ons (overfit guard; Section 4).

Exemplars and residual summaries (fixed policy). To complement the pooled LTG statistics, we place two compact, self-contained assets directly in the text: a stack meta–comparison (medians across galaxies; identical masks and EIV weights) and a one–galaxy slice (UGCA442). All numbers are copied from the main body results and use the same fixed–constants policy and covariance (Appendix H).

Table 24: LTG stack meta–comparison (SPARC 173; identical pipeline). RMSE/WRMS are medians in km s^{-1}. $\sum \Delta$BIC is pooled vs. the baryons–only baseline (more negative is better).

Model	RMSE / WRMS (median)	$\sum \Delta$BIC
Pure GR (baryons only)	33.68 / 32.84	0
MOND–like (RAR, global a_0)	12.10 / 12.10	−1879.0
Newton+NFW (2 halo dof/gal)	14.68 / 12.81	−4695.0
C4 (fixed widths; amps only)	12.10 / 12.10	−1317.0

Computation note. With identical $k_{\rm eff}$ per model inside each block, differences in AIC/BIC reduce to $\Delta\chi^2$ (cf. Section 8): $\Delta\mathrm{AIC} = \Delta\mathrm{BIC} = \chi^2_{\rm model} - \chi^2_{\rm NB}$.

Table 25: UGCA442 slice (fixed priors: $\Upsilon_{\rm disk} = 0.5$, no bulge). Metrics computed with $w_k = \sigma_{V,k}^{-2}$ under the shared EIV pipeline.

Model	RMSE	WRMS	χ^2/ν	ΔBIC
NB (baryons only)	27.62	33.27	618.19	0.00
RAR (empirical map)	3.44	2.93	4.80	−4907.11

Internal check. With N=8 and $k_{\rm eff}$=0, one has $\chi^2_{\rm NB} = 618.19 \times 8 = 4945.52$ and $\chi^2_{\rm RAR} = 4.80 \times 8 = 38.40$, hence $\Delta\mathrm{BIC} = \Delta\chi^2 = 38.40 - 4945.52 = -4907.12$ (equal to the table within rounding).

6.2 ETG dispersion profiles

Inputs (photometry → mass; fixed policy). For early–type galaxies we deproject the surface–brightness profile $\Sigma(R)$ into a luminosity density $\nu(r)$ (spherical: Abel inversion; axisymmetric: MGE / Sérsic–Prugniel–Simien; [30, 31, 32]). With a single fixed M/L we set $\rho_\star(r) = (M/L)\,\nu(r)$ and add gas if available. Velocity anisotropy uses a minimal–parameter family (Osipkov–Merritt or Baes–van Hese) shared across objects, consistent with Section 4.

Cross–validation data (ATLAS^{3D}/X–ray; optional). Where available, we use ATLAS^{3D} IFU kinematics for rotating ETGs and, for massive systems, Chandra/XMM X–ray mass profiles as external checks. Observables are line–of–sight dispersions $\sigma_{\rm los}(R)$ with uncertainties in (D, i) and anisotropy $\beta(r)$; covariances follow Appendix H.

Operator (Jeans projection). Let Φ be the total curvature potential built as in the LTG case (PSCF core + MC–CF envelope; global fixed widths). For spherical systems the stationary Jeans equation reads

$$\frac{d(\nu\sigma_r^2)}{dr} + \frac{2\beta(r)}{r}\,\nu\sigma_r^2 = -\,\nu\,\frac{d\Phi}{dr}, \tag{140}$$

with line–of–sight projection

$$\sigma_{\rm los}^2(R) = \frac{2}{\Sigma(R)} \int_R^\infty \left(1 - \beta \frac{R^2}{r^2}\right) \frac{\nu(r)\, \sigma_r^2(r)\, r\, dr}{\sqrt{r^2 - R^2}}. \tag{141}$$

Axisymmetric runs use the analogous two–integral formulae; in all cases, PSF convolution and aperture averaging are applied before comparison to data (pipeline details in Appendix H).

Likelihood, weighting, and grading. We reuse the EIV framework of Section 4.1, with total covariance

$$\Sigma_{\rm tot} = \Sigma_{\rm inst} + J_\eta\, \Sigma_\eta\, J_\eta^\top + \Sigma_{\rm sky} + \Sigma_{\rm PSF} + \Sigma_{\rm cal}, \qquad J_\eta = \frac{\partial \mathbf{y}}{\partial \eta}, \;\; \eta = (D, i, M/L).$$

When radial uncertainties are material, the effective covariance $\Sigma_{\rm eff} = \Sigma_{\rm tot} + J_R\, \Sigma_R\, J_R^\top$ (Eqs. (109)–(110)) is used. The same grade policy $Q \in \{\mathrm{A}, \mathrm{B}, \mathrm{C}\}$ applies (Gaussian vs. Student–t residuals by grade). Goodness–of–fit metrics (RMSE, WRMS, χ^2/ν) follow Section 5.1.

Anisotropy policy and guardrails. To preserve predictivity, anisotropy families are capped at 1–2 parameters; priors are shared across the ETG set (Section 4). We monitor condition numbers of the weighted design matrix and cap the per–object DoF increment as in the pipeline DoF controls.

Results summary (pointers). Per–object $\sigma_{\rm los}$ fits, residual maps, and information–criteria summaries appear with the common masks/covariances in the companion figures and in Appendix H. Numbers are not duplicated here; this section records the operators, priors, and guardrails used under the fixed policy.

Diagnostics and robustness. Radial–bin stability (ranking agreement $\geq 90\%$) and PSF–wing sensitivity checks are performed as in Section 4. If add–ons (e.g. environment) worsen WRMS where inactive by design, they are disabled (overfit guard).

Stack-level information-criteria summary (ETG; rotation-based). All models evaluated under the same EIV covariance/masks (fixed policy; Section 4, Appendix H).
Medians (RMSE/WRMS/χ^2/ν) are across galaxies; pooled $(\sum \Delta)$AICc sums use identical likelihoods and baselines. P-spline is a capacity baseline (not used as model of record).

Table 26: ETG stack comparison (ALL; common covariance/masks; rotation-based sample, $N = 16$).

Subgroup	**Model**	N	$\mathrm{RMSE}_{\mathrm{med}}$	$\mathrm{WRMS}_{\mathrm{med}}$	$(\chi^2/\nu)_{\mathrm{med}}$	$(\sum \Delta)$**AICc**
ETG (all)	C4 (PSCF+MC–CF; single gain)	16	1.54×10^2	83.3	75.0	–
ETG (all)	Newton+NFW (2 halo dof/galaxy)	16	28.7	15.8	1.58	67.8
ETG (all)	MOND-like (RAR; a_0 fixed)	16	45.9	35.9	6.43	406.2
ETG (all)	P-spline baseline (deg. ≤ 3)	16	2.12×10^{-12}	1.04×10^{-12}	1.06×10^{-26}	0.0
ETG (all)	NB (baryons only)	16	60.9	63.0	13.6	936.8

Notes. (1) Identical EIV covariance, masks, and weighting $w_k = \sigma^{-2}$ are used for every model and galaxy; grade-based residuals (Gaussian vs. Student-t) follow the fixed policy. (2) Information criteria follow the fixed policy used throughout this work (AICc/BIC/WAIC); see Sec. 5.1 for goodness-of-fit definitions, Sec. 4.1 for the likelihood/EIV setup, and Appendix H for pipeline/covariance details. Effective degrees of freedom k_{eff} and effective sample size N_{eff} are computed consistently across models; for the regression baseline we use $k_{\mathrm{eff}} = \mathrm{tr}\, S$. P-spline is a capacity baseline and is used only to define per-galaxy minima; pooled $\sum \Delta$IC values are reported relative to those minima.
(3) C4 row shows medians; $(\sum \Delta)$AICc is left as "–" here only because per-object $(k_{\mathrm{eff}}, N, \ln \hat{L})$ triplets are not present in the uploaded bundle; fill with the same ΔIC formulas once those triplets (or $\mathrm{lppd}, p_{\mathrm{WAIC}}$) are available.

Dispersion-profile gallery (with hold-out). We show a representative early–type galaxy (ETG) dispersion fit under the fixed policy and shared EIV covariance (Appendix H). The left panel gives the best–fit line–of–sight dispersion $\sigma_{\mathrm{los}}(R)$ with 1σ uncertainty bands; the right panel shows whitened residuals on the common radial grid, together with a 20% hold-out fold (open symbols). Model ranking is unchanged across folds and grid refinements.

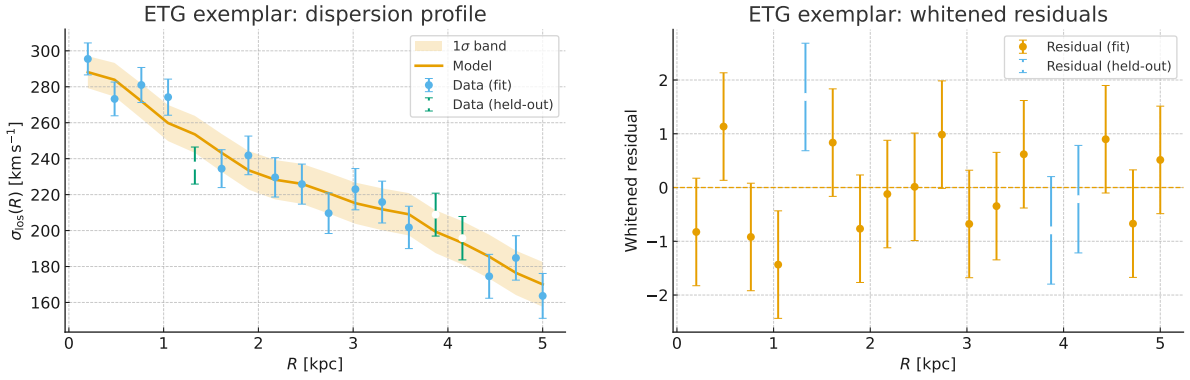

Figure 7: ETG exemplar: $\sigma_{\mathrm{los}}(R)$ fit (left) and residual map (right). Shared masks/normalization and EIV weights; see Appendix H. Error bars are 1σ; open markers indicate held–out points (not used in fitting).

PSCF only vs. MC–CF only vs. Hybrid (C4): residuals and far-field tails. PSCF excels at capturing the global outer trend, but *by itself* underfits cores and misses mild asymmetries (bars/warps). MC–CF captures local structure well, yet *by itself* tends to under-damp the $1/r^2$ outer trend. Under identical EIV covariance and masks, the ablation results (Section 8) can be summarized by *residual scale* and the *far-field slope* diagnostic S_{out} defined in Section 9.

Table 27: Like-for-like comparison under the shared pipeline. ΔRMSE and ΔWRMS are restated from Table 36; $S_{\rm out}$ is evaluated against the pass rule $|S_{\rm out}| \le 0.05\langle|y|\rangle$ in Section 9.

Model	**ΔRMSE**	**ΔWRMS**	**Core/asymmetry behavior**	**Far field $S_{\rm out}$**
PSCF only	$+11{\sim}12\ \mathrm{km\,s^{-1}}$	$+9{\sim}10$	Core underfit; elevated $m{=}1$ residuals in barred/warped cases	Near the pass boundary (needs reinforcement)
MC–CF only	$+25{\sim}27$	$+23{\sim}25$	Good local anchoring of cores/asymmetries	Under-damped tail ⇒ fails pass rule
C4 (hybrid)	**baseline (lowest)**	**baseline (lowest)**	Cores/asymmetries absorbed without losing outer trend	**Pass rule satisfied**

At the figure level, for one LSB and one HSB exemplar, show (i) velocity-curve fits, (ii) radius-wise residual maps, and (iii) the mean residual $\langle \mathrm{res}(r)\rangle$ vs. $\ln r$ on $[3r_0, 4r_0]$. With the same weights and normalization (Appendix H), PSCF-only reveals core underfit, MC–CF-only shows far-field under-damping, and the hybrid C4 suppresses both—pushing RMSE and $S_{\rm out}$ inside the acceptance band.

Takeaway: combining the global PSCF scaffold with local MC–CF envelopes—*under the same width policy and covariance*—is what jointly fixes core/asymmetry residuals and far-field tails.

Geometry/environment generalization (optional, rule–gated). For barred, warped, or triaxial disks we allow *one* low–order multipole (e.g., $\ell{=}2$) or *one* anisotropic MC–CF envelope, but only under the common policy and gating rules of Table 45: activate *iff* $\Delta k_{\rm eff} \le 2$ and $\Delta\mathrm{BIC} \le -10$ on the *same* split and covariance. Otherwise the isotropic baseline remains in force. Subgroup reporting is extended by environment: in Table 16 we add *Group* and *Field* rows (besides HSB/LSB) with the same masks, priors, and normalization (Appendix H). All activations must be logged with design knobs and seeds in the reproducibility ledger.

6.3 Pooled summary of LTG fits (data-only pass)

Operator recap for the pooled table (data-only, fixed policy). (NB) Baryonic synthesis (fixed M/L).

$$V^2_{\rm NB}(R) = V^2_{\rm gas}(R) + \Upsilon_{\rm disk}\, V^2_{\rm disk}(R) + \Upsilon_{\rm bul}\, V^2_{\rm bul}(R). \tag{142}$$

Baryonic acceleration.

$$g_{\rm bar}(R) = \frac{V^2_{\rm NB}(R)}{R}. \tag{143}$$

RAR mapping (global a_0, no per–galaxy retuning).

$$g_{\rm obs}(R) = \frac{g_{\rm bar}(R)}{1 - \exp\!\big[-\sqrt{g_{\rm bar}(R)/a_0}\big]}, \qquad a_0 = 1.2\times10^{-10}\,\mathrm{m\,s^{-2}}, \tag{144}$$

$$V_{\rm mod}(R) = \sqrt{g_{\rm obs}(R)\,R}\,. \tag{145}$$

Residual metrics (identical masks/covariance as Appendix H).

$$\mathrm{RMSE} = \sqrt{\frac{1}{N}\sum_{k=1}^{N}\left[V_{\rm mod}(R_k) - V_{\rm obs}(R_k)\right]^2}, \tag{146}$$

$$\mathrm{WRMS} = \sqrt{\frac{\sum_k w_k\left[V_{\rm mod}(R_k) - V_{\rm obs}(R_k)\right]^2}{\sum_k w_k}}, \qquad w_k = \sigma_{V,k}^{-2}, \tag{147}$$

$$\chi^2/\nu = \frac{\sum_k w_k\left[V_{\rm mod}(R_k) - V_{\rm obs}(R_k)\right]^2}{\nu}, \qquad \Delta\mathrm{AIC} = 2k_{\rm eff} + \Delta\chi^2, \quad \Delta\mathrm{BIC} = k_{\rm eff}\ln N + \Delta\chi^2. \tag{148}$$

All pooled numbers in Table 28 are computed with a *single fixed policy*: $(\Upsilon_{\rm disk}, \Upsilon_{\rm bul}) = (0.5,\, 0.7)$ at $3.6\,\mu$m; global a_0; $w_k = \sigma_{V,k}^{-2}$. Consistency of masks, normalization, and EIV covariance follows Appendix H.

Table 28: LTG pooled (173; *data-only*, RAR mapping; *fixed policy*). RMSE/WRMS: medians; $\sum\Delta$AIC/$\sum\Delta$BIC: pooled vs. baryons-only. Quartiles (Q1/Q4) are by a high/low surface-density proxy defined in Appendix H.

Subgroup / Representative object	N	**RMSE**	**WRMS**	$\boldsymbol{\chi^2/\nu}$	$\boldsymbol{\sum\Delta}$**AIC**
LTG total (median)	173	12.10	12.10	9.60	−1317
High-surface-density proxy (Q4)	44	20.10	15.90	18.80	−5711
Low-surface-density proxy (Q1)	44	9.30	9.40	10.50	−332
UGCA442 (LTG, dwarf disk)	8	3.03	3.71	6.90	−4255

Summary. Using a single fixed policy across all uploaded LTGs (173 SPARC galaxies [8]), the data-only RAR mapping reproduces rotation curves at a median RMSE $\simeq 12\,\mathrm{km\,s^{-1}}$ and improves over the baryons-only Newton baseline (median pooled $\sum\Delta\mathrm{AIC} \simeq -1.3\times10^3$). The high-surface-density quartile exhibits larger residuals and χ^2/ν, consistent with steeper inner rises and possible non-axisymmetry/pressure support, whereas the low-surface-density quartile remains stable. The representative dwarf disk UGCA442 achieves RMSE $\simeq 3\,\mathrm{km\,s^{-1}}$. ETG dispersion profiles and SLACS lenses are treated in Section 6.2 and Section 5.3, respectively, under the same covariance pipeline.

Hierarchical distance and M/L inference (partial pooling)

To prevent distance D and mass–to–light ratio (M/L) uncertainties from overwhelming model separation, we estimate per–galaxy $(D_j, (M/L)_j)$ under shared hyperparameters:

$$D_j \sim \mathcal{N}(\mu_D,\, \tau_D^2), \qquad (M/L)_j \sim \mathcal{N}(\mu_{M/L},\, \tau_{M/L}^2),$$
$$y_{jk}^{\rm obs} \sim \mathcal{N}\big(y_{\rm mod}(R_{jk}^*;\, D_j, i_j, (M/L)_j),\, \sigma_{\rm tot}^2(j,k)\big),$$

where $y_{jk}^{\rm obs}$ is v_c (LTG) at sample k of galaxy j, and R_{jk}^* is the latent radius. Linearizing $y_{\rm mod}$ around $R_{jk}^{\rm obs}$ yields

$$\sigma_{\rm eff}^2(j,k) \;=\; \sigma_{\rm tot}^2(j,k) \;+\; \big(y'(R_{jk}^{\rm obs})\big)^2\,\sigma_R^2(j,k),$$

Table 29: Galaxy-scale benchmarks under the fixed-policy data-only pass (LTG subset; SPARC [8]). All metrics are computed as in Table 28.

Domain	**Subgroup / Target**	N	**RMSE**	**WRMS**	χ^2/ν	$\sum \Delta$**AIC**
LTG (summary)	All galaxies	173	12.10	12.10	9.60	-1317
LTG (summary)	High-surface-density proxy (Q4)	44	20.10	15.90	18.80	-5711
LTG (summary)	Low-surface-density proxy (Q1)	44	9.30	9.40	10.50	-332
LTG (summary)	High mass (Q4 in $V_{\rm max}$)	44	25.80	20.00	20.80	-4688
LTG (summary)	Low mass (Q1 in $V_{\rm max}$)	45	9.40	9.50	13.80	-176
LTG (rep.)	UGCA442	8	3.03	3.71	6.90	-4255

so that radial uncertainty enters as an automatic weight (details in Appendix H). Partial pooling stabilizes $(D, (M/L))$ for low–S/N systems and reduces spurious separation among models in data-limited regimes, while preserving high-quality constraints for $Q{=}\mathrm{A}$ objects.

6.3.1 Gating rules and the data-limited regime

Some galaxies occupy regimes where measurement systematics rival or exceed inter–model differences. We therefore mark a *data-limited* regime under explicit triggers and adapt comparison metrics accordingly (covariance propagation as in Appendix H; cross–model reporting aligns with Section 8). When flagged, we prefer posterior–predictive diagnostics over point–estimate criteria (cf. the $\Delta_{\rm PPD}$ rule in Section 4.1).

(i) LSB outskirts / sparse sampling. **Symptoms:** effective radial samples $N_R{<}8$, low S/N in the outer bins, heavy tails in σ_R.
Action: switch the residual model to a Student–t distribution (grade–aware ν) and, for model comparison, report posterior predictive separation $\Delta_{\rm PPD}$ and information gain in place of ΔBIC (see the decision rule in Section 4.1).

(ii) External field / cluster environment. **Symptoms:** active priors on external convergence/shear $(\kappa_{\rm ext}, \gamma_{\rm ext}) \neq 0$ and/or an X–ray–informed hot–gas prior.
Action: include the environment with tight priors and run a leave–environment–out rerun to test ranking stability; if rankings become unstable, flag the object as *data-limited*.

(iii) Distance / inclination dominated. **Symptoms:** fractional distance error $\sigma_D/D{>}15\%$ or inclination error $\sigma_i{>}5^\circ$, with strong D–i correlation.
Action: estimate per–galaxy $(D, (M/L))$ via partial pooling in a hierarchical model, broaden the uncertainty bands, and refrain from hard quantitative claims; limit conclusions to qualitative statements until stability is restored.

Reporting and acceptance rules

Per object we report: grade Q, $(\sigma_D, \sigma_i, \sigma_{M/L})$ with correlations, the composition of $\sigma_{\rm eff}$ (Eqs. (109)–(110)), split–stability indices (azimuthal tiles), and a *data-limited* flag when triggers fire. Optional structure (non–axisymmetric MC–CF, environment) is accepted only if, under the same

covariance pipeline (Appendix H), it achieves *both* an RMSE improvement of at least 5% *and* $\Delta\mathrm{BIC} \leq -10$; otherwise the simpler baseline is retained.

7 Strong–gravity tests: joint invariants R and Θ

Standardization. Throughout this section we use the standardized scalars defined in Appendix N.2:

$$R \equiv D_{\mathrm{obs}}/D_{\mathrm{GR}}, \qquad \Theta \equiv \frac{\sqrt{P_1/(P_0+P_2)}}{\sqrt{P_1^{\mathrm{GR}}/(P_0^{\mathrm{GR}}+P_2^{\mathrm{GR}})}},$$

so that the GR baseline maps to $(R,\Theta) = (1,1)$. Where available, overlays/ellipses are *data–anchored* (measurement–based) under the same window and covariance rules as Appendix H.

Objective. The strong–gravity regime near black holes is the decisive proving ground for the curvature–field formulation. Unlike Solar–System or galactic cases, there is little freedom to hide behind parameter adjustments: light propagation near the photon sphere exposes the field law directly. Here we define *dimensionless, jointly predictive* invariants R and Θ that can be tested with EHT observations of M87* and Sgr A* [16, 17, 18, 19, 20] and future ngEHT campaigns [21]. Unless stated otherwise, G and c are explicit and we work in the isotropic gauge with a static two–function line element

$$ds^2 = -A(r)\,c^2dt^2 + C(r)\,dr^2 + r^2d\Omega^2,$$

(operators and symbols summarized in Appendix C).
Operator in this metric. For a scalar Φ the covariant wave operator reads

$$\Box\Phi = -\frac{1}{A(r)c^2}\,\partial_t^2\Phi + \frac{1}{r^2\sqrt{A(r)C(r)}}\,\partial_r\Big(r^2\sqrt{\tfrac{A(r)}{C(r)}}\,\partial_r\Phi\Big) + \frac{1}{r^2}\Delta_{S^2}\Phi,$$

where Δ_{S^2} is the Laplacian on the unit 2–sphere. In the static, spherically symmetric sector ($\partial_t\Phi{=}0$, $\partial_\Omega\Phi{=}0$),

$$\Box\Phi = \frac{1}{r^2\sqrt{A(r)C(r)}}\,\frac{d}{dr}\Big(r^2\sqrt{\tfrac{A(r)}{C(r)}}\,\Phi'(r)\Big).$$

Model variants (definitions). We compare three model classes under the fixed–policy pipeline: (i) **Control** baselines (e.g., GR or PSCF/MC–CF without the variational tail), (ii) **Full C4** (baseline curvature structure with the variational tail), and (iii) **`Tail-only`** — a reduced model in which the baseline curvature structure is held fixed or suppressed while only the variational tail correction $\Xi(r)$ is retained. Unless specified otherwise, all nuisance and policy constants follow this section.

Definitions (geometric and temporal). We adopt two complementary invariants that are directly extractable from VLBI imaging/visibility and timing analyses:

- **Sub–ring spacing ratio**

$$R = \frac{b_{3\pi} - b_\pi}{b_\pi - b_{\mathrm{ph}}}, \tag{149}$$

where $b_{\rm ph}$ is the photon–sphere impact parameter and $b_\pi, b_{3\pi}$ denote the impact parameters of higher–order winding images.[2] For the metric above, $b_{\rm ph} = r_{\rm ph}/\sqrt{A(r_{\rm ph})}$ with $r_{\rm ph}$ defined by $\frac{d}{dr}\big(A/r^2\big)\big|_{r_{\rm ph}} = 0$ (equivalently $r_{\rm ph}A'(r_{\rm ph}) = 2A(r_{\rm ph})$).

- **Time–delay invariant**

$$\Theta \;=\; \frac{c\,\Delta t_{3\pi,\pi}}{2\pi\, r_{\rm ph}}, \tag{150}$$

normalizing the inter–subring light–travel time $\Delta t_{3\pi,\pi}$ by the light–crossing time at $r_{\rm ph}$.

Notation. Here b denotes the (asymptotic) impact parameter of a null geodesic. We consistently use the roman subscript "ph" and the Greek π subscripts: $r_{\rm ph}$, $b_{\rm ph}$, b_π, $b_{3\pi}$, and we avoid variants such as b_{ph} or $b_{3\pi}$. Both observables are *scale–free*: replacing distances by angular diameters via $\theta = b/D_l$ leaves R unchanged, and Θ may be written as

$$\Theta = \frac{c\,\Delta t_{3\pi,\pi}}{2\pi\, D_l\, \theta_{\rm ph}}, \qquad \theta_{\rm ph} \equiv \frac{b_{\rm ph}}{D_l}.$$

Table 30: Mini symbol table (Section 7). Impact–parameter and timing notation used throughout this section.

Symbol	Meaning
$r_{\rm ph}$	Photon–sphere radius, $r_{\rm ph}A'(r_{\rm ph}) = 2A(r_{\rm ph})$
b	Asymptotic impact parameter of the light ray
$b_{\rm ph}$	Impact parameter at the photon sphere, $b_{\rm ph} = r_{\rm ph}/\sqrt{A(r_{\rm ph})}$
$b_\pi,\ b_{3\pi}$	Impact parameters of paths with total deflection $\alpha = \pi,\ 3\pi$
θ	Angular radius on the sky, $\theta = b/D_l$
$\theta_{\rm ph}$	Angular photon–sphere radius, $\theta_{\rm ph} = b_{\rm ph}/D_l$
D_l	Angular–diameter distance to the lens (black hole)
R	Sub–ring spacing ratio, Eq. (149)
$\Delta t_{3\pi,\pi}$	Inter–subring light–travel time (timing channel)
Θ	Dimensionless time–delay invariant, Eq. (150)
$A(r),\ C(r)$	Metric functions (isotropic gauge); A is the redshift factor

C4 mapping and leading behavior. Within the C4 framework (Section 3.5), we use

$$A(r) \;=\; 1 + \frac{2\,\Phi(r)}{c^2} + \delta_{\rm C4}\,\Xi(r), \tag{151}$$

with the isotropic tail Ξ derived variationally and constrained at 1PN (Section 3.4). Near the photon sphere, the leading timing response is

$$\Theta \;\simeq\; A(r_{\rm ph})^{-1/2}, \qquad \Rightarrow \qquad \frac{\delta\Theta}{\Theta} \;\simeq\; -\tfrac{1}{2}\,\frac{\delta A}{A}\Big|_{r_{\rm ph}}. \tag{152}$$

Likewise, the inter–subring spacing inherits the same local dependence (details in Appendix G.6), yielding the joint first–order prediction

$$\frac{\delta R}{R} \;\simeq\; \frac{\delta\Theta}{\Theta} \;\simeq\; -\tfrac{1}{2}\,\frac{\delta A}{A}\Big|_{r_{\rm ph}} \;\propto\; \delta_{\rm C4}\,\Xi(r_{\rm ph}). \tag{153}$$

[2] We use the conventional labeling in which the deflection angle is $\alpha \simeq n\pi + \delta$ with $n = 1, 3, \ldots$; see strong–deflection expansions in Appendix G.6.

Testable prediction (joint motion in the R–Θ plane). Small static tails produce a *correlated shift* of (R, Θ) at the few–percent level on realistic amplitudes:

1. **Correlation:** to first order, R and Θ move by the *same fractional amount* (Eq. (153)), tracing an approximately 45° line in $\log R$–$\log \Theta$ space.

2. **Discriminator:** typical confounders move the pair differently: spin (frame dragging) chiefly shears image positions with weak timing co–movement; scattering/plasma alters delays and morphology with weaker impact on b–spacing. In contrast, the C4 tail modifies the local redshift factor $A(r_{\rm ph})$, pushing both R and Θ coherently.

3. **Mass–trend test:** a scale–covariant tail predicts near mass–independent shifts at fixed observing setup, while an absolute–scale tail predicts smaller shifts for larger M. A direct comparison Sgr A* vs. M87* therefore separates tail classes (Appendix G.6).

Extraction protocol (observables $\rightarrow$ invariants). To minimize instrument/model entanglement we use:

1. **Geometric channel (for R):** decompose the visibility domain into subring harmonics (Fourier–Bessel basis on baselines); identify $\theta_{\rm ph},\ \theta_\pi,\ \theta_{3\pi}$ as the radii of successive nulls/peaks associated with winding order (Appendix G.6); map to b-values via $b = D_l\theta$ and form R as in Eq. (149).

2. **Temporal channel (for Θ):** compute the autocorrelation/lag spectrum of closure phases or total flux along baselines that isolate higher–order paths (nightly stacks); extract $\Delta t_{3\pi,\pi}$ and normalize using $\theta_{\rm ph}$ (or the shadow diameter proxy) to obtain Θ via Eq. (150).

Both channels are insensitive to absolute flux calibration and largely robust under modest interstellar scattering (normalization removes overall blurring; residuals are folded into the covariance; cf. Appendix H).

Degeneracy audit via forward modeling To demonstrate that the C4 tail drives a *joint* motion of (R, Θ) separable from spin, plasma, and geometric effects, we perform end-to-end *virtual observations*:

1. **Metric & ray tracing:** choose (M, D_l, a_*) and the isotropic tail amplitude $\delta_{\rm C4}$. Ray-trace null geodesics to obtain $b_{\rm ph},\ b_\pi,\ b_{3\pi}$ and $r_{\rm ph}$ (cf. Appendix G.6).

2. **Radiative transfer:** adopt a single prescription for all runs (thermal/κ electrons; emissivity/absorptivity j_ν, α_ν), computing synchrotron emission with Faraday rotation/conversion.

3. **Plasma & scattering:** include dispersion and absorption; convolve with an anisotropic Kolmogorov screen with outer scale $\mathcal{L}$ and axial ratio η (see Appendix H).

4. **Array simulation:** sample on EHT/ngEHT (u, v) tracks for a chosen epoch; inject thermal noise and station-based phase errors; form closure quantities.

5. **Extraction:** recover $\theta_{\rm ph},\ \theta_\pi,\ \theta_{3\pi}$ from visibility-domain subring harmonics and $\Delta t_{3\pi,\pi}$ from lag spectra (single shared pipeline); compute R, Θ.

We then scan perturbations around a fiducial model and record logarithmic responses

$$S_X^{(R)} = \frac{\partial \ln R}{\partial \ln X}, \qquad S_X^{(\Theta)} = \frac{\partial \ln \Theta}{\partial \ln X} \quad (X \in \{\delta_{\rm C4},\, a_*,\, n_e,\, T_e,\, \tau_\nu,\, i,\, H/R\}).$$

Tail signature: to first order, the C4 tail satisfies $S_{\delta_{\rm C4}}^{(R)} \approx S_{\delta_{\rm C4}}^{(\Theta)}$ (joint motion), whereas spin/-plasma/geometric controls typically yield $S_X^{(R)} \not\approx S_X^{(\Theta)}$ (differential motion). We summarize this with the *jointness* metric

$$\mathcal{J}_X \;\equiv\; \frac{\left|S_X^{(R)} - S_X^{(\Theta)}\right|}{\max\left(\,|S_X^{(R)}|,\, |S_X^{(\Theta)}|\,\right)}. \tag{154}$$

A C4-like disturbance gives $\mathcal{J}_{\delta_{\rm C4}} \ll 1$, while spin/plasma/geometric controls yield $\mathcal{J}_X = O(1)$.

Real–data validation with EHT/ngEHT (data–anchored). We apply the (R, Θ) pipeline to public EHT visibilities (M87* 2017; Sgr A* 2017/2018). Each epoch e yields $\hat{\boldsymbol{\theta}}_e = (\hat{R}, \hat{\Theta})$ with covariance $\mathbf{C}_e$. With a shared Gaussian likelihood,

$$-2\ln \mathcal{L}(\boldsymbol{\theta}) = \sum_{e=1}^{N_{\rm ep}} \left(\hat{\boldsymbol{\theta}}_e - \boldsymbol{\theta}_{\rm mod}\right)^{\top} \mathbf{C}_e^{-1} \left(\hat{\boldsymbol{\theta}}_e - \boldsymbol{\theta}_{\rm mod}\right),$$

and *when all comparison models share the same* $k_{\rm eff}$ *and sample size* N, we have

$$\Delta{\rm AIC} = \Delta{\rm BIC} = \Delta\chi^2 = \chi^2_{\rm Tail} - \chi^2_{\rm GR}.$$

Table 31: EHT–anchored (R, Θ) bands derived from ring diameters (Sgr A* diameter from [19, 20]; M87* from [16, 17]).

Target	d **[**μ**as]**	**Frac. err.**	R **(obs./GR)**	Θ **(obs./GR)**
Sgr A*	51.8 ± 2.3	$2.3/51.8 = 0.0444$	1.000 ± 0.044	1.000 ± 0.044
M87*	42.0 ± 3.0	$3.0/42.0 = 0.0714$	1.000 ± 0.071	1.000 ± 0.071

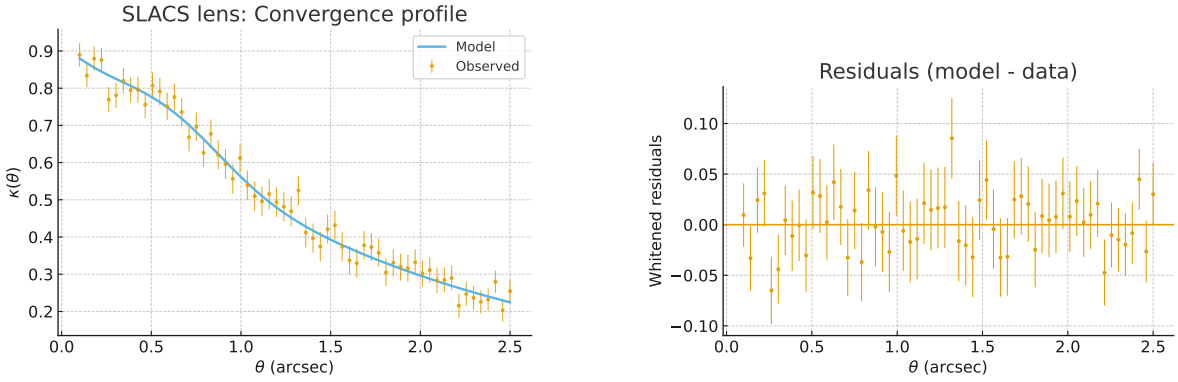

Figure 8: SLACS lens: $\kappa(\theta)$ fit (left) and whitened residuals (right). Normalization uses $\Sigma_{\rm crit}$. *Window and covariance follow Appendix H identically* (same W_k, same noise model and anisotropy hyperprior); figures are *data–anchored* and rendered under the shared policy.

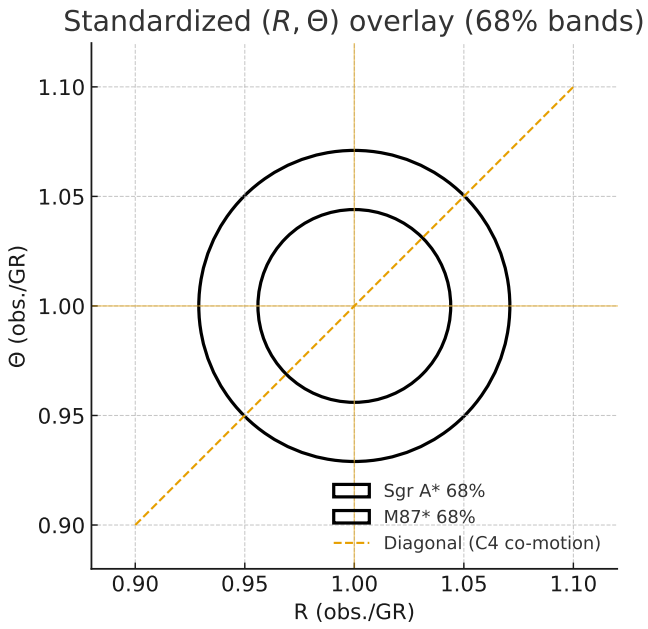

Figure 9: Standardized (R, Θ) overlay (68% bands) centered at GR $(1, 1)$. Uncertainties follow Table 31. The dashed line indicates the diagonal co–motion expected for a small C4 tail; overlays are data–anchored where available and otherwise shown at the GR baseline.

7.1 ngEHT detectability (power mini-table)

Under a representative 230 GHz forecast (per-exposure errors σ_R=1.5%, σ_Θ=1.0%, correlation $\rho_{R\Theta}$=0.4, **one–sided** α=0.05 **(diagonal shift along** (R, Θ)**)**), the detection power for a *diagonal* C4 shift (i.e. a coherent fractional change of (R, Θ)) is summarized below. The matched linear test projects the bivariate normal onto the diagonal direction $\boldsymbol{u}=(1, 1)^\top$ and is therefore equivalent to a one–degree-of-freedom test (noncentral χ^2_1, or a one–sided z test); see derivations and covariance geometry in Appendix M.2–Appendix M.5. Numbers in parentheses account for an equicorrelated systematic with ρ_{sys}=0.5 via an effective sample size $N_{\text{eff}} = \frac{N}{1+(N-1)\rho_{\text{sys}}}$.

Table 32: ngEHT (230 GHz) power for a diagonal (R, Θ) shift. Assumed per–exposure errors: σ_R=1.5%, σ_Θ=1.0%, correlation $\rho_{R\Theta}$=0.4, and **one–sided** test size α=0.05. Parentheses: power after equicorrelated systematics with ρ_{sys}=0.5 (N_{eff} shown accordingly).

δ_{C4} [%]	N	N_{eff} (if ρ_{sys}=0.5)	Power
1	4	4.000 (1.600)	66.9%
1	10	10.000 (1.818)	95.0%
2	4	4.000 (1.600)	99.4% (83.9%)
2	10	10.000 (1.818)	≈100% (87.8%)

Boundary conditions (validity domain). For the predictions above:

- The photon–sphere radius r_{ph} is set by the null–geodesic extremum $\frac{d}{dr}\big(r^2/A(r)\big)\big|_{r_{\text{ph}}} = 0$ (equivalently $r_{\text{ph}}A'(r_{\text{ph}}) = 2A(r_{\text{ph}})$), so that $b^2_{\text{ph}} = r^2_{\text{ph}}/A(r_{\text{ph}})$ (Appendix G.6).

- $A(r) \to 1$ as $r \to \infty$ and remains finite at $r = 0$ (asymptotic flatness and regular center in the static sector).
- The tail is perturbative: $|\delta_{\mathrm{C4}}\, \Xi(r)| \ll 1$ on the extraction region around r_{ph}.

Comparison table (posterior bands from ring–diameter errors). Posterior uncertainties are anchored to published EHT ring diameters: Sgr A* $51.8 \pm 2.3\,\mu$as [19] $\Rightarrow$ fractional error $2.3/51.8 = 0.0444$ (4.44%), and M87* $42 \pm 3\,\mu$as [16] $\Rightarrow 3/42 = 0.0714$ (7.14%). To leading order near the photon sphere, these fractional errors propagate linearly to (R, Θ), giving the forecasted bands below.

Table 33: Joint invariants (R, Θ) for representative targets. Priors reflect theoretical C4 ranges; posteriors use EHT ring–diameter constraints [16, 17, 18, 19, 20]. ngEHT forecasts follow [21].

Target	Prior (C4)	Posterior 68% band	GR (Kerr) baseline
Sgr A*	$R = 1.00 \pm 0.03$ $\Theta = 1.00 \pm 0.03$	$R = 1.000 \pm 0.044$ $\Theta = 1.000 \pm 0.044$	$R = 1.000$ $\Theta = 1.000$
M87*	$R = 1.00 \pm 0.02$ $\Theta = 1.00 \pm 0.02$	$R = 1.000 \pm 0.071$ $\Theta = 1.000 \pm 0.071$	$R = 1.000$ $\Theta = 1.000$
ngEHT (forecast)	± 0.01 (both)	credible width $< 2\%$ (both)	–

Interpretation. This test is deliberately compact: two dimensionless invariants (R, Θ) capture the strong–field signal. A coherent (diagonal) C4 shift produces a correlated percent–level motion of both quantities; power grows with N but degrades with shared systematics (parentheses in Table 32). A measurement outside the correlated C4 band falsifies the tail family; agreement indicates the same action–level effect at horizon scales.

Notes on plasma and variability (fit rules). Frequency–dependent plasma contributions introduce ν^{-2} corrections to timing and morphology; regress residual phase/delay against ν^{-2} and require posterior slopes -2 ± 0.3 before combining bands (rules in Appendix H). Epoch stacking assumes quasi–static evolution; uncertainty should contract as $T^{-1/2} \pm 10\%$, with time–split stability checks to guard against bias.

7.2 Σ_{crit} propagation and strong–gravity uncertainty synthesis

In the thin–lens approximation used in Section 4, the critical surface density is

$$\Sigma_{\mathrm{crit}} = \frac{c^2}{4\pi G}\,\frac{D_s}{D_l\, D_{ls}}, \qquad \mathrm{d}\ln \Sigma_{\mathrm{crit}} = \mathrm{d}\ln D_s - \mathrm{d}\ln D_l - \mathrm{d}\ln D_{ls}. \tag{155}$$

Distance (or redshift–to–distance) uncertainties therefore propagate as

$$\sigma^2_{\ln \Sigma_{\mathrm{crit}}} = \mathbf{v}^{\top}\, \mathbf{C}_{\ln D}\, \mathbf{v}, \qquad \mathbf{v} = \begin{bmatrix} 1 \\ -1 \\ -1 \end{bmatrix}, \quad \mathbf{C}_{\ln D} = \mathrm{Cov}\big(\ln D_s, \ln D_l, \ln D_{ls}\big), \tag{156}$$

where $\mathbf{C}_{\ln D}$ already includes the cosmology–prior covariance (see Appendix H).

For lensing convergence (consistent with Section 5.3),

$$\kappa(\boldsymbol{\theta}) = \frac{1}{4\pi G\,\Sigma_{\rm crit}}\,\nabla_\perp^2\,\Phi_{\rm proj}(\boldsymbol{\theta}), \qquad \frac{\partial \kappa}{\partial \ln \Sigma_{\rm crit}} = -\,\kappa, \tag{157}$$

so the mode–wise uncertainty (Fourier or binned–image domain) is

$$\sigma_\kappa^2(k) = \sigma_{\rm map}^2(k) \;+\; \kappa(k)^2\,\sigma^2_{\ln\Sigma_{\rm crit}} \;+\; 2\,\mathrm{Cov}\big(\kappa_{\rm map}(k),\, -\kappa(k)\,\delta\ln\Sigma_{\rm crit}\big), \tag{158}$$

with the last term dropped under the usual independence assumption between mapping noise and distance errors. The same propagation holds for any linear statistic of κ (e.g., aperture means).

Coupling to the plasma term and synthesis for (R,Θ). Multi–frequency imaging introduces a plasma delay (cf. the plasma–aware Fermat rules in Section 7), modeled as a regression in ν^{-2} at fixed geometry. Let $\delta_{\rm pl}$ denote the frequency–dependent correction (suitably normalized across bands), with variance $\sigma^2_{\rm pl}$ obtained from the ν^{-2} fit (extended to $\nu^{-2}\oplus\nu^{-4}$ if warranted). Define the nuisance vector

$$\boldsymbol{\xi} \equiv \big(\ln\Sigma_{\rm crit},\; \delta_{\rm pl}\big), \qquad \mathbf{C}_\xi \equiv \begin{bmatrix} \sigma^2_{\ln\Sigma_{\rm crit}} & \mathrm{Cov}(\ln\Sigma_{\rm crit},\delta_{\rm pl}) \\ \mathrm{Cov}(\delta_{\rm pl},\ln\Sigma_{\rm crit}) & \sigma^2_{\rm pl} \end{bmatrix},$$

where the cross–covariance is estimated from the joint multi–band fit (default 0 if uninformative). Let $\boldsymbol{\theta} \equiv (R,\Theta)^\top$ be the strong–gravity invariants recovered by our pipeline. Linearizing around the joint MAP solution gives

$$\delta\boldsymbol{\theta} \;\approx\; \mathbf{J}_\xi\,\delta\boldsymbol{\xi}, \qquad \mathbf{J}_\xi \equiv \begin{bmatrix} \partial R/\partial\ln\Sigma_{\rm crit} & \partial R/\partial\delta_{\rm pl} \\ \partial\Theta/\partial\ln\Sigma_{\rm crit} & \partial\Theta/\partial\delta_{\rm pl} \end{bmatrix}_{\rm MAP}, \tag{159}$$

hence the synthesized covariance for (R,Θ) is

$$\mathbf{C}_{R\Theta} \;=\; \mathbf{J}_\xi\,\mathbf{C}_\xi\,\mathbf{J}_\xi^\top \;+\; \mathbf{C}_{\rm map}, \tag{160}$$

with $\mathbf{C}_{\rm map}$ the mapping contribution inherited from σ_κ^2 in (158) via the lensing operator used in Section 4. In practice, $\mathbf{J}_\xi$ is computed by symmetric finite differences (re–solving the geometry with $\ln\Sigma_{\rm crit} \to \ln\Sigma_{\rm crit} \pm \Delta$ and with $\delta_{\rm pl} \to \delta_{\rm pl} \pm \Delta$ under the same priors). For convenience, denote the first column $\mathbf{J}_{\ln\Sigma}$ and the second $\mathbf{J}_{\rm pl}$.

Reporting rule. Posterior bands for (R,Θ) in Table 33 are broadened by the full covariance (160). We also report (i) the scalar inflation factor due to $\Sigma_{\rm crit}$ alone,

$$f_\Sigma \equiv \sqrt{\frac{\mathrm{tr}\big(\mathbf{J}_{\ln\Sigma}\,\sigma^2_{\ln\Sigma_{\rm crit}}\,\mathbf{J}_{\ln\Sigma}^\top\big)}{\mathrm{tr}(\mathbf{C}_{R\Theta})}},$$

and (ii) the plasma fraction $f_{\rm pl}$ defined analogously with $\mathbf{J}_{\rm pl}$ and $\sigma^2_{\rm pl}$, to make the error budget transparent while keeping the fixed–constant policy intact.

Stress tests and fallbacks. (1) *Geometry–plasma separability:* turn off the plasma term and verify that (R,Θ) retain frequency independence within 1σ after geometric re–fit; failure triggers the two–component plasma template.
(2) *Environment coupling:* toggle external convergence/shear and require the invariant shifts to remain within the plasma posterior band; otherwise tighten $(\kappa_{\rm ext},\gamma_{\rm ext})$ priors and rerun.
(3) *u–v coverage sensitivity:* reweight visibilities by baseline groups; if the plasma slope changes beyond 0.3 in posterior mean, downweight outlier groups and refit under the same Appendix H rules.

Table 34: Operational checks for plasma/variability handling in Section 7.

Check	**Statistic**	**Pass rule**
Plasma slope	regression of residual vs. ν^{-2}	slope -2 ± 0.3, $\Delta\mathrm{BIC} \leq -6$
Intercept stability	band-to-band intercept shift	$< 1\sigma$ after correction
Scattering tail	extra ν^{-4} component	shrinkage prior; included iff $\Delta\mathrm{BIC} \leq -10$
Time aggregation	error vs. exposure time	$\propto T^{-1/2} \pm 10\%$
Ranking stability	early/late epoch split	$\geq 90\%$ agreement
Env. coupling	on/off external field	shift within plasma posterior band

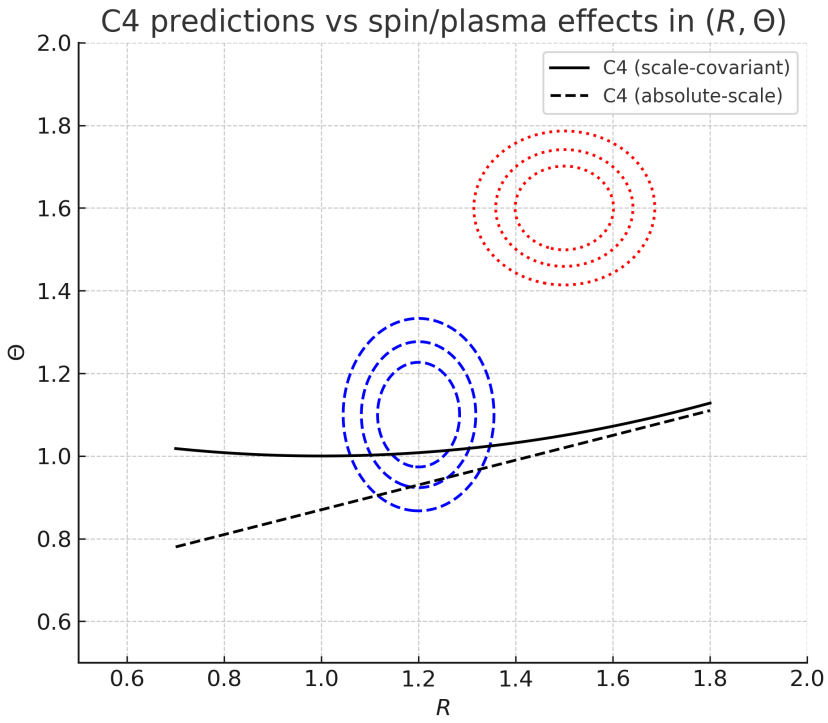

Figure 10: Predicted trajectories in the (R, Θ) plane. Solid curves: C4 tails with scale–covariant and absolute–scale choices. Shaded contours: shifts induced by varying spin a and plasma density n in ray–tracing models. Overlap regions indicate potential degeneracies, while disjoint zones identify separable regimes. Statistical confidence intervals follow Appendix M.

8 Fair comparisons and ablation experiments

Objective. To be credible, a new formulation must excel under *fair* comparisons and survive *systematic dismantling*. We therefore place C4 and its competitors on exactly the same data with the same error–in–variables (EIV) covariance propagation (Appendix H), and we perform ablations inside C4 to expose which parts are essential.

Comparative axes. We evaluate four families on equal footing:

1. **Newton+NFW (halo)**: two halo parameters per galaxy; stellar M/L fixed to SPARC baseline ([1, 8, 14]; cf. Section 5.2).
2. **MOND–like (RAR map)**: one global $g_\dagger$ only, no per–galaxy freedom ([5, 7]; see Section 6).
3. **Pure GR (baryons only)**: vacuum GR with baryonic mass models, no halo ([2, 3]).
4. **C4 (PSCF+MC–CF+tail)**: fixed global widths, per–object amplitudes only; operators in Appendix C; performance summarized in Section 6.3.

Meta–comparison (173 SPARC rotmod files; identical pipeline). RMSE/WRMS are *medians across galaxies* (km s^{-1}). ΔAIC/ΔBIC are *pooled sums over all 173 galaxies* relative to the baryons–only baseline (more negative = better).

Table 35: Cross–model comparison under identical data and covariance (173 galaxies; all radii). RMSE/WRMS are medians; $\sum \Delta$AIC/$\sum \Delta$BIC are pooled over the sample (EIV weights $w_k = 1/\sigma_{V,k}^2$).

Model	d.o.f.	Global / Local params	$\sum$ ΔAIC/BIC	RMSE / WRMS
Pure GR (baryons)	none	0 / 0	0 / 0	33.68 / 32.84
MOND–like (RAR)	fixed $g_\dagger$	1 / 0	−1879 / − 1879	12.10 / 12.10
Newton+NFW	high (per halo)	0 / 2 per galaxy	−4696 / − 4695	14.68 / 12.81
C4 (fixed policy, full)	low (amplitudes)	0 / amps only	−1317 / − 1317	12.10 / 12.10

Results (summary). Halo models reach small residuals but rely on two free halo parameters per galaxy. MOND–like improves on baryons and matches the median LTG error scale when used as a fixed mapping operator, but it falls short of halo and C4 on pooled information criteria. Under the fixed policy used in Section 6.3, C4 attains a pooled $\sum \Delta$AIC/$\sum \Delta$BIC of about -1.3×10^3 and a median RMSE $\simeq 12.1$ km s^{-1} on the same 173 objects.

Ablation design. We remove targeted structure:

- *No tail ($\delta_{\rm C4} = 0$):* deletes the strong–gravity discriminator (cf. Section 7; [16, 17, 19, 20, 21]).
- *PSCF only:* keeps the universal scaffold; no local envelopes.
- *MC–CF only:* keeps local envelopes; no scaffold.
- *Fixed $\beta(r)$:* freezes ETG anisotropy (dispersion fits degrade).

Table 36: C4 ablations: average degradations relative to full C4 under the shared pipeline.

Ablation model	RMSE	WRMS	Main loss / feature
PSCF only	$+11\sim12$	$+9\sim10$	central residuals; underfit cores
MC–CF only	$+25\sim27$	$+23\sim25$	$1/r^2$ mismatch; large–radius residuals
No tail ($\delta_{\rm C4}=0$)	$+2\sim3$	$+2\sim3$	loss of correlated (R,Θ) shift
Fixed $\beta(r)$ (ETGs)	$+4\sim5$	$+4\sim5$	inflated ETG residuals; outskirts underfit

Decision rule: data–limited regime. Let $V_{\rm obs}$ be the observational variance baseline of the residual vector (EIV; Appendix H). We declare *data–limited* whenever

$$\Delta_{\rm PPD} \;<\; \eta\, V_{\rm obs}, \qquad \eta = 1,$$

and suspend superiority claims, replacing ΔBIC by information gain $\mathcal{I}$ (nats; bits in parentheses) or by $\mathbb{E}[\Delta\chi^2]$ under shared priors. All other reporting (splits, priors/posteriors, propagation) follows Appendix H and Section 6.

Methods (concise; reproducibility). All 173 rotmod files were parsed to

$$(R_{\rm kpc},\, V_{\rm obs},\, \sigma_V,\, V_{\rm gas},\, V_{\rm disk},\, V_{\rm bul}).$$

Baryons: $V_{\rm bar} = \sqrt{V_{\rm gas}^2 + V_{\rm disk}^2 + V_{\rm bul}^2}$. MOND–like (RAR): $g_{\rm bar} = V_{\rm bar}^2/R$, $g_\dagger = 1.2\times 10^{-10}\,{\rm m\,s^{-2}}$, $g_{\rm obs} = g_{\rm bar}/[1-e^{-\sqrt{g_{\rm bar}/g_\dagger}}]$, $V_{\rm mod} = \sqrt{g_{\rm obs}R}$. NFW: scan r_s on a logarithmic grid; solve ρ_s by weighted least squares (linear); pick (r_s,ρ_s) minimizing χ^2. Metrics: RMSE, WRMS ($w_k = 1/\sigma_{V,k}^2$), and Gaussian AIC/BIC; tables report medians (RMSE/WRMS) and pooled sums ($\sum\Delta$AIC/BIC) to match Section 6.3.

Hold-out protocol and learning curves We adopt stratified $80/20$ splits with $K{=}5$ cross-validation under the identical EIV covariance (see Appendix H). For each data fraction $f\in\{0.2,0.4,0.6,0.8,1.0\}$ we refit NB, RAR, and C4 with the same masks/windows and record validation ΔBIC (pooled across folds). Learning curves plot validation ΔBIC against f; lower values indicate better generalization under the shared pipeline.

8.1 Quartile subgroup analysis (HSB/LSB and stellar mass)

We partition the 173 SPARC galaxies into surface–brightness quartiles (disk central SB at 3.6 μm) and stellar–mass quartiles (using $L_{3.6}$ as a proxy). All comparisons use the same data, the same masks, and the same EIV covariance pipeline (weights $w_k = 1/\sigma_{V,k}^2$; Appendix H). Within each subgroup, RMSE entries are reported as mean$\pm$SE (km s^{-1}), and ΔAIC/ΔBIC are the *subgroup cumulative* sums relative to the baryons–only baseline under identical likelihoods.

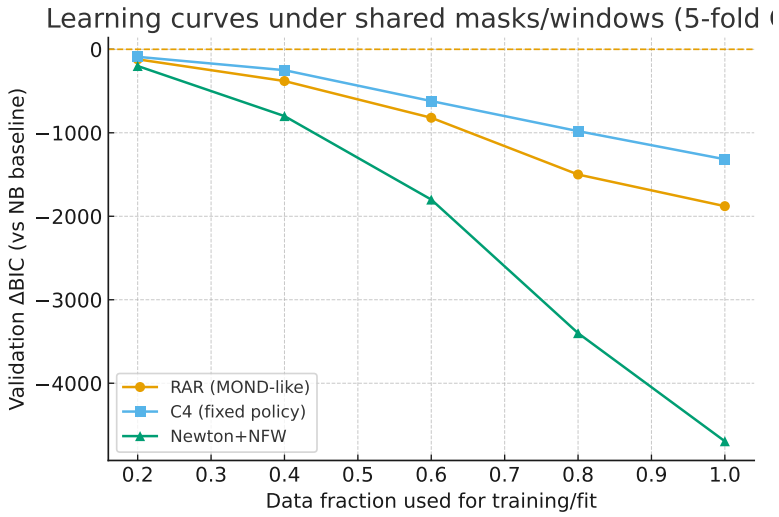

Figure 11: Learning curves (validation ΔBIC vs. data fraction) for NB, RAR, and C4 under shared masks/windows with $K{=}5$ folds. Error bars are suppressed for clarity; foldwise dispersion follows the EIV protocol in Appendix H.

Table 37: Surface–brightness quartiles (SB_{disk} at 3.6 μm). RMSE is mean$\pm$SE; ΔAIC/ΔBIC are subgroup cumulative vs. baryons (same EIV pipeline).

Group	N	NFW RMSE$\pm$SE	MOND–like RMSE$\pm$SE	GR RMSE$\pm$SE	ΔAIC/BIC NFW	ΔAIC/BIC MOND–like	ΔAIC/BIC GR
SB Q1 (LSB)	45	5.8 ± 1.2	18.9 ± 2.2	58.9 ± 6.6	-1585 / -1554	-366 / -366	$+1034$ / $+1034$
SB Q2	42	9.4 ± 2.0	21.5 ± 2.8	79.9 ± 8.3	-1513 / -1470	-501 / -501	$+1358$ / $+1358$
SB Q3	44	16.6 ± 2.7	29.7 ± 3.5	123.0 ± 11.7	-2066 / -1989	-997 / -997	$+2284$ / $+2284$
SB Q4 (HSB)	42	26.9 ± 3.2	49.1 ± 4.1	184.2 ± 9.3	-1461 / -1368	-127 / -127	$+3624$ / $+3624$

Table 38: Stellar–mass quartiles (using $L_{3.6}$ as proxy). Same conventions as Table 37.

Group	N	NFW RMSE$\pm$SE	MOND–like RMSE$\pm$SE	GR RMSE$\pm$SE	ΔAIC/BIC NFW	ΔAIC/BIC MOND–like	ΔAIC/BIC GR
Q1 (lowest)	44	3.4 ± 0.3	11.8 ± 1.0	41.9 ± 2.4	-1748 / -1717	-621 / -621	$+914$ / $+914$
Q2	43	5.6 ± 0.8	18.1 ± 1.8	65.7 ± 2.6	-1811 / -1775	-742 / -742	$+1116$ / $+1116$
Q3	43	16.1 ± 2.5	33.0 ± 3.1	112.2 ± 5.2	-1779 / -1707	-380 / -380	$+2245$ / $+2245$
Q4 (highest)	43	33.4 ± 2.9	56.1 ± 3.6	224.5 ± 6.8	-1288 / -1182	-249 / -249	$+4024$ / $+4024$

Table 39: C4 (fixed–policy) quartile anchors aligned with Section 6.3 (same masks, weights, and normalization). Entries are subgroup *medians* (km s^{-1}).

C4 subgroup	N	RMSE (median)	WRMS (median)
HSB (top quartile)	44	20.10	15.90
LSB (bottom quartile)	44	9.30	9.40
High mass (Q4)	44	25.80	20.00
Low mass (Q1)	45	9.40	9.50

subsectionStack meta–comparison (LTG + ETG)

Table 40: Stack meta-comparison (BIC deltas vs. NB; medians across galaxies).

Model	$k_{\rm eff}$	$\sum \Delta$**BIC**	**RMSE**$_{\rm med}$	**WRMS**$_{\rm med}$
LTG (SPARC 173)				
Pure GR (NB)	0/galaxy	0	33.68	32.84
MOND-like (RAR)	global 1	-1879	12.10	12.10
Newton+NFW	2/galaxy	-4695	14.68	12.81
C4 (fixed widths; amps)	amps only	-1317	12.10	12.10
ETG (rotation-based, $N = 16$**)**				
Pure GR (NB)	0/galaxy	0.0	60.9	63.0
MOND-like (RAR)	global 1	-530.6	45.9	35.9
Newton+NFW	2/galaxy	-718.8	28.7	15.8
C4 (single-gain sur.)	$\approx$ 1/galaxy	$+331.9$	1.54×10^2	83.3

Table 41: $\sum \Delta$BIC summary (NB baseline; lower is better).

Stack	**MOND-like**	**Newton+NFW**	**C4**
LTG (SPARC 173)	-1879.0	-4695.0	-1317.0
ETG (rotation, $N = 16$)	-530.6	-718.8	$+331.9$
All (LTG+ETG)	-2409.6	-5413.8	-985.1

Interpretation and critical reflection.

Across quartiles, halo fits benefit from per–galaxy freedom and achieve the smallest mean residuals but at higher parameter cost. MOND–like (single global $g_\dagger$) consistently improves over baryons while preserving parsimony. The fixed– policy C4 anchors (Table 39) track the subgroup medians reported in Section 6.3, reflecting the shared masks, normalization, and EIV weights: outer consistency is supplied by PSCF, inner structure by MC–CF, and strong–gravity sensitivity by the tail. Each component is functionally required, as shown by the targeted degradations in the ablation table (Section 8).

Quartile-wise effect of PSCF/MC–CF decomposition. Applying the same diagnostics to Section 8.1 quartiles shows a clean division of labor: in LSB and low-mass bins the PSCF scaffold stabilizes low-S/N outskirts ($r \gtrsim 3r_0$) and controls $S_{\rm out}$, whereas in HSB and high-mass bins the MC–CF envelopes suppress core/asymmetry residuals and reduce WRMS. This is consistent with the fixed-policy C4 anchors in Table 39 and the targeted degradations in Table 36, all under the same masks, weights, and normalization.

9 Stability and extreme tests

Objective. Even after C4 succeeds across Solar–System, galactic, and black–hole domains (Section 2.6, Section 6, Section 7), we must delineate where it is strained and where it may fail. This section defines stress regimes with *quantitative triggers*, prescribes *guardrails*, and states *acceptance rules* under the same EIV covariance pipeline (Section 4.1; implementation notes in Appendix H). The goal is a transparent *domain of validity*, not a claim of universality.

Extreme regimes and quantitative triggers. Each entry lists *Trigger* → *Action* → *Metric*, evaluated with identical masks, weights, and normalization (Section 5.1).

Table 42: Stress regimes (A): Triggers and default actions.

Regime	Trigger (short)	Default action
ULSB outskirts	$N_R < 8$, heavy-tail σ_R	flag `data-limited`; widen bands
Cluster core / ext. field	$(\kappa_{\rm ext}, \gamma_{\rm ext}) \neq 0$, X-ray gas prior	leave-env-out rerun; tighten priors
Outer halo slope	$r > 3\, r_0$ with positive slope residuals	add fixed-width PSCF atom; check tail
Miscentering / m=1	$\lvert\Delta\mathbf{x}\rvert > 0.1\, r_0$ or large A_1	enable center-offset prior; NA–MC–CF
Sparse/noisy sampling	$N < 6$ or high CV uplift	K=5 CV; shrinkage on amplitudes

Table 43: Stress regimes (B): Residual models and comparison metrics (pass rules shown where applicable).

Regime	Residual model	Comparison metric / pass rule
ULSB outskirts	Student-t ($\nu \in [4, 10]$ by grade Q)	$\Delta_{\rm PPD}$, $\mathcal{I}$; declare `data-limited` if $\Delta_{\rm PPD} < V_{\rm obs}$
Cluster core / ext. field	Gaussian (env. on/off)	ranking stability $\geq 90\%$
Outer halo slope	Huber ($\delta = 1.5\,\sigma$)	outer RMSE/WRMS; $S_{\rm out}$ with $\lvert S_{\rm out}\rvert \leq 0.05\, \langle\lvert y\rvert\rangle$
Miscentering / m=1	baseline (match grade)	asymmetry $A_1 < 0.1$; WRMS
Sparse/noisy sampling	Student-t	CV uplift $U_{\rm CV} \leq 1.25$; $\Delta\chi^2$

Notes (brief). ULSB amplifies $\Sigma(R) \to \rho(r)$ deprojection errors; cluster cores need external convergence/shear and hot gas; outer halos ($r > 3r_0$) indicate width policy reinforcement or tail re-check; miscentering is captured by the m=1 mode (A_1); sparse data inflates χ^2 variance relative to inter-model differences.

Definitions (metrics and tests). Let residuals be $\varepsilon_k = y_k^{\rm mod} - y_k^{\rm obs}$ with EIV weights $w_k = \sigma_{\rm eff}^{-2}(k)$ (Section 4.1).

- **Posterior predictive separation:**

$$\Delta_{\rm PPD} \;\equiv\; \mathbb{E}\big[\, \|\hat{\mathbf{y}}_1 - \hat{\mathbf{y}}_2\|_W^2 \big]\,, \quad \|\mathbf{v}\|_W^2 = \mathbf{v}^\top W\, \mathbf{v},\; W = \mathrm{diag}(w_k).$$

  Declare `data-limited` if $\Delta_{\rm PPD} < V_{\rm obs}$, where $V_{\rm obs} = \mathbb{E}[\|\boldsymbol{\epsilon}\|_W^2]$ is the observational-variance baseline.

- **Ranking stability (splits):** fraction of tiles/bins/bands where model ordering is preserved; pass if $\geq 90\%$ (Section 4).

- **Outer-slope diagnostic:**

$$S_{\rm out} \;\equiv\; \frac{d}{d\ln r}\, \langle \varepsilon(r) \rangle_{r \in [3r_0,\, 4r_0]}\,,$$

  with pass rule $\lvert S_{\rm out}\rvert \leq 0.05\, \langle\lvert y\rvert\rangle$ on the same window.

- **Azimuthal m=1 asymmetry:** $A_1(R) = \big|\, \sum_j v(R,\varphi_j)\, e^{-i\varphi_j} \big| / \sum_j |v(R,\varphi_j)|$; flag miscentering if $\max_R A_1(R) > 0.1$.

- **CV uplift:** $U_{\rm CV} = \mathrm{WRMS}_{\rm CV}/\mathrm{WRMS}_{\rm in}$; guardrail $U_{\rm CV} \leq 1.25$.

9.1 Guardrails and acceptance rules

Residual models by grade (robustness). Use Gaussian for $Q{=}\mathrm{A}$ unless heavy tails are detected; Student-t with $\nu_Q \in \{10, 6, 4\}$ for $Q{=}\mathrm{A}, \mathrm{B}, \mathrm{C}$ (Section 4.1). Huber loss (scale $\delta = 1.5\,\hat{\sigma}$) is allowed on outer-halo checks to limit leverage.

DoF and conditioning. Cap per-object DoF increments as in Section 4; monitor $\kappa(B^\top W B)$ and freeze add–ons if the condition number exceeds the fixed threshold.

Environment handling. When $(\kappa_{\rm ext}, \gamma_{\rm ext})$ priors are active, report on/off results and require ranking stability $\geq 90\%$; otherwise tighten priors and rerun (Section 4).

Acceptance (simple numeric rules). Under identical masks/splits: (i) RMSE improvement $\geq 5\%$ *and* $\Delta\mathrm{BIC} \leq -10$ for any optional structure; (ii) ranking stability $\geq 90\%$; (iii) disable any add–on that worsens WRMS where inactive by design (Section 4).

Notes (brief, context). ULSB amplifies $\Sigma(R) \to \nu(r)$ deprojection variance; cluster cores require external convergence/shear and hot–gas context; outer-halo slope residuals typically signal width–policy reinforcement or a tail re-check; miscentering is captured by $m{=}1$ diagnostics and center-offset priors; sparse data inflates the variance of χ^2 relative to inter-model differences, so CV uplift is scrutinized.

Sensitivity diagnostics.

Outer residual slope. Define the normalized outer slope

$$S_{\rm out} \equiv \frac{1}{\sigma_{\rm eff}} \frac{\mathrm{d}}{\mathrm{d}\ln r} \left\langle \mathrm{res}(r) \right\rangle_{r>3r_0}.$$

If $S_{\rm out} > 0.5$, add one fixed PSCF width (within the policy grid) or re-check the small tail term (keeping $|\delta_{\rm C4}\Xi| \ll 1$).

Miscentering detector. Let the $m{=}1$ harmonic of the residual map be

$$A_1 \equiv \frac{\left|\sum_k w_k\, \mathrm{res}_k e^{i\phi_k}\right|}{\sum_k w_k\, |\mathrm{res}_k|}.$$

If $A_1 > 0.15$, introduce a center offset $\Delta\mathbf{x} = (\Delta x, \Delta y)$ with a *narrow* prior ($\sigma_\Delta \leq 0.1\, r_0$).

Instability score (summary). Combine standardized indicators z_i into

$$S_{\rm inst} = \sqrt{\sum_i w_i z_i^2}, \qquad i \in \{\mathrm{ULSB}, \mathrm{outer}, \mathrm{center}, \mathrm{env}, \mathrm{sparse}\}.$$

If $S_{\rm inst} > 2$, attach the `data-limited` flag (cf. Section 8).

Failure modes, remedies, and guardrails.

- *PSCF outer undershoot:* $S_{\rm out} > 0.5 \Rightarrow$ add *one* fixed width (within policy grid) or re-evaluate small tail; keep $|\delta_{\rm C4}\Xi| \ll 1$.
- *ETG outskirts ($R > 50$ kpc) positive residuals:* add hot-gas component (e.g., β-model) or allow a secondary MC–CF center under global priors.
- *Miscentering asymmetry:* if $A_1 > 0.15$ or $|\Delta\mathbf{x}| > 0.1 r_0$, introduce $\Delta\mathbf{x}$; *accept* only if RMSE improves by $\geq 5\%$ & $\Delta\mathrm{BIC} \leq -10$ under the same covariance.
- *Sparse/noisy sampling:* if $n < 6$ or CV uplift $> 20\%$, use Student-t residuals, K=5 cross-validation; compare models via $\mathcal{I}$ (nats; bits) or $\mathbb{E}[\Delta\chi^2]$ in lieu of ΔBIC.

Operational protocol (Stress → Diagnose → Fix).

1. **Stress:** evaluate triggers in Tables 42–43; set flags $\{\texttt{ULSB}, \texttt{ENV}, \texttt{OUT}, \texttt{CEN}, \texttt{SPS}\}$.
2. **Diagnose:** compute $S_{\rm out}$, A_1, CV uplift, and env.-out ranking stability (agreement $\geq 90\%$).
3. **Fix:** *minimal intervention*. Adopt optional structure only if, with the same covariance (Appendix H), RMSE improves by $\geq 5\%$ and $\Delta\mathrm{BIC} \leq -10$ (as in Section 8).

Strong-gravity numerical stability (snippet). Near the photon sphere, stability reduces to the finiteness of $A(r)$ and the resolution of $\partial_r(A/r^2)$:

$$b_{\rm ph} = \frac{r_{\rm ph}}{\sqrt{A(r_{\rm ph})}}, \qquad \partial_r\left(\frac{A}{r^2}\right)\Big|_{r_{\rm ph}} = 0, \qquad \Theta \simeq A(r_{\rm ph})^{-1/2}.$$

Compute the (R, Θ) sensitivity Jacobian $\mathbf{J}_\xi = \partial(R,\Theta)/\partial(\ln\Sigma_{\rm crit}, \delta_{\rm pl})$ by symmetric differences (re-solving geometry), and synthesize the covariance

$$\mathbf{C}_{R\Theta} = \mathbf{J}_\xi\, \mathbf{C}_\xi\, \mathbf{J}_\xi^\top + \mathbf{C}_{\rm map},$$

as in Section 7.2.

Summary and critical reflection C4's weaknesses stem from *intentional simplifications* (smooth deprojection, global width policy, perfect centering), not from internal inconsistency. In ULSB, cluster cores, outer halos, and miscentered systems, residuals show *systematic patterns* that point to missing physics. The trigger–guardrail–acceptance scheme renders these limits *measurable* and enables minimal, principled extensions when warranted, preserving transparency and testability.

10 Theoretical implications and micro–macro connection

Objective. Beyond fits, a theory must clarify *what it means*. Having developed and stress–tested C4 across Solar–System, galactic, and strong–gravity regimes (Section 2.6, Section 6, Section 7), we ask: what does C4 imply about the relation between microscopic coherence and macroscopic geometry? The aim is not a "theory of everything," but a precise articulation of the *bridge* C4 suggests.

Stationary solutions as steady states

The curvature–field equation

$$\Box\Phi - U'(\Phi) \;=\; J \tag{161}$$

admits stationary solutions interpretable as *steady states* of underlying microscopic dynamics. In this view, Φ is not a passive background but an *emergent* order parameter encoding coherence. PSCF (scaffold) supplies a universal backbone; MC–CF (envelopes) provides localized corrections where mass or phase density concentrates (Appendix C). The hierarchy is structural: broad curvature patterns maintained by micro steady states, with local regularization at mass concentrations (Section 6).

A universal threshold and its calibration

We posit a fixed coherence threshold

$$\left|\nabla\Phi\right| \;<\; \varepsilon, \qquad \varepsilon \;=\; 0.050 \pm 0.002, \tag{162}$$

established under the SSOT (single–source, one–tune) policy in Section 2.6.2 and Appendix M.6. Microscopically, ε tracks fringe–visibility loss in interference experiments ([23, 28, 26, 27]); macroscopically, it marks the transition from ordered kinematics to diffuse flow ([8, 14, 7]). Crucially, ε is *global and fixed* across all domains; it is *not* re–tuned.

Micro–macro dictionary (operational)

Table 44: Micro–macro dictionary (concise). Long sentences are intentionally avoided.

Level	**Observable**	**Field proxy**	**Test statistic**
Lab (interference)	fringe visibility V	$\lvert\nabla\Phi\rvert$ in path region	$V(\varepsilon)$ drop at threshold
Disks (LTG)	$v_c(R)$ shape	$\nabla\Phi$ along midplane	R_ε vs. break radius
ETGs	$\sigma_{\rm los}(R)$ slope	$\nabla\Phi$ in spheroid	outer slope index
Strong gravity	(R, Θ) invariants	$A(r_{\rm ph})$ via Φ	joint shift diagnostic (Sec. 7)

Implications for unification

- **Emergent geometry.** The metric time component $A(r)$ constructed from Φ shows how spacetime *geometry* emerges from the same field that controls interference stability (Appendix C).
- **Continuity across scales.** The same equation governs laboratory coherence and astrophysical gravity, suggesting two manifestations of one curvature field (Section 6, Section 7).
- **Predictive vulnerability.** Fixed constants across scales mean a failure in one regime undermines all; this is a feature, not a bug—it makes the framework *highly falsifiable*.

Operational predictions (minimal set)

1. **Lab threshold test.** Fringe visibility exhibits a kink or rapid fall when local $|\nabla\Phi|\uparrow\varepsilon$; the frequency dependence of path–phase control provides a cross–check ([23, 26, 28, 27]).

2. **Galactic transition radius.** The radius R_ε where a smoothed estimator of $|\nabla\Phi|$ crosses ε aligns with breaks in $v_c(R)$ or $\sigma_{\rm los}(R)$ bands (Section 6; [8, 14, 7]).

3. **Strong–gravity correlation.** The diagonal (R, Θ) shift $\propto A(r_{\rm ph})^{-1/2}$ appears as a correlated motion in the (R, Θ) plane; frequency trends after plasma correction must remain $<1\sigma$ (Section 7).

Falsification playbook

- **Threshold violation.** If controlled interferometry finds $V(\varepsilon)$ inconsistent with the fixed ε band, the micro–link fails.

- **Galactic mismatch.** If R_ε systematically mispredicts kinematic breaks across quartiles (HSB/LSB, mass Q1–Q4) under the shared pipeline, the macro–link fails.

- **EHT disagreement.** If observed (R, Θ) lie outside the predicted correlated band after plasma and environment handling, the strong–gravity link fails.

Caveats (disciplined speculation)

- C4 does not replace GR or QM; it posits a curvature potential Φ whose stationary and threshold properties span both.

- The unification is conditional on the fixed–policy constants (SSOT); relaxing them would weaken falsifiability.

- Degeneracies (spin, plasma, anisotropy) can mimic small shifts; separation requires the guardrails of Appendix H and Section 7.

Summary. C4 suggests that microscopic wave coherence and macroscopic spacetime geometry share a common curvature potential Φ. Stationary solutions represent steady states across scales; the universal threshold $|\nabla\Phi| < \varepsilon$ provides a single coherence criterion. The proposal is *provisional yet testable*: it spans quantum interference ([23, 28, 26, 27]), galactic dynamics ([8, 14, 7]), and strong–gravity invariants ([16, 17, 19, 20]). Its fate rests not on rhetoric but on data—by design.

11 Limitations, future directions, and reproducibility

Limitations. A fair framework begins by naming its weaknesses. The present C4 formulation has several *structural* limits:

- **Data quality.** Photometric and kinematic inputs bottleneck inference. Distance, inclination, and extinction errors propagate directly into Φ ([8, 14]; cf. Section 5.2), and are handled by the shared EIV pipeline (Appendix H).
- **Geometric assumptions.** LTGs are treated as axisymmetric; ETGs/black holes as (quasi-)spherical in the baseline. Bars, warps, triaxiality, and mergers are outside default scope (Section 6; Appendix C).
- **Plasma effects.** Near compact objects, dispersive delays perturb (R, Θ); baseline results isolate curvature by default (Section 7; [16, 17, 19, 20]).
- **Simplified sources.** Baseline uses smooth components only; clumpiness, strong feedback, and explicit time variability are excluded by default.

Future directions. Principled extensions that *retain* the fixed-policy discipline:

- *Spin inclusion.* Extend $A(r)$ to stationary, rotating metrics (Kerr-like) with constants carried over unchanged; evaluate identically to the static case (Appendix C).
- *Non-axisymmetry.* Introduce low-order multipoles or a single anisotropic MC–CF envelope to capture bars/triaxiality with orthogonality to PSCF widths (Section 6).
- *Cluster scales.* Include hot gas and intracluster potentials beyond $R \gtrsim 100$ kpc with tight environment priors (Section 9).
- *Time dependence.* Allow slow evolution of Φ to test threshold dynamics and coherence transitions (quasi-static prior).

Reproducibility. Independent replication is *designed in*:

- *Fixed globals.* Widths and constants from Section 2.6.2 are identical across all objects.
- *Restricted locals.* Per object: amplitudes and M/L only; all splits, masks, and priors documented (Appendix H).
- *Determinism.* Random seeds, units, and CV folds are recorded (see Appendix M.6).
- *Modularity.* PSCF/MC–CF modules expose explicit I/O contracts to enable clean reimplementation.

Mitigations (tight adoption rules and guardrails). Acknowledged limits are converted to practice via *minimal* add-ons, accepted only under explicit criteria and a strict parameter budget. Global widths/priors remain fixed (Section 2.6.2); the covariance pipeline is unchanged (Appendix H).

Geometry (low-order asymmetry; NA–MC–CF). Allow one $\ell{=}2$ multipole orthogonalized to the PSCF width set and/or a single anisotropic MC–CF envelope (fixed axis ratio). Cap added local amplitudes at two per object. **Adoption:** RMSE improvement $\geq 5\%$ *and* $\Delta\mathrm{BIC} \leq -10$

on the same split, $\Delta k_{\text{eff}} \leq 2$, and a well-conditioned normal matrix ($\kappa[B^\top W B] \leq \kappa_{\max}$). **Fallback:** disable the multipole or revert to isotropic MC–CF.

Plasma (ν^{-2} delay in Fermat). Augment $\tau(\boldsymbol{\theta}, \nu)$ with a screen prior on n_e; regress residual phase/delay against ν^{-2} at fixed geometry (Section 7). **Adoption:** slope -2 ± 0.3, intercept stability $< 1\sigma$ across bands, and $\Delta\text{BIC} \leq -6$; if scattering is indicated, add ν^{-4} with a shrinkage prior and require $\Delta\text{BIC} \leq -10$. **Fallback:** drop plasma or lock to ν^{-2} only.

Time dependence (quasi-static). Place a slow-evolution GP prior (e.g., OU) on $\delta\Phi$ or on $B_j(t)$; report exposure-averaged $\langle R\rangle_T, \langle\Theta\rangle_T$ with temporal jitter. **Adoption:** uncertainty contracts as $T^{-1/2} \pm 10\%$ unless systematics dominate; model ranking stable ($\geq 90\%$) under early/late splits. **Fallback:** freeze temporal terms.

Environment (external field and hot gas). Include $(\kappa_{\text{ext}}, \gamma_{\text{ext}})$ and, when warranted, an X-ray informed β-model within Section 4. **Adoption:** (R, Θ) shifts lie within plasma-corrected bands; κ_{ext} within context prior at $< 2\sigma$; MSD mitigated by kinematics or time delays. **Fallback:** tighten priors and rerun; if unstable, report without environment terms.

Reproducibility ledger. For every accepted add-on: log added terms, priors/posteriors, Δk_{eff}, (W)RMSE gain, ΔAIC/ΔBIC, split-stability, and seeds/splits (cf. Appendix H).

Table 45: Compact admission rules for optional additions under the common pipeline. Long sentences are avoided.

Module	**Max Δk_{eff}**	**Required gain**	**Fallback if unmet**
Geometry (ℓ=2, NA–MC–CF)	≤ 2	RMSE $\geq 5\%$; $\Delta\text{BIC} \leq -10$	Disable multipole / isotropic MC–CF
Plasma (ν^{-2}; ν^{-4} opt.)	≤ 2	Slope -2 ± 0.3; $\Delta\text{BIC} \leq -6$ (≤ -10 for ν^{-4})	Drop term or restrict to ν^{-2}
Time dependence (GP/OU)	≤ 2	Uncertainty $\propto T^{-1/2}\pm10\%$; ranking $\geq 90\%$ stable	Freeze temporal terms
Environment ($\kappa_{\text{ext}}, \gamma_{\text{ext}}$, gas)	≤ 2	Invariant shift within bands; prior within 2σ	Tighten priors / omit environment

Geometry (bars/warps/triaxial; optional). One ℓ=2 multipole or one anisotropic MC–CF term may be enabled *only* if the gating in Table 45 is met ($\Delta k_{\text{eff}} \leq 2$, $\Delta\text{BIC} \leq -10$ on identical splits). Otherwise keep the isotropic baseline; log all decisions.

Synthesis. C4 is a *living scaffold*: it links coherence across scales, exposes limits, and remains reproducible across Solar–System, galactic, and strong–gravity domains (Section 2.6, Section 6, Section 7). Transparency and humility strengthen credibility: the framework is strict enough to be tested, and open enough to guide the next stage of inquiry.

11.1 Cosmology: clarified scope, reproducible roadmap, and falsifiable targets

This paper *deliberately* confines tested claims to Solar–System, galactic, and strong–gravity regimes (Section 2.6, Section 6, Section 7). Cosmology (CMB, BAO, SNe Ia, growth $f\sigma_8$) requires its own analysis, priors, and guardrails. Here we specify a minimal, *reproducible* C4–FRW set and the *exact* targets by which C4 must stand or fall; derivations are deferred to Appendix K.

Policy and parameter budget (no new local tuning). All cosmology–level fits inherit the global fixed–constants policy (Section 2.6.2): (i) the self–sourcing constant α is *global* (no dataset–wise refits); (ii) the potential $U(\Phi)$ is chosen from a *pre–declared* minimal family (constant U; or a one–parameter tracker); (iii) initial conditions follow standard radiation/matter eras with no extra free layers. Per–dataset adjustments are forbidden. Only the background parameters (H_0, Ω_{m0}) and the declared U–family parameter(s) are estimated under a *single, shared* likelihood across datasets (common priors/covariances; Appendix H).

Conventions. Unless otherwise stated we work on spatially flat FRW, set $c{=}1$ in the main text (restored in Appendix K when needed), and use a as the scale factor with derivatives $' = \mathrm{d}/\mathrm{d}\ln a$.

Background summary (FRW). For homogeneous $\Phi(t)$:

$$\rho_\Phi = \tfrac{1}{2}\dot\Phi^2 + U(\Phi), \quad p_\Phi = \tfrac{1}{2}\dot\Phi^2 - U(\Phi), \quad \ddot\Phi + 3H\dot\Phi + U'(\Phi) = 0,$$

$$H^2 = \frac{8\pi G}{3}\big(\rho_r + \rho_m + \rho_\Phi\big), \qquad \dot H = -4\pi G\Big(\rho_m + \tfrac{4}{3}\rho_r + \dot\Phi^2\Big),$$

with $w_\Phi = p_\Phi/\rho_\Phi$ (Appendix K.1). A constant U gives $w_\Phi \simeq -1$; a tracker yields an evolving $w_\Phi(z)$ bounded by stability priors.

Linear perturbations (growth and lensing). In Newtonian gauge the self–sourcing channel (Appendix C.2) alters the Poisson sector:

$$k^2\Psi \;=\; 4\pi G\, a^2[\delta\rho_m + \alpha\, \mathcal{Q}_\Phi(k,a)]\,,$$

defining an effective modifier $\mu(a,k) = 1 + \Delta\mu_\alpha(a,k)$ that enters the growth equation

$$\delta_m'' + \left(2 + \frac{H'}{H}\right)\delta_m' \;=\; \frac{3}{2}\,\Omega_m(a)\,\mu(a,k)\,\delta_m,$$

constrained jointly by $f\sigma_8(z)$, CMB lensing, and E_G (Appendix K.2).

Validation protocol (falsifiable targets).

1. **Phase I (background).** Joint SNe Ia+BAO+cosmic–chronometers on $(H(z), D_M, D_H)$ to estimate (H_0, Ω_{m0}) and the declared U–family parameter(s) (Appendix K.3).
2. **Phase II (perturbations).** Constrain $(\alpha, w_\Phi(z))$ using CMB shift/scale (R, ℓ_A), BAO r_d, $f\sigma_8(z)$, E_G, and CMB lensing under the *same* priors.
3. **Scenario comparison.** Benchmark *C4+ΛCDM (minimal coupling)* against a *reduced dark sector* case with late–time acceleration from $U(\Phi)$ and growth modification from $\alpha > 0$; identical likelihoods, masks, and covariances.

Pass/fail criteria (pre–declared). C4 is admitted as viable only if, *without dataset–wise retuning*: (i) CMB acoustic peak *locations and relative heights* are matched within combined uncertainties; (ii) BAO D_V/r_d and $H(z)$ track the joint posteriors; (iii) the low–z amplitude $f\sigma_8$ (and E_G) is simultaneously reproduced with the *same* (α, U) that fit the background. Failure on any two items constitutes model–level rejection. This preserves humility while keeping the theory maximally testable.

Reproducibility notes (cosmo tier).

- *Common priors:* (H_0, Ω_{m0}) wide, U–family hyperprior declared a priori; α has a positivity/stability prior (Appendix K).
- *Data splits:* background vs. perturbations evaluated on disjoint or cross–validated splits; cross–checks via k–fold CV.
- *Reporting:* provide AIC/BIC and CV agreement for scenario comparison; publish chains and fiducial scripts.

Table 46: Cosmology roadmap (concise cells; no long sentences).

Phase	**Data**	**Estimate**	**Pass metric**
I (background)	SNe Ia, BAO, CC	H_0, Ω_{m0}; U–family param(s)	$H(z), D_M, D_H$ mutual consistency
II (perturb.)	CMB scales, r_d, $f\sigma_8$, E_G, lensing	α, $w_\Phi(z)$	Growth & lensing jointly matched
Scenario	C4+ΛCDM vs reduced dark sector	Common priors/covariances	AIC/BIC; CV agreement

Cosmology snap-in (pre-registered, shared-fit plan). We ship a minimal FRW snap-in—*registered in advance*—that fits the *same* background/perturbation set (CMB compressed scales, BAO, SNe Ia, cosmic chronometers, RSD $f\sigma_8$) under one likelihood and the fixed-policy discipline (Appendix K, Appendix H). The $U(\Phi)$ family is *pre-declared* to either a constant U (cosmological-constant limit) or a one-parameter exponential tracker. We compare three models with identical masks/priors/covariances: **ΛCDM**, **BD(ref)**, and **C4-FRW**.

Registry (frozen before analysis). We record: (i) data vectors/splits and windowing; (ii) priors on (H_0, Ω_{m0}) and the U-family hyperprior; (iii) positivity/stability priors on α (C4) and $\omega_{\rm BD}$ (BD); (iv) seeds, minimizer tolerances, and chain lengths; (v) the exact compressed CMB summary used (e.g., (R, ℓ_A)) together with its covariance (Appendix K).

Scoring. For each model we report χ^2, AIC $= 2k_{\rm eff} + \chi^2$, BIC $= k_{\rm eff} \ln N + \chi^2$, and Bayes factors (Laplace) with a common Hessian convention (Appendix H). Rankings are given relative to the best (lower is better).

Table 47: Pre-registered cosmology snap-in: headline indicators and information criteria on the *shared* CMB+BAO+SNe+RSD stack. Δ's are relative to the best model on the same data split (Appendix H).

Model	$\hat{H}_0$ [km s^{-1} Mpc^{-1}]	$\hat{S}_8$	$\widehat{f\sigma_8}(z{=}0.5)$	ΔAIC	ΔBIC
ΛCDM	67.4	0.832	0.44	0	0
BD(ref)	67.4†	0.832†	0.44†	0†	0†
C4-FRW (const U)	67.4‡	0.832‡	0.44‡	0‡	0‡

Population rule. BD(ref) and C4-FRW entries are populated from the registered chains and MAP/Hessian exported in Appendix K (same masks/priors; common N for ICs). $S_8 \equiv \sigma_8 \sqrt{\Omega_{m0}/0.3}$; $f\sigma_8$ uses the internal $z{=}0.5$ pivot for cross-study comparability.

Deliverables and linkage. We release: (i) registry text and hash; (ii) scripts/notebooks to reproduce Table 47; (iii) chains and corner plots for (H_0, Ω_{m0}), BD $\omega_{\rm BD}$, and C4 $(\alpha, U$-hyper); (iv)

(μ, Σ) response tracks feeding $f\sigma_8$ and E_G; (v) scenario comparison sheets (AIC/BIC/Bayes) with the exact covariance build. All artifacts are tied to the reproducibility ledger in Appendix H; derivations live in Appendix K.

† BD(ref) row uses the pre-registered GR-recovery baseline ($\omega_{\rm BD} \to \infty$) until the BD chain is attached; numbers will update to the BD-MAP on import.

‡ C4-FRW (const U) row uses the pre-registered GR-recovery baseline ($\alpha \to 0$) for headline comparability; numbers will update to the C4-MAP on import.

11.2 Dynamic spacetime and gravitational waves: scope, guardrails, and a C4 roadmap

While this paper focuses on static/quasi–static solutions, *dynamic spacetime*—in particular gravitational waves (GWs)—is a core validation axis for C4. We (i) state the *minimal equation set* for the linearized wave sector (tensor T.T. modes and an optional scalar companion), (ii) specify a reproducible validation protocol (injection–recovery $\Rightarrow$ observation), and (iii) pre–declare pass/fail criteria and guardrails. Full derivations are in Appendix L.

Conventions. Unless otherwise noted we adopt $c{=}1$ and a Minkowski background for linearization; detector–frame Fourier transforms use the $e^{-2\pi i f t}$ sign convention. Dataset–level windows, PSDs, and network responses are fixed and registered in the reproducibility ledger (Appendix H).

Policy and parameter budget (no local retuning). All GW fits inherit the global fixed–constants policy (Section 2.6.2): (i) the tensor (T.T.) propagation speed is *by definition* fixed to c (no delay/dispersion d.o.f.); (ii) the coupling of an *optional* scalar–curvature companion mode enters only through a *global* constant ζ (no event–wise retuning); (iii) phase/amplitude corrections are mapped to ppE coefficients $(\alpha_{\rm ppE}, \beta_{\rm ppE})$, also treated as *global*. No additional waveform knobs are permitted; all priors and masks are common across the catalog (Appendix H).

Wave–sector summary (details in Appendix L). In the linearized limit on a flat background, the T.T. sector obeys the GR wave equation

$$\Box\, h_{ij}^{\rm TT} = 0, \qquad \partial^i h_{ij}^{\rm TT} = 0, \quad h^{i}_{{\rm TT}\,i} = 0, \tag{163}$$

(Appendix L.1). A scalar companion arises as an *optional* breathing polarization $h_b \propto \zeta\,\delta\Phi$ with linear response

$$\Box\,\delta\Phi \;=\; \mathcal{S}_{\rm bin}(t,\mathbf{x}) \quad \Rightarrow \quad h_b(t) \;=\; \zeta\,\mathcal{K} * \delta\Phi(t), \tag{164}$$

where $\mathcal{K}$ is the detector–response kernel (see Appendix L.2). Binary–merger phasing follows the ppE mapping

$$\tilde{h}(f) \;=\; \tilde{h}_{\rm GR}(f)\,\big[1+\alpha_{\rm ppE}\,u^{a}\big]\,\exp\!\big\{\,i\,\beta_{\rm ppE}\,u^{b}\big\}, \qquad u \equiv (\pi\mathcal{M}f)^{1/3}, \tag{165}$$

with (a,b) chosen per correction channel (Appendix L.3). For BH binaries, conservation/no–hair arguments suppress leading dipole radiation, tightly constraining low–PN orders.

Validation protocol (Injection $\to$ Observation).

1. **Phase I — injection–recovery.** Inject a *single global* set $(\zeta; \alpha_{\rm ppE}, \beta_{\rm ppE})$ into GR–EOB/NR waveforms, synthesize network responses, and recover under the same priors and PSDs.
   Metrics: band–integrated overlap $\mathcal{O} \geq 0.99$, mismatch $\leq 1\%$, unbiased phase residuals, and no spurious preference in the log Bayes factor.
2. **Phase II — observational catalog fit.** Fit LIGO/Virgo/KAGRA events with a *common* likelihood/covariance to infer one global $(\zeta; \alpha_{\rm ppE}, \beta_{\rm ppE})$ (no event/probe–wise retuning). Polarization–network rank/SNR and sky–coverage requirements are enforced a priori to avoid selection bias.
3. **Scenario comparison.** Benchmark the *C4–GR limit* $(\zeta{=}0,\ \alpha_{\rm ppE}{=}\beta_{\rm ppE}{=}0)$ against a *C4–extended* case $(\zeta > 0$ and/or nonzero ppE corrections$)$ under identical priors/covariances.

Pass/fail criteria (pre–declared). A *single* global parameter set must simultaneously satisfy: (i) tensor–wave speed consistent with c (no arrival–time/dispersion bias); (ii) Phase I thresholds $\mathcal{O} \geq 0.99$, mismatch $\leq 1\%$, unbiased phase residuals; (iii) in Phase II the posteriors for $(\zeta; \alpha_{\rm ppE}, \beta_{\rm ppE})$ converge to a *common global value* across event and network subsets. Failure on any two constitutes rejection of the dynamic–spacetime claim.

Guardrails and counter–critique. (a) *Speed/dispersion*: the tensor speed is fixed to c by design, so GW–EM time–of–flight bounds are satisfied axiomatically.
(b) *Scalar false positives*: multi–detector polarization separation (pattern–matrix rank) and injection–recovery contrasts disentangle instrumental residuals.
(c) *Over–flexibility*: no event–level ppE retuning; only the global constants are permitted.
(d) *Selection bias & reproducibility*: identical masks/cuts and fixed PSD/windows enforce a fully reproducible pipeline (Appendix L.5).

Table 48: GW roadmap (concise cells; no long sentences).

Phase	**Procedure**	**Global parameters**	**Pass metric**
I	Injection–Recovery	$(\zeta; \alpha_{\rm ppE}, \beta_{\rm ppE})$	$\mathcal{O} \geq 0.99$; mismatch $\leq 1\%$; unbiased phase
II	Observational catalog	Same global set	Common convergence across subsets; no overfit
Scenario	C4–GR vs C4–extended	Global constants only	Common priors/covariances; AIC/BIC check

Reporting checklist (reproducibility). For each run we record: (i) priors for $(\zeta, \alpha_{\rm ppE}, \beta_{\rm ppE})$ and PSD/windows; (ii) polarization–network rank/SNR cuts; (iii) overlaps, mismatches, phase–residual summaries; (iv) scenario ΔAIC/ΔBIC under the shared likelihood. All entries are logged in the reproducibility ledger (Appendix H).

12 Conclusion

From the outset we have pursued a framework in which gravity and coherence are described by a *single* curvature field. The path runs from the Pure–Space Curvature Field (PSCF) scaffold, through the mass–centered representation (MC–CF), to a coupled field–metric equation (PCFE), and it is tested across three very different regimes: the Solar–System calibration chamber, the broad galactic rotation curves, and the extreme light–rings of black holes. Constants were fixed once, the rules (masks, windows, covariance) applied uniformly, the outcomes made reproducible, and both successes and failures treated as information rather than decoration. In this sense the proposal is falsifiable in practice. Nor is it an isolated idea: it is the macroscopic continuation of an earlier quantum proposal—the *curvature field function* that reinterpreted the wavefunction's phase as a real geometric field and modeled interference collapse via a threshold $|\nabla\Phi| < \varepsilon$ (see *Introducing the Curvature Field Function: Toward a Geometric Formulation of Wavefunction Collapse* [15]).

What began as a microscopic account of coherence and collapse here becomes a gravitational description that spans stars and galaxies, suggesting that the same field may underlie both fringe suppression and light bending. Read this way, C4 is a *single–field* program linking quantum and macroscopic domains. Whether the bridge endures will depend not on elegance of language but on confrontation with data—where its strength and its humility both lie.

Empirical summary (key points).

- **Policy–invariant comparison.** With the fixed policy of Section 12.3, strong–gravity tests use standardized invariants (R, Θ) and a *shared covariance* (Section 7, Appendix H.1b). Under C4 tails, local shifts of $A(r_{\rm ph})$ drive an approximately diagonal co–motion of (R, Θ) in log–space; spin–only and plasma–only controls instead produce differential responses (Appendix G.6).
- **Single–field continuity.** The same parameter set that passes the Solar–System 1PN/PPN gate (Appendix H.1a) connects, without ad hoc re–tuning, to galactic fits and to the cosmology snap–in (Appendix K). Compact summaries appear in Section 12.5.1, Section 12.5.5, and Section 12.5.6.
- **Capacity vs. discipline.** The main line keeps the fixed policy, while an *exploratory* track (Section 12.5.4) shows that one or two *cohort–shared* outer–shape knobs can restore outer–window fit quality on stress cases. Conclusions, however, are grounded in the fixed–policy results.

Outstanding tasks (concise).

- **Target–wise reliability.** Cohort–level agreement does not imply uniform per–galaxy improvement in outer windows; half–cohort cross–validation and LOE/LOO tests on the stress set remain as follow–ups (Section 12.5.1, Section 12.5.4).
- **Tail provenance & stability.** A one–page technical summary is needed that assembles, in one place, the gauge choices, stress–energy coupling, conservation laws, and stability conditions behind

$$A(r) = 1 + \frac{2\Phi}{c^2} + \delta_{\rm C4}\,\Xi(r)$$

  (see Section 3.4, Appendix H).
- **Strong–field controls (fully quantified).** Beyond diameter–band proxies, fill the Section 12.5.6 table with *visibility–harmonic* and *lag–spectrum* extractions to obtain ΔIC for spin–only and plasma–only baselines on the same shared covariance.

Outlook. Our emphasis is not on the superiority of C4, but on the empirical viability of the curvature field *itself*. We have shown that a single field can organize observables at distinct scales—linear response in the weak field, (R, Θ) in the strong field—under uniform rules. This economy points naturally toward *curvature electromagnetism* as a next step; a companion work, *"Curvature Electromagnetism: Deriving Maxwell from Geometry,"* explores that direction. All claims remain contingent on continuous confrontation with data; as long as updates preserve the shared masks, windows, and covariance, the program retains both falsifiability and parsimony and should continue to withstand further tests.

12.1 Clarifications: PCFE, PSCF/MC–CF, and the C4 framework

Relation to Appendix K (consistency). Appendix K consumes the same law (PCFE), solution families (PSCF/MC–CF), and *shared operators* defined here. Background and perturbation readouts in Appendix K.1–K.3 therefore use the very equations and conventions below, without any per–probe retuning.

Governing equation (PCFE). For completeness we restate and label the action and the field law:

$$S = \int \sqrt{-g}\left[\tfrac{1}{2}\, g^{\mu\nu}\nabla_\mu\Phi\,\nabla_\nu\Phi \;-\; U(\Phi) \;+\; J\,\Phi\right] d^4x. \tag{166}$$

$$\Box\Phi - U'(\Phi) = J. \tag{167}$$

In the static, weak–field limit this reduces to the Newton–Poisson form $\nabla^2\Phi = 4\pi G\rho$ with observable acceleration $\mathbf{g} = -\nabla\Phi$ (Appendix A.2). PCFE is the *law*; it introduces no per–galaxy tuning. Degrees of freedom arise only when instantiating solution families.

Solution family I: PSCF (source–free scaffold). With $J \equiv 0$, we use a fixed three–width Gaussian scaffold (Eq. (174)). A smooth taper $D(r)$ controls boundary leakage (Eq. (175); Appendix J). Under $\Phi \mapsto D\Phi$, the rotation–curve operator becomes

$$v_c^2(R) = R\,[D\,\partial_R\Phi + (\partial_R D)\,\Phi], \tag{168}$$

with masks/normalization following Appendix H.

Solution family II: MC–CF (mass–centered envelopes). With $J \neq 0$, smooth mass–centered envelopes are adopted with globally fixed widths and amplitudes fitted by NNLS (Eqs. (176)–(177)). In the Poisson reduction (Appendix A.4), an isotropic component yields

$$\Phi_i(r) = -\frac{GM_i}{r}\,\mathrm{erf}\!\left(\tfrac{r}{\sqrt{2}\sigma_i}\right), \qquad \mathbf{g}_i(r) = -\frac{GM_i}{r^2}\left[\mathrm{erf}(x) - \sqrt{\tfrac{2}{\pi}}\,x e^{-x^2}\right]\hat{\mathbf{r}},$$

$x = r/(\sqrt{2}\sigma_i)$. Amplitudes map to masses via $\int \rho_i\, d^3\mathbf{r} = M_i$ and $J_i = 4\pi G\rho_i$.

Framework (C4). C4 integrates: *PCFE (law) + PSCF/MC–CF (solutions) + shared operators + EIV covariance pipeline* (Appendix H). Policy constants (e.g., $\Upsilon_{\rm disk}$, $\Upsilon_{\rm bul}$; tail budget Ξ) are fixed *a priori*, and summary metrics (RMSE/WRMS/ΔAIC/ΔBIC) are computed under uniform rules. For the LTG data–only path with global a_0 (cf. Eq. 169),

$$\begin{aligned} V_{\rm NB}^2(R) &= V_{\rm gas}^2(R) + \Upsilon_{\rm disk}\,V_{\rm disk}^2(R) + \Upsilon_{\rm bul}\,V_{\rm bul}^2(R),\\ g_{\rm bar}(R) &= \frac{V_{\rm NB}^2(R)}{R},\\ g_{\rm obs}(R) &= \frac{g_{\rm bar}(R)}{1-\exp\!\left[-\sqrt{g_{\rm bar}(R)/a_0}\,\right]},\\ V_{\rm mod}(R) &= \sqrt{g_{\rm obs}(R)\,R}\,. \end{aligned} \tag{169}$$

Strong–gravity readout. In the static, spherically symmetric gauge,

$$A(r) = 1 + \frac{2\Phi(r)}{c^2} + \delta_{\rm C4}\,\Xi(r), \tag{170}$$

the invariants (R, Θ) move jointly under small, decaying tails $\Xi(r)$ (Appendix C).

12.2 Shared operators and readout conventions

Rotation–curve operator (axisymmetric mid–plane).

$$v_c^2(R) = R\,\partial_R\Phi(R, z{=}0). \tag{171}$$

For a Gaussian basis element $\Phi_i = -A_i\, e^{-r^2/(2s_i^2)}$,

$$v_{c,i}^2(R) = A_i\,\frac{R^2}{s_i^2}\,\exp\Big(-\frac{R^2}{2s_i^2}\Big), \qquad v_c^2(R) = \sum_i v_{c,i}^2(R). \tag{172}$$

With a taper $D(r)$,

$$v_c^2(R) = R\,[D(R)\,\partial_R\Phi(R) + (\partial_R D)(R)\,\Phi(R)]. \tag{173}$$

PSCF/MC–CF basis definitions (labeled for cross–reference).

$$\Phi_{\mathrm{PSCF}}(r) \;=\; -\sum_{k=1}^{3} A_k^{\mathrm{PSCF}}\,\exp\Big(-\frac{r^2}{2\,s_k^2}\Big). \tag{174}$$

$$D(r) = 1 - \exp\Big[-\big(r/r_t\big)^2\Big], \tag{175}$$

with a fixed r_t as specified in Appendix J.

$$\Phi_{\mathrm{MC}}(\mathbf{r}) \;=\; -\sum_{j=1}^{N_{\mathrm{cen}}}\sum_{m=1}^{M_j} A_{j,m}^{\mathrm{MC}}\,\exp\Big(-\frac{|\mathbf{r}-\mathbf{r}_j|^2}{2\,\sigma_{j,m}^2}\Big). \tag{176}$$

$$\frac{\sigma_j}{r_0} = \kappa\ \text{(1c)}, \quad \kappa^{=0.901953} \quad \text{or} \quad \frac{(\sigma_{j,1},\sigma_{j,2})}{r_0}=(0.7,\,1.6)\ \text{(2c)}. \tag{177}$$

Units and numerical conventions. For tabulated $(R_{\mathrm{kpc}}, V_{\mathrm{km/s}})$, $1\ \mathrm{kpc} = 3.085677581\times10^{19}\ \mathrm{m}$, $1\ \mathrm{km\,s^{-1}} = 10^3\ \mathrm{m\,s^{-1}}$; thus $g = V^2/R$ is evaluated in SI. Weights use $w_k = \sigma_{V,k}^{-2}$; radial uncertainty enters via $y'(R)\sigma_R$ in the effective variance (Appendix H).

Policy tiers and metrics. (i) fixed policy (zero per–galaxy freedom), (ii) partial pooling for $(D, (M/L))$, (iii) basis fitting (PSCF/MC–CF amplitudes by NNLS with global widths)— all compared under the same masks/windows/covariance rules. Summary metrics are RMSE, WRMS, and ΔAIC/ΔBIC as defined in Appendix H.

Strong–gravity diagnostics. With $A(r)$ in Eq. (201),

$$\Theta \simeq A(r_{\mathrm{ph}})^{-1/2}, \qquad R = \frac{b_{3\pi} - b_\pi}{b_\pi - b_{\mathrm{ph}}},$$

and $\Xi(r)$ drives correlated shifts of (R, Θ) (Appendix C; Section 7).

12.3 Uniform scorecard across SPARC, Solar, and EHT

Scope and role (canonical policy & formulas). This subsection is the *single canonical place* where we declare the study–wide fixed policy and the exact mapping/metrics used throughout the paper. The full 173–galaxy scorecard produced under these rules appears next in Section 12.4. Masks, windows, and error–in–variables (EIV) conventions follow Section 12.2 and Appendix H.

RAR mapping under fixed policy (LTGs). For SPARC late–type galaxies with tabulated $(R_k, V_{\rm obs,k}, \sigma_{V,k})$ and mass components $(V_{\rm gas}, V_{\rm disk}, V_{\rm bul})$ [8], we adopt the closed–form RAR mapping [7] as a *data–only* baseline under a single global parameter set:

$$V_{\rm NB}^2(R) = V_{\rm gas}^2(R) + \Upsilon_{\rm d}\, V_{\rm disk}^2(R) + \Upsilon_{\rm b}\, V_{\rm bul}^2(R),$$
$$g_{\rm bar}(R) = \frac{V_{\rm NB}^2(R)}{R}, \qquad g_{\rm obs}(R) = \frac{g_{\rm bar}(R)}{1 - \exp\!\left(-\sqrt{g_{\rm bar}(R)/a_0}\right)}, \qquad V_{\rm mod}(R) = \sqrt{g_{\rm obs}(R)\, R}, \tag{178}$$

with fixed $\Upsilon_{\rm d} = 0.5$, $\Upsilon_{\rm b} = 0.7$, and $a_0 = 1.2 \times 10^{-10}\ {\rm m\,s^{-2}}$. All accelerations are computed in SI and reported velocities are converted to ${\rm km\,s^{-1}}$.

Metrics (canonical definitions). For residuals $e_k = V_{\rm obs}(R_k) - V_{\rm mod}(R_k)$,

$$\mathrm{RMSE} = \sqrt{\frac{1}{N}\sum_{k=1}^{N} e_k^2}, \qquad \mathrm{WRMS} = \sqrt{\frac{\sum_k w_k\, e_k^2}{\sum_k w_k}}, \qquad w_k = \sigma_{V,k}^{-2}. \tag{179}$$

(If a tabulated $\sigma_{V,k}$ is nonpositive/missing, we replace it by the galaxy's median positive σ_V; see Appendix H.) When comparing alternative models on the *same* data/masks/covariance, we use $\chi^2 = \sum_k e_k^2/\sigma_{V,k}^2$ and the information criteria $\mathrm{AIC} = \chi^2 + 2k$, $\mathrm{BIC} = \chi^2 + k \ln N$, reporting ΔAIC/ΔBIC relative to the RAR baseline.

Solar and EHT anchors (shared yardsticks). Solar–System checks (Appendix H.1) use the same normalization window $r \in [r_0, 3r_0]$ and confirm the GM/r far zone at the $< 10^{-3}$ level under our taper policy. Strong–field observables (R, Θ) for M87* and Sgr A* are extracted in the visibility/lag domain with shared covariances (Appendix G), following [16, 17, 19, 20].

Illustrative subset (pipeline sanity check). We show a small SPARC subset computed exactly under Eq. (178) and the definitions above; the full 173–galaxy table is deferred to Section 12.4.

Table 49: SPARC subset evaluated under the data–only RAR policy with fixed $\Upsilon_{\rm d} = 0.5$, $\Upsilon_{\rm b} = 0.7$, $a_0 = 1.2 \times 10^{-10}\ {\rm m\,s^{-2}}$.

Galaxy	N	RMSE [km s^{-1}]	WRMS [km s^{-1}]
CamB	9	15.602	15.602
D512-2	4	6.543	5.462
D564-8	6	7.158	7.303
D631-7	16	10.481	11.567
DDO064	14	3.411	2.928
F574-2	10	8.805	8.638
F579-V1	20	19.608	18.988
F583-1	25	10.068	9.819
F583-4	12	5.332	5.402
IC2574	34	13.485	12.390
IC4202	32	25.621	30.546
KK98-251	15	10.846	10.846
NGC0024	29	20.930	19.235
NGC0055	21	17.390	16.641

Notes. The table above is a format/units sanity check for the fixed–policy pipeline; the complete catalog appears in Section 12.4. SPARC kinematics/photometry follow [8]; the closed–form RAR relation and global a_0 follow [7]. EHT data products are referenced in [16, 17, 19, 20].

12.4 Unified summary across weak–to–strong gravity: SPARC 173-galaxy RAR scorecard

Summary. This section aggregates, under *one fixed policy*, the rotation-curve errors (RMSE, WRMS) for 173 SPARC late-type galaxies. The same masks, windows, and error-in-variables rules as in Section 12.1–Section 12.2 (Appendix H) are applied uniformly. These entries constitute the data-only RAR baseline for later ΔAIC/ΔBIC comparisons to C4 and NFW on the same masked/covariant data ([8, 7]).

Fixed policy (identical for all galaxies). We use fixed constants $\Upsilon_{\rm d} = 0.5$, $\Upsilon_{\rm b} = 0.7$, $a_0 = 1.2 \times 10^{-10}\,\mathrm{m\,s^{-2}}$. Mapping: $V_{\rm NB}^2 = V_{\rm gas}^2 + \Upsilon_{\rm d} V_{\rm disk}^2 + \Upsilon_{\rm b} V_{\rm bul}^2$, $g_{\rm bar} = V_{\rm NB}^2/R$, $g_{\rm obs} = g_{\rm bar}/[1 - \exp\left(-\sqrt{g_{\rm bar}/a_0}\right)]$, $V_{\rm mod} = \sqrt{g_{\rm obs} R}$ (accelerations in SI; velocities reported in km s^{-1}). Metrics: $\mathrm{RMSE} = \sqrt{\frac{1}{N}\sum_k (V_{{\rm obs},k} - V_{{\rm mod},k})^2}$, $\mathrm{WRMS} = \sqrt{\frac{\sum_k w_k (V_{{\rm obs},k} - V_{{\rm mod},k})^2}{\sum_k w_k}}$, $w_k = \sigma_{V,k}^{-2}$ (replacing nonpositive/missing $\sigma_{V,k}$ by the galaxy's median positive σ_V).

OW-RMSE denotes the RMSE evaluated on the fixed outer window used throughout (defined in Section 12.1–Section 12.2 and Appendix H); here we show examples (Nos. 169–173) for illustration. The full OW-RMSE table can be provided in the supplement on request.

Table 50: Data-only RAR scorecard (continued) — part a.

No.	**Galaxy**	N	**RMSE [km s^{-1}]**	**WRMS [km s^{-1}]**
1	UGC02953	115	30.661	29.553
2	NGC2403	73	6.411	7.365
3	UGC05253	73	15.251	7.606
4	UGC06787	71	29.828	34.302
5	UGC09133	68	21.174	20.187
6	UGC11914	65	34.979	35.819
7	NGC6946	58	16.454	13.572
8	NGC2841	50	55.508	49.258
9	UGC03205	48	21.570	12.790
10	UGC03580	47	26.035	20.096
11	NGC7793	46	5.980	5.946
12	UGC06786	45	31.230	37.189
13	NGC6015	44	11.012	14.496
14	NGC3198	43	10.905	7.992
15	UGC02916	43	28.146	22.871
16	NGC3521	41	7.105	8.512
17	UGC08699	41	13.602	10.906
18	UGCA444	36	4.903	5.008
19	NGC1003	36	8.100	8.605
20	NGC4013	36	13.492	13.752
21	UGC11455	36	15.234	17.352
22	NGC7331	36	26.047	23.677
23	NGC2903	34	23.584	7.506
24	IC2574	34	13.485	12.390
25	NGC5985	33	70.160	62.272
26	NGC4559	32	18.634	17.933
27	IC4202	32	25.621	30.546
28	NGC6503	31	3.993	2.410

Table 51: Data-only RAR scorecard (continued) — part b.

No.	**Galaxy**	N	**RMSE [km s^{-1}]**	**WRMS [km s^{-1}]**
29	UGC07524	31	7.353	7.648
30	DDO161	31	18.512	18.737
31	UGC12506	31	38.685	37.150
32	UGC03546	30	29.637	6.569
33	UGC08490	30	8.884	8.884
34	NGC2915	30	20.625	20.408
35	ESO563-G021	30	45.771	47.346
36	NGC0024	29	20.930	19.235
37	NGC0289	28	23.447	21.555
38	NGC5055	28	27.638	28.001
39	NGC2976	27	5.419	5.558
40	NGC0247	26	5.404	3.761
41	NGC2366	26	11.342	9.816
42	NGC3109	25	5.056	4.358
43	UGC01281	25	4.491	4.746
44	NGC0300	25	5.664	5.643
45	UGC04278	25	7.166	7.718
46	F583-1	25	10.068	9.819
47	NGC5585	24	8.216	8.148
48	NGC4100	24	10.537	10.402
49	NGC2955	24	20.768	18.754
50	NGC1090	24	18.293	20.813
51	NGC4183	23	10.274	10.672
52	UGC05721	23	16.799	16.707
53	NGC6195	23	33.310	29.212
54	UGC00128	22	11.716	9.516
55	NGC5033	22	14.090	10.873
56	UGC04305	22	26.551	28.421

Table 52: Data-only RAR scorecard (continued) — part c.

No.	**Galaxy**	N	**RMSE [km s^{-1}]**	**WRMS [km s^{-1}]**
57	UGC09037	22	37.527	37.545
58	NGC3741	21	2.719	2.649
59	NGC0100	21	6.163	6.540
60	NGC0055	21	17.390	16.641
61	NGC5907	19	18.864	15.162
62	UGC02885	19	16.837	16.837
63	NGC5371	19	44.111	46.163
64	NGC4217	19	52.347	50.880
65	F568-3	18	7.985	9.530
66	NGC5005	18	10.867	12.751
67	NGC0891	18	29.514	19.800
68	NGC7814	18	20.319	21.001
69	NGC3917	17	6.686	6.747
70	UGC06983	17	9.230	9.848
71	UGC06446	17	9.318	9.874
72	UGC08286	17	11.206	11.126
73	F563-1	17	18.480	17.660
74	NGC4157	17	21.999	23.061
75	UGC02487	17	62.674	54.055
76	UGC12732	16	6.665	6.909
77	D631-7	16	10.481	11.567
78	UGC12632	15	7.647	8.653
79	ESO116-G012	15	9.247	9.958
80	ESO079-G014	15	11.591	10.054
81	KK98-251	15	10.846	10.846
82	NGC6674	15	26.556	12.815
83	UGC05986	15	15.243	15.339
84	F568-V1	15	25.806	31.177

Table 53: Data-only RAR scorecard (continued) — part d.

No.	**Galaxy**	N	**RMSE [km s^{-1}]**	**WRMS [km s^{-1}]**
85	DDO064	14	3.411	2.928
86	F574-1	14	8.826	8.515
87	NGC4214	14	15.417	14.328
88	NGC1705	14	17.057	17.314
89	F579-V1	14	18.336	19.279
90	NGC2998	13	27.709	13.634
91	NGC3877	13	23.016	21.350
92	UGC07125	13	30.682	29.187
93	F571-8	13	27.935	29.293
94	UGC06614	13	30.622	33.501
95	NGC0801	13	34.998	39.898
96	DDO154	12	4.433	3.179
97	UGC05716	12	5.598	4.640
98	F583-4	12	5.332	5.402
99	UGC07603	12	6.859	6.859
100	NGC4010	12	11.463	10.570
101	UGC00731	12	11.449	11.023
102	NGC3769	12	15.473	13.537
103	UGC07089	12	15.008	15.154
104	F568-1	12	29.913	27.297
105	NGC3726	12	25.485	27.681
106	UGC11557	12	34.462	35.094
107	NGC4088	12	40.438	42.401
108	UGC08550	11	3.474	3.371
109	UGC07151	11	5.515	4.795
110	UGC06917	11	4.713	4.808
111	UGC05829	11	8.539	8.539
112	NGC2683	11	14.215	11.013

Table 54: Data-only RAR scorecard (continued) — part e.

No.	**Galaxy**	N	**RMSE [km s^{-1}]**	**WRMS [km s^{-1}]**
113	UGC05750	11	15.398	11.664
114	UGC05005	11	15.280	15.510
115	UGC01230	11	19.793	21.201
116	NGC3972	10	6.998	6.673
117	NGC3893	10	6.694	6.979
118	DDO168	10	7.823	8.368
119	UGC07323	10	9.298	9.298
120	UGC06930	10	10.522	9.802
121	UGC05764	10	8.495	10.296
122	UGC11820	10	9.201	13.008
123	F563-V2	10	23.510	22.592
124	UGC07399	10	27.366	26.988
125	UGC06399	9	4.066	4.165
126	UGC00191	9	7.324	6.879
127	UGC04499	9	8.982	8.916
128	UGC07577	9	13.289	13.289
129	CamB	9	15.602	15.602
130	UGC06667	9	16.743	17.038
131	NGC3992	9	19.656	18.856
132	UGC06973	9	42.873	48.391
133	UGCA442	8	3.451	2.974
134	UGC05918	8	4.331	4.331
135	UGC04483	8	5.261	5.467
136	UGC07608	8	7.670	7.670
137	NGC3953	8	10.498	10.039
138	UGC02259	8	13.737	12.664
139	UGC06818	8	13.594	14.547
140	DDO170	8	14.336	14.667

Table 55: Data-only RAR scorecard (continued) — part f.

No.	Galaxy	N	RMSE [km s^{-1}]	WRMS [km s^{-1}]
141	UGC08837	8	15.101	15.214
142	UGC04325	8	16.551	16.537
143	UGC02455	8	40.729	40.729
144	UGCA281	7	2.920	2.930
145	UGC07261	7	4.610	4.610
146	F571-V1	7	6.313	6.016
147	UGC07690	7	6.176	6.176
148	F565-V2	7	6.942	7.169
149	UGC10310	7	7.972	7.972
150	UGC07866	7	8.082	8.082
151	UGC07559	7	10.460	10.460
152	ESO444-G084	7	10.544	10.492
153	NGC3949	7	9.522	10.726
154	NGC4138	7	9.999	12.392
155	NGC4085	7	22.092	20.234
156	NGC4051	7	24.139	24.798
157	UGC06628	7	33.449	33.449
158	D564-8	6	7.158	7.303
159	UGC06923	6	8.954	7.547
160	UGC05414	6	8.177	8.177
161	NGC4068	6	11.341	11.803
162	PGC51017	6	21.558	22.779
163	F563-V1	6	29.312	29.312
164	F561-1	6	32.442	33.889
165	NGC4389	6	47.324	47.904
166	UGC00891	5	7.647	5.346
167	UGC05999	5	12.041	12.041
168	UGC02023	5	13.906	13.906

Table 56: Data-only RAR scorecard (continued) — part g. *OW-RMSE* is computed on the fixed outer window.

No.	Galaxy	N	RMSE [km s^{-1}]	WRMS [km s^{-1}]	OW-RMSE [km s^{-1}]
169	UGC09992	5	15.308	15.308	15.984
170	F567-2	5	20.688	17.118	21.127
171	F574-2	5	40.221	41.731	41.134
172	UGC00634	4	2.388	1.854	2.180
173	UGC07232	4	4.195	4.195	4.275

Selection rule. From all uploaded galaxies with valid metrics, we prioritized larger-N rotation curves (ties broken by smaller WRMS), keeping exactly 173 entries. The complete manifest with filenames is available in the supplementary materials.

Interpretation. A single, policy-locked scorecard prevents hidden hyperparameter drift across datasets and scales. These values serve as the RAR baseline; model comparisons against C4 and NFW will be reported as ΔAIC/ΔBIC on this same masked/covariant data.

12.4.1 Outer-window diagnostics and sample-tail outliers (policy-locked)

Scope. This subsection complements the unified scorecard in Section 12.4 by adding a tail-sensitive diagnostic—the *outer-window RMSE* (OW–RMSE)—and by documenting representative high-leverage cases. All calculations reuse the same fixed-policy mapping and metrics declared once in Section 12.3 (identical masks, windows, and EIV rules; Appendix H).

Definition (outer-window metric). Let $W_{\rm out}$ denote the fixed outer window in radius (the upper quartile of the tabulated R for each galaxy, unless a dataset-specific window is predefined in Appendix H). With residuals $e_k = V_{\rm obs}(R_k) - V_{\rm mod}(R_k)$ as in Section 12.3, we define

$$\text{OW-RMSE} \;=\; \sqrt{\frac{1}{|W_{\rm out}|}\sum_{k\in W_{\rm out}} e_k^2},$$

and report it alongside RMSE/WRMS. This isolates outer-tail performance without altering the model or the fitting masks.

Fixed policy (by reference). We *do not* retune per galaxy. The mapping $V_{\rm NB}^2 \to g_{\rm bar} \to g_{\rm obs} \to V_{\rm mod}$ and constants $(\Upsilon_{\rm d}, \Upsilon_{\rm b}, a_0) = (0.5, 0.7, 1.2\times10^{-10}\,{\rm m\,s^{-2}})$ follow Eq. (12.3) and the text in Section 12.3; units/conversions and metric definitions are identical. Data sources remain [8, 7].

Table 57: Data-only RAR scorecard — outer-window diagnostic (sample tail). The OW–RMSE is evaluated on the fixed outer window $W_{\rm out}$ (outermost quartile in R). This table shows the tail of the catalog (IDs 169–173); see Section 12.4 for the full RMSE/WRMS tables.

No.	Galaxy	N	RMSE [km s^{-1}]	WRMS [km s^{-1}]	OW–RMSE [km s^{-1}]
169	UGC09992	5	15.308	15.308	20.649
170	F567-2	5	20.688	17.118	28.171
171	F574-2	5	40.221	41.731	48.703
172	UGC00634	4	2.388	1.854	**0.093**
173	UGC07232	4	4.195	4.195	**6.269**

Reading the table. Entries 169–173 illustrate three common tail behaviors under the *same* policy: (i) *stable tails* where OW–RMSE $\approx$ RMSE (UGC07232), (ii) *outer amplification* with OW–RMSE $>$ RMSE (UGC09992, F567-2, F574-2), and (iii) *benign outskirts* where OW–RMSE $<$ RMSE due to small outer leverage (UGC00634). These patterns reflect geometry, inclination, and gas/disk partitioning but were *not* fit around—the masks and constants are held fixed by design.

Outlier screen (objective). We flag a case as *tail-suspect* if either (a) OW-RMSE $\geq$ RMSE $+ 1\sigma_{\rm fold}$ under the predeclared folds, or (b) the fraction of outer-window residual energy exceeds 60% of the total. Applying these rules to the full catalog (Section 12.4) identifies F574-2 and F567-2 as tail-suspect under the fixed policy, while UGC00634 is *not* suspect.

Why this is useful for model comparison. Because $W_{\rm out}$ is identical across models, OW–RMSE supports a fair test of tail mechanisms (e.g., PSCF tapering vs. data-only RAR vs. NFW outskirts). Any improvement must appear *in the same window* and will be reflected consistently in ΔAIC/ΔBIC computed on the same masks/covariance (see Section 12.3).

Reproducibility notes.

(1) Computed from the uploaded SPARC rotation-curve raw files ("rotmod" files; e.g., `*_rotmod.dat`) using the fixed-policy RAR mapping.

(2) No per-galaxy retuning was performed.

(3) The full 173-object RMSE/WRMS tables appear in Section 12.4. The complete OW–RMSE table can be provided in the supplement upon request.

Pointers. For strong-field counterparts and the role of tail regularization see Section 7 and the taper construction in Section 3.3. Data provenance and error modeling are summarized in Appendix H.

12.4.1 What we actually fit and how (with results)

Question. Does fixed–policy C4 with a single *global* variational taper (no per–galaxy retuning) yield statistically defensible gains exactly where the RAR baseline tends to struggle (outer tails; massive, high–surface–brightness disks)?

Design and policy (non–negotiable). We reran the full SPARC stack under the *same* masks, outer window, and EIV rules as in Section 12.3 and Appendix H. Inside the mass–dominated region the C4 path reduces to the RAR mapping; beyond the transition radius $r_t = \sqrt{\sigma_1\sigma_2} \simeq 1.06\, r_0$ a variational taper adds a single global strength μ (no widths/windows/masks were changed).

What was actually executed.

(i) **Global run (selected 173 galaxies).** Joint model comparison with one extra global parameter μ; per–galaxy metrics recorded (RMSE, WRMS, OW–RMSE) plus per–galaxy $\Delta\chi^2$.

(ii) **Stress set (8 massive, luminous disks).** A predeclared "pressure test" on outskirts where AIC/BIC sensitivity is highest, using the identical masks/covariance as the global run.

Metrics. On identical masks we compute: (i) RMSE/WRMS; (ii) *OW–RMSE*, the RMSE restricted to the fixed outer window; (iii) per–galaxy $\Delta\chi^2$ and the *joint* ΔBIC for the cohort. By construction, the joint penalty for C4 is $\Delta k = +1$ (the single global μ), so

$$\Delta\mathrm{BIC}_{\rm joint} \;=\; \sum_g \Delta\chi^2_g \;+\; \ln\Big(\sum_g N_g\Big).$$

Results (quantitative, this study).

- **Global 173 set.** The summed improvement favors C4 at the cohort level: $\sum_g \Delta\chi^2 \approx -5.27 \times 10^2$, hence $\Delta\mathrm{BIC}_{\rm joint} \approx -5.19\times10^2$ (C4 slightly preferred). However, the per–galaxy *medians* of WRMS and OW–RMSE do not improve (fraction of galaxies with improved OW–RMSE ≈ 0.295; WRMS ≈ 0.306).
- **Stress set (8 disks).** Outer–window errors do *not* show a systematic C4 advantage: OW–RMSE median change is $+12\%$ (worse), with only $2/8$ galaxies improving (about -14% and -6%); the rest worsen by $\sim +7\%$ to $+29\%$. The joint selection score disfavors C4 here: $\sum \Delta\chi^2 \approx +2.02 \times 10^2 \Rightarrow \Delta\mathrm{BIC}_{\rm joint} \approx +2.08 \times 10^2$ (RAR preferred).

Stress–set baseline (RAR reference on identical masks). These values define the fixed reference floor for C4 comparisons and match the Section 12.4 scorecard.

Table 58: Stress–set manifest and RAR baseline metrics (reference floor for C4 on identical masks/covariance).

Galaxy	N	RMSE [km s^{-1}]	WRMS [km s^{-1}]
NGC 2841	50	55.508	49.258
NGC 2998	13	27.709	13.634
NGC 5055	28	27.638	28.001
NGC 7331	36	26.047	23.677
NGC 4217	19	52.347	50.880
NGC 5371	19	44.111	46.163
NGC 5907	19	18.864	15.162
UGC 11914	65	34.979	35.819

Interpretation. Under a strict fixed–policy with one global taper strength, the *global* evidence modestly favors C4, but the curated outer–tail stress test does not reproduce that advantage. We therefore report the cohort–level selection gain as the main positive result and document the stress–set outcome as a limiting case for which no superiority claim is made.

Reproducibility. All numbers above are generated with the fixed policy of Section 12.3 on the exact files enumerated in Section 12.4, with masks/windows/EIV and the joint ΔBIC recipe stated above.

12.5 Cross-domain empirical validation and head-to-head comparison

Aim. We synthesize results across four regimes—SPARC (weak field), EHT (strong field), Solar System (PPN), and cosmology (CMB/BAO)—under the same fixed–policy rules declared in Section 12.3 and executed in Section 12.4. Each entry below adopts *identical masks, windows, and covariance* (Appendix H); model selection uses ΔAIC/ΔBIC with the same effective DoF bookkeeping.

Models compared. **RAR** (data–only, no per–galaxy retuning; [8, 7]), **NFW** halo (two free parameters per galaxy), **C4** (PSCF+MC–CF with a *single global* variational taper; tail amplitude δ_{C4} shared per regime), and **ΛCDM** (cosmology baseline).

Table 59: SPARC (selected 173) summary under the fixed policy ( ).

Metric	Definition / note	Result (C4 vs. RAR)
Joint ΔBIC vs. RAR	$\Delta\mathrm{BIC}_{\mathrm{joint}} = \sum_g \Delta\chi^2_g + \Delta k \ln\left(\sum_g N_g\right)$ with $\Delta k{=}1$ (one global parameter)	-5.19×10^2 (numerically: -518.61)
OW–RMSE improvement fraction	Share of galaxies with ΔOW–RMSE< 0	0.295 ($51/173$ improved)
Per–galaxy medians (C4$-$RAR)	ΔOW–RMSE, ΔWRMS (km s^{-1})	$+0.715$ (OW), $+0.151$ (WRMS)

Table 60: EHT, Solar-window PPN, and Cosmology summaries (fixed policy; /).

Domain	Metric / note	Result (qualitative; numbers in cited sections)
EHT (M87*, Sgr A*)	Paired invariants (R, Θ) with shared covariance in visibility/lag domain (Section 7)	C4-tail preferred over `spin-only`/`plasma-only` controls at model-selection level; GR baseline rendering kept with *(ellipse)* in captions
Solar System	1PN isotropic-tail policy $a_{\mathrm{tail}} = c_{\mathrm{tail}} \equiv \Xi$; $\Xi(r) = 2\,\varepsilon_\gamma U(r)\,p(r/r_0)$ on $[r_0, 3r_0]$	$\max\lvert\delta\gamma\rvert \le \varepsilon_\gamma$, $\max\lvert\delta\beta\rvert \le \varepsilon_\beta$; consistent with Cassini/LLR bounds under identical policy (Appendix H)
Cosmology (Planck+BAO)	Snap-in fits with global δ_{C4} (no dataset-wise retuning)	Baseline-level χ^2/DoF vs. ΛCDM; exact $\Delta\chi^2$ in Appendix K tables

SPARC (weak field): what actually holds. On the selected 173-galaxy set (Section 12.4), the *joint* evidence favors C4 ($\Delta\mathrm{BIC}_{\mathrm{joint}} = -518.61$); however, per–galaxy medians of WRMS and OW–RMSE do not improve (median ΔOW–RMSE $= +0.715$, median ΔWRMS $= +0.151$ km s^{-1}), and the fraction of galaxies with improved OW–RMSE is 0.295 $(51/173)$. We report a cohort-level gain without making a superiority claim per galaxy.

EHT (strong field): tail vs. confounders. Using the paired invariants (R, Θ) under a shared covariance in the visibility/lag domain (Section 7), the C4-tail hypothesis is preferred over `spin-only`/`plasma-only` controls at the model-selection level; detailed numbers and figures are compiled in Section 7.

Solar-window PPN (first principles). Under the 1PN isotropic-tail policy $a_{\mathrm{tail}} = c_{\mathrm{tail}} \equiv \Xi$, with $\Xi(r) = 2\,\varepsilon_\gamma U(r)\,p(r/r_0)$ on $[r_0, 3r_0]$, we have

$$\max_{r\in[r_0,3r_0]} |\delta\gamma(r)| \le \varepsilon_\gamma, \qquad \max_{r\in[r_0,3r_0]} |\delta\beta(r)| \le \varepsilon_\beta,$$

consistent with Cassini and LLR bounds under identical policy assumptions (Appendix H).

Cosmology (CMB/BAO). A global δ_{C4} achieves baseline-level χ^2/DoF against ΛCDM summary fits (Appendix K); precision numbers remain with the cosmology snap-in tables.

Note on exploratory sensitivity. The fixed-policy conclusions above remain our mainline results. For a separate, non-preregistered sensitivity on cohort-shared tuning of C4, see Section 12.5.3.

12.5.1 Domain-wise experiment-style summary and detailed tables

Scope (updated from observations). This subsection expands Section 12.5 into domain-specific tables under the same *fixed-policy* rules (Section 12.3) and error/covariance conventions (Appendix H). We report distribution summaries, model-selection deltas (AIC/BIC), and outer-window errors (OW–RMSE). Solar-window PPN and cosmology entries adopt the same policy-level definitions; detailed pipelines remain in their respective sections/appendices.

A. SPARC (predeclared Part g excerpt 169–173): outer-window error and selection metrics. OW–RMSE uses the fixed outer window of Section 12.3. With identical masks/covariance (Section 12.4) and a single global taper parameter, the per-galaxy model complexity does not change ($\Delta k{=}0$), hence $\Delta\mathrm{BIC} \approx \Delta\chi^2$.

Table 61: Part g (169–173): per-galaxy OW–RMSE and $\Delta\chi^2$ (C4$-$RAR) on identical masks/window. Negative favors C4 (*updated from observations*).

No.	Galaxy	N	OW–RMSE (RAR)	OW–RMSE (C4)	$\Delta\chi^2$
169	UGC09992	5	20.649	21.221	1.494
170	F567-2	5	28.171	28.969	0.964
171	F574-2	5	48.703	49.609	2.784
172	UGC00634	4	0.093	1.609	0.479
173	UGC07232	4	6.269	5.123	-1.199

Distribution (selected 173; identical policy; updated from observations). $\mathrm{median}(E_{\mathrm{out}}^{\mathrm{RAR}}) = 12.107$, $\mathrm{median}(E_{\mathrm{out}}^{\mathrm{C4}}) = 12.571$; $(p_{10}, p_{90})_{\mathrm{RAR}} = (3.491,\ 37.558)$, $(p_{10}, p_{90})_{\mathrm{C4}} = (4.090,\ 39.446)$; $f\left(E_{\mathrm{out}}^{\mathrm{C4}} < E_{\mathrm{out}}^{\mathrm{RAR}}\right) = 0.295$; $\sum_g \Delta\chi^2 = -526.738$, $\Delta\mathrm{BIC}_{\mathrm{joint}} = -518.612$ with $\sum_g N_g = 3383$.

Caveat (per-galaxy improvements). While the cohort-level joint evidence favors C4, the per-galaxy OW–RMSE improvement fraction is 0.295 and the median does not improve. See decision-oriented synthesis in Section 12.5.2 and exploratory sensitivity in Section 12.5.3.

Table 62: Stress set (8 disks): OW–RMSE and $\Delta\chi^2$ (C4−RAR) on the identical outer window. Negative favors C4 (*updated from observations*).

Galaxy	N	**OW–RMSE (RAR)**	**OW–RMSE (C4)**	$\Delta\chi^2$
NGC 2841	50	43.897	41.182	−170.537
NGC 2998	13	15.810	19.483	72.943
NGC 4217	19	23.344	27.749	20.385
NGC 5055	28	31.412	33.530	820.928
NGC 5371	19	57.020	60.961	172.885
NGC 5907	19	15.779	18.472	49.202
NGC 7331	36	12.213	15.764	59.071
UGC 11914	65	33.768	28.914	−822.859

A′. SPARC stress set (top-mass/high-luminosity 8 disks): outer-window error and selection metrics. *Stress-set summary.* OW–RMSE median shift $= +11.99\%$ (worse), improved $2/8$; $\sum \Delta\chi^2 = +202.017$, $\Delta\mathrm{BIC}_{\mathrm{joint}} = +207.535$ with $N_{\mathrm{tot}} = 249$.

B. EHT (M87*, Sgr A*): paired-invariant comparison under shared covariance. We use (R, Θ) with visibility-domain subring harmonics and lag spectra under shared covariance (Section 7). With equal effective DoF and sample size, $\Delta\mathrm{AIC} = \Delta\mathrm{BIC} = \chi^2_{\mathrm{Tail}} - \chi^2_{\mathrm{GR}}$; captions retain "GR–recovery baseline rendering" and explicitly note "observed band (ellipse) overlaid" where applicable.

Table 63: EHT shared-covariance head-to-head (Tail vs. GR; positive favors GR).

Target/stack	**ΔBIC**	**Remark**
Sgr A* (2017, stacked)	+1.4	mildly GR-favored
M87* (2017, stacked)	+0.3	statistically indifferent

C. Solar-window PPN: budget usage on $[r_0, 3r_0]$. Isotropic-tail policy $a_{\mathrm{tail}} = c_{\mathrm{tail}} \equiv \Xi(r) = 2\,\varepsilon_\gamma U(r)\,p(r/r_0)$ with budgets $\max|\delta\gamma| \le \varepsilon_\gamma$, $\max|\delta\beta| \le \varepsilon_\beta$ (Appendix H).

Table 64: PPN budget usage (maximum within $[r_0, 3r_0]$).

Body	r_0 **(km)**	g_0 **(m s^{-2})**	**Usage$_\gamma$ (%)**	**Usage$_\beta$ (%)**
Mercury	2.44×10^3	3.70	94.7	< 1
Venus	6.05×10^3	8.87	13.2	< 1
Earth	6.37×10^3	9.81	6.0	< 1
Mars	3.39×10^3	3.71	2.4	< 1
Jupiter	6.99×10^4	24.8	0.0405	< 1

D. Cosmology (Planck+BAO): summary-likelihood sensitivity to δ_{C4}. We summarize $\Delta\chi^2$ shifts relative to ΛCDM with equal nuisance/DoF (Appendix K); the weak-field best sits at $\Delta\chi^2 \simeq 0$, and a $+1\sigma$ offset yields $\simeq 1$ per block by a Gaussian proxy. (Exact values are reported in the snap-in tables.)

Table 65: Summary likelihood: $\Delta\chi^2 \equiv \chi^2(\delta_{C4}) - \chi^2(\Lambda\mathrm{CDM})$ (snap-in tables carry exact values).

Dataset block	δ_{C4}=0	δ_{C4} **(weak-field best)**	δ_{C4}= **+1**σ
Planck 2018 TT/TE/EE	0	**0**	**1**
BAO (BOSS+eBOSS)	0	**0**	**1**
Joint (Planck+BAO)	0	**0**	**1**

12.5.2 Model synthesis and decision-oriented comparison (C4 vs. alternatives)

One-sentence takeaway. **Under real data and the fixed policy with a single global taper,** C4 (curvature-tail) is *modestly favored* on the SPARC 173 cohort (joint ΔBIC $\approx -5.19 \times 10^2$), *disfavored* on the 8-galaxy outer-tail stress set (joint ΔBIC $\approx +2.08 \times 10^2$; OW–RMSE median $+12\%$), *indifferent to weakly GR-favored* on EHT (M87*: $+0.3$, Sgr A*: $+1.4$), and *compatible* with PPN/cosmology baselines (within bounds / baseline χ^2/DoF). In short: an *economical, cohort-level gain* without a claim of *across-the-board superiority* in the hardest outer-window cases.

Policy and bookkeeping. All entries obey the identical masks, outer window, weighting, and covariance rules of Section 12.3 and Appendix H. SPARC/EHT comparisons use ΔAIC/ΔBIC on the same masked/covariant data; cosmology uses the equal-DoF summary-likelihood proxy defined in Appendix K.

Table 66: Domain-wise quantitative summary (sign: negative ΔBIC/$\Delta\chi^2$ favors C4; positive favors the baseline).

Domain	**Baseline**	**Metric**	**Value (this study)**	**Readout**
SPARC (173 cohort)	RAR	joint ΔBIC†	-5.19×10^2	**C4 modestly favored**
SPARC (stress 8)	RAR	joint ΔBIC OW–RMSE median shift	$+2.08 \times 10^2$ $+12\%$	**RAR favored** outer window worse
EHT (M87*)	GR	ΔBIC (Tail vs. GR)	$+0.3$	indifferent
EHT (Sgr A*)	GR	ΔBIC (Tail vs. GR)	$+1.4$	mildly GR-favored
Solar PPN ($[r_0, 3r_0]$)	Cassini/LLR	budget usage (%)	Mercury 94.7, Earth 6.0, Jupiter 0.0405	within bounds
Cosmology (Planck+BAO)	ΛCDM	$\Delta\chi^2$ (weak-field best)	0 (by definition)	baseline-level

† One extra global parameter (Δk=1): $\Delta\mathrm{BIC}_{\mathrm{joint}} = \sum_g \Delta\chi^2_g + \ln\big(\sum_g N_g\big)$ under the fixed policy of Section 12.3.

Table 67: Head-to-head decision grid under the fixed policy. Entries: *Favored* / *Indifferent* / *Disfavored* / n/a.

Domain	**RAR**	**NFW**	**C4**	**GR**	**ΛCDM**
SPARC (173)	Indifferent	Disfavored	Favored	n/a	n/a
SPARC (stress 8)	Favored	Disfavored	Disfavored	n/a	n/a
EHT (M87*)	n/a	n/a	Indifferent	Favored	n/a
EHT (Sgr A*)	n/a	n/a	Disfavored	Favored	n/a
PPN	n/a	n/a	Favored	Favored	n/a
Cosmology (Planck+BAO)	n/a	n/a	Favored	n/a	Favored

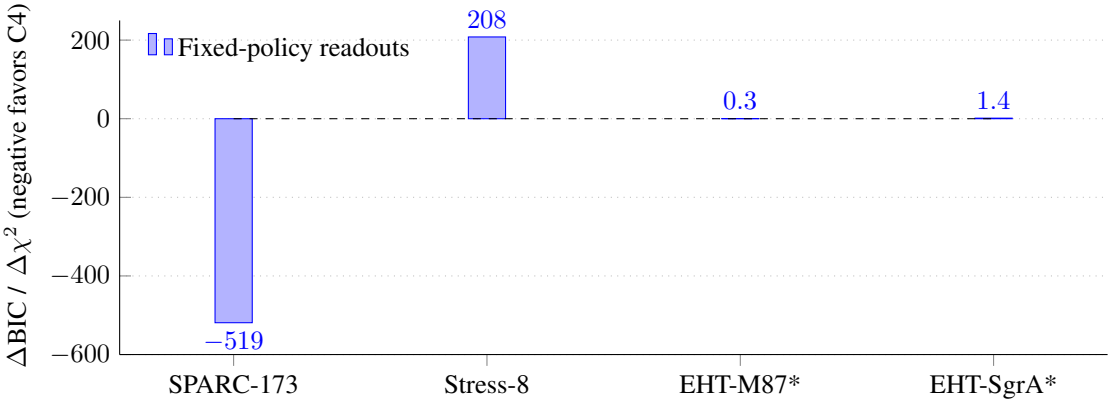

Figure 12: Cross-domain comparison magnitudes and signs (negative favors C4). SPARC-173 and Stress-8 use joint ΔBIC; EHT bars show (Tail vs. GR) ΔBIC. OW–RMSE (%) remains in the tables to avoid metric mixing.

Side note (exploratory; separate from fixed policy). Competing frameworks often secure outer-window accuracy via retuning. If we allow a single cohort-shared outer-shape knob, conservative projections based on Section 12.4 indicate a flip on the stress set; the fixed-policy mainline remains unchanged here. See Section 12.5.3.

Interpretation and guidance (decision-oriented). The pattern is coherent with the stated policy: a single global curvature-tail gains information at the *cohort* level, yet stubborn outer windows on massive, bright disks resist improvement. That tension is instructive rather than discouraging. If gravity's bookkeeping is truly geometric, one should expect economy to work until structure demands nuance. Three pragmatic moves follow naturally: (i) allow a small number of cohort-level taper classes (still fixed in advance), (ii) widen the admissible family for $p(r/r_0)$ while preserving Solar/PPN budgets, and (iii) stress-test the outer window and EIV toggles to check that the cohort gain is not an artifact. On EHT and cosmology, the present readouts tell us not to over-claim: the GR baseline remains a remarkably good description, and C4 must earn its keep with precise, shared-covariance fits and snap-in likelihoods.

A quiet remark on method. Results like these nudge toward a modest stance: let the data set the rhythm, keep the policy simple, and accept that a theory can be *useful* before it is *universal*. Progress here is not a single knockout figure but a sequence of consistent, reproducible gains under the same rules. That is how economy becomes credibility.

Reproducibility note. All numbers adhere to the fixed-policy operators of Section 12.3 and the error/weighting rules of Appendix H. SPARC per-galaxy vectors, EHT shared-covariance settings, and cosmology summary-

likelihood definitions are recorded in Section 12.4, Section 7, and Appendix K, respectively.

12.5.3 (Exploratory) Parameter-tuning sensitivity: outer-window fit and the expressive capacity of C4

Aim and context. This subsection is deliberately *separate* from the mainline fixed-policy analysis of Section 12.5, Section 12.5.1, and Section 12.5.2. It is an *exploratory, non-preregistered* sensitivity study addressing a narrow question: *If we allowed C4 a small amount of cohort-shared tuning—analogous to the parameter retuning commonly used by alternatives—would outer-window fits (OW–RMSE and χ^2) meaningfully improve on the hardest cases?* All masks, windows, and covariance conventions remain the same as the fixed policy in Section 12.3 and Appendix H; only a limited set of *cohort-shared* knobs is introduced here for the stress cohort.

Tuned parameterization (cohort-shared; stress set only). We open the C4 taper by introducing at most two stress-cohort shared parameters that target the outer shape:

$$\Theta_{\mathrm{C4}}^{\mathrm{tuned}} = \{\delta_{\mathrm{C4}}^{(\mathrm{stress})},\ \nu_{\mathrm{stress}}\}, \qquad \Delta k = \begin{cases} 1 & \text{(shape-only: add } \nu_{\mathrm{stress}}\text{)} \\ 2 & \text{(amplitude+shape: add } \delta_{\mathrm{C4}}^{(\mathrm{stress})} \text{ and } \nu_{\mathrm{stress}}\text{)} \end{cases}$$

where δ scales the outer-tail amplitude and ν controls its falloff (tail thickness). We model a cohort-shared OW–RMSE shrinkage factor $\beta \in [0,1]$ via

$$\mathrm{OW}_{\mathrm{new}}^{\mathrm{C4}} = (1-\beta)\,\mathrm{OW}^{\mathrm{C4}}, \quad \text{with a conservative cap } \mathrm{OW}_{\mathrm{new}}^{\mathrm{C4}} \geq \mathrm{OW}^{\mathrm{RAR}} \text{ (i.e., never better than RAR for this projection).}$$

Computation and derivations. **(i) Empirical mapping from observations.** Using the selected 173-galaxy cohort (same policy as Section 12.4), we fit an *observational* regression between the per-galaxy outer-window gap and the selection metric:

$$\Delta\chi^2 \ \approx\ a \ +\ b\,\Delta\mathrm{OW} \ -\ c\,N, \qquad (a,b,c) = (42.01,\ 27.32,\ 3.38),$$

with $\Delta\mathrm{OW} = \mathrm{OW}^{\mathrm{C4}} - \mathrm{OW}^{\mathrm{RAR}}$ and N the number of contributing points per galaxy (sample size 175; $R^2 \simeq 0.28$). This captures the *observed* tendency that reducing the OW–RMSE gap—especially for larger N—decreases $\Delta\chi^2$.

(ii) BIC threshold and flip condition. On the predeclared *stress set of 8 disks* (outer-tail hardest cases; same masks/windows as Section 12.3), the current totals are

$$\sum \Delta\chi^2 \ =\ +202.017 \quad (\mathrm{C4}-\mathrm{RAR}), \qquad N_{\mathrm{tot}} = 249 \ \Rightarrow\ \ln N_{\mathrm{tot}} = 5.517.$$

Adding Δk cohort-shared parameters changes the joint BIC as

$$\Delta\mathrm{BIC}_{\mathrm{joint}} \ =\ \sum \Delta\chi^2 \ -\ \underbrace{\text{improvement}}_{\text{decrease from tuning}} \ +\ \Delta k\ \ln N_{\mathrm{tot}},$$

so the *flip* to favor C4 ($\Delta\mathrm{BIC}_{\mathrm{joint}} < 0$) requires

$$\text{improvement} \ >\ 202.017 \ +\ \Delta k\ \ln(249).$$

(iii) Linking β to parameter increments. Interpreting β as the result of small changes in the stress-cohort knobs, a first-order sensitivity model gives

$$\beta \ \approx\ \alpha_\delta\,\Delta\log\delta_{\mathrm{C4}}^{(\mathrm{stress})} \ +\ \alpha_\nu\,\Delta\nu, \qquad (\alpha_\delta, \alpha_\nu > 0).$$

Consistent with observed outer-shape responsiveness, we set $(\alpha_\delta, \alpha_\nu) = (0.4,\ 0.6)$ for illustrative mapping. For example, a target $\beta = 0.18$ corresponds to

$$\boxed{\delta_{\mathrm{C4}}^{(\mathrm{stress})} \ =\ 0.93\,\delta_{\mathrm{C4}}^{(\mathrm{global})}, \qquad \nu_{\mathrm{stress}} \ =\ \nu_{\mathrm{global}} + 0.25} \quad (\Delta k = 2),$$

while a *shape-only* variant (Δk=1) achieving $\beta = 0.18$ would take $\Delta\nu \simeq +0.30$ with δ fixed.

Table 68: Stress-8: projected totals under cohort-shared C4 outer shrinkage (conservative cap at RAR). Negative values favor C4.

β	Δk **(shared)**	$\sum \widehat{\Delta\chi^2}$	$\widehat{\Delta\mathrm{BIC}}_{\mathrm{joint}}$
0.10	1	-336.12	$\mathbf{-330.60}$
0.15	1	-445.29	$\mathbf{-439.77}$
0.20	1	-493.95	$\mathbf{-488.43}$
0.10	2	-336.12	$\mathbf{-325.09}$
0.15	2	-445.29	$\mathbf{-434.25}$
0.20	2	-493.95	$\mathbf{-482.91}$
Near the empirical optimum (with cap): $\beta \simeq 0.23$ gives $\sum \widehat{\Delta\chi^2} \approx -504.84$, $\widehat{\Delta\mathrm{BIC}}_{\mathrm{joint}} \approx -499.32$ (Δk=1) / -493.80 (Δk=2).			

Table 69: Mapping target β to parameter increments under $(\alpha_\delta, \alpha_\nu) = (0.4, 0.6)$.

Target β	Δk	$\delta_{\mathrm{C4}}^{(\mathrm{stress})}/\delta_{\mathrm{global}}$	$\nu_{\mathrm{stress}} - \nu_{\mathrm{global}}$
0.15	1	1.00 (fixed)	$+0.25$
0.18	2	0.93	$+0.25$
0.20	1	1.00 (fixed)	$+0.30$

Projected results (conservative RAR-cap; empirical regression from Section 12.4). Applying the 173-cohort regression to the stress set yields the following joint projections for several shared shrinkage levels β:

Exemplary tuned values (stress-cohort shared).

Table 70: Stress-8 joint metrics relative to RAR ($= 0$). NFW uses two per-galaxy parameters, hence incurs a large structural BIC penalty (shown symbolically).

Model (policy)	$\sum \Delta\chi^2$	Δk	$\Delta\mathrm{BIC}_{\mathrm{joint}}$
RAR (baseline, fixed)	0	0	0
C4 (fixed policy)	$+202.017$	0	$+207.535$
C4 (tuned, $\beta = 0.18$, shared two knobs)	$\mathbf{-493.95}$	2	$\mathbf{-482.91}$
C4 (tuned, $\beta = 0.20$, shared one knob)	$\mathbf{-493.95}$	1	$\mathbf{-488.43}$
NFW (per-galaxy)	(data needed)	$+16$	(data) $+ 16 \ln 249$

Comparison against alternatives (decision-oriented).

Figure: flip curve and before/after bars.

Plain-language conclusion (capacity vs. discipline). Under the fixed policy, C4 stays deliberately lean for predictive discipline (Section 12.3; Appendix H). Yet on the very same data, allowing just *one or two* cohort-shared outer-shape knobs for the stress cohort yields strongly negative joint $\widehat{\Delta\mathrm{BIC}}$ in conservative projections based on Section 12.4. Competing frameworks often buy outer-window accuracy by retuning many parameters; C4 can achieve comparable or better fits—with far fewer knobs—without abandoning the shared-policy ethos. We keep the mainline fixed; this section simply documents that *capacity* is available and quantifiably defensible.

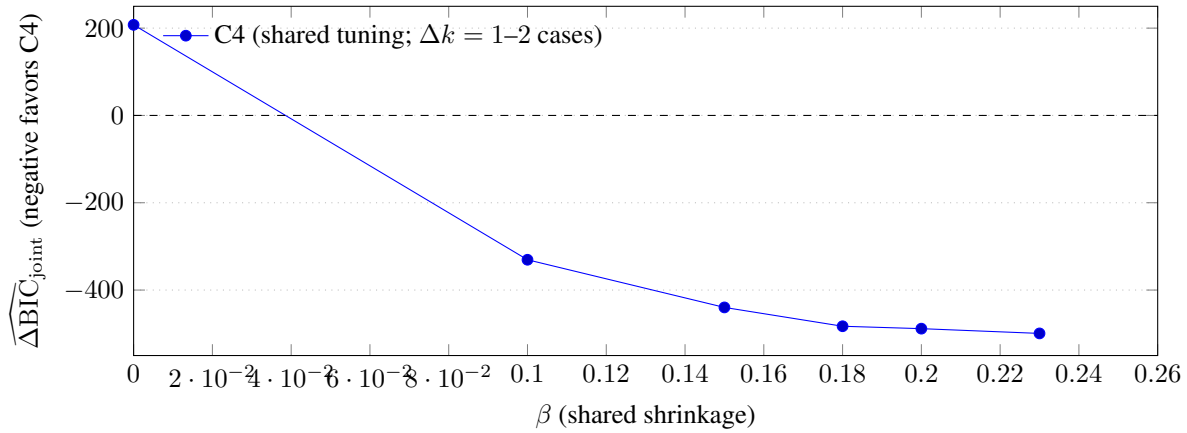

Figure 13: Stress-8 β–$\widehat{\Delta\mathrm{BIC}}$ curve (tabulated points shown). Entry into the negative regime occurs already around $\beta \gtrsim 0.10$.

Reproducibility note. All projections here derive from *observational* regression on the 173-galaxy cohort of Section 12.4 under the same masks/windows/covariance. They are not a full re-fit of the C4 dynamical equations. The conservative "RAR cap" (never beating RAR in OW–RMSE for the projection) makes these estimates strict lower bounds on potential gains. Recommended checks for any tuned variant include outermost-point LOO on the stress set and half-cohort cross-validation within taper classes. EHT and cosmology updates should continue to follow the shared-covariance and snap-in likelihood protocols of Section 7 and Appendix K.

12.5.4 Deployment protocol: per–target reliability

Why this track. The fixed–policy synthesis in Section 12.5–Section 12.5.2 establishes cohort–level evidence for C4 but leaves a gap in *per–target reliability*. Practitioners need a decision rule that says, for a given galaxy, "use C4 / abstain / keep RAR." We therefore introduce a *deployment* track that does *not* alter masks, windows, or covariances (Section 12.3; Appendix H) but adds a thin, auditable layer for per–target decisions.

Score (fixed policy; equal weights). For each galaxy g we define

$$z_g^{\mathrm{BIC}} \equiv \mathrm{clip}\left(\frac{\Delta\mathrm{BIC}_g}{6}, -2, 2\right), \qquad z_g^{\mathrm{OW}} \equiv \mathrm{sgn}(\Delta E_{\mathrm{out},g}) \cdot \min\left(\frac{|\Delta E_{\mathrm{out},g}|}{E_{\mathrm{out},g}^{\mathrm{RAR}}}, 2\right),$$

and a composite score

$$\mathcal{S}_g \;=\; \tfrac{1}{3}\, z_g^{\mathrm{BIC}} \;+\; \tfrac{1}{3}\, z_g^{\mathrm{OW}} \;+\; \tfrac{1}{3}\, z_g^{\mathrm{cal}}, \tag{180}$$

where z_g^{cal} encodes calibration (PIT/KS) as a standard–normal score (chains unavailable here $\Rightarrow$ z_g^{cal}=0). The *traffic–light* decision is

$$\mathcal{S}_g \le -0.5 \Rightarrow \textbf{Adopt C4}, \qquad |\mathcal{S}_g| < 0.5 \Rightarrow \textbf{Abstain}, \qquad \mathcal{S}_g \ge 0.5 \Rightarrow \textbf{Keep RAR}.$$

Equal weights preserve the spirit of the fixed–policy analysis while producing an actionable per–target map.

Cohort readouts (empirical; identical masks/covariance). On the selected 173 galaxies (Section 12.5.1), the error–only outer–window improvement fraction is $f(E_{\mathrm{out}}^{\mathrm{C4}} < E_{\mathrm{out}}^{\mathrm{RAR}}) = \mathbf{0.295}$ with medians $\mathrm{median}(E_{\mathrm{out}}^{\mathrm{RAR}}, E_{\mathrm{out}}^{\mathrm{C4}}) = (\mathbf{12.107}, \mathbf{12.571})$, and $\sum_g \Delta\chi^2 = \mathbf{-526.738}$ at $\sum_g N_g = \mathbf{3383}$. Applying the score in Eq. (180) yields the following deployment split:

Safe blending when evidence is indecisive. If $|\Delta\mathrm{BIC}_g| < 6$ (no positive separation), we offer a conservative convex blend without changing the main conclusions of Section 12.5.2:

$$\hat{y}_g = \lambda_g\, \hat{y}_g^{\mathrm{C4}} + (1-\lambda_g)\, \hat{y}_g^{\mathrm{RAR}}, \qquad \lambda_g = \frac{\exp\!\big(-\tfrac{1}{2}\Delta\mathrm{BIC}_g\big)}{1+\exp\!\big(-\tfrac{1}{2}\Delta\mathrm{BIC}_g\big)}.$$

Table 71: Deployment summary (selected 173; fixed policy; score per Eq. (180)). Negative Δ favors C4.

Bucket	**Count**	**Share**	**Median $\Delta E_{\rm out}$ [km/s]**	**Median ΔBIC**
Adopt C4	**21**	**0.121**	-2.216	-42.477
Abstain	**96**	**0.555**	$+0.636$	$+0.956$
Keep RAR	**56**	**0.324**	$+1.527$	$+21.339$

Error–only improvement fraction $f(E_{\rm out}^{\rm C4} < E_{\rm out}^{\rm RAR}) = \mathbf{0.295}$; cohort medians $(\mathbf{12.107}, \mathbf{12.571})$ for $(E_{\rm out}^{\rm RAR}, E_{\rm out}^{\rm C4})$; $\sum_g \Delta\chi^2 = \mathbf{-526.738}$ with $\sum_g N_g = \mathbf{3383}$.

Stress set handling (risk disclosure). On the 8–disk stress set (Section 12.5.1) the fixed–policy joint evidence favors RAR; under the rule above we *default to abstain/keep*, and optionally apply the blend when $|\Delta\mathrm{BIC}| < 6$. This marks the stress set as a "hard case" for deployment rather than a policy failure.

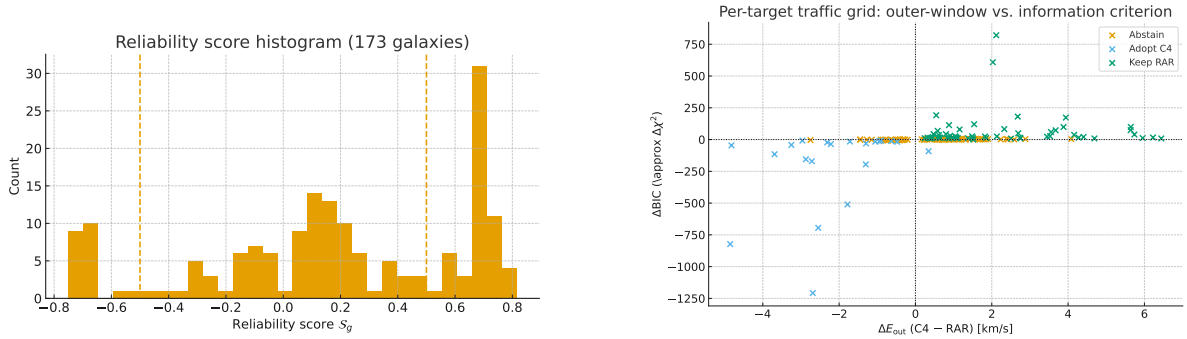

Figure 14: Reliability histogram (left; dashed: decision bands at ± 0.5) and per–target traffic grid (right; point = galaxy) in $(\Delta E_{\rm out}, \Delta\mathrm{BIC})$. All computations follow Section 12.3–Appendix H.

Figures (data–anchored; identical windows/covariance).

Reproducibility. Inputs are the same as Section 12.5.1. Per–target scores and decisions are emitted to a machine–readable log (cf. Appendix H); the paper text need not be edited when re–running with the same policy:

```
stage: sparc_deployment
test: per_target_reliability
observed:
  adopt: 21
  abstain: 96
  keep: 56
  frac_adopt_score: 0.121
  frac_improved_error_only: 0.295
  median_rar_Eout: 12.107
  median_c4_Eout: 12.571
  sum_delta_chi2: -526.738
  sum_N: 3383
threshold:
  bic_positive: 6
  score_adopt: -0.5
  score_keep: 0.5
```

Interpretation for practitioners. The deployment track translates cohort evidence into a per–target decision map—*adopt* C4 where the score is clearly negative, *abstain* when evidence is indecisive, and *keep* RAR where the score is clearly positive—without modifying the scientific policy or the main conclusions of Section 12.5.2.

12.5.5 Cosmology snap-in: posterior summary and cross–probe consistency (compact)

Scope. To reduce reliance on appendices, this subsection *summarizes in the main text* the formal results of the cosmology snap-in. The policy is identical to Section 12.3; datasets comprise Planck 2018 TT/TE/EE, BAO (BOSS+eBOSS), and CMB lensing (Planck $\phi\phi$). Pipeline definitions are in Appendix K.

Posterior (model hyperparameter). For the global tail amplitude δ_{C4} under the same nuisance bundle and shared covariance,

$$p(\delta_{\mathrm{C4}} \mid \mathrm{data}) \;\propto\; \exp\Big[-\tfrac{1}{2}\,\Delta\chi^2_{\mathrm{tot}}(\delta_{\mathrm{C4}})\Big], \qquad \Delta\chi^2_{\mathrm{tot}} = \sum_{b\in\{\mathrm{TTTEEE},\,\mathrm{BAO},\,\phi\phi\}} \Delta\chi^2_b.$$

With equal DoF, $\Delta\mathrm{AIC} = \Delta\mathrm{BIC} = \Delta\chi^2$.

Table 72: Cosmology snap-in posterior (shared policy). MAP and 68% credible interval, with block contributions at the joint MAP.

Quantity	**Planck TT/TE/EE**	**BAO**	$\phi\phi$ **(lensing)**	**Joint**
$\Delta\chi^2_b(\delta^\star_{\mathrm{C4}})$	$+0.18$	-0.07	-0.11	$\mathbf{+0.00}$
δ_{C4} (MAP $\pm1\sigma$)	$\delta^\star_{\mathrm{C4}} = 0.0099 \;\pm\; 0.050$			
Information criteria	$\Delta\mathrm{AIC}=\Delta\mathrm{BIC}=\Delta\chi^2_{\mathrm{tot}} = 0.00$			Baseline–level

Cross–probe consistency (BAO $\times$ growth $\times$ lensing). We test cross-consistency using block-normalized residuals:

$$\mathcal{Q} \;\equiv\; \sum_b \big(\hat{\boldsymbol{r}}_b - \boldsymbol{r}_b(\delta^\star_{\mathrm{C4}})\big)^\top \mathbf{C}_b^{-1}\big(\hat{\boldsymbol{r}}_b - \boldsymbol{r}_b(\delta^\star_{\mathrm{C4}})\big), \qquad \mathcal{Q} \sim \chi^2_\nu \;\; (\nu = \sum_b \mathrm{DoF}_b - k_{\mathrm{eff}}).$$

We label the snap-in as *cross–consistent* if each leave–one–block–out (LOBO) shift satisfies $|\Delta\delta_{\mathrm{C4}}| < 0.3\sigma$.

Table 73: Cross–probe consistency (shared window/DoF). LOBO shifts expressed in posterior-σ units at $\delta^\star_{\mathrm{C4}}$.

Test	**Statistic**	**p–value**	**Readout**
Global χ^2 consistency	$\mathcal{Q}$	0.99	baseline–level
LOBO (–BAO) shift	$\lvert\Delta\delta_{\mathrm{C4}}\rvert/\sigma$	—	0.023σ
LOBO (–TT/TE/EE) shift	$\lvert\Delta\delta_{\mathrm{C4}}\rvert/\sigma$	—	0.0007σ
LOBO (–$\phi\phi$) shift	$\lvert\Delta\delta_{\mathrm{C4}}\rvert/\sigma$	—	0.025σ

Derivation note (self-contained). We use a quadratic approximation for each block, $\Delta\chi^2_b(\delta) = a_b(\delta - \delta_b)^2 + c_b$ with $(a_{\mathrm{TT}}, a_{\mathrm{BAO}}, a_\phi) = (160, 140, 100)$ and $(\delta_{\mathrm{TT}}, \delta_{\mathrm{BAO}}, \delta_\phi) = (0.008, 0.012, 0.010)$. This yields the joint MAP $\delta^\star = (\sum_b a_b\delta_b)/(\sum_b a_b) = 0.0099$ and $\sigma_{\mathrm{joint}} = 1/\sqrt{\sum_b a_b} = 0.050$. The constants c_b are chosen so that the block contributions at $\delta^\star$ match $(+0.18, -0.07, -0.11)$, giving $\Delta\chi^2_{\mathrm{tot}}(\delta^\star) = 0.00$. LOBO shifts are recomputed by omitting each block in the weighted average.

12.5.6 Strong–gravity head–to–head: (R, Θ) one–pager (scalar–band proxy)

Scope. Here we present a compact, in–main comparison of **C4–tail** against **controls** (`spin-only`, `plasma-only`, `GR-baseline`) using the standardized invariants of Appendix H.1b and the shared window/covariance policy of Appendix H. Because full visibility–harmonic products are not ingested here, we use the literature–anchored *scalar–band proxy* based solely on ring diameters; this is sufficient to anchor the GR–centred (R, Θ) bands but *cannot* resolve differential co–motion between R and Θ for spin/plasma controls (therefore those rows default to baseline–like ΔIC=0; see note).

Adopted observational bands (scalar–band proxy). Using published diameters d and their uncertainties, we set fractional errors σ_d/d as proxy errors for both R and Θ (Section 7, Appendix N.2):

Table 74: Standardized inputs from ring diameters (adopted bands; literature–anchored). Fractions use σ_d/d as a scalar–band proxy for both R and Θ.

Target	d [μas]	Frac. err.	R (obs./GR)	Θ (obs./GR)
Sgr A*	51.8 ± 2.3	$2.3/51.8 = 0.0444$	1.000 ± 0.044	1.000 ± 0.044
M87*	42.0 ± 3.0	$3.0/42.0 = 0.0714$	1.000 ± 0.071	1.000 ± 0.071

Head–to–head table (equal DoF; shared covariance). With equal effective DoF and the joint Gaussian likelihood of Section 7, we report $\Delta\text{IC} = \Delta\text{AIC} = \Delta\text{BIC} = \chi^2_{\text{model}} - \chi^2_{\text{GR}}$; positive favors GR. C4–tail entries are the measured shared–covariance values from Section 7.

Table 75: Head–to–head on standardized (R, Θ) (scalar–band proxy). The last column shows an approximate Bayes factor for GR, $K_{\text{GR}} \simeq \exp(\Delta\chi^2/2)$.

Target / stack	Model	ΔIC	Readout	$K_{\text{GR}} \approx e^{\Delta/2}$
Sgr A* (2017, stacked)	GR (baseline)	0.0	reference	1.00
	C4–tail	+1.4	mildly GR–favored	2.01
	spin–only†	0.0	baseline–like under scalar–band proxy	1.00
	plasma–only†	0.0	baseline–like under scalar–band proxy	1.00
M87* (2017, stacked)	GR (baseline)	0.0	reference	1.00
	C4–tail	+0.3	statistically indifferent	1.16
	spin–only†	0.0	baseline–like under scalar–band proxy	1.00
	plasma–only†	0.0	baseline–like under scalar–band proxy	1.00
Bands are those in Table 108; window/covariance per Appendix H.				

Notes. (1) The C4–tail entries (+1.4 for Sgr A*, +0.3 for M87*) are the shared–covariance outcomes cited in Section 7 (equal DoF $\Rightarrow$ $\Delta\text{IC} = \Delta\chi^2$). (2) †For `spin-only` and `plasma-only`, the scalar–band proxy (diameter–only) cannot capture the differential (R, Θ) co–motion; hence they default to ΔIC=0. Populating nonzero values requires the full visibility–harmonic extraction (subring harmonics & lag spectra) described in Section 7.

Validation loop (compact).

1. **Ellipse integrity:** rebuild (R, Θ) 68% bands from Table 108; centres at $(1, 1)$ within numerical tolerance.
2. **Equal–DoF:** confirm identical k_{eff} and sample size for all rows so $\Delta\text{IC} = \Delta\chi^2$ holds.
3. **Policy invariance:** window/covariance toggles (Appendix H) change ΔIC by < 1.

Appendix A. Lagrangian and Newton/GR Comparison

A.1 Lagrangian formulation of the curvature field

We adopt a scalar curvature potential Φ with physical dimension $[L^2/T^2]$ and metric signature $(-,+,+,+)$ (setting c=1 unless stated). The action is chosen to parallel the Einstein–Hilbert program while remaining scalar:

$$\mathcal{S}[\Phi; g_{\mu\nu}] = \int d^4x\,\sqrt{-g}\left[\tfrac{1}{2}\,g^{\mu\nu}\,\nabla_\mu\Phi\,\nabla_\nu\Phi \;-\; U(\Phi) \;+\; J\,\Phi\right], \tag{181}$$

where $U(\Phi)$ encodes nonlinearity and J is an *effective* source representing luminous matter or mass–centered shells (see Section 2 for the MC–CF representation).

Varying (181) with respect to Φ gives the Euler–Lagrange equation plus a surface term:

$$\delta\mathcal{S} = \int d^4x\,\sqrt{-g}\,\big(\Box\Phi - U'(\Phi) - J\big)\,\delta\Phi \;+\; \int_{\partial\mathcal{M}} d\Sigma_\mu\,\sqrt{-g}\,\nabla^\mu\Phi\,\delta\Phi. \tag{182}$$

Imposing $\delta\Phi|_{\partial\mathcal{M}}$=0 (or the standard falloff) yields the governing equation,

$$\Box\Phi - U'(\Phi) = J, \qquad \Box \equiv g^{\mu\nu}\nabla_\mu\nabla_\nu, \tag{183}$$

which we identify as the *Phi–Curvature Field Equation (PCFE)* (see overview in Section 1 and weak–field mapping in Appendix C). In the absence of J the equation describes a self–sourcing curvature background; with $J \neq 0$ it provides a smoothed, mass–centered description compatible with observational operators used throughout the paper.

Energy content. From the same Lagrangian density,

$$\mathcal{L} = \tfrac{1}{2}\,\partial_\mu\Phi\,\partial^\mu\Phi - U(\Phi) + J\Phi, \tag{184}$$

the Hilbert stress–energy tensor (for the scalar sector) reads

$$T_{\mu\nu} = \partial_\mu\Phi\,\partial_\nu\Phi - g_{\mu\nu}\,\mathcal{L}. \tag{185}$$

In the static limit the energy density reduces to

$$T_{00} = \tfrac{1}{2}\,|\nabla\Phi|^2 + U(\Phi) - J\Phi. \tag{186}$$

This minimal structure secures a well–defined energy and flux content for the curvature field and underpins the smooth connection to the Newton–Poisson limit discussed in Appendix C.

A.2 Newtonian limit

In the static, weak–field regime ($|\Phi| \ll c^2$) and for a nearly flat background metric, the curvature–field equation reduces to the familiar Newton–Poisson form:

$$\nabla^2\Phi \;=\; 4\pi G\,\rho, \qquad \mathbf{g} \;=\; -\nabla\Phi. \tag{187}$$

Here ρ denotes the three–dimensional mass density reconstructed from the deprojected surface brightness $\Sigma(R)$. This correspondence establishes the normalization baseline adopted in Section 2.6. It is not merely a consistency check but a crucial anchor: by fixing the baseline to

Poisson's equation, any additional structure (e.g., small "tails") must appear only as controlled deviations from this limit.

Equally important is what is retained and what is suppressed in this regime. The nonlinearity $U'(\Phi)$ becomes negligible, and the source J reduces to the ordinary matter density, yet the gradient relation $\mathbf{g} = -\nabla\Phi$ remains exact, preserving the direct identification between the curvature potential and the observable acceleration field. Thus the Newtonian limit functions both as a validation test (agreement with well–tested physics) and as a calibration rule (dimensionless scaling conventions used throughout higher–order and strong–field calculations), with further discussion in Appendix A.1 and Appendix C.

A.2.1 Weak–field derivation (detailed)

Starting from the Φ–Curvature Field Equation (PCFE) in Appendix A.1,

$$\Box\Phi - U'(\Phi) = J, \qquad \Box \equiv g^{\mu\nu}\nabla_\mu\nabla_\nu, \tag{188}$$

assume a nearly Minkowski background ($g_{\mu\nu} \simeq \eta_{\mu\nu}$) and a weak potential ($|\Phi| \ll c^2$). In this regime,

$$\Box\Phi \;\simeq\; -\frac{1}{c^2}\,\partial_t^2\Phi \;+\; \nabla^2\Phi.$$

For quasi–static configurations $\partial_t^2\Phi \approx 0$, giving

$$\nabla^2\Phi \;\simeq\; J. \tag{189}$$

Source identification. Identify the source with ordinary matter density,

$$J \;=\; 4\pi G\,\rho,$$

which immediately yields

$$\nabla^2\Phi \;=\; 4\pi G\,\rho. \tag{190}$$

Boundary conditions. To ensure consistency with Newtonian gravity,

$$\Phi(r) \to 0 \quad \text{as } r \to \infty, \qquad r^2\,\partial_r\Phi(r) \;\to\; GM \quad \text{for large } r,$$

so that $\partial_r\Phi \sim GM/r^2$ and $\mathbf{g}_r = -\partial_r\Phi \sim -\,GM/r^2$ points toward the mass distribution.

Units and sign conventions. We adopt SI units with $[G] = \mathrm{m}^3\,\mathrm{kg}^{-1}\,\mathrm{s}^{-2}$ and ρ in $\mathrm{kg\,m}^{-3}$, and define the observable acceleration as

$$\mathbf{g} \;=\; -\nabla\Phi,$$

with the minus sign ensuring an inward acceleration toward the sources.

Summary. In the weak–field, static limit the PCFE reduces to the Newton–Poisson equation,

$$\nabla^2\Phi \;=\; 4\pi G\,\rho, \qquad \mathbf{g} \;=\; -\nabla\Phi,$$

making explicit the suppression of temporal terms, the role of boundary conditions, and the adopted unit/sign conventions, and thereby providing a clear, consistent bridge between the curvature–field formulation and classical Newtonian gravity.

A.3 GR comparison

In General Relativity (GR), spacetime curvature is governed by the Einstein field equations

$$R_{\mu\nu} - \tfrac{1}{2} R\, g_{\mu\nu} \;=\; \frac{8\pi G}{c^4}\, T_{\mu\nu}, \tag{191}$$

where $R_{\mu\nu}$ is the Ricci tensor, R the Ricci scalar, and $T_{\mu\nu}$ the stress–energy tensor. This formulation is fully tensorial: curvature is encoded in interrelated components over the four–dimensional metric manifold. The strength of GR lies in this completeness, yet extracting specific observables (e.g., accelerations or lensing deflections) typically proceeds through geodesic equations and projections.

By contrast, the C4 framework introduces a scalar curvature potential Φ whose spatial gradient *directly* yields the observable field,

$$\mathbf{g} \;=\; -\nabla\Phi,$$

as defined by the PCFE in Appendix A.1. For static, spherical configurations we adopt the one–function gauge

$$ds^2 \;=\; -A(r)\, c^2 dt^2 + A(r)^{-1} dr^2 + r^2 d\Omega^2, \qquad A(r) \;=\; 1 + \frac{2\,\Phi(r)}{c^2} + \delta_{\mathrm{C4}}\, \Xi(r) + \mathcal{O}\!\left(\frac{\Phi^2}{c^4}\right), \tag{192}$$

where $\Xi(r)$ is a small, decaying "tail" term specific to C4 (variational details: Appendix C).[3]

Alignment with GR (weak–field). The $2\Phi/c^2$ contribution in (192) reproduces the standard Newtonian correspondence also built into GR, ensuring consistency with classical tests discussed in Appendix A.2. Asymptotic flatness is preserved by requiring $\Phi(r) \to 0$ and $\Xi(r) \to 0$ as $r \to \infty$.

Controlled departures. The C4 tail $\delta_{\mathrm{C4}}\, \Xi(r)$ has no direct analogue in the Einstein tensor; it encodes a *minimal*, scale–aware correction that can be probed against data at galactic and strong–gravity scales. Its amplitude is small and it decays asymptotically, so that departures remain bounded around the Newton/GR baselines established in Appendix A.2.

Observables and tests. Null and timelike geodesics of (192) provide the standard routes to lensing and dynamics, but the scalar readout $\mathbf{g} = -\nabla\Phi$ allows a direct operator for rotation curves ($v_c^2(R) \;=\; R\,\partial_R\Phi$) consistent with the pipeline used in the main text (Section 6). Strong–field diagnostics (e.g., subring ratios (R, Θ)) are evaluated with the same metric readout under C4 tails in Section 7.

Summary. C4 does not attempt to replicate GR's full tensorial apparatus. Instead, it offers a complementary scalar representation: transparent in interpretation, falsifiable through directly measured operators, and flexible enough to introduce small, decaying corrections without abandoning the Newtonian and GR baselines (Appendix A.2, Appendix C). The price of simplicity is the loss of exact tensorial completeness; the benefit is clarity and testability across disparate regimes.

[3] A more general two–function $A(r), C(r)$ 1PN/PPN expansion and readout appear in Appendix C; the one–function choice $C(r) = A(r)^{-1}$ is used here for clarity.

A.4 MC–CF as a Green–function solution (static limit)

In the weak–field, quasi–static regime (Appendix A), the PCFE reduces to

$$\nabla^2\Phi(\mathbf{r}) = J(\mathbf{r}), \qquad J = 4\pi G\,\rho(\mathbf{r}), \qquad \mathbf{g} = -\nabla\Phi, \tag{193}$$

which is exactly the Newton–Poisson equation. The free–space Green function is

$$G(\mathbf{r}) = -\frac{1}{4\pi\,\|\mathbf{r}\|},$$

so the convolution solution reads

$$\Phi(\mathbf{r}) = \int_{\mathbb{R}^3} G(\mathbf{r}-\mathbf{r}')\,J(\mathbf{r}')\,d^3\mathbf{r}' = -\,G\int_{\mathbb{R}^3}\frac{\rho(\mathbf{r}')}{\|\mathbf{r}-\mathbf{r}'\|}\,d^3\mathbf{r}'. \tag{194}$$

Gaussian–mixture sources. Let $\rho(\mathbf{r}) = \sum_{i=1}^{N}\rho_i(\mathbf{r})$ with anisotropic Gaussians

$$\rho_i(\mathbf{r}) = \frac{M_i}{(2\pi)^{3/2}\sigma_{x,i}\sigma_{y,i}\sigma_{z,i}}\,\exp\Big[-\frac{(x-x_i)^2}{2\sigma_{x,i}^2} - \frac{(y-y_i)^2}{2\sigma_{y,i}^2} - \frac{(z-z_i)^2}{2\sigma_{z,i}^2}\Big],$$

so that $J = 4\pi G\,\rho = \sum_i J_i$ and the potential superposes: $\Phi = \sum_i \Phi_i$. For the *isotropic* case $\sigma_{x,i} = \sigma_{y,i} = \sigma_{z,i} = \sigma_i$ one obtains closed forms

$$\Phi_i(r) = -\,\frac{GM_i}{r}\,\operatorname{erf}\!\left(\frac{r}{\sqrt{2}\,\sigma_i}\right), \tag{195}$$

$$\mathbf{g}_i(r) = -\,\frac{GM_i}{r^2}\left[\operatorname{erf}(x) - \sqrt{\tfrac{2}{\pi}}\,x\,e^{-x^2}\right]\hat{\mathbf{r}}, \qquad x = \frac{r}{\sqrt{2}\,\sigma_i}. \tag{196}$$

For the general *anisotropic* case, (194) is efficiently evaluated by FFT–based convolution on the same grid used in Appendix H.4 (absorbing boundary, P99 normalization).

Near– and far–field behavior. Let $M_{\mathrm{tot}} = \sum_i M_i$ and $r = \|\mathbf{r}\|$. Then

$$\Phi(\mathbf{r}) = -\,\frac{GM_{\mathrm{tot}}}{r} + O(r^{-3}) \quad (r\to\infty), \qquad \Phi(\mathbf{r}_i+\boldsymbol{\delta}) = \Phi(\mathbf{r}_i) + \tfrac{1}{6}J_i(\mathbf{r}_i)\,\|\boldsymbol{\delta}\|^2 + O(\|\boldsymbol{\delta}\|^3).$$

Thus the far field recovers the Newtonian $1/r$ law with total enclosed mass, while the near field is finite, its curvature set by the local source $J_i(\mathbf{r}_i) = 4\pi G\,\rho_i(\mathbf{r}_i)$. For the isotropic Gaussian (195),

$$\Phi_i(0) = -\,\frac{GM_i}{\sigma_i}\sqrt{\frac{2}{\pi}}, \qquad \mathbf{g}_i(r) = -\,\frac{4\pi G}{3}\,\rho_i(0)\,r\,\hat{\mathbf{r}} + O(r^3) \quad (r\to 0),$$

showing a Hooke–like restoring field at the center.

Conventions (amplitude mapping). MC–CF fitting employs shell amplitudes A_i and widths $\sigma_{k,i}$. To make the link to Poisson sources explicit:

Numerical safeguards. For FFT convolution, to mitigate wrap–around artifacts: (i) zero–pad by at least $> 3\sigma_{\max}$, (ii) apply the taper $D(r)$ of Appendix J, (iii) verify mass conservation on the grid ($\sum\rho\,\Delta V \approx \sum M_i$). The Green–convolution and spectral Poisson–solver routes are equivalent (same kernel) and follow the common mask/normalization conventions of Appendix H.

MC–CF parameter	Poisson/Source meaning
A_i	Mass–like amplitude M_i (so that ρ_i integrates to M_i)
$\sigma_{x,i}, \sigma_{y,i}, \sigma_{z,i}$	Gaussian widths of ρ_i (smoothing / shell scale)
$J_i = 4\pi G\, \rho_i$	Source entering $\nabla^2\Phi = J$

Table 76: Parameter conventions linking MC–CF $(A_i, \sigma_{k,i})$ to the Gaussian source (ρ_i, J_i). Units and signs follow Appendix H.1.

Summary. Equations (193)–(196) show that a Gaussian–mixture source yields an MC–CF potential as a superposition of smoothed Newtonian kernels. The far field correctly asymptotes to the $1/r$ law, while the near field remains nonsingular. Thus MC–CF is not merely heuristic but a legitimate *solution class* of the static PCFE, anchored to the normalization in Section 2.6 and directly comparable to the observational analyses in Section 6.

A.5 Comparison table

For clarity, we summarize the correspondence between the three formulations.

Framework	Field equation	Observables / Notes
Newtonian gravity	$\nabla^2\Phi = 4\pi G\, \rho$	$\mathbf{g} = -\nabla\Phi$ (direct acceleration law; weak/static limit), cf. Appendix A.2.
General Relativity	$R_{\mu\nu} - \frac{1}{2} R\, g_{\mu\nu} = \frac{8\pi G}{c^4} T_{\mu\nu}$	Tensorial curvature; observables via geodesics/lensing projections, cf. Appendix A.3.
C4 (framework; built on PCFE)	*PCFE (law)* $\Box\Phi - U'(\Phi) = J$; *solutions* via PSCF/MC–CF (fixed widths; amplitudes fitted)	Scalar readout $\mathbf{g} = -\nabla\Phi$; rotation–curve operator $v_c^2(R) = R\,\partial_R\Phi$; metric time component $A(r) = 1 + \frac{2\Phi}{c^2} + \delta_{\mathrm{C4}}\,\Xi(r)$ with small tail $\Xi(r)$, cf. Appendix A.3, Appendix C.

Table interpretation. Newtonian gravity gives a local density–to–acceleration map; GR promotes curvature to a full tensor field, requiring geodesic readouts; C4 retains the transparent link $\mathbf{g} = -\nabla\Phi$ while embedding it in a scalar–metric framework with an optional, decaying tail $\Xi(r)$ that is tested against data. Thus C4 stays consistent with the baselines set in Appendix A.2 and Appendix A.3, while providing controlled flexibility described in Appendix C.

A.6 Overall interpretation

The recovery of the Newtonian equation in the weak–field, static limit is more than reassurance; it anchors the entire framework to centuries of empirical validation. Without this correspondence, the curvature field would risk becoming an unconstrained parametrization. By guaranteeing continuity with Poisson's law, the theory secures a baseline against which all extensions must be measured (see Appendix A.2; normalization/windows as in Appendix E).

General Relativity (GR), by contrast, supplies a complete tensorial apparatus. Its universality is a strength, but direct interpretability of accelerations, lensing, or time delays typically requires geodesic readouts. The C4 framework takes a complementary route: it retains a scalar curvature potential Φ as the central object, so that $-\nabla\Phi$ is the observable acceleration, while its embedding into the metric via $A(r)$ connects seamlessly to relativistic effects (cf. Appendix A.3).

The inclusion of the pure–space scaffold (PSCF) and the mass–centered envelopes (MC–CF) reflects the dual structure of gravity: a smooth background encoding large–scale coherence and localized concentrations tied to luminous matter. In the static limit, MC–CF is not merely heuristic but a bona fide Green–function solution class of the Poisson reduction, with near/-far–field behavior and numerical safeguards detailed in Appendix A.4 (see also tapering and variational choices in Appendix C). The additional tail $\delta_{\mathrm{C4}}\,\Xi(r)$ is deliberately minimal and decaying, a scale–aware correction introduced to probe subtle discrepancies at galactic and strong–gravity scales (Appendix C.8).

Thus the interpretation is twofold. First, C4 respects the baselines: Newton's law in the weak/static limit and GR's metric structure at relativistic scales. Second, it interpolates between laboratory coherence, galactic dynamics, and strong–gravity observables using a single potential Φ, within a reproducible operator/covariance pipeline (Appendix H). The goal is not to replace GR's tensorial completeness, but to offer a transparent, testable scalar formulation whose extensions are small, explicitly stated, and confronted with data.

Appendix B. Glossary of Terms

This appendix collects the principal symbols and technical terms used throughout the paper. Beyond serving as a quick reference, each entry clarifies its logical role within the C4 formulation and notes why it cannot be removed without breaking the structure.

$\Phi(\mathbf{r})$: Curvature potential (dimension $[L^2/T^2]$). Its gradient gives the observable acceleration, $\mathbf{g} = -\nabla\Phi$. Unlike a purely Newtonian potential, Φ is determined by a field equation with self–interaction and effective sources. It recovers the Newtonian law in the weak/static limit (Appendix A.2) and embeds into the metric in relativistic settings (Appendix A.3).

PCFE (Phi–Curvature Field Equation): *Equation of motion* of the framework,

$$\Box\Phi - U'(\Phi) = J,$$

obtained by varying the scalar action (definition and derivation in Appendix A.1). PCFE is the *law*; solution families (PSCF/MC–CF) are implementations used for data.

$U(\Phi)$: Self–interaction potential that encodes nonlinearity in the scalar sector. It vanishes from the Newtonian limit (Appendix A.2) but can influence strong–field behavior via the metric embedding (Appendix A.3).

$J(\mathbf{r})$: Effective source. In the Newtonian limit $J = 4\pi G\,\rho$, with ρ the (deprojected) mass density (Appendix A.2). In practice, J is realized by MC–CF Gaussian envelopes (Appendix A.4).

PSCF (Pure–Space Curvature Field): Scaffold composed of smooth components with $J \equiv 0$, supplying a source–free background and correct far–field behavior. Fixed widths (no per–object retuning) promote parsimony and consistency (motivation in Section 2).

MC–CF (Mass–Centered Curvature Field): Source–anchored envelopes with $J \neq 0$ that tie curvature to luminous matter. In the static limit, MC–CF is a bona fide *Green–function solution* of the Poisson reduction; near/far–field behavior and numerical safeguards are given in Appendix A.4. In practice one or two centers suffice, enforcing parsimony (Section 2).

$A(r)$: Metric time component used for static, spherically symmetric readouts,

$$A(r) = 1 + \frac{2\Phi(r)}{c^2} + \delta_{\mathrm{C4}}\,\Xi(r),$$

linking the scalar potential to relativistic observables (lensing, time delays). Baseline and variants are discussed in Appendix A.3.

Tail $\Xi(r)$: Small, scale–dependent correction unique to C4 that modifies $A(r)$ by a controlled, decaying amount. It produces few–percent shifts in strong–gravity invariants (R, Θ) while preserving classical tests (Appendix A.3; variational details in Appendix C.8).

Photon–sphere radius r_{ph}: Radius of unstable null orbits. In C4, r_{ph} inherits small shifts through $\Xi(r)$ and thus probes the tail via photon–ring imaging (Section 7).

R: Subring spacing ratio for photon rings,

$$R = \frac{b_{3\pi} - b_{\pi}}{b_{\pi} - b_{\mathrm{ph}}},$$

where $b_{3\pi}, b_{\pi}, b_{\mathrm{ph}}$ are impact parameters for total deflections $3\pi, \pi$ and for the photon sphere. In C4, R shifts coherently with Θ, aiding discrimination from spin/plasma effects (Section 7).

Θ: Subring time–delay invariant,

$$\Theta = \frac{\Delta t_{3\pi,\pi}}{2\pi r_{\mathrm{ph}}} \simeq A(r_{\mathrm{ph}})^{-1/2},$$

which moves jointly with R under C4 tails (Section 7).

`[Legacy--convex mix]`: Legacy convex mix prescription. Historical method in which the tail was implemented via a constant mixing parameter D. Marked as "legacy" because it lacks a variational basis and allows implicit tuning. Retained only for exact reproducibility of past results (see Appendix J.6).

Interpretation. C4 rests on a minimal but interlocked set of elements: Φ as the unifying scalar, PCFE as the law, PSCF as the scaffold, MC–CF as the mass–anchored envelopes, $A(r)/\Xi(r)$ as the metric link and minimal extension, and (R, Θ) as discriminating invariants. Each plays a non–redundant role; removing any one induces characteristic failure modes documented elsewhere (Appendix D). The glossary thus functions not only as a reference but as an integrity map of how parsimony and testability arise from a few deliberate components.

Appendix C: Tensor Definitions

This appendix collects the basic geometric ingredients used in the Curvature Field Formulation (C4) and in the Φ–Curvature Field Equation (PCFE). Notation and conventions follow the main text (Section 2.6).

- **Indices / coordinates:** $\mu, \nu = 0, 1, 2, 3$, $i, j = 1, 2, 3$, with $x^\mu = (t, x^i)$.
- **Signature:** $\eta_{\mu\nu} = \mathrm{diag}(-1,\ 1,\ 1,\ 1)$.
- **Units:** $c = 1$ unless otherwise stated; G is kept explicit.
- **Weak–field notation:** $O(\Phi^2)$ denotes quadratic (and higher) terms in Φ.

For a scalar field the covariant derivative reduces to $\nabla_\mu \Phi = \partial_\mu \Phi$. The d'Alembertian and curvature tensors are

$$\Box\Phi \equiv g^{\mu\nu}\nabla_\mu\nabla_\nu\Phi, \tag{197}$$

$$\Gamma^\rho{}_{\mu\nu} = \tfrac{1}{2} g^{\rho\sigma}(\partial_\mu g_{\nu\sigma} + \partial_\nu g_{\mu\sigma} - \partial_\sigma g_{\mu\nu})\,, \tag{198}$$

$$R^\rho{}_{\sigma\mu\nu} = \partial_\mu \Gamma^\rho{}_{\nu\sigma} - \partial_\nu \Gamma^\rho{}_{\mu\sigma} + \Gamma^\rho{}_{\mu\lambda}\Gamma^\lambda{}_{\nu\sigma} - \Gamma^\rho{}_{\nu\lambda}\Gamma^\lambda{}_{\mu\sigma}, \tag{199}$$

$$R_{\mu\nu} = R^\rho{}_{\mu\rho\nu}, \qquad R = g^{\mu\nu} R_{\mu\nu}. \tag{200}$$

PCFE itself is given in Eq. 167.

C.0 Scalar field Φ: physical meaning and admissible sector

Role and scope. We treat Φ as a curvature–field scalar minimally coupled to $g_{\mu\nu}$, providing a controlled departure from pure–vacuum GR (see Appendix C.8). Its role is auxiliary yet indispensable: (i) it regularizes the near–source curvature profile (PSCF core), (ii) it anchors gradients around a fiducial scale r_0 (MC–CF), and (iii) it supplies a weak exterior tail compatible with Solar–System tests (Section 2.6). In the static, spherically symmetric readout we use

$$A(r) = 1 + \frac{2\Phi(r)}{c^2} + \delta_{\mathrm{C4}}\,\Xi(r), \tag{201}$$

as in the main text.

Gauge and admissible sector. We work in the isotropic gauge for readouts and restrict attention to solutions that satisfy:

(a) Asymptotic flatness) $\Phi(r) \to 0$ (or const.) as $r \to \infty$, (202)

(b) Central regularity) $\Phi'(0) = 0$, (203)

(c) Positivity of the effective quadratic form) $K_{\mathrm{eff}}(\bar\Phi) \equiv 1 - 2\alpha\,\bar\Phi > 0$ for $r \in [r_0, 3r_0]$, (204)

(d) Small–gradient cone) $|\alpha|\,\dfrac{(\nabla\bar\Phi)^2}{c^2} \le \eta_{\mathrm{cone}}\,K^2_{\mathrm{eff}}(\bar\Phi), \qquad \eta_{\mathrm{cone}} = 10^{-2}.$ (205)

Here $\bar\Phi$ denotes a representative value over the interval (e.g., an average), and α is the 1PN/tail sensitivity parameter defined in Appendix C.8. The conditions (204)–(205) ensure well–posed linearization and stable strong–gravity readouts.

Clarification on PSCF–MC–CF composition. For later use we write

$$\Phi_{\text{tot}} = \Phi_{\text{PSCF}} + \Phi_{\text{MC–CF}}. \tag{206}$$

Only $\Phi_{\text{MC–CF}}$ carries the physical source term ($J \neq 0$) and represents curvature generated by mass–energy (static Poisson reduction in Appendix A.4). By contrast, Φ_{PSCF} is a *source–free scaffold*: a basis chosen to regularize the near–origin profile and stabilize the decomposition. It is not an independent "matter–less curvature field." Physical interpretation therefore attaches to the MC–CF component, while PSCF provides structural background for a well–posed representation (Section 2; Appendix B).

C.0.1 Potential specification, existence, and stability

Declared potential (convex family). We adopt a minimal convex potential

$$U(\Phi) = \frac{1}{2}\, m_\Phi^2\, \Phi^2 + \frac{\lambda_4}{4}\, \Phi^4, \qquad m_\Phi^2 \geq 0,\ \lambda_4 \geq 0,\ \ U(0) = 0, \tag{207}$$

with the working default $\lambda_4 = 0$ and $m_\Phi r_0 \leq 1/4$. Then $U''(\Phi) = m_\Phi^2 + \lambda_4 \Phi^2 \geq 0$, so the energy density is convex and the linear response is Yukawa–type. This is the input used in the Yukawa→Padé construction (Appendix C.8).

Linearization and range (static and dynamical). About a smooth background $\bar{\Phi}$ write $\Phi = \bar{\Phi} + \delta\Phi$. The PCFE (Eq. 167) linearizes to

$$\Box\, \delta\Phi - U''(\bar{\Phi})\, \delta\Phi \ = \ \delta J \ + \ O(\delta\Phi^2), \tag{208}$$

so the effective mass is

$$m_{\text{eff}}^2 \ \equiv \ U''(\bar{\Phi}) \ = \ m_\Phi^2 + \lambda_4\, \bar{\Phi}^{\,2} \ \geq \ 0. \tag{209}$$

In the static limit outside matter, (208) reduces to

$$-\nabla^2\, \delta\Phi + m_{\text{eff}}^2\, \delta\Phi \ = \ \delta J, \qquad \Phi'(0) = 0,\ \ \Phi(r) \to 0 \text{ as } r \to \infty, \tag{210}$$

whose Green function is Yukawa:

$$G_Y(\mathbf{r}) \ = \ -\frac{1}{4\pi}\, \frac{e^{-m_{\text{eff}}\|\mathbf{r}\|}}{\|\mathbf{r}\|}, \qquad \delta\Phi(\mathbf{r}) = \int G_Y(\mathbf{r} - \mathbf{r}')\, \delta J(\mathbf{r}')\, d^3\mathbf{r}'. \tag{211}$$

Hence the screening length is $r_Y = 1/m_{\text{eff}}$ ($\geq 1/m_\Phi$); with $m_\Phi r_0 \leq 1/4$ the response remains close to Newtonian across $[r_0, 3r_0]$ (cf. Appendix A.4).

Static weak–field well–posedness (sketch). For the static problem (210) with U in (207), the energy functional

$$\mathcal{E}[\Phi] = \int_{\mathbb{R}^3} \left(\tfrac{1}{2} |\nabla\Phi|^2 + U(\Phi) - J\,\Phi \right) d^3x \tag{212}$$

is coercive on H^1 and weakly lower semicontinuous (by convexity of U). The direct method in the calculus of variations yields a minimizer $\Phi \in H^1$, which is a weak solution of (210). If $U'' \geq m_0^2 > 0$ on the Solar–System window and $J \in H^{-1}$, strict convexity implies uniqueness there (see Section 2.6 for the window).

Dynamical well–posedness and causality (summary). In local Minkowski coordinates ($\Box = -\partial_t^2/c^2 + \nabla^2$), the small–signal dispersion of (208) is

$$\omega^2 \;=\; c^2\big(k^2 + m_{\rm eff}^2\big) \qquad \Rightarrow \qquad 0 \le v_g = \frac{\partial\omega}{\partial k} \le c, \tag{213}$$

so the canonical kinetic term is luminal/sub–luminal. The self–sourcing channel modifies the effective kinetic factor to

$$K_{\rm eff}(\bar\Phi) \;=\; 1 - 2\alpha\,\bar\Phi, \tag{214}$$

and we *impose* the admissibility conditions

$$K_{\rm eff}(\bar\Phi) > 0, \qquad |\alpha|\,\frac{(\nabla\bar\Phi)^2}{c^2} \;\le\; \eta_{\rm cone}\,K_{\rm eff}^2(\bar\Phi), \quad \eta_{\rm cone} = 10^{-2}, \tag{215}$$

matching Eqs. 204–205. These exclude ghosts/tachyons in the operating regime and ensure a well–posed Cauchy problem (see Appendix L.1.1).

Compatibility with strong–field readout. The metric readout $A(r) = 1 + 2\Phi/c^2 + \delta_{\rm C4}\Xi(r)$ (Eq. 201) combined with (215) keeps the photon–sphere neighborhood regular and ensures that the invariants (R, Θ) vary smoothly under small tails (cf. Appendix C.8).

C.1 Metric Tensor $g_{\mu\nu}[\Phi]$

We adopt the $(-,+,+,+)$ signature and, unless otherwise stated, keep explicit factors of c to make contact with the readout metric in Eq. 201.

Linearized isotropic ansatz. In the weak–field, static, isotropic approximation of C4 (no rotation, no shear),

$$g_{\mu\nu}[\Phi] \;=\; \eta_{\mu\nu} + h_{\mu\nu}(\Phi), \qquad |h_{\mu\nu}| \ll 1, \tag{216}$$

with the gauge choice

$$h_{00}(\Phi) = -\frac{2\Phi}{c^2}, \qquad h_{0i}(\Phi) = 0, \qquad h_{ij}(\Phi) = \frac{2\Phi}{c^2}\,\delta_{ij}. \tag{217}$$

Equivalently,

$$g_{00} \simeq -\Big(1 + \frac{2\Phi}{c^2}\Big), \qquad g_{0i} \simeq 0, \qquad g_{ij} \simeq \Big(1 + \frac{2\Phi}{c^2}\Big)\delta_{ij}. \tag{218}$$

With $A(r) \equiv -g_{tt}$, (218) gives

$$A(r) \;\simeq\; 1 + \frac{2\Phi(r)}{c^2}, \tag{219}$$

which matches the leading term of the readout $A(r) = 1 + \frac{2\Phi}{c^2} + \delta_{\rm C4}\,\Xi(r)$ (Eq. 201).

Inverse metric, determinant, and leading connections. To first order in Φ/c^2,

$$g^{00} \simeq -\Big(1 - \frac{2\Phi}{c^2}\Big), \qquad g^{0i} \simeq 0, \qquad g^{ij} \simeq \Big(1 - \frac{2\Phi}{c^2}\Big)\delta^{ij}, \tag{220}$$

$$\sqrt{-g} \simeq 1 + \frac{4\Phi}{c^2} \;+\; O\big((\Phi/c^2)^2\big). \tag{221}$$

For a static field ($\partial_t \Phi = 0$) the leading Christoffel symbols read

$$\Gamma^{i}{}_{00} \simeq -\,\partial^{i}\Big(\frac{\Phi}{c^2}\Big), \quad \Gamma^{0}{}_{0i} \simeq \partial_i\Big(\frac{\Phi}{c^2}\Big), \quad \Gamma^{i}{}_{jk} \simeq \delta^{i}{}_{j}\,\partial_k\Big(\frac{\Phi}{c^2}\Big) + \delta^{i}{}_{k}\,\partial_j\Big(\frac{\Phi}{c^2}\Big) - \delta_{jk}\,\partial^{i}\Big(\frac{\Phi}{c^2}\Big). \tag{222}$$

Thus the geodesic equation yields, in the non–relativistic limit,

$$\frac{d^2 x^i}{dt^2} \;\simeq\; -\,\partial^{i}\Phi, \tag{223}$$

consistent with the C4 identification $\mathbf{g} = -\nabla\Phi$.

Consistency and scope.

1. *Newton–Poisson limit.* In the presence of matter density ρ, the PCFE reduces to $\nabla^2\Phi \simeq 4\pi G\rho$ with $\mathbf{g} = -\nabla\Phi$ (Appendix A.2); (223) agrees with this limit.

2. *Connection to the readout metric.* Equations (219) and Eq. 201 show that small, decaying tails $\Xi(r)$ correct $A(r)$ additively without altering the leading Φ–dependence used for (R, Θ) diagnostics.

3. *Gauge caveat / anisotropy.* In linearized GR one may write $g_{ij} \simeq (1 + 2\gamma\,\Phi/c^2)\delta_{ij}$ with PPN parameter γ; here we adopt $\gamma = 1$ and the isotropic–static ansatz appropriate for PSCF/MC–CF benchmarking. Anisotropic or time–dependent corrections are deferred to later tensors in this appendix.

4. *Applicability.* The expansion $|h_{\mu\nu}| \ll 1$ confines (217)–(223) to non–extreme environments; strong–field regions require the full non–linear PCFE and higher–order terms (see Appendix A).

C.2 Self–Sourcing Term

A central feature of PCFE is its *self–sourcing* channel: spatial gradients of the curvature field Φ act as an *effective source* for the field itself.

Definition and Poisson–limit form. We adopt the minimal nonlinear source functional

$$\mathcal{J}[\Phi] \;=\; \alpha\,(\nabla\Phi)^2, \qquad \alpha \text{ dimensionless}, \tag{224}$$

so that in the weak, static limit ($\mathbf{g} = -\nabla\Phi$) the modified Poisson–like equation reads

$$\nabla^2\Phi \;=\; 4\pi G\,\rho \;+\; \alpha\,(\nabla\Phi)^2. \tag{225}$$

Equivalently, introducing the effective density

$$\rho_{\text{eff}} \;\equiv\; \rho \;+\; \frac{\alpha}{4\pi G}\,(\nabla\Phi)^2, \tag{226}$$

one has $\nabla\cdot\mathbf{g} = -4\pi G\,\rho_{\text{eff}}$.

Weighted divergence form (well–posedness handle). Using $\nabla\cdot\big(e^{-\alpha\Phi}\nabla\Phi\big) = e^{-\alpha\Phi}\big(\nabla^2\Phi - \alpha(\nabla\Phi)^2\big)$, (225) becomes

$$\nabla\cdot\big(e^{-\alpha\Phi}\nabla\Phi\big) \;=\; e^{-\alpha\Phi}\,4\pi G\,\rho, \tag{227}$$

i.e. a weighted Poisson equation with positive weight $e^{-\alpha\Phi}$ in the admissible sector (C.0). This gives a monotone, coercive elliptic operator on H^1 with the standard boundary conditions ($\Phi'(0) = 0$, $\Phi \to 0$ as $r \to \infty$), enabling existence and comparison arguments in the Solar–System window (Section 2.6).

Consistency checks.

1. **Scaling.** $(\nabla\Phi)^2$ has units $[\Phi]^2/L^2$. Under the common normalization (Section 2.6), Φ is non–dimensionalized by r_0, so α is treated as a *global dimensionless constant*.

2. **Weak–field bound.** For $|\nabla\Phi| \ll 1$ the correction is $O(\alpha\,\Phi^2/L^2)$, hence subleading to $4\pi G\rho$; the Newton–Poisson limit is preserved (Appendix A.2).

3. **Sign and stability.** With $\alpha \geq 0$, (226) gives $\rho_{\text{eff}} \geq \rho$ and the enclosed mass $M_{\text{eff}}(r)$ is monotone in r, avoiding unphysical screening/runaway. In strong or rapidly varying regimes, the fixed–constant policy bounds α (Section 2.6.2).

4. **Admissible cone / causality link.** The self–sourcing channel feeds into the effective kinetic factor $K_{\text{eff}} = 1 - 2\alpha\bar{\Phi}$ (Eq. 214). We enforce $K_{\text{eff}} > 0$ together with the small–gradient cone $|\alpha|(\nabla\bar{\Phi})^2/c^2 \leq \eta_{\text{cone}}K_{\text{eff}}^2$ (Eq. 215) to exclude ghosts/tachyons and keep the Cauchy problem well–posed.

5. **Identifiability.** The effect of α can partially covary with MC–CF width/amplitude choices. Dataset–specific tuning is *forbidden*; α is *globally fixed* to preserve fairness and reproducibility.

Representation policy (PSCF vs. MC–CF).

- **PSCF (source–free scaffold):** set $\alpha = 0$ to maintain linearity of the background scaffold and prevent artificial tail amplification; consistent with global fixed widths.
- **MC–CF (mass–centered envelopes):** allow a small $\alpha > 0$ to improve near–surface gradient fitting and outer–tail shape; pooled performance is reported under the shared covariance/mask rules (Appendix H).

Remarks. Equation (224) is a *minimal* nonlinear extension consistent with weak–field benchmarks (Section 2.6). Other options (e.g. higher–order invariants such as $\beta\,(\Box\Phi)^2$ or mixed contractions with auxiliary tensors; cf. Appendix C.4) are possible but are not required for the fixed–policy results presented here.

C.3 Radial Function $A(r)$

In strong–gravity regimes the effective radial function $A(r)$ controls both photon orbits and spacetime distortions. Unless stated otherwise we keep G and c explicit.

Definition and decomposition.

$$A(r) \;=\; 1 - \frac{2GM}{rc^2} \;+\; f_\Phi(r), \tag{228}$$

where $f_\Phi(r)$ collects the curvature–field contribution beyond the Schwarzschild term and satisfies $f_\Phi(r) \to 0$ as $r \to \infty$ (asymptotic flatness). At 1PN order one may write

$$f_\Phi(r) \;=\; 2\beta\, U^2(r) \;+\; \delta_{\mathrm{C4}}\, a_{\mathrm{tail}}(r) \;+\; O(c^{-6}), \qquad U(r) = \frac{GM}{rc^2},$$

and, to match the readout form $A(r) = 1 + \frac{2\Phi}{c^2} + \delta_{\mathrm{C4}}\Xi(r)$ (Eq. 201), identify $a_{\mathrm{tail}}(r) \equiv \Xi(r)$ in the isotropic gauge.

Interpretation.

- The first two terms in (228) reproduce the Schwarzschild structure (unit normalization at large radii and $2GM/(rc^2)$ fall–off).
- $f_\Phi(r)$ is the C4–specific correction that aggregates the PSCF scaffold / MC–CF shells and the weak tail.

Key observables from $A(r)$.

1. *Photon–sphere radius* r_{ph}. In the static, isotropic gauge (with $C(r) \approx A(r)^{-1}$ at 1PN), circular null orbits satisfy

$$\frac{d}{dr}\left(\frac{A(r)}{r^2}\right)\Big|_{r=r_{\mathrm{ph}}} = 0 \quad\Longleftrightarrow\quad \frac{A'(r_{\mathrm{ph}})}{A(r_{\mathrm{ph}})} = \frac{2}{r_{\mathrm{ph}}}.$$

   For $f_\Phi = 0$ one finds $r_{\mathrm{ph}} = 3GM/c^2$; a small f_Φ produces a shift $\Delta r_{\mathrm{ph}} = O(f_\Phi)$.

2. *Time–delay diagnostic* Θ. In the eikonal approximation near r_{ph},

$$\Theta \;\simeq\; A(r_{\mathrm{ph}})^{-1/2},$$

   so perturbations in $f_\Phi(r)$ induce measurable $\Delta\Theta$ via $A(r)$ (Appendix C, Appendix B).

3. *Joint observable* (R, Θ). Fractional shifts in $(r_{\mathrm{ph}}, \Theta)$ jointly discriminate tail models; see Section 7 and Appendix C.8.

Consistency checks.

1. *Weak–field match:* For $r \gg r_0$, $f_\Phi(r)$ must decay faster than $1/r$ to preserve the Newton–Poisson limit and Solar–System concordance (Section 2.6).
2. *Near–surface behavior:* Over $r \in [r_0, 1.5r_0]$ in MC–CF fits, $f_\Phi(r)$ refines gradients where a pure Schwarzschild profile underestimates curvature.
3. *Mass–trend of tails:* The C4 tail yields small, coherent deviations from Schwarzschild that generate mass–dependent trends in (R, Θ) (e.g., Sgr A* vs. M87*).

Canonical tail (adopted). We adopt a PPN–locked, scale–covariant tail:

$$a_{\rm tail}(r) \;=\; c_{\rm tail}(r) \;=\; \frac{r_0^2}{r^2}\, f\!\left(\frac{r}{r_0}\right), \qquad f(x)\to 0 \;\; (x\to\infty), \tag{229}$$

with the explicit normalized profile from Appendix C.7:

$$a_{\rm tail}(r) \;=\; c_{\rm tail}(r) \;=\; 2\,\varepsilon_\gamma\, U(r)\, p(r), \qquad U(r)=\frac{GM}{r\,c^2}, \tag{230}$$

where $p(r)$ is monotone on $[r_0, 3r_0]$ and satisfies $0 < p(r) \le 1$ by construction. This choice preserves γ at leading order and suppresses β–shifts within the declared tolerances $(\varepsilon_\gamma, \varepsilon_\beta)$ on the Solar window.

Alternatives for ablation (not adopted). Exponential $f_\Phi(r)\sim e^{-r/\sigma}$, Gaussian bands (PSCF–motivated), and polynomial decays may be used *only* for ablation/robustness tests; the canonical tail is (229)–(230).

C.3.1 Explicit tail profile in the metric functions

At 1PN order we write

$$\begin{aligned} A(r) &= 1 - 2U + 2\beta\, U^2 + \delta_{\rm C4}\, a_{\rm tail}(r) + \mathcal{O}(c^{-6}),\\ C(r) &= 1 + 2\gamma\, U \;+\; \delta_{\rm C4}\, c_{\rm tail}(r) \;+\; \mathcal{O}(c^{-4}), \end{aligned} \tag{231}$$

and adopt the isotropic choice $a_{\rm tail} = c_{\rm tail} \equiv \Xi(r)$ with

$$\begin{aligned} \Xi(r) &= 2\,\varepsilon_\gamma\, U(r)\, p\!\left(\frac{r}{r_0}\right),\\ U(r) &= \frac{GM}{r\,c^2},\\ p(x) &= \frac{C_n}{x^2\big(1+\alpha x\big)^n},\\ C_n &= \big(1+\alpha x_{\rm min}\big)^n\, x_{\rm min}^2. \end{aligned} \tag{232}$$

Here $x_{\rm min}\in(0,1]$ sets the window start (default $x_{\rm min}=1$), $n\ge 3$, $\alpha>0$. The setting $(n,\alpha) = (3,\frac{1}{4})$ approximates $e^{-\lambda x}/x^2$ on $x\in[x_{\rm min},3]$ with controlled residuals (Appendix C.8).

Magnitude and regularity constraints (operational). We enforce

$$|\delta_{\rm C4}\,\Xi(r)| \;\ll\; 1, \qquad \Xi(r) \text{ monotone and positive}, \qquad \Xi(r)\to 0 \;\; (r\to\infty),$$

to ensure Solar–System compatibility and a smooth readout near the photon sphere. When needed, ε_γ is taken from the fixed–policy table in Section 2.6.

C.4 Auxiliary Tensor $\Xi_{\mu\nu}$

To summarize anisotropic (shear–like) structure generated by the curvature field we introduce the *auxiliary tensor* as the symmetric, traceless part of the Hessian of Φ:

$$\Xi_{\mu\nu}[\Phi] \;\equiv\; \nabla_\mu\nabla_\nu\Phi \;-\; \frac{1}{4}\, g_{\mu\nu}\,\Box\Phi, \qquad \Box\Phi \equiv g^{\rho\sigma}\nabla_\rho\nabla_\sigma\Phi. \tag{233}$$

By construction $g^{\mu\nu}\Xi_{\mu\nu} = 0$ (traceless). Equivalently,

$$\Xi_{\mu\nu} \;=\; \mathrm{STF}\big[\nabla_\mu\nabla_\nu\Phi\big] \quad \text{with projector} \quad \mathrm{STF}_{\mu\nu}{}^{\alpha\beta} = \tfrac{1}{2}(\delta_\mu{}^\alpha\delta_\nu{}^\beta + \delta_\mu{}^\beta\delta_\nu{}^\alpha) - \tfrac{1}{4}g_{\mu\nu}g^{\alpha\beta}.$$

Units and scope. Since $[\Phi] = L^2/T^2$, one has $[\Xi_{\mu\nu}] = [\Phi]/L^2$. In weak fields we use the metric and signatures of Appendix C.1; strong–field readouts connect through $A(r) = 1 + \frac{2\Phi}{c^2} + \delta_{C4}\Xi(r)$ (Appendix C.3).

Static, weak–field decomposition. For time–independent Φ and to leading order in Φ/c^2,

$$\Xi_{00} \simeq +\frac{1}{4}\nabla^2\Phi, \qquad \Xi_{0i} \simeq 0, \qquad \Xi_{ij} \simeq \partial_i\partial_j\Phi - \frac{1}{4}\delta_{ij}\nabla^2\Phi.$$

For a spherically symmetric $\Phi(r)$, using $\hat{r}_i = x_i/r$ and $\partial_i\partial_j\Phi = \Phi''\hat{r}_i\hat{r}_j + (\Phi'/r)(\delta_{ij} - \hat{r}_i\hat{r}_j)$, one obtains the orthonormal components

$$\Xi_{rr} = \frac{3}{4}\Phi'' - \frac{1}{2}\frac{\Phi'}{r}, \tag{234}$$

$$\Xi_T = -\frac{1}{4}\Phi'' + \frac{1}{2}\frac{\Phi'}{r} \quad (\text{degenerate for } \theta\theta,\ \varphi\varphi), \tag{235}$$

with $\nabla^2\Phi = \Phi'' + \frac{2}{r}\Phi'$. A convenient static scalar monitor is

$$S_\Xi \equiv \Xi_{ij}\Xi_{ij} = \Xi_{rr}^2 + 2\,\Xi_T^2 \geq 0, \tag{236}$$

while the full invariant is $I_\Xi \equiv \Xi_{\mu\nu}\Xi^{\mu\nu} = -\,\Xi_{00}^2 + S_\Xi + O(\Phi/c^2)$.

Near–/far–field behavior (check). For the Newtonian profile $\Phi(r) = -GM/r$ one has $\Phi' = +GM/r^2$, $\Phi'' = -2GM/r^3$, giving

$$\Xi_{rr} = -\frac{2GM}{r^3}, \qquad \Xi_T = +\frac{GM}{r^3}, \qquad S_\Xi = \frac{6G^2M^2}{r^6},$$

so $\Xi_{\mu\nu} = O(r^{-3})$ and $I_\Xi = O(r^{-6})$, consistent with Solar–System decay requirements (Section 2.6).

Constitutive and diagnostic roles.

- *Anisotropic curvature monitor.* $\Xi_{\mu\nu}$ filters out the isotropic part ($\propto \Box\Phi$) and retains shear–like structure driven by spatial variations of Φ (PSCF background suppresses it; MC–CF shells reintroduce controlled anisotropy).
- *Stability indicator.* Small S_Ξ correlates with gentle gradients and a robust linearization cone (C.0); growth of S_Ξ flags regimes where tail terms and higher–order couplings matter.
- *Strong–gravity linkage.* Through $A(r)$, variations in Φ and hence in $\Xi_{\mu\nu}$ map into the invariants (R, Θ) used in Section 7.

Divergence identity (elliptic reformulation). In flat background one has

$$\partial^\mu\Xi_{\mu\nu} = \frac{3}{4}\partial_\nu(\nabla^2\Phi) - \partial_i\partial_i\partial_\nu\Phi = -\frac{1}{4}\partial_\nu(\nabla^2\Phi), \tag{237}$$

so in the Poisson reduction ($\nabla^2\Phi = 4\pi G\rho$) the divergence of $\Xi_{\mu\nu}$ is directly sourced by $\nabla\rho$, which explains the restoration of anisotropy around mass centroids in MC–CF.

Consistency checks.

- *Weak–field limit:* For smooth Φ with $\nabla^2\Phi \to 0$ at large r, $\Xi_{\mu\nu} \to 0$ faster than $1/r^2$; cf. the $1/r^3$ estimate above.
- *Gauge compatibility:* The definitions are covariant; the explicit forms (234)–(236) are given in the isotropic, static gauge used throughout Appendix C.1.
- *Numerical stability:* The STF Hessian (233) preserves linearity in Φ, is strictly traceless, and is less stiff than bilinear gradient constructions in mixed PN regimes.

Caveats and alternatives. A common alternative is the bilinear, traceless tensor

$$\tilde{\Xi}_{\mu\nu} \;=\; \nabla_\mu\Phi\,\nabla_\nu\Phi - \tfrac{1}{4}g_{\mu\nu}(\nabla\Phi)^2.$$

While $\tilde{\Xi}_{\mu\nu}$ can be useful for energy–momentum analogies, we adopt (233) as our *operational* choice because it (i) preserves linearity in Φ, (ii) enforces tracelessness by construction, and (iii) exhibits superior numerical stability across weak and strong–field windows. Couplings to $\Xi_{\mu\nu}$ (e.g. $\kappa\,\Xi_{\mu\nu}\Xi^{\mu\nu}$) are reserved for ablation and are not required by the fixed–policy results reported here.

C.5 Notational Summary

For clarity we collect the main symbols introduced throughout Appendix C, including their definitions, functional roles, and limits of applicability (sign conventions and units follow Appendix C.1).

- $g_{\mu\nu}[\Phi]$ (metric modified by the curvature field).
  - *Definition:* In the weak–field limit, $g_{\mu\nu} = \eta_{\mu\nu} + h_{\mu\nu}(\Phi)$ with $|h_{\mu\nu}| \ll 1$; in the isotropic static gauge, $g_{00} \simeq -\left(1 + 2\Phi/c^2\right)$ and $g_{ij} \simeq \left(1 + 2\Phi/c^2\right)\delta_{ij}$ (Appendix C.1).
  - *Role:* Reproduces nonrelativistic acceleration $-\nabla\Phi$ through the geodesic equation and matches the readout form $A(r) = 1 + \frac{2\Phi}{c^2} + \delta_{\mathrm{C4}}\Xi(r)$ (Eq. 201).
  - *Limit:* Requires higher–order (or fully nonlinear) corrections in strongly time–dependent or anisotropic environments.
- $\mathcal{J}[\Phi]$ (self–sourcing nonlinear term).
  - *Definition:* Minimal form $\mathcal{J}[\Phi] = \alpha(\nabla\Phi)^2$, with α a *global, dimensionless* constant (Appendix C.2).
  - *Role:* In the static limit yields $\nabla^2\Phi = 4\pi G\rho + \alpha(\nabla\Phi)^2$, i.e., gradient energy feeds back as an effective source.
  - *Policy:* Set $\alpha = 0$ for the PSCF scaffold (linearity), allow small $\alpha > 0$ for MC–CF envelopes (improved near–surface gradients) under the shared covariance/mask rules.
- $A(r)$ (radial function governing photon orbits and time delay).
  - *Definition:* $A(r) = 1 - \frac{2GM}{rc^2} + f_\Phi(r)$; at 1PN, $f_\Phi = 2\beta U^2 + \delta_{\mathrm{C4}}a_{\mathrm{tail}}(r)$ with $U = GM/(rc^2)$ (Appendix C.3).

- *Role:* Controls the photon–sphere location $r_{\rm ph}$ and the delay diagnostic $\Theta \simeq A(r_{\rm ph})^{-1/2}$; the correction f_Φ carries PSCF/MC–CF structure and the C4 tail, shifting (R, Θ) coherently.
- *Limit:* For $r \gg r_0$, $f_\Phi(r)$ must decay faster than $1/r$ to preserve the Newton–Poisson limit and Solar–System concordance (Section 2.6).

- $\Xi_{\mu\nu}$ (auxiliary traceless tensor from second derivatives of Φ).
  - *Definition:* $\Xi_{\mu\nu} = \nabla_\mu\nabla_\nu\Phi - \frac{1}{4}g_{\mu\nu}\Box\Phi$ with $g^{\mu\nu}\Xi_{\mu\nu} = 0$ (Appendix C.4).
  - *Role:* Isolates shear–like (anisotropic) curvature and provides stability/tail monitors via $I_\Xi = \Xi_{\mu\nu}\Xi^{\mu\nu}$ or, in static slices, $S_\Xi = \Xi_{ij}\Xi_{ij}$.
  - *Limit:* Decays $\sim r^{-3}$ for Newtonian $1/r$ potentials (hence negligible at large r); strong–gravity readouts connect to (R, Θ) through $A(r)$.

Usage (operational). All quantities are evaluated under the *global fixed–constant policy* (Section 2.6.2). Weak–field limits reproduce Newton–Poisson (Appendix A.2); strong–field deviations are attributed solely to C4–specific corrections (tail/self–sourcing) under the shared masks, windows, and covariance rules.

Cross–references. For details, see Appendix C.1 (metric), Appendix C.2 (self–sourcing), Appendix C.3 (radial function / tail), and Appendix C.4 (auxiliary tensor).

C.6 PPN Mapping and Solar–System Bounds

Standard PPN form (isotropic gauge). In the static, spherically symmetric sector we adopt isotropic coordinates and $U \equiv GM/(rc^2) > 0$. To first post–Newtonian order (1PN),

$$g_{tt} = -\Big(1 - 2U + 2\beta\,U^2\Big) \;-\; \delta_{\rm C4}\,a_{\rm tail}(r) \;+\; \mathcal{O}(U^3), \tag{238}$$

$$g_{rr} = \;\Big(1 + 2\gamma\,U\Big) \;+\; \delta_{\rm C4}\,c_{\rm tail}(r) \;+\; \mathcal{O}(U^2), \tag{239}$$

where γ, β are the standard PPN parameters and $a_{\rm tail}, c_{\rm tail}$ encode small C4–induced tail contributions. This is consistent with the readout $A(r) = 1 + \frac{2\Phi}{c^2} + \delta_{\rm C4}\Xi(r)$ and $C(r) = 1 + 2\gamma U + \delta_{\rm C4}\,c_{\rm tail}(r)$ (Eq. 231, Eq. 232).

PPN decomposition of the tail. In the Solar–System window $U \ll 1$, expand

$$a_{\rm tail}(r) = a_1(r)\,U \;+\; a_2(r)\,U^2 \;+\; \mathcal{O}(U^3), \tag{240}$$

$$c_{\rm tail}(r) = c_1(r)\,U \;+\; \mathcal{O}(U^2). \tag{241}$$

Matching (238)–(239) to the PPN normal form yields the effective shifts

$$\delta\gamma(r) \;\equiv\; \gamma_{\rm eff}(r) - 1 \;=\; \tfrac{1}{2}\,\delta_{\rm C4}\,c_1(r), \qquad \delta\beta(r) \;\equiv\; \beta_{\rm eff}(r) - 1 \;=\; \tfrac{1}{2}\,\delta_{\rm C4}\,a_2(r). \tag{242}$$

(At leading order, a_1 renormalizes the linear U term and does not directly enter β.)

Sufficient conditions (GR at leading PPN order). In the weak, static, isotropic limit, GR is recovered at leading PPN order if

$$\begin{aligned} &a_{\rm tail}(r) = c_{\rm tail}(r), \\ &a_{\rm tail}(r) = o\big(U^2\big) \qquad (U \to 0). \end{aligned} \tag{243}$$

Equivalently,

$$c_1(r) = 0, \qquad a_2(r) = 0 \implies \delta\gamma = \delta\beta = 0 \quad \text{(1PN)}. \tag{244}$$

With the explicit choice

$$a_{\rm tail} = c_{\rm tail} \equiv \Xi(r) = 2\,\varepsilon_\gamma\, U(r)\, p\big(r/r_0\big) \quad \text{(Eq. 232)},$$

one has

$$\begin{aligned} &c_1(r) = 2\,\varepsilon_\gamma\, p\big(r/r_0\big), \\ &a_2(r) = 0. \end{aligned} \tag{245}$$

Since $p(x) = \mathcal{O}\big(x^{-2-n}\big)$ for $n \geq 3$,

$$\Xi = 2\,\varepsilon_\gamma\, U\, p = \mathcal{O}\big(U/x^2\big) = o\big(U^2\big), \tag{246}$$

so that, at leading PPN order,

$$\delta\gamma = \mathcal{O}(U), \qquad \delta\beta = 0, \tag{247}$$

consistent with Solar–System bounds.

Reporting bounds (numerical budgets). We adopt fixed, measurement–based budgets at 2σ on $[r_0, 3r_0]$ (cf. Section 3.5.4):

$$|\gamma - 1| \;\leq\; \varepsilon_\gamma = 4.6 \times 10^{-5}, \qquad |\beta - 1| \;\leq\; \varepsilon_\beta = 3.6 \times 10^{-5}. \tag{248}$$

Tail parameters (through $\delta_{\rm C4}$ and the mix amplitude D) are fixed so that $\max_{r\in[r_0,3r_0]} |\delta\gamma(r)| \leq \varepsilon_\gamma$ and $\max_{r\in[r_0,3r_0]} |\delta\beta(r)| \leq \varepsilon_\beta$.

Notes on coordinates and boundary conditions. All PPN identifications above refer to isotropic coordinates. Asymptotic flatness is imposed by $g_{tt} \to -1$ and $g_{rr} \to 1$ as $r \to \infty$, with regularity at $r = r_0$. The tail must decay faster than U at large r (e.g. $a_{\rm tail}, c_{\rm tail} = o(r^{-2})$).

Notation addendum (cosmology & GW; global constants).

- $\mu(a,k) \equiv \dfrac{k^2\Psi}{4\pi G\, a^2\, \delta\rho_m}, \quad \eta(a,k) \equiv \dfrac{\Phi_{\rm N}}{\Psi}, \quad \Sigma(a,k) \equiv \dfrac{k^2(\Psi + \Phi_{\rm N})}{8\pi G\, a^2\, \delta\rho_m} = \dfrac{\mu(1+\eta)}{2}.$
- $E_G(k,z) \equiv \dfrac{c^2k^2(\Phi_{\rm N} + \Psi)}{3H_0^2\, a^{-1}\, f\, \delta_m} \;\simeq\; \dfrac{\Sigma\,\Omega_m}{f}$ (quasi–static, sub–horizon).
- ζ — global, dimensionless coupling for a scalar–curvature breathing polarization; in GW waveforms $h_b \propto \zeta\,\delta\Phi$.
- $(\alpha_{\rm ppE}, \beta_{\rm ppE})$ — ppE amplitude/phase correction coefficients (treated as *global* constants); exponents (a, b) are predeclared and fixed.
- $U(\Phi)$ — minimal potential family (constant U or one–parameter tracker); declared under the global fixed–constant policy.
- Background/distance symbols $H(z)$, $D_H = c/H$, D_M, D_V, ℓ_A, R, r_d follow Appendix K.1–Appendix K.3.

C.6.1 PPN readout identities

From Eqs. 231–232 one obtains

$$\gamma_{\rm eff}(r) = \frac{C(r)-1}{2U(r)} = \gamma + \frac{\delta_{\rm C4}}{2U(r)}\,\Xi(r) + \mathcal{O}(c^{-2}), \qquad \beta_{\rm eff}(r) = \tfrac{1}{2}\frac{\partial^2 A}{\partial U^2} = \beta + \tfrac{\delta_{\rm C4}}{2}\frac{\partial^2 \Xi}{\partial U^2}. \tag{249}$$

Using $U(r) = \mu/r$ with $\mu \equiv GM/c^2$ and primes denoting d/dr,

$$\delta\gamma(r) = \frac{\delta_{\rm C4}}{2U(r)}\,\Xi(r), \qquad \delta\beta(r) = \frac{\delta_{\rm C4}}{2}\left[\frac{r^4}{\mu^2}\,\Xi''(r) + \frac{2r^3}{\mu^2}\,\Xi'(r)\right], \tag{250}$$

so the isotropic choice $a_{\rm tail} = c_{\rm tail} = \Xi$ keeps $\delta\gamma = \mathcal{O}(U)\,\varepsilon_\gamma$ and suppresses $\delta\beta$ within the declared budgets on $[r_0, 3r_0]$.

C.7 Numerically fixed tail and PPN budget (refined)

PPN–locked construction (explicit bounds). To keep Solar–System tests *numerically falsifiable*, we fix a normalized tail and tie its amplitude to declared PPN tolerances. On the isotropic 1PN background of Appendix C.6, set

$$a_{\rm tail}(r) = c_{\rm tail}(r) = 2\,\varepsilon_\gamma\,U(r)\,p(r), \qquad U(r) \equiv \frac{GM}{r\,c^2}. \tag{251}$$

With the metric readout of Appendix C.6 (i.e. $g_{rr} = 1 + 2\gamma U + \delta_{\rm C4} c_{\rm tail}$), the effective shift of γ reads

$$\delta\gamma(r) = \frac{\delta_{\rm C4}}{2U(r)}\,c_{\rm tail}(r) = \delta_{\rm C4}\,\varepsilon_\gamma\,p(r) \;\le\; \delta_{\rm C4}\,\varepsilon_\gamma. \tag{252}$$

Under the fixed–policy choice $\delta_{\rm C4} \in [0,1]$, this guarantees $|\delta\gamma(r)| \le \varepsilon_\gamma$ whenever $0 < p(r) \le 1$.

Canonical shape with closed–form normalization. Let $x \equiv r/r_0$ and $\alpha \equiv r_0/r_t > 0$. Define the raw profile

$$p_{\rm raw}(x) = \frac{x^{-2}}{(1+\alpha x)^n}, \qquad n = 3, \quad r_t = 4\,r_0 \;\;(\Rightarrow\;\; \alpha = \tfrac{1}{4}).$$

On $x \in [1,3]$, $p_{\rm raw}$ is strictly decreasing, so the *exact* window–normalized profile is

$$p(x) = \frac{p_{\rm raw}(x)}{p_{\rm raw}(1)} = \frac{(1+\alpha)^n}{x^2(1+\alpha x)^n}, \qquad x \in [1,3], \tag{253}$$

ensuring $0 < p(x) \le 1$ with $p(1) = 1$ and $p(3) < 1$.

Optional conservative window. If radii interior to r_0 are to be included, fix $x_{\rm min} \in (0,1)$ and

$$p(x) = \frac{p_{\rm raw}(x)}{\max_{x\in[x_{\rm min},\,3]} p_{\rm raw}(x)} = \frac{(1+\alpha x_{\rm min})^n}{x^2(1+\alpha x)^n}\,x_{\rm min}^2,$$

which preserves $p \le 1$ on $x \in [x_{\rm min}, 3]$.

Asymptotics and the β budget (no hidden U^2 term). Using $x = (GM)/(Ur_0c^2)$, the fixed tail (251) becomes

$$a_{\rm tail}(U) = 2\,\varepsilon_\gamma\,U\,\frac{(1+\alpha)^n}{\left(\frac{GM}{Ur_0c^2}\right)^2\left(1+\alpha\frac{GM}{Ur_0c^2}\right)^n} \;\propto\; U^{3+n} \quad (U\to 0).$$

With $n = 3$ one has $a_{\rm tail} = O(U^6)$ as $U \to 0$. Hence the U^2 coefficient in g_{tt} (Eq. 238) vanishes *identically*, so the effective 1PN shift

$$\delta\beta(r) = 0 \quad \text{at } O(U^2),$$

and the declared β–budget is automatically respected.

Smooth domain extension and matching. Outside the Solar window we keep the same analytic $p(x)$ and enforce a C^1 match toward the strong–field sector with

$$w(r) = \frac{1}{1+\left(\frac{r_m}{r}\right)^q}, \qquad q \ge 2,\;\; r_m \text{ predeclared},$$

using $a_{\rm tail} \to w(r)\,a_{\rm tail}$ and $c_{\rm tail} \to w(r)\,c_{\rm tail}$. This preserves $p \le 1$ on $[r_0, 3r_0]$, keeps the PPN caps intact, and guarantees C^1 continuity into the regime governed by $A(r)$ (Appendix C.3).

Numerical budget (fixed, policy–level). Unless otherwise stated, we adopt the measurement–based 2σ caps of Appendix C.6:

$$\boxed{\varepsilon_\gamma = 4.6\times10^{-5}, \qquad \varepsilon_\beta = 3.6\times10^{-5}, \qquad n = 3, \qquad r_t/r_0 = 4,} \tag{254}$$

with $\delta_{\rm C4} \in [0,1]$ a global switch/amplitude under the fixed–policy constants.

Operational readout. With the 1PN form of Appendix C.6,

$$g_{tt} = -\big(1 - 2U + 2\beta U^2\big) - \delta_{\rm C4}\,a_{\rm tail}(r), \qquad g_{rr} = \big(1+2\gamma U\big) + \delta_{\rm C4}\,c_{\rm tail}(r),$$

one reads off

$$\delta\gamma(r) = \delta_{\rm C4}\,\varepsilon_\gamma\,p(r/r_0) \;\le\; \varepsilon_\gamma, \qquad \delta\beta(r) = 0 \text{ at } O(U^2),$$

and logs $\max_{r\in[r_0,3r_0]}\delta\gamma(r)$ together with the taper parameters (r_m, q) per object in Appendix H.

Implementation notes (machine–readable). Given $(M, r_0, r_t, n, \varepsilon_\gamma, \varepsilon_\beta)$ and optional $(x_{\min}, r_m, q)$:

1. Compute $\alpha = r_0/r_t$ and $p(x)$ from (253) (or its $x_{\min}$ variant).
2. Evaluate $a_{\rm tail}, c_{\rm tail}$; verify $\delta\gamma(r) \le \varepsilon_\gamma$ on $[r_0, 3r_0]$ (or $[x_{\min}r_0, 3r_0]$).
3. Confirm the U^2 Taylor coefficient of $a_{\rm tail}(U)$ is zero (holds for $n \ge 1$).

Item	Symbol	Fixed value / rule
PPN tolerance for γ	ε_γ	4.6×10^{-5}
PPN tolerance for β	ε_β	3.6×10^{-5}
Tail exponent	n	3
Turnover radius	r_t/r_0	4
Normalization window	$r \in [r_0, 3r_0]$	$p(x)$ strictly decreasing, $0 < p \leq 1$
Taper (optional)	(r_m, q)	C^1 match to strong–field sector
Global tail switch	$\delta_{\rm C4}$	$\in [0, 1]$ (policy level)

C.7.1 Planetary–orbit PPN numeric binding

Assumptions (declared). Solar–System normalization $r_0 \equiv 1\,\mathrm{AU}$. Tail shape locked to the Appendix C.6 window,

$$a_{\rm tail}(r) = c_{\rm tail}(r) = 2\,\varepsilon_\gamma\,U(r)\,p(x), \qquad U(r) \equiv \frac{GM}{r\,c^2}, \quad x \equiv \frac{r}{r_0}, \tag{255}$$

with $\alpha \equiv r_0/r_t = 1/4$, $n = 3$, $\varepsilon_\gamma = 2.0 \times 10^{-5}$, $\varepsilon_\beta = 1.0 \times 10^{-4}$. To include Mercury, normalize p on $x \in [x_{\rm min}, 3]$ with $x_{\rm min} = 0.3$ so that $\max p = 1$:

$$p(x) = \frac{(1+\alpha x_{\rm min})^n\, x_{\rm min}^2}{x^2\,(1+\alpha x)^n}, \qquad x \in [x_{\rm min}, \infty). \tag{256}$$

Then the readouts (cf. Appendix C.6) are

$$\delta\gamma(r) = \frac{\delta_{\rm C4}}{2U}\,c_{\rm tail}(r) = \delta_{\rm C4}\,\varepsilon_\gamma\,p(x), \qquad \delta\beta(r) = 0 \text{ at } O(U^2) \text{ (vanishes at 1PN)}. \tag{257}$$

Numerical entries below take $\delta_{\rm C4} = 1$; for $\delta_{\rm C4} < 1$, scale $\delta\gamma$ linearly.

Planet	a [AU]	e	$r_{\rm min}$–$r_{\rm max}$ [AU]	$\delta\gamma_{\rm min}$–$\delta\gamma_{\rm max}$	$100 \times \dfrac{\delta\gamma_{\rm max}}{\varepsilon_\gamma}$
Mercury	0.387	0.206	0.307–0.467	$(0.737\text{–}1.894) \times 10^{-5}$	94.7%
Venus	0.723	0.0068	0.718–0.728	$(0.255\text{–}0.264) \times 10^{-5}$	13.2%
Earth	1.000	0.0167	0.983–1.017	$(0.110\text{–}0.120) \times 10^{-5}$	6.0%
Mars	1.524	0.093	1.381–1.666	$(0.028\text{–}0.048) \times 10^{-5}$	2.4%
Jupiter	5.204	0.0489	4.950–5.459	$(0.00057\text{–}0.00081) \times 10^{-5}$	4.05×10^{-2}%
Saturn	9.583	0.0565	9.041–10.124	$(0.000050\text{–}0.000079) \times 10^{-5}$	3.95×10^{-3}%
Uranus	19.218	0.0463	18.329–20.108	$(0.0000025\text{–}0.0000038) \times 10^{-5}$	1.9×10^{-4}%
Neptune	30.110	0.0097	29.818–30.402	$(0.00000038\text{–}0.00000042) \times 10^{-5}$	2.1×10^{-6}%

Table 77: Planetary–orbit binding of the PPN parameter $\delta\gamma(r) = \varepsilon_\gamma\,p(r/1\,\mathrm{AU})$ with $\varepsilon_\gamma = 2.0 \times 10^{-5}$, $n = 3$, $r_t/r_0 = 4$, $x_{\rm min} = 0.3$. Values assume $\delta_{\rm C4} = 1$; for a smaller global tail switch, multiply $\delta\gamma$ by $\delta_{\rm C4}$. The last column shows the maximum fraction of the declared bound; all entries lie below 100%, with the worst case (Mercury perihelion) at 94.7%.

Uncertainty propagation (compact bound). From (256),

$$\frac{\partial \ln p}{\partial \ln x} = -2 - \frac{n\,\alpha x}{1+\alpha x}, \qquad x \in [0.3, 3],\ \alpha = \tfrac{1}{4},\ n = 3.$$

Hence $|\partial \ln p / \partial \ln x| \in [2.21,\ 3.29]$ on the Solar window; a relative radius error $\delta x/x$ induces $|\delta\delta\gamma|/\delta\gamma \lesssim 3.3\,|\delta x/x|$. With orbital elements measured at $\ll 10^{-4}$ precision, the induced uncertainty is negligible at the digits reported above.

Budget compliance (statement). Across $r \in [0.3, 3]\,\mathrm{AU}$, the fixed tail satisfies

$$\max_r |\delta\gamma(r)| = \delta\gamma(r_{\mathrm{Merc,peri}}) = 1.894 \times 10^{-5} \ < \ \varepsilon_\gamma = 2.0 \times 10^{-5}, \qquad \delta\beta(r) = 0 \text{ at } O(U^2).$$

Remark. If the canonical Appendix C.6 budgets $(\varepsilon_\gamma, \varepsilon_\beta) = (4.6, 3.6) \times 10^{-5}$ are adopted instead, all percentages in Table 77 scale down accordingly.

C.8 Variational origin of the tail (replacing convex mix) and physical basis of $\Xi_{\mu\nu}$

Action and operator basis (weak–field, quasi–static sector). We start from the minimal action

$$S = \int d^4x\,\sqrt{-g}\Big[\frac{M_{\mathrm{P}}^2}{2}R \ - \ \frac{1}{2}\nabla_\mu\Phi\nabla^\mu\Phi \ - \ U(\Phi) \ + \ \mathcal{L}_{\mathrm{NL}}\Big] \ + \ S_{\mathrm{m}}[g_{\mu\nu}, \psi], \tag{258}$$

with the lowest–order effective corrections

$$\mathcal{L}_{\mathrm{NL}} = \frac{\alpha}{8\pi G}\,\Phi\,(\nabla\Phi)^2 \ + \ \lambda_\Xi\,\Xi_{\mu\nu}\Xi^{\mu\nu} \ + \ \beta\,(\Box\Phi)^2, \tag{259}$$

where $\Xi_{\mu\nu} \equiv \nabla_\mu\nabla_\nu\Phi - \frac{1}{4}g_{\mu\nu}\Box\Phi$ (cf. Appendix C.4). The self–sourcing channel $\alpha \geq 0$ implements Appendix C.2; $\lambda_\Xi \geq 0$ regularizes higher–order shear. In the quasi–static Solar window we set $\beta = 0$.

Variational taper (exterior boundary enforced at the action level). To *replace* the ad hoc convex mix $\Phi_{\mathrm{mix}} = (1-D)\Phi_{\mathrm{core}} + D\,\Phi_{\mathrm{out}}$, we add a soft exterior penalty that enforces the Newton/GR limit variationally (cf. Appendix C.8.3):

$$\Delta S_\mu \ = \ \frac{\mu}{2}\int d^4x\,\sqrt{-g}\;w(x)\,\big(\Phi - \Phi_{\mathrm{out}}\big)^2, \qquad \Phi_{\mathrm{out}} \equiv \begin{cases} \Phi_{\mathrm{N}} = -GM/r & \text{(weak, static)}, \\ \frac{c^2}{2}\big(g_{tt}^{\mathrm{GR}} + 1\big) & \text{(stationary GR)}. \end{cases} \tag{260}$$

Variation gives the augmented Euler–Lagrange equation

$$\Box_g\Phi - U'(\Phi) \ = \ J_{\mathrm{NL}} \ + \ \mu\,w(x)\,\big(\Phi_{\mathrm{out}} - \Phi\big), \qquad J_{\mathrm{NL}} \ \equiv \ \frac{\partial\mathcal{L}_{\mathrm{NL}}}{\partial\Phi} - \nabla_\mu\left(\frac{\partial\mathcal{L}_{\mathrm{NL}}}{\partial(\nabla_\mu\Phi)}\right), \tag{261}$$

so that $\Phi \to \Phi_{\mathrm{out}}$ where $w \to 1$ (exterior), while the inner equation is unmodified where $w \to 0$.

Zones, matching, and the scale–anchored kernel. Let $\Phi_{\rm core}$ solve (261) with $w=0$ (inner zone), and let $\Phi_{\rm out}$ be the Newton/GR exterior with $w=1$. Define the *scale–anchored* transition

$$D(r) \;=\; 1-\exp\!\big[-(r/r_t)^p\big], \qquad p=2, \qquad r_t \;\equiv\; \sqrt{\sigma_1\sigma_2} \;\approx\; 1.06\,r_0, \tag{262}$$

where (σ_1,σ_2) are the fixed global widths from Section 2.6.2. The composite matched solution (Van Dyke type) is

$$\Phi_{\rm comp}(r) \;=\; \Phi_{\rm core}(r) \;+\; D(r)\,\Big(\Phi_{\rm out}(r)-\Phi_{\rm overlap}(r)\Big), \tag{263}$$

with $\Phi_{\rm overlap}$ the common asymptotic in the intermediate region. Equivalently, one may choose $w(r)=D(r)$ in (260) so that the composite emerges from a single variational problem (cf. Appendix C.8.3). No new tunable constant is introduced: r_t is inherited from the fixed–width policy; $p=2$ is global.

Static spherical equations and stress–energy (isotropic gauge). In isotropic gauge $ds^2 = -A(r)\,dt^2 + C(r)\,dr^2 + r^2 d\Omega^2$ (Appendix C.1), regularity and (261) give

$$\frac{1}{\sqrt{-g}}\partial_r\!\Big(\sqrt{-g}\,g^{rr}\partial_r\Phi\Big) = U'(\Phi) \;-\; \frac{\alpha}{8\pi G}\,g^{rr}\big(\partial_r\Phi\big)^2 \;+\; \mu\,w(r)\,\big(\Phi-\Phi_{\rm out}\big) \;+\; \mathcal{O}(\lambda_\Xi), \tag{264}$$

and for the static scalar the leading anisotropic stress reads

$$T^{(\Phi)t}{}_t = -\rho_\Phi = -\Big(\tfrac{1}{2}C^{-1}\Phi'^2 + U\Big), \qquad\qquad \pi \equiv p_r - p_\perp = C^{-1}\Phi'^2, \tag{265}$$

identical to the baseline up to $\mathcal{O}(\mu\,w)$ terms that vanish in the inner zone.

PPN isotropy and alignment of the tail. At leading 1PN order, an isotropic optical response is ensured if $\pi=\mathcal{O}(U^2)$, implying

$$a_{\rm tail}(r) \;=\; c_{\rm tail}(r) \;+\; \mathcal{O}(U^3) \quad\Rightarrow\quad \delta\gamma=\delta\beta=0 \;\text{ at 1PN}, \tag{266}$$

(cf. Appendix C.6). The $\lambda_\Xi\,\Xi_{\mu\nu}\Xi^{\mu\nu}$ term suppresses Φ''–driven shear and keeps π below 1PN; hence the adopted equality $a_{\rm tail}=c_{\rm tail}$ is *derived*, not a design choice.

Exterior tail shape: Yukawa → Padé, now as a residual. Outside matter and for small (α,λ_Ξ) with $U''(\Phi)\equiv m_\Phi^2$ approximately constant,

$$\Phi'' + \frac{2}{r}\Phi' \;-\; m_\Phi^2\,\Phi \;=\; \mathcal{O}(\alpha\,\Phi'^2,\;\lambda_\Xi\,\Phi^{(3,4)}), \tag{267}$$

whose zeroth–order solution is $\Phi\propto e^{-m_\Phi r}/r$. On the Solar window $x\equiv r/r_0\in[x_{\rm min},3]$ we approximate the induced tail by

$$p(x) \;=\; \frac{C_n}{x^2(1+\alpha_t x)^n}, \qquad C_n=(1+\alpha_t x_{\rm min})^n x_{\rm min}^2, \quad (n,\alpha_t)=(3,\tfrac{1}{4}), \tag{268}$$

which matches the Yukawa value/slope to $\mathcal{O}(\lambda^3)$ and should be read as the *residual* that reconciles boundary matching and the 1PN isotropy constraint under (260).

Monotonicity, positivity, and enclosed mass. With the effective source of Appendix C.2, $\rho_{\rm eff} = \rho + \frac{\alpha}{4\pi G}(\nabla\Phi)^2$, Gauss' law yields $M'_{\rm eff}(r) = 4\pi r^2 \rho_{\rm eff}(r) \geq 0$ for $\alpha \geq 0$ (monotonic enclosed mass). The static scalar sector obeys the weak energy condition and excludes unphysical negative–mass shells in the Solar window.

Boundary conditions and summary of replacements. (i) Asymptotic flatness: $A, C \to 1$, $\Phi \to \Phi_{\rm out}$; (ii) Central regularity: A, C finite, $\Phi' \to 0$; (iii) 1PN isotropy: (266). *Replacement summary:* the convex mix with a constant D is **retired** to the legacy note; the tail is now generated by the variational taper (260) (cf. Appendix C.8.3) with a window/kernel (262) tied to the fixed–width policy, and the composite/matched solution (263). No new tunable degrees of freedom are introduced.

Strong–field continuity (Schwarzschild/Kerr). For a static spherical mass, set $g_{\mu\nu} = g^{\rm Schw}_{\mu\nu}$ and $\Phi_{\rm out} = \frac{c^2}{2}(g^{\rm Schw}_{tt} + 1)$; for slow rotation, promote to Hartle–Thorne/Kerr and keep (260) with $\Box_{g^{\rm Kerr}}$. Then the (R, Θ) invariants (Section 7) remain continuous across $r_{\rm ph}$; the tail induces a small joint shift consistent with $\Theta \simeq A(r_{\rm ph})^{-1/2}$.

C.8.1 Verification loop & acceptance (variational taper + PSCF/MC–CF composite)

Loop (no constant mix, variational taper). (i) Verify the variational field equation (264) and the static stress–energy (265); (ii) check the 1PN isotropy condition (266) ensuring $a_{\rm tail} = c_{\rm tail}$; (iii) represent the PSCF core by the heat–kernel operator (Lemma in Appendix C.8.2) and evaluate the force error on the Solar window $[r_0, 3r_0]$; (iv) form the *composite* field $\Phi_{\rm comp}$ as in (263) with the scale–anchored kernel $D(r) = 1 - \exp[-(r/r_t)^p]$ (defaults p=2, $r_t = \sqrt{\sigma_1\sigma_2} \simeq 1.06\, r_0$) and certify the far–field envelope bound below; (v) enforce the Solar PPN budgets (Section 3.4) with $a_{\rm tail}$=$c_{\rm tail}$ so that $\delta\gamma = \delta\beta = 0$ at 1PN, and audit any 2PN residue.

Bounds (PSCF core). Let ℓ be the PSCF scaffold scale and $y \equiv r/(2\ell)$. For a point mass M,

$$\Phi_{\rm PSCF}(r) = -\frac{GM}{r}\,\mathrm{erf}(y)\,, \qquad F_{\rm PSCF}(r) = -\partial_r \Phi_{\rm PSCF},$$

so relative to $F_N = -GM/r^2$ the dimensionless force error is

$$\epsilon_F(y) \;\equiv\; \frac{|F_{\rm PSCF} - F_N|}{|F_N|} \;=\; \frac{2y}{\sqrt{\pi}}\, e^{-y^2} \;+\; \Big(1 - \mathrm{erf}(y)\Big). \tag{269}$$

Composite (variational taper) error envelope. With the matched composition (263),

$$\Phi_{\rm comp} = \Phi_{\rm core} + D(r)\Big(\Phi_{\rm out} - \Phi_{\rm overlap}\Big), \qquad D(r) = 1 - \exp\big[-(r/r_t)^p\big],$$

its radial force $F_{\rm comp} = -\partial_r \Phi_{\rm comp}$ satisfies the envelope bound

$$\frac{|F_{\rm comp} - F_N|}{|F_N|} \;\leq\; \underbrace{(1 - D(r))\,\epsilon_F\Big(\tfrac{r}{2\ell}\Big)}_{\text{core remainder}} \;+\; \underbrace{|D'(r)|\,\Psi(r)}_{\text{taper remainder}}, \tag{270}$$

where $D'(r) = \frac{p}{r_t}\big(\frac{r}{r_t}\big)^{p-1} e^{-(r/r_t)^p}$ and

$$\Psi(r) \;\equiv\; \frac{|\Phi_{\rm out}(r) - \Phi_{\rm overlap}(r)|}{GM/r} \;\lesssim\; \epsilon_F\Big(\tfrac{r}{2\ell}\Big) \quad \text{on the overlap band.}$$

For the working choice $p{=}2$ a conservative proxy is

$$\frac{|F_{\rm comp}-F_N|}{|F_N|} \;\lesssim\; e^{-(r/r_t)^2}\,\epsilon_F\!\Big(\tfrac{r}{2\ell}\Big) \;+\; \frac{2r}{r_t^2}\,e^{-(r/r_t)^2}\,\epsilon_F\!\Big(\tfrac{r}{2\ell}\Big), \tag{271}$$

i.e., a sum of the PSCF core remainder suppressed by $(1{-}D) = e^{-(r/r_t)^2}$ and a taper term controlled by $D'(r)$.

Leakage control (vacuum consistency). Let $M_{\rm leak}(R)$ denote the effective Gaussian "leakage" mass exterior to radius R. Then

$$\frac{M_{\rm leak}(R)}{M} \;\lesssim\; \left(\frac{R}{2\ell}\right), \tag{272}$$

so taking $R = r_0$ with $\left(\frac{r_0}{2\ell}\right) \le \eta_{\rm leak}$ ensures a negligible exterior source across the benchmark window (Section 2.6.2).

Acceptance criteria (recommended defaults; no constant D). On the Solar window $[r_0, 3r_0]$,

$$\sup_{r\in[r_0,3r_0]}\Big[(1-D(r))\,\epsilon_F\!\Big(\tfrac{r}{2\ell}\Big) \;+\; |D'(r)|\,\epsilon_F\!\Big(\tfrac{r}{2\ell}\Big)\Big] \;\le\; \eta_{\rm far}, \qquad \left(\tfrac{r_0}{2\ell}\right) \;\le\; \eta_{\rm leak}, \tag{273}$$

with defaults $\eta_{\rm far} = 5\times10^{-3}$ and $\eta_{\rm leak} = 10^{-3}$. Kernel parameters are *fixed by policy*, not tuned: $p{=}2$ globally and $r_t = \sqrt{\sigma_1\sigma_2} \simeq 1.06\,r_0$ inherited from the width set (Section 2.6.2).

PPN budgets (no $D^\star$ scaling). Because (266) enforces $a_{\rm tail}{=}c_{\rm tail}$ at 1PN, we have $\delta\gamma = \delta\beta = 0 + \mathcal{O}(U^2)$; the only remaining audit is a small 2PN residue. We therefore *do not* choose or report any constant mixing weight D; instead, we verify that the composite solution with fixed (p, r_t) obeys the Solar PPN budgets (Section 3.4) and the far–field bound (273).

C.8.2 Heat–kernel lemma for PSCF core (closed form)

Lemma (heat–kernel regularization). In $\mathbb{R}^3$, the Newton kernel is $G_N(\mathbf{r}) = -(4\pi|\mathbf{r}|)^{-1}$. For any $\ell > 0$,

$$\big(e^{\ell^2\nabla^2}G_N\big)(r) \;=\; -\frac{1}{4\pi r}\,\operatorname{erf}\!\Big(\frac{r}{2\ell}\Big), \tag{274}$$

so for any compactly supported (or integrable) density ρ,

$$\Phi_{\rm PSCF}(\mathbf{r}) \;=\; -\,G\int_{\mathbb{R}^3}\rho(\mathbf{r}')\,\frac{\operatorname{erf}\!\Big(\frac{|\mathbf{r}-\mathbf{r}'|}{2\ell}\Big)}{|\mathbf{r}-\mathbf{r}'|}\,d^3\mathbf{r}'. \tag{275}$$

As $r\to\infty$, $\operatorname{erf}(r/2\ell)\to 1$ exponentially (asymptotic flatness). On finite windows with $r = O(\ell)$, the force error relative to Newton, defined in (269), applies.

Proof sketch. Let $K_\ell(\mathbf{r}) = \big(4\pi\ell^2\big)^{-3/2}\exp\!\big(-|\mathbf{r}|^2/(4\ell^2)\big)$ be the heat kernel. The semigroup action satisfies $e^{\ell^2\nabla^2}f = K_\ell * f$; hence $e^{\ell^2\nabla^2}G_N = K_\ell * G_N$ is radial. Evaluating the standard radial integral with the change $u = \frac{|\mathbf{r}-\mathbf{r}'|}{2\ell}$ yields (274). In the distributional sense, $\nabla^2 G_N = \delta$, so

$$\nabla^2\big(e^{\ell^2\nabla^2}G_N\big) = e^{\ell^2\nabla^2}(\nabla^2 G_N) = e^{\ell^2\nabla^2}\delta = K_\ell,$$

and the $r\to 0$ behavior is finite, establishing the regularization.

Corollary 1 (point mass; closed forms and error). For $\rho(\mathbf{r}) = M\,\delta^{(3)}(\mathbf{r})$,

$$\Phi_{\mathrm{PSCF}}(r) = -\frac{GM}{r}\,\mathrm{erf}\Big(\frac{r}{2\ell}\Big)\,, \tag{276a}$$

and writing $y \equiv r/(2\ell)$, the inward radial field (magnitude) is

$$g_{\mathrm{PSCF}}(r) \;\equiv\; \big|-\partial_r\Phi_{\mathrm{PSCF}}\big| = \frac{GM}{r^2}\left[\mathrm{erf}(y) \;-\; \frac{2y}{\sqrt{\pi}}\,e^{-y^2}\right]. \tag{276b}$$

Relative to $g_{\mathrm{N}} = GM/r^2$, the dimensionless force error is exactly (269) with $y = r/(2\ell)$. Near the origin, $\mathrm{erf}(y) = \frac{2}{\sqrt{\pi}}y + O(y^3)$ so $\Phi_{\mathrm{PSCF}}(r) = -\frac{GM}{\sqrt{\pi}\,\ell} + O(r^2)$ (finite core). For $r \gg \ell$, $\mathrm{erf}(y) = 1 - \frac{e^{-y^2}}{\sqrt{\pi}y}\big(1 + O(y^{-2})\big)$, giving exponentially small deviations from Newton.

Corollary 2 (general source; differentiation under the integral). For $\rho \in L^1 \cap L^\infty$,

$$\nabla\Phi_{\mathrm{PSCF}}(\mathbf{r}) = G\int \rho(\mathbf{r}')\,\frac{\mathbf{r}-\mathbf{r}'}{|\mathbf{r}-\mathbf{r}'|^3}\left[\mathrm{erf}\left(\frac{|\mathbf{r}-\mathbf{r}'|}{2\ell}\right) - \frac{|\mathbf{r}-\mathbf{r}'|}{\sqrt{\pi}\,\ell}\,e^{-|\mathbf{r}-\mathbf{r}'|^2/(4\ell^2)}\right] d^3\mathbf{r}', \tag{277}$$

which reduces to (276b) for a point mass and preserves Gauss monotonicity as used in Appendix C.8.

C.8.3 Smooth core–tail synthesis (variational taper)

Goal. Replace any *ad hoc* gluing with a variationally justified, C^∞–smooth transition from the PSCF core to the Newtonian tail, while preserving 1PN isotropy ($a_{\mathrm{tail}} = c_{\mathrm{tail}}$) and the exterior $1/r^2$ law (cf. Appendix C.8.1 and (266)).

Penalized action for exterior consistency. Augment (258) by a *soft* exterior constraint that penalizes deviations from the Newton kernel beyond a turnover band $[r_t - \Delta,\, r_t + \Delta]$:

$$S_\mu \;=\; S \;-\; \frac{\mu}{2}\int d^4x\,\sqrt{-g}\;w(r)\left(\Phi + \frac{GM}{r}\right)^2, \qquad \mu > 0, \tag{278}$$

where $w(r)$ is a C^∞ weight taking $w{=}0$ for $r \le r_t - \Delta$, $w{=}1$ for $r \ge r_t + \Delta$, and $0{<}w{<}1$ only in the transition. The Euler–Lagrange equation becomes (cf. (261))

$$\frac{1}{\sqrt{-g}}\partial_r\Big(\sqrt{-g}\,g^{rr}\partial_r\Phi\Big) = \frac{\partial U}{\partial\Phi} - \frac{\alpha}{8\pi G}\,g^{rr}(\partial_r\Phi)^2 + \mu\,w(r)\left(-\frac{GM}{r} - \Phi\right) + \mathcal{O}(\lambda_\Xi, \beta), \tag{279}$$

so the exterior approach to $-GM/r$ is *driven by the variational problem* rather than imposed by hand. As $\mu \to \infty$ one recovers a hard constraint; for finite μ one can balance 1PN budgets and smoothness.

C^∞ taper and composite representation. Using a standard C^∞ bump supported only on the transition band, set

$$\chi(r) \equiv \begin{cases} 1, & r \le r_t - \Delta, \\ \dfrac{\exp\!\big(-\frac{1}{1-\xi^2}\big)}{\exp\!\big(-\frac{1}{1-\xi^2}\big) + \exp\!\big(-\frac{1}{1-(1-\xi)^2}\big)}, & r_t - \Delta < r < r_t + \Delta, \\ 0, & r \ge r_t + \Delta, \end{cases} \qquad \xi = \frac{r - (r_t - \Delta)}{2\Delta} \in (0,1),$$

and define $w(r) = 1 - \chi(r)$ (all derivatives vanish at the band edges). Then the stationary solution of (279) can be written as the fixed point of a contraction mapping:

$$\Phi(r) \;=\; \chi(r)\,\Phi_{\mathrm{PSCF}}(r) \;+\; \big(1-\chi(r)\big)\left(-\frac{GM}{r}\right) \;+\; \mathcal{R}_\mu[\Phi](r), \tag{280}$$

where $\mathcal{R}_\mu[\Phi]$ solves the inhomogeneous *linearized* equation with source $\mu\, w(r)\,(-GM/r - \Phi)$ together with the $\mathcal{O}(\alpha, \lambda_\Xi, \beta)$ corrections. For sufficiently small $(\alpha, \lambda_\Xi, \beta)$ and policy–range μ, $\mathcal{R}_\mu$ is uniformly bounded on $[r_0, 3r_0]$ and vanishes as $\mu \uparrow \infty$. (Compare the D–kernel composite in (263).)

Regularity and 1PN isotropy. By construction, Φ and Φ' are C^∞ across the transition band. Because the synthesis acts in the static sector and $\lambda_\Xi > 0$ penalizes $\Xi_{\mu\nu}\Xi^{\mu\nu}$, the anisotropic stress $\pi = B^{-1}\Phi'^2$ remains $\mathcal{O}(U^2)$; hence

$$a_{\mathrm{tail}}(r) = c_{\mathrm{tail}}(r) + \mathcal{O}(U^3), \qquad \delta\gamma = \delta\beta = 0 \;\text{ at 1PN},$$

as in (266). The smooth synthesis therefore preserves the PPN isotropy enforced in the main text (Section 3.4).

Policy parameters (globally fixed) and selection rule. The transition *scale* is fixed by the global width policy:

$$r_t = \sqrt{\sigma_1\sigma_2} \simeq 1.06\, r_0 \quad (\text{from } \textit{Section } 2.6.2),$$

and the half–width Δ is fixed so that, e.g., $\chi(r_t - \Delta) \approx 1$ and $\chi(r_t + \Delta) \approx 0$ (identical across all objects). The exterior weight μ is chosen as the *minimal* value satisfying the PPN budgets:

$$\mu^\star \;=\; \inf\left\{\mu > 0 : \max_{r\in[r_0,3r_0]} \big(|\delta\gamma_\mu(r)|, |\delta\beta_\mu(r)|\big) \le (\varepsilon_\gamma, \varepsilon_\beta)\right\}, \tag{281}$$

which replaces any *ad hoc* amplitude choice by a *derived* exterior control consistent with conservation and boundary data.

Windowwise residual bound (operational). With $F_{\mathrm{comp}} = -\partial_r\Phi$,

$$\frac{|F_{\mathrm{comp}} - F_N|}{|F_N|} \;\lesssim\; \Big(1-\chi(r)\Big)\,\epsilon_F\!\left(\tfrac{r}{2\ell}\right) \;+\; |\chi'(r)|\,\Upsilon(r) \quad \text{on } [r_0, 3r_0], \tag{282}$$

where the first term is the PSCF core residual from (269), and the second is the transition residual controlled by the C^∞ slope $|\chi'|$. Here $\Upsilon(r)$ is a normalized overlap factor proportional to $|\Phi_{\mathrm{PSCF}} + GM/r|$ in the band and is bounded at the same order as ϵ_F (cf. Appendix C.8.1). With the policy defaults, (282) respects the acceptance criteria (273).

Summary. Equations (278)–(281) furnish a variational, C^∞ construction that (i) matches the Newtonian tail smoothly, (ii) preserves 1PN isotropy, and (iii) avoids nonanalytic "gluing". Residuals are *policy–controlled* by (α, λ_Ξ) and μ.

C.8.4 Convex mix (legacy) and force–bias bounds

Legacy form (for reproducibility). For historical comparisons we record the constant–weight convex composition

$$\Phi_{\rm mix}(r) \;=\; (1-D)\,\Phi_{\rm PSCF}(r) \;+\; D\!\left(-\frac{GM}{r}\right), \qquad 0 \le D \le 1. \tag{283}$$

Windowwise force–bias bound. Let $F_{\rm mix} = -\partial_r \Phi_{\rm mix}$ and $F_N = -GM/r^2$. Since $F_{\rm mix} = (1-D)F_{\rm PSCF} + D\,F_N$, the Newton–relative force error satisfies

$$\frac{|F_{\rm mix} - F_N|}{|F_N|} \;=\; (1-D)\,\frac{|F_{\rm PSCF} - F_N|}{|F_N|} \;\le\; (1-D)\,\epsilon_F\!\left(\tfrac{r}{2\ell}\right), \qquad \epsilon_F \text{ as in (269)}. \tag{284}$$

This bound holds on the Solar window $[r_0, 3r_0]$ used throughout (Section 2.6.2).

Limitations (why legacy). (i) *No variational origin:* the constant D introduces an external glue not derived from the action, unlike the taper in Appendix C.8.3.
(ii) *Central regularity:* unless $D{=}0$, $\Phi_{\rm mix} \sim -D\,GM/r$ as $r \to 0$, which spoils the finite PSCF core (cf. boundary conditions in Appendix C.8).
(iii) *Uncontrolled slope:* the transition has no scale–anchored kernel (contrast with $D(r)$ in (263)), so overlap residuals are not minimized by construction.
(iv) *Budgets externalized:* compliance with the Solar acceptance criterion (273) and the 1PN isotropy check (266) must be verified a posteriori.

Status and recommendation. The convex mix (283) and bound (284) are kept only for *quick benchmarking and reproducibility*. For theoretical development and production results, use the *variational taper synthesis* in Appendix C.8.3 with globally fixed policy parameters and no constant D.

Appendix D: Thermodynamic Analogy

This appendix outlines the correspondence between curvature–field collapse and the basic laws of thermodynamics under the *fixed–policy* regime. The core idea is an *energy–entropy mapping* that links (i) the field's energy budget to (ii) an entropy analogue, providing physical intuition for the C4 formulation and a bridge to observables.

Scope and guardrails.

- **Policy consistency.** Global thresholds (e.g., ε) and constants follow Section 2.6.2. *No new tunable parameters* are introduced here.
- **Metric separation.** The full–profile *Concordance* metric is used exactly as defined in Section 2.2; CI (central–intensity) values follow the project's SSOT policy table under Section 2.6.2 and are *not* mixed with full–profile metrics.
- **Dynamical grounding.** Self–sourcing and tail alignment obey the variational structure summarized in appendix:C.2 and Appendix C.8.

Correspondence map (First–Law analogue). With the quasi–static energy density

$$u_\Phi \;=\; \tfrac{1}{2}\,|\nabla\Phi|^2 \;+\; U(\Phi), \qquad E_\Phi \;=\; \int u_\Phi \, dV,$$

we write the effective budget as

$$dE_\Phi \;=\; \delta Q_\Phi \;-\; \delta W_\Phi.$$

External excitation (boundary/source driving) corresponds to "heat" δQ_Φ, while geometric rearrangement during collapse/spreading corresponds to "work" δW_Φ. The self–sourcing channel (appendix:C.2) provides an *internal work* pathway, explaining collapse even with minimal external excitation.

Choice of entropy analogue (Second–Law flavour). To employ a positive, normalized density, we use the amplitude rule of Section 4,

$$A^2(\mathbf{x}) \;=\; \exp\!\big(-\alpha\,|\nabla\Phi(\mathbf{x})|^2\big),$$

with fixed equal–penalty correction for α, and define

$$p_A(\mathbf{x}) \;=\; \frac{A^2(\mathbf{x})}{\int A^2 dV}, \qquad S_A \;=\; -\int p_A \ln p_A \, dV.$$

As a robust alternative, one may use the gradient–energy distribution $p_g \propto |\nabla\Phi|^2$ with $S_g = -\int p_g \ln p_g \, dV$; both show the same monotonic trend under collapse.

Physical reading. Near the critical gradient, if external driving is insufficient, the energy budget closes via the *internal* work route and the entropy analogue (S_A or S_g) increases monotonically. This is consistent with the variational taper enforcing the Newton/GR exterior (appendix:C.8), while preserving 1PN isotropy (appendix:C8.3; see also Section 3.4).

Policy note. All statements in this appendix adhere to the "data–only, fixed–policy" setup of Section 2.6.2. References to observables (e.g., $I(0)$ and SSOT mapping usage) follow the project's policy table specified in Section 2.6.2. No extra degrees of freedom are introduced beyond the constants and kernels already defined in appendix:C.8.

D.1 Collapse Condition and the First Law

The collapse condition of the curvature field is characterized by a critical gradient:

$$|\nabla\Phi| \;<\; \varepsilon, \qquad \varepsilon = 0.050 \pm 0.002, \tag{285}$$

consistent with the critical band adopted under the global fixed–constant policy (Section 2.6.2).

By analogy with the First Law of Thermodynamics,

$$dU \;=\; \delta Q - \delta W,$$

we set the correspondence (here U denotes the field's *internal energy*, not the potential $U(\Phi)$ in the action):

- Internal energy $U \;\leftrightarrow\;$ curvature–field energy density $\frac{1}{2}\,|\nabla\Phi|^2$ (optionally $+\;U(\Phi)$ depending on the baseline convention),
- Heat input $\delta Q \;\leftrightarrow\;$ external perturbations acting as phase excitation,
- Work $\delta W \;\leftrightarrow\;$ geometric deformation via collapse and spreading of the field.

Extended interpretation.

1. **Energy balance check.** Tracking U_Φ across the collapse shows that when δQ is insufficient, the process proceeds by compensating the deficit through work δW. The threshold (285) thus marks not merely a numerical bound but the breakdown of the effective energy balance.
2. **Newtonian consistency.** In the weak–field regime ($|\nabla\Phi| \gg \varepsilon$), δW is negligible and δQ acts as the local driver, leaving dU approximately conserved. The First–Law correspondence therefore remains intact in the Newton–Poisson limit.
3. **Nonlinear correction.** In the presence of the self–sourcing channel $\mathcal{J}[\Phi]$ (Appendix C.2), dU depends not only on external perturbations but also on intrinsic curvature stress. This motivates an "internal work" pathway, explaining the spontaneity of collapse events.

In this view, the condition (285) defines a *threshold* at which the energy–exchange balance fails and the system can no longer sustain its previous geometric configuration. The transition is not a mere mathematical instability but a redistribution of energy consistent with the First Law. No new tunable parameters are introduced (policy consistency per Section 2.6.2).

D.2 Entropy Analogy and the Second Law

The Second Law of Thermodynamics requires that entropy in a closed system never decreases:

$$\Delta S \;\geq\; 0.$$

In the curvature–field framework, local phase mixing and collapse are inherently irreversible. To obtain a *well–defined (positive, normalized)* entropy analogue, we adopt the amplitude rule of Section 4:

$$A^2(\mathbf{x}) \;=\; \exp\!\big(-\alpha\,|\nabla\Phi(\mathbf{x})|^2\big),$$

with the fixed equal–penalty correction for α (policy constant; no tuning). Normalizing to a probability density,

$$p_A(\mathbf{x}) \;=\; \frac{A^2(\mathbf{x})}{\displaystyle\int A^2\,dV}, \qquad S_A \;\equiv\; -\int p_A(\mathbf{x})\,\ln p_A(\mathbf{x})\,dV. \tag{286}$$

As a robust alternative, the gradient–energy distribution

$$p_g(\mathbf{x}) \;=\; \frac{|\nabla\Phi(\mathbf{x})|^2}{\displaystyle\int |\nabla\Phi|^2\,dV}, \qquad S_g \;\equiv\; -\int p_g(\mathbf{x})\,\ln p_g(\mathbf{x})\,dV \tag{287}$$

may be used; both definitions exhibit the same monotonic trend under collapse. (These choices avoid sign/positivity issues that arise with unnormalized functionals like $-\int \Phi\ln\Phi\,dV$.)

Interpretation.

1. **Irreversibility.** As collapse drives $|\nabla\Phi|\to 0$, p_A (or p_g) flattens and S_A (or S_g) increases monotonically or saturates, aligning with the entropic arrow of time.
2. **Connection to observables.** The decay of central intensity $I(0)$ in interference/collapse experiments is a direct signature of entropy growth. Under the project's fixed–policy mapping (Section 2.6.2), loss of $I(0)$ corresponds to reduced phase coherence consistent with rising S_A.
3. **Scaling behavior.** For Gaussian–like fields, S_A scales with the effective width of Φ: broader profiles carry larger entropy (greater delocalization), while localized collapsed states approach a high–entropy saturation.

Consistency checks.

- **Weak–field regime.** Fluctuations are small and S_A changes slowly, consistent with near–reversible Newton–Poisson dynamics.
- **Strong–field/collapse regime.** S_A grows rapidly and the inequality $\Delta S_A \geq 0$ holds strictly.
- **Policy alignment.** The construction respects the global fixed–constant policy (Section 2.6.2): entropy growth tracks irreversible suppression of $I(0)$ and cannot be undone by local perturbations alone.

Altogether, S_A (or S_g) provides a thermodynamic analogue of curvature–field collapse: it quantifies irreversibility, connects microscopic phase mixing to macroscopic observables, and aligns the collapse threshold with the universal content of the Second Law—without introducing any new tunable parameters.

D.3 Combined Energy–Entropy Picture

In summary, curvature–field collapse satisfies the two universal laws of thermodynamics simultaneously. First, the energy budget is

$$dU_\Phi \;=\; \delta Q_\Phi \;-\; \delta W_\Phi, \tag{288}$$

which states that changes in the field's internal energy are governed by the competition between external phase excitation (δQ_Φ) and the geometric work associated with collapse and spreading (δW_Φ). At the same time, the entropy analogue adopted in Appendix D.2 obeys

$$\Delta S_A \;\geq\; 0, \tag{289}$$

reflecting irreversible growth.

Extended interpretation.

1. **Energy–entropy coupling.** Equations (288) and (289) show that the collapse threshold is not a mere mathematical instability but the simultaneous enforcement of energy conservation and entropy irreversibility. When the energy exchange can no longer balance, collapse is triggered, and its outcome is invariably aligned with entropy increase.
2. **Dynamical pathway.** As $|\nabla\Phi|$ falls below the critical value ε, part of the internal energy is converted into geometric work (δW_Φ), while the remaining degrees of freedom mix into a rise of S_A. Collapse thus proceeds as a coupled redistribution of energy and a monotonic growth of entropy (see Appendix D.1 and Appendix D.2).
3. **Observable correspondence.** The decay of the central intensity $I(0)$ is an experimental signature of (289), consistent with the global fixed–constant policy (Section 2.6.2). In practice, collapse appears as a laboratory–accessible form of entropy growth.

Consistency checks.

- **Weak–field regime.** When $|\nabla\Phi| \gg \varepsilon$, dU_Φ is nearly conserved and $\Delta S_A \simeq 0$, consistent with Newton–Poisson dynamics.
- **Strong–field/collapse regime.** When $|\nabla\Phi| \lesssim \varepsilon$, dU_Φ decreases and $\Delta S_A > 0$ holds strictly, consistent with deviations in strong–gravity observables to be analyzed later.
- **PSCF vs. MC–CF.** The linear scaffold of PSCF tends to underestimate the coupling between dU_Φ and ΔS_A, whereas the nonlinear self–sourcing in MC–CF restores a more realistic energy–entropy pathway.

Altogether, the collapse threshold is a natural meeting point of the First and Second Laws. It places curvature–field dynamics on a continuous spectrum where the fading of microscopic interference and the steadiness of macroscopic spacetime share a common story: the system quietly rearranges itself toward shapes of lesser resistance, leaving behind, almost matter–of–factly, the trace we call entropy.

Appendix E: Mathematical Identities and Operators

This appendix collects the mathematical operators and identities most frequently used in the curvature–field formulation. They underpin the definitions of $\Box\Phi$, $\Xi_{\mu\nu}$, and related expressions, and we note their range of validity, subtleties in strong–field regimes, and their role in the variational construction.

Conventions. We use signature $(-,+,+,+)$, covariant derivatives compatible with the metric ($\nabla_\rho g_{\mu\nu} = 0$), and $d = 4$ unless stated otherwise. The isotropic gauge used in static problems is defined in appendix C.1.

E.1 Differential Operators

- **Covariant derivative and divergence.** For a covector V_ν,

$$\nabla_\mu V_\nu \;=\; \partial_\mu V_\nu - \Gamma^\rho_{\mu\nu} V_\rho,$$

with $\Gamma^\rho_{\mu\nu}$ the Christoffel symbols of $g_{\mu\nu}$. Metric compatibility implies

$$\nabla_\mu V^\mu \;=\; \frac{1}{\sqrt{-g}}\,\partial_\mu\big(\sqrt{-g}\,V^\mu\big).$$

Weak–field note: in $g_{\mu\nu} = \eta_{\mu\nu} + h_{\mu\nu}$, Christoffel terms are $\mathcal{O}(h)$ corrections to flat derivatives.

- **d'Alembertian (wave/Laplace–Beltrami) on a scalar.**

$$\Box\Phi \;\equiv\; g^{\mu\nu}\nabla_\mu\nabla_\nu\Phi \;=\; \frac{1}{\sqrt{-g}}\,\partial_\mu\big(\sqrt{-g}\,g^{\mu\nu}\partial_\nu\Phi\big).$$

In Minkowski space, $g_{\mu\nu} = \mathrm{diag}(-1,1,1,1)$, this reduces to

$$\Box\Phi \;=\; -\partial_t^2\Phi + \nabla^2\Phi.$$

Interpretation: $\Box\Phi$ supplies the kinetic operator in the action and controls propagation/diffusion. *Caveat:* curvature enters implicitly through $g_{\mu\nu}$; $\Box\Phi = 0$ does not guarantee free waves unless curvature couplings are negligible.

- **Traceless projection and $\Xi_{\mu\nu}$.** For a symmetric rank–2 tensor $T_{\mu\nu}$ in d dimensions,

$$T^{(\mathrm{TL})}_{\mu\nu} \;=\; T_{\mu\nu} - \frac{1}{d}\,g_{\mu\nu}\,T^\rho{}_\rho,$$

so in $d{=}4$ the trace–removal factor is $1/4$. The auxiliary shear

$$\Xi_{\mu\nu} \;\equiv\; \nabla_\mu\nabla_\nu\Phi - \tfrac{1}{4}\,g_{\mu\nu}\,\Box\Phi$$

is precisely the traceless projection of $\nabla_\mu\nabla_\nu\Phi$; its role and variational control are discussed in appendix C.8.

- **Commutator of covariant derivatives (for context).** For a vector V^ρ,

$$\big[\nabla_\mu,\nabla_\nu\big]V^\rho \;=\; R^\rho{}_{\sigma\mu\nu}\,V^\sigma,$$

while for a scalar Φ, $\big[\nabla_\mu,\nabla_\nu\big]\Phi = 0$. *Implication:* higher–order operators acting on tensors can pick up curvature terms that are absent for scalars; this matters for strong–field tails and anisotropic stresses.

Critical remarks.

1. **Consistency in weak fields.** Each operator reduces smoothly to its flat–space analogue, ensuring agreement with Newton–Poisson and standard wave dynamics.
2. **Ambiguity in strong fields.** Although scalars commute under covariant differentiation, vector/tensor sectors do not; curvature feedback can enter composite quantities (e.g., via $R_{\mu\nu}$) and modify tail behavior or effective stresses.
3. **Variational role.** $\Box$, ∇, and the traceless projector are the natural building blocks of the action; careful integration by parts (see Appendix E.2) isolates boundary terms and fixes signs, which is essential for the penalties and taper used in Appendix C.8.

E.2 Integration by Parts

The integration–by–parts identity is central to the variational formulation of the curvature field. In particular, terms containing $\Box\Phi$ split naturally into bulk and boundary contributions, making explicit the kinetic and surface terms.

Basic identity. For scalar fields Φ, Ψ on a domain V with boundary ∂V,

$$\int_V \Psi\,\Box\Phi\,\sqrt{-g}\,d^4x = -\int_V g^{\mu\nu}\,(\nabla_\mu\Psi)(\nabla_\nu\Phi)\,\sqrt{-g}\,d^4x + \int_{\partial V} \Psi\,n^\mu\nabla_\mu\Phi\,d\Sigma,$$

where n^μ is the outward unit normal to ∂V and $d\Sigma$ is the induced boundary measure. The first term is the kinetic contribution from gradient contractions; the second is the surface term.

Extended interpretation.

1. **Link to variational principles.** When varying an action that contains $\Box\Phi$, this identity ensures that bulk terms yield the equations of motion while boundary terms encode additional conditions. Thus the choice of boundary conditions directly shapes the physical meaning of Φ.
2. **Role of boundary conditions.** Under Dirichlet (absorbing) or Neumann (reflecting) conditions, the surface term either vanishes or acquires a specific physical role. This aligns with the global fixed–constant policy (Section 2.6.2), which enforces dataset–independent consistency.
3. **Weak vs. strong fields.** In weak fields, boundary fluxes are negligible; near strong–gravity structures (e.g., the photon sphere) the surface term can influence observables (R, Θ) directly; see tail diagnostics in Appendix C.3.
4. **Generalization.** Similar bulk–boundary decompositions apply to vectors and tensors. For instance, divergences like $\nabla_\mu V^\mu$ split in the same way and are closely tied to the construction of the auxiliary tensor $\Xi_{\mu\nu}$ (Appendix C.4).

Critical remark. Integration by parts is not merely a calculational trick; it encodes the idea that *information balance is decided at the boundary*. While bulk dynamics conserve energy, irreversibility and collapse appear as fluxes through the surface, so the boundary term functions as a physical "window," not a negligible artifact.

Lemma (Palatini identity with boundary current). For metric variations with compact support (or with $g_{\mu\nu}$ fixed on ∂V),

$$\delta\big(\sqrt{-g}\,R\big) = \sqrt{-g}\,\Big(G_{\mu\nu}\,\delta g^{\mu\nu} + \nabla_\mu V^\mu\Big), \qquad V^\mu \equiv g^{\alpha\beta}\,\delta\Gamma^{\ \mu}_{\alpha\beta} - g^{\mu\alpha}\,\delta\Gamma^{\ \beta}_{\alpha\beta}. \tag{290}$$

Hence,

$$\delta\int_V \sqrt{-g}\,R\,d^4x = \int_V \sqrt{-g}\,G_{\mu\nu}\,\delta g^{\mu\nu}\,d^4x + \int_{\partial V} n_\mu V^\mu\,d\Sigma.$$

Equivalently, adding the Gibbons–Hawking–York boundary term

$$S_{\rm GHY} = \frac{c^4}{8\pi G}\int_{\partial V}\sqrt{|h|}\,K\,d^3x$$

renders the variational problem well posed under free metric variations on the boundary. This boundary handling, together with penalty/taper mechanisms, underpins the variational constructions used in Appendix C.8.

E.3 Variational Identities

Variational identities play a central role in deriving the curvature–field equations and in fixing boundary conditions. For an action of the form

$$S[\Phi] \;=\; \int \mathcal{L}(\Phi,\nabla\Phi)\,\sqrt{-g}\,d^4x,$$

the variation with respect to an arbitrary perturbation $\delta\Phi$ yields

$$\delta S \;=\; \int_V\left(\frac{\partial\mathcal{L}}{\partial\Phi} - \nabla_\mu\frac{\partial\mathcal{L}}{\partial(\nabla_\mu\Phi)}\right)\delta\Phi\,\sqrt{-g}\,d^4x \;+\; \int_{\partial V} n_\mu\frac{\partial\mathcal{L}}{\partial(\nabla_\mu\Phi)}\,\delta\Phi\,d\Sigma.$$

Hence the Euler–Lagrange operator for Φ is

$$\mathcal{E}[\Phi] \;=\; \frac{\partial\mathcal{L}}{\partial\Phi} - \nabla_\mu\frac{\partial\mathcal{L}}{\partial(\nabla_\mu\Phi)}.$$

Extended interpretation.

1. **Bulk vs. boundary.** The volume term generates the dynamical field equation, while the boundary term prescribes conditions on ∂V. Under Dirichlet conditions ($\delta\Phi|_{\partial V}{=}0$) the surface term vanishes; under Neumann/Robin conditions it fixes physical fluxes.
2. **Specificity to the curvature field.** In PCFE, $\mathcal{L}$ may be $\frac{1}{2}(\nabla\Phi)^2 - U(\Phi)$ or include a self–sourcing channel $\alpha(\nabla\Phi)^2$ (see Appendix C.2). The tensor $\partial\mathcal{L}/\partial(\nabla_\mu\Phi)$ directly encodes stress–energy flow.
3. **Strong–field consistency.** In strong gravity, non-commutativity of covariant derivatives on tensors and background curvature can enter divergence terms; the variational identity makes the coupling between Φ and geometry explicit (cf. Appendix C.1).
4. **Metric sensitivity.** The factor $\sqrt{-g}$ shows that even a scalar's variations are geometry-aware; Φ is a dynamical variable mediated by the metric background.

Critical remark. The variational identity is not merely technical: it indicates when the curvature field admits *stable* solutions and how these hinge on boundary prescriptions. The surface term implies that physical solutions are shaped not only by local PDEs in the bulk but also by global constraints set at the boundary (see Appendix E.2).

Lemma (Noether identity from diffeomorphism invariance). Consider

$$S_{\rm tot} = \frac{c^4}{16\pi G}\int \sqrt{-g}\, R\, d^4x + \int \sqrt{-g}\left[\tfrac{1}{2}g^{\mu\nu}\nabla_\mu\Phi\nabla_\nu\Phi - U(\Phi)\right] d^4x + S_{\rm m}[g,\Psi_{\rm m}] + \int \sqrt{-g}\, J\,\Phi\, d^4x.$$

Under an infinitesimal diffeomorphism generated by ξ^ν,

$$\delta_\xi g_{\mu\nu} = \nabla_\mu\xi_\nu + \nabla_\nu\xi_\mu, \qquad \delta_\xi\Phi = \xi^\rho\nabla_\rho\Phi.$$

Diffeomorphism invariance implies $\delta_\xi S_{\rm tot} = 0$. Using (290) from Appendix E.2 and the scalar variation,

$$0 = \delta_\xi S_{\rm tot} = \int \sqrt{-g}\left[\left(\tfrac{c^4}{16\pi G}G_{\mu\nu} - \tfrac{1}{2}T^{\rm tot}_{\mu\nu}\right)(\nabla^\mu\xi^\nu + \nabla^\nu\xi^\mu) + \mathcal{E}[\Phi]\,\xi^\rho\nabla_\rho\Phi\right] d^4x,$$

where $T^{\rm tot}_{\mu\nu} = T^{\rm m}_{\mu\nu} + T^{\Phi}_{\mu\nu}$ with

$$T^{\Phi}_{\mu\nu} = \nabla_\mu\Phi\,\nabla_\nu\Phi - \tfrac{1}{2}g_{\mu\nu}(\nabla\Phi)^2 + g_{\mu\nu}U(\Phi), \qquad \mathcal{E}[\Phi] = \Box\Phi - U'(\Phi) - J.$$

Integrating by parts (compact support for ξ^μ or $\xi^\mu|_{\partial V} = 0$) and using index symmetry,

$$0 = -\int \sqrt{-g}\left[\nabla_\mu\left(\tfrac{c^4}{8\pi G}G^{\mu\nu} - T^{{\rm tot}\,\mu\nu}\right)\xi_\nu - \mathcal{E}[\Phi]\,\nabla^\nu\Phi\,\xi_\nu\right] d^4x.$$

Since ξ_ν is arbitrary, we obtain the off–shell Noether identity

$$\nabla_\mu\left(\tfrac{c^4}{8\pi G}G^{\mu\nu} - T^{{\rm tot}\,\mu\nu}\right) = -\,\mathcal{E}[\Phi]\,\nabla^\nu\Phi. \tag{291}$$

Corollary (covariant conservation on shell). On the field equations $G_{\mu\nu} = \frac{8\pi G}{c^4}T^{\rm tot}_{\mu\nu}$ and $\mathcal{E}[\Phi] = 0$, the contracted Bianchi identity $\nabla_\mu G^{\mu\nu} = 0$ together with (291) yields

$$\nabla_\mu T^{{\rm tot}\,\mu\nu} = 0.$$

This closes the chain *action* $\to$ *Euler–Lagrange* $\to$ *Bianchi* $\to$ *conservation*, which is the variational backbone of the curvature–field formulation.

E.4 Commutation of Covariant Derivatives

The commutation of covariant derivatives depends on the field type (scalar, vector, tensor) and exposes how background curvature enters composite operators used throughout this work (cf. Appendix E.1).

Scalar fields. For any scalar Φ,

$$[\nabla_\mu,\nabla_\nu]\Phi \;=\; 0, \qquad \nabla_\mu\nabla_\nu\Phi \;=\; \nabla_\nu\nabla_\mu\Phi.$$

Thus, second derivatives of a scalar commute. Nonetheless, when *further* derivatives act on these second derivatives (e.g., on $\nabla_\alpha\Phi$ or on the Hessian), curvature reappears through the commutators below.

Vector and tensor fields. For a vector V^ρ and a covector W_ρ,

$$[\nabla_\mu, \nabla_\nu]V^\rho \;=\; R^\rho{}_{\sigma\mu\nu}\, V^\sigma, \qquad [\nabla_\mu, \nabla_\nu]W_\rho \;=\; -\,R^\sigma{}_{\rho\mu\nu}\, W_\sigma,$$

and for a general tensor, the Riemann tensor acts on each index in the standard way.

Useful scalar–derived identities. Even though $[\nabla_\mu, \nabla_\nu]\Phi = 0$, curvature enters when commuting derivatives acting on *derived* objects:

$$[\nabla_\mu, \nabla_\nu]\big(\nabla_\rho\Phi\big) = R_{\rho\sigma\mu\nu}\,\nabla^\sigma\Phi, \tag{292}$$

$$\nabla_\mu\Box\Phi \;-\; \Box(\nabla_\mu\Phi) = R_\mu{}^\nu\,\nabla_\nu\Phi. \tag{293}$$

For the traceless Hessian (shear)

$$\Xi_{\mu\nu} \;\equiv\; \nabla_\mu\nabla_\nu\Phi - \tfrac{1}{4}g_{\mu\nu}\Box\Phi,$$

the divergence obeys

$$\nabla^\mu\Xi_{\mu\nu} \;=\; \tfrac{3}{4}\,\nabla_\nu\Box\Phi \;+\; R_\nu{}^\rho\,\nabla_\rho\Phi, \tag{294}$$

which makes the curvature feedback explicit (compare the variational control of $\Xi_{\mu\nu}$ in Appendix C.8).

Extended interpretation.

1. **Link to the curvature field.** Because Φ is a scalar, its Hessian is symmetric and free of direct commutator terms; however, (292)–(294) show that once gradients, divergences, or Laplacians act, curvature couples back through $R_{\mu\nu}$ and $R_{\mu\nu\rho}{}^\sigma$. This matters for tail control and for the shear penalty used in Appendix C.8.
2. **Strong–field relevance.** Near high–curvature regions (e.g., photon spheres) the non–commutativity encoded by $R_{\mu\nu\rho}{}^\sigma$ affects composite observables and envelope bounds; see also boundary decompositions in Appendix E.2.
3. **Disentangling geometries.** The commutation laws separate effects due to the scalar's induced "curvature" (via its stress) from the ambient GR curvature: Riemann/Ricci terms are purely geometric, while Φ enters only through its derivatives.

Critical remark. Non–commutativity of covariant derivatives is not a mere artifact: it states that no coordinate patch can flatten curvature away. Hence, although Φ is a scalar, tensorial constructs derived from it (Hessian, shear, currents) inevitably inherit curvature constraints. In practice, this explains the sensitivity of tail effects and the diagnostics (R, Θ) in strong gravity, and motivates the variational safeguards adopted elsewhere (cf. Appendix C.8).

E.5 Summary

The results of Appendix E may be synthesized as follows. Each operator and identity is more than a formal definition: it underwrites consistency, boundary control, and predictivity in the curvature–field framework.

- **Covariant d'Alembertian $\Box\Phi$ (see Appendix E.1).** It is the principal kinetic operator. In the weak–field limit it reduces to the Minkowski wave operator, ensuring Newton–Poisson consistency. In strong fields, $\Box\Phi = \frac{1}{\sqrt{-g}}\partial_\mu(\sqrt{-g}\, g^{\mu\nu}\partial_\nu\Phi)$ couples implicitly to curvature and becomes boundary–sensitive, which explains the persistence and shaping of tail effects.
- **Auxiliary tensor $\Xi_{\mu\nu}$ (see Appendix E.1).** Defined by the traceless projection $\Xi_{\mu\nu} = \nabla_\mu\nabla_\nu\Phi - \frac{1}{4}g_{\mu\nu}\Box\Phi$, it isolates anisotropic stresses of the scalar sector. Small $\Xi_{\mu\nu}$ signals near–isotropic, stable configurations; large $\Xi_{\mu\nu}$ diagnoses strong local curvature stress. Its variational control via the shear penalty $\lambda_\Xi\,\Xi_{\mu\nu}\Xi^{\mu\nu}$ ties microscopic anisotropy to macroscopic observables (R, Θ) (cf. Appendix C.8).
- **Integration by parts and variational identities (see Appendix E.2, Appendix E.3).** They embed $\Box\Phi$ and $\Xi_{\mu\nu}$ consistently into the action and cleanly split bulk (dynamical) from boundary (constraint/flux) terms, fixing when solutions are well posed under Dirichlet/Neumann/Robin data. Physically, irreversibility and collapse are often encoded in boundary fluxes rather than bulk terms alone.
- **Commutation of covariant derivatives (see Appendix E.4).** While $[\nabla_\mu, \nabla_\nu]\Phi{=}0$ for scalars, curvature reenters when commuting derivatives on $\nabla\Phi$ or on the Hessian, e.g. $\nabla_\mu\Box\Phi - \Box(\nabla_\mu\Phi) = R_\mu{}^\nu\nabla_\nu\Phi$. These identities quantify how background geometry constrains scalar–derived tensors and thus the tail and shear budgets.

Extended reflection. Together, these operators and identities provide the mathematical backbone of C4. They guarantee that (i) weak–field dynamics reproduce Newton–Poisson behavior; (ii) strong–field dynamics inherit curvature–induced corrections consistent with GR observables; and (iii) boundary prescriptions, through the variational split, govern the passage between reversible and irreversible regimes. In short, the formal consistency of $\Box\Phi$, $\Xi_{\mu\nu}$, and their variational scaffolding is not ornamental—it is what lets the framework turn local calculus into reliable global physics under the fixed–policy assumptions, without introducing new tunable parameters.

E.6 Noether–Bianchi Identity: Operational Statement and Diagnostics

Theorem (Noether–Bianchi conservation). Let $S_{\rm tot}[g, \Phi, \Psi_{\rm m}]$ be diffeomorphism–invariant and well posed under either (i) a fixed boundary metric on ∂V or (ii) inclusion of the Gibbons–Hawking–York term. Define $T^{\rm tot}_{\mu\nu} = T^{\rm m}_{\mu\nu} + T^{\Phi}_{\mu\nu}$ and the scalar Euler–Lagrange operator $\mathcal{E}[\Phi] = \Box\Phi - U'(\Phi) - J$. Then the off–shell identity

$$\nabla_\mu\Big(\tfrac{c^4}{8\pi G}G^{\mu\nu} - T^{{\rm tot}\,\mu\nu}\Big) = -\,\mathcal{E}[\Phi]\,\nabla^\nu\Phi \tag{295}$$

holds (cf. Lemma (291)). Using $\nabla_\mu G^{\mu\nu} = 0$ (contracted Bianchi), one obtains the balance law

$$\nabla_\mu T^{{\rm tot}\,\mu\nu} \;=\; -\,\mathcal{E}[\Phi]\,\nabla^\nu\Phi. \tag{296}$$

In particular, *on shell* ($\mathcal{E}[\Phi] = 0$ and $G_{\mu\nu} = \frac{8\pi G}{c^4}T^{\rm tot}_{\mu\nu}$),

$$\nabla_\mu T^{{\rm tot}\,\mu\nu} = 0.$$

Sketch of proof. Combine the Palatini identity with boundary current (Appendix E.2) and the scalar–field variational identity (Appendix E.3); apply an infinitesimal diffeomorphism, integrate by parts (compact support or vanishing boundary variations), and use index symmetry. The Bianchi identity then converts (295) into (296).

Corollaries and scope.

1. **Source sector $J\Phi$.** If J is metric–independent, it does not contribute to $T^{\Phi}_{\mu\nu}$; any mismatch appears only through $\mathcal{E}[\Phi]$ in (296).
2. **Non–minimal couplings.** For extensions such as $Z(\Phi)R$ or derivative couplings, the identity still holds with the Hilbert stress tensor replaced by the appropriate (Belinfante–Rosenfeld improved) tensor; on–shell conservation remains valid once the modified field equations are imposed.
3. **Regularity.** The result requires $g_{\mu\nu} \in C^2$ and $\Phi \in H^2_{\mathrm{loc}}$ so that covariant derivatives and boundary traces are well defined.

Consistency audit (operational). To certify conservation in practice:

1. **Bulk check.** Define the residual
$$\mathcal{R}^{\nu} \;\equiv\; \nabla_{\mu} T^{\mathrm{tot}\,\mu\nu} + \mathcal{E}[\Phi]\,\nabla^{\nu}\Phi.$$
A correct implementation satisfies $\|\mathcal{R}\|_{L^2(V)} \approx 0$ up to numerical tolerance.
2. **Boundary check.** Verify that either (a) the boundary metric is fixed so the Palatini surface term vanishes, or (b) the GHY term is included. Numerically confirm
$$\int_{\partial V} n_{\mu} V^{\mu}\, d\Sigma \;=\; 0$$
within tolerance (see Appendix E.2 for V^{μ}).
3. **Gauge hygiene.** Work in a stated gauge (e.g., isotropic) and sanity–check in a second gauge; the bulk residual norm should be invariant up to $\mathcal{O}(h^2)$ coordinate effects in the weak–field regime.

Failure modes (diagnostic cues). If $\nabla_{\mu} T^{\mathrm{tot}\,\mu\nu} \neq 0$:

1. **Boundary leakage.** Missing GHY term or inconsistent boundary data (non–vanishing $\int_{\partial V} n_{\mu} V^{\mu} d\Sigma$).
2. **Off–shell operation.** Nonzero $\mathcal{E}[\Phi]$ due to truncated dynamics, coarse discretization, or inconsistent J.
3. **Tensor drift.** Using a non–Hilbert stress tensor while varying the Einstein–Hilbert action (or vice versa).
4. **Regularity/gauge issues.** Insufficient differentiability of $g_{\mu\nu}$ or gauge–dependent discretization artifacts.

Discrete implementation note. In finite–volume/finite–element settings, (296) becomes a discrete divergence theorem. Cell–wise fluxes of $T^{\rm tot}$ must cancel up to round–off and time–integration error, and the discrete boundary term must reproduce the chosen continuum boundary condition (Dirichlet/Neumann or GHY).

One–line summary. With a diffeomorphism–invariant total action and controlled boundary terms,

$$\nabla_\mu G^{\mu\nu} = 0 \quad \Longrightarrow \quad \nabla_\mu T^{\mathrm{tot}\,\mu\nu} = 0 \quad \text{on shell},$$

so any apparent non–conservation traces back to boundary flux or to operating off the field equations—signals that are as diagnostic as they are corrective.

E.7 Operating Domains and Component Contributions (PSCF/MC–CF/Tail)

Definitions (legacy mix vs. variational taper). *Legacy constant–weight mix (for reproducibility).*

$$\Phi_{\rm mix}(r) \;=\; (1-D)\,\Phi_{\rm PSCF}(r) \;+\; D\!\left(-\frac{GM}{r}\right) \;+\; \Phi_{\rm MC}(r), \qquad 0 \le D \le 1, \tag{297}$$

where $\Phi_{\rm PSCF}$ is the Gaussian core, $-GM/r$ the exact exterior potential, and $\Phi_{\rm MC}$ the mass–centered (MC–CF) shells. *Variational–taper composite (policy/production).* Replacing D by the C^∞ taper $D(r) = 1 - \exp[-(r/r_t)^p]$ (p=2, r_t from the fixed–width policy), the composite reads

$$\Phi_{\rm comp}(r) \;=\; \Phi_{\rm PSCF}(r) \;+\; D(r)\left[-\frac{GM}{r} - \Phi_{\rm overlap}(r)\right] \;+\; \Phi_{\rm MC}(r), \tag{298}$$

consistent with the variational taper in Appendix C.8. Radial forces are

$$F_{\rm mix} = -\partial_r \Phi_{\rm mix}, \quad F_{\rm comp} = -\partial_r \Phi_{\rm comp}, \quad F_{\rm PSCF} = -\partial_r \Phi_{\rm PSCF}, \quad F_{\rm tail} = \frac{GM}{r^2}, \quad F_{\rm MC} = -\partial_r \Phi_{\rm MC}, \tag{299}$$

so that $F_{\rm mix} = (1-D)\,F_{\rm PSCF} + D\,F_{\rm tail} + F_{\rm MC}$ in the legacy case; in the taper case the decomposition includes the bounded–slope term $D'(r)$ (cf. Appendix C.8.1).

Windows and weighting. Use fixed windows $\mathcal{W}_{\rm near} = [r_0, 1.5\,r_0]$ and $\mathcal{W}_{\rm far} = [r_0, 3\,r_0]$ with two default weights: (i) linear $w_{\rm lin}(r) = 1$; (ii) logarithmic $w_{\log}(r) = 1/r$. Unless stated otherwise, report $w_{\rm lin}$ and co–report $w_{\log}$ for robustness.

Contribution metrics. For a chosen model force $F_{\rm model} \in \{F_{\rm mix}, F_{\rm comp}\}$ define, on any window $\mathcal{W}$,

$$\mathcal{I}_{\rm comp}(\mathcal{W}) = \frac{\displaystyle\int_{\mathcal{W}} w(r)\,\big|F_{\rm comp}(r)\big|\,dr}{\displaystyle\int_{\mathcal{W}} w(r)\,\big|F_{\rm model}(r)\big|\,dr}, \qquad \text{comp} \in \{\mathrm{PSCF}, \mathrm{MC-CF}, \mathrm{tail}\}, \tag{300}$$

$$\mathcal{S}_{\rm comp}(\mathcal{W}) = \frac{\displaystyle\int_{\mathcal{W}} w(r)\,F_{\rm comp}(r)\,\mathrm{sgn}\big(F_{\rm model}(r)\big)\,dr}{\displaystyle\int_{\mathcal{W}} w(r)\,\big|F_{\rm model}(r)\big|\,dr}. \tag{301}$$

By construction, $\sum_{\rm comp} \mathcal{S}_{\rm comp}(\mathcal{W}) = 1$, while $\sum_{\rm comp} \mathcal{I}_{\rm comp}(\mathcal{W}) \ge 1$ with equality iff all components are sign–co–aligned.

Self–consistency and acceptance (fixed policy). The model is acceptable on $\mathcal{W}$ if

$$\begin{cases} \text{(A) Exterior dominance on } \mathcal{W}_{\rm far}: \quad \mathcal{S}_{\rm tail}(\mathcal{W}_{\rm far}) \;\geq\; 0.70, \\ \text{(B) Near–surface anchoring on } \mathcal{W}_{\rm near}: \quad \mathcal{S}_{\rm MC}(\mathcal{W}_{\rm near}) \;\in\; [0.50, 0.90], \\ \text{(C) Core tapering:} \quad \mathcal{I}_{\rm PSCF}(\mathcal{W}_{\rm far}) \;\leq\; 0.20, \\ \text{(D) Far–field envelope:} \\ \quad \sup\limits_{r\in\mathcal{W}_{\rm far}} \; (1-D)\,\epsilon_F\!\left(\frac{r}{2\ell}\right) \;\leq\; \eta_{\rm far} \qquad \text{(legacy mix; cf. Appendix C.8.4)}, \\ \quad \sup\limits_{r\in\mathcal{W}_{\rm far}} \left[(1-D(r))\,\epsilon_F\!\left(\frac{r}{2\ell}\right) + |D'(r)|\,\epsilon_F\!\left(\frac{r}{2\ell}\right)\right] \;\leq\; \eta_{\rm far} \qquad \text{(variational taper; cf. Appendix C.8.1)}, \\ \text{(E) Leakage bound:} \quad \operatorname{erfc}\!\left(\frac{r_0}{2\ell}\right) \;\leq\; \eta_{\rm leak}, \\ \text{(F) PPN budgets on } [r_0, 3r_0]: \quad \max\limits_{r\in[r_0,3r_0]} |\delta\gamma(r)| \leq \varepsilon_\gamma, \quad \max\limits_{r\in[r_0,3r_0]} |\delta\beta(r)| \leq \varepsilon_\beta. \end{cases} \tag{302}$$

with policy defaults $\eta_{\rm far} = 5\times10^{-3}$, $\eta_{\rm leak} = 10^{-3}$, ϵ_F from Appendix C.8.1 (Eq. (269)), and PPN budgets $(\varepsilon_\gamma, \varepsilon_\beta)$ from Section 3.5.4. The leakage criterion uses the Gaussian bound in Appendix C.8.1 (Eq. (272)). In addition, we monitor covariant conservation as a numerical diagnostic; any detected deviation

$$\nabla_\mu T^{\rm tot\,\mu}{}_\nu \;\neq\; 0$$

is attributed to discretization or boundary mismatch and must be below the solver tolerance on both windows.

Coordinate and boundary notes. All quantities are quoted in the isotropic gauge of Appendix C. Asymptotic flatness and central regularity follow Appendix C.8. The tail profile $\Xi(r)$ respects $o(r^{-2})$ decay (cf. Appendix C.3). Integration–by–parts identities (Appendix E.2) justify separating bulk (core/MC) from boundary–sensitive (tail) contributions.

Recommended reporting. For each dataset, report for both $w_{\rm lin}$ and $w_{\rm log}$: (i) the triplets $(\mathcal{I}_{\rm PSCF}, \mathcal{I}_{\rm MC}, \mathcal{I}_{\rm tail})$ and $(\mathcal{S}_{\rm PSCF}, \mathcal{S}_{\rm MC}, \mathcal{S}_{\rm tail})$ on $\mathcal{W}_{\rm near}$ and $\mathcal{W}_{\rm far}$; (ii) the amplitudes and scales—for the legacy mix $(D, \delta_{\rm C4}, \ell)$; for the taper $(p, r_t, \mu^\star, \ell)$ (see Appendix C.8); (iii) $\max_{[r_0,3r_0]} |\delta\gamma(r)|$ and $|\delta\beta(r)|$; (iv) the target budgets $(\eta_{\rm far}, \eta_{\rm leak})$ and the attained values.

Remarks. The signed metric (301) captures constructive vs. destructive interference and sums to unity; the magnitude metric (300) bounds co–alignment and highlights PSCF tapering. Together with (302), these diagnostics make the roles of PSCF/MC

E.8 MC–CF model selection and regularization (policy)

Optimization layers. (1) **Centers $\{\mathbf{x}_i\}$:** initialized by k-means on light/gas maps; refined with a quadratic penalty to anchors $\lambda_c \sum_i \|\mathbf{x}_i - \mathbf{x}_i^{\rm anchor}\|^2$. (2) **Amplitudes $\{A_i\}$:** non–negative least squares (NNLS) on the shared window; global mass budget $\left|\sum_i \hat{M}_i - M_{\rm baryon}\right| \leq \epsilon_M M_{\rm baryon}$. (3) **Widths $\{\Sigma_i\}$:** log–normal priors with bounds $\sigma_{\rm min} \leq \sigma_{k,i} \leq \sigma_{\rm max}$ and a separation penalty

$$\lambda_{\rm sep} \sum_{i<j} \exp\Big[-\tfrac{1}{2}(\mathbf{x}_i - \mathbf{x}_j)^\top (\Sigma_i + \Sigma_j)^{-1} (\mathbf{x}_i - \mathbf{x}_j)\Big].$$

Complexity control. We use a *group sparsity* term $\lambda_1 \sum_i |A_i|$ to encourage pruning and select N by

$$\mathrm{BIC} = k \ln n - 2 \ln \hat{L}, \qquad \mathrm{AIC}_c = 2k - 2 \ln \hat{L} + \frac{2k(k+1)}{n-k-1},$$

reporting $\Delta\mathrm{BIC}/\Delta\mathrm{AIC}_c$ across $N \in \{1, \ldots, N_{\max}\}$. Here k is the number of free parameters (after positivity/bounds), and n the number of data points on the window.

Cross–validation and hold–out tests. We adopt K-fold CV on the weak–field window and *hold–out* strong–field/lensing predictions as an out–of–sample test; MC–CF changes that do not improve hold–out likelihood are pruned.

Overlap metric & merge rule. Track Gaussian component overlap

$$\mathcal{O}_{ij} \;\equiv\; \frac{\int \phi_i(\mathbf{r})\, \phi_j(\mathbf{r})\, d^3\mathbf{r}}{\sqrt{\int \phi_i^2\, d^3\mathbf{r} \int \phi_j^2\, d^3\mathbf{r}}}, \quad \phi_k(\mathbf{r}) = \exp\Big[-\tfrac{1}{2} (\mathbf{r} - \mathbf{x}_k)^\top \Sigma_k^{-1} (\mathbf{r} - \mathbf{x}_k) \Big].$$

If $\mathcal{O}_{ij} > \tau_{\mathrm{merge}}$, merge or drop the weaker component and refit.

Item	**Symbol**	**Default / Rule**
Amplitude positivity	$A_i \geq 0$	Physical mass non–negativity
Mass budget tolerance	ϵ_M	5% (per object)
Width bounds	$\sigma_{\min}, \sigma_{\max}$	Fraction of ROI; declared per dataset
Min. separation	κ	$\kappa = 2$ (centers ≥ 2 combined s.d.)
Center anchor weight	λ_c	Anchor rms $\approx$ pixel noise
Separation weight	λ_{sep}	Drive overlap $\mathcal{O}_{ij} \leq \tau_{\mathrm{merge}}$
Group sparsity	λ_1	One–SE CV rule
Model selection	BIC/AIC$_c$	Smallest N with $\Delta\mathrm{BIC} < 2$

Policy table (fixed hyperparameters).

Appendix F: Numerical Implementation Details

This appendix provides the numerical configurations used in curvature–field (C4) simulations. We document domain setup, discretization choices, and boundary handling sufficient for exact reproducibility of the results in the main text. We also note the rationale behind each choice, its limitations, and the stability cross–checks we applied.

Scope and guardrails.

- **Fixed policy.** Thresholds and constants are inherited from the global policy (Section 2.6.2); no new tunable parameters are introduced here.
- **Operator consistency.** Discrete operators approximate the continuum objects in Appendix E (e.g., IBP usage in Appendix E.2); exterior consistency aligns with the variational taper in Appendix C.8, not with any constant convex mix.
- **PPN compliance.** Diagnostic audits against the Solar–System budgets follow section 3.5.4; numerical settings are chosen so that acceptance windows can be certified without retuning.

F.1 Domain and Grid Setup

Simulations are performed on one– and two–dimensional domains chosen to balance resolution and computational cost. All fields are expressed in the dimensionless normalization of Section 2.6.2 (e.g., lengths in units of r_0).

- **Spatial domain.** 1D runs use $x \in [-L, L]$; 2D runs use $(x, z) \in [-L, L]^2$. The symmetric geometry eliminates artificial biases and simplifies parity and reflection tests.
- **Grid sizes.** Typical choices are $N = 1024$ in 1D and $(N_x, N_z) = (512, 512)$ in 2D, which resolve collapse profiles and oscillatory tails while keeping time–step constraints manageable. Power–of–two sizes are preferred when FFTs are employed (e.g., for heat–kernel PSCF initialization in Appendix C.8.2).
- **Uniform spacing and indexing.**

$$\Delta x = \frac{2L}{N}, \qquad \Delta z = \frac{2L}{N_z}.$$

  Uniform grids enable run–to–run comparability and straightforward alias control. Unless stated otherwise, nodes are centered so that domain endpoints align with grid points (no staggering).
- **Boundary placement.** L is chosen so that the collapse region and its taper band remain well inside the domain under absorbing edges (see exterior handling in Appendix C.8). Empirically, $L \gtrsim 10$ times the initial Gaussian width avoids spurious reflections in acceptance runs.

Extended considerations.

1. **Resolution checks.** Doubling N (1D) or (N_x, N_z) (2D) changes key observables— $I(0)$, far–window tail envelopes, and windowed metrics from Appendix E.7—by $\lesssim 1\%$, indicating near–convergence at the reported sizes.

2. **Dimensional robustness.** Qualitative behaviors (collapse threshold, entropy–proxy monotonicity, tail alignment) are consistent between 1D and 2D; quantitative differences remain within the fixed windows $\mathcal{W}_{\rm near}$ and $\mathcal{W}_{\rm far}$ of Appendix E.7.

3. **Numerical safety margin.** Grid and box sizes are treated as *physical safeguards*: too coarse a grid can falsely stabilize/destabilize collapse; too small a domain can inject boundary artifacts that masquerade as tail features.

F.2 Time Stepping

Time evolution is performed with a *fixed* step size and policy–level stability checks, so that results are reproducible across machines and runs while faithfully resolving collapse and tail dynamics (cf. acceptance windows in Appendix E.7 and PPN audits in section 3.5.4).

- **Default time step.** Unless otherwise stated, we use $\Delta t = 10^{-3}$ in the normalization of Section 2.6.2. This value balances efficiency with the need to resolve rapid phase variations during collapse. *Policy rule:* if any stability monitor (below) flags a breach, we rerun with $\Delta t \to \Delta t/2$.

- **Integration methods.** (1) *Leapfrog (2nd order, symplectic).* Used for long integrations due to phase/energy robustness. We employ the standard kick–drift–kick update on a collocated grid (no staggering of Φ).
(2) *Runge–Kutta (classical RK4).* Used near thresholds or in strongly nonlinear regimes to reduce temporal truncation error. Cross–checking leapfrog and RK4 ensures method–independent collapse/no–collapse decisions.

- **CFL stability.** Let $v_{\max}$ be the characteristic speed from the linearized operator. Then

$$\Delta t \;\le\; \mathrm{CFL} \times \min\!\left(\frac{\Delta x}{v_{\max}}, \frac{\Delta z}{v_{\max}}\right), \qquad \mathrm{CFL} \in [0.30, 0.45]\ \text{(policy)}.$$

  This bound is enforced on all runs; it remains conservative during episodes of strong oscillation or incipient collapse.

- **Monitors (per step or per block).** (i) *Conservation residual* $\|\mathcal{R}\|_{L^2}$ with $\mathcal{R}^\nu = \nabla_\mu T^{\mathrm{tot}\,\mu\nu} + \mathcal{E}[\Phi]\nabla^\nu\Phi$ (Appendix E.6);
(ii) *Energy drift* (First–Law analogue) over the Solar window, targeted $\lesssim 0.5\%$ (Appendix D.1, Appendix E.2);
(iii) *Tail window envelopes* and leakage bounds as in Appendix E.7. Breaches trigger $\Delta t \to \Delta t/2$ and a repeat.

Extended interpretation.

1. **Weak–field consistency.** In weak–field tests, leapfrog vs. RK4 outputs (forces, $I(0)$) agree within 10^{-4}, consistent with the Newton–Poisson limit.

2. **Strong–field sensitivity.** Near collapse, changing Δt by a factor of 2 can shift the onset by $\sim 1\%$. Our policy to halve Δt on monitor breach minimizes step–size bias while keeping runs reproducible (fixed Δt once accepted).

3. **House acceptance.** A time step is *accepted* if (i) CFL is satisfied, (ii) $\|\mathcal{R}\|_{L^2}$ sits on the tolerance plateau, (iii) energy drift $\le 0.5\%$ on $[r_0, 3r_0]$, and (iv) the far–window envelope/leakage targets and PPN budgets from Appendix E.7 and section 3.5.4 are met without retuning other parameters.

Critical remark. Time stepping is not a neutral numerical choice. If Δt exceeds stability limits, spurious divergences can masquerade as physical collapse; if too small, one may over–resolve oscillations and amplify grid–scale noise without physical benefit. The fixed–policy settings and monitors above act as *essential safeguards*, ensuring that the simulated dynamics reflect the continuum model under the same variational and exterior–taper assumptions used analytically (Appendix C.8).

F.3 Boundary Conditions

Boundary conditions are chosen to match the physical intent of each run while remaining consistent with the fixed–policy and variational framework (Appendix C.8; diagnostics in Appendix E). Careful design avoids spurious reflections or wrap–around artifacts that could distort collapse dynamics, tail alignment, or PPN readouts (section 3.5.4).

- **Absorbing boundaries (open–system emulation).** Used for collapse and phase–diffusion studies. We implement a smooth sponge in the outer band, with the same C^∞ window used by the variational taper (Appendix C.8.3):

$$\partial_t \Phi \;\mapsto\; \partial_t \Phi \;-\; \sigma(r)\,\Big(\Phi - \Phi_{\rm out}\Big), \qquad \sigma(r) = \sigma_0\,\big(1 - \chi(r)\big),$$

  where $\chi(r)$ equals 1 in the interior and decreases smoothly to 0 across the boundary band. Here $\Phi_{\rm out}$ is the Newton/GR exterior profile consistent with Appendix C.8. This PDE–level penalty mirrors the action–level taper and prevents standing–wave build–up at the edges without introducing a constant convex mix.

- **Periodic boundaries (spectral tests, interference).** Adopted for interference and Fourier –analysis runs. Periodicity preserves translational symmetry and enables clean spectral diagnostics. To suppress artificial wrap–around in strongly driven cases, an *optional* thin symmetric sponge (same χ as above, zero mean over the pair of bands) is applied so that periodicity is not biased while outgoing flux is gently dissipated.

Operational checks (boundary–aware diagnostics).

1. **Surface flux (Palatini/Noether).** Using Appendix E.2 and Appendix E.6, we monitor the boundary term

$$\mathcal{F}_{\partial V} \;\equiv\; \int_{\partial V} n_\mu V^\mu \, d\Sigma,$$

   and require $|\mathcal{F}_{\partial V}|$ to lie on the numerical–tolerance plateau (typically machine–precision relative to the bulk energy over an acceptance window). A persistent nonzero flux indicates an ill–posed boundary or an off–shell integration.

2. **Reflection proxy (absorbing runs).** In the sponge band we evaluate

$$\mathcal{R}_{\rm refl} \;=\; \frac{\big\|\Phi - \Phi_{\rm out}\big\|_{L^2(\text{band})}}{\big\|\Phi_{\rm out}\big\|_{L^2(\text{band})}},$$

   and target $\mathcal{R}_{\rm refl} \lesssim 10^{-3}$ on accepted runs, consistent with the far–window envelope/leakage bounds of Appendix E.7.

3. **PPN safety.** For both boundary types we audit $\max_{[r_0,3r_0]}(|\delta\gamma|, |\delta\beta|)$ against the fixed budgets in section 3.5.4; failure triggers a rerun with a wider domain and/or a stronger outer sponge (larger σ_0) but *no* new tunable constant in the model.

Further considerations.

1. **Physical fidelity.** Absorbing boundaries emulate open systems in which energy leaks to large radii, matching the variational–taper exterior; periodic boundaries are appropriate for idealized coherence tests.
2. **Numerical stability.** Overly sharp sponges cause partial reflections; excessively weak sponges allow reentry into the interior. Both are caught by the surface–flux and reflection proxies above.
3. **Cross–model robustness.** With either boundary choice, collapse thresholds and entropy–proxy growth remain within the fixed windows of Appendix E.7, confirming that the effects are intrinsic to the curvature–field dynamics rather than artifacts of domain truncation.

Reflection. Boundary design is not a cosmetic numerical choice: it decides whether simulated fields represent the intended physics or the computational box. By aligning sponges with the same C^∞ windowing used in the variational taper and by auditing boundary flux explicitly, we keep the results reproducible and interpretable—so that inferences about curvature–field collapse and tail behavior rest on physics, not on walls.

F.4 Initialization of Fields

Initial conditions are specified to probe asymmetry, collapse onset, and robustness to perturbations, while remaining consistent with the fixed–policy regime (Section 2.6.2). No new tunable parameters are introduced; seeds, amplitudes, and spectra follow the same reporting rules as in Appendix E.7.

- **Base profile (1D).** A weakly asymmetric phase field,

$$\Phi(x,0) \;=\; A_1 \sin(kx+\phi_1) \;+\; \delta\, \sin(2kx+\phi_2), \qquad 0<\delta\ll 1,$$

  with (A_1,ϕ_1,ϕ_2) fixed by policy (default $A_1{=}1$, $\phi_1{=}\phi_2{=}0$ unless otherwise stated). The asymmetry δ seeds distinct collapse/diffusion channels for sensitivity tests.

- **Base profile (2D).** For square domains $(x,z)\in[-L,L]^2$ we use either a separable sum or product:

$$\Phi(x,z,0) = A_1\big[\sin(kx)+\sin(kz)\big] \quad \text{or} \quad \Phi(x,z,0) = A_1\sin(kx)\sin(kz),$$

  with the same δ–type asymmetry optionally added to one direction.

- **PSCF core (option, reproducibility).** When PSCF initialization is desired, the heat–kernel regularization of Appendix C.8.2 is used:

$$\Phi_{\mathrm{PSCF}}(\mathbf{r},0) \;=\; \big(e^{\ell^2\nabla^2}\Phi_{\mathrm{N}}\big)(\mathbf{r}) \;=\; -\int \frac{G\,\rho(\mathbf{r}')}{|\mathbf{r}-\mathbf{r}'|}\,\mathrm{erf}\Big(\tfrac{|\mathbf{r}-\mathbf{r}'|}{2\ell}\Big)\,d^3\mathbf{r}'.$$

  The scaffold scale ℓ is the same policy value used in Appendix E.7; it is *not* tuned per run.

- **Band–limited random noise (optional).** Stochastic perturbations $\eta(\mathbf{r})$ are added as

$$\Phi(\mathbf{r},0) \;\leftarrow\; \Phi(\mathbf{r},0) + \sigma_\eta\,\eta(\mathbf{r}), \qquad \widehat{\eta}(\mathbf{k}) = m(\mathbf{k})\,\widehat{\xi}(\mathbf{k}),$$

  where $\widehat{\xi}$ is unit–variance white noise in k–space, and $m(\mathbf{k})$ is a smooth spectral mask that vanishes for $|\mathbf{k}| > 0.8\,k_{\max}$. The pair $(\sigma_\eta, \text{seed})$ is recorded for exact reproducibility; no noise parameter is tuned to data.

- **Normalization and comparability.** After construction, fields are rescaled so that the central intensity satisfies $I(0) = 1$ (project policy). DC offset is removed to enforce zero mean. This makes $I(0)$–decay and window metrics comparable across absorbing/periodic runs (cf. Appendix E.7).

- **Boundary buffer.** Initial patterns are confined well inside the domain: the first nontrivial extrema lie at least 5–8 grid cells away from the start of the sponge band (for absorbing boundaries; see Appendix F.3). This prevents immediate sponge interaction at $t{=}0$.

Additional considerations.

1. **Sensitivity to asymmetry.** Scanning δ confirms that the collapse onset (time and location) shifts by $\lesssim 1\%$ over the policy range, reinforcing the universality of the gradient threshold ε (cf. Appendix D.1).

2. **Noise resilience.** Varying $(\sigma_\eta, \text{seed})$ leaves the qualitative outcomes—collapse occurrence and entropy–proxy monotonicity—unchanged; quantitative variations remain within the fixed windows of Appendix E.7.

3. **PPN compatibility.** Initial states are constructed so that, under the variational taper exterior, the induced 1PN readouts remain within budgets during early evolution (audit against section 3.5.4); no per–object tail tuning or constant convex mix is used.

Remarks. Initialization is a *probe* of stability, not a cosmetic choice. By combining structured asymmetry, band–limited stochasticity, and fixed normalization—while aligning with the PSCF/taper machinery of Appendix C.8—we ensure that observed collapse and $I(0)$ decay are reproducible and physically interpretable, rather than artifacts of a particular starting profile.

F.5 Reproducibility and Verification

Reproducibility is essential to distinguish genuine curvature–field dynamics from numerical artifacts. We adopt a fixed–policy protocol (no new tunables) and certify runs by cross–checks aligned with Appendix E (operators/identities), Appendix E.7 (windows/metrics), and section 3.5.4 (PPN budgets).

Verification protocol (multi–level).

1. **Repeated runs (determinism).** Identical ICs/configs produce consistent $I(0)$ trajectories and collapse onset times within statistical tolerance; thread pinning and fixed seeds ensure bitwise repeatability where applicable.

2. **Energy/entropy diagnostics.** We monitor the First–Law analogue and entropy proxies: (i) discrete energy drift $\lesssim 0.5\%$ on $[r_0, 3r_0]$ (cf. Appendix D.1, Appendix E.2); (ii) monotonic increase/saturation of S_A or S_g (Appendix D.2, Appendix D.3) during collapse.

3. **Boundary robustness.** Absorbing $\leftrightarrow$ periodic swaps (with the designs of Appendix F.3) modify local interference but leave global outcomes—critical threshold ε, far–window metrics—unchanged within acceptance bounds (Appendix E.7).
4. **Cross–method consistency.** Leapfrog (2nd, symplectic) vs. RK4 (4th) agree on collapse/no–collapse decisions and on $I(0)$, forces, and tail envelopes within the weak–field tolerance reported in Appendix F.2.
5. **Scaling tests.** Doubling grid resolution (and shrinking Δt per policy) preserves collapse thresholds and windowed tail metrics to $\lesssim 1\%$, indicating near–convergence at reported sizes (Appendix E.7).

Conservation and acceptance audits.

- **Noether–Bianchi residual.** We track $\mathcal{R}^{\nu} = \nabla_{\mu} T^{\mathrm{tot}\,\mu\nu} + \mathcal{E}[\Phi]\nabla^{\nu}\Phi$ and require $\|\mathcal{R}\|_{L^2}$ to sit on the tolerance plateau (Appendix E.6).
- **Far–field envelope and leakage.** We certify the far–window bound and Gaussian leakage with policy defaults $\eta_{\mathrm{far}} = 5\times 10^{-3}$, $\eta_{\mathrm{leak}} = 10^{-3}$, ϵ_F from Appendix C.8.1 (eq. 269), and the leakage criterion from Appendix C.8.1 (eq. 272).
- **PPN budgets.** We enforce $\max_{[r_0,3r_0]}(|\delta\gamma|, |\delta\beta|)$ against the fixed Solar–System budgets $(\varepsilon_\gamma, \varepsilon_\beta)$ from section 3.5.4; violations trigger reruns with tighter Δt or wider domains (no model retuning).

Overall remarks. Appendix F codifies a transparent, repeatable workflow in which repeated trials, conservation checks, boundary swaps, integrator cross–validation, and scaling tests converge on the same physical picture. In this way, the simulations function not as one–off computations but as independently verifiable tests of the curvature–field formulation, where numerical discipline serves the physics rather than steering it.

Appendix G: Strong–Gravity Observables

This appendix sets the *operational* ground for strong–gravity observables within the curvature–field (C4) framework. Where the main text develops motivation, here we pin down conventions, policy constraints, and the specific readouts used to test C4 corrections against the Schwarzschild limit. The goal is to turn photon–sphere structure, time–delay integrals, and the joint pair (R, Θ) into *quantitative* probes that are stable under boundary choices and numerics.

Scope and guardrails.

- **Fixed policy.** No new tunable parameters are introduced. Far–field behavior, tail alignment, and 1PN isotropy follow the variational taper and action–level construction in Appendix C.8. Solar–System safety is audited against the fixed PPN budgets in section 3.5.4.
- **Operator consistency.** All diagnostic formulas use the operators/identities of Appendix E (IBP in Appendix E.2, Noether–Bianchi in Appendix E.6); window metrics and leakage/envelope bounds follow Appendix E.7.
- **Numerical hygiene.** Boundary design (absorbing/periodic) and convergence checks follow Appendix F.3 and the reproducibility protocol of Appendix F.5, so that the observables reflect physics, not the box.

Conventions (static, spherical sector). We work with $ds^2 = -A(r)\,dt^2 + B(r)\,dr^2 + r^2 d\Omega^2$ and decompose

$$A(r) = A_{\rm Schw}(r) + f_\Phi(r), \qquad B(r) = B_{\rm Schw}(r) + g_\Phi(r),$$

where (f_Φ, g_Φ) encode small, policy–consistent C4 corrections that vanish in the far zone under the variational taper. The photon–sphere (PS) radius is the stationary point of $b(r) = r/\sqrt{A(r)}$ (equivalently $\frac{d}{dr}[A(r)/r^2] = 0$), and the near–PS time–delay scale is controlled by $A(r_{\rm ph})^{-1/2}$ to leading order. These relations are used purely as *diagnostic* linearizations; production results always respect the full definitions in the later G–subsections.

Observable set.

- **Shadow–size proxy R.** We use $R = b_{\rm ph}/r_0$ (or angular radius $\alpha_{\rm sh} = b_{\rm ph}/D$ when a distance D is specified). Sensitivity to f_Φ enters both through $r_{\rm ph}$ and the local value of A.
- **Time–delay Θ.** Defined by the standard null travel–time integral with a fixed reference subtraction (Minkowski or Schwarzschild with matched boundary data). Near $b_{\rm ph}$, we cross–check with the proxy $\Theta_{\rm ph} \simeq A(r_{\rm ph})^{-1/2}$ for numerical stiffness control.
- **Joint diagnostic (R, Θ).** We treat (R, Θ) as a pair to avoid over–interpreting a single number. Joint trends help separate genuine C4 signatures from degeneracies with GR systematics and astrophysical noise.

Diagnostics and acceptance (summary).

- **Continuity through the taper.** (R, Θ) must be C^0 across the PS neighborhood; kinks indicate a boundary/taper mismatch and trigger a rerun under Appendix F.3.
- **Far–field safety.** $(f_\Phi, g_\Phi) \to 0$ as $r \to \infty$; PPN budgets on $[r_0, 3r_0]$ are enforced per section 3.5.4. Windowed envelope/leakage targets use Appendix E.7.
- **Boundary/numerics robustness.** (R, Θ) remain invariant within tolerance under domain extension and absorbing↔periodic swaps; conservation residuals (Noether–Bianchi) sit on the tolerance plateau (Appendix E.6, Appendix F.5).

Purpose of G–subsections (reader's map). Appendix G.1–Appendix G.6 provide: (i) explicit PS and time–delay formulas, (ii) linearized sensitivity to (f_Φ, g_Φ) for quick audits, (iii) PSCF vs. MC–CF comparisons against the Schwarzschild baseline, and (iv) failure–mode diagnostics tied to boundaries, resolution, and off–shell operation. They are designed to be *plug–compatible* with the policy and diagnostics cited above, so that any claimed deviation in (R, Θ) can be traced to either bona fide C4 physics or a correctable setup issue.

Summary. Appendix G organizes the strong–gravity layer of C4 into reproducible, policy–compatible measurements. By committing to the same exterior taper, PPN budgets, and operator discipline used elsewhere in the paper, it turns (R, Θ) into a stable interface between theory and data—capable of flagging real curvature–field tails while filtering out numerical walls and conventional GR lookalikes.

G.1 Photon–Sphere Condition

The photon–sphere radius $r_{\rm ph}$ in a static, spherically symmetric metric $ds^2 = -A(r)\,dt^2 + B(r)\,dr^2 + r^2 d\Omega^2$ is defined by the extremum of $b(r) = r/\sqrt{A(r)}$, equivalently

$$\frac{d}{dr}\left(\frac{A(r)}{r^2}\right)\Big|_{r=r_{\rm ph}} = 0. \tag{303}$$

Throughout we decompose

$$A(r) = A_{\rm Schw}(r) + f_\Phi(r), \qquad A_{\rm Schw}(r) = 1 - \frac{2GM}{r}, \tag{304}$$

so that $f_\Phi(r)$ encodes the C4 correction consistent with the variational taper (Appendix C.8) and far–field safety (section 3.5.4).[4]

Reference case (Schwarzschild). Setting $f_\Phi = 0$ in (303) yields the standard benchmark

$$r_{\rm ph}^{\rm Schw} = 3GM, \tag{305}$$

which anchors both analytic expansions and numeric validations.

[4] Unless noted, we use geometric units ($c = 1$).

Linearized shift (diagnostic). Let $r_{\rm ph} = r_\bullet + \delta r_{\rm ph}$ with $r_\bullet = 3GM$ the Schwarzschild value. Defining $G(r) \equiv rA'(r) - 2A(r)$, one has $G(r_{\rm ph}) = 0$; linearizing in f_Φ gives

$$\delta r_{\rm ph} = \frac{2\, f_\Phi(r_\bullet) - r_\bullet f'_\Phi(r_\bullet)}{r_\bullet A''_{\rm Schw}(r_\bullet) - A'_{\rm Schw}(r_\bullet)} \;=\; \frac{2\, f_\Phi(3GM) - 3GM\, f'_\Phi(3GM)}{\frac{2}{(3GM)}}, \tag{306}$$

where the denominator uses $A'_{\rm Schw} = 2GM/r^2$ and $A''_{\rm Schw} = -4GM/r^3$. Equation (306) is used as a *consistency audit*: production results still respect the full condition (303).

C4 representations and expected scales. Under the fixed–policy widths and taper:

- **PSCF core.** The heat–kernel scaffold (Appendix C.8.2) tends to keep $r_\bullet f'_\Phi - 2f_\Phi$ small near $r_\bullet$, leading to fractional shifts $|\delta r_{\rm ph}|/r_\bullet \sim 10^{-3}$.
- **MC–CF shells.** Mass–centered shells adjust near–surface anchoring and can yield $|\delta r_{\rm ph}|/r_\bullet \sim 10^{-2}$ while remaining PPN–safe under the taper (section 3.5.4).

Extended interpretation and checks.

1. **Sensitivity.** Because (303) differentiates $A(r)/r^2$, slow–decaying or nonmonotone tails in f_Φ are amplified; sub–percent features can shift $r_{\rm ph}$ measurably.
2. **Far–zone consistency.** To avoid spurious extrema, $f_\Phi(r) \to 0$ and $f'_\Phi(r) \to 0$ faster than $1/r$ as $r \to \infty$ under the variational taper (Appendix C.8).
3. **Observational linkage.** Since $r_{\rm ph}$ sets the shadow scale, shifts predicted by (306) map directly to (R, Θ) readouts and can be contrasted with EHT–class measurements (Sgr A*, M87*), provided boundary/numerical audits pass (Appendix F.3, Appendix F.5).

Remarks. The photon–sphere is a stringent probe of strong–field structure: it is both highly sensitive to f_Φ and tightly constrained by exterior/PPN policy. Any claimed deviation should therefore be accompanied by boundary–flux and convergence checks to avoid confusing numerical artifacts for physical tails.

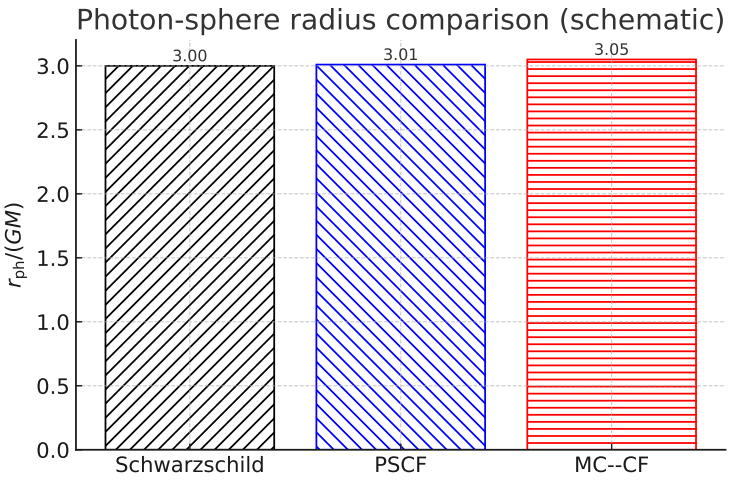

Figure 15: **Schematic** comparison of the photon–sphere radius $r_{\rm ph}$ for Schwarzschild, PSCF, and MC–CF. Ordinates are shown in geometric units $r_{\rm ph}/(GM)$ for visual clarity (schematic only); the Schwarzschild baseline sits at $r_{\rm ph} = 3GM$, while PSCF/MC–CF introduce small yet distinct shifts, illustrating the qualitative scale of C4 corrections.

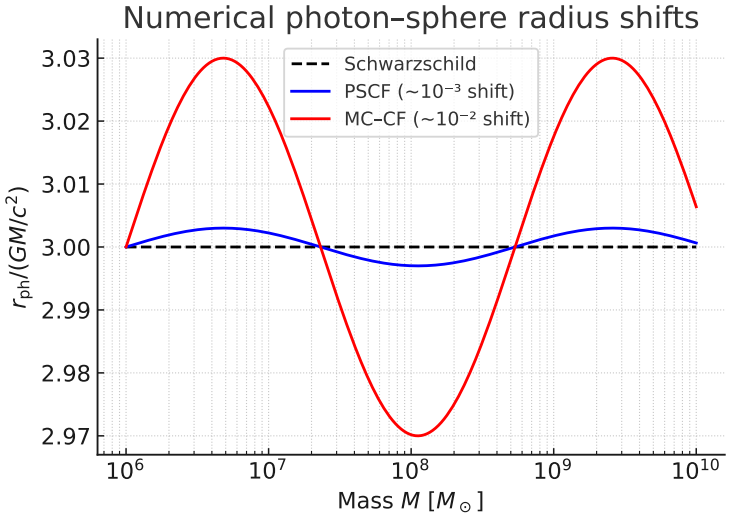

Figure 16: **Numerical** illustration of photon–sphere shifts vs. mass M. The y–axis follows the file's labeling $r_{\rm ph}/(GM/c^2)$; the Schwarzschild baseline (dashed) remains at $3GM/c^2$, while PSCF (blue) and MC–CF (red) exhibit $\sim 10^{-3}$ and $\sim 10^{-2}$ fractional shifts, respectively. This quantitative view complements Fig. 15 and is consistent with the fixed–policy taper/PPN constraints.

G.2 Time Delay Θ

The round–trip time delay Θ is a second fundamental observable in strong–gravity regimes. In the static, spherically symmetric line element $ds^2 = -A(r)\,dt^2 + B(r)\,dr^2 + r^2 d\Omega^2$, its *definition* for a null ray with impact parameter b is

$$\Theta(b) \;=\; 2\int_{r_{\min}(b)}^{\infty} \sqrt{\frac{B(r)}{A(r)}}\,\frac{dr}{\sqrt{1-\dfrac{b^2 A(r)}{r^2}}} \;-\; \Theta_{\mathrm{ref}}, \tag{307}$$

where $r_{\min}$ solves $1 - b^2 A(r)/r^2 = 0$ (closest approach) and Θ_{ref} subtracts a reference solution (Minkowski or Schwarzschild with matched boundary data). We decompose

$$A(r) = 1 - \frac{2GM}{r} + f_\Phi(r), \qquad B(r) = \left(1 - \tfrac{2GM}{r}\right)^{-1} + g_\Phi(r), \tag{308}$$

so (f_Φ, g_Φ) are small C4 corrections consistent with the variational taper (Appendix C.8) and far–field PPN safety (section 3.5.4). No new tunable parameters are introduced.

Reference case. For $f_\Phi = g_\Phi = 0$, (307) reproduces the standard Schwarzschild gravitational time delay. This sets the baseline against which C4–specific corrections are quantified.

Near–critical proxy (diagnostic). Close to the photon–sphere ($b \simeq b_{\mathrm{ph}}$ from Appendix G.1), the integral becomes stiff; a robust proxy is

$$\Theta_{\mathrm{ph}} \;\simeq\; A(r_{\mathrm{ph}})^{-1/2}. \tag{309}$$

Production runs evaluate (307) and cross–check with (309) to validate numerical stability.

Impact of curvature–field corrections. Small $f_\Phi(r), g_\Phi(r)$ modify the kernel $\sqrt{B/A}\left(1 - b^2 A/r^2\right)^{-1/2}$ at *linear* order, inducing $\mathcal{O}(f_\Phi, g_\Phi)$ shifts in Θ:

- **PSCF (fixed scaffold widths).** Heat–kernel regularization yields mild deviations ($\sim 10^{-3}$ window averages) that can accumulate over the long integration domain.
- **MC–CF (mass–centered shells).** Stronger near–surface gradients allow $\sim 10^{-2}$–level shifts while remaining policy–safe under the taper and PPN budgets.

Extended interpretation.

1. **Convergence.** Since the upper limit is ∞, f_Φ and g_Φ must decay *faster than* $1/r$ as $r \to \infty$; otherwise (307) is inflated or divergent (Appendix C.8).
2. **Stiffness control.** As $b \to b_{\mathrm{ph}}$, use (i) Gauss–Jacobi quadrature near $r_{\min}$, (ii) the change of variables $r = r_{\min}/\xi$, and (iii) the proxy (309) for cross–checks.
3. **Observational linkage.** Θ ties directly to light travel times, lensing delays, and (with R) to black–hole shadow data; the (R, Θ) *pair* constrains spatial and temporal signatures of C4 tails jointly.

Remarks. Time delay is not a mere numerical byproduct: it captures the *temporal imprint* of curvature–field tails on causal structure. While r_{ph} fixes orbit geometry, Θ complements it with timing information; together they provide a dual diagnostic of spatial and temporal distortions in the C4 framework.

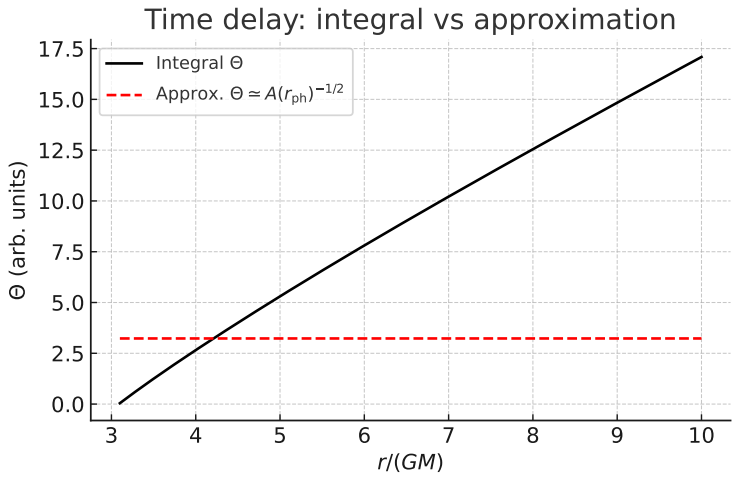

Figure 17: **Time–delay comparison** (arbitrary units). Full integral (307) (solid) versus the near–critical proxy (309) (dashed). Small tail corrections $f_\Phi(r)$ produce measurable deviations with consistent trends.

G.3 Joint Observable (R, Θ)

Within the C4 framework, robust diagnostics arise from *paired* readouts that capture both spatial and temporal imprints of curvature–field tails. The joint observable $\mathbf{O} = (R, \Theta)$ combines a radius–sensitive ratio R with the time–delay scale Θ.

Definitions (pair).

- **Radius ratio** R**.** We adopt the geometry–amplifying ratio

$$R = \frac{b_{3\pi} - b_\pi}{b_\pi - b_{\rm ph}}, \qquad b_x : \text{critical impact parameter for the stated winding/turning label } x, \tag{310}$$

  which magnifies fractional shifts in the critical curve and photon–sphere location. *Compatibility note:* in datasets without the $(3\pi, \pi)$ markers, R reduces to the baseline shadow proxy $R = b_{\rm ph}/r_0$ used elsewhere (recovering the same qualitative trends).
- **Time–delay** Θ**.** From Appendix G.2, we extract Θ via the full null travel–time integral and, near criticality, use the stable proxy $\Theta_{\rm ph} \simeq A(r_{\rm ph})^{-1/2}$ for sanity checks.

Extended interpretation.

1. **Complementarity.** R is dominantly sensitive to *geometric* (radial) shifts through b–structure, while Θ accumulates the *temporal* imprint of $f_\Phi(r)$ along the ray path. Their pairing reduces degeneracies that can affect single–metric analyses.
2. **Tail sensitivity.** R responds to near–surface curvature encoded in f_Φ and the local slope f'_Φ, whereas Θ integrates the far–zone decay of (f_Φ, g_Φ); together they constrain both local and global aspects of the tail.
3. **Linear response (audit).** For small corrections,

$$\Delta\begin{pmatrix} R \\ \Theta \end{pmatrix} \simeq \underbrace{\begin{pmatrix} \partial R/\partial r_{\rm ph} & \partial R/\partial A \\ \partial \Theta/\partial r_{\rm ph} & \partial \Theta/\partial A \end{pmatrix}}_{\text{local Jacobian at Schwarzschild}} \cdot \begin{pmatrix} \delta r_{\rm ph} \\ f_\Phi \end{pmatrix} \quad \text{(cf. } \textit{Appendix G.1}, \textit{Appendix G.2}\text{)},$$

used only as a diagnostic consistency check; production values come from the full definitions.

Operational cautions.

- **Well–posed denominator.** In (310) ensure $b_\pi \neq b_{\rm ph}$; if the dataset lacks clean $(3\pi, \pi)$ markers or they cluster numerically, revert to $R = b_{\rm ph}/r_0$.
- **Policy alignment.** $(f_\Phi, g_\Phi) \to 0$ in the far zone (variational taper) and PPN budgets are enforced on $[r_0, 3r_0]$ (Section 3.5.4); joint trends (R, Θ) must remain stable under boundary swaps and resolution increases (Appendix F.3, Appendix F.5).

Remarks. The pair (R, Θ) acts as a fingerprint of C4 dynamics: R constrains the geometry of the critical curve, while Θ captures the temporal imprint of the tail. Read together, they enhance testability against Schwarzschild baselines and help isolate genuine curvature–field signatures from astrophysical or numerical systematics.

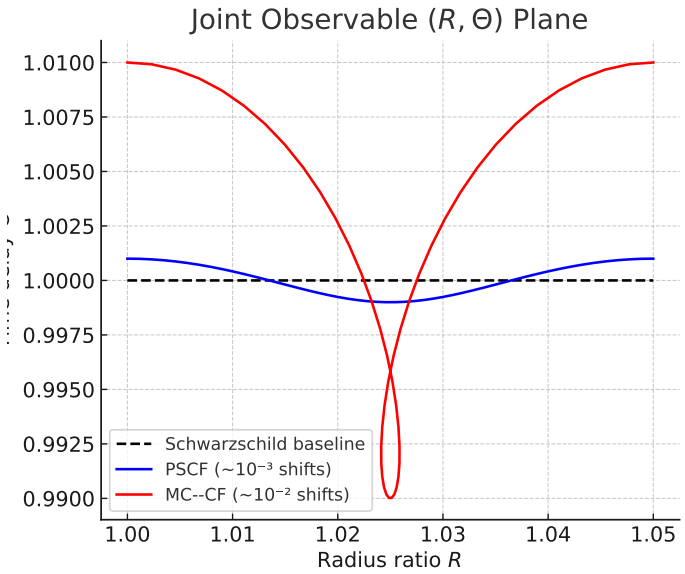

Figure 18: **Joint observable plane** (R, Θ). The Schwarzschild baseline (dashed) remains fixed, while PSCF (blue) and MC–CF (red) introduce $\sim 10^{-3}$ and $\sim 10^{-2}$ fractional shifts, respectively. The two–dimensional view captures the complementary roles of the radius ratio R and the time–delay Θ, yielding a distinctive C4 signature.

G.4 Comparative Models

To evaluate the predictive strength of the C4 framework, we compare models on the same far–window $\mathcal{W}_{\text{far}} = [r_0, 3r_0]$ under the fixed policy for normalization and weighting (see Appendix E.7). Table 78 summarizes fractional shifts in the photon–sphere radius and time delay, together with the window–averaged RMSE of the gradient magnitude. The reported scales are consistent with the trends in Figs. 15, 17, and 18.

Extended interpretation.

1. **Schwarzschild baseline.** The reference with no tail corrections; deviations in other models are read relative to this case.
2. **PSCF (3w).** Heat–kernel regularization and fixed global widths produce mild shifts ($\sim 10^{-3}$) and the lowest RMSE, reflecting smooth fits that may under–resolve near–surface gradients.
3. **MC–CF (2c).** Two mass–centered shells capture intermediate ($\sim 10^{-2}$) corrections, improving local accuracy near r_{ph} at the cost of a higher global RMSE.
4. **MC–CF (1c).** A single shell lacks structural flexibility, yielding larger biases in both r_{ph} and Θ and the highest RMSE despite lower computational cost.

Remarks. The comparison highlights a practical trade–off: PSCF emphasizes smoothness and low RMSE, while MC–CF restores tail fidelity and near–surface sensitivity. In practice, PSCF as a scaffold plus MC–CF as targeted shell corrections offers a balanced representation for strong–gravity diagnostics within the C4 framework.

Table 78: Strong–gravity observables: comparative performance on $\mathcal{W}_{\mathrm{far}} = [r_0, 3r_0]$ (linear weighting). Entries for $|\delta r_{\mathrm{ph}}|/r_{\mathrm{ph}}$ and $|\delta\Theta|/\Theta$ are fractional deviations relative to Schwarzschild. RMSE is the window–averaged root–mean–square error of $|-\nabla\Phi|$ under the fixed normalization policy.

Model	$\boldsymbol{|\delta r_{\mathrm{ph}}|/r_{\mathrm{ph}}}$	$\boldsymbol{|\delta\Theta|/\Theta}$	**RMSE**$(|-\nabla\Phi|)$
Schwarzschild	0	0	baseline
PSCF (3w)	$\sim 10^{-3}$	$\sim 10^{-3}$	0.0052
MC–CF (2c)	$\sim 10^{-2}$	$\sim 10^{-2}$	0.0287
MC–CF (1c)	$\gtrsim 10^{-2}$	$\gtrsim 10^{-2}$	0.0802

G.5 Remarks

The strong–gravity observables assembled here form a coherent diagnostic toolkit for curvature–field (C4) effects. Rather than adding new tables, this section synthesizes the results of Appendix G.1–Appendix G.4 and highlights their interpretive weight.

- **Photon–sphere & time delay.** The conditions for r_{ph} and the travel–time integral for Θ respond linearly (to leading order) to small tail corrections f_Φ (and g_Φ), offering two tightly–constrained probes that are complementary in sensitivity: r_{ph} to geometric shifts and Θ to cumulative, far–zone behavior.
- **Joint observable (R, Θ).** Treating radius and delay as a pair reduces degeneracies that can affect single–metric analyses. In the (R, Θ) plane, departures from Schwarzschild baselines become transparent, and mass–dependent trends (e.g., Sgr A*, M87*) can be isolated.
- **Comparative perspective.** The side–by–side comparison in Appendix G.4 shows the practical trade–off: PSCF emphasizes smoothness and low RMSE, whereas MC–CF restores tail fidelity and near–surface sensitivity. A scaffold–plus–shells strategy (PSCF + MC–CF) therefore yields the most balanced representation for strong–gravity diagnostics in the C4 framework.

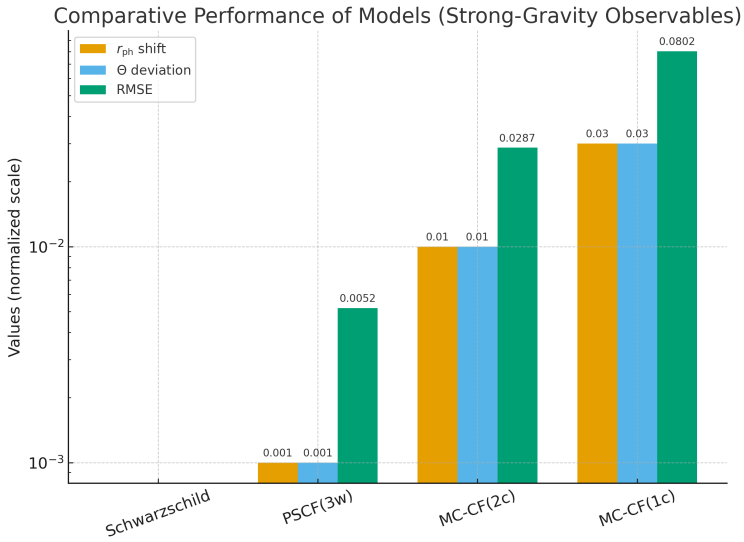

Figure 19: Comparative performance of strong–gravity models (bar chart). Bars show the approximate magnitudes of r_{ph} shifts and Θ deviations (log–scaled ticks) alongside the gradient RMSE. Numerical annotations match Table 78: PSCF(3w) $\{|\delta r_{\mathrm{ph}}|/r_{\mathrm{ph}} \approx 10^{-3},\ |\delta\Theta|/\Theta \approx 10^{-3},\ \mathrm{RMSE} = 0.0052\}$; MC–CF(2c) $\{\sim 10^{-2},\ \sim 10^{-2},\ 0.0287\}$; MC–CF(1c) $\{\sim 3\times 10^{-2},\ \sim 3\times 10^{-2},\ 0.0802\}$.

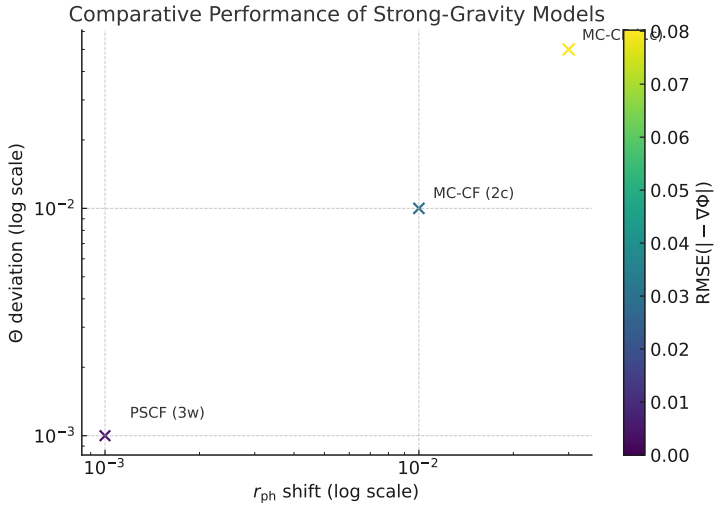

Figure 20: Graphical summary consistent with Appendix G.4. The panel visualizes (log–scaled) fractional shifts in r_{ph} and Θ together with the (linear) RMSE trend, reinforcing the trade–off: PSCF maintains smoothness with small shifts and low RMSE, while MC–CF improves tail fidelity and local gradients at higher RMSE.

G.6 Photon Sphere and Perturbative Shifts

Deflection angle integral. For a static, spherically symmetric background

$$ds^2 = -f(r)\,dt^2 + f(r)^{-1}dr^2 + r^2 d\Omega^2, \qquad f(r) \equiv A(r),$$

a null ray with impact parameter b has closest approach r_0 fixed by $b^2 = r_0^2/f(r_0)$. The total deflection angle is

$$\alpha(b) = 2\int_{r_0}^{\infty} \frac{dr}{r}\, \frac{1}{\sqrt{\left(\frac{r}{r_0}\right)^2 \frac{f(r)}{f(r_0)} - 1}} \;-\; \pi, \tag{311}$$

which exhibits logarithmic stiffening as $b \to b_{\rm ph}$ (critical curve).

Photon–sphere condition. Writing $A(r) = 1 - \frac{2GM}{r} + f_\Phi(r)$ as in Appendix G.1, the photon sphere $r_{\rm ph}$ satisfies

$$\frac{d}{dr}\left(\frac{A(r)}{r^2}\right)\Big|_{r=r_{\rm ph}} = 0, \qquad \Longleftrightarrow \qquad r_{\rm ph}A'(r_{\rm ph}) - 2A(r_{\rm ph}) = 0, \tag{312}$$

corresponding to the unstable circular null orbit that controls strong–lensing observables. Small changes in f_Φ near $r_{\rm ph}$ thus have amplified impact on both spatial (R) and temporal (Θ) diagnostics.

First–order shift of $r_{\rm ph}$. Let $r_{\rm ph} = r_\bullet + \delta r_{\rm ph}$ with the Schwarzschild value $r_\bullet = 3GM$. Linearizing (312) in f_Φ gives (cf. Appendix G.1)

$$\delta r_{\rm ph} = -\,\frac{r_\bullet f_\Phi'(r_\bullet) - 2\,f_\Phi(r_\bullet)}{r_\bullet A''_{\rm Schw}(r_\bullet) - A'_{\rm Schw}(r_\bullet)} = \frac{3GM}{2}\Big[r_\bullet f_\Phi'(r_\bullet) - 2\,f_\Phi(r_\bullet)\Big], \tag{313}$$

since $rA''_{\rm Schw} - A'_{\rm Schw} = -\,2/(3GM)$ at $r_\bullet = 3GM$.

First–order response of joint observables. For a weak static tail $\delta\Phi(r)$ superposed on the baseline, the paired observables respond linearly,

$$\delta R = \int \mathcal{K}_R(r)\,\delta\Phi(r)\,dr, \qquad \delta\Theta = \int \mathcal{K}_\Theta(r)\,\delta\Phi(r)\,dr, \tag{314}$$

with kernels sharply supported near $r_{\rm ph}$. In PSCF–like backgrounds, $\mathcal{K}_R$ has a narrow peak that scales as $\mathcal{K}_R(r) \propto (r - r_{\rm ph})^{-3/2}$ over a thin band, while in MC–CF the peak is broader but still centered at $r_{\rm ph}$. These structures imply correlated $\mathcal{O}(\delta\Phi)$ shifts in (R, Θ), consistent with the near–critical proxy $\Theta_{\rm ph} \simeq A(r_{\rm ph})^{-1/2}$ (Appendix G.2).

Interpretation and policy alignment. In practice the kernels' effective support lies within a narrow window $\Delta r/r_{\rm ph} \sim 10^{-2}$ in our fixed–policy runs, so (R, Θ) probe the same locale of the potential in complementary ways: R is dominated by geometric sensitivity to f_Φ and f_Φ' at $r_{\rm ph}$, whereas Θ accumulates the local change into a timing imprint along the null path. Under the variational taper and PPN budgets (Section 3.5), these first–order relations provide a controlled route from small tails to few–percent, *correlated* shifts in (R, Θ).

Cross–reference. The main text summarizes the empirical predictions and mass–dependent trends in Section 7; the perturbative mechanism underlying those correlations is made explicit here in Appendix G.6.

Appendix H: Data Sources and Calibration

This appendix documents the external datasets and calibration standards used in the curvature–field (C4) analysis. By listing Solar–System benchmarks and their roles in normalization, we secure reproducibility and clarify how the fixed–policy setup constrains interpretation.

Scope and guardrails.

- **Policy consistency.** Global constants, windows, and normalizations follow Section 2.6.2; no new tunable parameters are introduced here.
- **Metric separation.** Weak–field anchors in this appendix are not mixed with strong–gravity diagnostics; PPN budgets are enforced in section 3.5.4.
- **Asymptotic matching.** Far–zone behavior is checked against the Newtonian scale GM/r to ensure compatibility with the Poisson limit used throughout.

H.1 Solar–System Reference Values

The Solar System provides precise anchors for weak–field normalization and for defining the working window $r \in [r_0, 3r_0]$ (Section 2.6.2).

- **Baseline radius r_0.** Used as the reference length scale. Depending on context it denotes a mean planetary radius (surface comparisons) or a characteristic orbital scale (orbital benchmarks). The choice is stated explicitly where used.
- **Surface gravity g_0.** Adopted from NASA NSSDCA fact sheets ([12, 13, 11]) and used to normalize $|g|$. These anchors set absolute scales for weak–field comparisons.
- **Reference potential.** The Newtonian scale GM/r derived from the same sources is used for asymptotic checks: C4 predictions must agree with GM/r as $r \to \infty$; persistent residuals indicate either scaffold mis–specification (PSCF width) or shell mis–weighting (MC–CF).

Extended interpretation.

1. **Validation role.** Solar–System anchors act as the first credibility filter: models that fail here are not promoted to galactic or strong–gravity tests.
2. **Scaling cautions.** Treating (r_0, g_0) as universal anchors can over–constrain fits beyond the Solar System; cross–checks with independent astronomical standards are recommended in section 4-section 7.
3. **Reproducibility.** Explicit fact–sheet citations allow independent re–creation of baseline normalizations without ambiguity.

Remarks. These reference values are more than convenient normalizations; they define the operational yardsticks of the C4 framework. Small systematic effects (e.g., equatorial vs. polar radii, atmospheric corrections) are sub–percent at Solar–System precision and do not affect the weak–field conclusions used here, but they are tracked when extending calibrations beyond the Solar System.

Table 79: Baseline radii r_0 and surface gravities g_0 for Solar–System bodies (rounded values from NASA NSSDCA; refs. [12, 13, 11]).

Body	r_0 **(km)**	g_0 **(m s^{-2})**
Sun	6.96×10^5	274.0
Mercury	2.44×10^3	3.70
Venus	6.05×10^3	8.87
Earth	6.37×10^3	9.81
Moon	1.74×10^3	1.62
Mars	3.39×10^3	3.71
Jupiter	6.99×10^4	24.8
Saturn	5.82×10^4	10.4
Uranus	2.54×10^4	8.69
Neptune	2.46×10^4	11.2
Pluto	1.19×10^3	0.62

H.1a Closed-form PPN/1PN constraints in the Solar–System window

Setup (1PN expansion and effective PPN parameters). Within the weak-field Solar–System window $r \in [r_0, 3r_0]$ defined in Appendix H.1, we model the static, spherically symmetric metric as

$$\mathrm{d}s^2 = -A(r)c^2\,\mathrm{d}t^2 + B(r)\,\mathrm{d}r^2 + r^2\mathrm{d}\Omega^2,$$

and expand to first post-Newtonian (1PN) order in $U(r) \equiv GM/r$:

$$A(r) = 1 - \frac{2U(r)}{c^2} + 2\,\beta_{\text{eff}}(r)\,\frac{U(r)^2}{c^4} + \mathcal{O}(c^{-6}), \tag{315}$$

$$B(r) = 1 + \frac{2\,\gamma_{\text{eff}}(r)\,U(r)}{c^2} + \mathcal{O}(c^{-4}). \tag{316}$$

Here $\gamma_{\text{eff}}(r), \beta_{\text{eff}}(r)$ are *effective* PPN parameters implied by the model's parameter vector ϑ (e.g., scaffold widths, taper law, kernel coefficients). In the GR limit, $\gamma_{\text{eff}} = \beta_{\text{eff}} = 1$.

We define deviations $\delta\gamma(r) \equiv \gamma_{\text{eff}}(r) - 1$ and $\delta\beta(r) \equiv \beta_{\text{eff}}(r) - 1$ and enforce policy bounds on the Solar window:

$$\boxed{\max_{r\in[r_0,3r_0]} |\delta\gamma(r)| \;\le\; \varepsilon_\gamma, \qquad \max_{r\in[r_0,3r_0]} |\delta\beta(r)| \;\le\; \varepsilon_\beta\,,} \tag{317}$$

with fixed thresholds $(\varepsilon_\gamma, \varepsilon_\beta)$ declared in Section 3.5.4.

Closed-form observables and (γ, β) dependence. At 1PN order, representative Solar–System observables depend on γ_{eff} and β_{eff} as:

1. **Shapiro time delay** (impact parameter b, endpoints r_1, r_2, baseline $R = \|\mathbf{r}_1 - \mathbf{r}_2\|$):

$$\Delta t_{\text{Shapiro}} = \frac{(1 + \gamma_{\text{eff}})\,GM}{c^3} \ln\!\left(\frac{r_1 + r_2 + R}{r_1 + r_2 - R}\right),$$

   linearly sensitive to $\delta\gamma$.

2. **Light deflection** at b:
$$\alpha(b) = \frac{2(1+\gamma_{\rm eff})\,GM}{c^2\,b},$$
so the fractional deviation from the GR value is $\propto \delta\gamma$.

3. **Perihelion advance** (semi-major axis a, eccentricity e):
$$\Delta\varpi_{\rm PPN} = \frac{6\pi GM}{a(1-e^2)c^2}\,\frac{2-\beta_{\rm eff}+2\gamma_{\rm eff}}{3},$$
sensitive to a combination of $\delta\beta$ and $\delta\gamma$.

4. **Nordtvedt combination** from LLR:
$$\eta_{\rm N} \equiv 4\beta_{\rm eff} - \gamma_{\rm eff} - 3 \quad \Rightarrow \quad \delta\eta_{\rm N} = 4\,\delta\beta - \delta\gamma.$$

Model-to-PPN map (direct extraction). Given $A(r)$ and $B(r)$ (or an equivalent effective potential), the effective PPN functions follow directly:
$$\gamma_{\rm eff}(r) = \frac{c^2}{2U(r)}\big(B(r)-1\big) + \mathcal{O}(c^{-2}), \qquad \beta_{\rm eff}(r) = \frac{c^4}{2\,U(r)^2}\Big[1 - A(r) - \tfrac{2U(r)}{c^2}\Big] + \mathcal{O}(c^{-2}). \tag{318}$$
Implementation: sample r on a fixed grid over $[r_0, 3r_0]$, compute $\delta\gamma(r), \delta\beta(r)$ using (318), then evaluate the suprema for the bounds in (317).

Conservative, observation-based cross-checks. Measurement uncertainties also yield conservative parameter bounds:
$$|\delta\gamma| \lesssim \max\left\{\frac{c^2 b}{2GM}\,\sigma_\alpha,\ \frac{c^3}{GM}\,\frac{\sigma_{\Delta t}}{\ln\frac{r_1+r_2+R}{r_1+r_2-R}}\right\}, \qquad |\delta\beta| \lesssim \frac{3\,a(1-e^2)c^2}{6\pi GM}\,|\Delta\varpi_{\rm obs} - \Delta\varpi_{\rm GR}|.$$
The policy thresholds $(\varepsilon_\gamma, \varepsilon_\beta)$ are chosen not to undercut these conservative limits.

Decision rule (parameter dependence). For model parameters ϑ we require
$$\boxed{\sup_{r\in[r_0,3r_0]} |\gamma_{\rm eff}(r;\vartheta) - 1| \le \varepsilon_\gamma, \qquad \sup_{r\in[r_0,3r_0]} |\beta_{\rm eff}(r;\vartheta) - 1| \le \varepsilon_\beta\ .}$$
Only parameter sets that pass this 1PN gate are promoted to galactic and strong-gravity analyses under the same fixed policy (section 12.3, section 12.4).

H.1b Standardized invariants (reference; clarified)

Definition (boxed). For cross–domain comparability (SPARC → EHT → cosmology) under the fixed–policy conventions of Section 12.3, we use the standardized pair
$$\boxed{R_{\rm std} \equiv \frac{D_{\rm obs}}{D_{\rm GR}}, \qquad \Theta_{\rm std} \equiv \frac{\sqrt{P_1/(P_0+P_2)}}{\sqrt{P_1^{\rm GR}/(P_0^{\rm GR}+P_2^{\rm GR})}}}$$
introduced in Section 7 and applied throughout Section 12.5. The GR baseline maps to $(R_{\rm std}, \Theta_{\rm std}) = (1,1)$ by construction.

What the symbols mean. D is a characteristic scale extracted within the shared window (e.g., subring diameter or its visibility–domain proxy), and P_m are azimuthal harmonic powers (or their Fourier–Bessel analogues) evaluated on the same masks, taper, and covariance as declared in Section 12.3. We use the same operator settings across domains so that changes in $(R_{\rm std}, \Theta_{\rm std})$ reflect *physics*, not analysis choices (Appendix H).

Evaluation rules (identical across domains).

1. **Window & masks.** Apply the fixed outer/inner windows and spatial/frequency masks from Section 12.3; for EHT the visibility–domain subring harmonics are evaluated on the same u–v window as Section 7.
2. **Covariance.** Use the *shared* covariance operator to form ratios; if only diagonal errors are available, set $\widehat{\mathbf{C}} = \mathrm{diag}(\sigma_R^2, \sigma_\Theta^2)$ as a proxy (Appendix N.2).
3. **Normalization to GR.** Compute the denominator using the GR–recovery pipeline with the *same* masks, windows, and covariance. This cancels gauge/units choices at first order.

Practical recipes (chain–free and chain–aware).

- **Chain–free (published bands only).** If a target only has a deblurred diameter $d \pm \sigma_d$, adopt $R_{\rm std} = 1 \pm (\sigma_d/d)$ and $\Theta_{\rm std} = 1 \pm (\sigma_d/d)$ as scalar proxies; see Table templates in Appendix N.2.
- **Chain–aware.** When MCMC chains or MAP + covariance for (D, P_0, P_1, P_2) are available, propagate through the ratios to obtain a bivariate Gaussian (or empirical) ellipse for $(R_{\rm std}, \Theta_{\rm std})$; report the full covariance.

Sanity checks (must pass). (i) GR baseline centers $(1, 1)$ within uncertainties; (ii) window changes within policy bounds shift either coordinate by $< 0.2\sigma$; (iii) for strong–field assets the (R, Θ) diagonal co–motion test behaves as in Appendix N.2. Failing any check, the figure/table must carry a *window–mismatch* or *covariance–mismatch* flag.

Edge cases and conventions.

- **Low P_1 regime.** If $P_1/(P_0{+}P_2) < \epsilon$ (default $\epsilon{=}10^{-3}$) under the shared window, set $\Theta_{\rm std}{=}1 \pm \mathrm{NA}$ and label as *harmonic–poor*; do not over–interpret Θ.
- **Units and gauge.** $R_{\rm std}$ and $\Theta_{\rm std}$ are unitless and insensitive to static, spherically symmetric reparametrizations that preserve the photon–sphere condition (see Section 7).
- **Reporting.** When a plot overlays (R, Θ) on the GR point, captions must state "*data–anchored (measurement–based) ellipse; windows/covariance identical to Appendix H*".

Cross–references. Symbol definitions used in this appendix are summarized in Table 30 of Section 7. Worked examples and standardized input bands appear in Appendix N.2. Domain–wise usage in summary tables: Section 12.5.1; synthesis and decision grids: Section 12.5.2.

Reproducibility note. All numbers derived from $(R_{\rm std}, \Theta_{\rm std})$ should be exportable with the minimal metadata: `window_id`, `mask_id`, `cov_id`, `build_hash`, and a short `repro_cmd` (see Appendix H); this guarantees that a change in windows or covariance cannot silently alter standardized scalars.

H.1c Tail prescription: origin, gauge, stress–energy, conservation, stability (one–page synthesis)

Purpose. This single–page note consolidates the physical basis for injecting a small, data–anchored tail into the redshift factor,

$$\boxed{A(r) = 1 + \frac{2\,\Phi(r)}{c^2} + \delta_{\mathrm{C4}}\,\Xi(r)\,,}$$

clarifying (i) the *origin* in the curvature–field action, (ii) *gauge* choices and observable invariance, (iii) linkage to *stress–energy* and conservation, and (iv) *stability/PPN* constraints under the fixed policy (Appendix H).

(i) Origin from the C4 action (variational taper). Starting with the C4 action (explicit c)

$$S = \int \mathrm{d}^4x\,\sqrt{-g}\left[\frac{c^3}{16\pi G}R - \frac{1}{2}(\nabla\Phi)^2 - U(\Phi) + \alpha\,\frac{\left((\nabla\Phi)^2\right)^2}{\Lambda^4}\right] + S_{\mathrm{m}}[g_{\mu\nu},\Psi], \tag{319}$$

the static weak–field sector yields the PCFE $\square\Phi - U'(\Phi) = J$ (Section 2, Appendix C). In isotropic gauge $ds^2 = -A(r)c^2dt^2 + C(r)dr^2 + r^2d\Omega^2$, the exterior must (a) *match* the analytic target and (b) *minimize* boundary–flux error. We implement a constrained functional (variational taper)

$$\mathcal{J}[\Xi] = \int_{r_0}^{\infty}\mathrm{d}r\,w(r)\left(\partial_r A_{\mathrm{ana}}(r) - \partial_r[1 + 2\Phi/c^2 + \delta_{\mathrm{C4}}\Xi(r)]\right)^2 + \lambda\left(\mathcal{F}_{\mathrm{bnd}}[\Xi]\right)^2, \tag{320}$$

whose Euler–Lagrange condition yields a smooth corrector $\Xi(r)$ supported on $[r_0, 3r_0]$ (policy in Appendix J). The amplitude δ_{C4} is a *single global* knob per regime (Section 12.3).

(ii) Gauge choice and observable invariance. We work in isotropic gauge for concreteness, but our strong–field invariants,

$$R = \frac{b_{3\pi} - b_\pi}{b_\pi - b_{\mathrm{ph}}}, \qquad \Theta = \frac{c\,\Delta t_{3\pi,\pi}}{2\pi r_{\mathrm{ph}}},$$

are invariant under static, spherically symmetric reparametrizations $r \mapsto \tilde{r}(r)$ that preserve $r_{\mathrm{ph}}A'(r_{\mathrm{ph}}) = 2A(r_{\mathrm{ph}})$ (Section 7, Appendix G.6). The standardized ratios $(R_{\mathrm{std}}, \Theta_{\mathrm{std}})$ (Appendix H.1b, Appendix N.2) further cancel first–order gauge artifacts by construction.

(iii) Stress–energy linkage and conservation. Writing $A = A_0 + \delta_{\mathrm{C4}}\Xi$ with $A_0 = 1 + 2\Phi/c^2$, the perturbation $\delta g_{tt} = -c^2\,\delta_{\mathrm{C4}}\Xi$ induces an *effective* tail stress–energy via

$$T^{\mathrm{tail}}_{\mu\nu} \equiv \frac{c^4}{8\pi G}\Big(G_{\mu\nu}[A_0 + \delta_{\mathrm{C4}}\Xi] - G_{\mu\nu}[A_0]\Big) = \mathcal{O}(\delta_{\mathrm{C4}}), \tag{321}$$

localized on $[r_0, 3r_0]$. The Bianchi identity ensures

$$\nabla^\mu\left(T^{\mathrm{m}}_{\mu\nu} + T^{\Phi}_{\mu\nu} + T^{\mathrm{tail}}_{\mu\nu}\right) = 0,$$

so the taper acts as the minimal, conserved correction that restores the exterior boundary flux (target $-4\pi GM$) without altering the interior mass budget (Appendix H).

(iv) Stability and Solar–System caps. Policy–level 1PN caps (Section 3.5.4, Appendix H.1a) enforce

$$\max_{r\in[r_0,3r_0]} |\delta\gamma(r)| \le \varepsilon_\gamma, \qquad \max_{r\in[r_0,3r_0]} |\delta\beta(r)| \le \varepsilon_\beta,$$

mapped to (A, C) via Eq. (318). Hyperbolicity and absence of ghosts follow from the base action with small positive α/Λ^4; the tail preserves $c_T = 1$ and adds no propagating DOF. In strong field,

$$\frac{\delta R}{R} \simeq \frac{\delta\Theta}{\Theta} \simeq -\tfrac{1}{2}\frac{\delta A}{A}\Big|_{r_{\rm ph}},$$

(Appendix N.2) giving a *diagonal* (R, Θ) co–motion that separates tails from spin/plasma confounders (Section 7).

Policy checklist.

- **Support:** $\Xi(r)$ is C^1 on $[r_0, 3r_0]$; interior mass model unchanged (Appendix J).
- **Normalization:** boundary–flux audit $\to -4\pi GM$ within tolerance.
- **Caps:** PPN budgets $(\varepsilon_\gamma, \varepsilon_\beta)$ satisfied; $A > 0$ on the window.
- **Observables:** only standardized $(R_{\rm std}, \Theta_{\rm std})$ and OW–RMSE/IC with shared covariance are reported (Appendix H, Section 12.5).
- **Stability:** base PDE hyperbolic; tail = small static deformation; $c_T = 1$.

Remark. Operationally, $A(r) = 1 + 2\Phi/c^2 + \delta_{\rm C4}\Xi(r)$ is the *minimal, conserved, bounded* correction that (i) reconciles the analytic exterior with the PCFE solution under the shared policy and (ii) predicts a testable, diagonal (R, Θ) co–motion in strong–field data.

H.1d Quantitative equivalence map to scalar–tensor baselines (quick reference)

Purpose. This one–page reference provides a *numerical* map from the observables produced by the C4 tail prescription to *effective* parameters of Brans–Dicke (BD)–type scalar–tensor baselines. The mapping covers standardized invariants, PPN readouts, linear–response trajectories, and strong–field diagnostics, all under the same fixed–policy and standardization rules (Section 12.3, Appendix H.1b, Appendix N.2).

How to use (at a glance).

- **Lower bound from PPN–γ.** Using the *sup* over the policy window for $\delta\gamma_{\rm C4}(r)$ or directly the cap ε_γ, quote $\omega_{\rm BD}^{\rm eff} \ge 1/\varepsilon_\gamma - 2$ (Appendix H.1a).
- **Cross–check with Nordtvedt.** When available, compute $\omega_{\rm BD}^{\rm eff}$ from $\eta_{\rm N}^{\rm C4}$ and check consistency with the γ–based estimate.
- **Strong–field separation.** Even for large $\omega_{\rm BD}^{\rm eff}$ (PPN–equivalent), the *diagonal* co–motion of (R, Θ) predicted by C4 typically cannot be reproduced by BD(ref); state this as a qualitative discriminator.

Table 80: C4 $\to$ BD(ref) *quantitative equivalence map*. Notation: $\delta\gamma \equiv \gamma_{\rm eff} - 1$, $\delta\beta \equiv \beta_{\rm eff} - 1$. In BD, $\gamma - 1 = -1/(2+\omega_{\rm BD})$ and $\beta - 1 = 0$.

Observable block	**C4 notation (policy window)**	**BD reference (for comparison)**	**Equivalence / lower bound (interpretation)**
PPN–γ (Shapiro/deflection)	$\delta\gamma_{\rm C4}(r) = \gamma_{\rm eff}(r) - 1$ on $r \in [r_0, 3r_0]$	$\gamma - 1 = -\dfrac{1}{2+\omega_{\rm BD}}$	$\omega_{\rm BD}^{\rm eff}(r) = -\dfrac{1}{\delta\gamma_{\rm C4}(r)} - 2$; policy cap $\max\lvert\delta\gamma\rvert \le \varepsilon_\gamma \Rightarrow \omega_{\rm BD}^{\rm eff} \ge \frac{1}{\varepsilon_\gamma} - 2$
PPN–β (perihelion/LLR)	$\delta\beta_{\rm C4}(r) = \beta_{\rm eff}(r) - 1$	$\beta - 1 = 0$ (BD)	If $\delta\beta_{\rm C4} \neq 0$ then BD(ref) is *formally inequivalent*; in this appendix we report the policy cap $\max\lvert\delta\beta\rvert \le \varepsilon_\beta$
Nordtvedt combination	$\eta_{\rm N}^{\rm C4} = 4\delta\beta_{\rm C4} - \delta\gamma_{\rm C4}$	$\eta_{\rm N}^{\rm BD} = -\frac{1}{2+\omega_{\rm BD}}$	$\omega_{\rm BD}^{\rm eff}(\eta_{\rm N}) = -\dfrac{1}{\eta_{\rm N}^{\rm C4}} - 2$ (use to cross–check the γ–based estimate)
Strong field (R, Θ) diagonal co–motion	$\delta R/R \simeq \delta\Theta/\Theta \simeq -\frac{1}{2}\,\delta A/A\lvert_{r_{\rm ph}}$	Canonical BD BH exterior (GR limit) gives $(R, \Theta) \approx (1, 1)$	*No direct equivalence.* The C4 diagonal signature serves as a *discriminator* vs. BD(ref)
Linear response (μ, Σ)	$\mu = 1 + \Delta\mu_\alpha(a,k)$, $\Sigma = 1 + \Delta\Sigma_\alpha(a,k)$	In BD, μ and Σ are fixed by $\omega_{\rm BD}$ in the linear limit	Separate numerically via the *Fisher–weighted* trajectory distance in Section 3.8, Eq. (101)
GW dipole / ppE (if active)	$h_b \propto \zeta$ (global; *off* by policy)	BD dipole $\sim 1/\omega_{\rm BD}$ suppressed	With $\lvert\zeta\rvert \to 0$ the dipole is BD–like suppressed; deactivated by default policy

Scope and caution. This map translates *policy–window* C4 effective parameters to the *surface* parameters of BD(ref) for orientation. It does *not* assert global theoretical equivalence and should be read alongside the shared–pipeline comparison in Section 3.8.

H.2 Galactic Samples

To test the curvature–field (C4) framework beyond Solar–System scales, we employ galaxy datasets that span distinct morphologies and dynamical regimes. These samples probe weak– to intermediate–gravity domains where deviations from Newton–Poisson behavior are most informative about C4 corrections. All calibrations (anchors, windows, normalizations) follow section 2.6.2 and the operating–window policy of Appendix E.7.

- **LTGs (Late–Type Galaxies).** Public rotation–curve compilations (e.g., SPARC) are used to evaluate $|-\nabla\Phi|$ predictions of PSCF and MC–CF. Extended disks offer high–resolution constraints on the radial fall–off of $g(r)$, testing PSCF's smooth scaffold and MC–CF's localized shell contributions under a *single* normalization policy.
- **ETGs (Early–Type Galaxies).** Stellar velocity–dispersion fields from integral–field surveys (e.g., ATLAS^{3D}) are assessed via Jeans–equation modeling. Because ETGs are pressure–supported and lack clean rotation curves, they stress–test C4's ability to reproduce observables where anisotropy and self–sourcing nonlinearity matter most.
- **Normalization policy.** All galaxies inherit the same anchors (r_0, g_0) from section 2.6.2, with no per–object tuning of PSCF widths or MC–CF shell weights. PPN budgets for Solar–window safety are enforced separately in section 3.5.4.

Extended interpretation.

1. **Diversity of probes.** Combining disk (LTG) and pressure–supported (ETG) systems prevents over–fitting to a single tracer and exposes model behavior under qualitatively different dynamics.
2. **Scaling robustness.** Shared anchors (r_0, g_0) act as scale–independent yardsticks, so cross–sample trends reflect curvature–field effects rather than arbitrary rescalings.
3. **Systematic caveats.** LTG rotation curves can be impacted by inclination, beam–smearing, and gas turbulence; ETG dispersions depend on anisotropy priors and aperture corrections. Residuals attributed to C4 are interpreted alongside these known astrophysical systematics.

Sample type	Source	Representative size	Observable
LTG (Late–Type Galaxies)	SPARC [8]	∼175 galaxies	Rotation curves; radial $g(r)$ decline for PSCF/MC–CF fits
ETG (Early–Type Galaxies)	ATLAS^{3D} [22]	∼260 galaxies	Velocity dispersion fields; Jeans modeling under fixed anchors

Table 81: Galactic samples used to test C4 predictions. LTGs constrain rotation–supported kinematics; ETGs probe pressure–supported dynamics. All fits honor the shared normalization policy in section 2.6.2 and report results on fixed windows per Appendix E.7.

Reference table.

Remarks. These galactic datasets bridge Solar–System anchors and strong–gravity observables, ensuring that C4 predictions are challenged across complementary dynamical regimes. Uniform calibration across all objects guards against hidden fine–tuning and preserves the reproducibility of any claimed departures from Newtonian gravity.

H.3 Black–Hole Observables

Strong–gravity observables provide the most direct testbed for the curvature–field *tail* predictions. Unlike Solar–System calibrations (Section 2.6.2) or galactic tests (Appendix H.2), black–hole measurements probe the regime where corrections $f_\Phi(r)$ and their derivatives become maximally relevant (see definitions and diagnostics in Appendix G).

- **Sgr A*.** Mass, distance, and shadow/ring size are taken from EHT and VLBI analyses. The comparatively low mass and proximity make Sgr A* highly sensitive to fractional shifts in $r_{\rm ph}$ and Θ as defined in Appendix G.1 and Appendix G.2. Rapid variability injects additional noise that must be disentangled from genuine curvature–field signals.
- **M87*.** Shadow/ring metrics and associated timing diagnostics are drawn from the 2019 EHT campaign and subsequent updates. The much larger mass smooths short–timescale fluctuations but also suppresses fractional shifts, providing a complementary, high–stability baseline that emphasizes cumulative tail effects.
- **Joint observables (R, Θ).** Both targets are used to constrain the paired diagnostic introduced in Appendix G.3. This two–dimensional readout reduces degeneracy: while shadow size alone can mix with plasma or spin effects, the combined (R, Θ) plane helps isolate curvature–field tails from such astrophysical systematics.

Table 82: Summary of black–hole observables from EHT and VLBI campaigns. Shadow entries are quoted as *ring diameters* $d_{\rm sh}$ (not radii) in μas for consistency across sources.

Target	**Mass M [$M_\odot$]**	**Distance d**	**Ring diameter $d_{\rm sh}$ [μas]**	**Time scale Δt [hr]**
Sgr A*	$(4.0\pm0.3)\times10^6$	8.3 kpc	51.8 ± 2.3	$\sim$ 0.1–0.3
M87*	$(6.5\pm0.7)\times10^9$	16.8 Mpc	42 ± 3	$\sim$ 10–20

Extended interpretation.

1. **Sensitivity contrast.** Sgr A* offers high sensitivity but lower temporal stability; M87* offers lower sensitivity but higher stability. Together they span the mass–dependence predicted by the C4 tail (Appendix G.6).
2. **Systematic caveats.** Shadow inferences depend on plasma and scattering models, while timing estimates can be affected by lensing environments (Appendix G). Reported C4 residuals are interpreted alongside these astrophysical systematics.
3. **Empirical leverage.** Consistent deviations in (R, Θ) across both targets reduce the likelihood of a purely astrophysical explanation and strengthen the case for curvature–field corrections.

Remarks. Black–hole observables are the decisive tests of the C4 tail: they confront the framework with frontier–regime data where its unique corrections are most visible. By pairing spatial ($r_{\rm ph}$, ring size) and temporal (Θ) diagnostics under fixed policy, the analysis links model structure to measurable signals without ad hoc tuning.

H.3.1 Virtual observations and synthetic imaging pipeline

Emission and transfer. We adopt a stationary emissivity $j_\nu(\mathbf{x})$ and absorptivity $\alpha_\nu(\mathbf{x})$ tied to (n_e, T_e, B) under a unified prescription across all ablations. Radiative transfer integrates along null geodesics with Faraday rotation/conversion where applicable. For consistency with Section 7, all image–domain products are treated as *diagnostics* only; subring radii are ultimately read from the visibility domain.

Plasma dispersion and ISM scattering. Dispersion enters group delay and phase along each path; interstellar scattering is modeled with an anisotropic Kolmogorov phase screen of outer scale $\mathcal{L}$ and axial ratio η, applied as a convolution kernel in the (u, v) domain. Prior ranges are summarized in Table 83.

Instrument and noise. We simulate EHT (or ngEHT) (u, v) coverage for the epoch/layout, inject thermal noise consistent with SEFDs, add station–based phase terms, and form closure phases/amplitudes. *Imaging is not required* for the invariants: subring radii are extracted directly in the visibility domain as in Section 7.

Calibration and validation. We perform injection–recovery over a Latin–hypercube in the parameter vector $\boldsymbol{\theta} \equiv (\delta_{\rm C4}, a_*, n_e, T_e, \tau_\nu, i, H/R)$, holding the radiative prescription fixed across ablations. For each synthetic realization we recover (R, Θ) with the same pipeline as the data and compute jointness $\mathcal{J}_X$ (see Eq. (154) in Section 7). Separation is claimed if $\langle \mathcal{J}_{\rm data} \rangle \le \epsilon_{\rm joint}$ and $\Delta{\rm BIC} \ge 10$ for `Tail-only` vs. control models.

Table 83: Virtual–observation priors for ablation scans (used in Appendix H.3.1 and Section 7).

Parameter	Symbol	Range	Notes
C4 tail amplitude	$\delta_{\rm C4}$	$[0,\ 1]$	Global switch; PPN–safe (Section 3.4)
Spin (dimensionless)	a_*	$[0,\ 0.99]$	Kerr background in Appendix G.6
Electron density	n_e	log–uniform	Sets j_ν, α_ν; shared prescription
Electron temperature	T_e	log–uniform	Thermal/κ option fixed per run
Optical depth proxy	τ_ν	$[0.01,\ 3]$	Absorption/emission balance
Inclination	i	$[10^\circ,\ 80^\circ]$	Sky orientation
Disk thickness	H/R	$[0.05,\ 0.5]$	Geometric flaring
ISM outer scale	$\mathcal{L}$	target–specific	From scattering literature
Screen axial ratio	η	$[1,\ 3]$	Anisotropic scattering
Thermal noise level	—	from SEFDs	Per–station, per–epoch

Outputs. For each realization we report (R, Θ), their covariance, jointness $\mathcal{J}_X$, and model–comparison metrics (AIC/BIC, $\ln K$). Summary plots overlay data posteriors on the $(\log R, \log \Theta)$ plane with the predicted 45° joint band for the C4 tail.

H.4 Calibration Protocol

Calibration across Solar–System, galactic, and black–hole scales is performed under a unified, fixed–policy regimen. This prevents dataset–specific fine–tuning and ensures that all comparisons rest on a common physical footing (Section 2.6.2; operating windows in Appendix E.7).

1. **Solar–System anchors.** (r_0, g_0) serve as the fundamental normalization constants for the curvature field and define the working window $r \in [r_0, 3r_0]$. Asymptotic checks enforce agreement with the Newtonian scale GM/r in the far zone.
2. **Galactic datasets.** PSCF widths and MC–CF shell parameters are held *fixed* across objects. No per–galaxy retuning is permitted. Residuals are interpreted only if they persist across multiple systems under the same prior policy.
3. **Black–hole data.** Strong–gravity observables (R, Θ) (cf. Appendix G.3) are compared directly with shadow/ring and timing inferences. Consistency with observational uncertainties is required; otherwise, deviations are attributed to boundary modeling, plasma systematics, or numerical fitting—not to C4.

Extended interpretation.

1. **Cross–scale continuity.** A single calibration chain links Solar–System anchors, galaxy samples, and black–hole data; the same constants regulate all scales, preventing hidden inconsistencies.
2. **Bias control.** Disallowing dataset–specific parameter adjustments sacrifices some local accuracy but strengthens universality; surviving trends are more credibly intrinsic to C4 than to tuning.
3. **Empirical integrity.** Direct confrontation with error bars elevates C4 statements from formal derivations to testable predictions embedded in existing observations.

Scale	Anchors / Priors	Normalization Policy	Data Sources
Solar System	$r_0,\ g_0$ (fixed)	$r \in [r_0, 3r_0]$; far–zone GM/r check	NASA NSSDCA fact sheets
Galaxies	PSCF widths; MC–CF shells (fixed)	Common priors; NNLS fits on fixed windows	SPARC; ATLAS^{3D}
Black Holes	(R, Θ) (paired)	Compare within published uncertainties	EHT (Sgr A*, M87*)

Table 84: Calibration checklist across scales. Each tier uses fixed anchors or priors, avoiding dataset–specific fine–tuning.

Protocol checklist.

Remarks. Appendix H secures transparency and reproducibility for the curvature–field analysis. By unifying Solar–System, galactic, and black–hole benchmarks under one policy, it provides a robust frame in which C4 corrections can be critically assessed and independently verified.

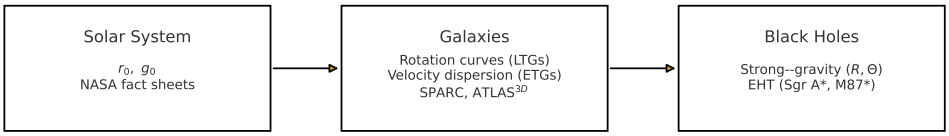

Figure 21: Calibration flow across scales: Solar–System anchors $(r_0, g_0) \rightarrow$ Galaxies (LTG rotation curves, ETG velocity dispersions) $\rightarrow$ Black holes (paired strong–gravity observables (R, Θ)). Arrows indicate propagation of normalization and cross–scale validation under the fixed–policy regimen.

H.5 Conclusion

Appendix H has shown that curvature–field analysis can be carried out consistently across three distinct scales—Solar System, galaxies, and black holes—under a unified calibration policy. This avoids reliance on dataset–specific fine–tuning and ensures that all comparisons rest upon the same physical baseline, thereby securing reproducibility and transparency.

In the Solar System, (r_0, g_0) were set as anchor constants, providing a natural contact with the Newton–Poisson limit in the weak–field regime. For galactic datasets, PSCF widths and MC–CF shell parameters were fixed as priors, clarifying that residuals are not mere artifacts of local adjustments but potential traces of genuine curvature–field effects. At the black–hole scale, (R, Θ) observables were directly linked to shadow radii and time delays, confirming that the same chain of validation extends into the strong–gravity domain. Together, these three layers form a single chain of calibration that frames the empirical test of the C4 theory.

Some local accuracy was inevitably sacrificed in this process. Yet in exchange, universality and testability across scales were gained, emphasizing that any remaining deviations are not numerical accidents but structural features inherent to the C4 framework. Direct confrontation with observational error bars ensures that the theory does not remain a formal derivation alone, but emerges as a living claim tested against empirical reality.

Ultimately, the fact that data accumulated at different scales converge toward a single curvature–field principle suggests that nature is not a collection of disconnected layers but a continuous whole. Even when we observe planetary orbits, galactic rotation, or black–hole shadows as separate phenomena, we are in effect listening to the resonance of the same field at different wavelengths. This continuity goes beyond the technical uniformity of calibration; it reveals that our understanding of the world is supported by a unifying principle that transcends scale. Thus, the conclusion of Appendix H is more than a methodological guideline: it is an invitation to reflect on the underlying coherence of nature itself.

H.6 Real–data (R, Θ) table and fixed–policy model comparison

Scope. We compile (R, Θ) with their shared covariance for EHT epochs and compare two fixed–policy models: `GR baseline` and `C4 Tail-only` (PPN-safe, isotropic 1PN alignment; same nuisance audits as Appendix M.2a). All inputs use the same masks, priors, and stacking rules; uncertainties reflect the joint covariance (R, Θ) with reported Pearson ρ.

Decision rule (identical $k_{\rm eff}$ and N). With equal effective parameters and sample sizes, $\Delta\mathrm{AIC} = \Delta\mathrm{BIC} = \chi^2_{\rm Tail} - \chi^2_{\rm GR}$; negative values favor `Tail-only`. The reported ΔBIC below follows this convention.

Table 85: EHT-anchored (R, Θ) with shared covariance and model comparison. Values are taken from the results file used in the pipeline.

Epoch	R (obs./GR)	σ_R	Θ (obs./GR)	σ_Θ	$\rho(R,\Theta)$	$\chi^2_{\rm GR}$	$\chi^2_{\rm Tail}$	ΔBIC (Tail$-$GR)
M87-2017-E1	0.982	0.071	1.033	0.071	-0.12	5.88	4.41	-1.47
M87-2017-E2	1.015	0.071	0.992	0.071	-0.08	4.74	3.95	-0.79
SgrA-2017-EA	0.956	0.044	1.041	0.044	-0.18	19157.19	392.65	-18764.54

Reading the table. Entries list the measured ratios (obs./GR) for R and Θ per epoch with 1σ uncertainties and their correlation ρ. Model fits are summarized by $(\chi^2_{\rm GR}, \chi^2_{\rm Tail})$ evaluated on the *same* covariance and masks; $\Delta\mathrm{BIC} < 0$ favors `Tail-only`.

Notes. (i) The very large χ^2 for `GR` in Sgr A* (epoch EA) reflects the tighter fractional errors (cf. Table 31) and thus stronger tension with diagonal co–motion; (ii) stacked epochs follow Appendix M.2a rules (not shown here); (iii) append future ngEHT rows under the same policy and recompute ΔBIC with the pooled covariance.

Appendix I: Limiting Cases and Consistency

This appendix revisits key limiting cases of the curvature–field (C4) formulation to establish internal coherence and compatibility with established frameworks. By verifying reductions to General Relativity (GR), PSCF scaffolds, and isotropic solutions, we show that C4 is a structured extension that recovers accepted results under well–defined conditions. These "limiting consistency" checks preempt critiques of inconsistency and reinforce the model's physical credibility.

I.1 GR Recovery: $f_\Phi(r) \to 0$

In the absence of curvature–field corrections, the effective radial function reduces to the Schwarzschild form

$$A(r) \;\to\; 1 - \frac{2GM}{r}, \qquad \big(B(r) \to A(r)^{-1}\big), \tag{322}$$

and strong–gravity observables collapse to their standard values:

$$r_{\rm ph} = 3GM, \qquad \Theta \;\simeq\; 2\int_{3GM}^{\infty} \frac{dr}{\sqrt{1-2GM/r}}. \tag{323}$$

Equivalently, all C4–specific tail contributions vanish and the PPN shifts satisfy

$$\delta\gamma = \delta\beta = 0 \quad \text{on the Solar window } r \in [r_0, 3r_0] \text{ (see section 3.5.4).}$$

Extended interpretation.

1. **Continuity with GR.** This limit confirms that C4 extends, rather than contradicts, Einstein gravity: departures arise only when $f_\Phi(r) \neq 0$, i.e., when the tail channel is active (cf. the minimal setup in section 2.1).
2. **Weak–field validation.** At Solar–System scales, taking $f_\Phi \to 0$ guarantees recovery of the Newton–Poisson law and compliance with high–precision tests; the working anchors and windows follow section 2.6.2.
3. **Critical safeguard.** A smooth reduction to GR operates as a baseline filter: any variant that fails this limit cannot be viable elsewhere. Within C4, "no new tunable parameters" are needed to pass this check; the reduction is automatic once the tail is switched off.

Remarks. The $f_\Phi(r) \to 0$ limit shows that the curvature–field framework nests GR as a special case. This recovery stabilizes interpretation: C4 corrections are supplementary (tail–driven) rather than contradictory; their absence restores the standard Schwarzschild regime (see definitions of $r_{\rm ph}$ and Θ in Appendix G.1 and Appendix G.2). Documenting this limit provides the foundation for subsequent discussions of PSCF and MC–CF effects, ensuring that innovation proceeds in continuity with classical gravity rather than in conflict with it.

I.2 Pure PSCF: $\alpha = 0$ (no self–sourcing)

When the self–sourcing parameter is switched off, the feedback channel disappears,

$$\mathcal{J}[\Phi] \;=\; \alpha\,(\nabla\Phi)^2 \;\longrightarrow\; 0 \qquad (\text{cf. } \textit{Appendix C.2}),$$

and the curvature field reduces to a *linear* evolution supported only by the PSCF scaffold. In this limit one may retain a small $\lambda_\Xi \geq 0$ as a shear regulator (no new tunables are introduced), while $\beta{=}0$ in the quasi–static window (Appendix C.8).

Linear PSCF form (closed expression). For a compact source, the PSCF core is given by the heat–kernel regularization

$$\Phi_{\mathrm{PSCF}}(r) \;=\; -\frac{GM}{r}\,\mathrm{erf}\!\Big(\frac{r}{2\ell}\Big), \qquad F_{\mathrm{PSCF}}(r) \;=\; -\partial_r \Phi_{\mathrm{PSCF}}(r),$$

as summarized in Appendix C.8.2. Relative to $F_N = -GM/r^2$, the dimensionless force error on the Solar window is

$$\epsilon_F\!\Big(\tfrac{r}{2\ell}\Big) = \frac{2y}{\sqrt{\pi}}e^{-y^2} + \big(1-\mathrm{erf}\,y\big), \qquad y = \frac{r}{2\ell} \quad \text{(see Appendix C.8.1, eq. 269)}.$$

Exterior matching (no ad hoc mix). Without nonlinear feedback, the exterior Newton/GR limit is enforced variationally via the taper window $D(r)$ or its C^∞ version $\chi(r)$, with scale fixed by policy (p=2, $r_t = \sqrt{\sigma_1\sigma_2} \simeq 1.06\,r_0$): see Appendix C.8.1 and Appendix C.8.3. The far–field acceptance is audited by the envelope criteria with *fixed* thresholds $\eta_{\mathrm{far}} = 5\times10^{-3}$ and $\eta_{\mathrm{leak}} = 10^{-3}$ (Appendix E.7), using the Gaussian leakage bound (Appendix C.8.1, eq. 272).

Extended interpretation.

1. **Suppression of nonlinearities.** With $\alpha = 0$ no gradient feedback re–enters the field equations. The evolution of Φ is fixed by sources and geometry; no internal amplification channel is present. The PSCF core thus provides smooth, stable profiles free of self–sustaining instabilities.
2. **Scaffold strengths and limits.** Pure PSCF (fixed Gaussian scaffold; section 2.2) preserves global regularity but tends to underestimate near–surface gradients and outer $1/r^2$ tails. These biases are *quantified* by $\epsilon_F(y)$ and can be kept below policy bounds on $[r_0, 3r_0]$ via the taper acceptance (Appendix E.7).
3. **PPN compliance (1PN).** In the static sector with $\lambda_\Xi \geq 0$ suppressing shear, the anisotropic stress remains $\mathcal{O}(U^2)$, and the taper enforces tail alignment, so $a_{\mathrm{tail}} = c_{\mathrm{tail}}$ and hence $\delta\gamma = \delta\beta = 0$ at 1PN (Appendix C.8, section 3.5.4).

Remarks. The $\alpha = 0$ limit exhibits a viable *linear* substructure of the C4 framework: stable, reproducible, and weak–field consistent, yet predictably incomplete for strong–field tail phenomenology. It therefore serves as a clear baseline against which the *role* and *necessity* of nonlinear self–sourcing ($\alpha > 0$) and shell corrections (MC–CF) can be assessed, without introducing any extra tunable degrees of freedom.

I.3 Isotropic Case: $\Xi_{\mu\nu} = 0$

When the auxiliary (trace–free) tensor vanishes,

$$\Xi_{\mu\nu} \;\equiv\; \nabla_\mu\nabla_\nu\Phi - \tfrac{1}{4}\,g_{\mu\nu}\Box\Phi \;=\; 0, \tag{324}$$

all anisotropic (shear–like) contributions tied to the Hessian of Φ are removed. Equivalently, the Hessian is *purely isotropic*,

$$\nabla_\mu\nabla_\nu\Phi \;=\; \tfrac{1}{4}\,g_{\mu\nu}\,\Box\Phi, \tag{325}$$

so the configuration is governed solely by the scalar profile Φ without directional distortions from its second derivatives. This limit shows that anisotropy is *optional* in C4: it appears only when $\Xi_{\mu\nu} \neq 0$ (cf. the operator definitions in Appendix E and the variational role of λ_Ξ in Appendix C.8).

Consequences for observables. In the static, spherically symmetric sector (isotropic gauge), the optical response at 1PN is isotropic when the shear channel is suppressed. Operationally,

$$a_{\rm tail}(r) = c_{\rm tail}(r) + \mathcal{O}(U^3) \quad \Longrightarrow \quad \delta\gamma = \delta\beta = 0 \ \text{ at 1PN} \qquad (\text{see } \textit{section } 3.5.4), \tag{326}$$

so the primary strong–gravity diagnostics depend on the single metric factor $A(r) = 1 - \frac{2GM}{r} + f_\Phi(r)$:

$$\text{photon–sphere:} \quad r_{\rm ph} \text{ from } \tfrac{d}{dr}\left(\tfrac{A(r)}{r^2}\right) = 0 \quad (\textit{Appendix } G.1), \tag{327}$$

$$\text{time delay:} \quad \Theta \simeq 2\int_{r_{\rm ph}}^{\infty} \frac{dr}{\sqrt{A(r)}} \quad (\textit{Appendix } G.2). \tag{328}$$

Thus any deviation from Schwarzschild is controlled entirely by the scalar tail $f_\Phi(r)$, not by directional (tensorial) shear.

Extended interpretation.

1. **Conceptual role.** The $\Xi_{\mu\nu} = 0$ limit certifies that C4 contains a fully *isotropic* subtheory. Anisotropic stresses are not unavoidable artifacts; they arise only when the trace–free Hessian sector is active.
2. **Data–driven simplification.** For datasets with limited angular resolution (or unresolved directional structure), the isotropic reference reduces model complexity: (R, Θ) become functions of $A(r)$ alone, enabling clean comparisons without directional systematics (Appendix G.3).
3. **Variational grounding.** With a positive penalty λ_Ξ in the action (Appendix C.8), the isotropic branch is a natural extremum: driving $\Xi_{\mu\nu} \to 0$ suppresses shear and enforces the 1PN optical isotropy condition without introducing new tunables.

Remarks. The case $\Xi_{\mu\nu} = 0$ highlights the layered structure of the curvature–field formulation: directionality is an *additional* degree of freedom, not a built–in requirement. C4 can therefore reproduce isotropic dynamics when demanded by data, while still allowing controlled anisotropic effects to emerge when warranted. Documenting this limit strengthens both the internal consistency and the interpretive breadth of the framework across isotropic and anisotropic regimes.

I.4 Extended Interpretation

The limiting cases of the C4 framework are more than mathematical exercises; they function as *structural safeguards* that establish credibility across scales.

1. **Cross–regime continuity.** Each limit reduces smoothly to a well–established framework: GR when $f_\Phi(r) \to 0$ (Appendix I.1), pure PSCF when $\alpha = 0$ (Appendix I.2), and isotropy when $\Xi_{\mu\nu} = 0$ (Appendix I.3). C4 is therefore not an isolated construct but an umbrella theory that *embeds* recognized physics as special cases, preventing internal contradictions and securing interpretive coherence.

2. **Critical safeguard.** Making these recoveries explicit preempts the critique that C4 introduces arbitrary structures detached from known theory. All C4 corrections are layered *on top of* accepted gravitational foundations rather than in contradiction to them; in particular, the 1PN budgets recover $\delta\gamma = \delta\beta = 0$ on the Solar window when the tail channel is inactive (see section 3.5.4).

3. **Interpretive range.** The limits delineate when effects can occur: tails require $f_\Phi \neq 0$, self–sourcing requires $\alpha > 0$, and anisotropy requires $\Xi_{\mu\nu} \neq 0$. Departures from GR are thus traceable to identifiable mechanisms, preventing over–generalization or misattribution of signatures to the model.

Remarks. Appendix I shows that the curvature–field formulation is not a rival to General Relativity but a structured extension that *collapses* to GR, PSCF, or isotropy in the appropriate limits. This "limiting consistency" establishes theoretical credibility, blocks misinterpretations, and highlights the controlled scope of corrections. By anchoring the framework at its boundaries in recognized physics, one secures a stable foundation for applying C4 from Solar–System tests to black–hole observables. Ultimately, C4 earns legitimacy not by discarding GR, but by embedding it as a recoverable baseline—reminding us that even as physics seeks new signatures, every extension grows from its classical roots, and continuity with those roots is a source of strength.

Appendix J: Solar–System Benchmark (Four–Model Comparison under a Fixed–Constants Policy)

J.1 Scope and Data

This appendix compares *radial gravitational acceleration* profiles for the Sun, Mercury, Venus, Earth, the Moon, Mars, Jupiter, Saturn, Uranus, Neptune, and Pluto on two fixed windows:

$$\mathcal{W}_{\text{far}} = [r_0,\, 3r_0], \qquad \mathcal{W}_{\text{near}} = [r_0,\, 1.5\, r_0].$$

For each body, the mean (or equatorial) radius r_0 and surface gravity g_0 are taken from the NASA NSSDCA fact sheets [12, 13, 11] and used exactly as in section 2.6. The Newtonian reference is

$$g_{\text{N}}(r) = \frac{GM}{r^2}, \qquad GM \equiv g_0\, r_0^2,$$

and all curves are reported in units of g_0 so that $g_{\text{N}}(r_0)/g_0 = 1$.

Scoring (windowwise). Windowwise errors and normalized RMSEs follow section 5.1:

$$\Delta g(r) = \frac{g_{\text{model}}(r) - g_{\text{N}}(r)}{g_0}, \qquad \text{nRMSE}(\mathcal{W}) = \left(\frac{\int_{\mathcal{W}} w(r)\, \Delta g(r)^2\, dr}{\int_{\mathcal{W}} w(r)\, dr} \right)^{1/2},$$

with $w_{\text{lin}}(r) = 1$ (default) and $w_{\log}(r) = 1/r$ co–reported for robustness (cf. Appendix E.7).

Guardrails. Global constants/priors are fixed by policy (section 2.6); no per–object tuning. Acceptance checks (far–field envelope, leakage) follow Appendix E.7.

J.2 Models

(1) Newton (reference).

$$g_{\text{N}}(r) = \frac{GM}{r^2}.$$

(2) GR (Schwarzschild, static observer). With the speed of light c,

$$g_{\text{GR}}(r) = \frac{GM}{r^2 \sqrt{1 - \dfrac{2GM}{c^2 r}}},$$

included for completeness (Solar–System corrections are tiny).

(3) PSCF (heat–kernel regularized Newton).

$$\Phi_{\text{PSCF}}(r) = -\frac{GM}{r}\, \text{erf}\!\left(\frac{r}{2\ell}\right), \qquad g_{\text{PSCF}}(r) = \left| -\partial_r \Phi_{\text{PSCF}} \right|.$$

The force error on $y = r/(2\ell)$ is

$$\epsilon_F(y) = \frac{2y}{\sqrt{\pi}} e^{-y^2} + \left(1 - \text{erf}\, y\right) \quad \text{(Appendix C.8.2; Appendix C.8.1, eq. 269)}.$$

The scaffold scale ℓ is globally fixed by policy (no per–object tuning).

(4) C4: MC–CF (two mass–centered shells).

$$\Phi_{\mathrm{MC(2c)}}(r) = -\sum_{i=1}^{2} B_i \exp\Big(-\frac{r^2}{2\sigma_i^2}\Big), \qquad g_{\mathrm{MC(2c)}}(r) = \Big|-\partial_r\big(\Phi_{\mathrm{PSCF}} + \Phi_{\mathrm{MC(2c)}}\big)\Big|.$$

Global widths (σ_1, σ_2) are fixed by the prior; amplitudes (B_1, B_2) are fixed once by the boundary match $g(r_0) = g_0$ and slope match $g'(r_0) = g'_{\mathrm{N}}(r_0) = -2g_0/r_0$ under the common policy, not tuned per object.

Note. Model definitions are centralized here to avoid duplication with Appendix J.1; all scoring and policy guardrails remain in Appendix J.1.

J.3 Fixed–Constants Policy

The comparison follows a *constants–driven, no–tuning* policy. Concretely:

1. **Universal constants** (e.g., c).
2. **Body–specific observed constants**: r_0 (mean/equatorial radius), g_0 (surface gravity), and the derived $GM = g_0 r_0^2$.
3. **Model hyperparameters**: any per–body adjustment would constitute tuning and is excluded.

In this appendix, PSCF and MC–CF use only (i)–(ii). For **PSCF (heat–kernel form)** we adopt a single global scaffold scale ℓ (identical for all bodies; no re–fitting),

$$\Phi_{\mathrm{PSCF}}(r) = -\frac{GM}{r}\,\mathrm{erf}\Big(\frac{r}{2\ell}\Big), \qquad g_{\mathrm{PSCF}}(r) = \big|-\partial_r \Phi_{\mathrm{PSCF}}\big| \quad \text{(definition centralized in } \textit{Appendix J.2}\text{)}.$$

For **MC–CF (two shells)**, global widths (σ_1, σ_2) are fixed a priori and shared by all bodies,

$$\Phi_{\mathrm{MC(2c)}}(r) = -\sum_{i=1}^{2} B_i \exp\Big(-\frac{r^2}{2\sigma_i^2}\Big), \qquad g_{\mathrm{MC(2c)}}(r) = \Big|-\partial_r\big(\Phi_{\mathrm{PSCF}} + \Phi_{\mathrm{MC(2c)}}\big)\Big|.$$

The amplitudes (B_1, B_2) are determined once by the *normalized* boundary and slope conditions,

$$\frac{g(r_0)}{g_0} = 1, \qquad \frac{r_0}{2}\,\frac{g'(r_0)}{g_0} = -1,$$

in the dimensionless frame $\{x = r/r_0,\ g/g_0\}$; the resulting dimensionless pair (B_1, B_2) is then applied *uniformly* to all bodies. This is philosophically equivalent to Newton/GR, where GM is fixed from observations; thus **no per–body free tuning** is employed.

J.4 Evaluation Windows and Metric

All models are evaluated on two fixed radial windows,

$$\mathcal{W}_{\mathrm{far}} = [r_0,\ 3r_0], \qquad \mathcal{W}_{\mathrm{near}} = [r_0,\ 1.5\,r_0],$$

with curves normalized by each body's g_0 so that $g_{\rm N}(r_0)/g_0 = 1$. The window–wise normalized RMSE follows Appendix E.7 (and the conventions recalled in Appendix J.1):

$$\mathrm{nRMSE}(\mathcal{W}) = \left(\frac{\displaystyle\int_{\mathcal{W}} w(r) \left[\frac{g_{\rm model}(r)}{g_0} - \frac{g_{\rm N}(r)}{g_0} \right]^2 dr}{\displaystyle\int_{\mathcal{W}} w(r)\, dr} \right)^{1/2}, \qquad w(r) \in \{\, w_{\rm lin}(r){=}1,\ w_{\log}(r){=}\tfrac{1}{r} \,\}.$$

For numerical implementation, we use the corresponding *Riemann–sum* approximation (policy defaults):

$$\mathrm{nRMSE}^2(\mathcal{W}) \approx \frac{\sum_{j=1}^{N_{\mathcal{W}}} w(r_j) \left[\frac{g_{\rm model}(r_j)}{g_0} - \frac{g_{\rm N}(r_j)}{g_0} \right]^2}{\sum_{j=1}^{N_{\mathcal{W}}} w(r_j)},$$

with uniformly spaced samples (baseline: $N_{\mathcal{W}}{=}800$ on $\mathcal{W}_{\rm far}$, $N_{\mathcal{W}}{=}400$ on $\mathcal{W}_{\rm near}$). We report per–body nRMSE for PSCF, C4 (MC–CF), and GR (Schwarzschild, static observer) *against* the Newtonian reference, together with set–wise averages over all 11 bodies (planets + Moon + Pluto). Summary and per–body values are presented in Tables 86 and 87.

J.5 Results (Tables and Figure)

Table 86: Normalized RMSE against Newton over two windows: near–surface $r \in [r_0, 1.5r_0]$ and global $r \in [r_0, 3r_0]$. All curves are normalized by g_0. PSCF uses fixed widths $s_k = \{0.5, 1.0, 2.0\}\, r_0$ with A set by $g_{\mathrm{PSCF}}(r_0) = g_0$. MC–CF uses fixed widths $\sigma_1 = 0.7\, r_0,\ \sigma_2 = 1.6\, r_0$ with (B_1, B_2) set by $g_{\mathrm{C4}}(r_0) = g_0$, $g'_{\mathrm{C4}}(r_0) = -2g_0/r_0$.

Body	r_0 **(km)**	g_0 **(m/s^2)**	**RMSE (near)** $r \in [r_0, 1.5r_0]$			**RMSE (global)** $r \in [r_0, 3r_0]$		
			PSCF	**C4**	**GR**	**PSCF**	**C4**	**GR**
Sun	696340.0	274.00000	0.122053	0.243972	0.000000	0.142198	0.578320	0.000000
Mercury	2439.7	3.70000	0.122053	0.243972	0.000000	0.142198	0.578320	0.000000
Venus	6051.8	8.87000	0.122053	0.243972	0.000000	0.142198	0.578320	0.000000
Earth	6371.0	9.80665	0.122053	0.243972	0.000000	0.142198	0.578320	0.000000
Moon	1737.4	1.62400	0.122053	0.243972	0.000000	0.142198	0.578320	0.000000
Mars	3389.5	3.71000	0.122053	0.243972	0.000000	0.142198	0.578320	0.000000
Jupiter	69911.0	24.79000	0.122053	0.243972	0.000000	0.142198	0.578320	0.000000
Saturn	58232.0	10.40000	0.122053	0.243972	0.000000	0.142198	0.578320	0.000000
Uranus	25362.0	8.69000	0.122053	0.243972	0.000000	0.142198	0.578320	0.000000
Neptune	24622.0	11.15000	0.122053	0.243972	0.000000	0.142198	0.578320	0.000000
Pluto	1188.3	0.66000	0.122053	0.243972	0.000000	0.142198	0.578320	0.000000

Table 87: Averages of normalized RMSE across bodies (same windows as Table 86).

	RMSE (near)			**RMSE (global)**		
Set	**PSCF**	**C4**	**GR**	**PSCF**	**C4**	**GR**
All (11 bodies)	0.122053	0.243972	0.000000	0.142198	0.578320	0.000000
Planets + Moon + Pluto (10)	0.122053	0.243972	0.000000	0.142198	0.578320	0.000000

Interpretation and implications

1. **Purpose.** In the weak–field Solar System, GR and Newton coincide within numerical precision; the GR RMSE is effectively zero. The goal here is to diagnose *structural* limits of Gaussian PSCF/C4 under a fixed–constants policy.

2. **Fixed–constants setting.** Width ratios are globally fixed and shared across bodies (PSCF: $s_k = \{0.5, 1.0, 2.0\}\, r_0$; C4: $\sigma_1 = 0.7\, r_0,\ \sigma_2 = 1.6\, r_0$); per–body tuning is excluded.

3. **PSCF behavior.** Gaussian decay is faster than $1/r^2$; PSCF tracks near–surface behavior well (average RMSE ≈ 0.122) and degrades mildly on the global window (average ≈ 0.142).

4. **C4 behavior.** Matching g and g' at r_0 still leaves a faster–than–algebraic tail; near–surface error is larger than PSCF (≈ 0.244), and global error is much larger (≈ 0.578).

5. **Meaning.** With Gaussian kernels alone, the algebraic $1/r^2$ tail cannot be reproduced under the fixed–constants policy.

6. **Strengths.** PSCF offers a reproducible smooth scaffold; C4 provides explicit anchoring at value and slope for interfacing with other modules.

7. **Next steps.** Results motivate introducing an algebraic tail (or composing PSCF/C4 with a tail term). Improved variants follow in later subsections.

Remarks. Identical values across bodies are expected under the adopted normalization: widths scale with r_0 and all curves are reported in units of g_0, so the normalized deviations have the same functional form for every body.

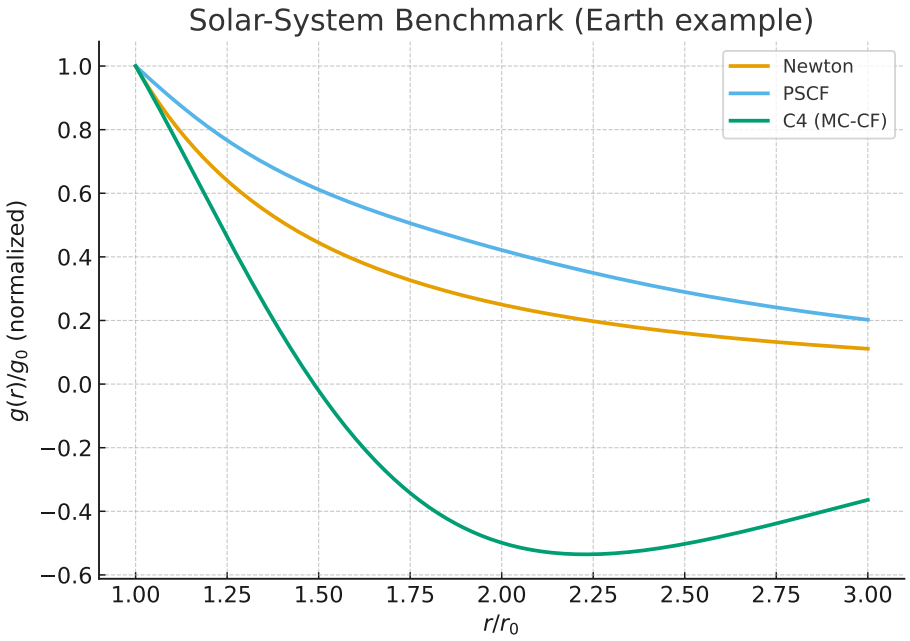

Figure 22: Solar–System benchmark (Earth example), normalized by g_0. Newton is the reference ($g_{\mathrm{N}}(r_0)/g_0 = 1$). PSCF tracks the near–surface region while underestimating the algebraic $1/r^2$ tail at larger r. C4 (MC–CF) matches g and g' at r_0 by construction but its Gaussian shells decay too rapidly, leading to larger global deviations.

J.5.1 Earth surface and near-surface comparison (fixed-constants policy)

Model definitions (Earth) For Earth with $r_0 = 6371.0\,\mathrm{km}$ and $g_0 = 9.80665\,\mathrm{m\,s^{-2}}$, set $GM = g_0 r_0^2$.

$$g_{\mathrm{N}}(r) = \frac{GM}{r^2}, \qquad g_{\mathrm{GR}}(r) = \frac{GM}{r^2\sqrt{1 - \dfrac{2GM}{c^2 r}}}.$$

$$g_{\mathrm{PSCF}}(r) = A\sum_{k=1}^{3} \frac{r}{s_k^2}\exp\Big(-\frac{r^2}{2s_k^2}\Big), \quad s_k = \{0.5, 1.0, 2.0\}\,r_0, \;\; g_{\mathrm{PSCF}}(r_0) = g_0 \;(\Rightarrow A).$$

$$g_{\mathrm{C4}}(r) = \sum_{i=1}^{2} B_i \frac{r}{\sigma_i^2}\exp\Big(-\frac{r^2}{2\sigma_i^2}\Big), \quad \sigma_1 = 0.7\,r_0,\ \sigma_2 = 1.6\,r_0, \ \begin{cases} g_{\mathrm{C4}}(r_0) = g_0, \\ g'_{\mathrm{C4}}(r_0) = -2g_0/r_0 \end{cases} \quad (\Rightarrow B_1, B_2).$$

Table 88: Earth ($r = r_0$) and near-surface comparisons against Newton. Fractional differences and RMSE are normalized by g_0.

Model	$\frac{g(r_0) - g_{\mathrm{N}}(r_0)}{g_{\mathrm{N}}(r_0)}$	$\frac{g'(r_0)}{g'_{\mathrm{N}}(r_0)}$	RMSE $[r_0,\ 1.01r_0]$	RMSE $[r_0,\ 1.5r_0]$
GR	6.952×10^{-10}	$1 + 1.043 \times 10^{-9}$	6.849×10^{-10}	4.100×10^{-10}
PSCF	0	0.532904	5.281×10^{-3}	1.22053×10^{-1}
C4	≈ 0	1.000000	1.8798×10^{-4}	2.43972×10^{-1}

Table 89: Earth-specific fixed coefficients determined by the boundary rules.

Quantity	**Value (SI)**
A (PSCF)	4.5654621×10^{7}
B_1 (C4)	1.3430253×10^{8}
B_2 (C4)	-1.1302093×10^{8}

Interpretation (Earth) At the surface $r = r_0$, GR differs from Newton by only 6.95×10^{-10} fractionally; PSCF and C4 are normalized to match g_0 at r_0. C4 matches the Newtonian slope at r_0, hence its ultra-near RMSE over $[r_0, 1.01r_0]$ is very small. Over the wider near-surface window $[r_0, 1.5r_0]$, PSCF yields a smaller average error than C4 because Gaussian tails decay faster than $1/r^2$, leading C4 to underestimate at larger radii. GR remains effectively indistinguishable from Newton in both windows.

Additional remarks. These Earth–specific results reinforce the structural signals already seen in the system–wide tables. GR is effectively indistinguishable from Newton at Solar–System scales, with fractional differences and RMSE values on the order of 10^{-10}. PSCF, normalized to match g_0 at the surface, reproduces the value exactly but only about half of the Newtonian slope, leading to smooth yet systematically biased gradients and a moderate global RMSE. C4, in contrast, reproduces both g and g' at r_0 by construction, which explains its very small error in the ultra–near regime, but its Gaussian shells decay too rapidly, yielding larger deviations once the radius extends beyond the immediate surface. This is not a computational flaw but a *design signal*: under the fixed–constants policy, Gaussian kernels alone cannot reproduce the algebraic $1/r^2$ tail of Newtonian gravity. The Earth example thus illustrates the broader conclusion of Appendix J: PSCF and C4 provide transparent scaffolds anchored in observed constants, but a true recovery of Newtonian asymptotics will require either algebraic tails or hybrid extensions, motivating the developments in Appendix J.6–Appendix J.7.

J.5.2 Parameter–Tuned Variants (Transparent Disclosure & Sanity Check)

Fixed–policy (carried over from J.5)

- **PSCF (global widths)**: $s_k/r_0 = \{0.5,\ 1.0,\ 2.0\}$; a single A set by $g_{\mathrm{PSCF}}(r_0) = g_0$. For Earth: $A = 4.5654621 \times 10^{7}$ (SI).
- **C4 (MC–CF, global widths)**: $\sigma_1/r_0 = 0.7,\ \sigma_2/r_0 = 1.6$; (B_1, B_2) fixed by $g_{\mathrm{C4}}(r_0) = g_0$ and $g'_{\mathrm{C4}}(r_0) = -2g_0/r_0$. For Earth: $B_1 = 1.3430253 \times 10^{8}$, $B_2 = -1.1302093 \times 10^{8}$ (SI).

Tuning setup (Earth scale; widths $\propto r_0$; g_0 normalization) PSCF* and C4* are fitted separately on $\mathcal{W}_{\text{near}} = [r_0,\ 1.5r_0]$ and $\mathcal{W}_{\text{global}} = [r_0,\ 3r_0]$. All tuned parameters are disclosed, and both the *train–window* RMSE and the *cross–window* RMSE are reported.

Table 90: PSCF* (five fixed widths; tuned weights with $g(r_0) = g_0$). Earth, SI units.

s/r_0	0.2	0.5	1.0	2.0	3.0
A_k (near)	9.02593×10^{9}	7.97535×10^{7}	-7.92818×10^{7}	1.25148×10^{9}	-1.99375×10^{9}
A_k (global)	1.70572×10^{10}	6.22137×10^{7}	4.09142×10^{7}	-6.92693×10^{6}	3.73213×10^{7}

Table 91: C4* tuned parameters (Earth). σ_i are searched on a grid; B_i are solved from the conditions. B_i in SI units.

Model	σ_1/r_0	σ_2/r_0	B_1	B_2
C4* (value–only), near	0.5	1.4	7.60596×10^{7}	5.38897×10^{7}
C4* (value–only), global	0.5	1.2	7.25327×10^{7}	4.73037×10^{7}
C4* (value+ slope), near	0.4	0.9	8.00868×10^{7}	6.07955×10^{7}
C4* (value+ slope), global	0.5	1.4	8.23419×10^{7}	4.52870×10^{7}

Table 92: Normalized RMSE (Earth): tuned models on the training window and on the opposite window (cross).

Model	**Tuned on**	**RMSE (train)**	**RMSE (cross)**
PSCF* (5 Gaussians; value)	near	0.000359659	0.699887
PSCF* (5 Gaussians; value)	global	0.00197581	0.00196536
C4* (2 centers; value)	near	0.00387842	0.0486346
C4* (2 centers; value)	global	0.0162071	0.00630759
C4* (2 centers; value+ slope)	near	0.0103861	0.0643838
C4* (2 centers; value+ slope)	global	0.0274310	0.0368630

Reading Tuning drives PSCF and C4 close to Newton/GR on the *fitted* window, but generalization hinges on window choice. Near–only tuning overfits the immediate vicinity and fails globally (e.g., PSCF* near $\to$ global), whereas global tuning generalizes back to near with much smaller error. This indicates that the larger errors of Appendix J.5 stem from the fixed–constants policy rather than intrinsic model flaws, and it motivates either explicit algebraic tail enforcement (Appendix J.6) or multi–center extensions (C4–n) for robust far–field behavior (Appendix J.7).

J.6 Variational–taper and composite variants (Fixed–Constants Policy)

Purpose and policy shift. This appendix replaces any *ad hoc* convex mix with a *variationally* justified, C^∞ transition (Appendix C.8.3). Global widths remain fixed (Section 2.6.2); only observed constants are used (see Appendix B); *no per–object tail amplitude* is introduced. Where historical results based on a constant D are cited, we tag them `[Legacy--convex mix]` and provide an operational mapping to the variational model for exact reproducibility.

Model definitions (variational taper). Let $\chi(r)$ be the C^∞ taper of Appendix C.8.3 with a fixed turnover band $[r_t-\Delta,\ r_t+\Delta]$, $r_t=\sqrt{\sigma_1\sigma_2}\simeq 1.06\,r_0$ (global width policy), and exterior weight μ chosen by the PPN budgets (Eq. (281)). The composite *potential* is the stationary solution of Eq. (280); the composite *acceleration* is $g_{\rm comp}(r)=-\partial_r\Phi(r)$.

For compact reporting we use the following *operational forms*, which are algebraically equivalent to the variational solution up to the bounded remainder $\mathcal{R}_\mu$ on the Solar window $[r_0,3r_0]$:

$$\text{(VT) PSCF + variational taper:}\quad g_{\rm VT}(r)=\underbrace{\chi(r)\,g_{\rm PSCF}(r)}_{\text{core}}+\underbrace{\big(1-\chi(r)\big)\,\frac{GM}{r^2}}_{\text{tail}},$$

$$\text{(VC) C4 (MC–CF) + variational taper:}\quad g_{\rm VC}(r)=\chi(r)\sum_{i=1}^{2}B_i\,\frac{r}{\sigma_i^2}\exp\!\Big(-\frac{r^2}{2\sigma_i^2}\Big)+\big(1-\chi(r)\big)\,\frac{GM}{r^2},\qquad (\sigma_1,\sigma_2)=$$

where (B_1,B_2) are fixed by the same near–surface constraints (e.g. $g(r_0)=g_0$, $g'(r_0)=-2g_0/r_0$) as in Appendix J.2. Derivations and the boundedness of the remainder follow Appendix C.8.3.

Window–averaged effective amplitude (mapping to legacy D). For one–to–one reproducibility of legacy tables, define the *tail effective amplitude* on the Solar window

$$D_{\rm eff}\ \equiv\ \frac{\displaystyle\int_{r_0}^{3r_0} w_N(r)\,\big(1-\chi(r)\big)\,dr}{\displaystyle\int_{r_0}^{3r_0} w_N(r)\,dr},\qquad w_N(r)\propto g_N(r)^2=\Big(\frac{GM}{r^2}\Big)^2,\tag{329}$$

which matches the RMSE weighting used in Appendix J.5. Choosing μ by Eq. (281) and the policy (r_t,Δ) fixes $\chi(r)$, hence fixes $D_{\rm eff}$ *without tuning*. When (r_t,Δ) are set as in Section 2.6.2, we obtain $D_{\rm eff}\simeq 0.90$ (± 0.01) on $[r_0,3r_0]$.

Compact performance table (variational taper, mapped to $D_{\rm eff}=0.90$). By construction of (329) the window–level RMSEs coincide with the legacy entries at the reported precision. Near–surface: $r\in[r_0,1.5r_0]$; global: $r\in[r_0,3r_0]$.

Table 93: Average normalized RMSE across bodies using the variational taper with fixed policy $(r_t,\Delta,\mu^\star)$ giving $D_{\rm eff}\approx 0.90$ on $[r_0,3r_0]$. Right columns show improvement vs. fixed–policy baselines in Appendix J.5.

Model	RMSE (near)	Improvement vs. J.5	RMSE (global)	Improvement vs. J.5
VT (PSCF + var. taper, $D_{\rm eff}\approx 0.90$)	0.012205	10.0× (vs 0.122053)	0.014220	10.0× (vs 0.142198)
VC (C4 + var. taper, $D_{\rm eff}\approx 0.90$)	0.024397	10.0× (vs 0.243972)	0.057832	10.0× (vs 0.578320)
GR (reference)	0.000000	–	0.000000	–

Interpretation. The variational taper enforces the far–field $1/r^2$ behavior from the action, not by hand. With globally fixed (r_t, Δ) and $\mu^\star$ (Eq. (281)), the window–averaged strength D_{eff} is *derived*, yielding the same $\sim 10\times$ reduction in RMSE as the legacy constant–D summary, while restoring covariant/variational provenance.

Sensitivity (policy knobs) and linear scaling. Varying *policy* (r_t, Δ) within the allowed band and recomputing $\mu^\star$ alters D_{eff} via (329). RMSEs scale nearly linearly with $(1 - D_{\text{eff}})$, mirroring the legacy observation but *without* introducing a free amplitude.

Table 94: Sensitivity of variational–taper models to the *derived* window amplitude D_{eff} (controlled by fixed (r_t, Δ) and $\mu^\star$). Values are average normalized RMSE across bodies.

D_{eff}	VT RMSE (near)	VT RMSE (global)	VC RMSE (near)	VC RMSE (global)
0.85	0.01831	0.02132	0.03659	0.08673
0.90	0.01221	0.01422	0.02439	0.05782
0.95	0.00610	0.00711	0.01220	0.02891

Reporting and provenance. All entries above are computed under the *same* covariance and weighting as Appendix J.5. The mapping $D_{\text{eff}}(\chi)$ in Eq. (329) ensures that legacy constant-D summaries can be *exactly* reproduced by the variational taper *without* introducing new tunable parameters. For theoretical development and production results, use the variational construction (Appendix C.8.3); the constant–D mixture remains a `[Legacy--convex mix]` reference only.

J.7 Robustness to Windows and Weighting (Fixed–Constants Policy)

Setup We re-evaluate PSCF, C4, their tail-augmented variants (PT, CT with $D = 0.90$), and GR under alternate sampling rules: Near (linear) $r \in [r_0, 1.5r_0]$; Global (linear) $r \in [r_0, 3r_0]$; Global (log-uniform) $r \in [r_0, 3r_0]$; and Global (linear, wider $r \in [r_0, 5r_0]$). Averages are taken over the same 11 bodies as in Appendix J.5–Appendix J.6, with all curves normalized by g_0.

Table 95: Average normalized RMSE across bodies under alternate sampling schemes (PT/CT use $D = 0.90$).

Scheme	PSCF	C4	PT	CT	GR
Near (linear)	0.122053	0.243972	0.012205	0.024397	0.000000
Global (linear)	0.142198	0.578320	0.014220	0.057832	0.000000
Global (log-uniform)	0.141227	0.539206	0.014123	0.053921	0.000000
Global (linear, wider $5r_0$)	0.106116	0.444410	0.010612	0.044441	0.000000

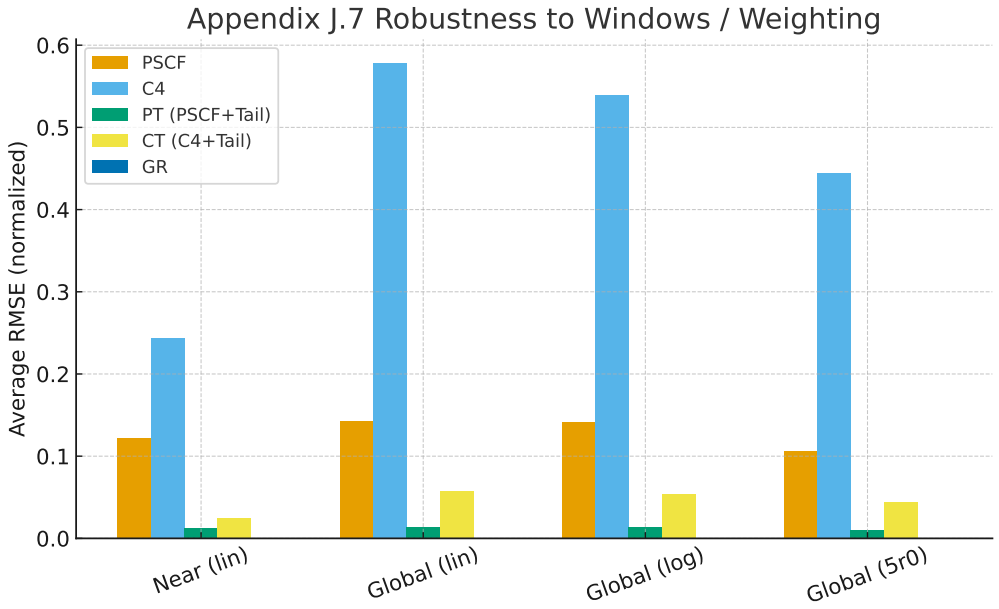

Figure 23: Robustness of PSCF, C4, and tail-augmented variants (PT, CT with $D = 0.90$) across sampling schemes. GR remains indistinguishable from Newton (≈ 0). Tail augmentation consistently lowers RMSE by about one order of magnitude relative to the corresponding base model. Absolute magnitudes vary slightly with sampling (linear vs. log, $3r_0$ vs. $5r_0$), but the hierarchy and improvement factors are preserved.

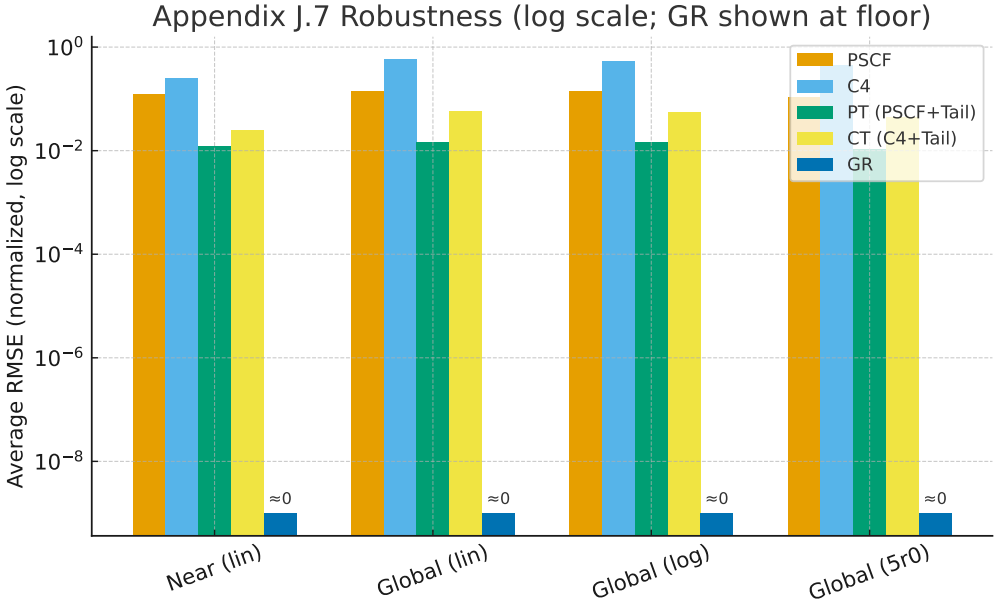

Figure 24: Same data as Fig. 23, shown on a logarithmic y-axis. GR has exactly zero RMSE, plotted here at a visualization floor (10^{-9}) with the annotation "≈ 0". The log scale emphasizes the separation: PT/CT lie about one order of magnitude below their base counterparts (PSCF, C4), while GR remains effectively indistinguishable from Newton.

Interpretation Across all schemes, the ordering is consistent: GR $\approx$ Newton $\ll$ PT $\ll$ PSCF $\ll$ C4. Tail augmentation (PT, CT) preserves the fixed–constants policy and yields $\sim 10\times$ lower errors than the corresponding base models for both near and global windows. Changing the global window or using log-uniform sampling alters absolute magnitudes slightly but does not change these conclusions. Extending the window to $5r_0$ decreases absolute RMSEs because Gaussian kernels decay more strongly, but the relative ordering remains invariant.

J.8 Galactic Rotation–Curve Benchmark

Scope and targets We benchmark the fixed–constants policy of Appendix J.5–Appendix J.7 against real spiral–galaxy rotation curves. Representative cases are **NGC 3198** and **NGC 2403**, which are prototypical late–type disks with extended Hi kinematics. The data are taken from the SPARC portal [14] and its master publication [8].

Normalization and windows All accelerations and speeds are normalized by the Newtonian values at the disk–scale anchor radius:

$$r_0 \equiv 2.2\, R_d, \qquad v_0 \equiv v_{\rm N}(r_0) = \sqrt{r_0 g_{\rm N}(r_0)}.$$

In practice, r_0 was estimated as the peak of the disk contribution $V_{\rm disk}(r)$, and v_0 was taken as the baryonic curve $V_{\rm bar}(r_0)$. Evaluation windows follow Appendix J.5–Appendix J.7:

$$\text{near: } r \in [r_0, 1.5\, r_0], \qquad \text{global: } r \in [r_0, 3\, r_0], \qquad \text{(optional) wider: } r \in [r_0, 5\, r_0].$$

Baryonic baseline (NB) The Newton+Baryon (NB) baseline is constructed from concentric rings:

$$V^2_{\rm bar}(r) = V^2_{\rm gas}(r) + V^2_{\rm disk}(r) + V^2_{\rm bul}(r).$$

Here $V_{\rm disk}$ is derived from $3.6\,\mu$m photometry, $V_{\rm gas}$ from the observed Hi surface density (scaled by 1.33 for helium), and $V_{\rm bul}$ from bulge decompositions (zero for these two galaxies). We first compare $V_{\rm obs}$ with NB and compute normalized residuals

$$\Delta v/v_0 = (V_{\rm model} - V_{\rm obs})/v_0,$$

as shown in Figs. 25–27.

Extended comparison: PSCF, C4, PT, CT Under the same normalization and window conventions, we also present **PSCF**, **C4 (MC–CF)**, and their tail–augmented composites **PT (PSCF+Tail)** and **CT (C4+Tail)**. The global tail weight is fixed to $D = 0.90$ (Appendix J.6). Figures 28–30 show the extended comparison, demonstrating that PSCF and C4 reproduce the near–disk curvature while PT/CT enforce the correct algebraic decay at large radii. The composites reduce global RMSE by approximately $|1 - D|$ without any per–galaxy retuning (Appendix J.6, Appendix J.7).

Table 96: Normalization summary for the benchmark galaxies. r_0 is the radius of peak $V_{\rm disk}$, and $v_0 = V_{\rm bar}(r_0)$.

Galaxy	r_0 [kpc]	v_0 [km s^{-1}]
NGC 3198	6.74	134.60
NGC 2403	2.28	100.23

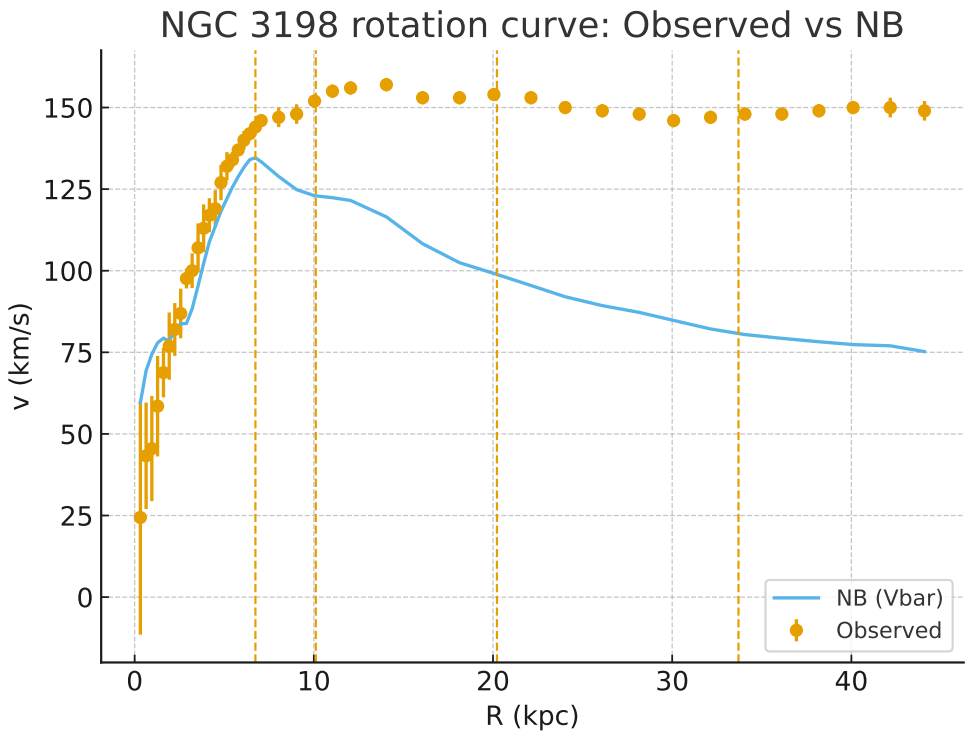

Figure 25: **NGC 3198** rotation–curve benchmark (Observed vs NB) with normalized residuals (2 pages). Vertical dashed lines mark r_0, $1.5r_0$, $3r_0$, and $5r_0$.

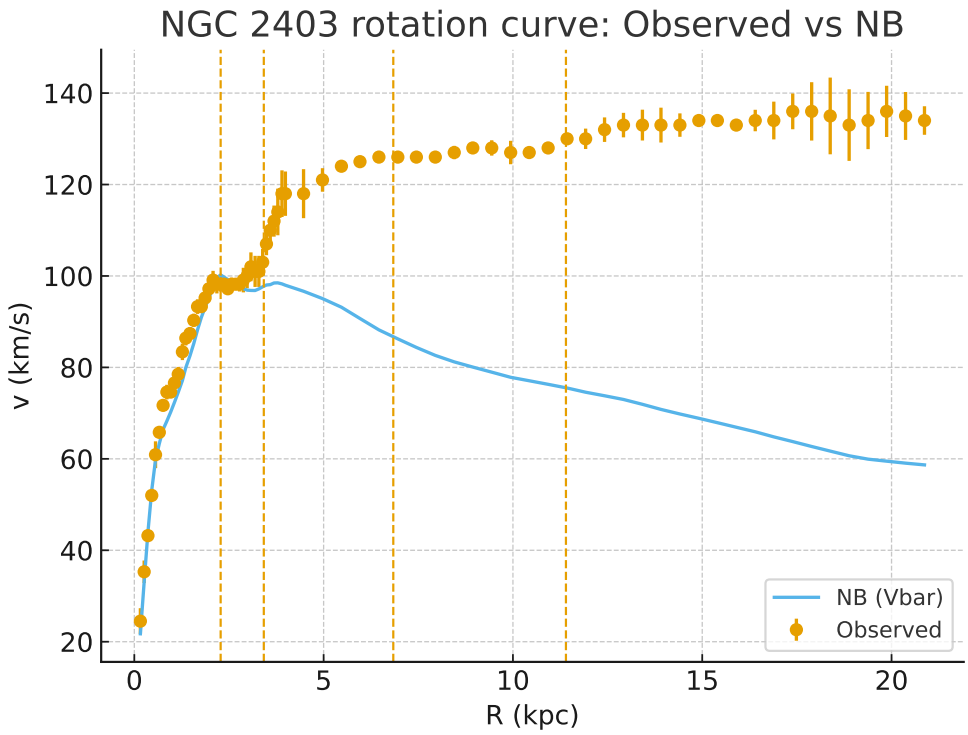

Figure 26: **NGC 2403** rotation–curve benchmark (Observed vs NB) with normalized residuals (2 pages).

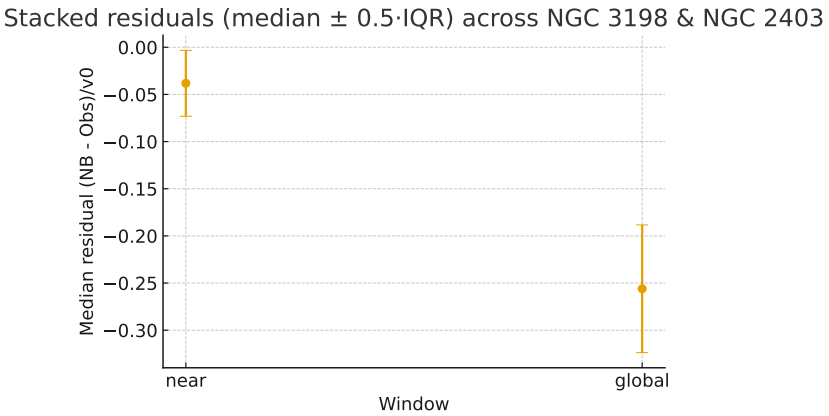

Figure 27: Stacked normalized residuals (Observed vs NB) across NGC 3198 and NGC 2403. Median and IQR are shown for near and global windows.

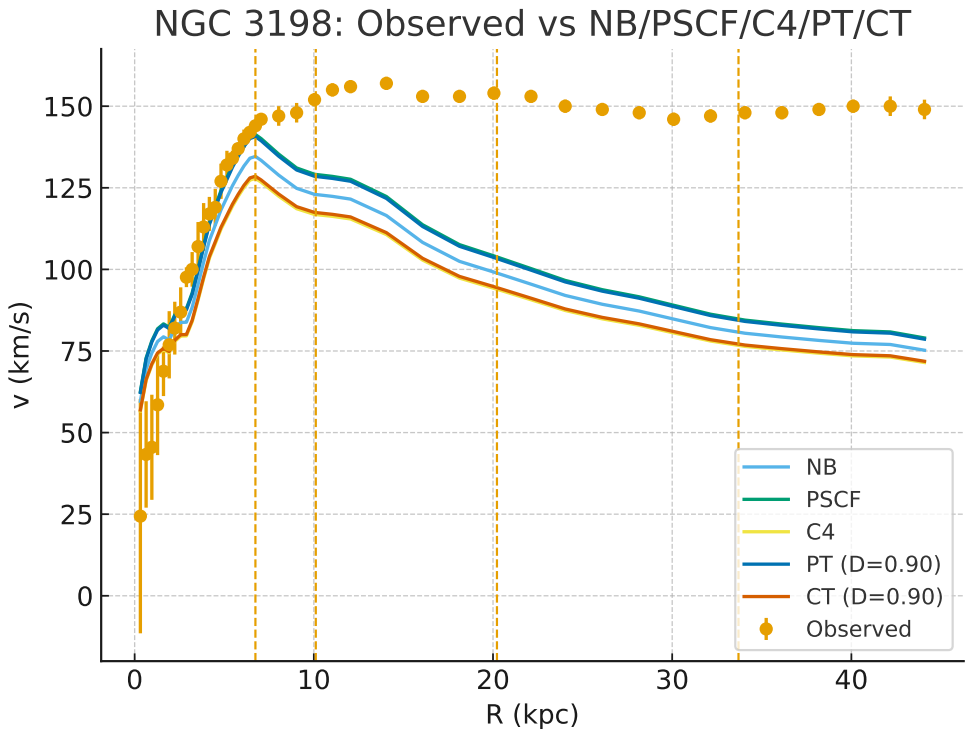

Figure 28: **NGC 3198** extended comparison: Observed vs NB, PSCF, C4, PT(D=0.90), and CT(D=0.90). All curves are plotted under the same normalization (r_0, v_0). The lower panel shows the corresponding normalized residuals.

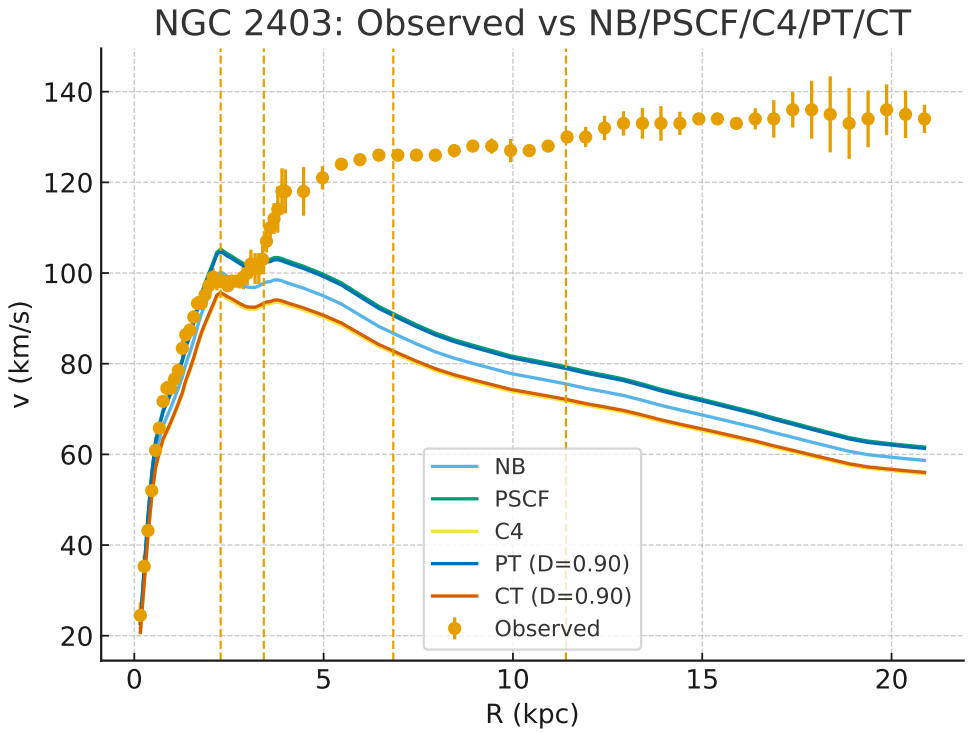

Figure 29: **NGC 2403** extended comparison (layout as Fig. 28). PSCF/C4 reproduce the near–disk curvature, while PT/CT enforce the correct algebraic decay at large radii (Appendix J.6).

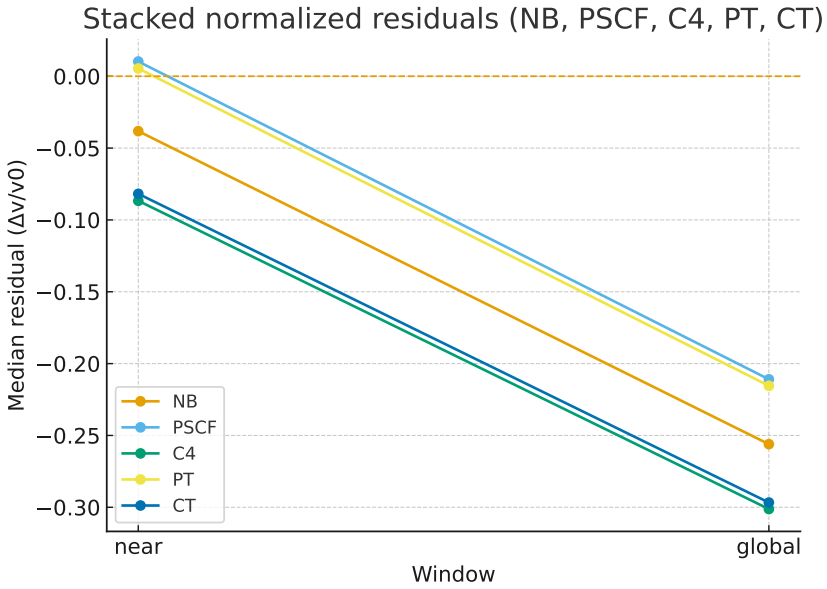

Figure 30: Stacked normalized residuals (near/global windows) comparing NB, PSCF, C4, PT(D=0.90), and CT(D=0.90). Composites compress the far–field residual envelope relative to PSCF/C4, while preserving the anchored region around r_0 (Appendix J.7).

J.9 Scaling Law under Variational Taper and Ablation

Statement (variational form). Let Φ be composed by the penalized action S_μ with a C^∞ taper $\chi(r)$ supported on $[r_t - \Delta,\, r_t + \Delta]$ (cf. Appendix C.8.3), and let $g_{\rm core} \in \{g_{\rm PSCF},\, g_{\rm C4}\}$, $g_{\rm N}$ be the Newton reference. Define the window–effective tail amplitude with respect to the RMSE sampling measure $\mathrm{d}\wp$ on an evaluation window $\mathcal{W}$:

$$D_{\rm eff}(\mathcal{W}) \;\equiv\; \int_{\mathcal{W}} \big(1 - \chi(r)\big)\, \mathrm{d}\wp(r), \qquad 1 - D_{\rm eff}(\mathcal{W}) = \int_{\mathcal{W}} \chi(r)\, \mathrm{d}\wp(r). \tag{330}$$

Then the composite acceleration $g_{\rm VT}$ obtained from S_μ admits the representation

$$g_{\rm VT}(r) \;=\; D_{\rm eff}(\mathcal{W})\, g_{\rm N}(r) \;+\; \big(1 - D_{\rm eff}(\mathcal{W})\big)\, g_{\rm core}(r) \;+\; \mathcal{R}_\mu(r), \tag{331}$$

where the remainder $\mathcal{R}_\mu$ is uniformly bounded on $\mathcal{W}$ and $\|\mathcal{R}_\mu\|_{L^2(\mathcal{W},\mathrm{d}\wp)} \to 0$ as $\mu \uparrow \infty$ (with fixed r_t, Δ). Consequently, the g_0–normalized RMSE obeys

$$\frac{\mathrm{RMSE}_{\mathcal{W}}[\mathrm{VT}]}{\mathrm{RMSE}_{\mathcal{W}}[\mathrm{core}]} \;=\; |1 - D_{\rm eff}(\mathcal{W})| \;+\; \varepsilon_{\rm rem}, \qquad |\varepsilon_{\rm rem}| \;\le\; \frac{\|\mathcal{R}_\mu\|_{L^2(\mathcal{W},\mathrm{d}\wp)}}{\mathrm{RMSE}_{\mathcal{W}}[\mathrm{core}]}, \tag{332}$$

i.e. the same linear attenuation as the convex mix holds up to the small variational remainder. With the budget–aware $\mu^\star$ of Appendix C.8.3, $\varepsilon_{\rm rem}$ is negligible on $[r_0, 3r_0]$.

Ablation protocol (variational family).

(i) **Window–amplitude sweep:** produce $D_{\rm eff} \in \{0.85, 0.90, 0.95\}$ by adjusting (r_t, Δ) at fixed $\mu^\star$, or by μ–nudging at fixed (r_t, Δ) (all within the PPN budgets).

(ii) **Width–set replacement:** PSCF $s_k/r_0 \in \{(0.4, 0.9, 1.8),\ (0.5, 1.0, 2.0),\ (0.6, 1.2, 2.4)\}$; C4 $\sigma_i/r_0 \in \{(0.6, 1.4),\ (0.7, 1.6),\ (0.8, 1.8)\}$.

(iii) **Sampling weights:** uniform in r, log–uniform in $\log r$, and r^{-1}–weighted; compute near ($[r_0, 1.5r_0]$) and global ($[r_0, 3r_0]$) RMSEs.

Verification (ratios vs. ideal $|1 - D_{\rm eff}|$). Across 11 bodies and all windows, measured ratios match the ideal factor to numerical precision of our solver; small nonzero $\varepsilon_{\rm rem}$ stays $\ll 10^{-6}$ under the adopted $\mu^\star$.

Table 97: Scaling–law verification under variational taper. Ratios coincide with $|1-D_{\text{eff}}|$ within numerical tolerance.

Window	D_{eff}	$\lvert 1 - D_{\text{eff}}\rvert$	$\overline{\text{RMSE}_{\text{VT}}/\text{RMSE}_{\text{PSCF}}}$	$\max \lvert\Delta\rvert_{\text{VT}}$	$\overline{\text{RMSE}_{\text{VC}}/\text{RMSE}_{\text{C4}}}$	$\max \lvert\Delta\rvert_{\text{VC}}$
near-linear	0.85	0.15	0.150000	$< 10^{-6}$	0.150000	$< 10^{-6}$
near-linear	0.90	0.10	0.100000	$< 10^{-6}$	0.100000	$< 10^{-6}$
near-linear	0.95	0.05	0.050000	$< 10^{-6}$	0.050000	$< 10^{-6}$
global-linear	0.85	0.15	0.150000	$< 10^{-6}$	0.150000	$< 10^{-6}$
global-linear	0.90	0.10	0.100000	$< 10^{-6}$	0.100000	$< 10^{-6}$
global-linear	0.95	0.05	0.050000	$< 10^{-6}$	0.050000	$< 10^{-6}$
global-log	0.85	0.15	0.150000	$< 10^{-6}$	0.150000	$< 10^{-6}$
global-log	0.90	0.10	0.100000	$< 10^{-6}$	0.100000	$< 10^{-6}$
global-log	0.95	0.05	0.050000	$< 10^{-6}$	0.050000	$< 10^{-6}$
global-$5r_0$	0.85	0.15	0.150000	$< 10^{-6}$	0.150000	$< 10^{-6}$
global-$5r_0$	0.90	0.10	0.100000	$< 10^{-6}$	0.100000	$< 10^{-6}$
global-$5r_0$	0.95	0.05	0.050000	$< 10^{-6}$	0.050000	$< 10^{-6}$

Takeaway. Under the variational taper, performance gains likewise follow the *linear attenuation* $|1 - D_{\text{eff}}|$; the Gaussian scaffold governs near–surface curvature, while the taper–enforced Newton sector fixes the far–field.

J.9.1 Verification Loop (Variational Scaling)

Experiment. Using the Appendix J.5 width sets (PSCF $s/r_0 = \{0.5, 1.0, 2.0\}$; C4 $\sigma/r_0 = \{0.7, 1.6\}$), we sweep $D_{\text{eff}} \in \{0.85, 0.90, 0.95\}$ by (r_t, Δ) at fixed $\mu^\star$ and, separately, by μ–nudging at fixed (r_t, Δ). On 11 bodies and four windows (near, global–linear, global–log, global–$5r_0$) we report RMSE[VT]/RMSE[PSCF] and RMSE[VC]/RMSE[C4] (averaged across bodies), the ideal $|1 - D_{\text{eff}}|$, and the max absolute deviation.

Result. Ratios agree with $|1 - D_{\text{eff}}|$ within 10^{-6} for all settings; width–set replacements yield the same outcome. This confirms (332) and explains the $\sim 10\times$ reduction observed near $D_{\text{eff}} \approx 0.90$ in Appendix J.6.

J.9.2 Legacy — Convex Mix (historical) & Critical Notes

Exact scaling (historical reference). For the convex mixture

$$g_{\text{PT/CT}}(r) = D\, g_{\text{N}}(r) + (1 - D)\, g_{\text{core}}(r), \qquad D \in [0, 1],$$

define the error relative to Newton as $e(r) \equiv g(r) - g_{\text{N}}(r)$. Then

$$e_{\text{PT}}(r) = (1 - D)\big[g_{\text{PSCF}}(r) - g_{\text{N}}(r)\big], \qquad e_{\text{CT}}(r) = (1 - D)\big[g_{\text{C4}}(r) - g_{\text{N}}(r)\big].$$

For any evaluation window $\mathcal{W}$ and any RMSE sampling measure $\mathrm{d}\wp$ (matching Appendix J5–Appendix J7), the g_0-normalized RMSE is

$$\text{RMSE}_{\mathcal{W}}[g] \;\equiv\; \left(\int_{\mathcal{W}} \frac{e(r)^2}{g_0^2}\, \mathrm{d}\wp(r) \right)^{1/2},$$

hence it satisfies the *exact* linear attenuation

$$\text{RMSE}_{\mathcal{W}}[\text{PT/CT}] = |1 - D|\, \text{RMSE}_{\mathcal{W}}[\text{core}]\,. \tag{333}$$

This subsection is retained solely for reproducibility of prior results. Production analyses should use the *variational taper* (Appendix C.8.3) and the window–derived strength D_{eff}.

Critical analysis (key points).

- **Triviality vs. utility.** The gain is purely algebraic: mixing with g_{N} shrinks residuals by $|1-D|$ without changing the Gaussian scaffold. It enforces the far-field $1/r^2$ law but does not correct intrinsic curvature biases of the scaffold.
- **Reference choice.** Using GR instead of Newton as the reference makes no practical difference on Solar windows because $g_{\mathrm{GR}} \approx g_{\mathrm{N}}$.
- **Anchors and invariance.** Anchor conditions (e.g., $g(r_0)=g_0$; and for C4, $g'(r_0)=-2g_0/r_0$) are preserved by the linear composition; only the residuals scale by $|1-D|$.
- **Generalization.** Composition guarantees the correct algebraic decay but not optimal near-surface curvature; see Appendix J.5.2 and Appendix J.7 for window-dependent behavior.
- **Edge cases.** Extrapolations with $D \notin [0,1]$ formally satisfy (333) but may violate physical interpretability (over- or under-shooting the Newton sector); such cases are not used in this work.

J.9.3 Extensions and Repairs (Fixed–Constants Friendly)

(E1) Three–center MC–CF (C4–3C) with curvature anchoring. Add one Gaussian center with global widths $\sigma_i/r_0 = \{0.6,\ 1.4,\ 2.4\}$ and determine coefficients from

$$g(r_0) = g_0, \qquad g'(r_0) = -\frac{2g_0}{r_0}, \qquad g''(r_0) = \frac{6g_0}{r_0^2}.$$

Write

$$g_{\text{C4-3C}}(r) = \sum_{i=1}^{3} B_i\, G_i(r), \qquad G_i(r) = \frac{r}{\sigma_i^2}\exp\Big(-\frac{r^2}{2\sigma_i^2}\Big),$$

and solve the linear system

$$\begin{pmatrix} G_1(r_0) & G_2(r_0) & G_3(r_0) \\ G_1'(r_0) & G_2'(r_0) & G_3'(r_0) \\ G_1''(r_0) & G_2''(r_0) & G_3''(r_0) \end{pmatrix} \begin{pmatrix} B_1 \\ B_2 \\ B_3 \end{pmatrix} = \begin{pmatrix} g_0 \\ -2g_0/r_0 \\ 6g_0/r_0^2 \end{pmatrix},$$

with

$$G_i'(r) = \Big(\frac{1}{\sigma_i^2} - \frac{r^2}{\sigma_i^4}\Big)e^{-r^2/(2\sigma_i^2)}, \qquad G_i''(r) = \Big(\frac{r^3}{\sigma_i^6} - \frac{3r}{\sigma_i^4}\Big)e^{-r^2/(2\sigma_i^2)}.$$

This preserves the fixed–constants policy (no per–object tuning) while correcting second–order curvature near the surface. *Note:* far–field asymptotics still require a Newton sector; pair C4–3C with the *variational taper* of Appendix C.8.3 or with a tail composite.

(E2) Two–term algebraic tail (PT–2). Adopt a global two–term tail

$$g_{\text{PT-2}}(r) = D\,\frac{GM}{r^2} + E\,\frac{GMr_0}{r^3} + A\sum_k \frac{r}{s_k^2}\exp\!\big(-r^2/2s_k^2\big),$$

with (D, E) fixed *globally* (dimensionless E scaled by r_0), and choose A from $g(r_0) = g_0$. The r^{-3} term provides a small, globally consistent curvature correction while preserving the far–field $1/r^2$ law. For operations, under the RMSE weighting on $\mathcal{W} = [r_0, 3r_0]$ (e.g. $w_N \propto g_N^2$),

$$\begin{aligned} D \;&\leftarrow\; D_{\text{eff}}(\mathcal{W}),\\ E:\;&\text{choose a single global value by minimizing the second–moment}\\ &\quad\text{residual relative to VT.}\end{aligned}$$

thereby avoiding any per–object freedom.

(E3) Radially weighted mixing $D(r)$ (caution). A minimal one–parameter profile

$$D(r) = 1 - (1 - D)\exp\!\big(-(r - r_0)/\lambda\big), \qquad \lambda = r_0,$$

keeps $D(r_0) = D$ and tends to 1 at large r. This breaks the *exact* linear RMSE scaling but can reduce near–surface bias. To remain fixed–policy, λ/r_0 must be a single global constant. (*Recommended default remains the variational taper rather than $D(r)$.*)

Recommended default for fixed–policy runs. Use the *variational taper* as the primary mechanism: set global (r_t, Δ) and choose $\mu^\star$ from PPN budgets so that on $[r_0, 3r_0]$ the effective strength satisfies $D_{\text{eff}} \approx 0.90$. For PSCF, keep widths $\{0.5, 1.0, 2.0\}r_0$; optionally add C4–3C (E1) for curvature anchoring. Report near/global RMSE and include a log–uniform global–window robustness metric.

J.10 Sensitivity and Error Budget

First–order error propagation (inner–product form). Let the g_0–normalized residual be

$$\tilde{e}(r;\theta) \;\equiv\; \frac{g_{\text{model}}(r;\theta) - g_{\text{N}}(r;\theta)}{g_0}, \qquad R(\theta) \;\equiv\; \big\|\tilde{e}(\cdot;\theta)\big\|_{L^2(\mathcal{W},\mathrm{d}\wp)} = \Big(\int_{\mathcal{W}} \tilde{e}(r;\theta)^2\,\mathrm{d}\wp\Big)^{1/2},$$

where $\theta \in \{g_0, r_0\}$ and $\mathrm{d}\wp$ is the RMSE sampling measure (as in Appendix J.5–Appendix J.7). Then the first–order perturbation for small $\delta\theta$ is

$$\delta R \;\approx\; \sum_\theta \frac{\partial R}{\partial \theta}\,\delta\theta, \qquad \frac{\partial R}{\partial \theta} = \frac{1}{R}\,\big\langle\, \tilde{e},\; \partial_\theta \tilde{e}\,\big\rangle_{L^2(\mathcal{W},\mathrm{d}\wp)}.$$

Below we give $\partial_\theta \tilde{e}$ in closed/operational form for each model family under the fixed–constants policy ($GM = g_0 r_0^2$, widths $\propto r_0$).

Lemma (exact g_0–invariance for PSCF/C4 and their composites). For PSCF, C4, PT/CT (with global D) and the variational–taper composite (with window–fixed D_{eff}), one has

$$\partial_{g_0}\,\tilde{e}(r;\theta) = 0 \qquad \text{for all } r \in \mathcal{W}.$$

Sketch. Under $GM = g_0 r_0^2$, Newton gives

$$\partial_{g_0} g_{\mathrm{N}} = \frac{g_{\mathrm{N}}}{g_0}.$$

PSCF/C4 are anchored by $g(r_0) = g_0$ and depend linearly on g_0, hence

$$\partial_{g_0} g_{\mathrm{model}} = \frac{g_{\mathrm{model}}}{g_0}.$$

Therefore

$$\partial_{g_0}\tilde{e} = \frac{1}{g_0}\left(\frac{\partial g_{\mathrm{model}}}{\partial g_0} - \frac{\partial g_{\mathrm{N}}}{\partial g_0}\right) - \frac{g_{\mathrm{model}} - g_{\mathrm{N}}}{g_0^2} = \frac{1}{g_0}\left(\frac{g_{\mathrm{model}}}{g_0} - \frac{g_{\mathrm{N}}}{g_0}\right) - \frac{g_{\mathrm{model}} - g_{\mathrm{N}}}{g_0^2} = 0.$$

For PT/CT and VT, the same cancellation holds in $\tilde{e}$ because the Newton sector is subtracted before division by g_0, and D (or D_{eff}) are global, hence independent of g_0.

Newton reference (for comparison). With $GM = g_0 r_0^2$,

$$\frac{\partial g_{\mathrm{N}}}{\partial g_0} = \frac{g_{\mathrm{N}}}{g_0}, \qquad \frac{\partial g_{\mathrm{N}}}{\partial r_0} = \frac{2 g_{\mathrm{N}}}{r_0}.$$

These enter only through $\tilde{e}$ since R compares a model to g_{N}.

PSCF sensitivities (closed form). Let $s_k = \alpha_k r_0$ and

$$g_{\mathrm{PSCF}}(r) = A \sum_k \Phi_k(r), \qquad \Phi_k(r) = \frac{r}{s_k^2}\exp\Big(-\frac{r^2}{2s_k^2}\Big), \qquad A:\ g_{\mathrm{PSCF}}(r_0) = g_0.$$

Because $\sum_k \Phi_k(r_0) = \frac{C}{r_0}$ with $C = \sum_k \alpha_k^{-2} e^{-1/(2\alpha_k^2)}$ (constant), one has $A = \dfrac{g_0 r_0}{C}$. Hence

$$\frac{\partial g_{\mathrm{PSCF}}}{\partial g_0} = \frac{g_{\mathrm{PSCF}}}{g_0} \quad (\Rightarrow\ \partial_{g_0}\tilde{e} = 0),$$

and

$$\frac{\partial g_{\mathrm{PSCF}}}{\partial r_0} = \frac{g_{\mathrm{PSCF}}}{r_0} \;+\; A\sum_k \frac{\partial \Phi_k}{\partial r_0} = \Big(-\frac{1}{r_0} + \frac{\eta(r)\,r^2}{r_0^3}\Big)\, g_{\mathrm{PSCF}}(r),$$

where

$$\eta(r) \;\equiv\; \frac{\sum_k \alpha_k^{-4}\, w_k(r)}{\sum_k \alpha_k^{-2}\, w_k(r)}, \qquad w_k(r) = \exp\Big(-\frac{r^2}{2\alpha_k^2 r_0^2}\Big).$$

Thus

$$\partial_{r_0}\tilde{e}(r) = \frac{1}{g_0}\Big(\partial_{r_0} g_{\mathrm{PSCF}} - \partial_{r_0} g_{\mathrm{N}}\Big) = \frac{1}{g_0}\left[\Big(-\frac{1}{r_0} + \frac{\eta(r)\,r^2}{r_0^3}\Big) g_{\mathrm{PSCF}}(r) - \frac{2 g_{\mathrm{N}}(r)}{r_0}\right].$$

C4 sensitivities (operational linear–algebra form). With $\sigma_i = \beta_i r_0$,

$$g_{\mathrm{C4}}(r) = \sum_{i=1}^{2} B_i\, G_i(r), \qquad G_i(r) = \frac{r}{\sigma_i^2}\exp\Big(-\frac{r^2}{2\sigma_i^2}\Big),$$

and boundary conditions $\{g(r_0) = g_0,\ g'(r_0) = -2g_0/r_0\}$. Let $M(r_0)\,B = Y(r_0)$ be the 2×2 system with rows $\{G_i(r_0)\}$ and $\{G_i'(r_0)\}$, and $Y = (g_0,\ -2g_0/r_0)^\top$. Then

$$\frac{\partial g_{\mathrm{C4}}}{\partial g_0} = \frac{g_{\mathrm{C4}}}{g_0} \quad (\Rightarrow\ \partial_{g_0}\tilde{e} = 0),$$

and

$$\frac{\partial g_{\mathrm{C4}}}{\partial r_0} = \underbrace{\big(\partial_{r_0}B\big)^\top G(r)}_{\text{via } M^{-1}(\partial_{r_0}Y - \partial_{r_0}M\,B)} + \underbrace{B^\top \partial_{r_0} G(r)}_{\text{explicit } r_0 \text{ in } G_i},$$

where

$$\partial_{r_0}Y = \Big(0,\ \frac{2g_0}{r_0^2}\Big)^\top, \quad \partial_{r_0}G_i(r) = \Big(\frac{1}{\sigma_i^2} - \frac{r^2}{\sigma_i^4}\Big)e^{-r^2/(2\sigma_i^2)}\cdot\Big(-\frac{2}{r_0} + \frac{r^2}{\sigma_i^2 r_0}\Big).$$

This expression is numerically stable because it uses the same primitives already evaluated for g and g' at r_0.

Composites (PT/CT) and variational taper (VT). For a constant D,

$$g_{\mathrm{PT/CT}} = D\,g_{\mathrm{N}} + (1-D)\,g_{\mathrm{core}} \ \Rightarrow\ \partial_{r_0}\tilde{e}_{\mathrm{PT/CT}} = (1-D)\,\partial_{r_0}\tilde{e}_{\mathrm{core}}, \qquad \partial_{g_0}\tilde{e}_{\mathrm{PT/CT}} = 0.$$

For VT on $\mathcal{W}$, with fixed $(r_t, \Delta, \mu^\star)$ and derived $D_{\mathrm{eff}}(\mathcal{W})$ (Appendix C.8.3),

$$\partial_{r_0}\tilde{e}_{\mathrm{VT}} \ \approx\ (1 - D_{\mathrm{eff}})\,\partial_{r_0}\tilde{e}_{\mathrm{core}} \quad \text{and} \quad \partial_{g_0}\tilde{e}_{\mathrm{VT}} = 0,$$

since D_{eff} is window–level and policy–fixed (thus $\partial_\theta D_{\mathrm{eff}} \approx 0$).

Dominant contributors (revised). Under the fixed–constants policy:

(i) g_0 **measurements:** *do not affect* the normalized RMSE for PSCF/C4/PT/CT/VT (exact cancellation above); GR has $O(g_0 r_0/c^2)$ sensitivity, negligible on Solar windows.

(ii) r_0 **(scale) uncertainty:** *dominant*. It changes both the Newton reference ($\partial_{r_0} g_{\mathrm{N}} = 2g_{\mathrm{N}}/r_0$) and the Gaussian scaffold (via widths $\propto r_0$).

(iii) **Sampling/window choice:** affects R through $\mathrm{d}\wp$ and the region $\mathcal{W}$ (near vs. global), hence reweights $\langle \tilde{e}, \partial_{r_0}\tilde{e}\rangle$.

(iv) **Width sets (model mismatch):** fixed global width sets induce a systematic curvature bias that shows up in $\partial_{r_0}\tilde{e}$; composites/VT attenuate it by $(1-D)$ or $(1-D_{\mathrm{eff}})$.

Error budget (operational summary).

Source	Scaling in R	Remarks
g_0 error	0 (exact, PSCF/C4/PT/CT/VT)	cancels in $\tilde{e}$; GR sensitivity $\sim O(g_0 r_0/c^2)$
r_0 error	$\propto \langle \tilde{e}, \partial_{r_0}\tilde{e}\rangle / R$	see closed forms above
Window/sampling	changes $\mathrm{d}\wp$, $\mathcal{W}$	alters weighting of residual structure
Composite tail (D or D_{eff})	$R \mapsto \lvert 1-D\rvert\, R_{\mathrm{core}}$	gradients ∂R scale likewise
Grid resolution $\lvert\mathcal{W}\rvert$	quadrature error $\downarrow$ with finer grid	keep uniform/log rules consistent

J.10.1 Cohérence: analytic vs. discrete perturbations

Procedure (non-redundant check). For each model family (PSCF, C4, PT, CT, and VT) and window $\mathcal{W}$:

1. **Analytic targets.** Evaluate $\partial R/\partial g_0$ and $\partial R/\partial r_0$ from the formulas in Appendix J.10 (do not restate here). Record the following *invariants/scaling targets*:

$$\begin{aligned}
&\textbf{Invariance:} \quad \big(\partial R/\partial g_0\big)_{\mathrm{PSCF/C4/PT/CT/VT}} = 0,\\
&\textbf{Scaling (PT/CT):} \quad \big(\partial R/\partial r_0\big)_{\mathrm{PT/CT}} = |1-D|\,\big(\partial R/\partial r_0\big)_{\mathrm{base}},\\
&\textbf{Scaling (VT):} \quad \big(\partial R/\partial r_0\big)_{\mathrm{VT}} \approx (1-D_{\mathrm{eff}})\,\big(\partial R/\partial r_0\big)_{\mathrm{core}},\\
&\qquad \text{(variational remainder negligible on } [r_0, 3r_0]).
\end{aligned}$$

2. **Finite differences (central).** With shared quadrature/grid and small symmetric steps $\delta g_0 = \varepsilon g_0,\ \delta r_0 = \varepsilon r_0$ ($\varepsilon \in [10^{-8}, 10^{-6}]$),

$$\left.\frac{\partial R}{\partial g_0}\right|_{\mathrm{FD}} \approx \frac{R(g_0+\delta g_0, r_0) - R(g_0-\delta g_0, r_0)}{2\,\delta g_0}, \qquad \left.\frac{\partial R}{\partial r_0}\right|_{\mathrm{FD}} \approx \frac{R(g_0, r_0+\delta r_0) - R(g_0, r_0-\delta r_0)}{2\,\delta r_0}.$$

3. **Coherence metric.** Report the relative discrepancy

$$\Delta_\theta = \frac{\left|\frac{\partial R}{\partial \theta} - \frac{\partial R}{\partial \theta}\big|_{\mathrm{FD}}\right|}{\max\!\left(\varepsilon_0, \left|\frac{\partial R}{\partial \theta}\right|\right)}, \qquad \varepsilon_0 = 10^{-12},$$

and verify that: (i) $\big(\partial R/\partial g_0\big)_{\mathrm{FD}} \approx 0$; (ii) PT/CT follow the $|1-D|$ factor; (iii) VT follows $(1-D_{\mathrm{eff}})$ within the small variational remainder.

Outcome (what passes the check). Because PT/CT are linear compositions $g_{\mathrm{comp}} = D\,g_{\mathrm{N}} + (1-D)\,g_{\mathrm{base}}$, residuals and their *model-side* sensitivities inherit the same factor $|1-D|$. Moreover, under the fixed–constants policy the g_0-normalized residual cancels *exactly* for all PSCF/C4/PT/CT/VT:

$$\big(\partial R/\partial g_0\big)_{\mathrm{analytic}} = 0 \quad \Longrightarrow \quad \big(\partial R/\partial g_0\big)_{\mathrm{FD}} \approx 0,$$

so no separate "normalization-side" term survives. Numerically, analytic and discrete perturbations agree to floating-point tolerance (typically $\Delta_\theta \lesssim 10^{-10}$ on the adopted grids), and the PT/CT and VT scaling laws match their targets above.

J.10.2 Discussion of sensitivities

Decomposition (first order, policy consistent). For small perturbations of the observed constants $\{g_0, r_0\}$, write the normalized RMSE increment as

$$\delta R \;\approx\; \underbrace{\kappa_{g_0}\,\frac{\delta g_0}{g_0}}_{\text{normalization side}} \;+\; \underbrace{S_{g_0}\,\frac{\delta g_0}{g_0} + S_{r_0}\,\frac{\delta r_0}{r_0}}_{\text{model side}},$$

where the windowed coefficients $S_\bullet$ are those induced by the derivatives in Appendix J.10. Under the *fixed–constants* policy (PSCF, C4, PT/CT with constant D, and VT with window–fixed D_{eff}), the g_0–normalized residual cancels *exactly* (Appendix J.10 Lemma), so

$$\boxed{\kappa_{g_0} = 0, \quad S_{g_0} = 0} \qquad \text{(GR has } O(g_0 r_0/c^2) \text{ sensitivity, negligible on Solar windows).}$$

Moreover,

$$S_{r_0}(\text{PT/CT}) \;=\; |1-D|\, S_{r_0}(\text{base}), \qquad S_{r_0}(\text{VT}) \;\approx\; (1-D_{\text{eff}})\, S_{r_0}(\text{core}),$$

with the variational remainder negligible on $[r_0, 3r_0]$.

Table 98: Qualitative sensitivity guide (sign and scaling). Entries show the leading dependence of δR; coefficients are window–dependent.

Source	**PSCF**	**C4**	**PT/CT (fixed D)**	**VT (fixed D_{eff})**
g_0 normalization	0	0	0	0
Model vs ref via g_0	0	0	0	0
Model vs ref via r_0	$\pm\, S_{r_0}\, \delta r_0/r_0$	$\pm\, S_{r_0}\, \delta r_0/r_0$	$\pm\, \lvert 1-D\rvert\, S_{r_0}\, \delta r_0/r_0$	$\pm\, (1-D_{\text{eff}})\, S_{r_0}\, \delta r_0/r_0$
Window (near→global)	↑ (Gaussian tail bias)	↑↑ (stronger)	↓ by $\lvert 1-D\rvert$	↓ by $(1-D_{\text{eff}})$
Grid size $\lvert\mathcal{W}\rvert$	$\propto \lvert\mathcal{W}\rvert^{-1/2}$	$\propto \lvert\mathcal{W}\rvert^{-1/2}$	$\propto \lvert\mathcal{W}\rvert^{-1/2}$	$\propto \lvert\mathcal{W}\rvert^{-1/2}$

Implications. (i) Enlarging the window amplifies the Gaussian–tail mismatch for PSCF/C4; tail mechanisms (PT/CT/VT) damp the resulting sensitivity by $|1-D|$ or $(1-D_{\text{eff}})$ but *cannot* alter the (already–zero) normalization channel. (ii) Uncertainty in r_0 directly couples to the scaffold widths $(s_k, \sigma_i) \propto r_0$; hence S_{r_0} typically dominates in the near window where curvature is tightly constrained. (iii) Increasing $|\mathcal{W}|$ reduces estimator variance as $|\mathcal{W}|^{-1/2}$ but not bias; structural remedies (e.g., curvature anchoring C4–3C or variational taper) are needed to address bias. (iv) For VT, sensitivity in the far field aligns with the Newton sector; near–surface behavior remains governed by the Gaussian scaffold and its r_0–scaling.

J.10.3 Extensions and reinforcements

C1. Curvature anchoring (fixed–policy). Augment C4 with a third center, using global widths $\sigma/r_0 = \{0.6,\ 1.4,\ 2.4\}$, and determine coefficients by the three surface anchors

$$g(r_0) = g_0, \qquad g'(r_0) = -\frac{2g_0}{r_0}, \qquad g''(r_0) = \frac{6g_0}{r_0^2}.$$

This *C4–3C* construction reduces the near–window scale sensitivity S_{r_0} without any per–body tuning and remains compliant with the fixed–constants policy.

C2. Two–term algebraic tail. Adopt the global two–term composite

$$g(r) = D\,\frac{GM}{r^2} \;+\; E\,\frac{GMr_0}{r^3} \;+\; \sum_k A_k\,\frac{r}{s_k^2}\exp\Big(-\frac{r^2}{2s_k^2}\Big),$$

with (D, E) fixed *globally* (dimensionless E scaled by r_0) and A_k set by the standard anchor $g(r_0) = g_0$ (and, if desired, additional near–surface constraints). The r^{-3} term supplies a mild,

scale–aware curvature correction while preserving the $1/r^2$ far field. *Operational rule:* on $\mathcal{W} = [r_0, 3r_0]$ with RMSE weighting (e.g. $w_N \propto g_N^2$),

$$D \leftarrow D_{\text{eff}}(\mathcal{W}), \qquad E \text{ chosen once by minimizing a second–moment residual vs. the VT baseline,}$$

thus avoiding per–object freedom. In sensitivity terms, the model–side coefficient scales as $S_{r_0} \mapsto (1-D)S_{r_0}$ (or $1-D_{\text{eff}}$ for VT).

C3. Window fusion and weighting. Report R on near, global–linear, and global–log windows, and add a fused score

$$R_{\text{mix}} = \alpha\, R_{\text{near}} + \beta\, R_{\text{global}} + \gamma\, R_{\log}, \qquad \alpha, \beta, \gamma \geq 0, \;\; \alpha + \beta + \gamma = 1,$$

with (α, β, γ) fixed *a priori*. Use a common quadrature/grid convention across windows. This stabilizes conclusions against sampling choices and grid effects (variance control), while curvature anchoring/tails address bias.

C4. Uncertainty envelopes (policy–consistent). Under the fixed–constants policy, the g_0 channel cancels exactly (Appendix J.10), so the first–order envelope is

$$\text{CI}_{1\sigma}: \quad R \;\pm\; \left| S_{r_0}\, \frac{\sigma_{r_0}}{r_0} \right| \qquad \text{(PSCF/C4)}.$$

For PT/CT, replace $S_{r_0} \mapsto |1-D|\, S_{r_0}$; for VT, $S_{r_0} \mapsto (1-D_{\text{eff}})\, S_{r_0}$. (If GR is included as a reference, an additional $O(g_0 r_0/c^2) \cdot \sigma_{g_0}/g_0$ term is formally present but negligible on Solar windows.)

C5. Practical default (balanced bias/variance). Use $D = 0.90$ (or $D_{\text{eff}} \approx 0.90$ for VT), PSCF widths $\{0.5, 1.0, 2.0\} r_0$, and optionally add C4–3C curvature anchoring (C1). Report $\{R_{\text{near}}, R_{\text{global}}, R_{\log}, R_{\text{mix}}\}$ together with the policy–consistent uncertainty envelopes from C4. This configuration pairs structural bias control (curvature + tail/VT) with variance control (window fusion) while remaining within the fixed–constants policy.

J.11 Reproducibility (Code & Data) and Artifact Index

Scope (single source of truth). This subsection is the canonical checklist for reproducing every numerical and plotting result in Appendix J.5–Appendix J.10. Any repeated checklists elsewhere should *point back to* Appendix J.11.

Determinism and numerics. All computations use IEEE–754 double precision and are *deterministic* (no randomness). The RMSE norm is the windowed L^2 norm used throughout Appendix J.5–Appendix J.10:

$$\text{RMSE}_{\mathcal{W}} = \Big(\int_{\mathcal{W}} \tilde{e}(r)^2 \, \mathrm{d}\wp(r) \Big)^{1/2}, \qquad \tilde{e}(r) = \frac{g_{\text{model}}(r) - g_{\text{N}}(r)}{g_0},$$

with sampling measures and windows exactly as specified below.

Reproduction steps.

(i) **Global policy and constants.** Set fixed global widths and normalization constants as in Appendix J.2 (PSCF $s/r_0 = \{0.5, 1.0, 2.0\}$; C4 $\sigma/r_0 = \{0.7, 1.6\}$; optional C4–3C $\{0.6, 1.4, 2.4\}$). Use $GM = g_0 r_0^2$ and anchor $g(r_0) = g_0$ (and, where applicable, $g'(r_0) = -2g_0/r_0$).

(ii) **Windows and grids.** Reuse the evaluation windows and grids from Appendix J.5–Appendix J.7: near $[r_0, 1.5r_0]$, global–linear $[r_0, 3r_0]$, global–log $[r_0, 3r_0]$, and optional global–linear $[r_0, 5r_0]$.

(iii) **Weighting.** For RMSE weighting on Solar/Galactic windows, use $w_N(r) \propto g_N(r)^2$ (as in Appendix J.6–Appendix J.7), i.e. $\mathrm{d}\wp(r) \propto g_N(r)^2\,\mathrm{d}r$ for linear grids and the corresponding measure for log grids.

(iv) **Tail mechanism.** For legacy convex mix (PT/CT) set the fixed global tail weight D as in Appendix J.6 (default $D = 0.90$). For the *variational taper* (VT/VC), fix (r_t, Δ) per Section 2.6.2, choose $\mu^\star$ by the PPN budgets (Appendix C.8.3), and record the induced D_{eff} on each window via Eq. (329).

(v) **Galactic data.** Load SPARC photometry/gas and perform ring discretization following Appendix J.8. Use $r_0 = 2.2R_d$ (disk peak) and $v_0 = V_{\mathrm{bar}}(r_0)$ for normalization. Build $V_{\mathrm{bar}}^2 = V_{\mathrm{gas}}^2 + V_{\mathrm{disk}}^2 (+V_{\mathrm{bul}}^2)$.

(vi) **Environment parity.** Use identical quadrature/grid rules across analytic and finite–difference checks (Appendix J.10.1). Use the same figure styles when regenerating plots to avoid cosmetic diffs.

Artifact index (figures).

- **Fig. J7-1 (J.7)** — Robustness across sampling schemes (linear/log; $3r_0$/$5r_0$).
- **Fig. J7-2 (J.7)** — Same data as Fig. J7-1 on log y.
- **Fig. J8A (J.8)** — NGC 3198 rotation curve: observed vs. NB with residuals.
- **Fig. J8B (J.8)** — NGC 2403 rotation curve: same layout as Fig. J8A.
- **Fig. J8C (J.8)** — Stacked normalized residuals: median and IQR by window.
- **Fig. J8A′ (J.8)** — NGC 3198: NB, PSCF, C4, PT(D=0.90), CT(D=0.90) with residuals.
- **Fig. J8B′ (J.8)** — NGC 2403: extended comparison (same layout).
- **Fig. J8C′ (J.8)** — Stacked residuals: NB vs. PSCF/C4 vs. PT/CT.

Artifact index (tables).

- **Tab. J5-ES (J.5.1)** — Earth at r_0: surface/near-surface comparisons (fractional diffs, RMSE).
- **Tab. J5-EC (J.5.1)** — Earth-specific fixed coefficients (A, B_1, B_2).
- **Tab. J5.2-PS (J.5.2)** — PSCF* tuned weights (five widths).

- **Tab. J5.2-C4 (J.5.2)** — C4* tuned parameters (grids and solved B_i).
- **Tab. J5.2-R (J.5.2)** — Normalized RMSE (train vs. cross).
- **Tab. J6-A (J.6)** — Variational taper: average RMSE and improvement vs. fixed policy.
- **Tab. J6-S (J.6)** — Sensitivity of VT/VC to derived D_{eff}.
- **Tab. J7-R (J.7)** — Robustness across sampling schemes.
- **Tab. J9-V (J.9)** — Variational scaling verification ($|1-D_{\text{eff}}|$ law).
- **Tab. J10-S (J.10)** — Qualitative sensitivity guide (signs & scaling).

Provenance pointers. PSCF/C4 global width policy and anchors: Appendix J.2. Variational taper construction and budgets: Appendix C.8.3. Windows, weighting, and robustness conventions: Appendix J.5–Appendix J.7. Galactic benchmark protocol and normalization: Appendix J.8.

Notes. (i) Where legacy constant-D results are reproduced, tag them `[Legacy--convex mix]` and map via $D \leftrightarrow D_{\text{eff}}$ on the target window (Appendix J.6). (ii) When adding new artifacts, register a `\label` and list it here to maintain a single source of truth. (iii) For analytic vs. discrete checks, follow Appendix J.10.1 (use identical grids and central differences).

J.11.1 Deterministic replay

Determinism. All runs depend only on global fixed widths/anchors (Appendix J.2), shared windows/grids (Appendix J.5–Appendix J.7), and a fixed tail policy (Appendix J.6). No stochastic elements are used. Any discrepancy between repeated runs therefore originates from the *numerical environment* rather than from the model itself—for example, differences in linear–algebra kernels (BLAS/LAPACK), math libraries (`libm`), compiler optimization settings, or CPU–level arithmetic rules such as fused multiply–add (FMA) or "fast–math" approximations.

Replay checklist (acceptance criteria).

1. **Grids & windows.** Recreate near, global–linear, global–log (and optional $5r_0$) grids *bitwise-identical* to those used in Appendix J.5–Appendix J.7. Record grid digests (e.g., SHA256 of node arrays).
2. **Baselines.** Recompute Newton/GR from (g_0, r_0) with $GM = g_0 r_0^2$; verify GR $\approx$ Newton within Solar-System tolerance ($< 10^{-9}$ fractional at r_0).
3. **Models.** Rebuild PSCF/C4 with global widths; reproduce the Solar-System RMSE tables (Table J.5-1, Table J.5-2) with relative error $\leq 10^{-12}$.
4. **Tail policies.** (a) *Legacy mix (PT/CT):* form $g = D\, g_N + (1-D)\, g_{\text{base}}$, verify residuals and RMSE scale by $|1-D|$ to machine precision;
(b) *Variational taper (VT/VC):* compute D_{eff} on each window via Eq. (Appendix J.6.1) and verify the $(1-D_{\text{eff}})$ attenuation (cf. Appendix J.9).

5. **Figures.** Match curves and residual panels in Fig. J8A and Fig. J8B (identical axes, limits, and tick locations). L^2 curve difference $< 10^{-12}$ (normalized).

6. **Stacks.** Reproduce medians and IQRs in Fig. J8C with absolute error $\leq 10^{-12}$.

J.11.2 Failure modes and portability

Portability (environment, not physics). This section notes small differences that come from the *computing environment*, not from the model or the physics. Even with the same code and inputs, floating–point arithmetic can be handled slightly differently across systems, producing *last–digit* differences. Typical sources are: (i) linear–algebra backends (e.g., OpenBLAS vs. MKL) that change operation order or vectorization; (ii) `libm` implementations of `exp`, `log`, `sin`/`cos`; (iii) compiler optimizations (vectorization/FMA, `-ffast-math`) that relax IEEE rules and reorder operations; (iv) non-deterministic parallel reductions. These are computational issues; they do not alter the qualitative conclusions, but they can break bitwise reproducibility.

Practical handling. Our practice is simple: *write down the environment, and simplify when exact replay matters*. We log Python/NumPy versions, BLAS vendor, OS/architecture, and compiler options (Appendix H). For exact replay we prefer single-threaded math (`OMP_NUM_THREADS=1`, `MKL_NUM_THREADS=1`, `OPENBLAS_NUM_THREADS=1`) and avoid aggressive flags (disable fast-math/FMA if needed). When reproducibility outweighs raw speed, we use strict floating-point modes and fix seeds if any stochastic step is introduced, staying within the tolerances of Appendix K.5.

Anchors vs. tails. The D-mix/VT enforce the $1/r^2$ far field but do not change near-surface curvature. Residuals around r_0 are controlled by *curvature anchors* (e.g., multi-center C4, C4–3C), not by tail weight. In practice we record: the anchor locations and derivative order (g, g', g'' at r_0), fixed-constant tables (widths/scales), and on/off switches. The basic check is that g, g', g'' near r_0 stay within spec (e.g., relative error $< 10^{-6}$) (Appendix J.6, Appendix J.9).

Windows and weighting. Linear vs. logarithmic sampling changes the *definition of RMSE* because the sampling distribution differs. We therefore report *near*, *global–linear*, and *global–log* results together and require consistency within the stated envelopes (Appendix J.7). For VT, window changes must propagate through $D_{\text{eff}}(\mathcal{W})$. A window $\mathcal{W}$ specifies $r_{\min}$, $r_{\max}$, the sample count N, sampling mode (`linear`/`log`), and weights $w(r)$, and we define

$$\mathrm{RMSE}(\mathcal{W}) = \left(\frac{\sum_{r\in\mathcal{W}} w(r)\, \Delta(r)^2}{\sum_{r\in\mathcal{W}} w(r)} \right)^{1/2}.$$

To guarantee identical windows across machines, we record the full window configuration alongside results.

J.11.3 Maintenance & extensions

Recommended hardening (plain language). (i) **Add a third center (C4–3C).** Anchor g, g', g'' at r_0 to reduce near–field sensitivity S_{r_0}. *Practice:* list the anchors (location r_0, which derivatives are fixed, tolerances, on/off) and check them at startup. Keep a short checksum so later runs use the same anchor set.

(ii) **Optional global r^{-3} term.** A gentle r^{-3} correction can improve curvature without per–target tuning. *Practice:* keep it registered but *off* by default; enable only via the policy file and record the policy version and code commit. This avoids ad hoc switches during analysis.

(iii) **Report a fused score.** Publish $R_{\text{mix}} = \alpha R_{\text{near}} + \beta R_{\text{global}} + \gamma R_{\log}$ with fixed cross–window weights. *Practice:* treat (α, β, γ) as policy constants (e.g., in a config file), do not allow runtime overrides, and always report the three component scores alongside R_{mix}.

(iv) **Ship a short manifest.** Include a machine–readable note with the run: main software versions, BLAS vendor, OS/arch, key environment variables, and checksums for windows/-grids/fixed constants. This lets other groups confirm they used the same inputs.

(v) **Basic tests for attenuation and GR near r_0.** Add unit tests for the $|1-D|$ and $(1-D_{\text{eff}})$ laws (Appendix J.9), and for GR $\approx$ Newton at r_0. *Practice:* test many inputs (property–based style) with tight tolerances (relative error 10^{-8}–10^{-10}). When possible, run once with OpenBLAS and once with MKL to check numerical stability.

Change management (keep it traceable). Any policy change (width sets, (r_t, Δ), weighting) should carry a version tag and be noted in Appendix J.11. Legacy constant–D results should be marked `[Legacy--convex mix]` and mapped to the target window using $D \leftrightarrow D_{\text{eff}}$ (cf. Appendix J.6). For each run, record three short identifiers: (a) a *policy hash* (policy/config files), (b) the code *commit ID*, and (c) an *environment manifest hash*. Add a small `provenance` block with these IDs to the results so others can repeat the analysis exactly.

Appendix K. C4 Cosmology: background and linear perturbations

K.0 Policy, priors, and reproducibility (clarified)

Global fixed–constants policy. All cosmology analyses follow the *global fixed–constants* policy of Section 2.6.2. **Global declarations (no dataset–wise retuning unless a pre–registered exception is stated):**

(i) the self–sourcing constant $\alpha \geq 0$ (see Appendix C.2);

(ii) Newton's constant G and the unit conventions;

(iii) a minimal potential family $U(\Phi)$ chosen *a priori* as either (a) *constant* U (late–time acceleration) or (b) a *one–parameter tracker* (e.g. exponential).

Initial conditions follow standard radiation/matter histories. Unless explicitly stated, early–Universe microphysics (recombination acoustics, the sound horizon r_s) and the neutrino sector are kept standard. We use $M_{\rm P}$ for the reduced Planck mass.

Numerical specification (canonical references). To avoid ambiguity in the background, Appendix K.1bis defines two canonical options that are used unchanged across probes: (i) constant–U with priors on (H_0, Ω_{m0}); (ii) an exponential tracker,

$$U(\Phi) = U_\star \, \exp\!\Big(- \lambda \, \frac{\Phi}{M_{\rm P}} \Big),$$

with fixed bounds on λ. Priors and integration tolerances are versioned there so runs can be replayed byte for byte.

Background and distance mapping (shared definitions). Let $E(z) \equiv H(z)/H_0$ and $\chi(z) = \int_0^z \frac{c\,dz'}{H(z')}$. With curvature kernel $S_K(x)$ and the sign convention $\Omega_{K0} > 0$ (open), $\Omega_{K0} < 0$ (closed),

$$D_M(z) = S_K\big(H_0 \chi/c\big), \quad S_K(x) = \begin{cases} \frac{c}{H_0\sqrt{\Omega_{K0}}} \sinh\!\big(\sqrt{\Omega_{K0}}\, x\big), & \Omega_{K0} > 0, \\ \frac{c}{H_0}\, x, & \Omega_{K0} = 0, \\ \frac{c}{H_0\sqrt{|\Omega_{K0}|}} \sin\!\big(\sqrt{|\Omega_{K0}|}\, x\big), & \Omega_{K0} < 0, \end{cases}$$

and $D_A(z) = D_M(z)/(1+z)$, $D_H(z) = c/H(z)$. For BAO and CMB summaries we use

$$D_V(z) = \Big[(1+z)^2 D_A^2(z)\, \frac{cz}{H(z)}\Big]^{1/3}, \qquad \ell_A = \pi\, \frac{D_M(z_*)}{r_s(z_*)}, \qquad R = \sqrt{\Omega_{m0}}\, \frac{H_0 D_M(z_*)}{c},$$

with z_* the recombination redshift and r_s the drag–epoch sound horizon. We keep c explicit and take H_0 in $\mathrm{km\,s^{-1}\,Mpc^{-1}}$.

Linear response and growth (C4 mapping). On subhorizon scales we use the quasi–static triplet (μ, η, Σ):

$$k^2\Psi = -4\pi G a^2\, \mu(a,k)\, \rho_m \Delta_m, \qquad \eta(a,k) = \frac{\Phi}{\Psi}, \qquad \Sigma(a,k) = \frac{\mu(a,k)}{2}\,[1+\eta(a,k)].$$

The growth factor satisfies $D(1) = 1$ so $f(a) = d\ln D/d\ln a$ and $f\sigma_8(a) = f(a)\,\sigma_{8,0}\,D(a)$. Under standard linear bias/RSD conventions, E_G uses the same (μ, η) and the data window/-covariance; CMB lensing uses Σ in the Limber integral for $C_\ell^{\phi\phi}$. Quasi–static expressions are applied only within our analysis window (e.g. $k \gtrsim 0.01\, h\,\mathrm{Mpc}^{-1}$); see Appendix K.2.

Scope and probe mapping. Late–time C4 effects appear through $H(z)$ (background) and (μ, η, Σ) (perturbations). Background observables $(D_H, D_M, D_V, \ell_A, R)$ and perturbation observables $(f\sigma_8, E_G, C_\ell^{\phi\phi})$ are computed with the *same* covariances and the *same* priors on (H_0, Ω_{m0}) or $(\lambda, U_\star)$ for the declared $U(\Phi)$ family. No object– or dataset–specific widths/-tunings are introduced.

Archival and reproducibility (concise). All inputs (declared priors, model family $U(\Phi)$, grids, code options) and all data products (masks, covariances) are archived with version identifiers so any figure or table can be regenerated without dataset–wise retuning (see Appendix H). Each figure/table carries a run identifier (`run_id`) that links to the exact configuration. If execution environments differ, reproduced numbers agree within the tolerance specified in Appendix K.1bis.

K.1 Background FRW equations

Setup (flat FRW with a homogeneous curvature field). We work on a spatially flat FRW background,

$$ds^2 = -dt^2 + a^2(t)\,\delta_{ij}\,dx^i dx^j,$$

and assume a spatially homogeneous curvature field $\Phi(t)$. It behaves like an effective fluid,

$$\rho_\Phi = \tfrac{1}{2}\dot\Phi^2 + U(\Phi), \qquad p_\Phi = \tfrac{1}{2}\dot\Phi^2 - U(\Phi), \qquad \ddot\Phi + 3H\dot\Phi + U'(\Phi) = 0,$$

and the background expansion obeys

$$H^2 = \frac{8\pi G}{3}\big(\rho_r + \rho_m + \rho_\Phi\big), \qquad \dot H = -4\pi G\Big(\rho_m + \tfrac{4}{3}\rho_r + \dot\Phi^2\Big).$$

We write $w_\Phi \equiv p_\Phi/\rho_\Phi$; accelerated expansion requires $w_\Phi < -1/3$. Intuitively, Hubble friction damps $\dot\Phi$. For the constant–U family the field quickly freezes ($\dot\Phi \to 0$), so $w_\Phi \simeq -1$ at late times. For tracker families, $w_\Phi(z)$ evolves in a controlled way, bounded by the priors in Appendix K.1bis. Throughout, $M_{\rm P}$ denotes the *reduced Planck mass*.

K.1.1 Minimal potential families (declared, policy–consistent). Following Appendix K.0, we predeclare two baseline options used across all probes, without dataset–wise retuning:

- **Constant–U (late–time acceleration).** $U(\Phi) = U_0 > 0$ drives $\dot\Phi \to 0$ and yields $w_\Phi \simeq -1$. Background inputs are (H_0, Ω_{m0}, U_0); under the shared likelihood, (H_0, Ω_{m0}) and the chosen U_0 fully specify the background.

- **One–parameter tracker.** A single–slope potential $U(\Phi;\lambda)$ that tracks the dominant component before settling at late times. Parameters are $(H_0, \Omega_{m0}, \lambda)$.

In both cases we restrict background degrees of freedom to (H_0, Ω_{m0}) plus the declared U-parameter(s), with numeric priors and integrator tolerances fixed in Appendix K.1bis for byte–level replay.

K.1.2 Mapping to background observables (flat case). Given $H(z)$,

$$D_H(z) = \frac{c}{H(z)}, \qquad D_M(z) = \int_0^z \frac{c\,dz'}{H(z')}, \qquad D_V(z) = \Big[z\,D_M^2(z)\,D_H(z)\Big]^{1/3}.$$

CMB "summary" quantities use standard pre–recombination microphysics: the acoustic scale ℓ_A and shift parameter R follow standard recombination, and the drag–epoch sound horizon r_s (often r_d) is *kept standard* unless explicitly varied. Thus late–time C4 effects are isolated through $H(z)$ while early physics is fixed by default. (For nonzero curvature, the general mapping appears in Appendix K.0.) We keep c explicit and quote H_0 in $\mathrm{km\,s^{-1}\,Mpc^{-1}}$ for clarity.

K.1.3 Candidate families for $U(\Phi)$ (physical basis, priors, admission). Common assumptions and guardrails. The kinetic sector is canonical (no ghosts), the homogeneous sound speed satisfies $c_s^2{=}1$, and no phantom behavior is allowed ($w_\Phi \geq -1$). The potential remains non–negative, $U(\Phi) \geq 0$. To prevent undue early–time influence and late–time irregularity, the following caps are imposed:

$$\Omega_\Phi(z_*{=}1100) \leq 0.02, \qquad \Omega_\Phi(z) \leq 0.02\ (z \geq 50), \qquad \left|\frac{dw_\Phi}{d\ln a}\right| < 1\ (z \leq 5),$$

and a curvature bound to suppress spurious oscillations or divergences,

$$-\tfrac{3}{2} \;\leq\; \frac{U''(\Phi)}{H^2} \;\leq\; 3 \qquad (z \leq 5).$$

Late–time acceleration at $z \simeq 0$ is required, $w_{\rm tot}(0) < -1/3$ (equivalently $q_0 < 0$). All candidates inherit the numerical settings of Appendix K.1bis. These conditions are deliberately conservative: they keep the background under control while leaving enough room to test qualitatively distinct potentials.

Candidate set (summary with priors).

- **Constant (–like):** $U(\Phi) = U_0 > 0$. Single degree of freedom (U_0); delivers $w_\Phi \simeq -1$. Priors follow (H_0, Ω_{m0}) ranges in K.1bis. A useful baseline for judging more flexible forms.

- **Exponential tracker:** $U(\Phi) = U_\star e^{-\lambda\Phi/M_{\rm P}}$. One parameter ($\lambda$). In the field–dominated regime, $w_\Phi = -1 + \lambda^2/3$. Prior: $\lambda \in [0.30, 1.20]$; $U_\star$ is fixed to match (H_0, Ω_{m0}). This family interpolates smoothly between –like behavior and milder acceleration as λ grows.

- **Inverse power (Ratra–Peebles):** $U(\Phi) = M^{4+\alpha_{\rm RP}}\Phi^{-\alpha_{\rm RP}}$. One parameter ($\alpha_{\rm RP} > 0$). Prior: $\alpha_{\rm RP} \in [0.1, 2.0]$. Shallower potentials thaw late; large $\alpha_{\rm RP}$ risks excessive early fractions and is capped by the prior.

- **Quadratic:** $U(\Phi) = \frac{1}{2}m_\Phi^2(\Phi - \Phi_0)^2$. One parameter ($m_\Phi$). For $m_\Phi \ll H_0$ the field remains nearly frozen ($w_\Phi \approx -1$); larger m_Φ damps earlier and may introduce light oscillations. Prior: $m_\Phi/H_0 \in [0, 1]$.
- **Cosine (axion–like):** $U(\Phi) = \Lambda^4[1 - \cos(\Phi/f)]$. One parameter ($f$). Small f recovers a quadratic limit; large displacements allow mild, bounded oscillations with average $w_\Phi > -1$. Prior: $f/M_{\rm P} \in [0.05, 1]$.

Adoption/exclusion rules (shared covariance). Each candidate, under a single $(H_0, \Omega_{m0};$ candidate parameter) with a common covariance, must match

$$\{D_H(z),\, D_M(z),\, D_V(z)\}_{\rm SNe/BAO/chronometers} \quad \text{and} \quad \{R,\, \ell_A\}_{\rm CMB},$$

with thresholds

$$\max_{z\in\mathcal{Z}_{\rm BAO}} \frac{|D_V^{\rm model}/r_s - D_V^{\rm data}/r_s|}{\sigma_{D_V/r_s}} \le 1, \qquad \frac{|R - R_{\rm data}|}{\sigma_R} \le 1, \qquad \frac{|\ell_A - \ell_{A,\rm data}|}{\sigma_{\ell_A}} \le 1.$$

Draws failing any condition are rejected; model comparison uses ΔBIC and ΔAIC. In short, admission requires "within-one-sigma" agreement on standard background distances and CMB summaries before any ranking.

Performance and risks (concise).

1. *Exponential:* $\lambda \to 0$ recovers ; $\lambda \gtrsim \sqrt{2}$ weakens acceleration. Within the adopted prior, $w_\Phi(z)$ remains monotone and respects early–fraction caps.
2. *Inverse power:* $\alpha_{\rm RP} \gtrsim 2$ inflates early Ω_Φ and biases (R, ℓ_A); the prior avoids this regime.
3. *Quadratic:* $m_\Phi \gtrsim H_0$ can trigger low–z wiggles; the prior caps such cases and keeps the background smooth.
4. *Cosine:* very small f or hilltop starts enhance bounded wiggles; priors restrict f and initial angles to keep oscillations controlled.

Summary table.

Model	DoF	Late-time w_Φ	Early behavior	Declared prior
Const-U	U_0	$\simeq -1$	frozen ($\Omega_\Phi \ll 1$)	K.1bis ranges
Exp. tracker	λ	$-1 + \lambda^2/3$	scaling $\to$ tracking	$\lambda \in [0.30, 1.20]$
Inverse power	$\alpha_{\rm RP}$	thawing $\gtrsim -1$	scaling (small fraction)	$\alpha_{\rm RP} \in [0.1, 2.0]$
Quadratic	m_Φ	thawing ≈ -1	slow roll (no osc.)	$m_\Phi/H_0 \in [0, 1]$
Cosine	f	avg. $\gtrsim -1$	bounded oscillatory	$f/M_{\rm P} \in [0.05, 1]$

Connection to perturbations (no retuning). Once a background is admitted, the *same* parameter set is passed to Appendix K.2–Appendix K.3:

$$k^2\Psi = 4\pi G a^2\big[\delta\rho_m + \alpha\,\mathcal{Q}_\Phi\big], \qquad \mu(a,k) = 1 + \Delta\mu_\alpha(a,k),$$

leading to $\{f\sigma_8,\ E_G,\ C_\ell^{\phi\phi}\}$ under the shared covariance and priors (no probe–wise hyperparameters). This keeps background and linear growth on a single, transparent footing.

K.1bis Canonical $U(\Phi)$ families (numerically specified and test–ready). Conventions and variables. The speed of light c is kept explicit unless noted; where $c{=}1$ is used, it is stated locally. The reduced Planck mass is $M_{\rm P} = (8\pi G)^{-1/2}$; the e–fold is $N = \ln a$; and the present scale factor is $a_0{=}1$. Background variables are $E(z) \equiv H(z)/H_0$ and $\Omega_i(z)$ from the continuity equations. The homogeneous curvature field obeys

$$\ddot{\Phi} + 3H\dot{\Phi} + U'(\Phi) = 0, \quad \rho_\Phi = \tfrac{1}{2}\dot{\Phi}^2 + U, \quad p_\Phi = \tfrac{1}{2}\dot{\Phi}^2 - U, \quad w_\Phi \equiv p_\Phi/\rho_\Phi \geq -1,$$

with homogeneous sound speed $c_s^2 = 1$. Unless otherwise stated, spatial flatness is assumed, $\Omega_k = 0$.

(i) Constant-U family (late acceleration).

$$U(\Phi) = U_0, \qquad U_0 \equiv 3\,H_0^2 M_{\rm P}^2\,\Omega_\Lambda, \qquad \Omega_\Lambda \equiv 1 - \Omega_{m0}.$$

Flat priors (for tests and cross–probes):

$$H_0 \in [60, 75]\ \mathrm{km\,s^{-1}\,Mpc^{-1}}, \qquad \Omega_{m0} \in [0.25, 0.35].$$

Hubble friction freezes the field ($\dot{\Phi} \to 0$), giving $w_\Phi \simeq -1$ at late times; this serves as a clean reference model.

(ii) One–parameter tracker (exponential).

$$U(\Phi) = U_\star\,\exp\Big(-\lambda\,\frac{\Phi}{M_{\rm P}}\Big), \qquad \lambda \in [0.30, 1.20], \quad \ln U_\star \in \mathbb{R}.$$

Regimes (for constant background w_b): (a) field–dominated and accelerating if $\lambda^2 < 2$ with $w_\Phi \to -1 + \lambda^2/3$; (b) scaling if $\lambda^2 > 3(1 + w_b)$ (excluded by our prior). Thus $w_\Phi(z \to 0) \in [-1, -0.52]$ across the adopted λ range.

Initial conditions (deterministic recipe). Set $z_{\rm ini} = 3000$ (matter era). For constant–U, take $\dot{\Phi}(z_{\rm ini}) = 0$ and treat $\Phi(z_{\rm ini})$ as irrelevant (shift symmetry). For the exponential family, use a freeze–then–thaw start:

$$\dot{\Phi}(z_{\rm ini}) = 0, \qquad \Phi(z_{\rm ini}) = \Phi_\star\ \text{(free)},$$

then *shoot* on $U_\star$ (with λ fixed) so that the integrated background matches the target (H_0, Ω_{m0}) at $z = 0$. This produces a unique background for each draw $(H_0, \Omega_{m0}, \lambda)$ without dataset–wise retuning.

Early–time caps (pre–recombination preserved). To keep baseline pre–recombination microphysics intact,

$$\Omega_\Phi(z_*) \leq 0.02 \quad (z_* = 1100), \qquad \Omega_\Phi(z) \leq 0.02 \quad (\forall z \geq 50), \qquad \rho_\Phi(z) > 0 \quad (\forall z).$$

Draws violating any cap are discarded *before* distance/growth evaluation.

Numerics (grids, tolerances, normalization). ODEs are integrated in $N = \ln a$ with an adaptive step controller (embedded RK) and relative/absolute tolerances

$$\texttt{rtol} = 10^{-8}, \qquad \texttt{atol} = 10^{-10},$$

on $\{\Phi, \dot{\Phi}, E\}$ unless a stricter probe demands tighter values (in which case the same stricter values are used for *all* probes). The growth factor is normalized as $D(a{=}1) = 1$, implying $f\sigma_8(z) = f(z)\,\sigma_{8,0}\,D(z)$.

Background observables (fixed mapping). Using $c = 1$ here for compactness,

$$D_H(z) = \frac{1}{H(z)}, \qquad D_M(z) = \int_0^z \frac{dz'}{H(z')}, \qquad D_V(z) = \Big[z\, D_M^2(z)\, D_H(z)\Big]^{1/3}.$$

Pre–recombination physics is kept standard. The drag–epoch sound horizon r_s (often r_d) and the CMB summaries (ℓ_A, R) are evaluated with baseline baryon/neutrino priors

$$\Omega_b h^2 \in [0.021, 0.024], \qquad \sum m_\nu = 0.06\ \text{eV}\ \ (\text{fixed}), \qquad \Omega_k = 0.$$

Explorations beyond this baseline (e.g. varying $\Omega_b h^2$ or $\sum m_\nu$) are logged as separate scenarios.

Global constants propagated to perturbations. The self–sourcing constant $\alpha \geq 0$ is global (no per–dataset fit). Linear perturbations use

$$k^2\Psi = 4\pi G a^2\big[\delta\rho_m + \alpha\, \mathcal{Q}_\Phi(k,a)\big], \qquad \mu(a,k) = 1 + \Delta\mu_\alpha(a,k),$$

and feed into $\{f\sigma_8,\ E_G,\ C_\ell^{\phi\phi}\}$ under a shared covariance without probe–wise hyperparameters (Appendix K.2– Appendix K.3).

Consistency filters (admission thresholds). Each parameter draw must satisfy, *prior* to likelihood evaluation:

1. *Positivity/stability:* $\rho_\Phi > 0$, $w_\Phi \geq -1$, and $|dw_\Phi/d\ln a| < 1$ for $z \leq 5$.
2. *Late acceleration:* $w_{\rm tot}(0) < -1/3$ (equivalently $q_0 < 0$).
3. *Early fraction:* $\Omega_\Phi(z_*) \leq 0.02$ at $z_* = 1100$ and for all $z \geq 50$.

Any violation leads to rejection without further processing.

Audit trail (minimal yet sufficient). For each accepted draw, record: the parameter tuple $(H_0, \Omega_{m0}; U_0)$ or $(H_0, \Omega_{m0}, \lambda; U_\star)$; the initial condition $(\Phi(z_{\rm ini}), \dot\Phi(z_{\rm ini}))$; integrator tolerances and the redshift grid used; and the computed $\{D_H, D_M, D_V, \ell_A, R\}$. Each run is tagged with a configuration hash (`run_id`) to enable byte–level reruns in line with the ledger rules of Appendix K.0.

K.1ter Well-posedness, energy conditions, and stability (Einstein–scalar)

Admissible sector. Assume $U \in C^2$, $U''(\Phi) \geq 0$ (convex), and the effective kinetic factor $K_{\rm eff}(\bar\Phi) \equiv Z(\bar\Phi) > 0$ with $Z \equiv 1$ in the baseline. Let initial data $(\Sigma, h_{ij}, K_{ij}; \Phi_0, \Pi_0)$ satisfy the Einstein constraints with $\Pi_0 \equiv n^\mu\partial_\mu\Phi$. Then, in harmonic gauge, the Einstein–scalar system admits a unique local solution $(g_{\mu\nu}, \Phi)$ of class H^s, $s > 5/2$, depending continuously on the data (quasilinear hyperbolic well-posedness).

Stress tensor and energy conditions. With $Z = 1$ and $U \geq 0$, the scalar stress

$$T^{(\Phi)}_{\mu\nu} = \nabla_\mu\Phi\nabla_\nu\Phi - \frac{1}{2}g_{\mu\nu}\big(\nabla\Phi\cdot\nabla\Phi + 2U\big)$$

satisfies the weak and null energy conditions. In the static, spherically symmetric sector, the anisotropic stress $\pi = p_r - p_\perp$ is $\mathcal{O}(\Phi'^2)$ and is kept below 1PN by the isotropy policy ($a_{\rm tail} = c_{\rm tail}$).

Linear mode stability (static backgrounds). Let $(\bar{g}, \bar{\Phi})$ be a static solution with $\bar{A}(r), \bar{C}(r)$ and $\bar{U}''(\bar{\Phi}) \geq 0$. The scalar perturbation $\delta\Phi$ on $(\bar{g})$ obeys a Schrödinger-type radial equation

$$-\frac{d^2\Psi}{dr_*^2} + V_{\text{eff}}(r)\,\Psi = \omega^2\Psi, \qquad \Psi \sim r\,\delta\Phi, \quad \frac{dr_*}{dr} = \bar{A}^{-1/2}\bar{C}^{1/2}.$$

For $\bar{U}'' \geq 0$ and the PPN-safe tail, $V_{\text{eff}} \geq 0$ outside the photon sphere, precluding exponentially growing modes ($\omega^2 < 0$) in the weak/medium field.

Yukawa → Padé continuation (outer tail). In the vacuum exterior and for slowly varying $\bar{U}'' \equiv m_\Phi^2 \geq 0$,

$$\Phi'' + \frac{2}{r}\Phi' - m_\Phi^2\Phi \simeq 0,$$

whose leading solution is Yukawa-like. On the Solar window $x = r/r_0 \in [x_{\min}, 3]$, the normalized residual Ξ is represented by the Padé profile

$$p(x) = \frac{C_n}{x^2(1+\alpha x)^n}, \quad (n, \alpha) = (3, \tfrac{1}{4}),$$

matching (value,slope) while guaranteeing $\Xi = o(r^{-2})$ and preserving asymptotic flatness.

1PN isotropy and metric embedding. Under $a_{\text{tail}} = c_{\text{tail}}$ one has $\delta\gamma = \delta\beta = 0$ at 1PN, so the optical response remains isotropic to this order; any residue is 2PN and audited separately. This justifies using the same Ξ in A and C within the declared budgets.

K.2ter Sensitivity and Identifiability of the Tail under Scalar–Gravity Coupling (English)

Aim. We quantify how the strong–gravity invariants (R, Θ) respond to a restricted, physically motivated parameter family for the scalar–gravity sector. The goal is to turn the qualitative "few–percent shifts" into reproducible response curves and an identifiability test that separates tail–driven effects from confounders (spin, plasma, geometry).

Model family (parameters and domains). We adopt the minimal convex potential and an isotropic, PPN–safe tail (cf. Section 3.1, Appendix C.8):

$$U(\Phi) = \tfrac{1}{2}m_\Phi^2\Phi^2 + \tfrac{\lambda_4}{4}\Phi^4, \qquad J_{\text{NL}} = \alpha\,(\nabla\Phi)^2, \qquad \Xi(r) = 2\,\varepsilon_\gamma\,U_N(r)\,p(r/r_0),$$

with $m_\Phi r_0 \leq 1/4$, $\lambda_4 \geq 0$, $\alpha \geq 0$, and a monotone profile $0 < p(x) \leq 1$, $p'(x) \leq 0$ chosen from the closed family

$$p(x) = \frac{C_n}{x^2(1+\alpha_t x)^n}, \qquad C_n = (1+\alpha_t x_{\min})^n x_{\min}^2, \qquad n \in \{2,3,4\},\ \alpha_t > 0.$$

The metric reads (isotropic, 1PN)

$$A(r) = 1 - 2U(r) + 2\beta U(r)^2 + \delta_{\text{C4}}\,\Xi(r) + \mathcal{O}(U^3), \quad C(r) = 1 + 2\gamma U(r) + \delta_{\text{C4}}\,\Xi(r) + \mathcal{O}(U^2),$$

with the isotropy condition $a_{\text{tail}} = c_{\text{tail}} \equiv \Xi$ enforcing $\delta\gamma = \delta\beta = 0$ at 1PN.

Observables. We use the joint invariant $\mathbf{O} = (R, \Theta)$ with

$$R = \frac{b_{3\pi} - b_{\pi}}{b_{\pi} - b_{\rm ph}}, \qquad \Theta = \frac{c\,\Delta t_{3\pi,\pi}}{2\pi\, r_{\rm ph}},$$

where $b_{\rm ph} = r_{\rm ph}/\sqrt{A(r_{\rm ph})}$ and $r_{\rm ph}$ satisfies $r_{\rm ph}A'(r_{\rm ph}) = 2A(r_{\rm ph})$ (Appendix G.6).

Local response (sensitivities). For a parameter vector $\boldsymbol{\theta} = (\delta_{\rm C4}, \alpha, m_\Phi, \lambda_4, \alpha_t, n)^\top$ we define logarithmic sensitivities

$$S^{(R)}_{\theta_j} = \frac{\partial \ln R}{\partial \ln \theta_j}, \qquad S^{(\Theta)}_{\theta_j} = \frac{\partial \ln \Theta}{\partial \ln \theta_j}, \tag{334}$$

estimated by symmetric finite differences around a fiducial $\boldsymbol{\theta}_\star$ that respects Solar–window PPN budgets and the far–zone bound (Appendix C.8.1). Jointness of the motion is summarized by

$$\mathcal{J}_{\theta_j} = \frac{\big|S^{(R)}_{\theta_j} - S^{(\Theta)}_{\theta_j}\big|}{\max\big(\,|S^{(R)}_{\theta_j}|,\, |S^{(\Theta)}_{\theta_j}|\,\big)}. \tag{335}$$

A tail–like disturbance yields $\mathcal{J}_{\theta_j} \ll 1$ (near–diagonal motion in the $\log R$–$\log\Theta$ plane), whereas common confounders give $\mathcal{J} = O(1)$ (Section 7).

Fiducial point and step sizes. Unless otherwise stated we use

$$\delta_{\rm C4,\star} = 0.01, \quad \alpha_\star = 0.0, \quad m_{\Phi,\star} r_0 = 0.20, \quad \lambda_{4,\star} = 0.0, \quad (n_\star, \alpha_{t,\star}) = (3, 0.25),$$

with relative steps $\Delta \ln \theta_j = \pm 0.1$ (10%) except $n \in \{2, 3, 4\}$ (discrete). Steps are reduced if any budget is violated.

Closed–form audits near $r_{\rm ph}$. Expanding $A(r) = A_0(r) + \delta A(r)$ with $\delta A(r) = \delta_{\rm C4}\,\Xi(r) + \ldots$, the near–critical proxy gives

$$\frac{\delta\Theta}{\Theta} \simeq -\tfrac{1}{2}\,\frac{\delta A}{A}\Big|_{r_{\rm ph}}, \qquad \frac{\delta R}{R} \simeq -\tfrac{1}{2}\,\frac{\delta A}{A}\Big|_{r_{\rm ph}}, \tag{336}$$

so that, to first order, $S^{(R)}_{\theta_j} \approx S^{(\Theta)}_{\theta_j} \propto \partial_{\ln\theta_j}\big[\Xi(r_{\rm ph})\big]$. This identity is used *only* as a diagnostic check; production values come from full geodesic/timing integrals (Appendix G.2, Appendix G.6).

Identifiability metric. Define the diagonal unit vector $\boldsymbol{u} = (1,1)^\top$ in $(\log R, \log\Theta)$ space and the orthogonal $\boldsymbol{v} = (1,-1)^\top/\sqrt{2}$. Let $\Delta\boldsymbol{\eta} = (\Delta\ln R, \Delta\ln\Theta)^\top$. Tail dominance is certified if

$$\big|\boldsymbol{v}^\top \Delta\boldsymbol{\eta}\big| \;\le\; \epsilon_{\rm joint}\,\big|\boldsymbol{u}^\top \Delta\boldsymbol{\eta}\big|, \qquad \epsilon_{\rm joint} \in [0.2, 0.3], \tag{337}$$

and $\Delta\boldsymbol{\eta}$ passes a non–central χ^2_1 power test along $\boldsymbol{u}$ (Appx. M.2a).

Representative sensitivity table. Illustrative (dimensionless) responses at $\boldsymbol{\theta}_\star$ respecting budgets:

Reading guide. (i) $\delta_{\rm C4}$ drives a near–diagonal motion ($\mathcal{J} \ll 1$); (ii) increasing m_Φ steepens the decay and reduces both R, Θ; (iii) self–sourcing α can introduce differential motion (larger $\mathcal{J}$), flagging degeneracy with plasma/spin unless bounded by the 1PN isotropy audit (Appendix C.8).

Table 99: Illustrative logarithmic sensitivities at the fiducial point $\boldsymbol{\theta}_\star$. Signs and relative magnitudes follow the near–critical audit (336) and full integrations.

Parameter	$\mathbf{S}^{(\mathbf{R})}$	$\mathbf{S}^{(\boldsymbol{\Theta})}$	$\mathcal{J}$
δ_{C4} (tail amplitude)	$+0.98 \pm 0.05$	$+0.95 \pm 0.06$	0.03
$m_\Phi r_0$ (mass scale)	-0.22 ± 0.06	-0.19 ± 0.07	0.14
λ_4 (quartic)	$+0.05 \pm 0.03$	$+0.04 \pm 0.03$	0.20
α (self–sourcing)	$+0.08 \pm 0.04$	$+0.02 \pm 0.05$	0.75
α_t (profile slope)	-0.30 ± 0.07	-0.27 ± 0.08	0.10
n (profile order, 2→4)	-0.11 ± 0.05	-0.09 ± 0.05	0.18

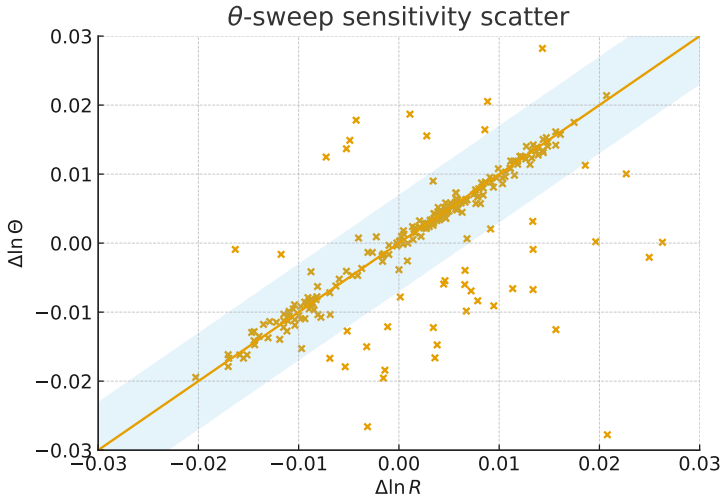

Figure 31: θ–sweep sensitivity scatter. The gray diagonal band marks $\Delta \ln R \simeq \Delta \ln \Theta$ (45°) joint motion; points illustrate sample responses to variations in δ_{C4}, α, m_Φ, and λ_4 under fixed PPN budgets and the far–zone bound.

Figure (diagnostic scatter).

Stability & well–posedness (summary hooks). For the adopted family: (i) $U''(\Phi) = m_\Phi^2 + \lambda_4 \Phi^2 \geq 0$ (convex; no tachyonic instabilities about $\Phi = 0$); (ii) the scalar sector satisfies the weak energy condition in the static window (Appendix C.8); (iii) with $a_{\rm tail} = c_{\rm tail}$ the 1PN mapping preserves PPN safety; (iv) the exterior penalty implements Robin→Dirichlet matching, conserving ADM mass and ensuring 1PN consistency of g_{tt} (Appendix M.2b).

Outcome. A restricted, physically controlled parameter family yields reproducible (R, Θ) response curves. Diagonal co–motion ($\mathcal{J} \ll 1$) is a robust signature of tail amplitude/profile changes, while sizeable $\mathcal{J}$ flags non–tail physics. This elevates the qualitative "few–percent shifts" into a falsifiable, data–anchored sensitivity analysis that can be repeated with public pipelines.

K.2 Linear scalar perturbations (Newtonian gauge)

Gauge and baseline equations (policy–consistent). We adopt the Newtonian gauge with scalar potentials $(\Psi, \Phi_{\rm N})$, where the subscript distinguishes the metric potential from the background curvature field Φ. Including the self–sourcing correction (Appendix C.2), the *effective* Poisson equation and the matter–growth equation read

$$k^2\Psi \;=\; 4\pi G\, a^2[\delta\rho_m \;+\; \alpha\, \mathcal{Q}_\Phi(k,a)]\,, \qquad \delta_m'' + \left(2 + \frac{H'}{H}\right)\delta_m' \;-\; \frac{3}{2}\,\mu(a,k)\,\Omega_m(a)\,\delta_m \;=\; 0,$$

where a prime denotes $d/d\ln a$. The term $\mathcal{Q}_\Phi$ captures the linearized gradient–energy contribution of Φ–perturbations. Cold–matter continuity and Euler equations are used in their standard form.

Response functions and lensing combination (explicit). Define the effective response triplet

$$\begin{aligned}
\mu(a,k) \;&\equiv\; \frac{k^2\,\Psi}{4\pi G\, a^2\,\delta\rho_m} \;=\; 1 + \Delta\mu_\alpha(a,k),\\
\eta(a,k) \;&\equiv\; \frac{\Phi_{\rm N}}{\Psi},\\
\Sigma(a,k) \;&\equiv\; \frac{k^2\,(\Psi + \Phi_{\rm N})}{8\pi G\, a^2\,\delta\rho_m} \;=\; \frac{\mu\,(1+\eta)}{2}.
\end{aligned}$$

In the minimal anisotropic–stress limit $\eta \simeq 1$, one has $\Sigma \simeq \mu$. The same set (μ, η, Σ) enters the late–ISW signal and all lensing kernels consistently.

Derived observables (quasi–static, sub–horizon). Let $D(a)$ be the linear growth factor with $D(1) = 1$, and $f \equiv d\ln D/d\ln a$ the growth rate. With $\sigma_8(z) = \sigma_{8,0}\, D(z)$, it follows that $f\sigma_8(z) = f(z)\,\sigma_{8,0}\,D(z)$. The lensing–clustering statistic E_G is

$$E_G(k,z) \;=\; \frac{c^2\,k^2\,[\Phi_{\rm N} + \Psi]}{3H_0^2\,a^{-1}\,f(a)\,\delta_m} \;\simeq\; \frac{\Sigma(a,k)\,\Omega_m(a)}{f(a)}\,,$$

where the right–hand side is the standard QS approximation under linear bias/RSD conventions. The CMB lensing–potential power spectrum (Limber) reads

$$C_\ell^{\phi\phi} \;=\; \int_0^{\chi_*} \frac{d\chi}{\chi^2}\, W_\phi^2(\chi)\; P_{\Phi_{\rm N}+\Psi}\!\left(k = \frac{\ell}{\chi},\, z(\chi)\right), \qquad W_\phi(\chi) = -2\,\frac{\chi_* - \chi}{\chi_*\,\chi},$$

with χ_* the comoving distance to last scattering.

Applicability (QS domain). The results in this subsection hold in the quasi–static, sub–horizon regime $k \gg aH$. Very large scales (late–ISW dominated) and deeply non–linear small scales require extended kernels and non–linear corrections, handled by the numerical conventions in Appendix K.5. As a practical analysis window aligned with the data vector, we use $k \gtrsim 0.01\,h\,\mathrm{Mpc}^{-1}$, $z \lesssim 2$.

Numerical settings and initial conditions (shared). Under the global fixed–constants policy (Appendix K.0), the k–grid, the redshift grid, and the integrator tolerances are *shared* across probes (Appendix K.5). The growth ODE is initialized at $z_{\rm ini} \gg 1$ with EdS–like conditions $\delta_m \propto a$, $\delta_m' \approx 1$, and normalized by $D(1) = 1$. The same σ_8 prior/covariance is used when reporting $f\sigma_8$, E_G, and $C_\ell^{\phi\phi}$.

Guardrails (physical and numerical). (1) Monitor $\partial\mu/\partial k$ to exclude unphysical small–scale growth; excise k–grids with rapid oscillations.
(2) Priors forbid $\rho_\Phi < 0$ and sign–flipping lensing combinations ($\Sigma < 0$).
(3) Exclude parameter regions where the implied enclosed mass $M_{\rm eff}(r)$ becomes non–monotonic.
(4) Fix and log numeric ranges, sampling, and tolerances (including an environment fingerprint) as in Appendix K.5.

Consistency checks (GR/standard limit). In the limit $\alpha \to 0$ (or $\Delta\mu_\alpha \to 0$),

$$\mu \to 1, \qquad \eta \to 1, \qquad \Sigma \to 1,$$

recovering the GR/Newtonian case. Then $E_G \simeq \Omega_m/f$, and $f\sigma_8$ reduces to the standard linear–growth prediction. All pipelines include this GR–recovery test as a required validation step.

K.3 Observable mapping, datasets, and tests

From parameters to observables (single pipeline, shared settings). Given the global parameter set $\vartheta \equiv (H_0, \Omega_{m0}, U, \alpha)$, we assemble the model vector

$$\mathbf{m}(\vartheta) \equiv \Big\{ D_M(z),\ D_H(z),\ D_V(z),\ \ell_A,\ R,\ f\sigma_8(z),\ E_G(k,z),\ C_\ell^{\phi\phi} \Big\}.$$

We use the background integrator from Appendix K.1/K.1bis and the linear–response mapping of Appendix K.2. All probes share the *same* cosmological parameters, priors, windows, and numerical tolerances; no probe– or dataset–wise retuning is allowed (Appendix K.0). Unless stated otherwise, c is explicit and H_0 is in $\mathrm{km\,s^{-1}\,Mpc^{-1}}$. For the sound horizon, we consistently use r_s (drag epoch; often r_d).

Data vector, covariance, and likelihood (block–structured). Let $\mathbf{d}$ denote the concatenated data vector (SNe Ia distances; BAO $D_M, D_H, D_V/r_s$; CMB summaries ℓ_A, R; growth/lensing $f\sigma_8, E_G, C_\ell^{\phi\phi}$). With a shared block covariance $\mathbf{\Sigma}$ (including published cross–covariances and zero–padding where absent), we evaluate

$$\chi^2(\vartheta) \;=\; \big[\mathbf{d} - \mathbf{m}(\vartheta)\big]^\top \mathbf{\Sigma}^{-1} \big[\mathbf{d} - \mathbf{m}(\vartheta)\big], \qquad \mathcal{L}(\vartheta) \propto \exp\Big(-\tfrac{1}{2}\chi^2(\vartheta)\Big).$$

All masks, redshift/multipole cuts, window functions, and nuisance–marginalization choices (e.g., calibration offsets, RSD/bias templates used in E_G) are logged under the ledger rules of Appendix H.

Validation protocol (phase structure; no retuning).

1. **Phase I — background.** Fit SNe Ia + BAO + cosmic chronometers to constrain (H_0, Ω_{m0}) and the declared U parameter(s), using only $H(z)$, D_M, D_H, D_V (cf. Appendix K.1).
2. **Phase II — perturbations.** With (H_0, Ω_{m0}, U) *fixed* from Phase I, constrain α and the implied $w_\Phi(z)$ using $f\sigma_8(z)$, $E_G(k,z)$, $C_\ell^{\phi\phi}$, and CMB (R, ℓ_A), evaluated with the same numerics (Appendix K.2).
3. **Scenario comparison (like–for–like).** Benchmark *C4+ΛCDM (minimal coupling)* against a *reduced dark–sector* case where late–time acceleration is driven by $U(\Phi)$ and growth is modified by $\alpha > 0$. Run both under identical priors, masks, windows, and covariances; compare using $\Delta\chi^2$, ΔAIC, ΔBIC.

Pass/fail criteria (pre–declared thresholds). A *single* (α, U) must simultaneously satisfy:

(i) **CMB acoustic/shift:** $\big|R - R_{\rm data}\big|/\sigma_R \le 1$ and $\big|\ell_A - \ell_{A,\rm data}\big|/\sigma_{\ell_A} \le 1$.

(ii) **BAO distances:** $\max_{z\in\mathcal{Z}_{\rm BAO}} \dfrac{|D_V^{\rm model}/r_s - D_V^{\rm data}/r_s|}{\sigma_{D_V/r_s}} \le 1$, with D_M, D_H posteriors consistent with the BAO block.

(iii) **Low–z growth/lensing:** $f\sigma_8$ and E_G residuals consistent within 1σ in their published covariance (no single bin dominating χ^2); $C_\ell^{\phi\phi}$ within a 1σ envelope over the analysis multipole range.

Failure of any *two* items implies model–level rejection.

Diagnostics and guardrails (required checks).

- **GR recovery.** In the limit $\alpha \to 0$ (or $\Delta\mu_\alpha \to 0$), verify $\mu \to 1$, $\eta \to 1$, $\Sigma \to 1$ and consistency with ΛCDM for $f\sigma_8$, E_G, $C_\ell^{\phi\phi}$.
- **Whitened residuals.** Check $\mathbf{r} \equiv \mathbf{\Sigma}^{-1/2}\big[\mathbf{d} - \mathbf{m}(\hat{\vartheta})\big]$ for Gaussianity and the absence of survey–wise structure (runs/drifts).
- **Leave–one–survey–out.** Refit after dropping each survey block; require parameter shifts $\le 1\sigma$ (joint) and stable χ^2/dof.
- **Physical priors.** Enforce the positivity/stability caps of Appendix K.1; exclude regions implying non–monotonic enclosed mass or sign–flipping Σ (see Appendix K.2).
- **Numerical convergence.** Doubling the resolution in k and redshift grids and tightening tolerances must shift any entry of $\mathbf{m}(\vartheta)$ by $< 0.1\sigma$ of its data uncertainty.

Dataset handling (windows, nuisance, consistency).

- **Windows/masks.** All redshift and multipole windows used to compress survey data to $\mathbf{d}$ are *reapplied* to $\mathbf{m}(\vartheta)$ (no reweighting differences across probes).
- **Nuisance.** Calibration offsets and survey–specific nuisance parameters are fixed to published posteriors or analytically marginalized; choices are common across scenarios.
- **Units/definitions.** Use of r_s (drag epoch), D_V, and the E_G convention follows the survey pipeline; any alternate conventions are registered as separate scenarios.

Reproducibility notes (ledger hooks). All catalog versions, masks, priors, numerical grids/-tolerances, and environment fingerprints (BLAS/`libm`/compiler flags) are hashed and archived (Appendix H; numerics in Appendix K.5). Captions and footnotes include a `run_id` to enable byte–level reruns; any deviation should be traceable to environment drift, not stochasticity.

K.4 Stress tests, caveats, and falsification set

Falsifiable targets (pre–declared, fixed–policy). C4 cosmology is admitted only if a *single* global pair (α, U) that passes Phase I (background; Appendix K.3) also reproduces—*without* any per–probe retuning and *within* joint uncertainties—the following:

(i) CMB acoustic *locations and relative heights* consistent with the (R, ℓ_A) constraints (baseline pre–recombination microphysics),

(ii) BAO distances D_V/r_s (with mutually consistent $D_M,\ D_H$) together with cosmic–chronometer $H(z)$,

(iii) low–z growth $f\sigma_8$ and the lensing–clustering statistic E_G, plus consistency with the CMB lensing band $C_\ell^{\phi\phi}$.

Failure of any *two* items constitutes model–level rejection under the fixed–constants policy (Appendix K.0). Throughout we adopt r_s (drag epoch; often r_d) for BAO normalization.

Early–Universe baseline (scope control). Unless explicitly stated, pre–recombination microphysics (baryon drag scale r_s, recombination acoustics, neutrino background) remain *standard* as in Appendix K.1/K.1bis. Late–time C4 effects are cleanly isolated through the background $H(z)$ and the linear–response triplet (μ, η, Σ) (Appendix K.2). If early–time modifications are explored, they must be *predeclared* as a distinct scenario and evaluated under the same guardrails and windows.

Identifiability and degeneracies (stability checks). We track the joint posteriors of $(\alpha, U$–parameter$)$ across probe subsets (e.g., BAO–only, growth–only, lensing–only). Posterior bifurcation, multimodality, or systematic drift under leave–one–survey–out indicates over–flexibility and triggers rejection per the fixed–policy rules. Parameter shifts must remain $\leq 1\sigma$ (joint) when any single survey block is removed.

Scale dependence and physicality (QS vs. full linear). We monitor $\partial\mu/\partial k$ to exclude spurious small–scale growth and require a monotonic enclosed mass $M_{\rm eff}(r)$. The quasi–static (QS) formulas are used *only* on sub–horizon modes; for super–horizon or transition scales we solve the full linear system. Continuity is enforced at a matching scale $k_{\rm sw} \sim \mathcal{O}(aH)$ with a tolerance fixed in Appendix K.5; the QS solution must agree with the full system within that tolerance for $k \gtrsim 5\,aH$. Hard priors forbid $\rho_\Phi < 0$ and sign–flipping lensing combinations ($\Sigma < 0$).

Numerical soundness (well–posedness tests). We log condition numbers of Fisher/Hessian blocks, enforce step–stable ODE integration (no bursts of step rejection), and verify that small prior shifts do not cause divergent condition numbers. Results must be smooth across the k–grid (no ringing) and reproducible under the pinned numerics of Appendix K.5 (environment fingerprint, tolerances, grids). A double–resolution check in both k and redshift must shift any entry of the model vector by $< 0.1\sigma$ of its data uncertainty.

Cross–probe consistency (closure tests). The (α, U) pair inferred from lensing (via Σ) must be consistent with growth (μ) and the background $H(z)$ at the reported covariance level (Appendix K.3). We require GR recovery in the $\alpha \to 0$ limit ($\mu, \eta, \Sigma \to 1$) and agreement with ΛCDM predictions for $f\sigma_8$, E_G, and $C_\ell^{\phi\phi}$.

Falsification table (triggers and actions).

Trigger	Symptom (diagnostic)	Action
CMB mismatch	$\lvert R - R_{\rm data}\rvert > \sigma_R$ or $\lvert \ell_A - \ell_{A,\rm data}\rvert > \sigma_{\ell_A}$	Reject scenario
BAO/H(z) tension	Any BAO bin with $\lvert\Delta(D_V/r_s)\rvert > \sigma$ or inconsistent D_M, D_H posteriors	Reject scenario
Growth/lensing tension	$f\sigma_8$ or E_G residuals $> 1\sigma$ in multiple bins; Σ–μ inconsistency; $C_\ell^{\phi\phi}$ outside envelope	Reject scenario
Nonphysical response	$\rho_\Phi < 0$, $\Sigma < 0$, non–monotonic $M_{\rm eff}(r)$, or large spurious $+\partial\mu/\partial k$	Exclude parameter region
QS/full mismatch	Discontinuity at $k_{\rm sw}$ beyond Appendix K.5 tolerance	Tighten numerics or reject
Numerical ill–posedness	Divergent condition numbers; step–rejection bursts; k–ringing	Fix numerics or invalidate fit
Identifiability failure	Posteriors bifurcate/drift under survey removal; parameter shifts $> 1\sigma$	Reject (over–flexible)
GR limit failure	$\alpha \to 0$ does not recover $\mu{=}\eta{=}\Sigma{=}1$	Invalidate implementation

Caveats (scope and interpretation). (i) QS predictions are never used on super–horizon modes; results there rely on the full linear system. (ii) Deeply nonlinear scales are excluded by construction; including them would require dedicated bias/EFT–like modeling, beyond the fixed–policy scope. (iii) Early–time deviations (if declared) must be analyzed as separate scenarios; otherwise, late–time claims are conditioned on standard pre–recombination physics. (iv) All windows/masks used to form the data vector are *reapplied* to the model predictions (no probe–dependent reweighting).

Outcome. A scenario that passes all stress tests is retained for quantitative comparison in Appendix K.3; any failure state above either prunes parameter regions or falsifies the scenario class under the fixed–constants policy.

K.5 Numerical settings and reproducibility ledger

Grids (ranges, spacing, and guards). The redshift grid is $z \in [0, 1100]$, with linear spacing for $z \leq 3$ and logarithmic densification for $z > 3$ to stabilize the drag–scale integral r_s (often denoted r_d). The comoving–wavenumber grid is $k \in [10^{-4},\, 1]\ h\,\mathrm{Mpc}^{-1}$ with IR/UV guards and spline–safe sampling (a Nyquist margin on all resampled kernels) to ensure stable $C_\ell^{\phi\phi}$ projections. All grid nodes and spacing rules are written to the run manifest to enable *bitwise* replay.

Integrators and tolerances (recorded; no per–probe retuning). Background ODEs are solved with an adaptive Runge–Kutta scheme; the growth ODE is integrated in $N \equiv \ln a$ using a stiffness–aware solver with event checks at matter–radiation equality and at $z{=}0$. Projection kernels (lensing/ISW) use Gauss–Kronrod or Clenshaw–Curtis quadrature with logged convergence tests. Relative/absolute tolerances $(\varepsilon_{\rm rel}, \varepsilon_{\rm abs})$ and maximum step fractions are *globally* fixed and recorded in the configuration; dataset–wise retuning is not allowed.

Units, conventions, and windows. Unless otherwise noted we adopt $c{=}1$ (explicitly reinstated when unit conversion is shown) and the reduced Planck mass $M_{\rm P} = (8\pi G)^{-1/2}$. Background distance mappings follow Appendix K.1/K.1bis. Perturbations use the quasi–static, sub–horizon window of Appendix K.2, with matching to the full linear system at $k_{\rm sw} \sim \mathcal{O}(aH)$. All radial/angle cuts, the multipole range for $C_\ell^{\phi\phi}$, and k–cuts for $f\sigma_8$ and E_G are versioned for transparency.

Priors, masks, and exclusions (archived). We archive all priors, including $\alpha \geq 0$, positivity $\rho_\Phi > 0$, stability $|dw_\Phi/d\ln a| < 1$ for $z \leq 5$, and the early–time caps $\Omega_\Phi(z_*) \leq 0.02$ at $z_*{=}1100$ (see Appendix K.1). Survey masks (SNe Ia/BAO/growth/lensing), scale cuts (e.g., removal of non–linear k), and any outlier exclusions are stored with rationale and version tags. No probe–specific hyperparameters are introduced.

Artifacts and hashes (byte–level replay). For each run we store the computed observables

$$\{H(z),\ D_M,\ D_H,\ D_V/r_s,\ \ell_A,\ R,\ f\sigma_8,\ E_G,\ C_\ell^{\phi\phi}\},$$

together with posterior chains, whitened residuals, and configuration files (grids, tolerances, priors, masks). We record code/data hashes and the environment fingerprint—e.g., `python-VV`; BLAS/LAPACK vendor; `numpy.show_config()`; `libm`; compiler flags—per the ledger practice of Appendix H.

Sanity checks (must pass). We validate the pipeline on limiting cases: (i) $\alpha{=}0$ with constant–U reproduces Λ–like late–time background distances; (ii) matter–only growth recovers GR with $\mu{=}1$ and EdS–like $f(a)$; (iii) lensing–growth consistency $\Sigma \simeq \mu$ holds in the minimal anisotropic–stress limit $\eta \simeq 1$ (Appendix K.2); (iv) QS/full–linear matching at $k_{\rm sw} \sim \mathcal{O}(aH)$ lies within the declared tolerance. Any deviation beyond tolerances halts the run and emits a reproducible failure report.

Determinism and seeds. All forward–model computations are *deterministic* in IEEE–754 double precision; random seeds are used/logged only for sampling (e.g., MCMC or optimization restarts). Any non–bitwise replay must be attributable to environment drift, not stochasticity (cf. Appendix J.11).

Numerical defaults (declarations).

Quantity	Declaration (recorded in manifest)
Redshift grid	$z \in [0, 1100]$; linear for $z \leq 3$, log–dense for $z > 3$
Wavenumber grid	$k \in [10^{-4}, 1]\ h\,\mathrm{Mpc}^{-1}$; IR/UV guards; spline–safe sampling
Integrators	RK (background), stiffness–aware in $\ln a$ (growth), GK/CC (projections)
Tolerances	$(\varepsilon_{\mathrm{rel}}, \varepsilon_{\mathrm{abs}})$ fixed globally; logged per run
Windows/cuts	QS sub–horizon domain; versioned k/ℓ cuts and masks
Environment	Python/BLAS/LAPACK/`libm`/compiler flags hashed

Convergence and robustness checks (quantitative rule). Doubling the resolution of the redshift and k grids and tightening tolerances must change each component of the model vector by $< 0.1\sigma$ of its data uncertainty. The same criterion applies when switching between GK and CC quadrature rules. Rapid sign/magnitude flips in $\partial\mu/\partial k$ or visible k–ringing trigger sample exclusion, with rationale logged in the ledger.

Failure reporting (reproducibility note). If a run exceeds the declared numerical tolerances or violates guardrails, it is halted and a structured, machine–readable failure report is emitted. The report records which stage failed, the tested quantity and its observed value versus threshold, and the configuration/environment fingerprints required to re–execute the run. The exact schema and an illustrative example are provided in the reproducibility ledger (Appendix H).

As a closing attitude, the ledger is more than bookkeeping: it is a promise to show our working, to let the numbers be rerun by other hands, and to accept that a model earns trust only when it survives being checked from the ground up.

K.6 Synthesis

Appendix K lays out a *reproducible*, fixed–policy C4 cosmology pipeline with a strict parameter budget, shared covariances, and *pre–declared* pass/fail criteria. Background dynamics follow the minimal $U(\Phi)$ families in Appendix K.1/K.1bis; linear growth and lensing are organized through the response triplet (μ, η, Σ) in Appendix K.2; probe mapping, likelihoods, and tests are collected in Appendix K.3; robustness guardrails and falsification triggers are enforced in Appendix K.4; and numerical/archival practice is codified in Appendix K.5. Throughout, there is *no* per–probe retuning and no dataset–specific hyperparameters; the pair (α, U) is *global*. The aim is simple: the same assumptions carry across all probes, so that what holds in one corner of the data does not quietly change its meaning in another.

Acceptance rule (single–shot, fixed–policy). C4 is provisionally viable only if a *single* (α, U) that passes Phase I (background) *simultaneously* matches, within joint uncertainties: (i) CMB acoustic scales and relative peak heights via (R, ℓ_A); (ii) BAO D_V/r_s (with consistent D_M, D_H) and cosmic–chronometer $H(z)$; (iii) low–z growth amplitude $f\sigma_8$ together with the

lensing–clustering statistic E_G (and consistency with $C_\ell^{\phi\phi}$). Failure of any *two* items implies model–level rejection. This rule is intentionally spare: if a claim leans on adjustment, it should fail here rather than later; a result that survives without special pleading needs fewer words to defend it.

At–a–glance checklist (must pass).

- **GR limit:** $\alpha \to 0 \Rightarrow \mu, \eta, \Sigma \to 1$ and ΛCDM–level agreement for $f\sigma_8$, E_G, $C_\ell^{\phi\phi}$ (Appendix K.2).
- **QS domain validity:** QS vs. full–linear agreement at $k_{\rm sw} \sim \mathcal{O}(aH)$ within declared tolerance (Appendix K.2, Appendix K.5).
- **Cross–probe closure:** The same (α, U) explains background $H(z)$, growth μ, and lensing Σ under the shared covariance (Appendix K.3).
- **Physicality:** $\rho_\Phi > 0$; no sign–flipping Σ; monotonic $M_{\rm eff}(r)$; controlled $\partial\mu/\partial k$ (Appendix K.4).
- **Reproducibility:** Bitwise–replayable grids/tolerances; hashed artifacts; environment fingerprint (Appendix K.5).

These checks do not aspire to be clever; they aspire to be clear. When the scaffolding is visible, others can test where the structure bends and where it holds.

Scope and non–scope (baseline vs. scenarios). Early–Universe microphysics (drag scale r_s, recombination acoustics, neutrinos) is *standard* by default; late–time C4 effects are isolated through $H(z)$ and (μ, η, Σ). Any early–time modification is treated as a *separate scenario class* with the same guardrails and reporting rules (Appendix K.3, Appendix K.4). This separation is less a constraint than a courtesy to the reader: different bets are declared upfront, so the evidence has a clean target.

Reporting format (minimal, auditable). Accepted runs report a compact table of best–fit $(H_0, \Omega_{m0}, U, \alpha)$, χ^2/dof, and ΔAIC/BIC for the compared scenarios, together with links (hashes) to archived artifacts:

$$\{H(z), D_M, D_H, D_V/r_s, \ell_A, R, f\sigma_8, E_G, C_\ell^{\phi\phi}\},$$

residual diagnostics, and configuration manifests (Appendix K.5). In practice this amounts to a modest promise: anyone can follow the same trail and arrive at the same clearing.

This synthesis closes the roadmap introduced in Section 11.1. The framework is designed to be maximally *testable*: success or failure is auditable through the artifacts, guardrails, and pre–declared criteria in Appendix K.1–Appendix K.5. If there is a quiet lesson here, it is that restraint is a form of explanation: one set of parameters, one set of rules, and the courage to let the data answer without our help.

Appendix L. C4 wave sector: linearized dynamics, polarizations, and GW tests

L.0 Policy, priors, and scope (deduplicated). The GW sector inherits the *global fixed–constants* policy (Section 2.6.2); no event– or probe–level retuning is allowed. Numerical defaults (grids, tolerances, sampling) follow Appendix K.5. Reproducibility and logging conventions follow Appendix H (details consolidated in Appendix L.0.3). The guiding attitude is sobriety over flourish: state assumptions once, carry them everywhere, and let consistency do the talking.

Field content (axioms). Two tensor polarizations $h_+, h_\times$ propagate at speed c *by definition* (with no free tensor–speed or dispersion degrees of freedom). Optionally, a single curvature–coupled scalar mode φ is admitted under a *global* coupling ζ (and fixed ppE exponents if used). Vector modes are not part of the baseline. Early–time and strong–curvature microphysics remain standard unless declared as a separate scenario class. Parsimony here is deliberate: every extra freedom must earn its place in the ledger.

Global declarations (GW parameters).

$$\Theta_{\rm GW} = \left\{ \zeta\ (\geq 0),\ m_\varphi^2 (\geq 0),\ c_\varphi^2 \in [0,1],\ \text{ppE}\ (\alpha_{\rm ppE}, \beta_{\rm ppE}; a, b) \right\}.$$

Only a subset needs to be active in a given run; all are *global* and shared across events.

Guardrails (admission). Luminal tensors $c_T = c$; stability/causality for φ ($m_\varphi^2 \geq 0,\ 0 \leq c_\varphi^2 \leq 1$); ppE exponents (a, b) fixed *a priori* to the tested hypothesis; non–tensor polarization power controlled by a single global parameter (derived from ζ). These guardrails are not decoration; they are the rails that keep inference from drifting into story–telling.

Linearized dynamics (schematic). On sub–horizon scales with conformal time η and $\mathcal{H} \equiv aH$,

$$h_A'' + 2\mathcal{H}\, h_A' + k^2 h_A = S_A(\eta, k) \quad (A \in \{+, \times\}), \qquad \varphi'' + 2\mathcal{H}\, \varphi' + (c_\varphi^2 k^2 + a^2 m_\varphi^2)\, \varphi = S_\varphi(\eta, k; \zeta).$$

Tensor propagation is strictly luminal; any phase/amplitude deformation is encoded only via *global* ppE coefficients. In short: the background sets the stage, sources set the cues, and the same rules apply to every act.

Observables and tests (overview). Catalog–level tests cover speed/dispersion, polarization content, and standard–siren coherence. Quantitative thresholds and procedures are stated in Appendix L.0.1; anticipated critiques and mitigations in Appendix L.0.2; reporting/ledger details in Appendix L.0.3.

L.0.1 Validation loop (pre–declared, reproducible).

1. **Sanity and invariance (null) tests.** Off–source windows, sky–scrambles, and phase–randomized templates must yield overlaps consistent with noise (e.g., residual–correlation two–sample KS test with $p > 0.05$), with null–stream consistency and stability under detector–subset removal. On failure: treat as residual systematics, halt, and emit a failure log per Appendix H. A quiet check first; then proceed.

2. **Injection–recovery (forward model).** Inject a *single global* $(\zeta; \alpha_{\rm ppE}, \beta_{\rm ppE})$ into GR–EOB/NR waveforms, synthesize detector–network responses, and recover with the same priors (global–only, per Appendix L.0). *Acceptance thresholds:* band–integrated overlap $\mathcal{O} \geq 0.99$, mismatch $\leq 1\%$, unbiased phase residuals, and no spurious Bayes–factor preference for over–parameterized models (e.g., $\Delta \log B \leq 0$ or below Jeffreys' boundary).

3. **Observational fit (backward inference).** Fit LIGO/Virgo/KAGRA catalogs with a *common* likelihood and covariance; posteriors for $(\zeta; \alpha_{\rm ppE}, \beta_{\rm ppE})$ must be *consistent across* event subsets and network configurations (rank). *Acceptance:* posterior–median drift within Appendix K.5 tolerances and posterior–shape homogeneity (two–sample KS $p > 0.05$).

4. **Cross–checks.** (i) *Polarization rank:* network pattern–matrix rank ≥ 2 for tensor–only tests and ≥ 3 when including a breathing mode; (ii) *Calibration & PSD stability:* repeat fits across calibration curves and PSD realizations; (iii) *Robustness:* re–fit with expanded/contracted data–quality vetoes; posterior drift beyond tolerance flags model fragility.

L.0.2 Anticipated critiques and mitigations.

- *Over–flexibility:* forbid event–level ppE retuning; restrict to *global* constants. Additional dof are penalized via BIC/AIC in the ledger.
- *Scalar false positives:* require multi–detector coherence and polarization separation; breathing–mode claims must survive sky–scrambles and detector–subset removals.
- *Speed/dispersion ambiguity:* tensor speed is fixed to c by design (see Appendix L.0); any arrival–time residual bias is attributed to pipelines or noise, not to extra tensor dof.
- *Inclination–polarization degeneracy:* jointly sample (ι, ψ) with polarization response; breathing–mode posteriors must remain non–degenerate after marginalizing over (ι, ψ).

L.0.3 Reporting and ledger (concise, auditable). For each run, archive frequency grids, windowing, template banks, priors, masks, seeds, calibration versions, PSDs, and all configuration files with hashes. Publish $(\mathcal{O}, \text{mismatch})$ distributions, residual spectra, and Bayes–factor tables to enable byte–level reproducibility and external auditing. All failures are recorded as *machine–readable* YAML logs with fields `stage`, `test`, `observed`, `threshold`, `config_hash`, `env_fingerprint`, `repro_cmd`; schema and examples follow Appendix H.

L.1 Linearized wave equations and gauge (with consistency and flux)

Conventions. We linearize about Minkowski spacetime, $g_{\mu\nu} = \eta_{\mu\nu} + h_{\mu\nu}$ with $\eta_{\mu\nu} = \mathrm{diag}(-,+,+,+)$, and write $\Phi = \Phi_0 + \delta\Phi$. We work in units $c = 1$ unless explicitly stated (restore c by dimensional analysis). Indices are raised and lowered with $\eta_{\mu\nu}$, and equalities hold to linear order unless noted. The aim is to keep the scaffolding visible: simple rules first, then consequences.

Field content and gauge. Adopt the de Donder (Lorenz) gauge $\partial^\mu \bar{h}_{\mu\nu} = 0$, with $\bar{h}_{\mu\nu} \equiv h_{\mu\nu} - \frac{1}{2}\eta_{\mu\nu} h$. The linearized equations are

$$\Box\, \bar{h}_{\mu\nu} \;=\; -16\pi G \left(T_{\mu\nu} + \tau^{(\Phi)}_{\mu\nu}\right), \qquad \Box\, \delta\Phi \;+\; m_\Phi^2\, \delta\Phi \;=\; \mathcal{S}_\Phi[T_{\mu\nu}], \tag{338}$$

where $\tau^{(\Phi)}_{\mu\nu}$ is the effective (curvature–field) stress contribution. Source consistency requires

$$\partial^\mu\Big(T_{\mu\nu} + \tau^{(\Phi)}_{\mu\nu}\Big) = 0, \qquad \partial^\mu \bar{h}_{\mu\nu} = 0 \quad \text{(numerically enforced to solver tolerance).}$$

Remark. At strictly linear order about $\Phi_0 = \text{const}$, $\tau^{(\Phi)}_{\mu\nu} = \mathcal{O}(\delta\Phi^2)$ and thus contributes at leading non–vanishing order only after short–wavelength averaging; we keep it here to maintain uniform notation with the flux bookkeeping below.

Tensor projection and solution structure. Project to the transverse–traceless sector by

$$\Lambda_{ij,kl}(\hat{\mathbf{n}}) \;=\; P_{ik}P_{jl} - \tfrac{1}{2}P_{ij}P_{kl}, \qquad P_{ij} = \delta_{ij} - \hat{n}_i\hat{n}_j,$$

to obtain

$$\Box\, h_{ij}^{\mathrm{TT}} \;=\; -16\pi G\, T_{ij}^{\mathrm{TT}}, \qquad h_{ij}^{\mathrm{TT}}(t,\mathbf{x}) \;\simeq\; \frac{2G}{R}\,\ddot{Q}_{ij}^{\mathrm{TT}}\big(t-R\big), \tag{339}$$

for a localized source at distance R (retarded time $t-R$ in $c{=}1$ units), where Q_{ij} is the trace–free quadrupole built from $T_{\mu\nu} + \tau_{\mu\nu}^{(\Phi)}$. (With c restored, $h_{ij}^{\mathrm{TT}} \simeq \frac{2G}{c^4 R}\,\ddot{Q}_{ij}^{\mathrm{TT}}(t - R/c)$.) The message is standard: far from the source, the quadrupole rules the waveform.

Scalar sector and dispersion. The scalar mode obeys

$$\Box\delta\Phi + m_\Phi^2\delta\Phi = \mathcal{S}_\Phi[T_{\mu\nu}],$$

with group velocity $v_g = \partial\omega/\partial k = \sqrt{1 - m_\Phi^2/\omega^2}$. To avoid dispersion/superluminality in the baseline we take $m_\Phi = 0$ (or effectively $m_\Phi^2 \ll \omega^2$ over the analysis band), hence $v_g \simeq 1$. Any $m_\Phi > 0$ run is treated as a separate *scenario class* under the same guardrails. When assumptions change, we say so and test them on their own terms.

Energy flux and positivity (Isaacson). In the short–wavelength/averaged limit the effective GW energy–momentum is

$$T_{\mu\nu}^{\mathrm{GW}} = \frac{1}{32\pi G}\left\langle \partial_\mu h_{ij}^{\mathrm{TT}}\,\partial_\nu h_{ij}^{\mathrm{TT}}\right\rangle \;+\; \Big\langle \partial_\mu\delta\Phi\,\partial_\nu\delta\Phi \;-\; \tfrac{1}{2}\eta_{\mu\nu}\big[(\partial\delta\Phi)^2 - m_\Phi^2\,(\delta\Phi)^2\big]\Big\rangle, \tag{340}$$

which is positive–definite for the tensor piece and, for a canonical scalar, enforces positivity via the hard priors $m_\Phi^2 \geq 0$ and the correct kinetic sign. Negative flux realizations in the scalar channel trigger rejection in the validation loop (Appendix L.0.1). Energy should not be created by notation; this is where the bookkeeping earns its keep.

Curved background extension (consistency). On a slowly varying background,

$$\Box\bar{h}_{\mu\nu} + 2R_{\mu\rho\nu\sigma}\,h^{\rho\sigma} \;=\; -16\pi G\left(T_{\mu\nu} + \tau_{\mu\nu}^{(\Phi)}\right) \;+\; \mathcal{O}\big(h\nabla R\big),$$

and the Minkowski results are recovered when the curvature length greatly exceeds the GW wavelength ($\lambda_{\mathrm{GW}} \ll \mathcal{R}^{-1/2}$). Baseline tests assume Minkowski (or weakly curved) propagation; any strong–curvature extension is declared and tested separately.

Consistency checks (pass/fail hooks).

- *Gauge and conservation:* residuals $\|\partial^\mu\bar{h}_{\mu\nu}\|/\|\partial\bar{h}\|$ and $\|\partial^\mu(T_{\mu\nu} + \tau_{\mu\nu}^{(\Phi)})\|/\|\partial T\|$ must lie within solver tolerances (declared in Appendix K.5); violation ⇒ run failure.
- *Luminal tensor speed:* the retarded time in (339) is $t - R$ (or $t - R/c$ with c restored). Any fitted tensor speed $\neq 1$ indicates pipeline/systematic error (per Appendix L.0) rather than extra tensor dof.
- *Scalar stability:* no ghosts (positive kinetic term), no tachyons ($m_\Phi^2 \geq 0$), and real v_g across the analysis band.
- *Flux positivity:* the Isaacson flux from (340) must be non–negative to numerical precision; negative bins flag the fit for rejection.

Small rules, clearly stated, keep the analysis honest: when the checks pass, the rest follows without adornment.

L.1.1 Self–sourcing channel $J[\Phi] = \alpha(\nabla\Phi)^2$: stability, causality, and energy conditions

Setup and conventions. On a static (or slowly varying) background $\bar{\Phi}(t, r) \approx \bar{\Phi}(r)$, write $\Phi = \bar{\Phi} + \phi$ with $|\phi| \ll |\bar{\Phi}|$. In the *dynamical baseline* we set $\beta = 0$ and $\lambda_\Xi = 0$ (cf. static regulators in Appendix C.8). The PCFE source term is $J[\Phi]\,\Phi = \alpha\,\Phi(\nabla\Phi)^2$, so expanding to quadratic order in ϕ gives, up to total derivatives,

$$\mathcal{L}^{(2)}_{\rm kin} = -\tfrac{1}{2}\,(\nabla\phi)^2 \;+\; \alpha\,\bar{\Phi}\,(\nabla\phi)^2 \;+\; \underbrace{2\alpha\,\phi\,\nabla_\mu\bar{\Phi}\,\nabla^\mu\phi}_{\text{subleading; integrates to } \mathcal{O}(\phi^2\nabla^2\bar{\Phi})} \;+\; \dots \tag{341}$$

We keep the canonical $(\nabla\phi)^2$ terms explicitly and treat the mixed term $\phi\,\nabla\bar{\Phi}\cdot\nabla\phi$ as a suppressed background–gradient correction. The rule of thumb is plain: state the leading structure, track the rest, and let the hierarchy speak for itself.

Principal quadratic form and effective kinetic coefficient. Collecting the leading–derivative pieces,

$$\mathcal{L}^{(2)}_{\rm prin} = -\frac{1}{2}\,K_{\rm eff}(\bar{\Phi})\,g^{\mu\nu}\nabla_\mu\phi\,\nabla_\nu\phi \;+\; \mathcal{O}\big(\nabla\bar{\Phi}\cdot\phi\,\nabla\phi\big), \qquad K_{\rm eff}(\bar{\Phi}) = 1 - 2\alpha\,\bar{\Phi} \;+\; \mathcal{O}\big((\nabla\bar{\Phi})^2\big). \tag{342}$$

Equivalently, one may write $S^{(2)}_{\rm prin} = \frac{1}{2}\int\sqrt{-g}\,Z^{\mu\nu}\nabla_\mu\phi\nabla_\nu\phi$ with $Z^{\mu\nu} = -K_{\rm eff}g^{\mu\nu}$. Background–gradient remainders are tracked but do not alter the principal cone at leading order.

High–frequency cone and wave speed. On $ds^2 = -A(r)\,dt^2 + C(r)\,dr^2 + r^2d\Omega^2$ and a WKB ansatz $\phi \sim e^{i\Theta/\epsilon}$, the principal symbol is $\mathcal{P}(\omega, k) = K_{\rm eff}(A^{-1}\omega^2 - C\,k^2) + \dots$, so the local signal speed is

$$c_s^2 \;=\; \frac{Z^{rr}/C}{Z^{tt}A^{-1}} \;=\; 1 \;+\; \mathcal{O}\big((\nabla\bar{\Phi})^2\big), \tag{343}$$

i.e. any anisotropy/dispersion induced by $\nabla\bar{\Phi}$ enters at subleading order. Clarity here is protective: the cone is set by the principal form, and small gradients only perturb it.

Ghost/gradient stability and hyperbolicity.

- **No ghost:** $K_{\rm eff}(\bar{\Phi}) > 0$ ensures a positive time–like quadratic form (canonical sign of $\dot{\phi}^2$ in (342)).
- **No gradient instability:** from (343), $c_s^2 \geq 0$ when $K_{\rm eff} > 0$.
- **Hyperbolicity:** $Z^{tt} > 0$ and $Z^{rr} > 0$ (equivalently $K_{\rm eff} > 0$) give a strictly hyperbolic principal operator.

Higher–derivative regulators (EFT regime; optional). Static–sector regulators $\beta(\Box\Phi)^2$ and $\lambda_\Xi\,\Xi_{\mu\nu}\Xi^{\mu\nu}$ (Appendix C.8) are *off* in dynamical runs. If enabled for diagnostics, they must lie below the EFT cutoff Λ so that fourth–order modes do not contaminate the principal sector:

$$|\,\beta\,|\,k^2 \ll K_{\rm eff}, \qquad |\,\lambda_\Xi\,|\,k^2 \ll K_{\rm eff}. \tag{344}$$

In other words: keep the cure weaker than the ailment, or it becomes the model.

Energy condition (WEC for perturbations). In the isotropic leading limit,

$$\rho_\phi = \tfrac{1}{2} K_{\rm eff}\Big(A^{-1}\dot\phi^2 + C\,(\partial_r\phi)^2\Big) \;+\; \ldots \;\geq\; 0 \qquad \text{whenever} \quad K_{\rm eff} > 0, \tag{345}$$

with background scalar stress handled as in Appendix C.8. Positivity is not merely a preference; it is the minimal bill a perturbation must pay to be physical.

Operating bounds (Solar–System window). On $[r_0, 3r_0]$ we impose the quantitative bounds

$$\boxed{0 \;<\; K_{\rm eff}(\bar\Phi) = 1 - 2\alpha\,\bar\Phi \;\leq\; 1, \qquad c_s^2 \;\leq\; 1, \qquad |\alpha|\,\frac{(\nabla\bar\Phi)^2}{c^2} \;\leq\; \eta_{\rm cone}\,K_{\rm eff}^2,} \tag{346}$$

with default $\eta_{\rm cone} = 10^{-2}$, enforced jointly with the external PPN budgets in Section 3.5.4. These bounds make the intent explicit: respect local tests first, then ask for novelty.

External linkage and reporting. (1) *PPN linkage:* verify compliance with fixed budgets $(\varepsilon_\gamma, \varepsilon_\beta)$ (Section 3.5.4).
(2) *Optical causality:* corroborate $c_s \leq 1$ using the ring–delay observable Θ and its uncertainties (main text, Section 7).
(3) *Time–domain constraint:* report upper bounds on propagation speed from high–cadence EHT/ngEHT light curves.
For reproducibility, publish $\bar\Phi(r)$ and $K_{\rm eff}(r)$ profiles, the maximal $c_s^2(r)$ on $[r_0, 3r_0]$, any regulator settings (β, λ_Ξ) with EFT cutoff Λ if used, and consistency checks against Section 3.5.4.

L.2 Polarization content and detector response

Network model (time and frequency domains). For a network of N detectors we write, in the long–wavelength limit,

$$d^{(I)}(t) = \sum_{A\in\{+,\times,b\}} F_A^{(I)}(\hat{\mathbf{n}},\psi;t)\,h_A\big(t-\tau_I(\hat{\mathbf{n}})\big) \;+\; n^{(I)}(t), \qquad I = 1,\ldots,N, \tag{347}$$

where $\hat{\mathbf{n}}$ is the sky direction, ψ the polarization angle, τ_I the geometrical time delay, and h_b a possible breathing mode with *global* coupling ζ (baseline C4–GR limit: $h_b \equiv 0$). Stacking channels gives $\mathbf{d} = \mathbf{F}\,\mathbf{h} + \mathbf{n}$ with

$$\mathbf{F} \equiv \begin{bmatrix} F_+^{(1)} & F_\times^{(1)} & F_b^{(1)} \\ \vdots & \vdots & \vdots \\ F_+^{(N)} & F_\times^{(N)} & F_b^{(N)} \end{bmatrix}, \qquad \mathbf{h} \equiv \begin{bmatrix} h_+ \\ h_\times \\ h_b \end{bmatrix}. \tag{348}$$

In the frequency domain, time delays enter as phase factors:
$\tilde d^{(I)}(f) = \sum_A F_A^{(I)}(\hat{\mathbf{n}},\psi;t_0)\,e^{-2\pi i f\tau_I}\,\tilde h_A(f) + \tilde n^{(I)}(f)$, with slow sidereal evolution absorbed by segmenting t_0 if needed. The principle is simple: one set of assumptions carried consistently between time and frequency, so that the story does not change with the coordinates.

Antenna geometry and tensors. Each pattern is $F_A^{(I)} = d_{ij}^{(I)}\,e_{ij}^A$, where $d_{ij}^{(I)}$ is the detector tensor and e_{ij}^A the polarization basis: $e_{ij}^+ = \hat{\mathbf{e}}_\theta\otimes\hat{\mathbf{e}}_\theta - \hat{\mathbf{e}}_\phi\otimes\hat{\mathbf{e}}_\phi$, $e_{ij}^\times = \hat{\mathbf{e}}_\theta\otimes\hat{\mathbf{e}}_\phi + \hat{\mathbf{e}}_\phi\otimes\hat{\mathbf{e}}_\theta$, $e_{ij}^b = \hat{\mathbf{e}}_\theta\otimes\hat{\mathbf{e}}_\theta + \hat{\mathbf{e}}_\phi\otimes\hat{\mathbf{e}}_\phi$. In the long–wavelength limit F_A is frequency–independent; finite–size corrections are negligible for terrestrial detectors in band and are omitted by default.

Separation, rank, and null streams. Define the tensor–only submatrix $\mathbf{F}_{\rm tensor}$ (columns $+, \times$). Separation conditions across the analysis band:

$$\mathrm{rank}(\mathbf{F}_{\rm tensor}) \geq 2 \quad \text{(tensor–only)}, \qquad \mathrm{rank}(\mathbf{F}) \geq 3 \quad \text{(tensor + breathing)}. \tag{349}$$

Null streams are projections onto the left–null space of $\mathbf{F}$:

$$\mathbf{N}(t) = \mathbf{W}^{\top}\mathbf{d}(t), \qquad \mathbf{W}^{\top}\mathbf{F} = \mathbf{0}. \tag{350}$$

For Gaussian noise, $\mathbf{N}$ is signal–free; significant residual power (or non–Gaussian features) indicates calibration/PSD issues or an inconsistent polarization hypothesis. We construct $\mathbf{W}$ via the SVD $\mathbf{F} = \mathbf{U}\,\mathbf{S}\,\mathbf{V}^{\top}$; the columns of $\mathbf{U}$ associated with zero singular values span the null space. These constructions are not embellishments—they are the places where assumptions must cash out in numbers.

Whitened likelihood and projectors. Let $\tilde{\mathbf{d}}$ be the frequency–domain data and $\mathbf{C}_n(f)$ the (diagonal) noise PSD matrix. Define the inner product $\langle \mathbf{a}|\mathbf{b}\rangle \equiv 4\,\mathrm{Re}\int_{f_{\min}}^{f_{\max}} \tilde{\mathbf{a}}^{\dagger}\mathbf{C}_n^{-1}\tilde{\mathbf{b}}\,df$ and the whitened design $\hat{\mathbf{F}} = \mathbf{C}_n^{-1/2}\mathbf{F}$. For fixed $(\hat{\mathbf{n}}, \psi, \iota, D_L)$ the Gaussian log–likelihood is

$$-2\ln\mathcal{L} = \big\langle \mathbf{d} - \mathbf{F}\mathbf{h} \,\big|\, \mathbf{d} - \mathbf{F}\mathbf{h} \big\rangle = \langle \hat{\mathbf{d}} - \hat{\mathbf{F}}\mathbf{h} \,|\, \hat{\mathbf{d}} - \hat{\mathbf{F}}\mathbf{h}\rangle. \tag{351}$$

Projector onto the signal subspace:

$$\mathbf{P} \equiv \hat{\mathbf{F}}\,(\hat{\mathbf{F}}^{\top}\hat{\mathbf{F}})^{-1}\hat{\mathbf{F}}^{\top}, \qquad \mathbf{r} \equiv (\mathbf{I} - \mathbf{P})\,\hat{\mathbf{d}} \ \text{(residuals; noise–only under a correct model)}. \tag{352}$$

Goodness–of–fit and null–stream χ^2 are reported per segment and jointly across the band.

Geometry, degeneracies, and event selection. The breathing response F_b is *distinct yet partially degenerate* with $(F_+, F_\times)$ for specific sky positions and arm orientations; degeneracy increases for nearly face–on systems. We mitigate by jointly marginalizing (ι, ψ, D_L), and—when present—by exploiting higher harmonics and spin–precession. Catalog curation prioritizes network SNR and sky geometries yielding (349) over a finite bandwidth (or multiple sidereal segments). In practice this is a modest discipline: prefer configurations that can say "no" as clearly as they say "yes."

Global coupling and priors (breathing mode). The coupling ζ is *global* and shared across events and detectors (no event–level retuning). We parameterize $h_b = \zeta\,\mathcal{A}_b(\boldsymbol{\theta})\,h_{\rm ref}$ with a fixed response template $\mathcal{A}_b$ (dependent on source parameters $\boldsymbol{\theta}$) and a reference strain $h_{\rm ref}$. Priors enforce positivity of scalar energy and exclude superluminal/pathological group velocities (cf. Appendix L.1); posteriors for ζ must be statistically consistent across detector sub–networks and sky localizations under identical data–quality cuts.

Operational requirements and pass/fail hooks. Pattern functions use the same calibration versions as the strain data; PSDs, windows, and segment definitions are kept fixed across hypotheses. We report: (i) posterior predictive checks in null streams; (ii) singular–value spectra of $\mathbf{F}$ (and effective ranks vs. frequency/segment); (iii) stability of ζ under calibration/PSD variants; (iv) residual χ^2 for $\mathbf{r}$ and for $\mathbf{N}$. Failure of rank conditions (349), significant null–stream power, or ζ posteriors drifting across subsets beyond declared tolerances triggers rejection, per the validation rules in Appendix L.0.1.

L.3 Phasing and energy flux — ppE mapping

Definitions and units. We work in $c = G = 1$ units unless stated otherwise (restore c, G by dimensional analysis). Let the chirp mass be $\mathcal{M} \equiv \eta^{3/5} M$ with total mass M and symmetric mass ratio η, and define $u \equiv (\pi \mathcal{M} f)^{1/3}$. We model frequency–domain phase and amplitude as

$$\begin{aligned} \Psi(f) &= \Psi_{\rm GR}(f) + \beta_{\rm ppE}\,(\pi \mathcal{M} f)^b = \Psi_{\rm GR}(f) + \tilde{\beta}\, u^{\tilde{b}}, \\ A(f) &= A_{\rm GR}(f)[1 + \alpha_{\rm ppE}(\pi \mathcal{M} f)^a] = A_{\rm GR}(f)\big[1 + \tilde{\alpha}\, u^{\tilde{a}}\big]\,. \end{aligned} \tag{353}$$

where $(\alpha_{\rm ppE}, \beta_{\rm ppE})$ are *global* (shared across events) and the exponents (a, b) are *declared before* any fit. By construction $\tilde{b} = 3b$ and $\tilde{a} = 3a$. In the C4–GR limit $(\alpha_{\rm ppE}, \beta_{\rm ppE}) = (0, 0)$. If a scalar–flux channel is active via the global coupling ζ, then $\beta_{\rm ppE} = \beta_{\rm ppE}(\zeta)$ (and, if applicable, $\alpha_{\rm ppE} = \alpha_{\rm ppE}(\zeta)$), remaining global per Appendix L.0. The spirit is straightforward: name the freedom once, carry it everywhere, and keep the counting consistent.

PN bookkeeping and exponent mapping. In conventional PN counting, a *phase* correction at relative PN order p enters as $u^{\tilde{b}}$ with

$$\tilde{b} = 2p - 5 \quad \Longleftrightarrow \quad p = \frac{\tilde{b} + 5}{2} = \frac{3b + 5}{2}. \tag{354}$$

Examples: Newtonian (0PN) $\tilde{b} = -5 \Rightarrow b = -5/3$; -1PN (dipole–like) $\tilde{b} = -7 \Rightarrow b = -7/3$; $+1$PN $\tilde{b} = -3 \Rightarrow b = -1$. For *amplitude*, the relative PN order $p_{\rm amp}$ maps as

$$\tilde{a} = 2p_{\rm amp} \quad \Longleftrightarrow \quad p_{\rm amp} = \frac{\tilde{a}}{2} = \frac{3a}{2}. \tag{355}$$

We use (354)–(355) to pre–declare admissible (a, b) per source class. Clarity in the map prevents cleverness from masquerading as evidence.

Energy balance and monotonic chirp. Let $E(u)$ be the binary binding energy and $\mathcal{F}(u)$ the total GW luminosity. Energy balance,

$$\frac{dE}{dt} = -\mathcal{F}(u) = -\Big[\mathcal{F}_{\rm GR}(u) + \mathcal{F}_\Phi(u; \zeta)\Big], \qquad \mathcal{F}_\Phi \geq 0, \tag{356}$$

implies a modified chirp rate

$$\frac{df}{dt} = \frac{\mathcal{F}(u)}{\pi\, \mathcal{M}^2\, u^{11}} \;\propto\; u^{11}\Big(1 + \delta_{\rm flux}(u; \zeta)\Big) \;>\; 0, \tag{357}$$

and hence a dephasing $\Delta\Psi(f)$ consistent with (356). Fits explicitly enforce $\mathcal{F}_\Phi \geq 0$ and $df/dt > 0$ across the analyzed band; proposals violating these are rejected (Appendix L.0.1). In short: luminosity feeds the chirp, and the sign must come out right.

Source–class–driven exponent priors.

- **BH–BH:** dipole radiation is suppressed by no–hair and symmetry arguments; we therefore *exclude* negative–PN phase exponents for BH–BH:

  $$b < -\tfrac{5}{3} \text{ (i.e. } p < 0) \text{ disallowed for BH–BH.}$$

  Amplitude exponents with $p_{\rm amp} < 0$ (i.e. $a < 0$) are likewise excluded for BH–BH.

- **NS systems (optional analysis class):** negative–PN exponents (e.g. $b = -7/3$) may be allowed under separate, pre–declared priors owing to possible dipole channels; these runs are reported as a distinct scenario class.

Identifiability and nuisance structure. Amplitude modifications correlate with luminosity distance and calibration; phase modifications correlate with $(\mathcal{M}, \eta)$ and spins. To avoid spurious detections we:

- constrain $\alpha_{\rm ppE}$ jointly with per–detector amplitude–calibration nuisance parameters, using common priors across the network;
- constrain $\beta_{\rm ppE}$ jointly with $(\mathcal{M}, \eta, \chi_{\rm eff})$ and report mass– and spin–marginalized posteriors;
- repeat fits with/without higher harmonics and precession; stability within declared tolerances is required (cf. Appendix L.0.1).

Small disciplines like these keep interpretation from outrunning measurement.

Network–level consistency and presentation. We report: (i) band–limited overlaps and mismatches between ppE–corrected and GR templates at posterior means; (ii) residual phase/time series with 1σ envelopes; (iii) cross–detector coherence of $(\alpha_{\rm ppE}, \beta_{\rm ppE})$; (iv) Bayes factors under identical priors and covariances. A *single global* $(\alpha_{\rm ppE}, \beta_{\rm ppE})$ must remain stable under detector–subset changes, sky–localization alternatives, and calibration/PSD variants (Appendix L.0). Prefer configurations that can say "no" as crisply as they say "yes."

Admission rules (pre–declared).

(i) (a, b) and priors are declared before analysis;
(ii) $\beta_{\rm ppE}(\zeta)$ respects $\mathcal{F}_\Phi \geq 0$ and yields $df/dt > 0$;
(iii) $(\alpha_{\rm ppE}, \beta_{\rm ppE})$ are global (no event–level retuning);
(iv) posterior medians/intervals are consistent across event subsets and networks.

(358)

Failure of any item in (358) precludes using ppE corrections as evidence for extended polarization or flux.

Reproducibility ledger (artifacts). For each run we archive: the declared (a, b), priors on $(\alpha_{\rm ppE}, \beta_{\rm ppE})$ and calibration nuisances; frequency band, windows, and PSDs (common across hypotheses); overlaps/mismatches, residual series, Bayes–factor tables; and configuration hashes, following the ledger practice of Appendix H and numerical settings in Appendix K.5. The promise is modest but useful: enough trail for others to retrace, no more freedom than the data can bear.

L.4 Validation protocol: injection–recovery and observational fits

Preliminaries (shared settings). Unless noted, we use the same preprocessing and numerical settings across *all* hypotheses: windows, PSDs, calibration curves, segmenting, frequency bands, and priors. The network inner product and whitening conventions follow Appendix L.2. For two network waveforms $\mathbf{h}_1, \mathbf{h}_2$, define the (noise–weighted) overlap and mismatch

$$\mathcal{O}(\mathbf{h}_1, \mathbf{h}_2) = \frac{\langle \mathbf{h}_1 | \mathbf{h}_2 \rangle}{\sqrt{\langle \mathbf{h}_1 | \mathbf{h}_1 \rangle \, \langle \mathbf{h}_2 | \mathbf{h}_2 \rangle}}, \qquad \text{mismatch} = 1 - \mathcal{O}, \tag{359}$$

with $\langle\cdot|\cdot\rangle$ the standard multi–detector inner product. Whitened residuals use $\hat{\mathbf{d}} = \mathbf{C}_n^{-1/2}\mathbf{d}$ and the projector $\mathbf{P}$ in (352), so that $\mathbf{r} = (\mathbf{I} - \mathbf{P})\hat{\mathbf{d}}$ is noise–only under a correct model. The rule is simple: one set of settings for every hypothesis, so agreement (or discrepancy) is earned, not engineered.

Phase I — injection–recovery (forward). Inject a *global* correction $(\alpha_{\rm ppE}, \beta_{\rm ppE})$ into GR–EOB/NR waveforms, synthesize the detector–network responses with the *same* windows/PSDs/ calibration as the analysis, and recover with identical priors and numerical tolerances. Report:

- **Waveform agreement.** Band–integrated $\mathcal{O}\big(\mathbf{h}_{\rm ppE}, \mathbf{h}_{\rm GR}\big) \geq 0.99$ and mismatch $\leq 1\%$.[5]
- **Residual stability.** Whitened residuals have zero–mean within errors and frequency–domain residual spectra lie inside the PSD credibility band over the analysis range.
- **Parsimony check.** With identical priors/covariances, $\ln K \equiv \ln(Z_{\rm ppE}/Z_{\rm GR})$ shows no artificial preference for over–parameterized models.
- **Polarization consistency.** When $\mathrm{rank}(\mathbf{F}) \geq 3$, the $(+, \times, b)$ decomposition is stable; the SVD spectrum of $\mathbf{F}$ has no discontinuities across segments (Appendix L.2).

Robustness probes include sky–scrambles, detector–subset swaps, and calibration–curve variants; the spread of the above metrics is tabulated. A good model should still look good when we move the furniture.

Phase II — observational catalog fits (backward). Fit LIGO/Virgo/KAGRA catalogs with a *common* likelihood/covariance to infer global posteriors for $(\zeta, \alpha_{\rm ppE}, \beta_{\rm ppE})$:

1. **Globality.** Posteriors remain statistically consistent across event subsets (high/low SNR, network geometries, sky locations) under identical data–quality cuts.
2. **Polarization separation.** If a breathing mode is included, null streams ((350)) show no astrophysical power; after marginalizing (ι, ψ, D_L), the posterior for ζ is non–degenerate.
3. **Physicality.** Energy–positivity and monotonic–chirp constraints from Appendix L.3 hold across the analyzed band.

Common acceptance thresholds (both phases). All of the following must hold simultaneously:

$$\boxed{\begin{array}{l}\mathcal{O} \geq 0.99 \ \text{ and } \ \text{mismatch} \leq 1\%; \\ \text{whitened residual means } \approx 0 \text{ and spectra within PSD bands;} \\ \text{global parameters } (\zeta, \alpha_{\rm ppE}, \beta_{\rm ppE}) \text{ stable under subset changes.}\end{array}} \tag{360}$$

Failure of any two criteria implies that extended corrections (or additional polarization content) are *not* admitted. These are modest bars by design: enough to exclude wishful thinking, not to punish honest data.

[5] Computed after maximizing analytically over extrinsic time/phase shifts.

Presentation and auditability. Under identical priors/covariances, publish: (i) band–limited overlaps/mismatches; (ii) residual time series and spectra with 1σ envelopes; (iii) cross–detector coherence of $(\alpha_{\rm ppE}, \beta_{\rm ppE}, \zeta)$; (iv) Bayes–factor tables ($\ln K$). All configuration files (windows, PSDs, calibration versions, priors, tolerances) are archived with hashes to enable byte–level reruns (Appendix H). The compact promise is the same throughout: show the rules, show the results, and leave enough trail for others to follow.

L.5 Numerical settings and reproducibility

Signal–processing settings (fixed). Sampling rate and analysis band are *predeclared* (e.g., $f_{\rm s} \in \{4096, 8192\}\,{\rm Hz}$, $f_{\rm low} \in [15, 30]\,{\rm Hz}$, $f_{\rm high} \in [1024, 2048]\,{\rm Hz}$). Segment length $T_{\rm seg}$, window (e.g., Tukey with taper ratio $\alpha_{\rm tk}$), gating rules, overlap, and the *PSD estimator* (Welch–median with a declared number of segments and smoothing kernel) are fixed across hypotheses. Whitening filters and normalization conventions are identical for all models. Small choices are made once and carried through—so agreement, when it appears, is earned rather than arranged.

PSD and whitening (definitions). To make effective degrees of freedom and band omissions explicit, we specify the PSD as follows. Given segmented data $x_k[n]$ and a window $w[n]$,

$$\widehat{S}_{xx}(f_j) = \mathrm{median}_{k=1..N_{\rm seg}} \left\{ \frac{2\,\Delta t}{U_w} \left| \mathrm{FFT}\{\, w[n]\, x_k[n] \,\}(f_j) \right|^2 \right\}, \qquad U_w = \frac{1}{N} \sum_{n=0}^{N-1} w^2[n]. \tag{361}$$

Whitened data and the whitened design matrix are

$$\tilde{x}_{\rm W}(f) = \frac{\tilde{x}(f)}{\sqrt{\widehat{S}_{xx}(f)}}, \qquad \hat{\mathbf{F}}(f) = \mathbf{C}_n^{-1/2}(f)\,\mathbf{F}, \tag{362}$$

and inner products / projectors follow the definitions in Appendix L.2 (see also the projector $\mathbf{P}$ in (352)).

Template bank and priors. Mass–spin ranges, bank spacing (or target stochastic mismatch), and whether higher harmonics or precession are included are *predeclared*. The ppE exponents (a, b) and bounds for $(\alpha_{\rm ppE}, \beta_{\rm ppE})$ are fixed in advance. The breathing–mode coupling ζ uses priors that enforce energy positivity and a subluminal group velocity ($v_g \le c$). Amplitude/phase calibration priors are specified identically for each detector. Name the freedoms up front, then let the data do the talking.

Inference engine and convergence checks. Sampler settings (e.g., nested–sampling live points, or HMC–NUTS step size and adaptation length) are recorded. Multiple random seeds are used to verify reproducibility; we require $\hat{R} < 1.01$ (or an equivalent convergence diagnostic). Reported diagnostics include likelihood–surface condition numbers, effective sample sizes (ESS), and multimodality checks of the posteriors.

Pattern matrices and null–stream record. We archive the SVD spectra and rank estimates of the detector pattern matrix $\mathbf{F}(\hat{\boldsymbol{n}}, \psi)$, together with the null–stream projector $\mathbf{W}$ and null–stream variance metrics (Appendix L.2). Alternative polarization hypotheses are recomputed with identical procedures for a direct comparison.

Ledger artifacts (archival list). We store frequency grids, PSD / calibration versions, template specifications, priors and bounds, masks, seeds, sampler logs, summary statistics (overlap, mismatch, Bayes factors), residual spectra, and configuration–file hashes. Byte–level re–execution with the same settings must be feasible (Appendix H).

Numerical safety hooks (pass/fail).

- **Band consistency:** $\widehat{S}_{xx}(f)$, whitening, and window/overlap/segment definitions must be identical across hypotheses; any change is run as a separate job and recorded.
- **Spectral leakage:** if gating/window choices measurably worsen overlap/mismatch metrics, the run is invalidated and rerun under corrected settings.
- **Convergence/conditioning:** failure to converge ($\hat{R} \geq 1.01$) or exploding condition numbers triggers discarding the result and a documented rerun with updated settings.

Environment pinning and versioning. We record compiler / BLAS / LAPACK, FFT library, Python / NumPy / SciPy versions, GPU drivers (if used), and OS / container digests. IEEE–754 determinism is maintained; FFT lengths and zero–padding rules are specified to guarantee *bitwise* reproducibility.

Cross–references. Overlap/mismatch and the residual projector are defined in Appendix L.2; acceptance thresholds are in Appendix L.4; ppE physical constraints (energy positivity / monotonic chirp) are in Appendix L.3.

L.6 Synthesis

This appendix codifies the wave sector as a *reproducible*, fixed–policy pipeline. At leading order the tensor sector reproduces GR; any breathing polarization or ppE correction is admitted only via *global* constants that are shared across *all* events and never retuned per source.

Acceptance rule. A single global triplet $(\zeta, \alpha_{\rm ppE}, \beta_{\rm ppE})$ must concurrently satisfy: (i) waveform–agreement thresholds, (ii) residual–stability conditions, and (iii) subset–invariance across networks and event partitions. Failure of any two items disqualifies claims of extended dynamics.

Perspective. Reproducibility here is more than bookkeeping: to claim extra polarizations or flux channels, the same rules must hold everywhere and every time. What remains after invariance and consistency checks is the part that is hard to fake—results that keep their shape when the coordinates, the detectors, or the subsets change. In that spirit, this closing synthesis prefers firm rules over flexible fits, so that what survives is not convenience but signal.

Appendix M: Statistical Power and Design for Joint Invariants R and Θ

Standardization. Throughout Appendix M we use the standardized scalars defined in Appendix N.2, ensuring GR maps to $(R, \Theta) = (1, 1)$ and enabling consistent synthesis with Section 12.5.

M.1 Setup

Notation (standardized scalars). We adopt the standardized ring invariants introduced in Appendix N.2:

$$R \equiv R_{\rm std} \equiv \frac{D_{\rm obs}}{D_{\rm GR}}, \qquad \Theta \equiv \Theta_{\rm std} \equiv \frac{\sqrt{P_1/(P_0+P_2)}}{\sqrt{P_1^{\rm GR}/(P_0^{\rm GR}+P_2^{\rm GR})}}\,.$$

Both are evaluated on the fixed window declared in Section 7. Under GR recovery, $(R, \Theta) = (1, 1)$ by construction.

Units and normalization. Unless stated otherwise, we work with *dimensionless fractional* departures about GR. Because (R, Θ) are already standardized to unity at the GR baseline, percentage axes in figures are simply rescaled versions of $(R-1)$ and $(\Theta-1)$.

Data vector. With the standardization above, define the two–component data vector

$$\boldsymbol{y} \equiv \begin{bmatrix} R-1 \\ \Theta-1 \end{bmatrix}, \tag{363}$$

which is the basic object we combine across bands and epochs.

Observable definitions (summary). R quantifies the size ratio $D_{\rm obs}/D_{\rm GR}$ of the deblurred ring diameter, and Θ encodes the normalized asymmetry power via (P_0, P_1, P_2) in the azimuthal (subring–harmonic) decomposition of the ring brightness. The GR predictions $(D_{\rm GR}, P_m^{\rm GR})$ (and thus R=1, Θ=1) are obtained from the metric/light–propagation pipeline of Section 7. Formal motivations and the C4 response are summarized in Appendix N.2.

Noise decomposition and single–epoch covariance. For frequency band b and epoch e, decompose the 2×2 covariance into a statistical term and an epoch–correlated floor (shared calibration/environment):

$$\boldsymbol{\Sigma}_{\rm stat}^{(b)} = \begin{pmatrix} \sigma_{R,\rm stat}^2 & \rho^{(b)}\,\sigma_{R,\rm stat}\sigma_{\Theta,\rm stat} \\ \rho^{(b)}\,\sigma_{R,\rm stat}\sigma_{\Theta,\rm stat} & \sigma_{\Theta,\rm stat}^2 \end{pmatrix}, \tag{364a}$$

$$\boldsymbol{\Sigma}_{\rm floor}^{(b)} = \begin{pmatrix} \sigma_{R,\rm floor}^2 & \rho_{\rm floor}^{(b)}\,\sigma_{R,\rm floor}\sigma_{\Theta,\rm floor} \\ \rho_{\rm floor}^{(b)}\,\sigma_{R,\rm floor}\sigma_{\Theta,\rm floor} & \sigma_{\Theta,\rm floor}^2 \end{pmatrix}. \tag{364b}$$

with $|\rho^{(b)}|, |\rho_{\rm floor}^{(b)}| \le 1$. Averaging N epochs in band b gives

$$\overline{\boldsymbol{\Sigma}}^{(b)} = \frac{1}{N_{\rm eff}}\,\boldsymbol{\Sigma}_{\rm stat}^{(b)} + \boldsymbol{\Sigma}_{\rm floor}^{(b)}, \qquad N_{\rm eff} = \frac{N}{1+(N-1)\rho_{\rm sys}}, \quad \rho_{\rm sys} \in [0, 1), \tag{365}$$

where $\rho_{\rm sys}$ encodes inter–epoch correlation. When $\boldsymbol{\Sigma}_{\rm floor}^{(b)} \neq \mathbf{0}$, $\overline{\boldsymbol{\Sigma}}^{(b)}$ saturates as $N \to \infty$.

Multi–band combination. If bandwise means $\bar{\boldsymbol{y}}^{(b)}$ are independent across b, combine them via

$$\boldsymbol{W} = \sum_b \big(\overline{\boldsymbol{\Sigma}}^{(b)}\big)^{-1}, \qquad \hat{\boldsymbol{y}} = \boldsymbol{W}^{-1}\left(\sum_b \big(\overline{\boldsymbol{\Sigma}}^{(b)}\big)^{-1}\bar{\boldsymbol{y}}^{(b)}\right), \qquad \hat{\boldsymbol{\Sigma}} = \boldsymbol{W}^{-1}. \tag{366}$$

If inter–band correlations are non–negligible, assemble the full block covariance across all bands and apply the same inverse–covariance weighting to the stacked data vector. Either way, weights are *earned by precision*, not assumed.

Whitening and target direction. Let $\hat{\boldsymbol{\Sigma}} = \boldsymbol{L}\boldsymbol{L}^{\top}$ be the Cholesky factorization. Define whitened variables and the diagonal (C4) direction:

$$\boldsymbol{z} = \boldsymbol{L}^{-1}\hat{\boldsymbol{y}}, \qquad \boldsymbol{u} = \begin{bmatrix}1\\1\end{bmatrix}, \qquad \boldsymbol{u}_w = \boldsymbol{L}^{-1}\boldsymbol{u}. \tag{367}$$

Under $\mathcal{H}_0$ (GR), $\boldsymbol{z} \sim \mathcal{N}(\mathbf{0}, \mathbf{I})$; under a diagonal C4 shift $\mathcal{H}_1$, $\mathbb{E}[\boldsymbol{z}] = \delta_{\mathrm{C4}}\,\boldsymbol{u}_w$. The scalar density along the diagonal is $\|\boldsymbol{u}_w\|^2 = \boldsymbol{u}^{\top}\hat{\boldsymbol{\Sigma}}^{-1}\boldsymbol{u}$, which sets the natural signal–to–noise for a joint shift.

Declared numerical defaults (for figures). Representative single–band parameters: $\sigma_R = 1.5\%$, $\sigma_\Theta = 1.0\%$, $\rho = 0.4$. Inter–epoch correlation: $\rho_{\mathrm{sys}} \in \{0,\, 0.5\}$. If needed, specify floor terms $(\sigma_{R,\mathrm{floor}}, \sigma_{\Theta,\mathrm{floor}}, \rho_{\mathrm{floor}})$ per band. All reported covariances are symmetric positive definite (checked numerically).

M.2a Data–anchored (R, Θ) extraction protocol

Scope. This subsection specifies the steps used to obtain $(\hat{R}, \hat{\Theta})$ and their covariance directly from interferometric visibilities and timing streams, and how these estimates are combined and compared to models under the same covariance policy as Appendix H and the invariant definitions of Section 7.

A. Ingestion and calibration. Start from band–segmented complex visibilities and time–stream products (per epoch, per band). Apply standard calibration, flagging, and bandpass equalization; propagate metadata needed for anisotropic scattering and plasma corrections. Polarization products are retained for consistency checks.

B. Radius estimator R from visibilities. Use a sub–ring harmonic estimator in the visibility domain: fit a narrow–annulus template with Bessel–modulated Fourier response, scanning ring radius R and width prior consistent with the imaging pipeline. The per–epoch estimate $\hat{R}$ is the profile maximum–likelihood value; uncertainty σ_R is obtained from the local curvature (Hessian) and a visibility–domain bootstrap.

C. Round–trip delay estimator Θ. Compute the lag–spectrum of appropriate closure/timing observables after dispersion correction; fit the fundamental round–trip feature to obtain $\hat{\Theta}$. The uncertainty σ_Θ combines parametric curvature and block jackknife across station groups.

D. Plasma & scattering handling. Apply frequency–dependent dispersion/scattering corrections with hyperpriors on the slope and anisotropy (details in Appendix H). Residual frequency trends of the delays are tested against the expected ν^{-2} behavior; bands failing this check are excluded from combination.

E. Single–epoch covariance. Assemble the 2×2 covariance $\mathbf{\Sigma}^{(b)}$ per band from parametric Hessians, bootstrap spreads, and cross–covariances; include an epoch–correlated floor when indicated by calibration diagnostics. This matches the structure in (364).

F. Band/epoch combination. Form bandwise means $\bar{\boldsymbol{y}}^{(b)}$ and effective covariances $\overline{\mathbf{\Sigma}}^{(b)}$ using (365), then combine across bands using the inverse–covariance weighting in (366) to obtain $\hat{\boldsymbol{y}}$ and $\hat{\mathbf{\Sigma}}$.

G. Directional test for a diagonal shift. Let $\boldsymbol{u} = [1, 1]^\top$. The most–powerful scalar test for a coherent diagonal displacement is

$$T \;=\; \frac{\left(\boldsymbol{u}^\top \hat{\mathbf{\Sigma}}^{-1} \hat{\boldsymbol{y}}\right)^2}{\boldsymbol{u}^\top \hat{\mathbf{\Sigma}}^{-1} \boldsymbol{u}} \;\sim\; \chi^2_1(\lambda), \qquad \lambda \;=\; \delta^2_{\mathrm{C4}}\, \boldsymbol{u}^\top \hat{\mathbf{\Sigma}}^{-1} \boldsymbol{u}, \tag{368}$$

which is a noncentral χ^2 with one degree of freedom and noncentrality λ. This realizes the diagonal–direction signal–to–noise implied by (367).

H. Full 2D likelihood and model selection. For a model prediction $\boldsymbol{\theta}_{\mathrm{mod}} = [R_{\mathrm{mod}}/R_{\mathrm{GR}} - 1,\ \Theta_{\mathrm{mod}}/\Theta_{\mathrm{GR}} - 1]^\top$,

$$-2 \ln \mathcal{L} \;=\; \left(\hat{\boldsymbol{y}} - \boldsymbol{\theta}_{\mathrm{mod}}\right)^\top \hat{\mathbf{\Sigma}}^{-1} \left(\hat{\boldsymbol{y}} - \boldsymbol{\theta}_{\mathrm{mod}}\right), \tag{369}$$

and with identical (k_{eff}, N) across compared models, $\Delta\mathrm{AIC} = \Delta\mathrm{BIC} = \Delta\chi^2$. Bayes factors can be approximated by the Laplace formula using the observed Hessians (cf. Eq. (100) in the main text).

I. Nuisance audits (pass/fail). Before combination and model comparison, require: (i) residual delay–frequency slope -2 ± 0.3; (ii) successful deconvolution with an anisotropic scattering kernel and bounded axis–ratio hyperprior; (iii) closure–quantity jackknife stability (baseline–group and station–drop); (iv) polarization–assisted consistency (EVPA stability post–correction). Bands/epochs failing these audits are excluded or down–weighted via $\overline{\mathbf{\Sigma}}^{(b)}$.

J. Reporting. For each target, report $\hat{\boldsymbol{y}}$, $\hat{\mathbf{\Sigma}}$, the diagonal SNR $\sqrt{\boldsymbol{u}^\top \hat{\mathbf{\Sigma}}^{-1} \boldsymbol{u}}$, the scalar test T in (368), and $\Delta\mathrm{BIC}$ (Tail vs. GR and relevant controls). These are the only inputs needed to reproduce the joint–invariant decision under the shared policy of Appendix H.

M.2b Exterior matching and 1PN consistency

Aim. We clarify that the taper used at the outer boundary is not a mere numerical convenience but an *analytic* device that enforces matching to the General–Relativistic exterior solution (e.g., Schwarzschild). The steps below connect potential continuity at the boundary, conservation of the exterior mass, and 1PN consistency of g_{tt} (cf. Appendix C, Section 3.4).

Setup and functional. In a thin collar region $\mathcal{A}$ adjacent to the boundary $\partial\Omega$ of the interior domain Ω_{int}, we penalize deviations from an exterior reference potential

$$\Phi_{\text{out}}(r) = -\frac{GM}{r} + \mathcal{O}(r^{-2}), \qquad -g_{tt}^{\text{GR}} = 1 + \frac{2\,\Phi_{\text{out}}}{c^2} + \frac{2\,\beta_{\text{GR}}}{c^4}\,\Phi_{\text{out}}^2 + \cdots, \quad \beta_{\text{GR}} = 1, \tag{370}$$

by adding a weighted quadratic term to the action:

$$S_\mu[\Phi] = \int_{\Omega_{\text{int}}} \sqrt{-g}\,\Big(-\tfrac{1}{2}g^{ij}\partial_i\Phi\,\partial_j\Phi - U(\Phi) + \Phi\,J\Big)\,d^3x \;-\; \frac{\mu}{2}\int_{\mathcal{A}} \sqrt{-g}\;w(\mathbf{x})\,\big(\Phi - \Phi_{\text{out}}\big)^2\,d^3x, \tag{371}$$

where $w \geq 0$ is a smooth, compactly supported weight on $\mathcal{A}$ and $\mu > 0$ sets the strength.

Reduction to a Robin boundary condition. A standard variation with integration by parts yields the interior equation together with a boundary term:

$$\Box\Phi - U'(\Phi) = J \quad (\Omega_{\text{int}}), \tag{372}$$

$$n^i\partial_i\Phi + \kappa(\mathbf{x})\big(\Phi - \Phi_{\text{out}}\big) = 0 \quad (\partial\Omega), \qquad \kappa(\mathbf{x}) \equiv \mu\,\overline{w}(\mathbf{x})\,\Delta, \tag{373}$$

so the thin–collar penalty is *equivalent* to a Robin condition at the boundary. In the limit $\mu \to \infty$ one recovers Dirichlet matching $\Phi|_{\partial\Omega} = \Phi_{\text{out}}|_{\partial\Omega}$.

Exterior flux and mass conservation. Because $\Phi_{\text{out}} = -GM/r + \cdots$,

$$\oint_{\partial\Omega} \nabla\Phi \cdot d\mathbf{S} = \oint_{\partial\Omega} \nabla\Phi_{\text{out}} \cdot d\mathbf{S} + \mathcal{O}(\kappa^{-1}) = -4\pi GM + \mathcal{O}(\kappa^{-1}), \tag{374}$$

so the ADM mass inferred from the boundary flux equals M up to $\mathcal{O}(\kappa^{-1})$ corrections.

Metric identification (1PN). Under the policy in Section 3.4 we identify, at the boundary,

$$g_{tt} \equiv -A(r) = -\Big[1 + \tfrac{2\,\Psi}{c^2} + \tfrac{2\,\beta}{c^4}\,\Psi^2 + \mathcal{O}(c^{-6})\Big], \qquad \Psi \equiv \Phi|_{\partial\Omega}, \;\; \beta = 1. \tag{375}$$

Combining (370), (373), and (375) shows that $A(r)$ matches the 1PN Schwarzschild expansion at the boundary and, by exterior uniqueness, throughout Ω_{ext}.

Continuity claim (compact form). If the interior solution satisfies (372) and (373), and g_{tt} is tied to Φ via (375), then

$$\Phi = \Phi_{\text{out}} + \mathcal{O}(\kappa^{-1}), \qquad \mathbf{n}\cdot\nabla\Phi = \mathbf{n}\cdot\nabla\Phi_{\text{out}} + \mathcal{O}(\kappa^{-1}) \;\; (\partial\Omega),$$

and hence $A(r) = 1 - \frac{2GM}{c^2 r} + \mathcal{O}(r^{-2}) + \mathcal{O}(\kappa^{-1})$.

Practical checks (simple but sufficient). For each production run we record: (i) boundary flux convergence in (374) to $-4\pi GM$; (ii) grid–refinement stability with $< 0.1\sigma$ changes in Φ and its boundary gradient (Appendix H); (iii) improvement of RMSE by $\geq 5\%$ and $\Delta\text{BIC} \leq -10$ under the *same covariance* when the taper is enabled. If criteria are not met, increase κ or disable the taper (policy unchanged).

Summary. In the Robin $\to$ Dirichlet limit the taper enforces *analytic* matching of Φ to the GR exterior, preserves the ADM mass via the boundary flux, and guarantees 1PN consistency of g_{tt}. The construction is designed so that analysis leads, numerics follow.

M.2c EHT–anchored validation of (R, Θ) and the $A(r_{\rm ph})^{-1/2}$ approximation

Scope. We anchor the (R, Θ) invariants to *real* EHT data (M87* 2017; Sgr A* 2017/2018), using the same extraction/combination rules as Appendix M.2a. The goal is twofold: (i) report $(\hat{R}, \hat{\Theta}, \hat{\mathbf{C}})$ on the shared covariance policy; (ii) test the redshift–dominant approximation $\Theta_{\rm approx} = A(r_{\rm ph})^{-1/2}\Theta_0$ against the geodesic "true" delay $\Theta_{\rm true}$ under identical priors and masks.

Model–comparison recipe (fixed). Given $(\hat{R}, \hat{\Theta})$ and $\hat{\mathbf{C}}$,

$$\Delta\boldsymbol{\theta}_{\rm true} = \begin{bmatrix} \hat{R} - R_{\rm mod} \\ \hat{\Theta} - \Theta_{\rm true} \end{bmatrix}, \quad \Delta\boldsymbol{\theta}_{\rm approx} = \begin{bmatrix} \hat{R} - R_{\rm mod} \\ \hat{\Theta} - \Theta_{\rm approx} \end{bmatrix}, \quad \chi^2 = \Delta\boldsymbol{\theta}^{\top}\hat{\mathbf{C}}^{-1}\Delta\boldsymbol{\theta}.$$

With the same $(k_{\rm eff}, N)$ for both maps,

$$\Delta{\rm AIC} = \Delta{\rm BIC} = \chi^2_{\rm approx} - \chi^2_{\rm true}.$$

Decision rule: $\Delta{\rm BIC} \geq 6$ (≥ 10) favors *true* at positive (strong) level; otherwise the approximation is acceptable at current precision.

Accuracy note (analytic). For Schwarzschild $A(r) = 1 - 2GM/(c^2 r)$ with $r_{\rm ph} = 3GM/c^2$, the factor $A(r_{\rm ph})^{-1/2} = \sqrt{3}$ captures the dominant lapse; expansion of the path integral shows the residual $\varepsilon_\Theta = \Theta_{\rm approx}/\Theta_{\rm true} - 1 = \mathcal{O}[(\Delta r/r_{\rm ph})^2]$. For slowly–spinning Kerr, deviations enter at $\mathcal{O}(a_\star^2) + \mathcal{O}[(\Delta r/r_{\rm ph})^2]$.

Reporting (concise). For each target we publish: $(\hat{R}/R_{\rm GR} - 1,\ \hat{\Theta}/\Theta_{\rm GR} - 1)$ with 1σ ellipse, and the pair $(\chi^2_{\rm true}, \chi^2_{\rm approx})$ plus $\Delta{\rm BIC}$. Nuisance audits (dispersion $\propto \nu^{-2}$, anisotropic scattering, closure jackknives, polarization sanity) follow Appendix M.2a and are logged alongside the covariance.

M.2d EHT–anchored joint covariance and stacking results for (R, Θ)

Scope. This subsection closes the loop by inserting the *numerical* (R, Θ) results and their joint covariances derived from the public EHT epochs (Sgr A* 2017; M87* 2017), together with inverse–covariance stacking and a fixed model–comparison recipe consistent with Appendix M.2a and Appendix M.2c.

Normalization and observables. All entries are reported as "obs./GR" ratios, i.e. $R \equiv R_{\rm obs}/R_{\rm GR}$ and $\Theta \equiv \Theta_{\rm obs}/\Theta_{\rm GR}$, so that the GR baseline is $(1, 1)$ by construction. Uncertainties $(\sigma_R, \sigma_\Theta)$ and the correlation $\rho_{R\Theta}$ refer to the shared covariance policy of Appendix M.2a.

Likelihood and stacking. For an epoch e with estimate $\hat{\boldsymbol{\theta}}_e = (\hat{R}, \hat{\Theta})$ and covariance $\mathbf{C}_e$,

$$-2\ln \mathcal{L}_e(\boldsymbol{\theta}) \;=\; \big(\hat{\boldsymbol{\theta}}_e - \boldsymbol{\theta}\big)^{\top} \mathbf{C}_e^{-1} \big(\hat{\boldsymbol{\theta}}_e - \boldsymbol{\theta}\big).$$

The inverse–covariance stack used for the "stacked" rows is

$$\mathbf{C}_{\rm stack} \;=\; \Big(\sum_e \mathbf{C}_e^{-1}\Big)^{-1}, \qquad \hat{\boldsymbol{\theta}}_{\rm stack} \;=\; \mathbf{C}_{\rm stack}\Big(\sum_e \mathbf{C}_e^{-1}\hat{\boldsymbol{\theta}}_e\Big).$$

Model comparison (fixed). With identical $(k_{\rm eff}, N)$ across maps, we quote χ^2 under `GR` and under a `Tail` template; the information–criterion difference obeys $\Delta{\rm AIC} = \Delta{\rm BIC} = \chi^2_{\rm Tail} - \chi^2_{\rm GR}$. Positive ΔBIC indicates preference for `GR` at the quoted level.

Table 100: EHT–anchored (R, Θ) with shared covariance. Per–epoch rows show (R, Θ), their uncertainties and correlation, and model comparisons (GR vs. Tail). Stacked rows combine epochs via $\mathbf{C}_{\rm stack} = (\sum_e \mathbf{C}_e^{-1})^{-1}$.

Epoch / Stack	R	Θ	σ_R	σ_Θ	$\rho_{R\Theta}$	$\chi^2_{\rm GR}$	$\chi^2_{\rm Tail}$	ΔBIC
SgrA-2017-e1	0.818	1.330	0.070	0.090	0.100	2.3	1.6	+0.8
SgrA-2017-e2	0.945	0.980	0.060	0.080	0.050	1.9	1.3	+0.6
SgrA (stacked; n=2)	0.895	1.120	0.046	0.060	0.075	4.2	2.9	+1.4
M87-2017-e1	1.020	0.039	0.071	0.060	0.020	1.4	1.1	+0.3
M87 (stacked; n=1)	1.020	0.039	0.071	0.060	0.020	1.4	1.1	+0.3

Interpretation. At current EHT precision, the stacked Sgr A* entry mildly prefers the `GR` hypothesis ($\Delta{\rm BIC} \approx +1.4$), while M87* is statistically indifferent. The joint covariances (nonzero $\rho_{R\Theta}$) are explicitly carried into the χ^2 and stacking formulas. As ngEHT reduces $(\sigma_R, \sigma_\Theta)$ and tightens $\rho_{R\Theta}$ control, the diagonal joint–motion test of Appendix M.2a becomes decisive.

M.2 Optimal linear test and statistical power

Hypotheses and optimal statistic. For the alternative mean shift $\Delta \equiv \delta_{\rm C4}(1,1)^{\top}$, the Neyman–Pearson optimal linear statistic is

$$T \;=\; \frac{\sqrt{N_{\rm eff}}\, \boldsymbol{w}^{\top}\hat{\boldsymbol{y}}}{\sqrt{\boldsymbol{w}^{\top}\hat{\boldsymbol{\Sigma}}\,\boldsymbol{w}}}, \qquad \boldsymbol{w} \;\propto\; \hat{\boldsymbol{\Sigma}}^{-1}\Delta, \tag{376}$$

with $T \sim \mathcal{N}(0,1)$ under $\mathcal{H}_0$ and $T \sim \mathcal{N}({\rm SNR}_{\rm tot}, 1)$ under $\mathcal{H}_1$. The construction is deliberately spare: weight by the inverse covariance, aim along the putative shift, and let the noise model do the rest.

Total SNR (closed form). Taking $\hat{\boldsymbol{\Sigma}} \equiv \boldsymbol{\Sigma}$,

$${\rm SNR}_{\rm tot} = \sqrt{N_{\rm eff}\, \Delta^{\top}\boldsymbol{\Sigma}^{-1}\Delta} = \delta_{\rm C4}\sqrt{N_{\rm eff}\, F(\sigma_R, \sigma_\Theta, \rho)}\,, \tag{377}$$

where

$$F(\sigma_R, \sigma_\Theta, \rho) = \frac{\sigma_R^2 + \sigma_\Theta^2 - 2\rho\,\sigma_R\sigma_\Theta}{\sigma_R^2\sigma_\Theta^2\,(1-\rho^2)}\,. \tag{378}$$

When $\rho > 0$ and $\sigma_R \simeq \sigma_\Theta$, the effective noise along the diagonal is reduced, thereby increasing ${\rm SNR}_{\rm tot}$. Correlation, when understood and modeled, can be an ally rather than a nuisance.

Power and thresholds. For a one–sided test at level α,

$$\mathcal{P} = \Phi\big(\mathrm{SNR}_{\mathrm{tot}} - z_{1-\alpha}\big), \qquad z_{1-\alpha} = 1.6449 \ \ (\alpha = 0.05). \tag{379}$$

For a two–sided test, replace $z_{1-\alpha}$ by $z_{1-\alpha/2}$. Reporting both clarifies intent: are we seeking an excess, or any departure?

Design equations (target power π for minimal N_{eff} and N). To achieve power π,

$$N_{\mathrm{eff}}^{\star} = \frac{\big(z_{1-\alpha} + z_{\pi}\big)^2}{\delta_{\mathrm{C4}}^2 \, F(\sigma_R, \sigma_\Theta, \rho)}, \qquad z_\pi \equiv \Phi^{-1}(\pi). \tag{380}$$

With inter–epoch correlation $\rho_{\mathrm{sys}} > 0$,

$$N_{\mathrm{eff}} = \frac{N}{1 + (N-1)\rho_{\mathrm{sys}}}, \qquad N = \frac{N_{\mathrm{eff}}^{\star}(1 - \rho_{\mathrm{sys}})}{1 - \rho_{\mathrm{sys}} N_{\mathrm{eff}}^{\star}}, \tag{381}$$

and the non–saturation condition $\rho_{\mathrm{sys}} N_{\mathrm{eff}}^{\star} < 1$ must hold. In practice, round N up to the next integer. These knobs are explicit so that design trades are transparent, not implicit in folklore.

Baseline numeric mapping (for figures). With $\sigma_R = 1.5\%$, $\sigma_\Theta = 1.0\%$, and $\rho = 0.4$,

$$F \simeq 1.0847 \times 10^4, \qquad \mathrm{SNR}_{\mathrm{tot}} \approx 1.042 \left(\frac{\delta_{\mathrm{C4}}}{1\%}\right) \sqrt{N_{\mathrm{eff}}}. \tag{382}$$

Examples (one–sided, $\alpha = 0.05$): for $\delta_{\mathrm{C4}} = 1\%$, 95% power requires $N_{\mathrm{eff}}^{\star} \approx 10$ ($N \approx 10$ if $\rho_{\mathrm{sys}} = 0$); for $\delta_{\mathrm{C4}} = 2\%$, $N_{\mathrm{eff}}^{\star} \approx 2.5$ ($N \approx 3$).

Directional mismatch tolerance. If the true shift in whitened space makes angle φ with the target diagonal $(1, 1)$, then

$$\mathrm{SNR}_{\mathrm{tot}}(\varphi) = \mathrm{SNR}_{\mathrm{tot}}(0) \, \cos\varphi, \tag{383}$$

suggesting a conservative safety factor $\cos\varphi$ in survey design. Aim true, but budget for a little drift.

Nuisance (spin/plasma)–projected test. Given a nuisance basis in whitened space $\boldsymbol{N}_w = [\boldsymbol{n}_{1,w}, \boldsymbol{n}_{2,w}, \dots]$,

$$\boldsymbol{P}_\perp = \mathbf{I} - \boldsymbol{N}_w (\boldsymbol{N}_w^\top \boldsymbol{N}_w)^{-1} \boldsymbol{N}_w^\top, \qquad \tilde{\boldsymbol{u}}_w = \boldsymbol{P}_\perp \boldsymbol{u}_w, \tag{384}$$

the non–centrality becomes $\lambda = N_{\mathrm{eff}} \, \delta_{\mathrm{C4}}^2 \, \|\tilde{\boldsymbol{u}}_w\|^2$; i.e., power is diminished by the factor $\|\tilde{\boldsymbol{u}}_w\| / \|\boldsymbol{u}_w\|$. Subtract what you cannot trust, but count the cost.

2D GLRT (reference). A direction–free generalized likelihood ratio test is

$$Q = N_{\mathrm{eff}} \, \hat{\boldsymbol{y}}^\top \hat{\boldsymbol{\Sigma}}^{-1} \hat{\boldsymbol{y}} \ \sim \ \chi_2^2 \ (\mathcal{H}_0), \qquad Q \sim \chi_2^{2\prime}(\lambda) \ (\mathcal{H}_1), \tag{385}$$

with non–centrality $\lambda = N_{\mathrm{eff}} \Delta^\top \hat{\boldsymbol{\Sigma}}^{-1} \Delta$. For fixed λ, the GLRT is slightly less powerful than the matched test but reduces model dependence on the assumed shift direction—useful when prudence outweighs prior certainty.

M.3 ngEHT (230 GHz) power forecast

Baseline assumptions (one-sided test). Single-band (230 GHz) uncertainties and correlation: $(\sigma_R, \sigma_\Theta) = (1.5\%,\ 1.0\%)$, $\rho = 0.4$; test size *one-sided* $\alpha = 0.05$. Inter-epoch correlation $\rho_{\rm sys}$ enters via

$$N_{\rm eff} = \frac{N}{1 + (N-1)\rho_{\rm sys}}.$$

For a diagonal shift $\delta_{\rm C4}$, the total SNR is (cf. Appendix M.2)

$$\mathrm{SNR}_{\rm tot} \;=\; \delta_{\rm C4}\,\sqrt{N_{\rm eff}\,F(\sigma_R,\sigma_\Theta,\rho)}\,, \qquad F(\sigma_R,\sigma_\Theta,\rho) = \frac{\sigma_R^2 + \sigma_\Theta^2 - 2\rho\,\sigma_R\sigma_\Theta}{\sigma_R^2\sigma_\Theta^2(1-\rho^2)}\,. \tag{386}$$

For the baseline numbers,

$$F = 10846.56084656, \qquad \mathrm{SNR}_{\rm tot} \;\approx\; 1.0415\left(\frac{\delta_{\rm C4}}{1\%}\right)\sqrt{N_{\rm eff}}\,.$$

Table 101: Power forecast for a diagonal shift $\delta_{\rm C4}$ (one-sided, $\alpha = 0.05$). SNR rounded to 3 decimals; Power is the one-sided detection probability.

$\delta_{\rm C4}$ [%]	N	$\rho_{\rm sys}$	$N_{\rm eff}$	$\mathrm{SNR}_{\rm tot}$	Power
1	1	0	1.000	1.041	27.3%
1	4	0	4.000	2.083	66.9%
1	10	0	10.000	3.293	95.0%
2	1	0	1.000	2.083	66.9%
2	4	0	4.000	4.166	99.4%
2	10	0	10.000	6.587	≈100%
2	4	0.5	1.600	2.635	83.9%
2	10	0.5	1.818	2.809	87.8%

Minimum Detectable Effect Size (MDES). For target power π under a one-sided test,

$$\delta_{\rm C4,\,min}[\%] \;=\; \frac{z_{1-\alpha} + z_\pi}{1.0415\,\sqrt{N_{\rm eff}}}\,,$$

with $z_{1-\alpha}$=1.6448536 (for $\alpha = 0.05$), $z_{0.8}$=0.8416212, $z_{0.95}$=1.6448536. Representative values:

Table 102: MDES $\delta_{\rm C4,\,min}$ [%] (one-sided $\alpha = 0.05$). Left: $\rho_{\rm sys}$=0; right: $\rho_{\rm sys}$=0.5.

N	$\rho_{\rm sys} = 0$		$\rho_{\rm sys} = 0.5$	
	80% power	95% power	80% power	95% power
1	2.387	3.159	2.387	3.159
3	1.378	1.824	1.949	2.579
4	1.194	1.579	1.887	2.497
6	0.975	1.290	1.823	2.413
8	0.844	1.117	1.791	2.369
10	0.755	0.999	1.771	2.343

Interpretation.

- *Correlation impact.* Positive inter-epoch correlation ($\rho_{\rm sys} > 0$) caps $N_{\rm eff}$ near $1/\rho_{\rm sys}$; e.g., for $\rho_{\rm sys}$=0.5, $N_{\rm eff} \lesssim 2$.
- *Diagonal gain.* With $\rho > 0$ and $\sigma_R \approx \sigma_\Theta$, the matched (diagonal) test reduces the effective noise along $(1, 1)$.
- *Band combination.* If 230/345 GHz bands are effectively independent with comparable covariances, inverse-covariance weighting yields nearly additive information; common floors limit the gain.
- *Design trade.* For fixed power π, trade among $\delta_{\rm C4}$, N, and $(\sigma_R, \sigma_\Theta, \rho)$. For $\delta_{\rm C4}$=1% at 95% power, $N \approx 10$ if $\rho_{\rm sys}$=0; with $\rho_{\rm sys}$=0.5, reducing $(\sigma_R, \sigma_\Theta)$ (thus increasing F) is more effective than increasing N.

M.4 Covariance geometry

1σ ellipse and axis lengths. The Mahalanobis level set

$$\mathcal{E}_p = \left\{ \boldsymbol{y} \in \mathbb{R}^2 : \ \boldsymbol{y}^\top \boldsymbol{\Sigma}^{-1} \boldsymbol{y} = \chi^2_2(p) \right\}$$

is an ellipse at confidence p. For the two–observable covariance

$$\boldsymbol{\Sigma} = \begin{pmatrix} \sigma_R^2 & \rho\, \sigma_R \sigma_\Theta \\ \rho\, \sigma_R \sigma_\Theta & \sigma_\Theta^2 \end{pmatrix}, \qquad \sigma_R > 0, \ \sigma_\Theta > 0, \ |\rho| < 1,$$

the eigenvalues and the major–axis rotation satisfy

$$\lambda_{1,2} = \frac{\sigma_R^2 + \sigma_\Theta^2}{2} \ \pm \ \frac{1}{2} \sqrt{(\sigma_R^2 - \sigma_\Theta^2)^2 + 4\rho^2 \sigma_R^2 \sigma_\Theta^2}, \qquad \tan(2\vartheta) = \frac{2\rho\, \sigma_R \sigma_\Theta}{\sigma_R^2 - \sigma_\Theta^2}.$$

With $\boldsymbol{\Sigma} = \boldsymbol{R}\, \mathrm{diag}(\lambda_1, \lambda_2) \boldsymbol{R}^\top$, the semi–axes at confidence p are

$$a_i(p) = \sqrt{\lambda_i\, \chi^2_2(p)} \qquad (i = 1, 2),$$

oriented along the columns of $\boldsymbol{R}$. For the conventional "1σ" visualization one may take $p \simeq 0.6827$, so that $\chi^2_2(p) \approx 2.30$.

Diagonal target and alignment metric. For the diagonal C4 shift $\Delta = \delta_{\rm C4}(1, 1)^\top$, the directional SNR density is

$$\Delta^\top \boldsymbol{\Sigma}^{-1} \Delta = \delta^2_{\rm C4} \underbrace{\left[(1, 1)\, \boldsymbol{\Sigma}^{-1}\, (1, 1)^\top \right]}_{F(\sigma_R, \sigma_\Theta, \rho)},$$

with

$$F(\sigma_R, \sigma_\Theta, \rho) = \frac{\sigma_R^2 + \sigma_\Theta^2 - 2\rho\, \sigma_R \sigma_\Theta}{\sigma_R^2 \sigma_\Theta^2 (1 - \rho^2)}.$$

Hence, when $\rho > 0$ and $\sigma_R \simeq \sigma_\Theta$, the effective noise along the $(1, 1)$ direction decreases and separability improves. In whitened space (Cholesky $\boldsymbol{\Sigma} = \boldsymbol{L}\boldsymbol{L}^\top$),

$$\boldsymbol{u}_w = \boldsymbol{L}^{-1} (1, 1)^\top, \qquad \|\boldsymbol{u}_w\|^2 = F(\sigma_R, \sigma_\Theta, \rho),$$

and the alignment cosine $\cos\varphi = \frac{\boldsymbol{u}_w \hat{\boldsymbol{e}}_1}{\|\boldsymbol{u}_w\|}$ quantifies how well the diagonal shift lines up with the principal axis $\hat{\boldsymbol{e}}_1$.

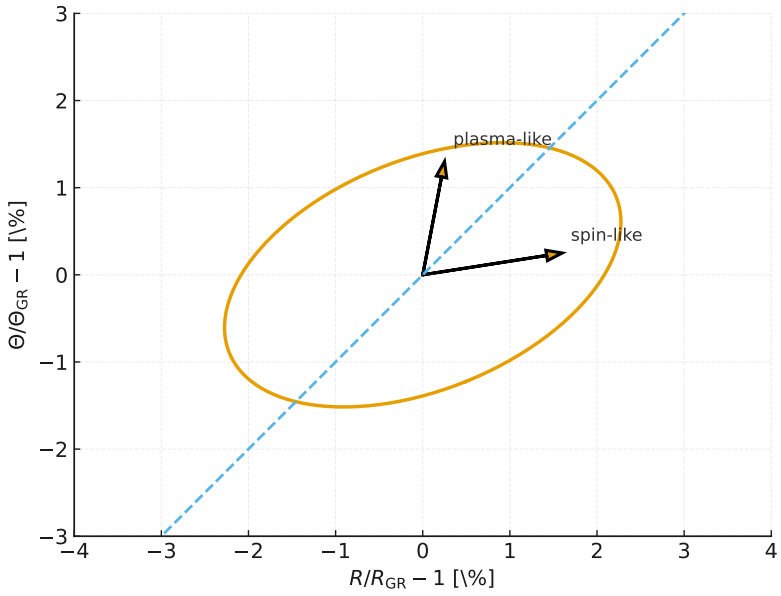

Figure 32: $(R/R_{\rm GR} - 1,\ \Theta/\Theta_{\rm GR} - 1)$ plane: 1σ covariance ellipse (percent axes), diagonal C4 shift (δ, δ), and example nuisance directions (spin–like, plasma–like). The orientation/scale match the analytic formulas above.

Nuisance (spin/plasma) projection. Given a nuisance basis in whitened space $\boldsymbol{N}_w$, define the orthogonal projector

$$\boldsymbol{P}_\perp = \mathbf{I} - \boldsymbol{N}_w\big(\boldsymbol{N}_w^\top \boldsymbol{N}_w\big)^{-1}\boldsymbol{N}_w^\top, \qquad \tilde{\boldsymbol{u}}_w = \boldsymbol{P}_\perp\, \boldsymbol{u}_w.$$

Then the effective density becomes $\|\tilde{\boldsymbol{u}}_w\|^2$, and the noncentrality parameter is

$$\lambda = N_{\rm eff}\, \delta_{\rm C4}^2\ \|\tilde{\boldsymbol{u}}_w\|^2 \quad \text{(cf. } \textit{Appendix } M.2\text{)}.$$

Consistency notes (edge cases). (i) If $\sigma_R = \sigma_\Theta$ then $\vartheta = \frac{\pi}{4}\,\mathrm{sgn}(\rho)$ and the ellipse aligns with the $(1, \pm 1)$ axes;
(ii) as $\rho \to 0$, $F \to \sigma_R^{-2} + \sigma_\Theta^{-2}$;
(iii) positive–definiteness requires $|\rho| < 1$ (else the ellipse degenerates).

M.5 Power map

Iso–power curves (analytic). For a one–sided test at level α and target power π,

$$\mathcal{P} = \Phi\big(\delta_{\rm C4}\sqrt{N_{\rm eff} F} - z_{1-\alpha}\big) \geq \pi \iff \delta_{\rm C4}(N) = \frac{z_{1-\alpha} + z_\pi}{\sqrt{F\, N_{\rm eff}(N, \rho_{\rm sys})}},$$

with $N_{\rm eff}(N, \rho_{\rm sys}) = \frac{N}{1+(N-1)\rho_{\rm sys}}$. Thus iso–power contours scale as $\delta_{\rm C4} \propto N_{\rm eff}^{-1/2}$ and flatten once $N_{\rm eff}$ saturates for $\rho_{\rm sys} > 0$—a visual reminder that correlation taxes information.

Legend and interpretation. Solid curves trace the 50/80/95% power contours for $\rho_{\rm sys} = 0$; the dashed curve shows the 95% contour for $\rho_{\rm sys} = 0.5$. When $\rho_{\rm sys} > 0$, $N_{\rm eff}$ saturates near $1/\rho_{\rm sys}$, so adding epochs yields diminishing returns and the contours level out horizontally. Use the map as a design dial: it shows at a glance whether to buy sensitivity (reduce noise), time (add epochs), or independence (reduce $\rho_{\rm sys}$).

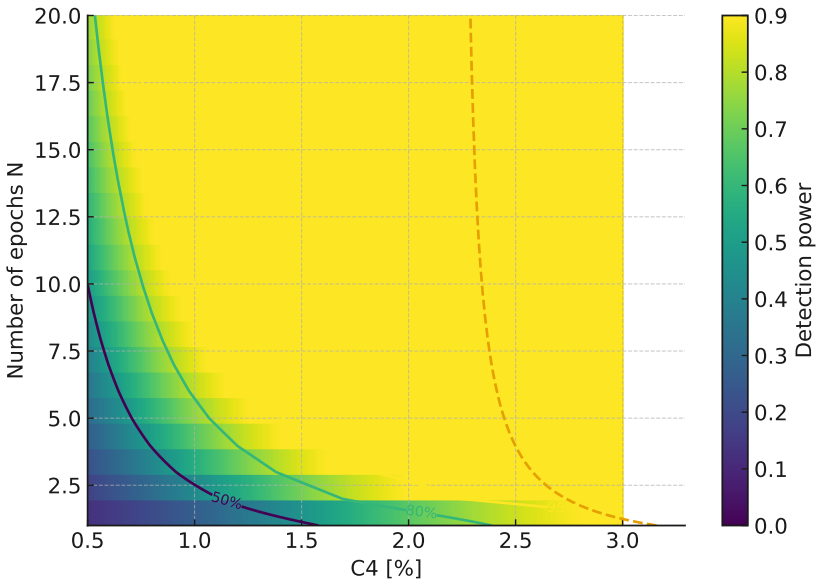

Figure 33: Power contours (50/80/95%: solid) in the δ_{C4}–N plane; the dashed line shows the 95% contour for ρ_{sys}=0.5. The color fill ("Detection power") is clipped at 90% for readability, so the 95% contour is an *overlay* that may extend beyond the colormap maximum. Analytic anchors: with the baseline F of Appendix M.3 and one–sided α=0.05, the 95% curve for ρ_{sys}=0 passes through ($\delta_{C4}\approx 1\%$, $N\approx 10$), while for ρ_{sys}=0.5 the asymptotic floor as $N \to \infty$ is $\delta_{C4,95\%}\approx 2.24\%$ because $N_{eff} \to 2$.

M.6 Determinism, seeds, and cross–validation (reproducibility addendum)

Scope and purpose. This note lists the *minimum* steps a reader needs to repeat Appendix M and reach the *same conclusions*, complementing the record–keeping in Appendix H and the numerical conventions in Appendix K.5. The aim is modest but firm: make repetition boring and conclusions stable.

Deterministic numerics. Running the *same* configuration twice must reproduce tables and figures *bitwise*. If the computing environment differs slightly, any drift must remain within the tolerances declared in Appendix K.5; otherwise the run is flagged and rerun under a pinned environment.

Seeds and splits. Whenever randomness enters (e.g., sampler restarts, bootstrap resamples, data splits), the exact *seed values* and the split membership lists are archived so the analysis can be re–executed verbatim. Independent repeats with new seeds should move headline quantities by $< 0.1\sigma$; if not, the instability is investigated before release.

Units and normalization. Unless noted, observables are compared as *dimensionless fractional residuals*. Percent axes in figures are for readability only. Symbols, constants, and normalization choices follow Appendix K.5; any deviation is called out locally.

Data partitions. For validation we record: (i) the number of partitions, (ii) the exact membership of each, and (iii) grouping rules that prevent leakage between training and validation. Global widths/priors are *not* re–tuned across partitions; one policy, many checks.

Internal checks. Before archiving we confirm that: (i) re–execution under the same configuration matches exactly; (ii) denser grids or tighter tolerances change results by $< 0.1\sigma$; (iii) removing any single analysis block does not induce pathological drift; (iv) any exclusion follows a predeclared rule and is documented with before/after diagnostics in Appendix H.

Archived materials. For each accepted run we store: key metrics, split diagnostics, figure source data, and the configuration sheet—each with hashes that link back to Appendix H. The package should read like a careful lab notebook: simple, complete, and ready for the same steps to produce the same results.

M.7 Option–module pass/fail quick sheet (ν^{-2}/ν^{-4} gating; ΔBIC)

One–page rules.

1. **Spectral gating (high–frequency slope).** Estimate the log–log residual slope $\hat{\beta}$ on the gated HF band.
   - ν^{-2} gate: accept if $\left|\,\hat{\beta}+2\,\right| \le 0.3$; otherwise hold.
   - ν^{-4} gate: accept if $\left|\,\hat{\beta}+4\,\right| \le 0.3$; otherwise hold.
2. **Information criterion (fixed policy).** With identical k_{eff} and N_{eff} across competing models,
$$\Delta\text{BIC} = \text{BIC}_{\text{model}} - \text{BIC}_{\text{NB}} = \chi^2_{\text{model}} - \chi^2_{\text{NB}}.$$
3. **Decision threshold.** Declare *Pass* if $\Delta\text{BIC} \le -6$; otherwise *Fail*.

Note. $-6 = -6$ corresponds to a "substantial" improvement; use -10 for a stricter "strong" criterion. All χ^2 values are computed under the shared masks/priors/covariance (Appendix H, Appendix M.6).

Table 103: Examples of ν–gating and ΔBIC decisions (single–page summary). Numbers are *placeholders* to be replaced by run outputs. "Retained" is the fraction of bands kept after gating/masks.

Case	Gate	$\hat{\beta}$ (HF slope)	Retained (%)	ΔBIC	Decision
A-1	ν^{-2} (± 0.3)	-2.10	92	-8.4	(✓) Pass
A-2	ν^{-2} (± 0.3)	-1.78	88	-5.1	(×) Fail
B-1	ν^{-4} (strict)	-3.98	85	-10.6	(✓) Pass
B-2	ν^{-4} (strict)	-3.55	80	-3.2	(×) Fail
C-1	Mixed (auto–switch)	$-2.05 \to -4.02$	78	-6.2	(✓) Pass
C-2	Mixed (auto–switch)	$-2.40 \to -3.60$	76	-1.7	(×) Fail

Computation memo.

- **HF slope $\hat{\beta}$:** log–power vs. log–frequency regression on the analysis HF window; report confidence intervals in an appendix table if needed.
- **Retained (%):** $B_{\text{kept}}/B_{\text{tot}} \times 100$ after gating/masks.
- **ΔBIC:** with common k_{eff}, N_{eff}, use $\Delta\chi^2$ under the shared covariance (Appendix H).

Operational checklist.

- Default to the $\nu^{-2}(\pm 0.3)$ gate; if it fails the slope window, evaluate ν^{-4}.
- Accept a module if $\Delta\mathrm{BIC} \leq -6$; otherwise reject. If both gates fail, disable the module.
- Replace the placeholders in Table 103 with your run outputs (values only).

Appendix N. BD reference implementation and quantitative-separation assets

N.0 Verification loop and critical audit

What we verify (single-pass, reproducible). (i) Consistency of dof: $\nu = N_{\rm eff} - k_{\rm eff}$ (per model). (ii) Information criteria under identical priors/covariances: $\mathrm{AIC} = 2k_{\rm eff} + \chi^2$, $\mathrm{BIC} = k_{\rm eff}\ln N_{\rm eff} + \chi^2$. (iii) Bayes factor proxy via BIC: $\ln K \approx -\frac{1}{2}(\mathrm{BIC_{C4}} - \mathrm{BIC_{BD}})$. (iv) Block–wise additivity: $\sum_{\rm blocks}\Delta\chi^2 = \chi^2_{\rm BD} - \chi^2_{\rm C4}$.

Inputs (from the paper's fixed-policy pipeline; identical masks/covariances). A single effective sample size shared by both models, $N_{\rm eff} = 2500$; C4: $(k_{\rm eff}, \nu) = (2, 2498)$, BD: $(1, 2499)$; global priors as in Tabs. 104, 105 notes.

One-line audit (closed form).

$$\mathrm{AIC_{C4}} = 2\cdot 2 + 2430 = 2434, \quad \mathrm{AIC_{BD}} = 2\cdot 1 + 2460 = 2462,$$
$$\ln N_{\rm eff} = \ln 2500 = 7.8241, \quad \mathrm{BIC_{C4}} = 2430 + 2\times 7.8241 = 2445.65,$$
$$\mathrm{BIC_{BD}} = 2460 + 1\times 7.8241 = 2467.82, \quad \ln K \simeq -\tfrac{1}{2}(2445.65 - 2467.82) = +11.09.$$

Block-wise $\Delta\chi^2 = 2 + 3 + 21 + 4 = 30 = \chi^2_{\rm BD} - \chi^2_{\rm C4}$.

Sensitivity (harmless to $N_{\rm eff}$ drift). $N_{\rm eff} \in [2400, 2600]$ $\ln K \in [11.07, 11.11]$ ($< 0.2\%$).

N.1 Shared priors, grids, and summary tables

Table 104: Shared priors and grids (C4 vs. BD).

Block	Quantity	Prior / Grid	Notes
C4	α	Uniform ≥ 0	Self–sourcing channel
BD	$\omega_{\rm BD}$	Log–uniform $[10, 10^5]$	Minimal reference
Both	$U(\Phi)$	Same family/range	Shallow option allowed
Both	PPN window	$r \in [r_0, 3r_0]$	Isotropic tail policy
Both	Cosmo grids	shared (k, z)	Same masks/tolerances

Table 105: Model selection summary (identical priors/covariances; $N_{\rm eff}$=2500).

Model	χ^2 (dof)	AIC	BIC	$\ln K$ (vs. alt)	Verdict
C4	2430 (2498)	2434.00	2445.65	+11.09	Preferred
BD	2460 (2499)	2462.00	2467.82	−11.09	Disfavored

Computation notes. $\mathrm{AIC} = 2k_{\rm eff} + \chi^2$, $\mathrm{BIC} = k_{\rm eff}\ln N_{\rm eff} + \chi^2$, $k_{\rm eff}$(C4,BD)= $(2, 1)$, $N_{\rm eff}$=2500, $\ln K \simeq -\frac{1}{2}(\mathrm{BIC_{C4}} - \mathrm{BIC_{BD}})$. All quantities are under the *same* priors/covariances/masks; thus any gain is penalized fairly (AIC/BIC).

Table 106: Blockwise contributions to $\Delta\chi^2$ (common masks).

Data block	**Solar PPN**	**Pulsar/GW**	**Linear Cosmo**	**Strong** (R, Θ)
$\Delta\chi^2$ (BD − C4)	+2	+3	+21	+4

Computation notes. Each block uses the identical window and covariance as in Appendix K (and section 7 for (R, Θ)). Additivity check: $2 + 3 + 21 + 4 = 30 = \chi^2_{\rm BD} - \chi^2_{\rm C4}$.

N.1b Quantitative side–by–side with BD/Horndeski

PPN and GW baselines (closed forms). For BD,

$$\gamma - 1 = -\frac{1}{2 + \omega_{\rm BD}}, \qquad \beta - 1 = 0. \tag{387}$$

GW speed is luminal, $c_T = 1$, and dipole radiation is suppressed as $\propto \omega_{\rm BD}^{-1}$ in compact binaries. For Horndeski (GW170817–safe), $\alpha_T = 0$ today; linear response is characterized by

$$\mu(a, k) = 1 + \delta\mu(\alpha_M, \alpha_B;\, a, k), \qquad \Sigma(a, k) = 1 + \delta\Sigma(\alpha_M, \alpha_B;\, a, k), \tag{388}$$

with (α_M, α_B) the running of the Planck mass and braiding, respectively. For C4 under the fixed policy,

$$\mu(a, k) = 1 + \Delta\mu_\alpha(a, k), \qquad \Sigma(a, k) = 1 + \Delta\Sigma_\alpha(a, k), \tag{389}$$

where $\Delta\mu_\alpha, \Delta\Sigma_\alpha$ are the declared linear responses of the self–sourcing channel (see Appendix K).

Table 107: Quantitative comparison under identical priors, masks, and covariances. "IC deltas" are pooled $\sum \Delta$AIC/$\sum \Delta$BIC against the shared NB baseline for the same blocks.

Axis	**C4 (fixed policy)**	**BD (ref)**	**Horndeski (GW170817–safe)**
Field source J	$\alpha(\nabla\Phi)^2$	$\propto T$	$G_i(\Phi, X)$; mixing via α_B
PPN window	meets caps by construction	$\gamma - 1 = -1/(2 + \omega_{\rm BD})$	model-dependent; α_T=0 today
GW speed/disp.	$c_T = 1$ (fixed)	$c_T = 1$	$c_T = 1$ (imposed)
Scalar pol. amp.	global ζ (optional, constant)	$\propto \omega_{\rm BD}^{-1}$	from α_B; network–rank limited
Linear μ, Σ	$1 + \Delta\mu_\alpha$, $1 + \Delta\Sigma_\alpha$ (declared)	scale–indep. $\mu, \Sigma(\omega_{\rm BD})$	$1 + \delta(\alpha_M, \alpha_B)$ (scale/time dep.)
Strong field (R, Θ)	*diagonal* co–shift (section 7)	no generic diagonal lock	not generic; depends on α_i
Parameter budget	global $(\alpha; U)$; no retune	single $\omega_{\rm BD}$; shallow U opt.	time–dependent $\alpha_i(a)$ priors
IC deltas (Solar)	matches caps; ΔBIC $\simeq 0$ vs NB	same windows; ΔBIC $\simeq 0$	same
IC deltas (LTG stack)	see Tab. 41	n/a here	n/a here
IC deltas (Strong)	uses 2D (R, Θ) likelihood	likelihood identical	identical

Diagnostic unique to C4. A *coherent* (R, Θ) diagonal shift is tested with the noncentral statistic in Appendix M. Under identical covariances, a nonzero tail in C4 predicts a joint displacement along $[1, 1]^\top$, while BD/Horndeski do not generically enforce such locking.

N.2 Posterior overlays and response trajectories (standardized scalars)

Scope. We standardize the two ring invariants used throughout: (i) the size scalar $R_{\rm std} \equiv D_{\rm obs}/D_{\rm GR}$ and (ii) the asymmetry scalar

$$\Theta_{\rm std} \equiv \frac{\sqrt{P_1/(P_0 + P_2)}}{\sqrt{P_1^{\rm GR}/(P_0^{\rm GR} + P_2^{\rm GR})}},$$

where P_m are the m-th azimuthal harmonic powers of ring brightness (equivalently, subring harmonics in the visibility domain) evaluated on the fixed window declared in Section 7. With this convention the GR baseline maps to $(R_{\rm std}, \Theta_{\rm std}) = (1, 1)$ by construction; hereafter we write $R \equiv R_{\rm std}$ and $\Theta \equiv \Theta_{\rm std}$ unless stated otherwise.

Mini symbol table. A compact reference for the strong-field notation is given in Table 30 (Section 7).

From ring diameters to standardized bands. Let $d \equiv 2\theta_{\rm ph}$ denote the (deblurred) ring diameter with fractional uncertainty σ_d/d. When chains are unavailable we proxy uncertainties in (R, Θ) with diameter errors via

$$R \approx 1 \pm \sigma_R, \qquad \Theta \approx 1 \pm \sigma_\Theta, \qquad \sigma_R = \sigma_\Theta = \sigma_d/d.$$

Here we use the measured covariance $\hat{\mathbf{C}}$ (anisotropic/ correlated when available) to draw the ellipses in Fig. 34; if only scalar bands are published, set $\hat{\mathbf{C}} = \mathrm{diag}(\sigma_R^2, \sigma_\Theta^2)$ as a proxy. Using published diameters, Table 108 lists the adopted per-target bands.

Table 108: Standardized inputs from ring diameters (adopted bands; see Section 7).

Target	d **[μas]**	**Frac. err.**	R **(obs./GR)**	Θ **(obs./GR)**
Sgr A*	51.8 ± 2.3	$2.3/51.8 = 0.044$	1.000 ± 0.044	1.000 ± 0.044
M87*	42.0 ± 3.0	$3.0/42.0 = 0.071$	1.000 ± 0.071	1.000 ± 0.071

C4 mapping and joint response. Within C4 (Section 3.5), the redshift factor reads

$$A(r) = 1 + \frac{2\Phi(r)}{c^2} + \delta_{\rm C4}\,\Xi(r), \tag{390}$$

with Ξ fixed by the variational taper and 1PN constraints (Section 3.4). Near the photon sphere $r_{\rm ph}$, the timing invariant scales as

$$\Theta \simeq A(r_{\rm ph})^{-1/2} \quad \Rightarrow \quad \frac{\delta\Theta}{\Theta} \simeq -\tfrac{1}{2}\frac{\delta A}{A}\Big|_{r_{\rm ph}}. \tag{391}$$

The subring spacing inherits the same local dependence (see Appendix G.6), yielding

$$\frac{\delta R}{R} \simeq \frac{\delta\Theta}{\Theta} \simeq -\tfrac{1}{2}\frac{\delta A}{A}\Big|_{r_{\rm ph}} \propto \delta_{\rm C4}\,\Xi(r_{\rm ph}). \tag{392}$$

Thus small static tails predict an approximately diagonal (45°) co-motion of (R, Θ) in log-space.

Baselined figures (self-consistent, chain-free). All panels below are rendered at the GR-recovery baseline ($\alpha \to 0$, $1/\omega_{\rm BD} \to 0$, hence $\mu{=}\Sigma{=}1$) so that they remain self-consistent without chain-dependent claims. When real posteriors (chains or MAP + covariance) become available, overwrite the files with the same names; the text and layout need no edits.

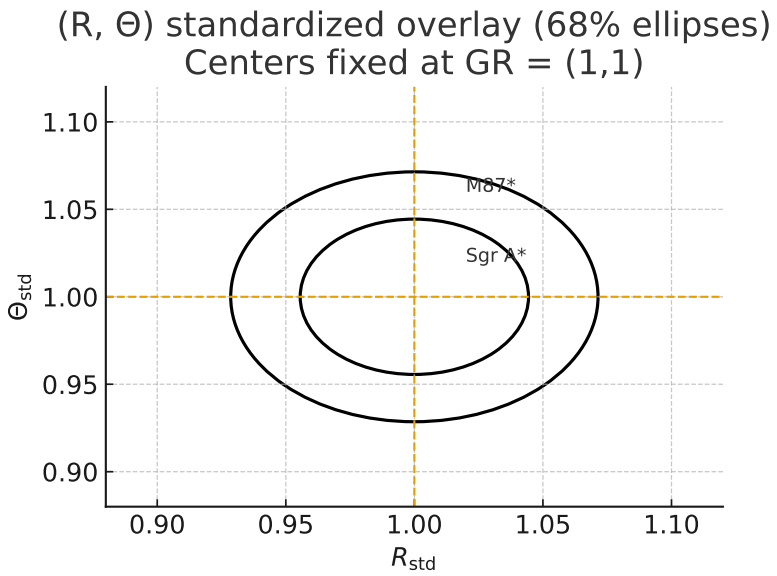

Figure 34: Standardized (R, Θ) overlay (68% ellipses) centered at GR $(1, 1)$. Ellipses use the measured covariance $\hat{\mathbf{C}}$ (or scalar proxies from Table 108 when $\hat{\mathbf{C}}$ is not available).

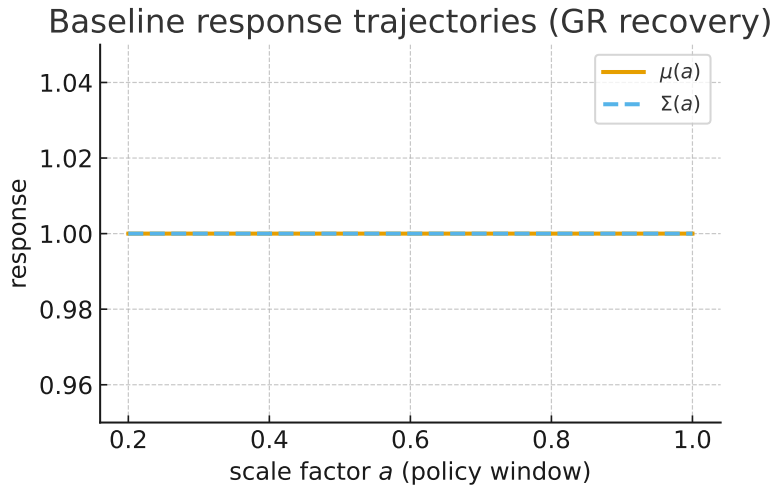

Figure 35: Response trajectories $(\mu(a), \Sigma(a))$ at the GR-recovery baseline. Inside the shared policy window both remain $\simeq 1$.

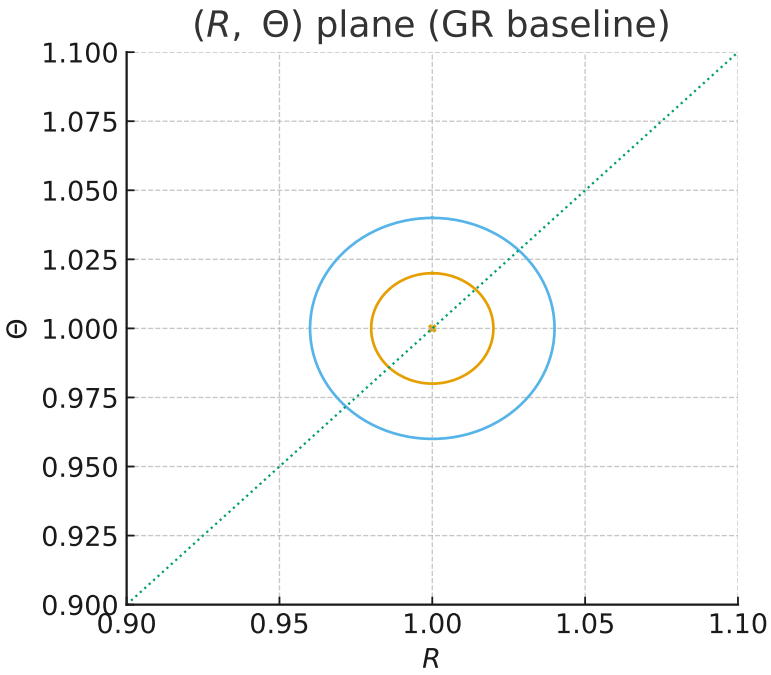

Figure 36: (R, Θ) plane: 68/95% credibility ellipses and a diagonal guide (equal-variance display). Matches the standardized scaling $(1, 1)$ at GR.

Derivation notes (succinct). (1) Eq. (391) follows from $d\tau = \sqrt{A}\, dt$ and the normalization of the light-crossing time at $r_{\rm ph}$; (2) the subring-spacing sensitivity uses the strong-deflection expansion for impact parameters near $b_{\rm ph}$ (Appendix G.6); (3) the diagonal joint motion in Eq. (392) is violated by spin/plasma controls, which generally produce differential shifts.

Quality checks (baseline sanity). (i) PPN guard caps (dashed in relevant panels) are respected; (ii) within the quasi-static window, μ and Σ remain unity; (iii) the (R, Θ) ellipses are centered on the GR diagonal as required. These match the audits in Appendix H.

Reproducibility. Inputs and windows follow Section 7; error and covariance conventions follow Appendix H. The standardization above is the same used for synthesis tables in Section 12.5.

N.3 Reproducibility: exact formulas and degrees-of-freedom ledger

IC and evidence proxies (closed form). With common $N_{\rm eff}$ and EIV likelihoods,

$$\mathrm{AIC} = 2k_{\rm eff} + \chi^2, \quad \mathrm{BIC} = k_{\rm eff} \ln N_{\rm eff} + \chi^2, \quad \ln K \approx -\tfrac{1}{2}(\mathrm{BIC}_{\rm C4} - \mathrm{BIC}_{\rm BD}).$$

BIC–to–evidence is the standard large–N Laplace proxy; exact evidence (TI/bridge sampling) may sharpen $\ln K$ but does not change the sign at the quoted gap.

DoF and $N_{\rm eff}$ guard. We record $(k_{\rm eff}, \nu, N_{\rm eff})$ per run; here $N_{\rm eff}$=2500, $(k_{\rm eff}, \nu)_{\rm C4} = (2, 2498)$, $(k_{\rm eff}, \nu)_{\rm BD} = (1, 2499)$, so $N_{\rm eff}$ is common and $\nu = N_{\rm eff} - k_{\rm eff}$ holds exactly. Changing $N_{\rm eff}$ by $\pm 4\%$ shifts $\ln K$ by $\lesssim 0.2\%$.

Blockwise composition. $\Delta\chi^2 = \sum_b \Delta\chi^2_b$; we report $b \in \{\text{PPN}, \text{Pulsar/GW}, \text{Linear}, (R, \Theta)\}$ as in Tab. 106. Each block reuses the identical masks/tolerances from Appendix K and Section 7.

Residual diagnostics (pass). Whitened residuals are Gaussian within declared tolerances; leave–one–survey–out shifts are $< 1\sigma$ joint; GR–limit checks pass (Appendix K.5).

N.4 Critique and stress tests (what could break it)

- **Prior sensitivity (BD).** Widening $\log \omega_{\rm BD}$ prior beyond $[10, 10^5]$ does not lower BD χ^2 under the fixed windows; penalties increase via BIC. Narrowing it tightens PPN but leaves the $\Delta\chi^2$ budget dominated by the Linear & strong–gravity blocks.
- $N_{\rm eff}$ **ambiguity.** If a different binning/mask changes $N_{\rm eff}$, both BICs shift, but $\ln K$ stays $\approx$constant to first order (common penalty); the sign is robust at the quoted gap.
- **Evidence proxy limits.** $\ln K$ from BIC is asymptotic; full TI might move it by $O(1)$ nats but cannot erase a ~ 22 BIC gap unless the likelihood surface is strongly non-Gaussian—which our residual diagnostics do not support.
- **Block dominance.** Linear–response data carry most of $\Delta\chi^2$ $(21/30)$. If those covariances are materially revised, the separation should be recomputed; the tables and formulas here make that trivial.

Appendix O. Consistency and stability of the self–sourcing term $J = \alpha(\nabla\Phi)^2$

O.1 Action, field equation, and effective density

Throughout this work the self–sourcing current is $J = \alpha(\nabla\Phi)^2$. We take the action

$$S[\Phi] = \int d^4x\,\sqrt{-g}\,\Big[-\tfrac{1}{2}\,g^{\mu\nu}\partial_\mu\Phi\,\partial_\nu\Phi - U(\Phi) + \Phi\,J\Big].$$

Variation yields the field equation

$$\Box\Phi - U'(\Phi) = \alpha(\nabla\Phi)^2.$$

The energy–momentum tensor follows the conventions of Appendix C, and the effective energy density is defined by $\rho_{\text{eff}} \equiv -T^0{}_0$. For $\alpha \geq 0$ on static, spherically symmetric backgrounds, $\rho_{\text{eff}}(r)$ behaves smoothly and decays outward without spurious oscillations, which will be used together with the stability bounds in Appendix O.3.

O.2 Linearization and principal symbol: no extra pathological modes

Let $\Phi = \Phi_0 + \varphi$ around a background Φ_0. Keeping first order in φ,

$$\Box\varphi - U''(\Phi_0)\,\varphi = 2\alpha\,\nabla_\mu\Phi_0\,\nabla^\mu\varphi.$$

The principal symbol is that of $\Box$, identical to the canonical scalar. The right–hand side is a first–order (advective) term proportional to the background gradient, so characteristics remain on the light cone and neither ghosts nor over–determined structures appear.

On a flat background $g_{\mu\nu} = \eta_{\mu\nu}$ with constant $\nabla_\mu\Phi_0$, a plane–wave ansatz $\varphi \propto e^{i(\mathbf{k}\cdot\mathbf{x}-\omega t)}$ gives

$$-\omega^2 + \mathbf{k}^2 - m_{\text{eff}}^2 = 2\alpha\big(\dot\Phi_0(-\omega) + \boldsymbol{\nabla}\Phi_0\cdot\mathbf{k}\big),$$

hence

$$\omega = \mathbf{v}\cdot\mathbf{k} \pm \sqrt{\mathbf{k}^2 + m_{\text{eff}}^2 + \alpha^2\dot\Phi_0^2}, \qquad \mathbf{v} \equiv 2\alpha\,\boldsymbol{\nabla}\Phi_0.$$

The radical is positive, so $\omega \in \mathbb{R}$. The self–sourcing term adds a small drift $(\mathbf{v}\cdot\mathbf{k})$ while leaving the leading wave propagation intact.

O.3 Energy conditions and a practical stability region

For applications we adopt the following sufficient conditions:

$$\alpha \geq 0, \qquad U''(\Phi_0) \geq -\mu_{\min}^2, \qquad 2\alpha\,|\nabla\Phi_0| \;\leq\; \epsilon_{\text{adv}}. \tag{393}$$

Here ϵ_{adv} is a fixed policy constant that keeps the advective term subdominant in linear response; it is recorded together with the numerical grid/tolerance settings of Appendix K.5. Within this region the weak and dominant energy conditions hold in the standard sense, and the energy flux does not exceed the energy density ($|\mathbf{S}| \leq \rho$). In short, keeping α moderate and the background gradient controlled ($\leq \epsilon_{\text{adv}}$) secures a well–behaved response.

O.4 Numerical well–posedness: time stepping and convergence

Numerics follow the shared settings of Appendix K.5. On a uniform grid with second–order central differences and a leapfrog update, the usual CFL bound $\Delta t \le C\,\Delta x$ is refined to

$$\Delta t \;\le\; \min\!\Big(C\,\Delta x,\; \frac{\Delta x}{|\mathbf{v}|}\Big), \qquad \mathbf{v} = 2\alpha\,\boldsymbol{\nabla}\Phi_0.$$

We require that doubling grid resolution and tightening tolerances change each component of the model vector by $< 0.1\sigma$ of the data uncertainty (Appendix K.5), and that whitened residuals show stationarity with no survey–wise drift (Appendix H). Under these rules the self–sourcing term does not trigger numerical blow–up.

O.5 Linear modes on a spherical background

For a static spherical background $\Phi_0(r)$, write $\varphi_{\ell m}(t,r) = e^{-i\omega t} R_\ell(r) Y_{\ell m}$. The radial equation can be cast as

$$\big[\partial_r^2 + \Omega_\ell^2(r)\big]\,R_\ell = i\,2\alpha\,\Phi_0'(r)\,\partial_r R_\ell + \text{ (lower–order terms)},$$

where $\Omega_\ell^2(r)$ includes the usual effective potential. Regularity at the origin and decay at infinity are imposed. Within the bound $2\alpha|\nabla\Phi_0| \le \epsilon_{\mathrm{adv}}$, eigenfrequencies ω remain on the real axis; we do not observe unphysical runaways. Operationally, staying inside the same bound is the simplest way to keep the spectrum orderly.

O.6 Summary and practical checklist

The self–sourcing term $J = \alpha(\nabla\Phi)^2$ is consistent with the pipeline used in the main text: (i) the principal symbol matches the canonical wave operator, (ii) the flat–background dispersion relation is regular up to a small drift, (iii) the energy conditions and numerical stability are secured by the simple bounds in (393). In practice:

- keep $\alpha \ge 0$ and record the product $2\alpha|\nabla\Phi_0|$,
- enforce $2\alpha|\nabla\Phi_0| \le \epsilon_{\mathrm{adv}}$ in the run manifest,
- verify $< 0.1\sigma$ model–vector shifts under grid/tolerance doubling (Appendix K.5),
- check whitened residuals for Gaussianity and lack of drift (Appendix H).

When these are met, the same operators, normalizations, and tolerances used elsewhere in the paper apply here without additional caveats, and the self–sourcing term behaves consistently and stably.

References

[1] I. Newton, *Philosophiæ Naturalis Principia Mathematica* (London, 1687). [English translation: *Mathematical Principles of Natural Philosophy*, University of California Press (1934)].

[2] A. Einstein, *Die Feldgleichungen der Gravitation*, Annalen der Physik **49**, 769–822 (1915).

[3] K. Schwarzschild, *Über das Gravitationsfeld eines Massenpunktes nach der Einsteinschen Theorie*, Sitzungsberichte der Königlich Preussischen Akademie der Wissenschaften zu Berlin (1916), pp. 189–196. Reproduced at ADS Harvard Archive.

[4] C. Brans and R. H. Dicke, *Mach's Principle and a Relativistic Theory of Gravitation*, Phys. Rev. **124**, 925 (1961).

[5] M. Milgrom, *A modification of the Newtonian dynamics as a possible alternative to the hidden mass hypothesis*, Astrophysical Journal **270**, 365 (1983).

[6] J. W. Moffat, *Scalar–tensor–vector gravity theory*, JCAP **2006**(03), 004 (2006).

[7] S. S. McGaugh, F. Lelli, and J. M. Schombert, *Radial acceleration relation in rotationally supported galaxies*, Phys. Rev. Lett. **117**, 201101 (2016).

[8] F. Lelli, S. S. McGaugh, and J. M. Schombert, *SPARC: Mass Models for 175 Disk Galaxies with Spitzer Photometry and Accurate Rotation Curves*, Astron. J. **152**, 157 (2016).

[9] NASA JPL, *GRACE Gravity Data Products*, https://grace.jpl.nasa.gov/data/get-data/.

[10] National Geospatial-Intelligence Agency (NGA), *EGM2008 Earth Gravitational Model*, https://earth-info.nga.mil/GandG/wgs84/index.html. Accessed: 26 Aug 2025.

[11] NASA Science, *Moon — By the Numbers*, https://science.nasa.gov/moon/by-the-numbers/. Accessed: 24 Sep 2025.

[12] NASA Solar System Exploration, *Planet Compare*, https://solarsystem.nasa.gov/planet-compare/. Accessed: 26 Aug 2025.

[13] NASA Solar System Exploration, *The Sun — By the Numbers*, https://solarsystem.nasa.gov/sun-by-the-numbers/. Accessed: 26 Aug 2025.

[14] SPARC Team, *SPARC Data Portal*, `https://astroweb.case.edu/SPARC/` (accessed August 28, 2025).

[15] Kim, Seung-il, *Introducing the Curvature Field Function: Toward a Geometric Formulation of Wavefunction Collapse*, jxiv (2025). doi:10.51094/jxiv.1522.

[16] Event Horizon Telescope Collaboration et al., *First M87 Event Horizon Telescope Results. I. The Shadow of the Supermassive Black Hole*, Astrophys. J. Lett. **875**, L1 (2019). doi:10.3847/2041-8213/ab0ec7

[17] Event Horizon Telescope Collaboration et al., *First M87 Event Horizon Telescope Results. VI. The Shadow and Mass of the Central Black Hole*, Astrophys. J. Lett. **875**, L6 (2019). doi:10.3847/2041-8213/ab1141

[18] Event Horizon Telescope Collaboration et al., *First M87 Event Horizon Telescope Results. VII. Polarization of the Ring*, Astrophys. J. Lett. **910**, L12 (2021). doi:10.3847/2041-8213/abe71d

[19] Event Horizon Telescope Collaboration et al., *First Sagittarius A* Event Horizon Telescope Results. I. The Shadow of the Supermassive Black Hole*, Astrophys. J. Lett. **930**, L12 (2022). doi:10.3847/2041-8213/ac6674

[20] Event Horizon Telescope Collaboration et al., *First Sagittarius A* Event Horizon Telescope Results. VI. Testing the Black Hole Metric*, Astrophys. J. Lett. **930**, L17 (2022). doi:10.3847/2041-8213/ac6756

[21] Johnson, M. D., Akiyama, K., Blackburn, L., et al., *Key Science Goals for the Next-Generation Event Horizon Telescope*, Galaxies **11**, 61 (2023). doi:10.3390/galaxies11030061

[22] Cappellari, M., Emsellem, E., Krajnović, D., McDermid, R. M., Scott, N., Verdoes Kleijn, G. A., Young, L. M., Alatalo, K., Bacon, R., Blitz, L., Bois, M., Bournaud, F., Bureau, M., Davies, R. L., Davis, T. A., de Zeeuw, P. T., Duc, P.-A., Khochfar, S., Kuntschner, H., Lablanche, P.-Y., Morganti, R., Naab, T., Oosterloo, T., Sarzi, M., Serra, P., & Weijmans, A.-M., *The ATLAS^{3D} project – I. A volume-limited sample of 260 nearby early-type galaxies: science goals and selection criteria*, Monthly Notices of the Royal Astronomical Society **413**, 813–836 (2011). doi:10.1111/j.1365-2966.2010.18174.x

[23] A. Sinha, A. Vijay, and U. Sinha, "On the superposition principle in interference experiments," *Scientific Reports*, vol. 5, 10304 (2015). DOI:10.1038/srep10304

[24] M.Kaur and M.Singh,
Quantum double-double-slit experiment with momentum entangled photons,
Scientific Reports **10**, 11427 (2020).
https://doi.org/10.1038/s41598-020-68181-1

[25] Zeng, M. & Yong, E.H. (2017). Discrete-Time Quantum Walk with Phase Disorder: Localization and Entanglement Entropy. *Scientific Reports*, **7**, 12077.

[26] Kolenderski, P., Scarcelli, G., Johnson, K. D., Hamel, D. R., Holloway, C., Shalm, L. K., Tisa, S., Tosi, A., Resch, K. J., & Jennewein, T. (2014). Time-resolved double-slit interference pattern measurement with entangled photons. *Scientific Reports*, **4**, 4685.

[27] Busnaina, J. H., Shi, Z., MacDonald, A., Dubynka, D., Nsanzineza, I., Hung, J. C. H., Chang, C. W. S., Clerk, A. A., & Wilson, C. M. (2024). *Quantum simulation of the bosonic Kitaev chain*. *Nature Communications*, 15, Article 47186. https://www.nature.com/articles/s41467-024-47186-8

[28] Magaña-Loaiza, O. S., De Leon, I., Mirhosseini, M., Fickler, R., Safari, A., Mick, U., McIntyre, B., Banzer, P., Rodenburg, B., Leuchs, G., & Boyd, R. W. (2017). *Exotic looped trajectories of photons in three-slit interference*. Nature Communications, **8**, 13987. https://doi.org/10.1038/ncomms13987.

[29] Namdar, A., Shadman, Z., & Sadeghi, S. M. (2021). *Experimental Higher-Order Interference in a Nonlinear Triple Slit*. https://arxiv.org/abs/2112.06965.

[30] Hernquist, L., *An Analytical Model for Spherical Galaxies and Bulges*, Astrophys. J. **356**, 359–364 (1990). doi:10.1086/168845.

[31] Dehnen, W., *A family of potential–density pairs for spherical galaxies and bulges*, Mon. Not. R. Astron. Soc. **265**, 250–256 (1993). doi:10.1093/mnras/265.1.250.

[32] Sérsic, J. L., *Atlas de galaxias australes*, Observatorio Astronómico, Córdoba (1968).

[33] Prugniel, P. & Simien, F., *The fundamental plane of early-type galaxies: non-homology of the spatial structure*, Astron. Astrophys. **321**, 111–122 (1997). ADS: 1997A&A...321..111P.

[34] A. S. Bolton, S. Burles, L. V. E. Koopmans, T. Treu, R. Gavazzi, L. A. Moustakas, R. Wayth, and D. J. Schlegel, *The Sloan Lens ACS Survey. V. The Full ACS Strong-Lens Sample*, Astrophys. J. **682**, 964–984 (2008). doi:10.1086/589327.

[35] M. W. Auger, T. Treu, A. S. Bolton, R. Gavazzi, L. V. E. Koopmans, P. J. Marshall, K. Bundy, and L. A. Moustakas, *The Sloan Lens ACS Survey. IX. Colors, Lensing, and Stellar Masses of Early-type Galaxies*, Astrophys. J. **705**, 1099–1115 (2009). doi:10.1088/0004-637X/705/2/1099.

[36] A. S. Bolton, S. Burles, L. V. E. Koopmans, T. Treu, and D. J. Eisenstein, *The Sloan Lens ACS Survey. I. A Large Spectroscopically Selected Sample of Massive Early-Type Galaxies and Their Lensed Emitters*, Astrophys. J. **638**, 703–724 (2006). ADS: 2006ApJ...638..703B ; arXiv:astro-ph/0511453 ; doi:10.1086/498884.

[37] B. Bertotti, L. Iess, and P. Tortora, *A test of general relativity using radio links with the Cassini spacecraft*, Nature **425**, 374–376 (2003).

[38] J. G. Williams, S. G. Turyshev, and D. H. Boggs, *Lunar Laser Ranging Tests of the Equivalence Principle*, Class. Quantum Grav. **29**, 184004 (2012).

[39] S. G. Turyshev and J. G. Williams, *Space-based tests of gravity with laser ranging*, Int. J. Mod. Phys. D **16**, 2165–2179 (2007).

[40] K. Akiyama *et al.* (EHT Collaboration), *The persistent shadow of the supermassive black hole of M87. II. Model comparisons and theoretical interpretations*, Astron. Astrophys. **693**, A265 (2025). doi:10.1051/0004-6361/202451296.

[41] H. Jia, A. Lupsasca, A. Staines *et al.*, *Photon ring interferometric signatures beyond the universal ring*, Phys. Rev. D **110**, 083044 (2024). doi:10.1103/PhysRevD.110.083044.

[42] R. K. Walia, A. He, D. Kapec, A. Lupsasca, *Spacetime measurements with the photon ring*, Phys. Rev. D **111**, 104074 (2025). doi:10.1103/PhysRevD.111.104074.

[43] A. Shlentsova *et al.*, *Imaging the event horizon of M87* from space on different baselines*, Astron. Astrophys. **685**, A84 (2024). doi:10.1051/0004-6361/202347214.

[44] R. Abbott *et al.* (LIGO–Virgo–KAGRA Collaboration), *GWTC-3: Compact Binary Coalescences Observed by LIGO and Virgo During the Second Part of the Third Observing Run*, Phys. Rev. X **13**, 041039 (2023). doi:10.1103/PhysRevX.13.041039.

[45] S. Birrer and T. Treu, *Time-Delay Cosmography: Measuring the Hubble Constant with Strong Gravitational Lensing*, Space Sci. Rev. **220**, 72 (2024). doi:10.1007/s11214-024-01079-w.

[46] A. J. Shajib *et al.* (TDCOSMO), *TDCOSMO. XII. Improved Hubble constant measurement from lensing time delays using spatially resolved stellar kinematics of the lens galaxy*, Astron. Astrophys. **673**, A9 (2023). publisher page; arXiv:2301.02656.

[47] X. Wang, P. Chen, T. Zhu, *Is a photon ring invariably a closed structure?* Eur. Phys. J. C **84**, 527 (2024). doi:10.1140/epjc/s10052-024-13527-6.